NASA TECHNICAL TRANSLATION

NASA TT F-807

NASA TT F-807

(NASA-TT-F-807) COSMIC RAYS (Kanner (Leo) Associates) 404 p HC $10.50 CSCL 04A

N75-16452
THRU
N75-16499
Unclas
H1/93 08526

COSMIC RAYS

Edited by S. N. Vernov and L. I. Dorman

"Nauka" Press
Moscow, 1972

NATIONAL AERONAUTICS AND SPACE ADMINISTRATION • WASHINGTON, D. C. • JANUARY 1975

1. Report No. NASA TT F-807	2. Government Accession No.	3. Recipient's Catalog No.
4. Title and Subtitle COSMIC RAYS		5. Report Date January 1975
		6. Performing Organization Code
7. Author(s) Editors in Chief, Academician S. N. Vernov, Dr. of Physical-mathematical Sciences, L. I. Dorman		8. Performing Organization Report No.
		10. Work Unit No.
9. Performing Organization Name and Address Leo Kanner Associates Redwood City, California 94063		11. Contract or Grant No. NASW-2481
		13. Type of Report and Period Covered Translation
12. Sponsoring Agency Name and Address National Aeronautics and Space Admin. Washington, D. C. 20546		14. Sponsoring Agency Code

15. Supplementary Notes

Translation of "Kosmicheskiye Luchi, Sbornik Statey, No. 13," Nauka Press, Moscow, 1972, 260 pages

16. Abstract

Abstracts are included with individual papers.

17. Key Words (Selected by Author(s))	18. Distribution Statement
	Unclassified, unlimited STAR Category 29

19. Security Classif. (of this report)	20. Security Classif. (of this page)	21. No. of Pages	22. Price*
Unclassified	Unclassified	403	$10.50

* For sale by the National Technical Information Service, Springfield, Virginia 22151

TABLE OF CONTENTS

I. THEORY

THEORY OF COSMIC RAY VARIATIONS, L. I. Dorman 1

II. PRIMARY COSMIC RAYS AND PROBLEMS OF ORIGIN

ENERGY SPECTRUM OF GALACTIC ELECTRONS IN THE ENERGY RANGE $2 \cdot 10^{10} - 2 \cdot 10^{11}$ eV, V. I. Zatsepin, V. I. Rubstov, and N. S. Svirzhevskiy 102

THE RELATION BETWEEN THE CHEMICAL COMPOSITION OF SOLAR COSMIC RAYS AND THE DURATION SPECTRUM OF RADIOSPLASHES, N. P. Tsimakhovich 106

III. MODULATION EFFECTS OF COSMIC RAYS

SOLAR ACTIVITY AND COSMIC RAYS IN THE PERIOD 1963-1965, A. G. Zusmanovich, Ye. V. Kolomeyets, R. A. Chumbalova, Yu. A. Shakhova 112

THE COSMIC RAY BURST ON 28 January 1967, N. P. Chirkov, G. F. Krymskiy, I. S. Samsonov, V. I. Ipat'ev 120

SOLAR ACTIVITY AND ITS RELATION TO CERTAIN PARAMETERS OF PHENOMENA IN THE GEOPHYSICAL COMPLEX, T. S. Razmadze, A. M. Chkhetiya 125

ATMOSPHERIC EFFECTS AND SIDEREAL-DIURNAL VARIATIONS IN EXTENDED AIR SHOWERS, N. N. Efimov, D. D. Krasil'nikov, S. N. Nikol'skiy, F. K. Shamsutdinova 133

COMPARISON OF THE RESULTS OF SIMULTANEOUS COSMIC RAY MEASUREMENTS IN THE STRATOSPHERE AT THE OLENIA AND APATITY STATIONS, L. L. Lazutin 138

ALTITUDINAL, DIURNAL AND LATITUDINAL DEPENDENCES FOR IONIC CONCENTRATIONS FORMED BY CORPUSCULAR FLUXES IN THE STRATOSPHERE AND MESOSPHERE, Yu. A. Bragin 142

THE EFFECT OF COSMIC RAYS ON THUNDERSTORM ELECTRICITY, Yu. A. Bragin 145

PRECEDING PAGE BLANK NOT FILMED

POSSIBILITY OF CONTROLLING THE EARTH'S NEGATIVE CHARGE AND THE UNITARY VARIATION OF ITS ELECTRIC FIELD BY COSMIC RAYS, Yu. A. Bragin, S. S. Vorontsov, A. A. Kocheyev 148

EFFECT OF THRESHOLD RIGIDITY VARIATIONS ON THE ELECTRON PRODUCTION RATE IN THE ATMOSPHERE, L. I. Dorman, T. M. Krupitskaya, M. I. Tyasto 154

SECULAR VARIATIONS OF L, B-COORDINATES, I. V. Getselev, E. V. Gorchakov, V. A. El'tekov 159

POSSIBLE ISOTOPIC SHIFTS WITH CHANGES IN THE GEOMAGNETIC FIELD, Yu. P. Bulashevich, V. M. Yershov V. F. Zakharchenko 164

CALCULATIONS OF THE COSMIC RAY MODULATION IN INTERPLANETARY SPACE TAKING INTO ACCOUNT THE POSSIBLE DEPENDENCE OF THE TRANSPORT TRAVEL FOR THE SCATTERING OF THE PARTICLES AND OF THE VELOCITY OF THE SOLAR WINDS ON THE ANGLE THEY MAKE WITH THE HELIOEQUATOR PLANE (The Case of Isotropic Diffusion), L. I. Dorman, Z. Kobilinski 170

IV. MEASUREMENTS FROM SATELLITES AND ROCKETS

A STUDY OF COSMIC RAYS ON THE ARTIFICIAL MOON SATELLITES "LUNA-11" AND "LUNA-12", N. L. Grigorov, V. G. Kurt, V. N. Lutsenko, V. L. Maduyev, N. F. Pisarenko, I. A. Savenko 206

THE STUDY OF COSMIC RAYS FROM THE "PROTON" ARTIFICIAL EARTH SATELLITE, N. L. Grigorov, I. A. Savenko, R. N. Basilova, N. N. Volodichev, S. I. Voropayev, L. F. Kalinkin G. P. Kakhidze, V. A. Labutin, A. S. Melioranskiy, E. A. Pryakhin, I. D. Rapoport 227

MEASUREMENT OF PROTON SPECTRA ON SATELLITES FROM THE "COSMOS"SERIES OF ARTIFICIAL SATELLITES, Ye. Ye. Kovalev, V. I. Ostroumov, S. S. Skvortsov, L. T. Smirennyy 247

MEASUREMENT OF SPECTRA AND NEUTRON FLUXES ON ARTIFICIAL EARTH SATELLITES FROM THE "COSMOS"SERIES, V. Ye. Dudkin, Ye. Ye. Kovalev, M. R. Novikova, Yu. V. Potapov S. S. Skvortsov, L. N. Smirennyy 252

THE POSSIBILITY OF USING SUPERCONDUCTIVE SYSTEMS IN THE ANALYSIS OF THE COMPOSITION OF COSMIC RAYS, O. P. Anashkin, B. M. Belitskiy, V. B. Brodskiy, L. V. Kurnosova, N. N. Mikhaylov, L. A. Razorenov, T. M. Sidyakina, M. I. Fradkin 256

V. NUCLEAR AND ELECTROMAGNETIC INTERACTIONS

A STUDY OF THE INTERACTION OF NEUTRAL AND CHARGED PARTICLES, V. M. Kim 261

MEASUREMENT OF THE RELATIVISTIC INCREASE IN PRIMARY IONIZATION FORMED BY A CHARGED PARTICLE IN A STREAMER CHAMBER, V. A. Dav denko, B. A. Dolgoshein, V. K. Davidenk Semenov, S. V. Somov 264

VI. PROBLEMS OF METHOD AND EQUIPMENT

INSTALLATION FOR THE SEARCH OF HEAVY NONRELATIVISTIC PARTICLES AT SEA LEVEL, A. M. Gal'per, V. A. Gomozov, A. F. Iyudin, Yu. D. Kotov, B. I. Luchkov, A. A. Prilepin, A. I. Rogovskiy 268

THE FEASIBILITY OF CONSTRUCTING A STABILIZING PLATFORM FOR A COSMIC RAY STATION, I. A. Akhmadeyev, V. M. Bednazhevskiy, E. P. Tolpygin 272

LARGE NEUTRON COUNTERS FOR SUPERMONITORS, Ya. L. Blokh, L. I. Dorman, V. K. Koiyava, V. Kh. Leonov, Kh. Nariziev, V. G. Chaykovskiy 279

EFFECT OF ELECTRON DIVERGENCE IN AIR GAPS ON THE MEASUREMENT OF THE ENERGY OF CASCADES IN EMULSION CHAMBERS, A. V. Apanasenko, L. T. Baradzey, Ye. A. Kanevskaya, Yu. A. Smorodin 282

DESCRIPTION OF AN IONIZATION CALORIMETER COMPLEMENTED WITH PROPORTIONAL COUNTERS, Kh. P. Babayan, N. G. Boyadzhyan, V. V. Vasil'tsov, N. L. Grigorov, V. A. Sobinyakov, V. Ya. Shestoperov 287

A DISCHARGE-CONDENSATION METHOD FOR THE DETECTION OF TRACES OF CHARGED PARTICLES, Z. Sh. Mandzhavidze, V. N. Poynishvili 290

A SYSTEM FOR MULTICHANNEL RECORDING AND AUTOMATIC READING OF INFORMATION, E. A. Bogomolov, Ye. Ya. Evstal'ev, V. K. Karakad'ko, N. D. Lubyanaya, V. A. Romanov, M. G. Totubalina, M. A. Yamshchikov 293

INSTALLATION FOR THE STUDY OF THE ANGULAR DISTRIBUTION OF COSMIC MUONS WITH SUPER-HIGH ENERGIES AT LARGE ZENITH ANGLES, V. V. Borog, V. G. Kirillov-Ugryumov, A. A. Petrukhin, V. V. Shestakov 298

CERTAIN PROBLEMS IN THE DEVELOPMENT AND DESIGN OF SCINTILLATION AND CERENKOV COUNTERS, V. S. Chukin 302

STUDY OF SPARK CHAMBERS FILLED WITH VARIOUS GAS MIXTURES, G. S. Akopyan, N. Kh. Bostandzhyan, G. A. Marikyan, K. A. Matevosyan 308

A THREE-ELECTRODE STREAMER CHAMBER, N. N. Nurgozhin 314

INCREASING THE ISOTROPIC PROPERTIES OF A DISCHARGE SPARK CHAMBER WITH A LARGE GAP, N. N. Nurgozhin 321

GAS THRESHOLD CERENKOV COUNTERS, V. I. Logachev, V. G. Sinitsyna, V. S. Chukin 327

BACKGROUND ESTIMATION IN A (νe)-DIFFUSION DETECTOR, V. I. Glotov 333

COMPARATIVE ANALYSIS OF ERRORS IN DIFFERENT METHODS OF CALCULATING L, B-COORDINATES, I. V. Getselev, V. A. El'tekov, V. I. Volga, V. A. Kuznetsov 337

AN INSTRUMENT FOR THE STUDY OF THE COMPOSITION OF THE ELECTRON COMPONENT OF COSMIC RAYS, E. A. Bogomolov, V. K. Karakad'ko, N. D. Lubyanaya, V. A. Romanov, M. G. Totuvalina, M. A. Yamshchikov 341

SPARK CALORIMETER--AN INSTRUMENT FOR DETERMINING PARTICLE ENERGY OF COSMIC RADIATION, A. A. Alakoz, V. N. Bolotov, M. I. Devishev, L. P. Klimanova, A. P. Shmeleva 349

GENERALIZATION OF FORMULAS FOR IONIZATION ENERGY LOSSES AND COLLISION CROSS SECTION IN THRESHOLD DETECTORS, V. K. Yermilova, L. P. Kotenko, G. I. Merzon, V. A. Chechin 355

DISTORTION OF THE ALTITUDE DEPENDENCE AND ENERGY SPECTRUM OF THE NEUTRON COMPONENT NEAR THE EARTH'S SURFACE, G. V. Gorshkov, O. S. Tsvetkov 361

THE EFFECT OF THERMAL NEUTRON FIELD SLAGGING CAUSED BY CYLINDRICAL BF_3 COUNTERS IN DIFFUSION MEDIA, G. V. Gorshkov, O. S. Tsvetkov, R. M. Yakovlev 366

STUDY OF COSMIC RAY MOTION IN COSMIC SPACE NEAR THE EARTH, V. K. Budilov, V. I. Ivanov, L. V. Kozak, L. A. Mirkin, I. G. Tsukerman 372

DETERMINATION OF THE COUPLING COEFFICIENTS AT VARIOUS ZENITH ANGLES ON THE BASIS OF THE COSMIC RAY AZIMUTH EFFECT, S. A. Bel'skiy, B. A. Dmitriev, A. M. Romanov 380

MEASUREMENT OF SUPERSMALL QUANTITIES OF Ar^{37} and H^3,
G. E. Kocharov, V. O. Naydenov 385

PLASTIC SCINTILLATION COUNTERS WITH AN AREA OF 2 m^2,
T. A. Yegorov, N. N. Yefimov, D. D. Krasil'nikov,
I. Ye. Sleptsov 389

THEORY OF FLUCTUATIONS OF EXTENDED AIR SHOWERS,
L. G. Dedenko 394

N75 16453

I. THEORY
THEORY OF COSMIC RAY VARIATIONS

L. I. Dorman

Abstract

1. Integral multiplicites and coupling coefficients for meson nucleon and electron-photon components are calculated on the basis of contemporary concepts about a nuclear-meson cascade of cosmic rays in the terrestial atmosphere with due account of the energy spectrum of the generated particles, their angular distribution and fluctuations in the elementary event. Calculations were performed in reference to the primary nucleons, α-particles and heavier nuclei incident at different angles to the zenith. The results of the calculations in the low energy range are compared with integral multiplicities and total coupling coefficients determined by the geomagnetic effects of cosmic rays and the data on cosmic ray variations. Variation of the parameters characterizing the state of the terrestial atmosphere in the theoretical expression obtained makes it possible to determine the partial barometric coefficients and the densities of temperature coefficients for the above components.

2. Set forth in the paper is information about the relation between the solar wind and large-scale characteristics of the solar wind during an eleven-year cycle. The large-scale characteristics are determined by measurements of the spectrum of protons and α-particles in the non-relativistic energy range, by measurements of radial and transverse gradients of intensity, by cosmic anisotropy in the interplanetary space, as well as by the results of explorations of hysteresis events in eleven-year and twenty-seven-day variations of galactic cosmic ray particles of different energies. This study of hystereses is based on a dynamic model using the anisotropic diffusion equation.

The results thus obtained make it possible to determine the size of the spiral field, the distance from the Sun to the effective border of the solar wind with the interstellar magnetic field, transport travels for the dispersion of particles of different energies and characteristics of the regular and irregular components of the interplanetary magnetic field at various distances from the Sun up to 100-200 AU.

The pure energy spectrum of the cosmic rays beyond the solar system is discovered and it is shown that the low-energy cosmic rays play a significant role in limiting solar wind spreading. While studying the solar-terrestial relations affected not by way of the direct influence of the Sun on the Earth but through the processes occurring in interplanetary space, it should be taken into account that the solar wind characteristics at great distances are determined with a considerable

delay with respect to the solar activity processes which cause the above variations.

3. The true chemical composition and the Sun's generation spectrum are determined on the basis of the nuclear composition and energy spectrum of the solar cosmic rays with the account of distortions due to their propagation in interplanetary space. Possible mechanisms of generation of chromospheric flares are discussed and the role of nuclear interrelations is estimated. Also discussed are possibilities of extraflare generation of solar cosmic rays and cases of abrupt increases, predominately in heavy nuclei.

The initial anisotropic and isotropic spaces of solar cosmis ray spreading in interplanetary space thus obtained are compared with the results of direct observations in the region adjacent to the Earth's orbit and with the results of explorations of the eleven-year and twenty-seven-day variations of the cosmic rays in more distant regions.

1. Main Trends in the Development of a Theory of Cosmic Ray Variations in Conjunction with the IYQS (International Year of the Quiet Sun) Program

/5*

For a number of reasons the period of the quiet Sun was of especial interest to cosmic ray investigators. The point is that when the activity of the Sun is at a minimum, all modulation effects are sharply attenuated, and therefore it is possible to study more thoroughly other classes of cosmic ray variations, variations of atmospheric and geomagnetic origin and variations of galactic origin. In addition to this, the information on how the twenty-seven day and daily solar variations, the Forbush effects and various variations related to changes in the solar activity vary with the activity of the Sun is very important. The continuous observations carried out in the years 1954 through 1966 (including the International Geophysical Year and the International Year of the Quiet Sun) made it possible to obtain valuable information about eleven-year cosmic ray variations. An equally important fact is that in the International Year of the Quiet Sun it was possible to measure the energy spectrum and nuclear composition of primary cosmic rays which are closest to the real ones beyond the solar system (although, as we will show below, even in the period when solar activity is minimal there is considerable modulation and distortion of the spectrum and nuclear composition in low energy ranges).

The theoretical studies of cosmic ray variations in conjunction with the IYQS program were carried out in several directions.

---

*Numbers in the margin indicate pagination in the foreign text.

1. The development of a theory of meteorological effects, perfection of the method of coupling coefficients; classification of cosmic ray variations, taking into account the penumbra and interference effects of various origin.

2. Development of a theory of geomagnetic effects, calculation of cutoff rigidities and asymptotic directions of the incoming particles in models of the geomagnetic field which approach the real field, the account of the effect of extra-ionospheric and ionospheric flux systems, of the effect of compression of the magnetosphere, its nonsphericity, and, in particular, the effect of the tail of the magnetosphere on the cutoff rigidity, the asymptotic directions of the incoming particles and the reception cones of the receptors.

3. A study of the modulation effects of cosmic rays (11-year, 27-day, daily solar variations and the Forbush effect) on the basis of various models for the effect of the solar wind on cosmic rays using isotropic and anisotropic diffusion approximations, as well as kinetic theory; an account of the geometric effects and obtaining information about characteristics of the solar wind and its boundary with the interstellar space, and the energy spectrum and nuclear composition of primary cosmic rays beyond the solar system. /6

4. A study of the propagation of solar cosmic rays in interplanetary space and the mechanisms which generate them in the Sun's atmosphere.

5. A study of the sidereal-diurnal variation of cosmic rays and its distortion in interplanetary space, removal from observation data of false effects caused by the complex amplitude phase modulation of daily solar variations, and a comparison of the data about sidereal-diurnal variation and the energy spectrum with various models of the origin of cosmic rays.

Substantial progress was made in all the investigations mentioned above. Experiments were developed on a wide scale, precision instruments such as neutron and meson supermonitors were incorporated into the global network of ground stations, the energy spectrum and nuclear composition were measured with the aid of balloons, satellites and space rockets, all of which served as a powerful stimulus for the development of a theory of cosmic ray variations. The study of cosmic ray variations led to the conclusion that cosmic radiation carries valuable information about electromagnetic conditions in space, and that it is a very sensitive probe which can be used to study not only the microcosm, but also the vast regions of the universe.

Great difficulties are encountered on this path, which are connected with the very nature of cosmic radiation (a wide energy spectrum of the charged particles, whose trajectories are distorted considerably in the magnetic fields of the Earth, the interplanetary space and in the fields of the Galaxy) and with the character of the recording instruments (a great part of which are below the layer which fluctuates with time in the Earth's atmosphere, and which monitor, to a considerable extent, the entire particle flux on the basis of the energies and the directions of arrival).

The information received is differentiated by a rather complex procedure which includes the following successive stages:

1. The introduction of special meteorological corrections;

2. Taking into account the direct effect of changes in the Earth's magnetosphere on the geomagnetic cutoff rigidity and the trajectory of the particles;

3. Recalculations of the variations observed by various instruments in the stratosphere at mountain and sea level, at various latitudes and longitudes and at various depths below the Earth's surface into variations of the primary spectrum beyond the boundary of the main part of the Earth's atmosphere;

4. Finding (from the data about the trajectories of particles of various rigidity in the real magnetic field on the basis of the information about variations in the energy spectrum) the space distribution beyond the boundaries of the Earth's magnetosphere, the incoming particles of various energy, which are responsible for the given type of variation[1]

Thus, in spite of the integrating character of the recording apparatus when the separating properties of the Earth's atmosphere, screens and properties of the geomagnetic field are used and also the method of coupling coefficients, it is possible to obtain valuable information about the energy distribution of cosmic ray variations in space, i.e., the differential characteristics of the variations. In this regard, the presence of a wide energy spectrum of cosmic radiation, a negative factor, becomes a factor which enriches considerably the information obtained,

1. The individual stages of the procedure are not necessary when the observations are carried out beyond the boundaries of the Earth's atmosphere or beyond the boundaries of the magnetosphere. In a number of cases, the meteorological effects are insignificant also when recording takes place below the layer of the atmosphere.

since particles having various energy are sensitive to the conditions in various regions of space (for example, particles with energy up to several tens of billion electron volts are sensitive to conditions in interplanetary space, particles with an energy of several thousand billion electron volts and more, are sensitive to conditions in the galaxy and practically insensitive to conditions in interplanetary space, etc.). /7

To obtain the astrophysical information on the basis of the data about cosmic ray variations, it is necessary to study carefully all possible mechanisms that can cause a particular type of cosmic ray variation. Naturally, the reliability of the data about electromagnetic conditions in space which are obtained from the study of cosmic ray variations is determined not only by the reliability of the set of experimental data about the variations, but also by how close the variation mechanisms under consideration are to the real ones.

2. Classification of Cosmic Ray Variations and Their Character

2.1. Customary Classification

The fundamental formula in the general theory of cosmic ray variations used at the present time to identify the variations is the expression (Chap. 4, Article [1])

$$\frac{\delta I_k^i(h_0)}{I_k^i(h_0)} = \int_{R_k}^{\infty} \frac{\delta m^i(R, h_0)}{m^i(R, h_0)} W_k^i(R, h_0)\, dR - \delta R_k W_k^i(R_k, h_0) + \int_{R_k}^{\infty} \frac{\delta D(R)}{D(R)} W_k^i(R, h_0)\, dR, \tag{2.1}$$

which is obtained by varying the expression

$$I_k^i(h_0) = \int_{R_k}^{\infty} m^i(R, h_0)\, D(R)\, dR \tag{2.2}$$

over all possible changes in the parameters R_k, $m^i(R, h_0)$, $D(R)$ (which ultimately determine a priori all types of variations) and using the definition for the coupling coefficient between the primary cosmic ray component and the secondary component of the i-th type

$$W_k^i(R, h_0) = \frac{m^i(R, h_0) D(R)}{I_k^i(h_0)}. \qquad (2.3)$$

Here $I_k^i(h_0)$ is the intensity of the component of cosmic rays of the i-th type at the point k with the geomagnetic cutoff rigidity R at pressure h_0, $m^i(R, h_0)$ is the integral multiplicity (i.e., the number of recorded particles of the i-th type from one primary particle with rigidity R) and D(R) is the differential spectrum of the primary cosmic radiation over the rigidities.

The first term in expression (2.1) corresponds to cosmic ray variations of atmospheric origin (class I variations) which, in turn, is subdivided into the temperature and barometric effects, the second term corresponds to variations of geomagnetic origin (class II variations), and the third term to variations of extraterrestrial origin (class III variations, which, in turn, is divided into three subclasses, caused by: a. generation of cosmic rays on the Sun, b. modulation effects in interplanetary space and c. variations of galactic and extragalactic origin).

2.2. Critique of Customary Classification /8

In deriving (2.1) it was assumed that : 1. a definite cutoff rigidity of the particles R_k exists which can vary with the changes in the geomagnetic field; 2. the possible changes in the parameters R_k, m^i and D(R) are relatively small (so that on the basis of the assumption it was not necessary to take into account the possible interference of various effects and use the superposition principle).

This approximation should be regarded as a first step toward a comprehensive and sufficiently complete classification of cosmic ray variations by their character. In its own time, it was fully justified, since it simplified considerably the analysis of the nature of the variations and could be used to develop very effective methods for the study of cosmic ray variations which are used widely today, such as the method of coupling coefficients (which can be used to find the spectrum of primary variations beyond the boundary of the Earth's atmosphere from the observed secondary variations) and the integral method for the calculation of meteorological corrections (from the data from atmospheric temperature and pressure probes) [1, 2].

However, at the present time, when it is possible to understand to a considerable extent the nature of various types of cosmic ray variations, because of the many studies based on observation data from a worldwide network of cosmic ray stations, satellites and rockets in the IGY-IPQS, it is feasible to make the next step and discard the aforementioned simplifying assumptions. This must also be done because, due to the highly developed worldwide network of stations, the sharply improved recording accuracy, the development of a theory for the effect of the geomagnetic field and the Earth's atmosphere on cosmic rays, it is already possible to detect interference effects which cannot be interpreted within the framework of expression (2.1) (for example, changes in the barometric coefficient with changes in the spectrum of primary cosmic rays, etc.)

2.3 Classification of Cosmic Ray Variations taking into account the Penumbra in the Presence of Interference Effects

The presence of the penumbra is described by the function $f_k(R)$, which takes on the values 1 and 0, respectively, for the permissible and forbidden directions at the observation point k. In the presence of a penumbra, the geomagnetic cutoff rigidity is a quantity which is not completely defined by the coordinates of the observation point as assumed formerly [1]; it also depends on the properties of the cosmic radiation and its variations [3-7] (supplement 1). From this point of view, perhaps it would be more useful to abandon altogether the concept of the effective geomagnetic cutoff rigidity, and to use directly the function $f_k(R)$ to determine the effect of the geomagnetic field on cosmic rays. Then

$$I_k^i(h_0) = \int_0^\infty f_k(R)\, m^i[R, h_0, T_0(h')]\, D(R)\, dR, \qquad (2.4)$$

where $m^i(R, h_0, T_0(h'))$ is the integral multiplicity with which secondary particles are generated, taking into account the temperature distribution in the atmosphere above the observation point. Generally $f_k(R)$ can vary, due to changes in the geomagnetic field, $m^i[R, h_0, T_0(h')]$ due to changes in the pressure h_0 and the temperature distribution $T_0(h')$, $D(R)$ due to processes of extraterrestrial origin. Taking into consideration that these variations are not small, we obtain

$$\frac{\Delta I_k^i(h)}{I_k^i(h_0)} = \int_0^\infty \frac{\Delta m^i[R, h, T(h')]}{m^i[R, h_0, T_0(h')]} W_k^i[R, h_0, T_0(h')] \left[1 + \frac{\Delta f_k(R)}{f_k(R)} + \right.$$

$$\left. + \frac{\Delta D(R)}{D(R)} + \frac{\Delta f_k(R)}{f_k(R)} \frac{\Delta D(R)}{D(R)}\right] dR + \int_0^\infty \frac{\Delta f_k(R)}{f_k(R)} W_k^i[R, h_0, T_0(h')] \times \qquad (2.5)$$

$$\times \left[1 + \frac{\Delta D(R)}{D(R)}\right] dR + \int_0^\infty \frac{\Delta D(R)}{D(R)} W_k^i[R, h_0, T_0(h')]\, dR,$$

where

$$\Delta I_k^i(h) = I_k^i(h) - I_k^i(h_0);\ \Delta f_k(R) = \tilde{f}_k(R) - f_k(R);$$

$$\Delta m^i[R, h_0, T(h')] = m^i[R, h, T(h')] - m^i[R, h_0, T_0(h')];$$

$$\Delta D(R) = \tilde{D}(R) - D(R);\ W_k^i[R, h_0, T_0(h')] = \frac{f_k(R)\, m^i[R, h_0, T_0(h')]\, D(R)}{I_k^i(h_0)} \qquad (2.6)$$

In expression (2.1) the first term corresponds to variations of class I, but unlike, in the usual expression, the effects of the changes in the geomagnetic field and primary spectrum on the meteorological coefficients are taken into account; the second term corresponds to variations of class II caused by changes in the Earth's magnetosphere (taking into account the effect of changes in the primary spectrum on this effect). The third term describes variations of class III.

2.4. Approximate Account of the Interference Effects

Unfortunately, at the present time, it is not possible to use the exact expression (2.5) in the study of cosmic ray variations since, for the time being, $f_k(R)$ has not been calculated for the real geomagnetic field and its changes. However, to estimate approximately the role played by the penumbra during the interference effects of cosmic rays, supplement 1 gives the results of calculations of the changes of the effective geomagnetic cutoff rigidity.

If the study of cosmic ray variations is carried out with an accuracy which makes it possible to ignore the negligible effects of the penumbra, or takes these into account approximately, using the formulas in supplement 1, it is possible to find a general formula for the variations from expression (2.2), in which the dependence of m^i on the temperature distribution in the atmosphere need only be taken into account. Then we obtain analogously as in (2.5),

$$\frac{\Delta I_k^i(h)}{I_k^i(h_0)} = \int_{R_k}^{\infty} \frac{\Delta m^i(R, h, T)}{m^i(R, h_0, T_0)} W_k^i(R, h_0, T_0)\left\{1 + \Delta R_k \delta(R - \bar{R}_k) \times \right.$$
$$\left. \times \left[1 + \frac{\Delta D(R)}{D(R)}\right]\right\} dR - \Delta R_k W_k^i(\bar{R}_k, h_0, T_0)\left[1 + \frac{\Delta D(\bar{R}_k)}{D(\bar{R}_k)}\right] + \qquad (2.7)$$
$$+ \int_{R_k}^{\infty} \frac{\Delta D(R)}{D(R)} W_k^i(R, h_0, T_0)\, dR,$$

where $\bar{R}_k$ lies in the interval R_k, $R_k + \Delta R_k$ and $\delta(R - \bar{R}_k)$ is the δ-function. The coupling coefficient in (2.7) is defined by the expression

$$W_k^i(R, h_0, T_0) = \frac{m^i(R, h_0, T_0) D(R)}{I_k^i(h_0)}. \qquad (2.8)$$

In expression (2.7) and also in (2.5), the terms in the right members correspond to variations of class I-III. Formula (2.7) defines a new system of variations taking into account the mutual interference of various types of cosmic ray variations. /10

3. Development of the Coupling Coefficient Method

The method of coupling coefficients is important for the study of temporary variations in the intensity of cosmic rays [1]. It can be used to find from the set of experimental data from a worldwide network of stations the primary variations in the energy spectrum beyond the boundaries of the Earth's atmosphere, and then (taking also into account the trajectories of motion of charged particles in the geomagnetic field) also in interplanetary space beyond the boundaries of the Earth's magnetosphere.

The coupling coefficients for a number of secondary components were determined in [1] from the data about the latitudinal effect of cosmic rays. In the 15 BeV energy range, the coupling coefficients were found through extrapolation. The greatest indeterminacy occurs for the μ-meson component which has a very small latitudinal effect ($\lesssim$10%). At the same time, the values of the coupling coefficients for the μ-meson components are especially large when cosmic ray variations are studied in the high energy region (according to data from ionization chambers, cubic and crossed telescopes[2] on the earth's surface and on various

2. Literal translation.

observation levels below the earth's surface).

The voluminous experimental material cannot be used effectively without a sufficiently accurate knowledge of the coupling coefficients for the μ-meson component in the high energy range. This fact led to a different approach to the problem, an attempt to calculate the coupling coefficients not from the data about the latitudinal effect, but on the basis of a study of nuclear interactions of primary neutrons in the atmosphere. The first such attempt to calculate numerically the integral multiplicity for the generation of μ-mesons was made in article [8] (since it is precisely the integral multiplicity which determines the coupling coefficients for a particular type of differential energy spectrum of the primary component). A one-dimensional model was studied in the case of a vertical incident particle. The angular divergence of particles in the elementary event was taken into account in article [3].

In the analysis of many of types of variations, it is very important to know the coupling coefficients of cosmic rays incident to the boundary of the atmosphere at an oblique angle. This case is studied in article [9]. Our study is based on the assumptions about the character of the elementary event which were adopted in article [10]. Basically these assumptions reduce to the following: It is assumed that in each interaction event, the particle isolated on the basis of the energy loses the same fraction of energy, while only π-mesons are formed. We consider two generations of π-mesons: the first generation formed in all collisions of the primary neutron, and the second generation formed in the collisions of first-generation π-mesons. The subsequent generations of π-mesons, and also the π-mesons formed in the collisions of δ-nucleons can be ignored, since their contribution to the total number of π-mesons is small. The assumption that the transverse impulse $\mathbf{P}_\perp$ of all π-mesons that have been generated is constant in all events is essential. It leads to a definite form of the angular and energy distribution function of the particles, and simplifies the problem considerably. The computational results are given in supplement 2.

4. Development of a Theory of Cosmic Ray Variations of Atmospheric Origin /11

4.1. General Remarks

The interest in the meteorological effects of cosmic rays increased sharply in recent years due to the development of a network of supermonitors and supertelescopes. In our opinion, this is explained by two reasons.

1. Ground measurements are apparently the only possible way of obtaining sufficiently accurate information about variations in a high energy particle flux.

2. The sharp improvement in the accuracy of the data obtained increases correspondingly the requirements on the accuracy with which the meteorological corrections are calculated.

4.2. Experimental Verification of the Theory of the Temperature Effect

The investigators who verified the definition of the temperature effect of the μ-meson component of cosmic rays presented in article [1] reached the conclusion that the densities of the temperature coefficients presented in article [1] must be mutiplied by certain correction factors which are (according to P. M. Mathews [11]) 0.76 ± 0.03, (according to S. Lindgrean and F. Lindholm [12]) 0.65 ± 0.10, and (according to M. Wada [13]), 0.84 ± 0.12. However, a more accurate comparison carried out by T. Carmichael, et al., [14] using the multiple correlation method, taking into account changes in the intensity of the neutron component, has shown that this factor is actually 1.018 ± 0.017, i.e., it is close to 1 within the measurement error. This shows that the theoretical densities of the temperature coefficients for the μ-meson components determined in article [1] are close to the true densities.

A study of the temperature effect of the neutron component is of great interest. This effect was calculated theoretically in Chapter V in study [1]. The first results beyond the range of experimental error were obtained by N. S. Kaminer, et al., [15] by subtracting the seasonal waves of the neutron component at the Chicago and Harvard stations (whose cutoff rigidities were close, but which were located in opposite hemispheres). If we take into consideration the fact that the difference in the seasonal waves which was found is caused only by the temperature effect, it is 1.8 times the expected difference from theory [1]. An analogous result is obtained by correlating variations in the intensity of the neutron component from day to day with the expected variations due to the temperature effect [16].

An analogous study was carried out recently by M. Bercovitch and B. Robertson [17] using observation data obtained with the aid of a neutron supermonitor, who found by regressing the expected changes in the intensity on the observed changes the value 1.7 for the regression coefficient (according to [1] Chap. V, para. 21). However, after the humidity effect was taken into account, the value of the regression coefficient was

reduced to 1.3, which differs insignificantly from 1, if we take into consideration the fact that the errors in the regression coefficient in study [17] are rather large.

The humidity coefficient which was obtained (0.09% per g/cm^2 of water vapor) [17] was used to determine the contribution of the seasonal changes in the absolute temperature humidity to the intensity of the neutron component [18]. The data about the humidity were obtained from measurements at altitudes from the Earth's surface to ~ 5.5 km. The expected seasonal change in the intensity of the neutron component caused by changes of the humidity content in the atmosphere is approximately 0.3%. If a correction for the humidity effect is introduced into the results of the studies of H. S. Kaminer and his associates [15, 16], /12 the mean seasonal wave of temperature origin in the neutron component decreases over 5 years from 0.89 to 0.59%, and the ratio of the measured temperature effect to the calculated effect from ~ 2.1 to ~ 1.45. The new ratio which was found is close to that obtained in study [17], and it is 1.28 ± 0.10.

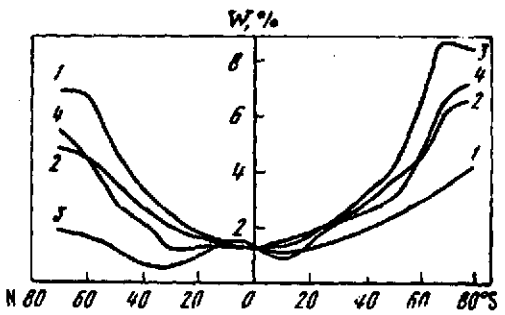

Fig. 1. Latitudinal variations in the seasonal values of the temperature corrections in 1962 on the Asiatic belt.
1. Winter period (on Northern hemisphere;
2. Spring period;
3. Summer period;
4. Fall period.

4.3. Planetary Distribution of the Intensity of Cosmic Rays and the Temperature Effect

When the planetary, in particular, longitudinal distribution of the intensity of cosmic rays is studied, it is necessary to take into account the temperature conditions in the atmosphere. It was shown already in study [1] that when the temperature effect is taken into account, the longitudinal intensity curve of μ-mesons changes considerably.

It is of interest to determine the temperature corrections from the data for the planetary distribution of the temperature in the atmosphere, and to evaluate on the basis of the result obtained, the data from a series of studies which measured the longitudinal course of the meson component. Such study was carried out in the

work of N. S. Kaminer, et al., [19]. The study used data from 55 stations which probed the temperature in the atmosphere, and which were situated in three continents: the American continent, the European continent and the Asiatic continent. The mean latitudinal distance between the stations was ~ 10^{o}. The monthly mean values of the temperature corrections were calculated in the period 1960-1962, using the data about the temperature on standard isobar contours, by the method of L. I. Dorman [1].

It turned out that the latitudinal changes in the temperature corrections vary considerably from season to season and are very asymmetric with respect to the equator in the summer and winter seasons (see, for example, Fig. 1 for the Asiatic strip). The mean seasonal latitudinal course of the temperature

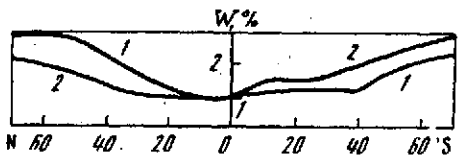

Fig. 2

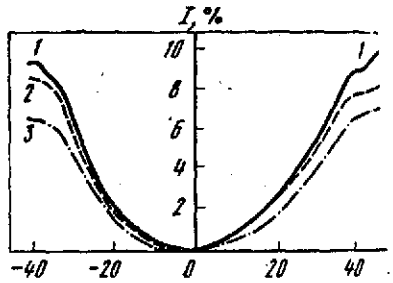

Fig. 3

Fig. 2. Temperature effect of the neutron component in 1962 (mean over the Asiatic, European and American strips)

1. Winter; 2. Summer over northern hemisphere

Fig. 3. Latitudinal effect of hard component of cosmic rays at sea level

1. Measurements carried out by A. Compton and R. N. Turner [21]; 2. Latitudinal effect corrected for temperature above Earth's surface [21]; 3. Latitudinal effect corrected in article [19] using the method of L. I. Dorman [1].

corrections varies little from year to year, the variations do not /12
exceed 0.5%, and they have approximately the same amplitude in all three longitudinal belts. The latitudinal course of the mean yearly temperature correction values varies from year to year in the 1% range.

The latitudinal variations in the temperature corrections for the neutron components were also calculated on the basis of the results in studies [15-18], in [19] for the summer and winter seasons. The latitudinal variations in the neutron component caused by the temperature effect are 1.5-2% (see Fig. 2).

The role played by the temperature effect during the measurements of latitudinal variations in the intensity of cosmic rays was estimated in [20]. This estimate was based on data of poor quality and on nonhomogeneous data. Therefore, an attempt was made in study [19] to estimate again the contribution of the temperature effect, using the data about the global temperature distribution in the free atmosphere, which were discussed above. The results of this estimate are given in Fig. 3.

4.4. Dynamic Effect of Atmospheric Winds in Cosmic Rays

The reason for the origin of the dynamic effect is that, due to the Bernoulli effect, the pressure measured on the surface of the Earth is always smaller than the weight of the air column which determines the barometric effect in cosmic rays. If v(h) is the horizontal velocity component for the displacement of air in a layer with pressure h, the difference Δh between the weight and pressure is

$$\Delta h = \frac{1}{2}\int_0^{h_0} \rho(h)\, v^2(h)\, dh, \tag{4.1}$$

where ρ(h) is the density of the air at the depth h. From the above, we can determine the expected effect of the wind in cosmic rays

$$\frac{\Delta N}{N} = -\beta \Delta h, \tag{4.2}$$

where β is the barometric coefficient.

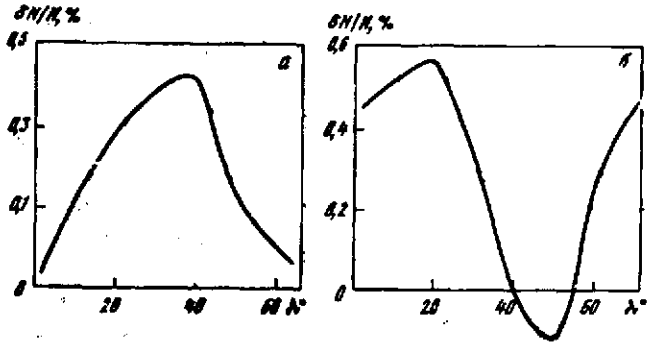

Fig. 4. Expected effect of wind on the latitudinal change in the intensity of the neutron component for, a. northern, and b. southern hemisphere

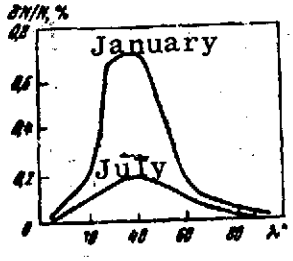

Fig. 5. Dynamic effect vs. latitude in winter and summer in the northern hemisphere

It can be seen that the dynamic effect is caused by the wind regime in the entire layer of the atmosphere. Therefore, strictly speaking, one must restrict oneself only to taking into account the dynamic effect in the layer of the atmosphere near the Earth's surface as G. A. Lockwood and A. R. Calawa [22] and also J. Dubinski, et al., [23] did, since at higher altitudes the velocity of the wind increases rapidly, so that the contribution of layers at high altitudes can be considerable. In this regard, study [24] estimated the magnitude of the dynamic effect in the neutron component of cosmic rays, taking into account the wind regime in the atmosphere at altitudes from the surface of the Earth to ~ 15 km (Fig. 4). Figure 4 shows that the effect has an extremum at mean latitudes whose magnitude is ~ 0.5%. In addition to this, in the northern hemisphere the dynamic effect changes with the latitude in the winter and summer (Fig. 5). It can be seen that the seasonal change in the intensity caused by the dynamic effect attains ~ 0.5%. /14

4.5. Theory of Cosmic Ray Variations of Atmospheric Origin Taking into Account Interference Effects

In expression (2.7) the term corresponding to variations of atmospheric origin has the most complex form. It can be expressed directly in terms of parameters which determine the state of the Earth's atmosphere.

To do this, we take into consideration [25], that in the general case the integral multiplicity of the generated particles of type i is determined (according to [2], Chap. III) from the expression

$$m^i[R, h_0, T_0(h')] = \int_0^{h_0} F^i[R, h_0, T_0(h'), h']\, dh', \tag{4.3}$$

where $F^i[R, h_0, T_0(h'), h']$ is a function determined by the development of a meson-nucleon cascade from the primary particle with rigidity R in the atmosphere, which leads to the generation of secondary particles of the i-th type. Since $\Delta m^i(R,h,T) \equiv m^i(R, h, T) - m^i(R, h_0, T_0)$, we obtain

$$\frac{\Delta m^i(R, h, T)}{m^i(R, h_0, T_0)} = \beta^i(R, h_0, T_0, \bar{h})\,\Delta h + \int_0^{h_0} \alpha^i[R, h_0, T_0(h')]\,\Delta T(h')\,dh', \tag{4.4}$$

where $\bar{h}$ lies in the interval h, h_0,

$$\Delta h = h - h_0;\ \Delta T(h') = T(h') - T_0(h'). \tag{4.5}$$

The coefficients β^i and α^i can be decomposed into a constant and a variable part (which depends on Δh and ΔT for the given observation point):

$$\beta^i = \bar{\beta}^i + \tilde{\beta}^i;\ \alpha^i = \bar{\alpha}^i + \tilde{\alpha}^i, \tag{4.6}$$

where

$$\bar{\beta}^i = [m^i(R, h_0, T_0)]^{-1} \left\{F^i[R, h_0, T_0(\bar{h}), \bar{h}] + \int_0^{h_0} \frac{\partial F^i[R, h_0, T_0(h'), h']}{\partial h_0}\, dh'\right\}, \tag{4.7}$$

$$\tilde{\beta}^i = [m^i(R, h_0, T_0)]^{-1} \left\{\frac{\partial F^i[R, h_0, T_0(\bar{h}), \bar{h}]}{\partial h_0}\,\Delta h + \right.$$
$$+ \frac{\partial F^i[R, h_0, T_0(\bar{h}), \bar{h}]}{\partial T_0}\,\Delta T(\bar{h}) + \int_0^{h_0} \left[\frac{1}{2}\,\frac{\partial^2 F^i[R, h_0, T_0(\bar{h}), \bar{h}]}{\partial^2 h_0}\,\Delta h + \right.$$
$$\left.\left. + \frac{1}{2}\,\frac{\partial^2 F^i[R, h_0, T_0(h'), h']}{\partial h_0 \partial T_0}\,\Delta T(h') + \ldots\right] dh'\right\}, \tag{4.8}$$

$$\frac{\partial F^i[R, h_0, T_0(h'), h']}{m^i(R, h_0, T_0)\,\partial T_0(h')},$$

$$\tilde{\alpha}^i = [m^i(R, h_0, T_0)]^{-1}\left[\frac{1}{2}\frac{\partial^2 F^i[R, h_0, T_0(h'), h']}{\partial^2 T_0}\Delta T(h') + \right.$$
$$\left. + \frac{1}{2}\frac{\partial^2 F^i[R, h_0, T_0(h'), h']}{\partial T_0 \partial h_0}\Delta h + \ldots\right]. \qquad (4.10)$$

It should be noted that in many real cases Δh and ΔT are relatively small, so that $\tilde{\beta}^i \ll \bar{\beta}^i$; $\tilde{\alpha}^i \ll \bar{\alpha}^i$, and one can restrict oneself only to the constant component of α^i and β^i.

Substituting (4.4)-(4.10) in the first term in the right member of (2.7), we obtain for a variation of atmospheric origin

$$\left[\frac{\Delta I_k^i(h)}{I_k^i(h_0)}\right]_{\text{атм}} = B_k^i(h_0, T_0, \bar{h})\,\Delta h + \int_0^{h_0} A_k^i[h_0, T_0(h'), h']\,\Delta T(h')\,dh', \qquad (4.11)$$

where

$$B_k^i(h_0, T_0, h') = [I_k^i(h_0)]^{-1}\int_{R_k}^{\infty}[D(R) + \Delta D(R)]\left\{F^i[R, h_0, T_0(\bar{h}), \bar{h}] + \right.$$
$$+ \frac{\partial F^i[R, h_0, T_0(\bar{h}), \bar{h}]}{\partial h_0}\Delta h + \frac{\partial F^i[R, h_0, T_0(\bar{h}), \bar{h}]}{\partial T_0}\Delta T(\bar{h}) +$$
$$+ \int_0^{h_0}\left[\frac{\partial F^i[R, h_0, T_0(h'), h']}{\partial h_0} + \frac{1}{2}\frac{\partial^2 F^i[R, h_0, T_0(h'), h']}{\partial h^2}\Delta h + \right.$$
$$\left.\left. + \frac{1}{2}\frac{\partial^2 F^i[R, h_0, T_0(h'), h']}{\partial h_0\,\partial T_0}\Delta T(h') + \ldots\right]dh'\right\}dR + [I_k^i(h_0)]^{-1}\Delta R_k \times \qquad (4.12)$$
$$\times [D(\bar{R}_k) + \Delta D(\bar{R}_k)]\left\{F^i(\bar{R}_k, h_0, T_0(\bar{h}), \bar{h}) + \frac{\partial F^i(\bar{R}_k, h_0, T_0(\bar{h}), \bar{h})}{\partial h_0}\Delta h + \right.$$
$$+ \frac{\partial F^i(\bar{R}_k, h_0, T_0(\bar{h}), \bar{h})}{\partial T_0(\bar{h})}\Delta T(\bar{h}) + \int_0^{h_0}\left[\frac{\partial F^i(\bar{R}_k, h_0, T_0(\bar{h}), \bar{h})}{\partial h_0} + \right.$$
$$\left.\left. + \frac{1}{2}\frac{\partial^2 F^i(\bar{R}_k, h_0, T_0(h'), h')}{\partial h_0^2}\Delta h + \frac{1}{2}\frac{\partial^2 F^i(\bar{R}_k, h_0, T_0(h'), h')}{\partial h_0\,\partial T_0}\Delta T(h') + \ldots\right]dh'\right\},$$

$$A_k^i[h_0, T_0(h'), h'] = [I_k^i(h_0)]^{-1}\left\{\int_{R_k}^{\infty}\left[\frac{\partial F^i[R, h_0, T_0(h'), h']}{\partial T_0(h')} + \right.\right.$$

$$+\frac{1}{2}\frac{\partial^2 F^i[R, h_0, T_0(h'), h']}{\partial T_0^2(h')}\Delta T(h') + \frac{1}{2}\frac{\partial^2 F^i[R, h_0, T_0(h'), h']}{\partial T_0 \partial h_0}\Delta h + \ldots\Big] \times \qquad (4.13)$$

$$\times [D(R) + \Delta D(R)]\, dR + \Delta R_k [D(\bar{R}_k) + \Delta D(\bar{R}_k)]\left[\frac{\partial F^i[\bar{R}_k, h_0, T_0(h'), h']}{\partial T_0(h')} + \right.$$

$$\left.\left.+\frac{1}{2}\frac{\partial^2 F^i[\bar{R}_k, h_0, T_0(h'), h']}{\partial T_0^2(h')}\Delta T(h') + \frac{1}{2}\frac{\partial^2 F^i[\bar{R}_k, h_0, T_0(h'), h']}{\partial T_0(h')\,\partial h_0}\Delta h + \ldots\right]\right\}.$$

The interference effects due to the simultaneous presence of $\Delta D(R)$ and ΔR_k can be taken into account by the method of successive approximations. The usual formulas for the meteorological effects (see [1], Chap. V) which follow from (4.12) and (4.13) when $\Delta D(R) = \Delta R_k = 0$ can be used as the first approximation. By introducing these corrections in the observation data, we eliminate in the first approximation local effects of atmospheric origin, and determine $\Delta D(R)$ and ΔR_k from the corrected data from the worldwide network of stations. Next, using formulas (4.11)-(4.13), the atmospheric effect corrections can be found more accurately, and then also the $\Delta D(R)$ and ΔR_k more accurately. The rate at which this process converges depends on the particular type of cosmic ray variation investigated. Basically, since the variable component of the coefficients in (4.12) and (4.13) is considerably smaller than the constant component, it suffices, given the present accuracy of the measurements, to find the second approximation (i.e., the $\Delta D(R)$ and ΔR_k must be taken into account at least roughly. /16

4.6. Calculation of the Meteorological Coefficients for the μ-Meson Component Taking into Account the Three-Dimensional Model of the Elementary Event

Article [1] developed a theory of cosmic ray variations of atmospheric origin without taking into account the possible dependence of the meteorological coefficients on the geomagnetic cutoff rigidity and the form of the primary spectrum. These can be taken into account by studying a nuclear-meson cascade in the real (non-isothermal) Earth's atmosphere. Such attempts were made in study [26] which was based on the three-dimensional model of the elementary event with the assumptions described in Section 3 according to which the integral multiplicity determined from expression (4.3) is:

$$m^{\mu}[E_0, h_0, T(h)] = \frac{\frac{m_\pi R}{\tau_\pi} m_\pi^2}{2\pi(m_\pi^2 - m_\mu^2)} \sum_{i=1}^{i_1} \frac{A_N^i}{(i-1)!} \int_0^1 \frac{d\cos\gamma}{(\lambda\cos\gamma)^i} \int_0^{h_0} \frac{dh}{h} T(h) \times$$

$$\times \int_{\Delta\varepsilon_\mu^i}^{\varepsilon_\mu^{\max(i)}} \frac{d\varepsilon_\mu}{\varepsilon_\mu} \int_0^{\infty} \frac{d\cos\theta}{\cos\theta} \int_{\frac{m_\pi^2}{m_\mu^2}\left[\varepsilon_\mu + \frac{K_\mu(h_0-h)}{\cos\theta}\right] \le \varepsilon_\pi^{\max(i)}} \frac{d\varepsilon_\pi \varepsilon_\pi^{-\tau} \exp\left[-q\widetilde{T}(h, h') - \frac{h}{\lambda\cos\theta}\right]}{(\varepsilon_\pi^2 - m_\pi^2)} \times \quad (4.14)$$

$$\times \int_0^h \exp\left[-\frac{h'}{\lambda}\frac{\cos\gamma - \cos\theta}{\cos\gamma\cos\theta}\right] (h')^{i-1} dh' \exp\left[-\frac{m_\mu R}{\tau_\mu} \widetilde{\widetilde{T}}(h, \varepsilon_\mu\cos\theta)'\right].$$

Here

$$q = \frac{m_\pi R}{g\tau_\pi \cos\theta \sqrt{\varepsilon_\pi^2 - m_\pi^2}}, \quad \widetilde{T}(h', h) = \int_{h'}^{h} \frac{dh'' T(h'')}{h''}.$$

$$\alpha = \sqrt{\frac{\varepsilon_\pi^2 - m_\pi^2 - p_\perp^2}{\varepsilon_\pi^2 - m_\pi^2}} \cos\gamma - \frac{p_\perp}{\varepsilon_\pi^2 - m_\pi^2} \sin\gamma; \quad (4.15)$$

$$\widetilde{\widetilde{T}}(h, \varepsilon_\mu, \cos\theta) = \int_h^{h_0} \frac{dh' T(h')}{h'\left[\varepsilon_\mu - \frac{(h'-h)K_\mu}{\cos\theta}\right]};$$

$$\varkappa = \sqrt{\frac{\varepsilon_\pi^2 - m_\pi^2 - p_\perp^2}{\varepsilon_\pi^2 - m_\pi^2}} \cos\gamma + \frac{p_\perp}{\varepsilon_\pi^2 - m_\pi^2} \sin\gamma; \quad (4.16)$$

$$L = \sqrt{1 - \frac{\varepsilon_\pi^2 - m_\pi^2 - p_\perp^2}{\varepsilon_\pi^2 - m_\pi^2} - \cos^2\theta - \cos^2\gamma + 2\cos\gamma\cos\theta\sqrt{\frac{\varepsilon_\pi^2 - m_\pi^2 - p_\perp^2}{\varepsilon_\pi^2 - m_\pi^2}}}; \quad (4.17)$$

h is the decay level of the π-meson, γ is the angle of incidence of the primary neutron, θ is the angle of jump of the π-meson, k_μ is the ionization loss factor of μ-mesons, λ is the free path for the neutron and π-meson (assumed to be the same). The remaining notation here is the same as in Section 3. /17

Before it is varied over temperature and pressure, expression (4.14) will be reduced to a more convenient form. We have a multiple integral with a large number of successive integrations. Its direct evaluation through successive integration and summation using approximate formulas is connected with an exceptionally large number of operations which sharply reduces the reliability

of the computer, increases the probability of an error and makes the debugging of the program difficult. Finally, the cumulative computational error can be of an order of magnitude which is comparable to the result.

Two methods exist for evaluating numerically multiple integrals, the Monte Carlo method and the theoretical numerical method. The essence of the latter consists of the following. Suppose that we have a sufficiently smooth function $f(x_i \ldots x_s)$ which is defined in the s-dimensional unit cube for which formula

$$\int_0^1 \cdots \int_0^1 f(x_1 \ldots x_s)\, dx_1 \ldots ds = \frac{1}{N} \sum_{k=1}^{N} f\left(\left\{\frac{a_1 k}{P}\right\} \ldots \left\{\frac{a_s k}{P}\right\}\right) - R, \qquad (4.18)$$

is valid, where the $a_i \ldots a_s$ are the so-called optimal coefficients, p is a scaling factor called the modulus, and R is the approximation error. The above formula can be used to obtain any desired accuracy with a comparatively small number of operations.

However, to use this method, the expression for m^{μ} must be represented in the appropriate form. This is easily achieved by a change of variables. We introduce the variables

$$x = \frac{\varepsilon_\mu - \Delta\varepsilon_\mu}{f}; \quad f = \varepsilon_\mu^{\max(i)} - \Delta\varepsilon_\mu; \quad y = \frac{h}{h_0}. \qquad (4.19)$$

Also, writing for the sake of convenience

$$F = fx + \frac{k_\mu h_0 (1 - y)}{\cos\gamma}; \qquad (4.20)$$

$$Q = \frac{m_\mu R}{\tau_\mu g} \qquad (4.21)$$

and carrying out a number of simplifications based on the behavior of the individual terms in different altitude and energy ranges, we reduce the expression for $m^{\mu}[E_0, h_0, T(h)]$ to the form

$$m^{\mu}[E_0, h_0, T(h)] = \frac{m_{\pi}^4 R}{2\pi\tau_{\pi} g (m_{\pi}^2 - m_{\mu}^2)} \sum_{i=1}^{i_1} \frac{A_N^{(i)}/h_0^i}{(i-1)!} \int_0^1 \frac{d\cos\gamma}{(\lambda\cos\gamma)^i} \times$$

$$\times \int_0^1 dy \frac{T(y)}{y} \int_0^1 \frac{dx}{fx + \Delta\varepsilon_{\mu}} \int_{F}^{\frac{m_{\pi}^2}{m_{\mu}^2} F \leqslant \varepsilon_{\pi}^{\max(i)}} \frac{d\varepsilon_{\pi}\varepsilon_{\pi}^{-r}}{(\varepsilon_{\pi}^2 - m_{\pi}^2)} \int_{\alpha}^{\pi} \frac{d\cos\theta}{L\cos^2\theta} \exp \times \tag{4.22}$$

$$\times \left[- Q\tilde{\tilde{T}}(y, h_0) \int_0^{h'} (h')^{i-1} \exp\left[- q\tilde{T}(y, h') - \frac{yh_0}{\lambda\cos\theta} \right] \exp \times \right.$$

$$\left. \times \left[- h_0 \frac{h'\cos\gamma - \cos\theta}{\lambda\cos\gamma\cos\theta} \right] dh',$$

where $r \approx 2.5 - 2.7$ is the exponent in the generation spectrum of π-mesons. /18

The triple integral with respect to x, y, cos γ is calculated using the above method. The integral with respect to $\varepsilon_{\pi}\cos\theta$, h' with variable limits of integration is calculated using a special subprogram for each set of x, y, cos γ, where again another preliminary change of variables can be made in accordance with formula (4.18).

Since we must have in the concrete calculations the expression for m^{μ} in this form, we will vary it over the temperature in this form. The result of the variation, as can be easily seen, will have the form

$$\frac{\delta m^{\mu}}{m^{\mu}} = \frac{1}{m^{\mu}} \frac{m_{\pi}^4 R}{2\pi g\tau_{\pi}(m_{\pi}^2 - m_{\mu}^2)} \sum_{i=1}^{i_1} \frac{A_N^{(i)}/h_0^i}{(i-1)!} (A + B + C), \tag{4.23}$$

where

$$A = \int_0^1 \frac{dy}{y} \delta T(y) \int_0^1 \frac{d\cos\gamma}{(\lambda\cos\gamma)^i} \int_0^1 \frac{dx}{fx + \Delta\varepsilon_\mu} \int_0^y dh' (h')^{i-1} \times$$

$$\times \int_\alpha^\varkappa \frac{d\cos\theta}{\cos^2\theta} \exp\left[-\frac{h_0 h'}{\lambda} \frac{\cos\gamma - \cos\theta}{\cos\gamma\cos\theta}\right] \int_F^{\frac{m_\pi^2}{m_\mu^2} F \leqslant \varepsilon_\pi^{\max(i)}} \frac{d\varepsilon_\pi \varepsilon_\pi^{-r}}{(\varepsilon_\pi^2 - m_\pi^2) L} \times \tag{4.24}$$

$$\times \exp\left[-q\tilde{T}(h', y) - \frac{h_0 y}{\lambda\cos\theta}\right] \exp\left[-Q\tilde{\tilde{T}}(y, h_0)\right].$$

$$B = \int_0^1 \frac{dh''}{h''} \delta T(h'') \int_{h''}^1 \frac{T(y)}{y} dy \int_0^1 \frac{d\cos\gamma}{(\lambda\cos\gamma)^i} \int_0^1 \frac{dx}{fx + \Delta\varepsilon_\mu} \times$$

$$\times \int_0^{h''} dh' (h')^{i-1} \int_\alpha^\varkappa \frac{d\cos\theta}{\cos^2\theta} \exp\left[-\frac{h_0 h'}{\lambda} \frac{\cos\gamma - \cos\theta}{\cos\gamma\cos\theta}\right] \times$$

$$\times \int_F^{\frac{m_\pi^2}{m_\mu^2} F \leqslant \varepsilon_\pi^{\max(i)}} \frac{d\varepsilon_\pi \varepsilon_\pi^{-r}}{(\varepsilon_\pi^2 - m_\pi^2) \cdot L} (-q) \exp\left[-q\tilde{T}(h', y) - \frac{h_0 y}{\lambda\cos\theta}\right] \exp\left[-Q\tilde{\tilde{T}}(y, h_0)\right]. \tag{4.25}$$

$$C = \int_0^1 \frac{dh''}{h''} \delta T(h'') \int_0^{h''} \frac{T(y)}{y} dy \int_0^1 \frac{d\cos\gamma}{(\lambda\cos\gamma)^i} \int \frac{dx}{fx + \Delta\varepsilon_\mu} \times$$

$$\times \int_F^y dh' (h')^{i-1} \int_\alpha^\varkappa \frac{d\cos\theta}{\cos^2\theta} \exp\left[-\frac{h_0 h'}{\lambda} \frac{\cos\gamma - \cos\theta}{\cos\gamma\cos\theta}\right] \times$$

$$\times \int^{\frac{m_\pi^2}{m_\mu^2} F \leqslant \varepsilon_\pi^{\max(i)}} \frac{d\varepsilon_\pi \varepsilon_\pi^{-r}}{(\varepsilon_\pi^2 - m_\pi^2) \cdot L} \left[-\frac{Q}{(fx + \Delta\varepsilon_\mu)\cos\theta}\right] \times \tag{4.26}$$

$$\times \exp\left[-q\tilde{T}(h', y) - \frac{h_0 y}{\lambda\cos\theta}\right] \exp\left[-Q\tilde{\tilde{T}}(y, h_0)\right].$$

Variation over h_0 is carried out analogously. To do this we can use the expression for m^μ which was derived for the isothermal atmosphere. As a result, we obtain the partial barometric coefficient $\beta(E_0, h_0)$ which was derived in [27]: /19

$$\beta(E_0, h_0) = -\frac{dm^2}{m^2 dh_0} \frac{(0{,}7\, m_\pi^2}{m_\pi^2 - m_\mu^2} \left\{ \sum_{i=1}^{i_1} \frac{i\, \Lambda_N^{(i)} \left(\frac{h_0}{\lambda}\right)^{i-1}}{\lambda\,(i-1)!} \times \right.$$

$$\times \int_0^1\int_0^1\int_0^1 dx\, dy\, d\cos\gamma\, y^{i-1}\, e^{-\frac{yh_0}{\lambda(0{,}7\cos\gamma+0{,}3)}} \frac{1}{(0{,}7\cos\gamma+0{,}3)^i} \left[\frac{y\,(fx+\Delta\varepsilon_\mu)}{F}\right]^{QT/F_1} \times$$

$$\times \int_{F_1}^{\frac{m_\pi^2}{m_\mu^2}F \leqslant \varepsilon_\pi^{\max(i)}} \frac{d\varepsilon_\pi \varepsilon_\pi^{-r}}{(\varepsilon_\pi^2 - m_\pi^2)\sqrt{(0{,}7\cos\gamma+0{,}3)^2 - \frac{p_\perp^2}{\varepsilon_\pi^2 - m_\pi^2}}} + \sum_{i=1}^{i_1} \frac{\Lambda_N^{(i)} \left(\frac{h_0}{\lambda}\right)^{i-1}}{(i-1)!} \times$$

$$\times \int_0^1\int_0^1\int_0^1 dx\, dy\, d\cos\gamma \frac{y^{i-1}}{(0{,}7\cos\gamma+0{,}3)^i} e^{-\frac{yh_0}{\lambda(0{,}7\cos\gamma+0{,}3)}} \times$$

$$\times (A_1 + B_1 + C_1) \int_{F_1}^{\frac{m_\pi^2}{m_\mu^2}F \leqslant \varepsilon_\pi^{\max(i)}} \frac{d\varepsilon_\pi \varepsilon_\pi^{-r}}{(\varepsilon_\pi^2 - m_\pi^2)\sqrt{(0{,}7\cos\gamma+0{,}3)^2 - \frac{p_\perp^2}{\varepsilon_\pi^2 - m_\pi^2}}} +$$

$$+ \sum_{i=1}^{i_1} \frac{A_N^i \left(\frac{h_0}{\lambda}\right)^{i-1}}{(i-1)!} \int_0^1\int_0^1\int_0^1 dx\, dy\, d\cos\gamma\, y^{i-1} e^{-\frac{yh_0}{\lambda(0{,}7\cos\gamma+0{,}3)}} \times \qquad (4.27)$$

$$\times \frac{1}{(0{,}7\cos\gamma+0{,}3)^i} \left[\frac{y\,(fx+\Delta\varepsilon_\mu)}{F_1}\right]^{QT/F_1} \times$$

$$\times \left\{ \frac{\left(\frac{m_\pi^2}{m_\mu^2}F_1\right)^{-r} \frac{k_\mu(1-y)}{0{,}7\cos\gamma+0{,}3}}{\left[\left(\frac{m_\pi^2}{m_\mu^2}F_1\right)^2 - m_\pi^2\right]\sqrt{(0{,}7\cos\gamma+0{,}3)^2 - \frac{p_\perp^2}{\left(\frac{m_\pi^2}{m_\mu^2}F_1\right)^2 - m_\pi^2}}} - \right.$$

$$\left. - \frac{F_1^{-r} \frac{k_\mu(1-y)}{0{,}7\cos\gamma+0{,}3}}{[F_1^2 - m_\pi^2]\sqrt{(0{,}7\cos\gamma+0{,}3)^2 - \frac{p_\perp^2}{F_1^2 - m_\pi^2}}} \right\},$$

where

$$A_1 = -\frac{y}{\lambda(0{,}7\cos\gamma + 0{,}3)}\left\{\frac{y(fx+\Delta e_\mu)}{F_1}\right\}^{QT/F_1}; \tag{4.28}$$

$$B_1 = \frac{QT}{F_1^2}\frac{k_\mu(1-y)}{0{,}7\cos\gamma+0{,}3}\ln\frac{y(fx+\Delta e_\mu)}{F_1}; \tag{4.29}$$

$$C_1 = -\frac{k_\mu(1-y)}{0{,}7\cos\gamma+0{,}3}\frac{QT}{F_1^2 y(fx+\Delta e_\mu)}; \tag{4.30}$$

$$F_1 = fx + \Delta e_\mu + \frac{k_\mu n_0(1-y)}{0{,}7\cos\gamma+0{,}3}. \tag{4.31}$$

4.7. Partial Barometric Coefficient

/20

One of the most widely used instruments today is the neutron monitor (and supermonitor). For the neutron component of cosmic rays, the most important effect is the barometric effect since the temperature effect is rather small (see Section 4.2). The concept of the barometric effect was generalized in study [27], by taking into account not only the possible effect of the primary spectrum on it, but also the changes in the cutoff rigidity due to the variable Earth's magnetosphere. By varying (2.2) over h_0 we obtain for the usual barometric coefficient

$$-\beta_k^i(h_0) = \frac{1}{I_k^i(h_0)}\frac{\partial I_k^i(h_0)}{\partial h_0} = \frac{1}{I_k^i(h_0)}\int_{R_k}^{\infty}\frac{\partial m^i(R,h_0)}{\partial h_0}D(R)\,dR. \tag{4.32}$$

In practice $\beta_k^i(h_0)$ is determined by correlating linearly variations in pressure with variations in the cosmic ray intensity (more precisely, with the change in the logarithm of the intensity). However, when (4.32) was derived, it was assumed that D(R) and R_k are constant and that the variations in h_0 are small. In the general case, the variable intensity is

$$I_k^i(h) = \int_{R_k}^{\infty} m^i(R,h)\,D'(R)\,dR, \tag{4.33}$$

where $D'(R) = D(R) + \Delta D(R)$ and $R_k^i = R_k + \Delta R_k$, $h = h_0 + \Delta h$, and where $\Delta D(R)$, ΔR_k and Δh are finite (not necessarily small)

increments. Writing also $I_k^i(h) = I_k^i(h_0) + \Delta I_k^i(h)$, $m^i(R,h) = m^i(R,h_0) + \Delta m^i(R,h)$, we obtain from (4.33)

$$\begin{aligned}\Delta I_k^i(h) = &- \Delta R_k m^i(\bar{R}_k, h_0)\, D(\bar{R}_k) - \Delta R_k m^i(\bar{R}_k, h_0)\, \Delta D(\bar{R}_k) - \\ &- \Delta R_k \Delta m^i(\bar{R}_k, h)\, D(\bar{R}_k) - \Delta R_k \Delta m^i(\bar{R}_k, h)\, \Delta D(\bar{R}_k) + \\ &+ \int_{R_k}^{\infty} m^i(R, h_0)\, \Delta D(R)\, dR + \int_{\bar{R}_k}^{\infty} \Delta m^i(R, h_0)\, D(R)\, dR + \\ &+ \int_{\bar{R}_k}^{\infty} \Delta m^i(R, h_0)\, \Delta D(R)\, dR,\end{aligned} \tag{4.34}$$

where $R_k \leq \bar{R}_k \leq R_k + \Delta R_k$ and the fact that $I_k^i(h_0)$ is determined from (2.2) was taken into account.

Breaking up (4.34) into $I_k^i(h_0)$ and using the coupling coefficients (2.3) that were determined, we obtain

$$\begin{aligned}\frac{\Delta I_k^i(h)}{I_k^i(h_0)} = &- \Delta R_k W_k^i(\bar{R}_k, h_0) - \Delta R_k \frac{\Delta D(\bar{R}_k)}{D(\bar{R}_k)} W_k^i(\bar{R}_k, h_0) - \\ - \Delta R_k \frac{\Delta m^i(\bar{R}_k, h_0)}{m^i(\bar{R}_k, h_0)} &W_k^i(\bar{R}_k, h_0) - \Delta R_k \frac{\Delta m^i(\bar{R}_k, h_0)}{m^i(\bar{R}_k, h_0)} \frac{\Delta D(\bar{R}_k)}{D(\bar{R}_k)} W_k^i(\bar{R}_k, h_0) + \\ &+ \int_{R_k}^{\infty} \frac{\Delta D(R)}{D(R)} W_k^i(R, h_0)\, dR + \int_{\bar{R}_k}^{\infty} \frac{\Delta m^i(R, h_0)}{D(R)} W_k^i(R, h_0)\, dR + \\ &+ \int_{\bar{R}_k}^{\infty} \frac{\Delta m^i(R, h_0)}{m^i(R, h_0)} \frac{\Delta (DR)}{D(\ )} W_k^i(R, h_0)\, dR.\end{aligned} \tag{4.35}$$

In expression (4.35), the effect due to variation in pressure is defined by the ratio $\Delta m^i(R,h)/m^i(R,h_0)$. We will express this ratio in terms of the barometric coefficient of the integral multiplicity with which secondary particles are generated, /21

$$\beta^i(R, h) = - \frac{\partial m^i(R, h)}{m^i(R, h)\, dh}, \tag{4.36}$$

which can be called the partial barometric coefficient. Substituting (4.36) in (4.32), and using definition (2.3), it can be easily shown that the relation between $\beta_k^i(h_0)$ and $\beta^i(R,h_0)$ is defined by the expression

$$\beta_k^i(h_0) = \int_{R_k}^{\infty} \beta_i(R, h_0) W_k^i(R, h_0) dR. \tag{4.37}$$

Formula (4.37) gives a method which can be used to find $\beta^i(R,h_0)$. In fact, measuring $\beta_k^i(h_0)$ experimentally, as a function of the geomagnetic cutoff rigidity R_k, we can then find $\partial\beta_k^i(h_0)/\partial R_k$, from which the unknown partial barometric coefficient

$$\beta^i(R_k, h_0) = -\frac{\partial\beta_k^i(h_0)/\partial R_k}{W_k^i(R_k, h_0)} + \beta_k^i(h_0). \tag{4.38}$$

is easily determined on the basis of (4.37).

When the measurements of $\beta_k^i(h_0)$ which are carried out depend not only on R_k but also on h_0, using (4.38) we find $\beta^i(R,h)$ in the interval $R \lesssim 15$ BV (this can be done, for example, using the measurement results [28]). For large values of R, evidently $m^i(R,h)$ must be calculated numerically taking into account cascading processes in the Earth's atmosphere (see Section 4.6), and then $\beta^i(R,h)$ must be found according to (4.36). Thus, in principle, $\beta^i(R,h)$ can be found without any difficulties. On the other hand, the concept of the partial barometric coefficient is very useful in the study of the barometric effect as we will see later.

The solution of equation (4.36) with the initial condition $m_i(R,h)\big|_{h=h_0} = m^i(R,h_0)$ is

$$m^i(R, h) = m^i(R, h_0) \exp\left[-\int_{h_0}^{h} \beta^i(R, h) dh\right]. \tag{4.39}$$

Using (4.39), the unknown ratio

$$\frac{\Delta m^i(R, h)}{m^i(R, h_0)} \equiv \frac{m^i(R, h) - m^i(R, h_0)}{m^i(R, h_0)} = \exp\left[-\int_{h_0}^{h} \beta^i(R, h)\, dh\right] - 1. \qquad (4.40)$$

can be easily expressed in terms of $\beta^i(R,h)$.

Let us substitute (4.40) in (4.35) and break up $\left[\frac{\Delta I_k^i(h)}{I_k^i(h_0)}\right]_{obs}$ into

$$\left[\frac{\Delta I_k^i(h)}{I_k^i(h_0)}\right]_{obs} = \left[\frac{\Delta I_k^i(h)}{I_k^i(h_0)}\right]_{bar} + \left[\frac{\Delta I_k^i(h)}{I_k^i(h_0)}\right]_{prim}, \qquad (4.41)$$

where

$$\begin{aligned}\left[\frac{\Delta I_k^i(h)}{I_k^i(h_0)}\right]_{bar} = &-\Delta R_k W_k^i(\bar{R}_k, h_0)\left\{\exp\left[-\int_{h_0}^{h} \beta^i(\bar{R}_k, h)\, dh\right] - 1\right\} - \\ &- \Delta R_k \frac{\Delta D(\bar{R}_k)}{D(\bar{R}_k)} W_k^i(\bar{R}_k, h_0)\left\{\exp\left[-\int_{h_0}^{h} \beta^i(\bar{R}_k, h)\, dh\right\} - 1\right\} + \\ &+ \int_{\bar{R}_k}^{\infty} \left\{\exp\left[-\int_{h_0}^{h} \beta^i(R, h)\, dh\right] - 1\right\} W_k^i(R, h_0)\, dR + \\ &+ \int_{\bar{R}_k}^{\infty} \left\{\exp\left[-\int_{h_0}^{h} \beta^i(R, h)\, dh\right] - 1\right\} \frac{\Delta D(R)}{D(R)} W_k^i(R, h_0)\, dR. \end{aligned} \qquad (4.42)$$

/22

and

$$\begin{aligned}\left[\frac{\Delta I_k^i(h)}{I_k^i(h_0)}\right]_{prim} = &-\Delta R_k W_k^i(\bar{R}_k, h_0) - \Delta R_k \frac{\Delta D(\bar{R}_k)}{D(\bar{R}_k)} W_k^i(\bar{R}_k, h_0) + \\ &+ \int_{\bar{R}_k}^{\infty} \frac{\Delta D(R)}{D(R)} W_k^i(R, h_0)\, dR. \end{aligned} \qquad (4.43)$$

Evidently the problem must be solved using the method of successive approximations. First, from formula (4.42) when $\Delta R_k = 0$, $\Delta D = 0$ we evaluate for the individual observation points

$$\left[\frac{\Delta I_k^i(h)}{I_k^i(h_0)}\right]_{\text{bar}} = \exp\left[-\int_{h_0}^{h} \beta_k^i(h)\,dh\right] - 1, \tag{4.44}$$

where $\beta_k^i(h)$ is determined from expressions (4.32) and (4.37) and is found directly from experimental data (the approximation (4.44) is discussed in article [29]). When the barometric correction is evaluated, using Equation (4.43), we can find in first approximation ΔR_K and $\Delta D(R)$, which, in turn, are substituted in (4.42), and $\left[\frac{\Delta I_k^i(h)}{I_k^i(h_0)}\right]_{\text{bar}}$ is found more accurately.

5. Theory of Cosmic Ray Variations of Geomagnetic Origin (Class II)

Observations have shown that during the principal phase of auroral storms, the cutoff rigidity changes. S. Chapman [30] was the first to draw attention to the possible variation in the magnetic cutoff rigidity, by assuming that the total variation in the field inside and outside the flux ring responsible for the principal phase of the auroral storm, leads to an increase in the geomagnetic threshold, which, in turn, reduces the cosmic ray intensity (Forbush effect). However, as T. G. Johnson [31] has shown, this explanation of the Forbush effect is inconsistent. If the magnetic field increases outside the flux ring, inside the ring it decreases and the sign of the effect will depend on the radius of the flux ring [31]. The calculations of S. Hiyakawa and J. N. Nishimura [32] and also of S. B. Treiman [33] have shown that the critical value of the radius of the ring when the effects of the regions with the increased and reduced magnetic field mutually compensate one another is 1.3 times the radius of the Earth. Many investigations of the magnetic field during auroral storms give a radius of the ring flux which is considerably larger than 1.3 R_E.

Consequently, during auroral storms we must observe a reduced rigidity threshold and an increase in the cosmic ray intensity on the surface of the Earth.

From this standpoint the experimental data about variations in the cosmic ray intensity during auroral storms are exceptionally important. First, many studies show that practically during all effective auroral storms, a decrease in cosmic ray intensity rather than an increase is observed. Thus, the principal effect of auroral storms on cosmic rays must have an entirely different character which is not related to variations in the structure of the geomagnetic field [1]. /23

The effect of the ring flux is isolated from the background of the considerable Forbush effect only with great difficulty. It was only possible to solve this problem to a considerable extent on the basis of the experimental studies that were carried out in accordance with the IGY program [34-37]. However, from a theoretical point of view, this important and interesting problem of the direct effect of distortions of the geomagnetic field on cosmic rays is far from solved.

The motion of a charged particle in a complex dipole and ring flux field in the plane of the equator was studied for the first time by K. Stormer [38]. Later, E. S. Ray [39] studied the effect of such ring flux on the latitudinal effect of primary cosmic radiation in an 11-year cycle of solar activity. E. S. Ray assumed that the threshold rigidity in an 11-year cycle varies as a result of variations in the parameters of the ring flux which vary with solar activity, which could possibly be the reason for the displacement along the latitude of the "bend" of the latitudinal effect of cosmic rays. It can be easily shown that this explanation gives an incorrect sign of the 11-year variation. A further study of variations in cutoff rigidity is of interest. In such a study it is important to calculate the threshold rigidities for particles arriving at the zenith at different angles, to take into account the spreading of the flux along the latitude, the finiteness of the geomagnetic field due to the action of solar plasma, the asymmetry of the ring flux, etc.

Theoretical studies of class II variations have recently been carried out mainly only in the Soviet Union [40-41] and in Japan [45]. Variations in the geomagnetic cutoff rigidity of cosmic rays incident to the Earth at different geomagnetic latitudes and different zenith and azimuth angles were calculated (in the presence of a filament equatorial ring flux) [40]. The calculations were carried out for flux rings whose radii were 3, 5 and 9 times the radius of the Earth, and the magnetic moments of the rings were 1, 3/2 and 2 times the magnetic dipole moments of the Earth. A more complex problem was solved in paper [41], which studied the effect on the geomagnetic cutoff rigidity of a given flux distributed over a sphere. Article [42] studied the effect of fluxes distributed over surfaces generated by

by rotating the magnetic lines of force about the dipole axis on the cutoff rigidity, i.e., the effects of fluxes in radiation belts were taken into account. The effect of the compression of the magnetosphere and its effect on the cutoff rigidity as well as on the trajectory of cosmic ray particles at the geomagnetic latitudes 50° and 60° were studied in article [43]. Using a concrete model of radiation belts (a model of three-dimensional fluxes), S. I. Akasofu and S. Chapman [46], found the expected cosmic ray effect in article [44]. It turned out that the amplitudes of the calculated effects were much larger than that of the effects that were observed (see supplement 3). The calculations were based on the coupling coefficients [47]. This implies that model [46] must be reexamined.

An interesting study of the effect of the asymmetry of a geomagnetic cavity on the distribution of the goemagnetic cutoff rigidity was carried out in paper [45], where it was shown that for 0, 6, 12 and 18 hours local time, a difference arises in the process which is equal to hundreds of a fraction of a billion volt which leads to a daily solar variation: in primary cosmic rays with an amplitude of ~0.6-1.5% at the latitudes from 30 to 50°, respectively, for the neutron component at sea level with an amplitude of 0.18-0.10% at the latitudes 30 to 50°, respectively, and with an amplitude of 0.04% for the μ-meson component at sea level at the latitude 30°. Within the accuracy of the calculations, a daily variation of local origin should not occur on the equator (because of the asymmetry of the geomagnetic cavity). The calculations [45] which took into account the penumbra were carried out on an electronic computer (direct calculation of trajectories). /24

6. Theory of Cosmic Ray Variations of Extraterrestrial Origin (Class III)

If variations of class I and I are eliminated from the observation data, we obtain the variations of class III.

Variations of class III can, in turn, be divided into three subclasses, each of which is of great interest in the study of electromagnetic properties of solar corpuscular fluxes in interplanetary space, processes on the Sun and in the Galaxy. Variations of class IIIa, the modulation effects of cosmic rays which characterize the electromagnetic conditions in interplanetary space in corpuscular fluxes and are completely determined by the activity of the Sun, are of great interest.

Variations of class IIIb, associated with the generation of cosmic particles on the Sun and their distribution in interplanetary space and in magnetic traps of solar corpuscular fluxes, receive a tremendous amount of attention not only because a study

of variations of this class yields exceptionally valuable data about the processes taking place in the depths of the Sun's atmosphere and the corona, the mechanisms by which the cosmic particles and solar radiation are generated, the character of the ejection of solar corpuscular fluxes and the magnetic fields in these, the electromagnetic conditions in interplanetary space, but also because the generation of solar cosmic rays represents a serious radiation hazard to space flights, and because a thorough study and forecasting of these phenomena will make it possible to develop the necessary measures for reducing and averting this hazard.

Variations of cosmic rays, class IIIc, which are associated with the diffusion of particles from the galaxy are also of tremendous interest. These variations are extremely important not only for estimating the structure of the magnetic fields in the galaxy, but also for determining the life of particles of various energy in the galaxy with regard to diffusion, which, in turn, makes it possible to estimate more accurately the energy transferred from the sources to the cosmic rays.

7. Modulation Effects of Cosmic Rays (Variations of Class IIIa)

7.1. Nature of Modulation Effects

According to contemporary concepts (see, for example, [2], [25], [48]), the modulation effects of cosmic rays are highly interrelated and reflect the complex and varied interaction of magnetic solar clusters and various perturbations of the cosmic rays which arrive from galactic space in interplanetary space. Thus, the 11-year variations, the displacement of the bend of the latitudinal effect, and the possible increase in the intensity of cosmic rays, the greater their distance from the Sun and from the plane of the ecliptic, are basically the same phenomenon brought on by the total action of the radial flux of magnetic inhomogeneities moving from the Sun on the galactic cosmic rays. The asymmetry in this flux of inhomogeneities (which is related to the longitudinal asymmetry of the distribution of active regions on the Sun) leads to the formation of 27-day cosmic ray variations (the presence of a quasi-radial interplanetary magnetic field which reduces considerably the azimuth diffusion of cosmic ray particles is essential for creating these variations). The anisotropy of cosmic rays originating in interplanetary space leads to a daily and semi-daily variation in solar time, due to the presence of electric fields indicated by the movement of the magnetic fields, and due to the drift of cosmic rays relative to Earth, due to the radial flux of inhomogeneities and the rotation of the Sun, and finally due to the density gradients of cosmic rays in the presence of quasi-regular magnetic fields. /25

To study the character with which conditions change in interplanetary space, it is also important to study the changes in the anisotropy of cosmic rays related to the solar activity cycle, the 27-day variations, auroral storms, etc.

One of the most characteristic modulation effects is the Forbush effect (a sharp reduction in the intensity of cosmic rays immediately after an auroral storm and its subsequent restoration several days later).

The flux of inhomogeneities from the Sun can be represented in the form of three parts: 1. a permanent, almost symmetric part, whose intensity may depend on the solar activity level, but which is not directly connected with active formations, 2. a recurrent part, consisting of corpuscular fluxes having a long life which are related to flocculi and sunspots, which cause auroral storms in successions, and 3. a nonrecurrent part consisting of isolated bursts of magnetized plasma from powerful chromospheric flares causing sudden auroral storms. All these parts of the solar wind cause 11-year variations, the first and second parts participate in the creation of 27-day variations whereas the third part, as a rule, only "reduces" the 27-day wave, and Forbush effects of large amplitudes are mainly caused by the third part.

7.2. Anisotropic Diffusion Approximation

Let the density of the cosmic rays in interplanetary space be $n(r, \theta, \varphi, R, Z, t)$, where r, θ, φ are spherical coordinates with center at the Sun, R and Z are the rigidity and the charge (in e units) of the particles, and t is time. Then in the diffusion approximation, n will be determined from equation

$$\frac{\partial n}{\partial t} + \sum_{\alpha=1}^{4} \frac{\partial j_\alpha}{\partial x_\alpha} = F(r, \theta, \varphi, R, z, t) \qquad (7.1)$$

with the boundary and initial conditions which are determined from the concrete problem of variations under investigation. It is assumed that the energy density of cosmic particles in interplanetary space is much smaller than the energy density of the magnetic fields and the kinetic energy of motion of the plasma, so that the reverse effect of cosmic radiation on the conditions in interplanetary space can be ignored. It should be noted that for galactic cosmic rays at distances on the order of the radius of the Earth's orbit this condition is amply satisfied and can only be violated at great distances, since the density of the galactic cosmic particles increases the farther they are away

from the Sun, and the density of the energy of motion of the plasma and the magnetic fields decreases faster than r^{-2}. This condition is also satisfied for powerful solar cosmic ray flares (apparently only with rare exceptions).

In Equation (7.1) F is a function of the source, j are the components of the particle flux which are functions of r, θ, φ, R. We will take into account that in the presence of anisotropic diffusion the three-dimensional flux is /26

$$j_i = -\varkappa_{ik}\frac{\partial n}{\partial x_k} + u_{dr,i}n, \tag{7.2}$$

where $\varkappa_{ik}$ is the tensor diffusion coefficient and u_{dr} is the drift velocity of cosmic rays in interplanetary space. Below we will show that u_{dr}, which arises as a result of the radial motion of the plasma emitted from the rotating Sun, will contain the components $u_{dr,r}$ and $u_{dr,\varphi}$.

Then expression (7.2) can be rewritten in a heliocentric spherical coordinate system:

$$j_r = -\varkappa_{rr}\frac{\partial n}{\partial r} - \frac{\varkappa_{r\theta}}{r}\frac{\partial n}{\partial\theta} - \frac{\varkappa_{r\varphi}}{r\sin\theta}\frac{\partial n}{\partial\varphi} + u_{dr,r}n, \tag{7.3}$$

$$j_\theta = -\varkappa_{\theta r}\frac{\partial n}{\partial r} - \frac{\varkappa_{\theta\theta}}{r}\frac{\partial n}{\partial\theta} - \frac{\varkappa_{\theta\varphi}}{r\sin\theta}\frac{\partial n}{\partial\varphi} \tag{7.4}$$

$$j_\varphi = -\varkappa_{\varphi r}\frac{\partial n}{\partial r} - \frac{\varkappa_{\varphi\theta}}{r}\frac{\partial n}{\partial\theta} - \frac{\varkappa_{\varphi\varphi}}{r\sin\theta}\frac{\partial n}{\partial\varphi} + u_{dr,\varphi}n. \tag{7.5}$$

We will now find the flux $j_k = ndR/dt$ along the rigidity axis, caused by the fact that during the radial divergence of the magnetic inhomogeneities from the Sun a systematic loss of energy of the particles occurs due to preferred scattering during the the lagging collisions (in the directions θ and φ) [49, 50].

Since during each such collision the energy ε of the particles is reduced on the average by $\Delta\varepsilon = -\varepsilon v\Delta u/c^2$, where $\Delta u = \Delta\Lambda/r$ and the intercollision time is $\Delta t = \Lambda/v$ and the energy is reduced only in directions which are perpendicular to r, we obtain

$$\frac{d\varepsilon}{dt} = -\frac{2}{3}\frac{\varepsilon p^2}{c^2}\frac{u}{r}. \tag{7.6}$$

Since

$$\varepsilon = Ze\sqrt{R^2 + \left(\frac{Am_0c^2}{Ze}\right)^2}, \quad d\varepsilon = \frac{ZeRdR}{\sqrt{R^2 + \left(\frac{Am_0c^2}{Ze}\right)^2}}; \tag{7.7}$$

$$\frac{v^2}{c^2} = \frac{R^2}{R^2 + \left(\frac{Am_0c^2}{Ze}\right)^2},$$

we obtain

$$\frac{dR}{dt} = -\frac{2}{3}\frac{u}{r}R. \tag{7.8}$$

Substituting (7.3)-(7.5) and (7.8) in (7.1), we obtain the fundamental equation for the investigation of the modulation effects of galactic cosmic rays in interplanetary space and the propagation of solar cosmic rays

$$\begin{aligned}\frac{\partial n}{\partial t} - \frac{1}{r^2}\frac{\partial}{\partial r}\left(-r^2 u_{dr,r} n + r^2 \varkappa_{rr}\frac{\partial n}{\partial r} + r\varkappa_{r\theta}\frac{\partial n}{\partial \theta} + \frac{r\varkappa_{r\varphi}}{\sin\theta}\frac{\partial n}{\partial \varphi}\right) - \\ - \frac{1}{r\sin\theta}\frac{\partial}{\partial \theta}\left(\sin\theta\varkappa_{\theta r}\frac{\partial n}{\partial r} \frac{\sin\theta\varkappa_{\theta\theta}}{r}\frac{\partial n}{\partial \theta} + \frac{\varkappa_{\theta\varphi}}{r}\frac{\partial n}{\partial \varphi}\right) - \\ - \frac{1}{r\sin\theta}\frac{\partial}{\partial \varphi}\left(\varkappa_{r\varphi}\frac{\partial n}{\partial r} + \frac{\varkappa_{\varphi\theta}\partial n}{\partial \theta} + \frac{\varkappa_{\varphi\varphi}}{r\sin\varkappa}\frac{\partial n}{\partial \varphi} - u_{dr,\varphi} n\right) - \\ - \frac{2}{3}\frac{u}{r}\frac{\partial}{\partial R}(Rn) = F(r, \theta, \varphi, R, Z, t).\end{aligned} \tag{7.9}$$

7.3. Determination of the Diffusion Tensor in Interplanetary Space /27

To determine $\varkappa_{ik}$, the following must be taken into account:

1. The electromagnetic conditions in interplanetary space which, in the final analysis, are determined by the anisotropic diffusion tensor $\varkappa_{ik}$ and the velocity u with which the plasma moves, do not remain constant, but vary with time, where these variations are lagged relative to the process which generate the plasma fluxes on the Sun by the time $t_{lag} \approx r/u$. If we denote by S the factor which controls the emission of the plasma from the Sun (the number of sunspots, chromospheric flares, calcium,

flocculi, etc.), $\varkappa_{ik}$ will be, at a distance from the Sun,

$$\varkappa_{ik} = \varkappa_{ik}[r, \Omega(t - r/u)]. \tag{7.10}$$

2. The density of the kinetic energy of the plasma emitted by the Sun will be much greater than the density of the adjacent magnetic fields. This relation which is valid and has been verified by direct measurements in the neighborhood of the Earth's orbit must also hold at great distances from the Sun, since the density of the kinetic energy decreases as $\sim r^{-2}$ and the density of the magnetic energy decreases in the same way. Therefore, we should expect that basically the plasma moves radially. Then the locus of the plasma sectors emitted from one solar region is a spiral of Archimedes

$$r - r_{\odot} = -\frac{u(\theta_{\odot}, \varphi_{\odot})}{\Omega(\theta_{\odot})}(\varphi - \varphi_{\odot}) = -a(\varphi - \varphi_{\odot}), \tag{7.11}$$

because the Sun rotates with an angular frequency $\Omega = 2\pi/T$ (where $T \approx 27$ days is almost independent of the polar angle θ). Here, $\theta_{\odot}$ and $\varphi_{\odot}$ are, respectively, the polar angle and the helio longitude generating the plasma in a region on the surface of the Sun $r_{\odot}$. The large-scale magnetic field will tend to elongate along these spirals.[3]

3. It should be noted that the quasispiral interplanetary magnetic field extends apparently over very large distances ~ 50-100 AU. This follows primarily from the large lag in the 27-day variation of cosmic rays relative to the 27-day variation in solar activity which was established in study [51]. Thus, the spiral of Archimedes makes a sufficiently large number of full turns in the region of modulating space (probably ~ 10-15). It is interesting to note, that, according to [51], the radius of the modulating space tends to change from ~ 30 in periods of low solar activity to ~ 80 in periods of high solar activity. This result agrees with the data about the 11-year variations of cosmic rays.

3. The angle between the magnetic rectilinear forces and the direction of the radial motion of the magnetic inhomogeneities

$$\psi = \operatorname{arctg}\left[\frac{r\sin\theta_{\odot})\,\Omega(\theta_{\odot})}{u(\theta_{\odot}, \varphi_{\odot})}\right] \tag{7.12}$$

determines the transformations of the anisotropic diffusion tensor $\varkappa_{ik}$.

4. In the coordinate system in which the Ox axis was selected as the direction of the force of the interplanetary magnetic field at some point r, θ, φ, the tensor is /28

$$\overline{\varkappa}_{ik} = \varkappa\begin{pmatrix} 1 & 1 & 0 \\ 0 & (1+\omega^2\tau^2)^{-1} & \frac{\omega\tau}{1+\omega^2\tau^2} \\ 0 & -\frac{\omega\tau}{1+\omega^2\tau^2} & (1+\omega^2\tau^2)^{-1} \end{pmatrix}, \tag{7.13}$$

where $\tau = \Lambda/v$ is the mean intercollision time, $\omega = ZeH/Mc$ is the Larmor frequency of motion of the particle with the charge Ze and mass $M = Am_0c^2\left(1-\frac{v^2}{c^2}\right)^{-1/2}$ in the large-scale field H.

Taking into account that Λ depends on the rigidity $R = cp/Ze$ of the particle and that the radius of curvature in the magnetic field H is $\rho = R/300H$ (if R is measured in volts, H in gauss, then ρ is in centimeters) we obtain

$$\omega\tau = \Lambda/\rho = \frac{300\Lambda(R)H}{R}, \tag{7.14}$$

i.e., $\omega\tau$ is only a function of R, and it does not depend on the particle charge Ze and the velocity v. Substituting (7.14) in (7.13), we obtain

$$\tilde{\varkappa}_{ik} = \varkappa_0 \begin{pmatrix} 1 & 0 & 0 \\ 0 & \alpha_1 & +\alpha_2 \\ 0 & -\alpha_2 & \alpha_1 \end{pmatrix}, \tag{7.15}$$

where

$$\alpha_1 = \frac{R^2}{R^2 + 9\cdot 10^4 \Lambda^2 H^2}, \quad \alpha_2 = \frac{3\cdot 10^2 \Lambda H R}{R^2 + 9\cdot 10^4 \Lambda^2 H^2}. \tag{7.16}$$

We note that since $r > r_\delta$ and $H \approx H_\delta (r_\delta / r)$, for Λ = const (i.e., when Λ is independent of r) the term $\Lambda^2 H^2 \approx r^{-2}$ and it decreases rapidly as the distance from the Sun increases. Therefore, from some r onward, we can assume $3\cdot 10^2 \Lambda H << R$ and, according to (7.16) $\alpha_1 \to 1$, $\alpha_2 \to 0$. However, if Λ increases proportionally with r, then, in this case, $\Lambda^2 H^2 \approx$ const, and anisotropy also exists for large r.

5. It can be shown that the determinant of the transformation α_{ik} from the coordinate system associated with the magnetic forces to the r, θ, φ-coordinate system has the form (the sign at the top indicates that the forces leave the Sun and the sign at the bottom that they enter the Sun):

$$a_{ik} = \begin{pmatrix} c_1 & 0 & \pm c_2 \\ 0 & 1 & 0 \\ \mp c_2 & 0 & c_1 \end{pmatrix}, \tag{7.17}$$

where

$$c_1 = \cos\psi; \quad c_2 = \sin\psi. \tag{7.18}$$

In the r, θ, φ-system, the anisotropic diffusion tensor is

$$\varkappa_{ik} = \sum_{m,n} a_{mi} a_{nk} \bar{\varkappa}_{mn} = \varkappa_0 \begin{pmatrix} c_1^2 + \alpha_1 & c_2^2 \mp c_2\alpha_2 - c_1c_2(1-\alpha_1) \\ -c_2\alpha_2 & \alpha_1 & \pm\alpha_2 c_1 \\ -c_1c_2(1-\alpha_1) \mp \alpha_2 c_1 & c_2^2 + \alpha_1 c_1^2 \end{pmatrix} \tag{7.19}$$

or

$$\varkappa_{ik} = \varkappa_0 \begin{pmatrix} \cos^2\psi + \alpha_1 \sin^2\psi & \mp\alpha_1 \sin\psi & \pm\sin\psi\cos\psi(1-\alpha_1) \\ \pm\alpha_2 \sin\psi & \alpha_1 & \pm\alpha_2\cos\psi \\ -\sin\psi\cos\psi(1-\alpha_1) & \alpha_2\cos\psi & \sin^2\psi + \alpha_1\cos^2\psi \end{pmatrix}. \tag{7.20}$$

It should be kept in mind that in (7.19) and (7.20) Ψ is a function of $\theta_\odot$ and $\varphi_\odot$, according to (7.12), and $\varkappa_0 = v\Lambda/3$ is a function of $t - r/u$, θ and φ.

7.4. Determination of Drift Velocity of Cosmic Rays in Interplanetary Space

/29

When the plasma moves radially with the magnetic field $\vec{H}$ with the velocity $\vec{u} = \vec{ur}/r$, an electric field $\vec{E}$ is formed in the solar-stellar coordinate system. In this coordinate system, the charged cosmic radiation particles will drift, under the action of $\vec{E}$ and $\vec{H}$ with the velocity

$$\vec{u}_{dr} = \frac{\vec{H}\times(\vec{u}\times\vec{H})}{H^2} = \frac{\vec{ur}}{r} - \frac{u(\vec{rH})\vec{H}}{H^2 r}. \tag{7.21}$$

We will first discuss the drift under the action of a regular spiral interplanetary field. Since in this case the angle between $\vec{r}$ and $\vec{H}_0$ is determined from expression (7.12), we obtain from (7.21) for the components of the drift velocity (regardless of whether $\vec{H}_0$ is oriented toward or away from the Sun).

$$(u_{dr})_{rec} = \frac{u\Omega^2 r^2 \sin^2\theta}{u^2 + \Omega^2 r^2 \sin^2\theta}; \quad (u_{d\theta})_{rec} = 0;$$
$$(u_{d\varphi})_{rec} = -\frac{u^2\Omega r \sin\theta}{u^2 + \Omega^2 r^2}. \tag{7.22}$$

We will now consider the second extreme case. We will assume that the interplanetary field represents only a set of inhomogeneities in which the direction of the magnetic field $\vec{h}$ can be arbitrary with equal probability. Let the angle between $\vec{r}$ and $\vec{h}$ be ξ (in the counterclockwise direction from $\vec{r}$ to $\vec{h}$). Averaging expression (7.21) over all possible directions $\vec{h}$, we obtain

$$(u_{dr.r})_{turb} = \frac{2}{3}u; \quad (u_{dr.\theta})_{turb} = (u_{dr.\varphi})_{turb} = 0. \tag{7.23}$$

Taking into consideration (7.22) and (7.23) in the presence of inhomogeneities in the field on the background of the large scale regular field, and denoting the relative portion of the large-scale field by w we obtain:

$$u_{dr_r} = \frac{\beta u \Omega^2 r^2 \cdot \sin^2\theta}{u^2 + \Omega^2 r^2 \cdot \sin^2\theta} + \frac{2(1-\beta)u}{3};$$
$$u_{dr_\varphi} = \frac{\beta u^2 \Omega r \cdot \sin\theta}{u^2 + \Omega^2 r^2}; \quad u_{dr_\theta} = 0. \tag{7.24}$$

7.5. Time Variations and Three-Dimensional Anisotropy of Cosmic Rays

Domain of Applicability of Anisotropic Diffusion Model

Substituting (7.19) and (7.24) in (7.9), we obtain an equation which determines the space-time change in the cosmic ray density. The unknown function n(r, θ, φ, R, Z, t) can be found with the aid of this equation, using the boundary and initial conditions. Substituting the function n which was found and the expressions (7.19), (7.24) in (7.3)-(7.5), we then find the three-dimensional particle fluxes which determine the anisotropy of the cosmic rays: in the radial direction, the so-called 12 and 24 hour anisotropy (j_r/nv), in the direction which is perpendicular to the helioequatorial plane, the so-called north-south asymmetry (j_θ/nv), in the direction along the Earth's orbit, the 6 and 18 hour anisotropy (j_φ/nv).

When the theoretical results are compared with the experimental data, it must be kept in mind that equation (7.9) gives results which are referred to a helioequatorial coordinate system. This can be recalculated for the case when the observations /30

are carried out from the rotating Earth, whose helioaltitude changes during the year, and whose own axis of rotation is inclined 66.5° to the plane of the ecliptic, using the formulas given in article [52].

We will now discuss the domain of applicability of equation (7.9). It is known that the anisotropic diffusion approximation is best applied to the description of the process, the slower the changes in the densities and fluxes at a distance which is on the order of magnitude of the length of the free path. For the estimates we can use such criteria as:

$$\frac{1}{n}\frac{\partial n}{\partial x_\alpha}\Lambda \ll 1;\quad \frac{1}{j}\frac{\partial j}{\partial x_\alpha}\Lambda \ll 1. \tag{7.25}$$

In all cases of modulation of galactic cosmic rays which are of practical interest, criterion (7.25) is satisfied. In fact, according to the measurements [53] in interplanetary space in the region of the Earth's orbit, the magnitude of the relative radial cosmic ray intensity gradient was $\frac{1}{n}\frac{\partial n}{\partial r} \approx (12 \pm 4)\%/1$ AU in 1962 for particles of energy $\gtrsim$ 10 MeV. But at such distance from the Sun, for particles which are so soft, according to the study of the propagation of solar cosmic rays [54] $\Lambda \sim 10^{12}$ cm, hence, in the radial direction in 1962 $\frac{1}{n}\frac{\partial n}{\partial r}\Lambda \lesssim 0{,}01$.

For high energy particles Λ increases, but according to [55] the relative gradient must decrease by the same amount so that the given estimate does not depend substantially, for all practical purposes, on the energy of the particles. During maximum solar activity, the magnitude of the relative gradient must increase several times (this follows from the experimental data about the 11-year cosmic ray variations) while Λ decreases somewhat, since criterion (7.25) is still satisfied.

It can be easily shown that criterion (7.25) is equivalent to the condition $j/nv \ll 1$. But according to many studies of daily variations in the entire interval of rigidities $j/nv \lesssim 0.01$ studied, j/nv attains the values 0.03-0.05 only in isolated periods of large Forbush effects. The anisotropic diffusion approximation is only inapplicable to the study of the problem of how the anisotropic flux of galactic cosmic rays is transformed when the galactic cosmic rays pass through the solar system (the scattering reduces the degree of anisotropy of galactic origin). In this case, the transformation of the distribution function $f(\vec{r}, \vec{v}, t)$ must be studied kinetically.

A similar approach is also needed when the angular distribution of solar cosmic rays is studied in the initial phase, after they were generated in the chromospheric flare [56, 57]. The analysis shows that in all other cases of the propagation of solar cosmic rays in interplanetary space criterion (7.25) is satisfied, and the anisotropic diffusion approximation is fully applicable.

7.6. Selection of the Source Function, Boundary and Initial Conditions

The source function for the problem of the propagation of solar cosmic rays in interplanetary space is usually selected as a δ-function (instantaneous point source). This is fully justified for the entire propagation process, except for the initial phase, for which F depends essentially on t [58]. The source function for the problem of the propagation of solar cosmic rays and also galactic cosmic rays contains a term which takes into account the absorption of the cosmic rays by the planets and the Sun (which can be ignored in first approximation) as well as ionization losses and the transformation of the nuclear composition due to the interaction of cosmic rays with the Sun's atmosphere when they leave the chromospheric flare and the interaction with the interplanetary medium (the latter can also be ignored when the energies of the cosmic particles are not very low). /31

The initial conditions which are selected are the distribution for the density of the cosmic rays in interplanetary space on the background of which the given variation develops. For example, when the modulation resulting from the motion of a "semitransparent" magnetic piston is studied (the model of the Forbush effect [2]), the initial condition selected is the solution found from the study of 11-year variations. The same initial condition is selected when 27-day variations are studied (when the dependence of $\varkappa$ and u on Ψ is important). Many variations of cosmic rays have a periodic character (11-year, 27-day variations and others), and for these a quasiperiodic solution is found which is characterized by a definite lag effect relative to changes in the conditions on the Sun. These solutions do not depend, for all practical purposes, on the initial conditions.

The boundary conditions for the 11-year variation are studied in two variants: a spherical symmetric model, and a model in which the possible absence of emissions of magnetic inhomogeneities from the region of high heliolatitudes are taken into account [52]. In addition to the conditions which change with the cycle of solar activity in interplanetary space, the possible changes in the dimensions of the modulation region with time are also taken into account (the boundary conditions on the moving boundary). Variable conditions on the moving

boundary are also selected in the solution of the problem of the modulation of galactic and solar cosmic rays during the motion of a "semitransparent" magnetic piston.

8. Anisotropy of Cosmic Rays in Interplanetary Space

8.1. General Formula for Anisotropy

Writing the regular component of the interplanetary magnetic field in the form

$$H_r = H_{r\delta} r_\delta^2 r^{-2}; \quad H_\varphi = H_{r\delta} r_\delta \Omega u^{-1} r_\delta r^{-1} \sin\theta; \quad H_\theta = 0, \tag{8.1}$$

and substituting (7.18) and (7.16) in (7.19), taking into account (7.12), we obtain, using the notation

$$f_1 = r^{-2} + \Omega^2 u^{-2} \sin^2\theta; \quad f_2 = 1 + r_\delta^2 \Omega^2 u^{-2} \sin^2\theta; \quad \nu \approx 3 \cdot 10^2 H_\delta r_\delta, \tag{8.2}$$

$$\varkappa_{rr} = \frac{v\Lambda}{3}\left[1 - \frac{\Lambda^2\Omega^2 f_1 R_\delta^2 r_\delta^2 \sin^4\theta}{(r^2\Omega^2 + u^2)(R^2 f_2 + R_\delta^2 \Lambda^2 r_\delta^2 r^{-2} f_1)}\right]; \tag{8.3}$$

$$\varkappa_{r\theta} = \frac{v\Lambda}{3} \frac{r\Omega\Lambda R R_\delta r_\delta r^{-1} f_1^{1/2} f_2^{1/2} \sin\theta}{(r^2\Omega^2 + u^2)^{1/2}(R^2 f_2 + R_\delta^2 \Lambda^2 r_\delta^2 r^{-2} f_1)}; \tag{8.4}$$

$$\varkappa_{r\varphi} = \varkappa_{\varphi r} = \frac{v\Lambda}{3} \frac{R_\delta^2 \Omega r_\delta^2 r^{-1} f_1 (r^2\Omega^2 \cos^2\theta + u^2)^{1/2} \sin\theta}{(r^2\Omega^2 + u^2)(R^2 f_2 + R_\delta^2 \Lambda^2 r_\delta^2 r^{-2} f_1)}; \tag{8.5}$$

$$\varkappa_{\theta r} = \varkappa_{\theta\varphi} = -\varkappa_{\varphi\theta} = -\frac{v\Lambda}{3} \frac{R R_\delta \Lambda r_\delta r^{-1} f_1^{1/2} f_2^{1/2} (r^2\Omega^2 \cos^2\theta + u^2)}{(r^2\Omega^2 + u^2)^{1/2}(R^2 f_2 + R_\delta^2 \Lambda^2 r_\delta^2 r^{-2} f_1)}; \tag{8.6}$$

$$\varkappa_{\theta\theta} = \frac{v\Lambda}{3} \frac{R^2 f_2}{R^2 f_2 + R_\delta^2 \Lambda^2 r_\delta^2 r^{-2} f_1}, \tag{8.7}$$

$$\varkappa_{\varphi\varphi} = \frac{v\Lambda}{3} \frac{R^2 f_2 + R_\delta^2 \Lambda^2 \Omega^2 r_\delta^2 f_1 (r^2\Omega^2 + u^2)^{-1} \sin^2\theta}{R^2 f_2 + R_\delta^2 \Lambda^2 r_\delta^2 r^{-2} f_1}. \tag{8.8}$$

/32

Analogously for $\vec{u}_{dr}$ we obtain:

$$u_{dr_r} = \frac{\beta u \Omega^2 r^2}{u^2 + \Omega^2 r^2} + \frac{2(1-\beta)u}{3}; \quad u_{dr_\varphi} = \frac{\beta u^2 \Omega r \sin\theta}{u^2 + \Omega^2 r^2}; \quad u_{dr_\theta} = 0, \tag{8.9}$$

where $\beta \sim H_0(H_0 + h)^{-1}$ is a parameter which determines the relative role played by the regular (H_0) and irregular (h) components of the interplanetary fields. Here we assume that the structure of the field is determined in accordance with (8.1). Substituting (8.2)-(8.9) in (7.3)-(7.5) and then in $\vec{A} = 3j(nv)^{-1}$ (8.10), we find the components of the anisotropy vector. We will consider the expected properties of the anisotropy in various cases.

8.2. Anisotropy Near the Earth's Orbit

First, we will find the properties of the anisotropy near the Earth's orbit ($r = r_\delta, \theta = \pi/2$). We set $u = 3 \cdot 10^7$ cm/sec, and find $\Omega r_\delta = 4 \cdot 10^7 \text{cm/sec}$ $\Omega r_\delta = 1{,}33$, $\psi_\delta = 53° \cdot \Omega^2 r_\delta^2 (\Omega^2 r_\delta^2 + u^2)^{-1} = 0{,}64$; $1 + r_\delta^2 \Omega^2 u^2 = 2{,}78$. We write $R_{c\delta} = 3 \cdot 10^2 \Lambda H_\delta$ and $p = R/R_{c\delta}$. Then on the basis of (8.2)-(8.9), we obtain at the Earth's orbit near the plane of the helioequator

$$\varkappa_{rr} = \frac{v\Lambda}{3} \cdot \frac{0{,}36 + p^2}{1 + p^2}; \quad \varkappa_{r\theta} = \frac{v\Lambda}{3} \cdot \frac{0{,}8p}{1 + p^2}; \quad \varkappa_{r\varphi} = \varkappa_{\varphi r} = -\frac{v\Lambda}{3} \cdot \frac{0{,}8}{1 + p^2}; \tag{8.10}$$

$$\varkappa_{\theta r} = \varkappa_{\theta\varphi} = -\varkappa_{\varphi\theta} = -\frac{v\Lambda}{3} \cdot \frac{p}{1 + p^2}; \quad \varkappa_{\theta\theta} = \frac{v\Lambda}{3} \cdot \frac{p^2}{1 + p^2}; \quad \varkappa_{\varphi\varphi} = \frac{v\Lambda}{3} \cdot \frac{0{,}64 + p^2}{1 + p^2}. \tag{8.11}$$

We will estimate the quantity p. Since we should expect $\Lambda = ak_1$ because of the presence of a wide spectrum of the inhomogeneities,

$$p = (3 \cdot 10^2 a H_\delta)^{-1}. \tag{8.12}$$

Since from the analysis [59] of the propagation of solar cosmic rays from the flare which occurred on 4 May 1960 in the period of the initial anisotropic stage (based on an investigation of the solution of the kinetic equation) it follows that near the Earth's orbit $v\lambda/3 = 5 \cdot 10^{22}$ $\text{cm}^2\text{sec}^{-1}$ for particles with an effective hardness of ~ 3 BV (according to observations made with the aid of terrestrial neutron monitors), $a = 5/3 \cdot 10^3$.

Since, according to direct measurements of the interplanetary magnetic field $H_\delta = 5 \cdot 10^{-5}$ gauss, $p = 4 \cdot 10^{-2}$.

$$\varkappa_{rr} \approx 0{,}36 \cdot \frac{v\Lambda}{3}; \quad \varkappa_{r\varphi} = \varkappa_{\varphi r} = -0{,}8\,\frac{v\Lambda}{3}; \quad \varkappa_{\varphi\varphi} \approx 0{,}64\,\frac{v\Lambda}{3};$$
$$\varkappa_{r\theta} \approx 0{,}032\,\frac{v\Lambda}{3}; \quad \varkappa_{\theta r} = \varkappa_{\theta\varphi} = -\varkappa_{\varphi\theta}; \qquad (8.13)$$
$$\varkappa_{r\theta} \approx \varkappa_{\theta r} \approx \varkappa_{\theta\varphi} \approx \varkappa_{\varphi\theta} \approx \varkappa_{\theta\theta} \approx 0.$$

follows from here and from (8.11).

We will now estimate the drift velocity of particles near the Earth's orbit. Since, according to direct measurement data, $H_0 \sim h$, we let $\beta \approx 0.5$ and for $u = 3 \cdot 10^7$ cm/sec we obtain

$$u_{dr\varphi} = 2 \cdot 10^7 \text{ cm/sec} \quad u_{dr\theta} = 0{,}7 \cdot 10^6 \text{ cm/sec} \quad u_{dr\,r} = 0. \qquad (8.14)$$

Substituting (8.13) and (8.14) in (7.3)-(7.5) and then in (8.10), we obtain /33

$$A_{r\delta} = -0{,}36\,\frac{\Lambda}{n}\,\frac{\partial n}{r} + 0{,}8\,\frac{\lambda}{nr_\delta}\,\frac{\partial n}{\partial\varphi} + 0{,}2 \cdot 10^{-2}; \quad A_{\theta\delta} \approx 0;$$
$$A_{\varphi\delta} = 0{,}8\,\frac{\Lambda}{n}\,\frac{\partial n}{\partial r} - 0{,}64\,\frac{\Lambda}{nr_\delta}\,\frac{\partial n}{\partial\varphi} + 0{,}07 \cdot 10^{-2}. \qquad (8.15)$$

8.3. Daily Variation and Mean True Gradient of the Intensity of Cosmic Rays

When data which have been averaged over a period greater than the period of the rotation of the Sun are analyzed, the term $\frac{\partial n}{\partial\varphi} \to 0$ and expressions (8.15) simplify. Further, we take into account the fact that a definite relation exists between j_r and the mean cosmic ray intensity in the interior of a sphere of radium r_δ, i.e., when $j_r > 0$, n must decrease. Since the mean values of the intensity (for example, the mean monthly or yearly intensities) vary comparatively slowly with time, it can be shown that the mean values of $A_{r\delta}$ must be small.

In fact, during an 11-year solar activity cycle the intensity of the neutron component varies on the average by at most 10% in $T \approx 1$ year, i.e., $4\pi r_\delta^3 j_r T \approx 0{,}1\,\frac{4\pi}{3} r_\delta^3 n$. Hence, $j_r = \frac{0{,}1 r_\delta n}{3T}$ and $A_r = \frac{0{,}1 \cdot r_\delta}{vT} \sim 2 \cdot 10^{-6}$, since the observed daily variations are

larger by almost three orders of magnitude (~ 0.1%). In the range of smaller rigidities, the variations in the intensity are considerably larger, but do not exceed 100%/1 year, which gives $A \lesssim 2 \cdot 10^{-5}$. This magnitude can also be ignored.

Thus, on the average $A_{r\delta}^{+} = 0$, from which the expression (8.15) for $A_{r\delta}^{+}$ follows

$$\frac{\Lambda}{n}\frac{\partial n}{\partial r} \approx 0{,}56 \cdot 10^{-2}. \qquad (8.16)$$

Now we can estimate the expected mean radial density gradient near the Earth's orbit

$$\frac{r_\delta}{n}\frac{\partial n}{\partial r} \approx \frac{r_\delta}{\Lambda} \cdot 0{,}56 \frac{\%}{\text{AU}} \qquad (8.17)$$

If we set $\Lambda \approx aR$, where $a \approx 5/3 \cdot 10^3$ (see above) $\frac{r_\delta}{n}\frac{\partial n}{\partial r} \approx \frac{5}{h}\frac{\%}{1\ \text{AU}}$ which agrees with the available measurements of the radial gradient in the region of the Earth's orbit.

8.4. Mean Daily Variation Near the Earth's Orbit

Substituting (8.16) in (8.15), and taking into account that for the mean variation $\partial n/\partial \varphi = 0$, we obtain $A_{\varphi\delta}^{+} \approx 0.52\%$ in the direction of maximum anisotropy in 18 hours. The physical meaning of the diffusion mechanism of this variation was explained in the work of G. F. Krymskiy [60]. Due to the solar wind, a convective drift of the cosmic rays from the solar system occurs in the radial direction away from the Sun. This drift is compensated by the radial component of the diffused flux oriented mainly in the direction of the forces of the regular interplanetary field, the uncompensated tangential component, which gives the basic mean daily variation with the direction in 18 hours (an additional flux in the direction of the Earth's rotation about the Sun).

8.5. Measurements of Daily Variation Near the Earth's Orbit and Simultaneous Determination of the Radial and Azimuthal Gradients

/34

Experimental data have shown that actually $A_{r\delta}^{+}$ often differs considerably from zero. This difference may be caused by the nonsphericity of the solar wind, as a result of which the cosmic rays penetrate the solar system at large angles to the plane of helioequator and then are drifted by the solar wind (as in a jet

pump) [60, 61]. In addition, in measurements made over short time intervals, the terms containing $\partial n/\partial\varphi$ become important. When $A_{r\delta}$ and $A_{\varphi\delta}$ are measured simultaneously, the $\frac{\Lambda}{n}\frac{\partial n}{\partial r}$ and $\frac{\Lambda}{nr_\delta}\frac{\partial n}{\partial\varphi}$ can be found with the aid of (8.15):

$$\begin{aligned}\frac{\Lambda}{n}\frac{\partial n}{\partial r} &= 1{,}56A_{r_\delta} + 1{,}95A_{\varphi} - 0{,}52\cdot10^{-2};\\ \frac{\Lambda}{nr_\delta}\frac{\partial n}{\partial\varphi} &= 1{,}95A_{r_\delta} + 0{,}88_{\varphi} - 0{,}45\cdot10^{-2}.\end{aligned} \tag{8.18}$$

8.6. 27-Day Modulation of Daily Variation

We note that the quantity $\frac{\partial n}{\delta\varphi}$ is easily determined from observations of 27-day cosmic ray variations. For the neutron component, the 27-day variation is $\frac{\delta n}{n} = \beta\cos\varphi$ where φ is measured from the direction of maximum intensity. From here

$$\frac{\Lambda}{nr_\delta}\frac{\partial n}{\partial\varphi} = -\frac{\Lambda B}{r_\delta}\sin\varphi. \tag{8.19}$$

According to [2], [61], $B \sim R^{-1}$, where for $R \approx 5\cdot10^9$ V, $B \sim 0.5\cdot10^{-2}$, i.e., approximately $B \approx bR^{-1}$ where $b \approx 2.5\cdot10^7$. Since $\Lambda \approx 1.7\cdot10^3R$

$$\frac{\Lambda}{nr_\delta}\frac{\partial n}{\partial\varphi} \approx 0{,}28\cdot10^{-2}\sin\varphi. \tag{8.20}$$

Substituting (8.20) in (8.15), we obtain

$$\begin{aligned}A_{r_\delta} &= -0{,}36\frac{\Lambda}{n}\frac{\partial n}{\partial r} - 0{,}23\cdot10^{-2}\sin\varphi + 0{,}2\cdot10^{-2};\\ A_{\varphi_\delta} &= 0{,}8\frac{\Lambda}{n}\frac{\partial n}{\partial r} + 0{,}18\cdot10^{-2}\sin\varphi + 0{,}07\cdot10^{-2}.\end{aligned} \tag{8.21}$$

It can be seen from (8.21) that the amplitude and phase of a daily variation must be modulated considerably with the 27-day period, and that this modulation must be intimately related to the 27-day variation of intensity.

8.7. Fast Changes in Anisotropy

In addition to the basic changes in anisotropy, faster changes can occur, for example, during Forbush effects. In this case, the radial and azimuthal gradients increase sharply and change their direction, which leads, according to (8.15), to sharp changes in $A_{r\frac{+}{0}}$ and $A_{\omega\frac{+}{0}}$. In addition to this, considerable changes in the wind velocity u can also occur, which will also lead to considerable changes in the amplitude and phase of the daily variation (here, formulas (8.10), (7.3)-(7.5) and (8.2)-(8.9) must be used.

9. Hysteresis Phenomena in Cosmic Rays, Properties of the Solar Wind and the Energy Spectrum of Various Nuclei in the Galaxy /35

9.1. The Selection of a Parameter Controlling Variations in the Intensity of Cosmic Rays in Interplanetary Space

In articles [62-64] it was shown that in the study of 11-year cosmic ray variations it is necessary to take into account the lag in the electromagnetic conditions in interplanetary space with respect to the processes on the Sun which cause them. Basically, the phenomenon of this lag is determined by the dimensions of the modulation region, or, more accurately, by the time the solar wind (caused by the modulation of cosmic rays) moves from the Sun to the boundary with the galactic magnetic field. If this time is comparable with the period of the variation under investigation, considerable hysteresis should be observed in the relationship between the intensity of the cosmic rays and the solar activity parameter which determines the force of the wind.

However, first it must be determined what should be taken as this parameter. This can be the Zurich sunspot numbers (over the entire disk) with the aid of which solar activity is usually characterized, the sunspot numbers in a particular band of latitudes, the intensity of the green corona line, the number of chromospheric flares, the intensity of the solar radiation per 10 cm, etc. There is no single opinion on this matter, since it is not clear at all what is essential in the generation of the solar wind and the magnetic inhomogeneities, and basically on what the velocity of the wind and its force depend.

9.2. Integral or Differential Indices?

In article [62] the trial hypothesis was made that the parameter which determines changes in the solar wind are the Zurich sunspot numbers W (over the entire disk). Why was this parameter selected? It is well known that all characteristics of solar activity that were mentioned are in rough approximation,

sufficiently well correlated, so that in the beginning this question is meaningless. The exceptions are only the solar activity characteristics which refer to particular lattitude bands, since the zone where the activity concentrates is gradually displaced from the region of high latitudes to low latitudes during the solar activity cycle when it passes through the Royal zone (10-25° north and south from the helioequator) in the period of maximum solar activity. Therefore, changes in these characteristics are shifted in time relative to changes in the characteristics over the entire disk.

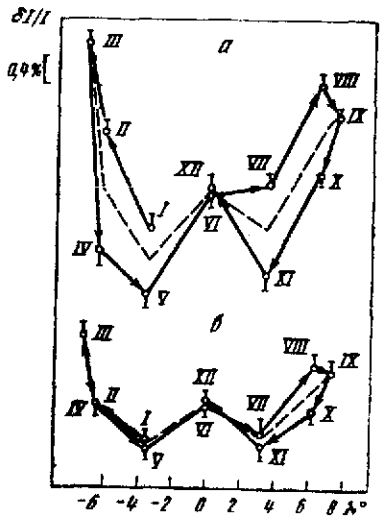

Fig. 6. Intensity of cosmic rays vs. Earth's heliolatitude according to data from a) worldwide network of neturon monitors, b) meson telescopes; in case b) corrections for the temperature effect have been introduced.

Roman numerals denote months, dashes indicate the mean course for the given heliolatitudes.

Thus, if the intensity of cosmic rays on Earth were controlled by solar activity in a narrow band of latitudes (which is possible in principle in the presence of a sufficiently regular quasi-radial interplanetary field which limits sharply diffusion in the direction perpendicular to the plane of the helioequator), a considerable part of the observed lag in the intensity of cosmic rays relative to the number of spots on the entire disk would have to be considered as fictitious. However, direct measurements of the magnetic fields in interplanetary space which have shown that inhomogeneous fields are comparable in magnitude with regular fields are a serious argument against such possibilities for high energy particles. In addition, according to the theory for the generation of the solar wind [48], its intensity must be mainly determined by the temperature of the corona, and therefore its flux can also be considerable at high heliolatitudes. /36

Another serious argument in favor of the characteristics of solar activity over the entire disk should be mentioned, namely, that according to study [65] based on data about the hard and neutron components obtained from the worldwide network of stations, the magnitude of the intensity gradient perpendicular to the plane of the ecliptic is very small $\leq$ 1%/0.1 AU (Fig. 6), i.e., almost one order of magnitude less than expected in [66] in the model of the solar wind bounded only by low latitudes. From this, it follows that the true modulation is close to that given by the spherical, symmetrical model. Therefore, probably the 11-year variation is controlled by solar activity indices over the entire disk.

9.3. Selection of a Model Taking into Account the Lag in the Processes in Interplanetary Space Relative to Solar Activity

An analysis of the anisotropic diffusion equations which was carried out in [67] has shown that when 11-year variations were investigated and the dimensions of the modulation region were sufficiently large, it was possible to use, in first approximation, a stationary isotropic diffusion model. The applicability of this model is limited to great rigidities ($R \sim 10^2 - 10^3$ BV), since for rigidities which are so large, the transport travels for the diffusion Λ in interplanetary space becomes comparable with the dimensions of the modulation region r_0, and a kinetic analysis must be used.

For small rigidities ($R \leq 1$ BV) the diffusion time of the particles $\sim r_0^2/\Lambda v$ becomes comparable with the characteristic times for the changes in intensity, and nonstationary equations must be considered.

Thus the data from the network of stations on Earth ($1 \text{ BV} \leq R \leq 10^2$ BV) lie in the region to which the stationary isotropic diffusion model can be applied.

But even in this simple model (which takes into account the damping of the particles which occurs due to the radial distribution of magnetic inhomogeneities), it is not possible to obtain analytic solutions which take into account the lag in the change $\Lambda(r)$ relative to the change w.

The exact solutions which were found in article [67], which are given in supplement 4 for the cases $\Lambda(r) = \text{const}$ and $\Lambda(r) \sim r$, show that they can be approximated with an accuracy up to 10% by the solutions of the balance equation for the particles, which is obtained from the condition for the equality of the diffusion flux $\varkappa\nabla n$ and the convection flux un. These solutions can be easily generalized to the case where the lag is taken into account.

These are the considerations which lead us to the conclusion that the sufficiently simple expressions for the modulation of cosmic rays in interplanetary space obtained in [62] /37

$$\frac{n(x, t, R)}{n_0(R)} = \begin{cases} \exp\left[-\dfrac{4{,}5u r_0 b}{v(R)\Lambda_{max}(R)}\right], & \text{if } \Lambda_{max}(R) \quad \text{const}, \\ \exp\left[-\dfrac{4{,}5u r_\delta d}{v(R)\lambda_\delta(R)}\right], & \text{if } \Lambda_{max}(R) \quad \Lambda_\delta(R) r_0 r/r_\delta, \end{cases} \tag{9.1}$$

are valid with a relative accuracy of about 10%.

Here $x \equiv r/r_0$, r_δ is the radius of the Earth's orbit, $\Lambda_{max}(R)$ is the transport travel for the diffusion at the maximum solar activity, and v(R) is the velocity of the particles. The b and d in (9.1) are determined from the variations in solar activity

$$b = \int_{x_\delta}^{1} \left[\frac{w(t - r_0 x/u)}{w_{max}}\right]^{-\alpha} dx; \quad d = \int_{x_\delta}^{1} \left[\frac{w\left(t - \frac{r_0 x}{u}\right)}{w_{max}}\right]^{-\alpha} \frac{dx}{x}, \tag{9.2}$$

where w_{max} is the Wolf sunspot number at maximum activity and $w(t - r_0 x/u)$ is the Wolf number at a particular instant of time, taking into account the lag in the processes in interplanetary space relative to the phenomena on the Sun, and u is the velocity of the solar wind, $x_\delta = r_\delta/r_0$.

With regard to the parameter α in (9.2), it determines the relation $\Lambda(r, t) \sim w^\alpha(t - r/u)$. Its magnitude is easily estimated. We will assume that inhomogeneities of various dimensions completely fill the interplanetary space[4] (i.e., the distance d between them is of the same order of magnitude as their dimensions b). Strictly speaking, the relation between the concentration of inhomogeneities $N(r, t) \sim d^{-3}$ and w is unknown, but it is natural to assume that $N(r, t) \sim w(t - r/u)$.

4. Direct observations of the magnetic fields show that probably this is the most realistic case.

Since $\Lambda \sim d^3 l^{-2}$ and $d \sim l$, $\Lambda(r, t) \sim w^{-1/3}(t - r/u)$, i.e., $\alpha = -1/3$.

9.4. Variation of Modulation Parameters with Solar Activity

Expression (9.1) takes into account, with the solar activity, only the variation in the single parameter Λ. However, in fact, the velocity of the wind changes (probably twice as much from minimum to maximum solar activity) and consequently also the radius of the modulation region

$$r_0 = 10^{-6} r_\delta u \sqrt{n_\delta} \min\{4 \cdot 10^{-6} H_{gal\perp}^{-1}; E_{c.r.}^{-1/2}\}, \qquad (9.3)$$

where n_δ is the solar wind concentration near the Earth's orbit, $H_{gal\perp}$ is the magnetic field which is perpendicular to the direction in which the solar wind of the component of the galactic magnetic field propagates in gauss; $E_{c.r.}$ is the density of the energy of cosmic rays reflected by the solar wind in eV/cm^3. It can be seen from (9.3) that r_0 must vary at least twice as much, and if the possible variation in n_δ with solar activity is taken into account, an even larger variation in r_0 should be expected.

Since in first approximation u and r are also related to w (as w increases, u and r_0 must also increase), their variation with the solar activity can be roughly taken into account by assuming that (9.1) includes a constant component u and r_0, and the variable component is reflected in (9.2) through the corresponding change in the parameter α. Since the exact value of α is not known, it can be estimated by comparing the expected variations in the intensity with the observed variations.

9.5. Comparison with Experiment, Determination of the Character of the Relation between Λ and r and the Estimate r_0 /38

Article [62] studied the case when $\Lambda_{max}(R)$ is independent of the distance from the Sun (Fig. 7a, b). As can be seen, the best agreement with the experimental data is obtained when r_0/u = 20 months and $\alpha = -1/3$.

It is of interest to study the case when $\Lambda_{max}(R)$ increases proportionally with r as the distance from the Sun increases (Fig. 7c, d). It can be seen from (9.1) that in this case, when the variations in the intensity are small, $\Delta n/n_0 = ad$, where $\alpha = \frac{4.5u_{dr}r_{\delta}}{v(R)\Lambda(R)}$ is a coefficient which depends only on the hardness of the particles. The character of the change d, according to (9.2), is determined for the given cycle of solar activity only by the parameter r_0/u.

Since the coefficient a is unknown, we will proceed as in [62]: we will join together the values for the maximum and minimum values of the intensity. The results of such a comparison of the intensity of the neutron component (cutoff rigidity 1.8 BV) with the expected values of the intensity when r_0/u - 20 months and α = - 1/3 are given in Fig. 7c. It can be seen from the figure that the observed hysteresis is larger than the expected hysteresis, even though for the same values of the parameters with Λ = const the experimental and theoretical hystereses were the same (Fig. 7b).

Physically, this result is related to the fact that when $\Lambda \sim r$, the radius of the region of space which plays an important role in the modulation is substantially smaller than the radius of the region of the vector r_0, since when Λ = const, these radii coincide. Figure 7c shows that when $\Lambda \sim r$, r_0/u must be much greater than 20 months, i.e., when $u = 3\cdot10^7$ cm/sec, r_0 must be greater than 100 AU. A hysteresis which is too narrow should also be expected when r_0/u = 40 months, i.e., $r_0 \approx 200$ AU. There is still considerable lack of correspondence even when r_0/u = 80 months, which corresponds to r_0 = 400 AU when $u = 3\cdot10^7$ cm/sec (Fig. 7d) /39

On the other hand, r_0 cannot be very large, since its magnitude is determined from expression (9.3), which follows from the condition for the equality of the solar wind pressure on one hand, and the galactic magnetic field and low energy cosmic rays reflected by the moving magnetic fields of the solar wind on the other hand. Assuming, for maximum solar activity, $u = 4\cdot10^7$ cm/sec $n_{\delta} = 10$ cm^{-3}, we obtain due to the finiteness of the magnetic field, $r_0/r_{\delta} = 170$ AU for $H_{gal\perp} = 3\cdot10^6$ gauss.

The solar wind along the magnetic field can spread over considerably larger distances. However, in addition to the anisotropic pressure of the magnetic field, the isotropic pressure of the low energy

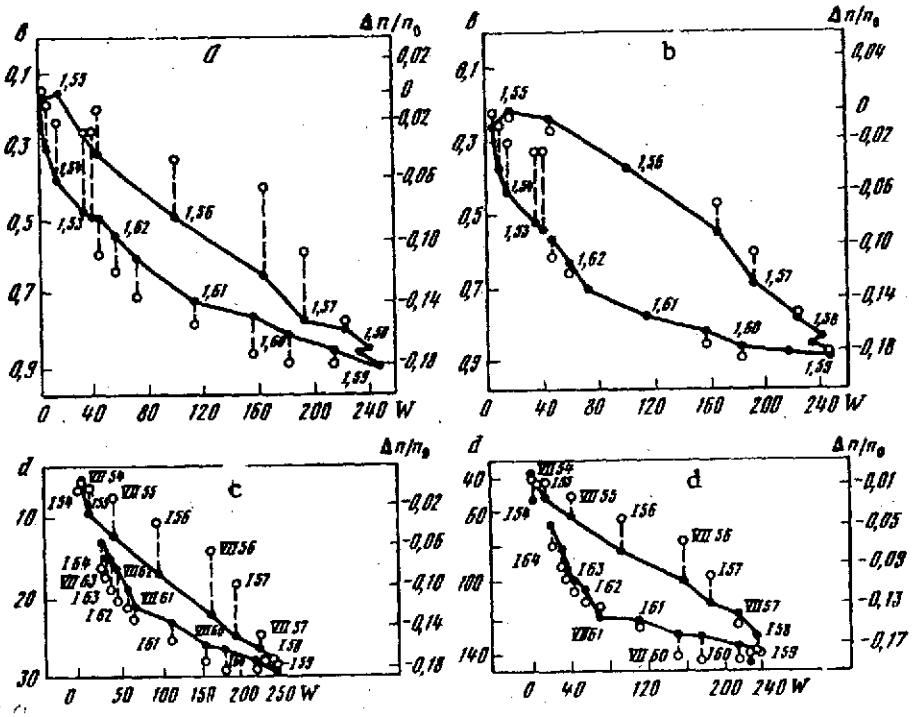

Fig. 7. Expected changes in the integrals b (Λ = const) and d ($\Lambda \sim r$) vs. the values of the sunspot numbers smoothed over a period of 12 months compared with observation data ($\Delta n/n_0$ on the neutron component of cosmic rays in Chicago (in Figs. c and d, the light circles indicate experimental values, and the dark circles the theoretical values. Roman numerals indicate months, Arabic numerals, years).

a--r_0/u = 10 months ($\Lambda \sim$ const); b--r_0/u = 20 months (Λ = const); c--c_0/u = 20 months ($\Lambda \propto r$); d--r_0/u = 80 months ($\Lambda \propto r$)

galactic cosmic rays reflected from the wind must also be taken into account. Since the energy density of these particles is $E_{c.r.} \approx 1$ eV/cm^3 (see below, Section 9.11), for the above-mentioned solar wind parameters, the maximum possible value is $r_0 \approx 120$ AU, the basic limitation must be produced by cosmic rays. This implies that the value $r_0 \geq 400$ AU

is inapplicable with a large margin and, hence, the case $\Lambda = r$ does not occur for some reason.

9.6. Model with Wide Spectrum of Magnetic Inhomogeneities

First, we note that according to the model for the magnetic clouds, i.e., according to the formula

$$\Lambda = d_\delta^3 \left(\frac{r}{r_\delta}\right)^3 \left[l_\delta + \frac{(r - r_\delta) u_{3B}}{u}\right]^{-2} \left[1 + \left(\frac{R}{300Hl}\right)^2\right] \qquad (9.4)$$

we must have in the region $R \geq 300\ Hl \sim R^2$ since it follows from the data [2] that this relation holds only when $R \geq 15$ BV, and in regions where R is smaller $\Lambda \sim R$ holds. This indicates that in accordance with the conclusions in [68] the scattering of the particles occurs in the wide spectrum of inhomogeneities, and the most effective are those particles whose dimensions are comparable with the Larmor radius in the magnetic field (when $\Lambda \sim R$).

According to [69], the transport travel for the scattering of the particles in the presence of a wide spectrum of inhomogeneities with the field $h \ll H$ in quasilinear approximation will be

$$\Lambda \approx \frac{v}{g\omega} \left(\frac{k}{H^2} \frac{dh^2}{dk}\right)^{-1}, \qquad (9.5)$$

where the coefficient $g \approx 2 - 3$, $\omega = \frac{ZeHc}{\epsilon}$, $k = \frac{\omega}{v}$, ϵ is the total energy of the particle and v is its velocity. From (9.5) it is easily seen that when $H \sim r^{-1}$, $w \sim r^{-1}$, $k \sim r^{-1}$ and $\Lambda \approx$ const with the condition that the spectrum dh^2/dk of the inhomogeneities is independent of r.

Beyond the boundaries of the Earth's orbit, the main role for the 11-year variation is played by the transverse diffusion coefficient

$$\varkappa_\perp \approx \frac{r\Lambda}{3(1 + \omega^2\tau^2)}, \qquad (9.6)$$

where $\omega\tau = \frac{300\,\Lambda H}{R}$.

When $\Lambda \sim$ const and $H \sim r^{-1}$, $\omega\tau \sim r^{-1}$ and in the main part of the modulation region $\omega\tau \lesssim 1$, so that $\varkappa_\perp \approx \frac{V\Delta}{4}$ = const which agrees with the results in Section 9.5. It should be mentioned /40
that in the wide interval of rigidities ($R \lesssim 15$ BV) the quantity $\omega\tau$ is independent of R, since $\Lambda \sim R$. Hence, the dependence of $\varkappa_\perp$ on R will be the same as for Λ, i.e., $\varkappa_\perp \sim R$.

However, in the range of very large rigidities ($\gtrsim 15$ BV), in [64] it was found that $\varkappa_\perp \sim R^2$. If $\omega\tau \lesssim 1$ (i.e., if $\Lambda \gtrsim \frac{R}{300H}$), this means that $\Lambda \sim R$. If $\omega\tau \gtrsim 1$ (i.e., if $\Lambda \gtrsim \frac{R}{300H}$), it follows from (9.6) that to explain $\varkappa_\perp \sim R^2$ we must assume that Λ is independent of R. But the condition $\omega\tau \gtrsim 1$ cannot be applied since $\varkappa_\perp \sim r^2$, which contradicts the results in Section 9.5. Nevertheless, if the condition $\omega\tau \gtrsim 1$ is used to obtain agreement with the results in Section 9.5 (i.e., that $\varkappa_\perp$ is independent of r), we must set $\Lambda \sim r^2$. Here, in the range $R \lesssim 15$ BV, $\Lambda \sim R$, and in the range $R \gtrsim 15$ BV (where $\varkappa_\perp \sim R^2$) $\Lambda \sim$ const, which is hardly applicable for very hard particles whose scattering takes place on the largest scale inhomogeneities, and due to multiple scattering at large angles we should expect $\Lambda \sim R^2$.

Thus, apparently we can assume that for the main part of the modulation range in the rigidity interval $\omega\tau \lesssim 1$ of interest, the diffusion is nearly isotropic.

9.7. The Relation Between the Effective Dimension of the Modulation Range and the Hardness of the Particles

The modulation of high-energy particles behind the boundaries of the Earth's orbit is mainly determined by the quasi-regular radially expanding interplanetary magnetic field whose lines of force have the form of spirals of Archimedes, in the presence of a sectorial structure and a wide spectrum of magnetic inhomogeneities. Behond the boundaries of several radii of the Earth's orbit from the Sun, the magnetic field is mainly azimuthal, the spiral of Archimedes gives a complete turn in an interval of approximately 6 AU (at a velocity of 300 km/sec) while the size of this interval does not depend, for all practical purposes, on the distance from the Sun. Thus, to create an 11-year cosmic ray variation, diffusion of the particles across the magnetic field is essential, and the maximum scale of the inhomogeneities will be the interval on which the spiral of Archimedes makes a complete turn, i.e., ~ 6 AU.

But also smaller scale inhomogeneities participate in the diffusion of particles (sectors which are 1-2 AU wide, etc.). Since the intensity of the magnetic field decreases as r^{-1}, the radius of curvature of the particles in the magnetic fields will be $\sim r$ as their distance from the Sun increases. But the maximum dimensions of the scattering formations do not vary with r, since for particles with a given rigidity R, for some $r > r_{max}$, the scattering will not be effective. For very hard particles, we may have $r_{max} < r_0$. In this case, the effective parameter which determines the magnitude of the hysteresis is not r_0/u but r_{max}/u, which will be smaller the harder the particles.

We will estimate r_{max} for the case when the neutron component was observed, when the effective energy of the recorded particles if R_{eff}. Since the azimuthal component of the interplanetary magnetic field near the Earth's orbit is $\sim 5\gamma$, $H(r) \sim t(r/r_\oplus)^{-1} \cdot 10^{-5}$ gauss. If we take for the maximum dimension of the inhomogeneity the quantity l_{max}, the condition R_{eff} implies

$$r_{max} \approx 225 l_{max}/R_{eff} \qquad (9.7)$$

where R_{eff} is measured in Bv.

If $l_{max} \sim 6$ AU and $R_{eff} \approx 30$ Bv((recorded by a neutron monitor on the equator), $r_{max} \approx 45$ AU. When the neutron component was recorded at medium latitudes, $R_{eff} \sim 7 - 10$ Bv and $r_{max} \sim 190 - 135$ AU.

Hence, for high energy particles the effective modulation region may turn out to be considerably smaller than the region occupied by the solar wind. For comparatively low energy particles $r_{max} \approx r_0$, and, in this case, the quantity which determines the modulation is r_0. /41

Figure 8 gives the observed variations in the intensity of the neutron component at several stations. The same figure shows the expected variations in the intensity when $\alpha = -1/3$, $\Lambda \sim$ const, $r_0/u = 10$, 20, 30 and 40 months (which corresponds to $r_0 = 50$, 100, 150 and 200 AU for $u = 3 \cdot 10^7$ cm/sec). It is evident from Fig. 8 that the magnitude of the hysteresis decreases as the effective rigidity of the recorded particle increases.

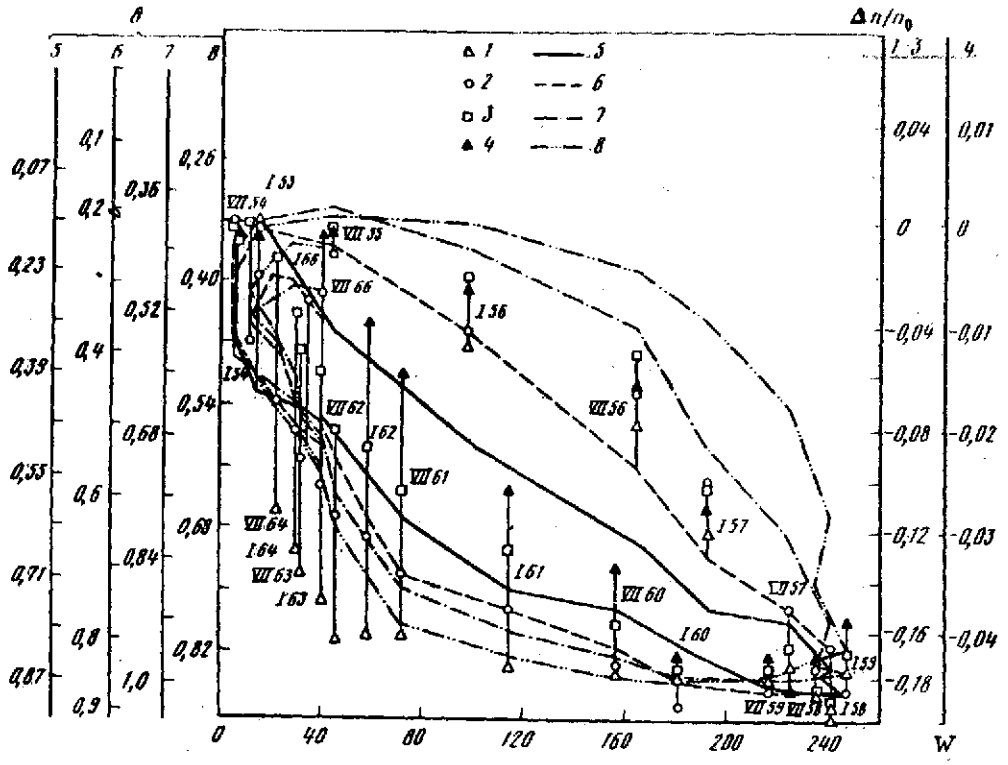

Fig. 8. Comparison of observed changes in the intensity of the neutron component of cosmic rays smoothed using a moving average with a period of 12 months vs. the smoothed sunspot numbers W with the same period and the expected variations when Λ = const, α = - 1/3.

1--Ottawa, cutoff rigidity 1.2 BV; 2--Chicago, 1.8 BV; 3--Climax, 3.2 BV; 4--Uankayo, 13 BV; 5-8--r_0/u = 10, 20, 30 and 40 months, respectively (left scales); the scales $\Delta n/n_0$ are reduced for the curves 1-4, Roman numerals indicate months, Arabic numerals, years.

9.8. The Validity of the Stationary Solution for the 11-Year Variation

In addition to the characteristic mentioned above, it follows from Fig. 8 that the restoration of the intensity after the period of maximum solar activity occurs with a considerable "lag," which is larger the less hard the particles. This "lag" is particularly large at the Ottawa station, where its duration is approximately 2-3 years, since 1961. However, it is already much smaller at the Chicago station. What is the reason for this phenomenon?

Basically, it may be related to the fact that we used the solution of the stationary equation, and thus ignored the lag with which the volume of wind is filled by galactic cosmic rays due to the finite diffusion time. We will estimate this time /42

$$t_{diff} \approx \frac{r_0^2}{2\lambda v}, \qquad (9.8)$$

which gives for r_0 = 100 AU, $v = 3 \cdot 10^{10}$ cm/sec, R ~ 30 - 40 BV (or, according to [62], $\Lambda \approx 7 \cdot 10^{13}$ cm), $t_{diff} = 5 \cdot 10^5$ sec $\leq$ 0.02 year, i.e., in this case t_{diff}, when compared with the "lag" under consideration, can be ignored. For particles of rigidity 6 - 10 BV (neutron monitors at medium latitudes) $\Lambda \sim 1.5 \cdot 10^{13}$ cm and $t_{diff} \approx 2.5 \cdot 10^6$ sec < 0.1 years, i.e., it is also substantially smaller than the "lag" time. Even for observations in the stratosphere in the high latitude range (R ≈ 2 - 3 Bv) $\Lambda \sim 3{,}6 \cdot 10^{12}$ cm and $t_{diff} \approx 0.3$ year, which is considerably less than the "lag" time.

Two important conclusions follow from the estimates of t_{diff} that were given.

1. Since, for particles with rigidity R $\geq$ 2 - 3 BV t_{diff} turned out to be considerably smaller than the characteristic times with which the intensity of cosmic rays varies in the 11-year variation, the global properties of the solar wind can be studied on the basis of measurement data using neutron monitors at sea level and at mountain level, and also the total intensity can be studied with the aid of balloons using the solution for the stationary problem.

2. When nonstationarity is taken into account in the study of 11-year variations, it does not explain the reason for the "lag" phenomenon that was detected in the restoration of the cosmic ray intensity in the period of declining solar activity.

9.9. The Existence of a Turbulent Layer Between the Solar Wind and the Interstellar Medium

On the basis of the discussion in Section 9.8, we are of the opinion that the real reason for the "lag" is the formation near the solar wind boundary with the galactic magnetic field

and the galactic low energy particles, of an almost stationary spherical layer with a relatively small transport travel for the scattering of the particles (i.e., a layer which does not reduce the intensity for all practical purposes). In the period of high solar activity a large number of magnetic inhomogeneities which do not have time to "scatter" in the interplanetary space are forced into this layer.

If the thickness of such "buffer" layer is L_b, the transport travel of the particles inside this layer is Λ_b, the time during which the lag occurs through restoration is

$$T_b \approx \frac{L_b^2}{2\lambda_b v} \qquad (9.9)$$

where v is the velocity of the particles. Assuming that $R \sim 3 - 5$ BV, $T_b \sim 3 \cdot 10^7$ sec, $v \approx 3 \cdot 10^{10}$ cm/sec, we obtain $L_b^2/\Lambda_b \sim 2 \cdot 10^{18}$ cm. When $L_b \sim r_0 \cdot 10^2$ AU, $L_b/\Lambda_b \sim 10^3$ and $\Lambda_b \sim 1.5 \cdot 10^{12}$ cm. But in order that particles of rigidity 3 BV be effectively scattered, it is necessary that this layer have inhomogeneities whose dimensions are $\sim 10^{12}$ cm with fields $H_b \sim 10^{-5}$ gauss. On the other hand, the intensity of the galactic field is $H_r \sim 3 \cdot 10^{-6}$ gauss and of the interplanetary field at a distance of $r \sim 100$ AU from the Sun, when $H \sim r^{-1}$, it is $\sim 5 \cdot 10^{-7}$ gauss.

Hence, the magnetic field in the "buffer" layer must be considerably strengthened, due to the large quantities of plasma with the "frozen" magnetic field forced into it in the period of high solar activity. The pressure of the "buffer" layer will be maintained by the galactic magnetic field, and the low energy galactic cosmic rays. Along with the compression of the magnetic field, /43
compression of the plasma must also occur, since its density in the buffer layer must be at least one order of magnitude greater than that usually assumed for solar plasma at such distances from the Sun.

The degree of "lag" in the period when the intensity of the cosmic rays is restored after solar activity has reached its maximum, depends, to a considerable extent, on the hardness of the particles. Figure 8 shows that if, on the rising branch of solar activity, the relative variations at the four stations that were mentioned are approximately the same, i.e., the spectrum of the variations changes relatively little in this period, on the descending branch, the spectrum of the variations

is considerably gentler, which can be seen clearly from the change in the ratio of the dip amplitudes. I (>1,2 BV): I (>1.8 BV): I (>3.2 BV): I(<13.5 BV). If we take these ratios in 1958-1959 as 1:1:1:1, the ratios will change as follows:

July 1960.	.1:0.98:0.75:0.60
January 1961	.1:0.88:0.75:0.60
July 1961.	.1:0.85:0.64:0.40
January 1962	.1:0.75:0.54:0.30
January 1963	.1:0.68:0.43:0.06

Thus, in January 1963 the role played by low energy particles (~ 2 - 3 BV) in comparison with high energy particles (~ 20 - 30 BV) was almost 15 times as great as during maximum solar activity. In our opinion this is mainly a consequence of the fact that in order that the low energy particles from the galaxy pass through the buffer layer into interplanetary space, much more time is needed than for high energy particles[5] so that for a long time, in spite of the considerable attenuation with which the particles are forced out from the galaxy, the intensity level remains almost the same as in the period of high solar activity (formally, according to [70], this is related to the fact that in this period the solution is determined by the diffusion equation with a modified boundary condition which corresponds to the reduced intensity on the boundary).

9.10. The Energy Spectrum of Cosmic Rays Beyond the Boundaries of the Solar System

It was shown in [71] that to find the spectra of the rigidities beyond the boundaries of the solar system and to determine independently the modulation parameters from the measurement data in n periods of solar activity which are modulated by the spectra of particles of the k-th type (with different Z/z), it is necessary to solve kn equations

$$D_{Mij}(R,r) = D_{0i}(R)\exp\{-\alpha_j(R,r)/\beta_i(R)\}, \qquad (9.10)$$

where $1 \leq i \leq k$, $1 \leq j \leq n$. Here $D_{M_{ij}}(R, r)$ is the observed modulated spectrum of a particle of type i in the solar activity

5. This is apparently due to the fact that Λ_b in formula (9.9) increases substantially with an increase in the particle rigidity.

period j; $D_{0j}(R)$ is the unperturbed spectrum beyond the boundaries of the modulation region of the particle of type i, $\alpha_j(R, r)$ is the modulation parameter which is determined in the spherical symmetrical model from the expression

$$a_j(R, r) = \frac{4,5}{c} \int_r^{r_0} \frac{\omega_{ij}\, dr}{\lambda_j(R)}. \qquad (9.11)$$

Finally $\beta_j(R)$ is the velocity of a particle of type i with charge $Z_i l$, and rest mass $A_i M$ in units of light velocity

$$\beta_i(R) = R\,[R^2 + (A_i M c^2/z_i e)^2]^{-1/2}. \qquad (9.12)$$

Considering $D_{0i}(R)$ and (R, r) as k + n unknowns, we obtain the consistency condition for the system of equations (9.10)

$$(D_{M1j}\, D_{M1j'})^{\beta_1} = (D_{M2j}\, D_{M2j'})^{\beta_2} = \ldots = (D_{Mkj}\, D_{Mkj'}) \qquad (9.13)$$

for any $j \neq j'$. It is easily seen that the number of independent consistency conditions (9.13) is k - 1 and n - 1. In the special case when protons and α-particles are measured, condition (9.13) can be rewritten in the form

$$\frac{\ln |D_{M2_i}(R, r)/D_{M22}(R, r)|}{\ln |D_{Mp1}(R, r)/D_{Mp2}(R, r)|} = \frac{\beta_p}{\beta_\alpha} = \sqrt{\frac{R^2 + 3,52}{R^2 + 0,88}}. \qquad (9.14)$$

Figure 9 gives R vs. $\ln [D_{M\alpha 1}/D_{M\alpha 2}]/\ln[D_{Mp1}/D_{Mp2}]$, for the periods 1963 (for the α-particles, the observation data [72-73] were used and for the protons, the data from [73-76] and 1965 (for the α-particles, the data [72, 73, 76] were used and for the protons, the data [73 and 76]). The theoretical relation between the above-mentioned ratio and k, according to (9.14), is also given. When it coincides with the experimental relation, the system of equations (9.13) is consistent. Unfortunately, so far, the complete interval in which the simultaneous measurements of the differential spectra of protons and α-particles were

carried out is comparatively small ($R \geq 0.5$ BV). Of greatest interest is the range of small rigidities where β_p and β_α are much smaller than 1, and differ from one another considerably (in the range of rigidities $R \geq 2$ BV condition (9.14) is satisfied with greater accuracy. Figure 9 shows that within the /45

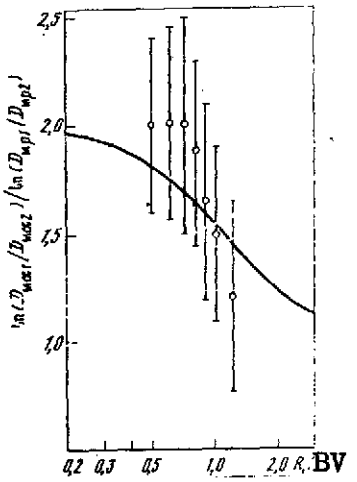

Fig. 9. Observed ratio (left member in expression (9.14) from the results of the measurements of the spectra of the proton and α-particles in 1963 and 1965 vs. the particle rigidity. The solid curve indicates the expected ratio [right member in expression (9.14)].

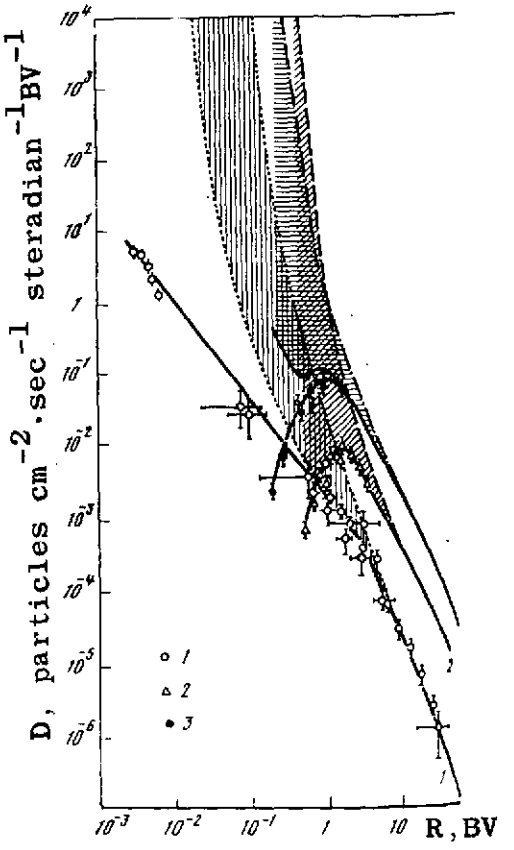

Fig. 10. Observed spectra of: (1) Electrons, (2) α-particles, (3) Protons according to various measurements carried out in balloons and satellites and expected spectra beyond the boundaries of the solar system (vertical dashes for electrons, slanted dashes for α-particles and horizontal dashes for protons).

experimental error, condition (9.14) is satisfied up to $R \geq 0.5$ BV. When condition (9.13) is satisfied, the system of equations (9.10) is consistent and the number of independent equations in this system reduces to $kn - (k - 1)(n - 1) = k + n - 1$ when the number of unknowns is $k + n$.

Thus, all $D_{0i}(R)$ and $\alpha_i(R, r)$ can be expressed in terms of one variable, which, in turn, must be found by some independent method. In particular, this method can be the taking into account of the hysteresis phenomenon in the 11-year cosmic ray variations as described above (see Section 9.3), which can be used to obtain the absolute values of the reduced intensity at any solar activity period.

We will try to correct the observation data on protons and α-particles (1963) and electrons (1962-1964) (Fig. 10). To do this we proceed as follows: comparing (see Fig. 8) the absolute modulation of the neutron intensity in Chicago (cutoof rigidity 1.8 BV) and in Climax (cutoff rigidity 3.2 BV), we find for 1963 $a(\bar{R}) \approx 1$, where $\bar{R} \approx 2.3$ BV. To make the transition to the low energy range, we must know how a depends on R. By comparing the data on the neutron and rigid components at the maximum and minimum solar activity, using the method of coupling coefficients, it was shown in article [64] that in the rigidity range $3 \text{ BV} \leq R \leq 12 \text{ BV}$ $a \sim R^{-1.8 \pm 0.2}$. The result was confirmed in [62]. On the other hand, from a comparison of the spectra of protons and α-particles, using rather coarse observation data from balloons in 1963, the values found were $a(1 \text{ BV}) \approx 1$, $a(0.7 \text{ BV}) \approx 2.4$ [77]. According to the analysis [78] which was based on more accurate measurements of the spectra of protons and α-particles on the IMP-1 satellite in late 1963 and early 1964, the values found were $a(1 \text{ BV}) = 0.22$, $a(0.5 \text{ BV}) = 0.51$. For the low energy range, apparently preference should be given to the more accurate result [78], according to which $a(R) \approx 0.25R^{-1}$ in the beginning of 1964.

This character of the relation also confirms well study [79] which was carried out on the basis of observation data on protons and α-particles [80, 81] on the IMP-1, 2, and 3 satellites in December 1963 through September 1965. The following relations which follow from (9.10) were used:

$$\ln \frac{D_{\text{мр1}}(R)}{D_{\text{мр2}}(R)} = \frac{\sqrt{R^2 + 0{,}88}}{R} [a_2(R) - a_1(R)];$$
$$\ln \frac{D_{\text{м}\alpha 1}(R)}{D_{\text{м}\alpha 2}(R)} = \frac{\sqrt{R^2 + 3{,}52}}{R} [a_2(R) - a_1(R)]. \qquad (9.15)$$

The difference $a_2(R) - a_1(R)$ can be found with the aid of (9.15) from measurements of the spectra of protons and α-particles at different instants of time. In [79] it was shown that $a_1(R) - a_2(R) = 0.12R^{-1}$ follows from a comparison of the data for December 1963-May 1964 (period 1) and October-November 1964 (period 2). A comparison of the data in periods 2 and 3 (June-September 1965) gives $a_2(R) - a_3(R) = 0.04\ R^{-1}$. Since, $a_1(R) - a_3(R) = 0.16\ R^{-1}$, it follows that at the end of 1963 a(R) was larger than $0.16\ R^{-1}$ (since in June-September 1965 there was still a residual modulation which is clearly seen in Fig. 8). This result applies to $R \geq 0.4$ BV. Thus, we can assume approximately for 1963-1964 $0.2\ R^{-1} \leq a(R) \leq 2 \cdot R^{-1}$.

Using these extreme values, the spectra of protons, α-particles and electrons can be corrected and the expected spectra of these particles beyond the modulation region can be found (see Fig. 10). On the basis of Fig. 10, the following conclusions can be made.

First, the undistorted spectra of protons and α-particles can be represented in the form $\sim R^{-2.5} - R^{-3}$ for large rigidities up to the rigidities 0.2 - 0.4 BV. The undistorted spectrum of electrons can be represented in the same form. It is possible that this form of the spectrum will be preserved all the way up to $R \sim 0.1$ BV. /46

Second, if we assume that the relation $a(R) \sim R^{-1}$ is preserved up to rigidities smaller than 0.1 BV, the exponent in the electron spectrum must increase considerably. The density of the electron energy must be many orders of magnitude greater than the energy of the magnetic fields in the galaxy, which is impossible for many reasons (tremendous magneto-inhibiting radiation would have to be observed, the relatively weak magnetic fields could not hold the particles). It follows that in the range of small rigidities the dependence of a on R is considerably weaker than say a(R) = const. In this range of rigidities up to several megavolts, the undistorted spectrum for electrons will differ from the observed spectrum by a constant factor (since for electrons we still have $v = c$). The study of the spectrum of the inhomogeneities of the magnetic field in interplanetary space [79] also supports this change in the character of the dependence of a on R.

9.11. The Density of the Energy of Cosmic Rays in the Galaxy

According to [82], the density of the energy of protons in the galaxy in the vicinity of the solar system is $W_p = 0.65\ eV/cm^3$, of α-particles, $W_\alpha = 0.18\ eV/cm^3$, of nuclei $W_{Z>2} = 0.08\ eV/cm^3$,

and of all cosmic rays $W_{c.r.} = 0.9$ eV/cm^3. These values were obtained from measurement data in 1955-1956. It was assumed that modulation of the spectrum did not take place in that period. However, Fig. 8 shows that even in this period the intensity of cosmic rays near the Earth's orbit was substantially lower than beyond the boundaries of the modulating region (for this period $a(R) \approx 0.3/R$, according to the same diagram for 1963, $a(R) \approx 1/R$, which agrees with the extreme values $2/R$ and $0.2/R$ that were adopted above). When $D_{0p}(R)$ is the undistorted spectrum of the protons,

$$W_i = 3 \cdot 10^{-9} \int_{R_{min}}^{\infty} \frac{4\pi}{\beta_i(R)} D_{0i}(R) E_{ki}(R) dR \text{ eV/cm}^3 \qquad (9.16)$$

where R - b BV, $\beta_i(R)$ is determined according to (9.12) and the kinetic energy of the particles is

$$E_{ki}(R) = \sqrt{Z_i^2 R^2 + (A_i Mc^2/Z_i e)^2} - A_i Mc^2.$$

Using the data for large rigidities which were given in [82], and the results that were obtained here for the range of small rigidities, we can write for 0.2 BV $\leq R \leq 10^3$ BV

$$D_{0i}(R) = K_i R^{-\gamma} \text{ particles} \cdot \text{cm}^{-2} \text{sec}^{-2} \cdot \text{Bv}^{-1}, \qquad (9.17)$$

where $K_p = 0.7$; $K_\alpha = 0.1$; $K_e = 0.01$; $K_{Z>2} = 0.087$.

The table gives the expected densities of the energy in cosmic rays in the range $R > R_{min}$.

The table shows that if modulation is taken into account, the density values of the energy of cosmic rays in galactic space that are usually used can increase several times. This implies, as we already mentioned in Section 9.4-9.5 that they can be the main barrier which limits the spreading of the solar wind.

EXPECTED VALUES OF THE ENERGY DENSITIES W(eV/cm^3) OF PRIMARY COSMIC RAYS BEYOND THE BOUNDARIES OF THE SOLAR SYSTEM. RIGIDITY $R \geq R_{min}$ WHEN $\gamma = 2.5$ /47

Particles	R_{min}, Bv							
	10.	2.5	1.5	0.5	0.2	0.1	0.02	0.01
Protons	0.18	0.32	0.37	0.52	0.77	1.04	2.18	3.04
α-particles	0.05	0.09	0.10	0.14	0.21	0.29	0.61	0.84
Nuclei Z > 2	0.02	0.04	0.05	0.06	0.09	0.13	0.27	0.38
Electrons	0.0036	0.0052	0.0067	0.0116	0.0184	0.026	0.058	0.082
Total W	0.25	0.46	0.53	0.73	1.09	1.49	3.12	4.34

9.12. The Possibility of Accelerating the Particles in the "Buffer" Layer

We already discussed in Section 9.9 the properties of the "buffer" layer between the solar wind and the interstellar medium. Due to intense turbulent motion of the magnetized plasma in this layer, the particles can be accelerated, or the energy of the low energy particles emitted from the galaxy into the solar system can be increased.[6]

In fact, the energy of the solar wind carried by them into the "buffer" layer is

$$W \approx \frac{\rho_\delta u^3}{2} u 4\pi r_\delta^2 \approx 3 \cdot 10^{25} \text{ erg/sec.}$$

If we assume that the main part of this energy is ultimately converted into the energy of the cosmic rays, we obtain for the power of this source $\sim 3 \cdot 10^{37}$ eV/sec. From the above (Section 9.9) it follows that the life of low energy particles in the "buffer" layer is ~ 2 years and if ionizing losses are ignored, the total

6. In principle, the cosmic ray particles can be accelerated by the turbulent pulsations also in the main part of the solar wind where the radial velocities are large. However, in this case apparently the antiphermium damping mechanisms, which diverges radially through the magnetic inhomogeneities, will dominate.

energy transferred to the cosmic rays in this time is $\sim 2 \cdot 10^{45}$ eV, which corresponds to an energy density of ~ 0.1 eV$\cdot$cm^3 which is comparable to the energy density in the low energy range of cosmic rays (when the thickness of the buffer layer is ~ 100 AU in a volume of $\sim 3 \cdot 10^{46}$ cm^3).

The acceleration parameter for non-relativistic particles is

$$\alpha = \frac{1}{e_k} \frac{de_k}{dt} = \frac{2u_6^2}{\Lambda_6 v},$$

where u_b are the random velocities with which the inhomogeneities move in the buffer layer, v is the velocity of the particles, and Λ_b is the transport travel for scattering. It can be easily seen that the acceleration is considerable if $\alpha > \frac{1}{\tau_1} 2 \cdot 10^{-8}$ sec^{-1} (where $\tau_1 \sim 6 \cdot 10^7$ sec is the life of the particle in the layer), which requires for $\Lambda_b \sim 10^{12}$cm, $v \sim 10^9 \sim 10^{10}$cm/sec, which is not impossible. The effect of the "buffer" layer on the energy of the relativistic particles will be negligible since Λ_b increases and T_1 decreases.

Thus the "buffer" layer can distort considerably the results of the diffusion model not only because of the "lag" phenomenon, but also because the particles may be accelerated in this layer. This fact is especially important for low energy particles.

Supplement 1. Estimate of Possible Variations in the Effective Geomagnetic Cutoff Rigidity due to the Presence of the Penumbra for a Constant Geomagnetic Field

/48

If $f_k(R)$ is a function which takes on the values 1 and 0, respectively for the permitted and forbidden directions at the observation point k, the effective cutoff rigidity R_k for the primary cosmic rays with the spectrum D(R) is determined from

the equation[7]

$$\int_{R_{kmin}}^{R_{kmax}} f_k(R)\, D(R)\, dR = \int_{R_{kmin}}^{R_{kmax}} D(R)\, dR, \qquad \text{(A1.1)}$$

where $R < R_{kmin}$ is the region of forbidden directions, and $R > R_{kmax}$ is the region of permitted directions, and $R_{kmin} \leq R \leq R_{kmax}$ is the region of the penumbra.

The effective cutoff rigidity R for the secondary component of type i is determined analogously when it is recorded on the observation level

$$\int_{R_{kmin}}^{R_{kmax}} f_k(R)\, m^i(R, h_0)\, D(R)\, dR = \int_{R_k^i(h_0)}^{R_{kmax}} m^i(R, h_0)\, D(R)\, dR \qquad \text{(A1.2)}$$

or

$$\int_{R_{kmin}}^{R_{kmax}} f_k(R)\, W_0^i(R, h_0)\, dR = \int_{R_k^i(h_0)}^{R_{kmax}} W_0^i(R, h_0)\, dR, \qquad \text{(A1.3)}$$

where $W_0^i(R, h_0)$ is the coupling coefficient at the observation point with zero cutoff rigidity. Strictly speaking, when the primary spectrum changes, the effective cutoff rigidity will also change somewhat according to the definition

$$\int_{R_{kmin}}^{R_{kmax}} f_k(R)\, W_0(R, h_0) \frac{\Delta^j D(R)}{D(R)}\, dR = \int_{R_k^{ij}(h_0)}^{R_{kmax}} W_0^i(R, h_0) \frac{\Delta^j D(R)}{D(R)}\, dR. \qquad \text{(A1.4)}$$

Taking into consideration that the interval R_{kmin} - R_{kmax} is comparatively small, the change in the coupling coefficient $W_0^i(R, h_0)$ can be represented as a power function

$$W_0^i(R, h_0) \sim R^{a_i}, \tag{A1.5}$$

where a_i is positive in the low energy range and negative in the high energy range. In exactly the same way, the primary variation can be represented in the interval R_{kmin} - R_{kmax} by the power function

$$\Delta^j D(R)/D(R) \sim R^{a_j}. \tag{A1.6}$$

Thus, the integrand in the right member of (A1.4) can be represented in the interval R_{kmin} - R_{kmax} in the form

$$W_0^i(R, h_0) \frac{\Delta^j D(R)}{D(R)} = AR^{b_{ij}}, \tag{A1.7}$$

where $b_{ij} = a_i + a_j$, and A is a constant which is not essential in the subsequent calculations. As we already mentioned, the function $f_k(R)$ can be expressed in the form /49

$$f_k(R) \begin{cases} 1, & \text{if } R_{k,2n-1} \leq R \leq R_{k,2n} \\ 0, & \text{if } R_{k,2n} \leq R \leq R_{k,2n+1}, \end{cases} \tag{A1.8}$$

where $1 \leq n \leq l$, when $R_{k,1} \equiv R_{kmin}$, $R_{k2l} \equiv R_{kmax}$. Substituting

7. It should be noted that the definition of the effective cutoff rigidity given in [4] by the equation $\int_0^\infty f_k(R)\, dR = \int_{R_k}^\infty$ is only valid for the case when the spectrum of the primary cosmic rays has the form D(R) = const. However, in the real case, definition (A1.2) or (A1.3) must be used.

(A1.7) and (A1.8) in (A.14), we obtain

$$\sum_{n=1}^{l}\left(R_{k,2n}^{b_{ij}+1}-R_{k,2n-1}^{b_{ij}+1}\right)=R_{k\max}^{b_{ij}+1}-\left|R_{k}^{ij}(h_0)\right|^{b_{ij}+1}, \qquad \text{(A1.9)}$$

from which we obtain the unknown effective cutoff rigidity

$$R_{k}^{ij}(h_0)=\left[R_{k\max}^{b_{ij}+1}-\sum_{n=1}^{l}\left(R_{k,2n}^{b_{ij}+1}-R_{k,2n-1}^{b_{ij}+1}\right)\right]^{\frac{1}{b_{ij}+1}}. \qquad \text{(A1.10)}$$

Thus, for each observation point, the effective cutoff rigidity is a function of b_{ij} which can be found from formula (A1.10). The results of the corresponding calculations [3] that were carried out for $j_k(R)$ for the geomagnetic latitudes λ = 30, 40, and 50° in the dipole approximation in the interval in which b_{ij} varies from + 3 to - 8 can be written, approximately, for the geomagnetic latitudes λ = 30, 40 and 50° in the form

$$R_{j}^{ij}(h_0)=\begin{cases}9.45+0.093b_{ij}\ \text{BV, when}\ \lambda=30^{\circ}\\ 5.38+0.045b_{ij}\ \text{BV, when}\ \lambda=40^{\circ}\\ 2.675+0.007b_{ij}\ \text{BV, when}\ \lambda=50^{\circ}\end{cases} \qquad \text{(A1.11)}$$

Examples of expected variations in the effective geomagnetic cutoff rigidity are given in Table 1. The values of the exponents a_i for various coupling coefficients were taken from [2]. It can be seen from the table that even in the quiet period the effective geomagnetic cutoff rigidity changes considerably when various components are recorded. At the geomagnetic latitude 30° the effective rigidity varies from 9.20 BV (recorded on satellites at low altitudes) to 9.33 BV (for the entire neutron component at sea level) and to 9.56 BV for the hard component at sea level).

Such changes must be taken into account in the analysis of latitudinal effects of various components in order to find the integral generation multiplicity and the coupling coefficients. It is important that this fact be also taken into account when the spectrum of the 11-year variation is determined in various periods of solar activity from the latitudinal effect.

Even greater changes should be expected for cosmic ray variations of primary origins of various types. For example, for the neutron component at sea level, the change in the cutoff rigidity when the geomagnetic field is constant, lies between the limits 9.28 - 8.79, 5.358 - 5.354 and 2.679 - 2.638 BV, respectively, for observations at the geomagnetic latitudes 30, 40 and 50°. For the hard component at sea level, the expected variations for the cutoff rigidity lie between the limits 9.52 - 8.98, 5.387 - 5.362 and 2.687 - 2.645 BV, respectively, at the latitudes 30, 40 and 50°.

It should be noted that since the calculations were carried out for the penumbra of a dipole field, the absolute values of the effective cutoff rigidities are not very important. What is important here are the variations in the effective cutoff rigidity that were found.

TABLE OF VALUES OF THE EFFECTIVE CUTOFF RIGIDITIES IN THE DIPOLE APPROXIMATION (IN BV) /50

Type of observation	Quiet Period			Solar cosmic ray bursts					
	$a_j = 0$			$a_j = -2$			$a_j = -4$		
	30°	40°	50°	30°	40°	50°	30°	40°	50°
I	9,20	5,369	2,656	9,01	5,360	2,642	8,84	5,351	2,628
II	9,30	5,375	2,686	9,10	5,366	2,671	8,92	5,358	2,655
III	9,30	5,377	2,68	9,10	5,369	2,665	8,92	5,359	2,649
IV	9,33	5,380	2,683	9,12	5,372	2,666	8,95	5,362	2,652
V	9,325	5,380	2,682	9,12	5,371	2,667	8,94	5,362	2,615
VI	9,56	5,389	2,690	9,36	5,380	2,675	9,16	5,371	2,660
VII	9,62	5,394	—	9,42	5,385	—	9,22	5,376	—
VIII	9,72	5,406	—	9,53	5,397	—	9,32	5,387	—

TABLE 1.

Modulation effects					
$a_j = -0,5$			$a_j = -1,0$		
30°	40°	50°	30°	40°	50°
9,15	5,367	2,652	9,10	5,364	2,649
9,25	5,368	2,682	9,19	5,371	2,677
9,25	5,375	2,676	9,19	5,373	2,673
9,28	5,378	2,679	9,22	5,376	2,675
9,28	5,378	2,678	9,22	5,376	2,675
9,52	5,387	2,687	9,47	5,385	2,683
9,57	5,391	—	9,53	5,389	—
9,87	5,403	—	9,62	5,401	—

Remarks on following page.

Remarks: Table I

I. On low flying satellites and in the stratosphere $a_i = -2.5$ for 30, 40 and 50°.

II. Neutron component for $h_0 = 3.12$ g/cm^2 (10 km), respectively: $a_i = -1.35; -1.1; 1.35$.

III. Neutron component at $h_0 = 680$ g/cm^2 (mountain level); $a_i = -1.53; -0.59; 0.59$.

IV. Neutron component at sea level at $h_0 = 1000$ g/cm^2, $a_i = -1.23; 0.0; 0.94$.

V. Hard component at $h_0 = 3.12$ g/cm^2 (10 km); $a_i = -1.26; 0.0; 0.88$.

VI. Hard component at sea level at $h_0 = 1000$ g/cm^2; $a_i = 1.12; 2.06; 1.94$.

VII. Hard component below the surface of the Earth at a depth of 3 m; $a_i = 1.67$ and 3.0 for 30 and 40°.

VIII. Hard component below the surface of the Earth at a depth of 7 m; $a_i = 2.7, 5.6$.

For the real goemagnetic field, results which are close are also obtained on the basis of the calculations of the penumbra [5]. The calculations of $R_k^{ij}(h_0)$ according to formula (A1.10) give for the interval $-8 \leq b_{ij} \leq 3$

$7.97 + 0.0265\ b_{ij}$ BV, for the point with coordinates 25.5°S, 50.7°E,

$4.718 + 0.0075\ b_{ij}$ BV, for the point 34.6°S, 23.2°F (according to the expansion of the field in [6]),

$4.622 + 0.0086\ b_{ij}$ BV, for the point 34.6°S, 23.2°E (according to the expansion of the field in [7]), (A1.12)

$3.714 + 0.0144\ b_{ij}$ BV, for the point 39.8°S, 22.5°E,

$2.021 + 0.0033\ b_{ij}$ BV, for the point 51.6°S, 23.7°E

From (A1.12) it follows that the difference in the effective cutoff rigidity for the two representations of the geomagnetic field is 0.097 BV in the quiet period, during measurements from low-altitude satellites for the neutron component at sea level 0.093 B , and for the hard component at sea level 0.112 BV.

Supplement 2. Calculations of Coupling Coefficients Taking Into Account the Three-dimensional Model of the Elementary Event

We will consider a neutron with energy E_0 and rest mass M incident to the boundary of the atmosphere at the angle γ to the vertical. In the i-th collision, its energy is reduced by the amount $\Delta E = K_N(E_{i-1} - M)$, where E_{i-1} is the energy of the nucleon after the $(i - 1)$-th collision and K_n is the nonelasticity coefficient in nucleon-nucleon interactions.[8] We will introduce the notation for the angles that determine the direction of motion of the π-mesons that are generated. Let α be the angle between the direction of motion of the π-meson and the primary nucleon, θ the angle between the direction of motion of the meson and the vertical line and φ be the azimuth angle. The relation between these angles is given by the expression

$$\cos\theta = \cos\alpha\cos\gamma + \sin\alpha\sin\gamma\cos\varphi. \qquad (A.21)$$

8. Here we took $c = 1$.

The number of charged π-mesons in the energy interval $\varepsilon_\pi + d\varepsilon_\pi$ and the angles $\alpha + d\cos\alpha$, $\varphi + d\varphi$ formed in the i-th collision at the depth h'' can be found. It is

$$dn_N^i(\alpha, \varepsilon_\pi, \varphi, h'', \gamma) = A_N^i \frac{\omega_N(\cos\alpha, \varepsilon_\pi)}{2\pi} d\varepsilon_\pi d\cos\alpha d\varphi d\psi_N^i. \qquad \text{(A2.2)}$$

In this expression $d\psi_N^i$ denotes the probability that the primary neutron will interact the i-th time in the layer dh'' at the depth h''. This probability is /51

$$d\psi_N^i(h'', \gamma) = \frac{(h'')^{i-1}}{(i-1)!(\lambda\cos\gamma)^{i-1}} \exp\left(-\frac{h''}{\lambda\cos\gamma}\right)\frac{dh''}{\lambda\cos\gamma}. \qquad \text{(A2.3)}$$

ω_N denotes the angular and energy distribution of the π-mesons generated in the elementary event.

The condition that the transverse pulse $p_\perp$ be constant can be used to express it in the following form:

$$W_N(\cos\alpha, \varepsilon_\pi) = \omega_N(\varepsilon_\pi)\,\delta\left(\cos\alpha - \sqrt{\frac{\varepsilon_\pi^2 - p_\perp^2 - m_\pi^2}{\varepsilon_\pi^2 - m_\pi^2}}\right). \qquad \text{(A2.4)}$$

This will further simplify considerably integration over the angles of jump of the mesons. Finally, A_N^i is the normalizing factor

$$A_N^i = \frac{2}{3}\frac{K_N(E_{i-1} - M)}{\int_{\varepsilon_{min}}^{\varepsilon_{max}} \varepsilon_\pi d\varepsilon_\pi \int_{(\cos\theta)_{min}}^{(\cos\theta)_{max}} \omega_N d\cos\theta}. \qquad \text{(A2.5)}$$

Next, we introduce the function $P(\varepsilon_\pi, \cos\theta, h', h'')$, which gives the probability that the π-meson generated in the i-th collision at the depth h'' whose energy lies in the interval $\varepsilon_\pi + d\varepsilon_\pi$ and which moves at an angle in the interval $\theta + d\cos\theta$,

attains the depth h'

$$P(\varepsilon_\pi \cos\theta, h', h'') = \left(\frac{h''}{h'}\right)^q \exp\left(-\frac{h'-h''}{\lambda \cos\theta}\right), \tag{A2.6}$$

where

$$q = \frac{RTm_\pi}{g\sqrt{\varepsilon_\pi^2 - m_\pi^2 \cos\theta}\tau_\pi};$$

λ is the mean travel for the collision (which is assumed to be the same for the neutron and the π-meson, τ_π is the life of the π-meson, R is the universal gas constant, g is acceleration due to gravity and T is temperature.[9]

Then, the number of π-mesons in the interval $\varepsilon_\pi + d\varepsilon_\pi$, $\cos\alpha + d\cos\alpha$, $\varphi + d\varphi$, generated in the i-th collision of the neutron at all levels which attain the depth h', is

$$dn_N^i = \int_0^{h'} dn_N^i P(\varepsilon_\pi, \cos\theta, h', h'') = \left[\Lambda_N^i \omega_N(\varepsilon_\pi) \times \right.$$
$$\times \frac{\delta\left(\alpha - \sqrt{\frac{\varepsilon_\pi^2 - m_\pi^2 - p_\perp^2}{\varepsilon_\pi^2 - m_\pi^2}}\right)}{2\pi(i-1)!\,(\lambda\cos\gamma)^i\,(h')^q} \cdot \left(\frac{\lambda\cos\gamma\cos\theta}{\cos\gamma - \cos\theta}\right)^{q+i} \exp\left(-\frac{h'}{\lambda\cos\theta}\right) \times \tag{A2.7}$$
$$\left. \times \int_0^{\frac{h'(\cos\gamma\cos\theta)}{\lambda\cos\gamma\cos\theta}} x^{q+i-1} e^x dx \right] d\varepsilon_\pi\, d\cos\alpha\, d\varphi.$$

Using (A2.1), we make the change of variable

$$d\varphi = -\frac{d\cos\theta}{\sqrt{1 - \cos^2\alpha - \cos^2\gamma - \cos^2\theta + 2\cos\gamma\cos\theta\cos\alpha}} \tag{A2.8}$$

9. For simplicity, it is assumed that the atmosphere is isothermal.

and integrate with respect to dφ. We obtain

$$dn_N^i = \frac{A_N^i \omega_N(e_\pi)}{2\pi(i-1)!(\lambda\cos\gamma)^i (h')^q} \times \frac{h'(\cos\gamma - \cos\theta)}{\lambda\cos\gamma\cos\theta} \times$$
$$\times \frac{\left(\frac{\lambda\cos\theta\cos\gamma}{\cos\gamma-\cos\theta}\right)^{q+i} \exp\left(-\frac{h'}{\lambda\cos\theta}\right)\int_0^x e^x x^{q+i-1}dx}{L} de_\pi d\cos\theta, \qquad \text{(A2.9)}$$

where

$$L = \sqrt{1 - \left(\frac{e_\pi^2 - m_\pi^2 - p_\perp^2}{e_\pi^2 - m_\pi^2}\right) - \cos^2\gamma - \cos^2\theta + 2\cos\theta\cos\gamma\sqrt{\frac{e_\pi^2 - m_\pi^2 - p_\perp^2}{e_\pi^2 - m_\pi^2}}}. \qquad \text{(A2.10)}$$

Finally, we obtain the total number of π-mesons that attained the depth h' from all collisions of the primary neutron at all possible depths

$$N_N(\gamma) = \int_0^{\pi/2} d\cos\theta \int_{\Delta e_\pi}^{e_{\pi max}} \Phi_1(h', e_\pi, \cos\theta, E_0, \gamma)\, de_\pi,$$

where

$$\Phi_1 = \sum_{i=1}^{i_1} \frac{A_N^i \omega_N(e_\pi)}{2\pi(i-1)!(\lambda\cos\gamma)^i (h')^q} \times \frac{h'(\cos\gamma - \cos\theta)}{\lambda\cos\gamma\cos\theta} \times$$
$$\times \frac{\left(\frac{\lambda\cos\gamma\cos\theta}{\cos\gamma-\cos\theta}\right)^{q+i} \exp\left(-\frac{h'}{\lambda\cos\theta}\right)\int_0^x e^x x^{q+i-1}dx}{L}. \qquad \text{(A2.11)}$$

The upper index in the summation over i is determined from the condition

$$K_N(E_{i-1} - M) \geqslant \Delta e_\pi, \qquad \text{(A2.12)}$$

where $\Delta\varepsilon_\pi$ is the minimum energy of the π-meson which is determined by the sensitivity of the recording apparatus.

We will now pass to the study of the second generation of π-meson-mesons generated in the meson-nuclear interactions.

We introduce the function $W_j(h'', h')$, the probability that a meson emitted at the level h'' in the angular interval $\theta + d\cos\theta$ with energy in the interval $\varepsilon_\pi + d\varepsilon_\pi$ attains the depth h' after the j-th collision. It is found as follows: /53

$$\begin{aligned} W_0(h'', h') &= (h''/h')^\eta \exp\left(-\frac{h'-h''}{\lambda\cos\theta}\right), \\ W_1(h'', h') &= \int_{h''}^{h'} P_\perp(h''', h')\cdot W_0(h'', h'')\frac{dh'''}{\lambda\cos\theta}, \\ &\cdots\cdots\cdots\cdots\cdots\cdots\cdots\cdots \\ W_j(h'', h') &= \int_{h''}^{h'} W_{j-1}(h''', h'')\cdot P_j(h''', h')\frac{dh'''}{\lambda\cos\theta}. \end{aligned} \tag{A2.13}$$

The function p_j used here differs from the function P since during each collision the π-meson loses a part of the energy. It has the form

$$P_j(h''', h') = \left(\frac{h'''}{h'}\right)^{q_i}\exp\left(-\frac{h'-h'''}{\lambda\cos\theta}\right), \quad \text{where } q_i = \frac{RTm_\pi}{g\sqrt{\varepsilon_{\pi j}^2 - m_\pi^2\cos\theta\tau_\pi}} \tag{A2.14}$$

The number of second generation π-mesons in the interval $\cos\alpha + d\cos\alpha$, $\varphi + d\varphi'$ with energy in the interval $\varepsilon'_\pi + d\varepsilon'_\pi$, generated by all possible collisions in the i-th event of the first generation π-meson in the layer dh' is

$$dn'_n = \sum_{j=1}^{K(\theta)} A_{n1}^j\omega_n(\varepsilon'_n)\,\delta\left(\cos\alpha' - \sqrt{\frac{\varepsilon_\pi^2 - m_\pi^2 - p_\perp^2}{\varepsilon_\pi^2 - m_\pi^2}}\right) W_{j-1}\,\frac{d\varepsilon'_\pi d\cos\alpha' d\varphi' dh'}{2\pi\cos\theta}. \tag{A2.15}$$

Making the change of variable

$$d\varphi' = -\frac{d\cos\theta'}{\sqrt{1-\cos^2\alpha' - \cos^2\theta - \cos^2\theta' + 2\cos\theta\cos\theta'\cos\alpha'}} \tag{A2.16}$$

and integrating with respect to $d\varphi'$, we obtain

$$dn'_\pi = \sum_{j=1}^{j_1} A^j_{\pi i}\omega_\pi(\varepsilon'_\pi)\, W_{j-1}\frac{dh'd\varepsilon'_\pi d\cos\theta'}{2\pi\lambda\cos\theta L'}, \qquad \text{(A2.17)}$$

where

$$L' = \sqrt{1-\cos^2\theta-\cos^2\theta'-\frac{\varepsilon'^2_\pi - m^2_\pi - p^2_\perp}{\varepsilon'^2_\pi - m^2_\pi}} + 2\cos\theta\cos\theta'\sqrt{\frac{\varepsilon'^2_\pi - m^2_\pi - p^2_\perp}{\varepsilon'^2_\pi - m^2_\pi}}. \qquad \text{(A.218)}$$

The flux of second generation π-mesons at the depth h' in the energy interval $\varepsilon'_\pi + \alpha\varepsilon'_\pi$ and the angular interval $\cos\theta' + d\cos\theta'$ from all possible collisions of the leading π-meson at all depths is equal to

$$dn_\pi = \int_{h'}^{h} dn'_\pi P_\pi(h'', h')\, d\varepsilon'_\pi d\cos\theta' = \sum_{j=1}^{j_1(i)} \frac{\Lambda^j_{\pi i}\omega_\pi(\varepsilon'_\pi)\, G_{j-1}(h', h')\, d\cos\theta\, d\varepsilon'_\pi}{2\pi L'}, \qquad \text{(A2.19)}$$

where

$$G_{j-1}(h'', h') = \int W_{j-1}(h''', h'')\left(\frac{h'''}{h'}\right)^{q'} \exp\left(-\frac{h'-h'''}{\lambda\cos\theta}\right)\frac{dh'''}{\lambda\cos\theta}. \qquad \text{(A2.20)}.$$

Integrating over the entire spectrum of first and second generation π-mesons, we obtain the expression for the entire second generation flux of π-mesons at the depth h' from all collisions of all first generation π-mesons at all depths

$$N_\pi = \int_{\Delta\varepsilon'_\pi}^{\varepsilon_{\pi\max}} d\varepsilon'_\pi \int_0^{\pi/2} \Phi_g d\cos\theta', \qquad \text{(A2.21)}$$

where

$$\Phi_2 = \sum_{i=1}^{i_1} \frac{A_{N_i}}{4\pi^2 (i-1)! (\lambda \cos\gamma)^i} \int_0^{\pi/2} d\cos\theta \times$$
$$\times \sum_{j=1}^{J_i(0) K_N(E_{N_{i-1}} - M)} \frac{A^j_{\pi_i} \omega_\pi(\varepsilon'_\pi) \left(\frac{\lambda \cos\gamma \cos\theta}{\cos\gamma - \cos\theta}\right)^{q+1} \omega_N(\varepsilon_\pi) D^i_{j-1} d\varepsilon_\pi}{I.I.'}, \qquad \text{(A2.22)}$$

$$D^i_{j-1} = \int_0^{h'} \frac{dh''}{\lambda \cos\theta} G_{j-1}(h'', h') \frac{1}{(h'')^q} \exp\left(-\frac{h''}{\lambda \cos\theta}\right) \int_0^{\frac{h''(\cos\gamma - \cos\theta)}{\lambda \cos\gamma \cos\theta}} e^x x^{q+i-1} dx. \qquad \text{(A2.23)}$$

Thus, we obtained the integral multiplicity of the π-mesons at the depth h' which is equal to the sum $N_X + N_N$.

From here, we will find the flux of μ-mesons. We assume that the single source for the generation of μ-mesons is $\pi \to \mu + \nu$ decay and that the μ-meson travels in the direction of the decayed π-meson. The energy of the μ-mesons lies in the range $\varepsilon_\pi \frac{m_\mu^2}{m_\pi^2} \leqslant \varepsilon_\mu \leqslant \varepsilon_\pi$ with an energy distribution $dN_\mu = \frac{m_\pi^2}{m_\pi^2 - m_\mu^2} \cdot \frac{d\varepsilon_\mu}{\sqrt{\varepsilon_\mu^2 - m_\pi^2}}$, where ε_π is the energy of the decayed π-meson. The ionizing losses will be taken into account by means of the coefficient K_μ. The probability that a π-meson with energy ε_π travelling at an angle θ will decay at the altitude h' + dh' is

$$dW_\pi = \frac{m_\pi RT}{g\tau_\pi \sqrt{\varepsilon_\pi^2 - m_\pi^2 \cos\theta}} \frac{dh'}{h'}. \qquad \text{(A2.24)}$$

The probability that a μ-meson with energy ε_μ generated at the depth h' will attain the depth h is, when ionizing losses are taken into account, according to [1]

$$P_\mu = \left\{\frac{h'\left[\varepsilon_\mu \cos\theta - (h-h')K_\mu\right]}{h\varepsilon_\mu \cos\theta}\right\}^{\frac{m_\mu RT}{\tau_\mu g(\varepsilon_\mu \cos\theta + h'K_\mu)}}, \qquad \text{(A2.25)}$$

or passing to the energy of the μ-meson at the observation level h,

$$\varepsilon'_\mu = \varepsilon_\mu - \frac{(h-h')K_\mu}{\cos\theta'}.$$

Thus, we obtain

$$P_\mu = \left\{\frac{h'\varepsilon'_\mu \cos\theta}{h\left[\cos\theta\varepsilon'_\mu + (h-h')K_\mu\right]}\right\}^{\frac{m_\mu RT}{\tau_\mu g(\varepsilon'_\mu \cos\theta + hK_\mu)}}. \qquad \text{(A2.26)}$$

The total number of μ-mesons at the observation level is

$$N_\mu = \int_0^{\pi/2} d\cos\theta \int_{\Delta\varepsilon_\mu}^{\varepsilon_{\mu\max}} \Phi d\varepsilon'_\mu + \int_0^{\pi/2} d\cos\theta' \int_{\Delta\varepsilon_\mu}^{\varepsilon_{\mu\max}} \Phi' d\varepsilon'_\mu. \qquad \text{(A2.27)}$$

Here

$$\Phi = \frac{m_\pi^3 RT}{(m_\pi^2 - m_\mu^2) g\tau_\pi \cos\theta} \int_0^h \frac{dh'}{h'} \int_{\varepsilon'_\mu}^{\frac{m_\pi^2}{m_\mu^2}\left[\varepsilon'_\mu + \frac{K(h-h')}{\cos\theta}\right] \leq \varepsilon_{\pi\max}} \frac{d\varepsilon_\pi}{\varepsilon_\pi^2 - m_\pi^2} \times \qquad \text{(A2.28)} \quad /55$$

$$\times \left\{\frac{h'\varepsilon'_\mu \cos\theta}{h\left[\cos\theta\varepsilon'_\mu + (h-h')K_\mu\right]}\right\} \frac{m_\mu RT}{g\tau_\mu(\varepsilon'_\mu \cos\theta + hK_\mu)} \cdot \Phi_1,$$

$$\Phi' = \frac{m_\pi^3 RT}{(m_\pi^2 - m_\mu^2)\, g\tau_\pi \cos\theta'} \int_0^h \frac{dh'}{h'} \int_{\varepsilon_{\mu}}^{\frac{m_\pi^2}{m_\mu^2}\left[\varepsilon'_\mu + \frac{K(h-h')}{\cos\theta}\right] \leqslant \varepsilon_{\pi\max}} \frac{d\varepsilon'_\pi}{\varepsilon_\pi^2 - m_\pi^2} \times \tag{A2.29}$$

$$\times \left\{ \frac{h'\varepsilon'_\mu \cos\theta'}{h\left[\cos\theta'\varepsilon'_\mu + (h-h')\, K_\mu\right]} \right\} \frac{m_\mu RT}{\tau_\mu g\left(\varepsilon'_\mu \cos\theta' + hK_\mu\right)} \cdot \Phi_2.$$

Now, since the integral multiplicity of the μ-mesons at the observation level is known, it is relatively easy to calculate the corresponding coupling coefficient

$$W_\mu(E_0, \Delta\varepsilon_\mu, \gamma) = \frac{D(E_0)\, N_\mu(E_0, \gamma)\, \omega^\mu_{N_0}(\gamma, \varphi)}{\int\limits_{\Delta\varepsilon_\pi}^{\varepsilon_{\pi\max}} dE_0 \int\limits_0^{2\pi} d\varphi \int\limits_0^{\pi/2} D(E_0)\, N_\mu(E_0, \gamma)\, \omega^\lambda_{N_0}(\gamma, \varphi)\, d\gamma}. \tag{A2.30}$$

In this expression $D(E_0)$ denotes the differential energy spectrum of the primary component and $\omega^{\pi}_{N_0}(\gamma, \varphi)$ the distribution of the primary neutrons by azimuth and zenith angles at the given latitude λ. The fluctuations in the elementary event are taken into account by varying the numerical values of the non-elasticity coefficient and by summing the corresponding terms with different weights.

Supplement 3. Estimate of the Effect of Fluxes in Radiation Belts on the Cutoff Rigidity of Cosmic Rays

We will estimate what variation in the cutoff rigidity is caused by fluxes generated by the motion of radiation particles captured according to the Akasof-Chapman model of radiation belts [46]. We will assume that ρ is the distance from the center of the Earth to some point, ψ is the latitudinal angle, φ is the geomagnetic longitude, and we will consider the points in the region occupied by the flux. Let $\rho = f_e R_3$ be the distance from the center of the Earth to the point M_e, at which the dipole line of force passing through the point M intersects the equatorial dipole plane. An element $d\ell$ of length of the line of force is

$$d\mu = \pi b^3 j dS = \pi j \rho_e^3 \sin^{10}\psi d\rho_e d\psi. \tag{A3.1}$$

Taking into account that the equation of the line of force for the given ρ_e is $\rho = \rho_e \sin^2\psi$, we find w (assuming that the selected line of force ρ_e is fixed). An element dS of the area in the meridional plane passing through the point M bounded by the lines of force ρ_e, $\rho_e + d\rho_e$ and the radii with latitudes ψ, $\psi + d\psi$ is

$$dS = h_1 dl, \quad \text{where} \quad h_1 = d\rho \cos\xi = \frac{d\rho\rho d\psi}{dl}. \tag{A3.2}$$

Hence, /56

$$dS = \rho_e \sin^3\psi d\rho_e d\psi. \tag{A3.3}$$

We will assume that the region with the flux is bounded by the lines of force $\rho_e^u \cdot \rho_e + d\rho_e$, which made contact with the Earth at the latitudes $\alpha_1 \pi - \alpha_1$ and α_2, $\pi - \alpha_2$.

The effective magnetic moment of the circular flux $d\mu$ with cross section dS in the meridional plane is

$$d\mu = \pi b^2 j dS = \pi j \rho_e^3 \sin^{10}\psi d\rho_e d\psi. \tag{A3.4}$$

By j we will mean the three-dimensional density of the flux perpendicular to the area dS in the given direction.

From here, we can easily write down the expression for the vector-potential of the elementary circular flux of cross section dS

$$dA = -\frac{2j\rho_e^{3/2}\sin^{1.5}\psi F(k)}{(R\cos\lambda)^{1/2}} d\rho_e d\psi, \tag{A3.5}$$

where the parameter k is determined from the expression

$$k^2 = \frac{4\rho_e \sin^3\psi R\cos\lambda}{(R\cos\lambda + \rho_e \sin^3\psi)^2 + (R\sin\lambda + \rho_e \sin^2\psi\cos\psi)^2}. \tag{A3.6}$$

In formula (A3.5), $F(k) = k\frac{2}{k}[K(k) - E(k)]^{-kK(k)}$, i.e., it is determined in terms of the difference of the eliptic integrals

$$K(k) = \int_0^{\pi/2} \frac{dv}{(1-k^2\sin v)^{1/2}}, \quad E(k) = \int_0^{\pi/2} (1-\sin v \cdot k^2)^{1/2} dv. \tag{A3.7}$$

The vector potential of the magnetic field created by the entire three-dimensional radiation belt flux modelled is obtained by integrating expression (A3.5) over ρ_e and ψ. The limits of integration for ρ_e lie between ρ_e and ρ_{e2}. The limits of integration for ψ are α and $\pi - \alpha$, where α is determined from the condition

$$R_3 = \rho_e \sin^2\alpha; \quad \alpha = \arcsin\sqrt{R^2/\rho_e}. \tag{A3.8}$$

Thus, the vector potential of the magnetic field of the three-dimensional flux is

$$A_3 = \frac{-2}{(R\cos\lambda)^{1/2}} \int_{\rho_{e1}}^{\rho_{e2}} \int_{\alpha}^{\pi-\alpha} j\rho_e^{3/2} \sin^{1/2}\psi F(k)\, d\rho_e d\psi. \tag{A3.9}$$

The first Störmer integral is written in the form

$$\sin\theta = \frac{2\gamma}{R\cos\lambda} - \frac{\cos\lambda}{R^2} - \frac{2I^4}{M(R\cos\lambda)^{1/2}} \int_{\rho_{e1}}^{\rho_{e2}} \int_{\alpha_1}^{\pi-\alpha} j\rho_e^{3/2} \sin^{1/2}\psi F(k)\, d\rho_e d\psi, \tag{A3.10}$$

where R, γ, ρ_e are expressed in Störmer units. The equations used to find the critical values of R_c and γ_c have the form

$$\frac{1}{R_c^2} - \frac{\beta'}{\sqrt{R_c}} \int_{\rho_{e1}}^{\rho_{e2}} \int_{\alpha}^{\pi-\alpha} j\rho_e^{3/2} \sin^{1/2}\psi \left[\frac{F(k)}{2} + R_c \frac{\partial F(k)}{\partial R_c}\right] d\rho_e d\psi = 1; \tag{A3.11}$$

$$R_c + \frac{1}{R_c} + \beta'\sqrt{R_c} \int_{\rho_{e1}}^{\rho_{e2}} \int_{\alpha}^{\pi-\alpha} j\rho_e^{3/2} \sin^{1/2}\psi F(k)\, d\rho_e d\psi = 2\gamma_c. \tag{A3.12}$$

Here $\beta' = 2\gamma^4/M$. Taking the derivative $\partial F(k)/\partial R_c$, we obtain

$$\frac{F(k)}{2} + R_c \frac{\partial F(k)}{\partial R_c} = \frac{R_c K}{2\rho_e \sin^3\psi}\left[K(k) - \frac{R_c^2 + \rho_e^2 \sin^4\psi (1 + 2\sin^2\varphi)}{R_c^2 - 2\rho_e R_c \sin^3\psi + \rho_e^2 \sin^4\psi} E(k)\right]. \qquad \text{(A3.13)}$$

Substituting (A3.13) in (A3.11), we obtain

$$\frac{1}{R_e^2} + \beta' \sqrt{R_c} \int_{\rho_{e1}}^{\rho_{e2}} \int_{\alpha}^{\pi-\alpha} j \rho_e^{1/2} \frac{\sin^{5/2}\psi}{2} k\,|K(k) - G(k)|\, d\rho_e d\psi = 1, \qquad \text{(A3.14)}$$

where

$$G_1 = \frac{R_c^2 + \rho_e^2 \sin^4\psi (1 - 2\sin^2\psi)}{R_c^2 - 2\rho_e R_c \sin^3\psi \sin^4\psi}. \qquad \text{(A3.15)}$$

We introduce the notation $\rho_e = f_e R_E$; $R_c = U_1 R_E$. Chapman and Akasofu calculated the density of the fluxes j for the following values of the parameters:

$$\rho_{e0} = f_0 R_E = 6R_E \text{ (or } f_0 = 6), \; n_0 = 1.0 \text{ cm}^{-3},$$
$$q = 1.517 \; a' = -0.5, \; n_0 E = 150 \text{ keV} \cdot \text{cm}^{-3} \qquad \text{(A3.16)}$$

where E is the energy of the captured particle and n is the concentration of the particle. For the given values of the parameters $j \approx j_0 \sin^{3/2}\psi_1$, where j_1 denotes

$$j_1 = f_e^2 \exp[-2{,}30(f_e - 6)](1 + 3\cos^2\psi)^{1/2} \times \left[\frac{0{,}2946 \sin^2\psi (1 + \cos^2\psi)}{(1 + 3\cos^2\psi)^3} + 1{,}3835 f_e (f_e - 6)\right]. \qquad \text{(A3.17)}$$

Here, $f_e = \rho_e/R_E$.

In Chapman and Akasofu when $n_0E = 150$ keV·cm^{-3}, $f_0 = 2.34\cdot10^{-15}$ CGSM. This value of j_0 and expression (A3.17) for j_1 determine the perturbation in the magnetic field on the surface of the Earth of 50 γ. In our notation, the expression for the perturbed field in the plane of the equator has the form

$$\Delta H_e = -j_0\iint\frac{j_1 k f_e^{7/2} R_3}{(\cos\lambda)^{7/2}}[K(k) - G_2E(k)]\sin^4\psi df_e d\psi, \tag{A3.18}$$

where

$$G_2 = \frac{1 + f_e\sin^4\psi(t \mp 2\sin^2\psi) + 2f_e\sin\lambda\sin^2\varphi\cos\psi}{1 + \sin^4\psi f_e^2 - 2f_e\sin^2\psi\sin^2\psi\sin(\lambda - \psi)}. \tag{A3.19}$$

Finally, substituting all constants we obtain similar equations for determining U_1 and γ_c:

$$\begin{aligned}&\frac{1}{u_1} - 0{,}192\cdot10^{-4}\sqrt{U_1}\iint jf_e^{7/2}\sin^4\psi k[K - G_1E]\,df_e d\psi = 0{,}0167P_1,\\ &0{,}129\sqrt{PU_1} + 7{,}73\sqrt{PU_1} + 2{,}95\cdot10^{-4}\sqrt{\frac{U_1}{P}}\iint j_1 f_e^{9/2}\sin^7\psi F(k)\,df_e d\psi = 2\gamma_c,\end{aligned} \tag{A3.20}$$

where **P** is the cutoff rigidity.

When u_1 and γ_c are known, we use as before the Störmer integral. For $R = R_E$, for vertical particles ($\theta = 0$), we obtain

$$P_{\gamma_c}^2 = P_{\text{dip}}^2(\lambda)\left[1 + \frac{3{,}83\cdot10^{-5}}{(\cos\lambda)^{7/2}}\iint j_1 f_e^{7/2}\sin^{11/2}\psi F(k)\,d\psi df_e\right]^2. \tag{A3.21}$$

Given U_1 (altogether 42 values of U_1 were given) we calculated the γ_c and on the basis of these γ_c we calculated

the magnitudes of the perturbed rigidity (Fig. 11). It can be seen from the figure that the perturbed cutoff rigidities can hardly be made to agree with the experimental data. In fact, using the results of the calculations for the expected /58

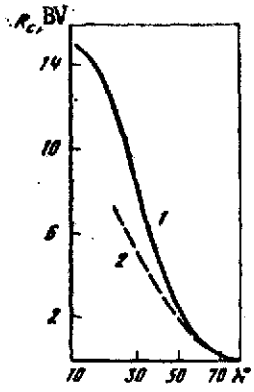

Fig. 11. Cutoff rigidity vs. geomagnetic latitude.

1--for dipole field; 2--taking into account the three-dimensional fluxes in the radiation belt according to model [46].

variations in the cutoff rigidity when $\Delta H = 50\ \gamma$ which are given in the diagram, we find with the aid of the coupling coefficients, that the expected increase in the intensity of the cosmic rays at sea level during such comparatively small magnetic perturbation will be: in the neutron component with amplitudes 17.5 and 12.5% at the geomagnetic latitudes 20 and 30°, respectively, in the μ-meson component with amplitude 3.9 and 2.7% at the latitudes 20 and 30°, respectively. The results that were presented contradict sharply the experimental data about the increase in the minimum Forbush effect observed until now.

Thus, the flux model studied by Akasofu and Chapman probably does not satisfy the variations in the cutoff rigidity observed on Earth.

Supplement 4. Spherical Symmetric Diffusion Model of Cosmic Rays in Interplanetary Space

Suppose that the intensity of the regular interplanetary field is $\vec{H}_0 = 0$. Then, according to (7.16),

$$\alpha_1 = 1; \quad \alpha_2 = 0 \tag{A4.1}$$

and according to (7.19),

$$\varkappa_{ik} = \varkappa_0 \cdot \begin{pmatrix} 100 \\ 010 \\ 001 \end{pmatrix}, \tag{A4.2}$$

i.e., isotropic diffusion takes place. Since in this case $\beta = H_0(H_0 + h) = 0$, according to (7.24), we obtain for the drift velocity of the particles in interplanetary space

$$u_{dr.r} = \frac{2}{3} u; \quad u_{dr.\varphi} = u_{dr.\theta} = 0. \tag{A4.3}$$

Substituting (A4.2) and (A4.3) in (7.9), we obtain

$$\frac{\partial n}{\partial t} - \frac{1}{r^2}\frac{\partial}{\partial r}\left(-r^2\frac{2}{3}un + r^2\varkappa_0\frac{\partial n}{\partial r}\right) - \frac{1}{r\sin\theta}\frac{\partial}{\partial\theta}\left(\frac{\sin\theta}{r}\varkappa\frac{\partial n}{\partial\theta}\right) - \\ - \frac{1}{r\sin\theta}\frac{\partial}{\partial\varphi}\left(\frac{\varkappa_0}{r\sin\theta}\frac{\partial n}{\partial\varphi}\right) - \frac{2}{3}\frac{u}{r}\frac{\partial}{\partial R}(Rn) = F(r, \theta, \varphi, R, Z, t). \tag{A4.4}$$

In equation (A4.4), the parameters $\varkappa_0$ and u are, generally, functions of r, θ, φ and t, a$\varkappa_0$ and also of R.

In the spherical symmetrical case $\frac{dn}{d\theta} = \frac{dn}{d\varphi} = 0$, and u is only a function of r, t, a$\varkappa_0$ and also of R. When the modulation of galactic cosmic rays is studied, we must set F = 0 (there are no galactic cosmic ray sources inside the modulation region under consideration). Thus equation (A4.4) takes on the form

$$\frac{\partial n}{\partial t} - \frac{1}{r^2}\frac{\partial}{\partial r}\left(-r^2\frac{2}{3}un + r^2\varkappa_0\frac{\partial n}{\partial r}\right) - \frac{2}{3}\frac{u}{r}\frac{\partial}{\partial R}(Rn) = 0. \tag{A4.5}$$

Steady-State Case, $\varkappa_0$ is Independent of r /59

We will assume that $\varkappa_0$ is independent of r, and that r_0 (the radius of the modulation region) depends little on t, so that the term $\partial n/\partial t$ can be ignored (this is valid to a considerable extent for the 11-year variations). We write

$$r/r_0 = \rho; \; n(r, R, t) = n_0(R) f(r, R, t), \tag{A4.6}$$

where $n_0(R)$ is the density of the cosmic rays of rigidity R beyond the boundaries of the modulating region. Substituting

(A4.6) in (A4.5) and taking into consideration that $\partial\varphi/dt = 0$, we obtain for $f(\rho, R, t)$ the equation

$$\frac{1}{r_0\rho}\frac{\partial}{\partial\rho}\left[\rho^2\left(-\frac{\varkappa}{r_0}\frac{\partial f}{\partial\rho}+\frac{2}{3}fu\right)\right]-\frac{2}{3}\frac{u}{r_0\rho}\frac{\partial}{\partial R}(R,f)-\frac{2}{3}\frac{u}{r_0\rho}\frac{\partial n_0/\partial R}{n_0}Rf=0 \qquad \text{(A4.7)}$$

with the boundary conditions

$$f(\rho, R, t)|_{\rho=0}<\infty;\quad f(\rho, R, t)|_{\rho=1}=1. \qquad \text{(A4.8)}$$

If we ignore the possible dependence of $\varkappa_0$ on R in the interval in which R varies in proportion to the penetration of the particles into the modulating region (this can be done for R > several billion volts, which corresponds to the estimates in [83], equation (A4.7) can be solved by separating the variables using the substitution $f(\rho, R, t) = A(R, t)\, B(\rho, t)$, where t is considered as the parameter

$$\frac{1}{\rho B}\frac{\partial}{\partial\rho}\left[\rho^2\left(-\frac{\varkappa_0}{r_0}\frac{dB}{d\rho}+B\frac{2}{3}u\right)\right]=\frac{2}{3}\frac{u}{A}\left[\frac{\partial}{\partial R}(R,A)+RA\frac{dn_0/dR}{n_0}\right]=\lambda. \qquad \text{(A4.9)}$$

Since $B(1,t) = 1$, equation (A4.8) implies $A(R,t) = 1$. Therefore,

$$\lambda=\frac{2}{3}u\left(1+R\frac{dn_0/dR}{n_0}\right). \qquad \text{(A4.10)}$$

When $n_0(R) = kR^{-\gamma}$,

$$\lambda=\frac{2}{3}u(1-\gamma). \qquad \text{(A4.11)}$$

Substituting (A4.11) in (4.9), we obtain

$$b\rho\frac{d^2B}{d\rho^2}-\left(\frac{2}{3}\rho-2\beta\right)\frac{dB}{d\rho}-\frac{2}{3}(\gamma-1)B=0, \qquad \text{(A4.12)}$$

where

$$\mathscr{E} \equiv \frac{\varkappa_0}{ur_0}. \tag{A4.13}$$

According to [84, 85], the solution of equation (A4.12) can be written in the form

$$B(\rho, t) = \frac{C_1}{b}\Phi\left(\gamma+1, 2\frac{2\rho}{3b}\right) + \frac{C_2}{\rho}\Phi\left(\gamma, 0, \frac{2\rho}{3b}\right), \tag{A4.14}$$

where C_1 and C_2 are arbitrary constants. Since $B(0,t) < \infty$, $C_2 = 0$. Since $B(1,t) = 1$, $C_1 = \frac{b}{\Phi\left(\gamma+1, 2\frac{2}{3b}\right)}$ so that finally

$$\frac{n(r, R, t)}{n_0(R)} = \frac{\Phi\left(\gamma+1, 2, \frac{2ur}{3\varkappa_0}\right)}{\Phi\left(\gamma+1, 2, \frac{2ur_0}{3\varkappa_0}\right)}. \tag{A4.15}$$

Using the asymptotic representation for Φ, we obtain /60

$$\frac{n(r, R, t)}{n_0(R)} = \frac{1 + \frac{ur(\gamma+1)}{3\varkappa_0} + \frac{(\gamma+1)(\gamma+2)}{27}\left(\frac{ur}{\varkappa_0}\right)^2 + \frac{(\gamma+1)(\gamma+2)(\gamma+3)}{486}\left(\frac{ur}{\varkappa_0}\right)^3 + \ldots}{1 + \frac{\gamma+1}{3}\frac{ur_0}{\varkappa_0} + \frac{(\gamma+1)(\gamma+2)}{27}\left(\frac{ur_0}{\varkappa_0}\right)^2 + \frac{(\gamma+1)(\gamma+2)(\gamma+3)}{486}\left(\frac{ur_0}{\varkappa_0}\right)^3 + \ldots}, \tag{A4.16}$$

from which for high energies when $ur_0/\varkappa_0 \ll 1$ follows

$$\frac{n(r, R, t)}{n_0(R)} = 1 - \frac{(\gamma+1)}{3}\frac{u(r_0 - r)}{\varkappa_0} + \left[\frac{3(\gamma+1)}{\gamma+2}\frac{r^2}{r_0^2} - 1\right]\frac{(\gamma+1)(\gamma+2)}{27}\left(\frac{ur_0}{\varkappa_0}\right)^2 + \ldots \tag{A4.17}$$

According to the elementary formula [48]

$$\frac{n(r, R, t)}{n_0(R)} = \exp\left[-\frac{u(r_0 - r)}{\varkappa_0}\right]. \tag{A4.18}$$

A comparison of the calculations based on (A4.15) and (A4.18) shows that the difference is negligible, so that expression (A4.18) can be used in the first approximation.

Steady-State Case, $\varkappa_0$ Depends on r

We will first consider the case when we can assume that the transport travel for the scattering of the particles Λ increases proportionally with r as the distance from the Sun increases. This case was studied in [60] in an approximation which is analogous to the one discussed above.

Thus, we will assume that b, which is determined from expression (A4.13) can be written in the form

$$\mathcal{E} = a\rho; \quad a = \frac{\varkappa_\delta}{ur_\delta} = \frac{v\lambda_\delta}{3ur_\delta}. \tag{A4.19}$$

Here $\varkappa_\delta$ and Λ_δ are, respectively, the diffusion coefficient and the transport travel for the scattering in the region of the Earth's orbit at the distance r_δ = 1 AU from the Sun. According to (A4.19), the expression for λ will be the same as before and the equation for B(ρ) will be transformed into the homogeneous equation

$$a\rho^2 B'' - \rho B'(1 - 3a) + \frac{2}{3}(\gamma + 2)B = 0, \tag{A4.20}$$

whose solution is

$$B(\rho) = C_1\rho^{\alpha_1} + C_2\rho^{\alpha_2}, \tag{A4.21}$$

where

$$\alpha_{1,2} = \frac{1}{3a} - 1 \pm \sqrt{\left(\frac{1}{3a} - 1\right)^2 + \frac{2}{3a}(\gamma + 1)}. \tag{A4.22}$$

The condition for the boundedness of the solution when $\rho = 0$ implies $C_2 = 0$ and the boundary condition $B(1) = 1$ implies $C_1 = 1$. Thus, we obtain

$$\frac{n(r, R, t)}{n_0(R)} = \left(\frac{r}{r_0}\right)^{\alpha_1}, \qquad \text{(A4.23)}$$

where

$$\alpha_1 = \frac{ur_\delta}{v\lambda_\delta} - 1 + \sqrt{\frac{u^2 r_\delta^2}{v^2\lambda_\delta^2} - \frac{2ur_\delta}{v\lambda_\delta} + 1 + \frac{2ur_\delta(\gamma+1)}{v\lambda_\delta}}. \qquad \text{(A4.24)}$$

When $ur_\delta^{\pm}/v\Lambda_\delta^{\pm} \ll 1$, expression (A4.24) can be written with an accuracy up to the terms $\sim\left(\frac{ur_\delta}{v\lambda_\delta}\right)^2$ in the form /61

$$\alpha_1 \approx \frac{ur_\delta}{v\lambda_\delta}(\gamma + 1), \qquad \text{(A4.25)}$$

When $\gamma = 2$, (A4.23) will be exactly the same as the expression found for this case in [86] on the basis of elementary concepts about the equality of the diffusion and convective fluxes. When $\gamma = 2.5$, the term $ur_\delta^{\pm}/v\Lambda_\delta^{\pm}$ in (A4.25) has the coefficient 3.5 instead of 3 as in [86].

The expected distribution of the intensity $n(r)/n(r_0)$ in interplanetary space for various values of the modulation parameter $ur_\delta^{\pm}/v\Lambda_\delta^{\pm}$ is given in Table 2. A comparison of Table 2 with the table given in [86] which was calculated using the formula $\frac{n(r)}{n(r_0)} = \left(\frac{r}{r_0}\right)^{\frac{3ur_\delta}{v\lambda_\delta}}$, shows that the difference is not very large.

TABLE 2. EXPECTED DISTRIBUTION OF INTENSITY $n(r)/n(r_0)$ IN INTERPLANETARY SPACE FOR VARIOUS VALUES OF THE MODULATION PARAMETER

r/r_0	$ur_\delta/\varkappa_\delta$							
	0,01	0,02	0,05	0,1	0,2	0,5	1,0	10,0
0,001	0,7868	0,6218	0,3112	0,1030	0,0131	$4,92\cdot10^{-5}$	$1,153\cdot10^{-6}$	$1,38\cdot10^{-64}$
0,002	0,8061	0,6521	0,3499	0,1294	0,0202	$1,331\cdot10^{-4}$	$7,218\cdot10^{-5}$	$3,499\cdot10^{-59}$
0,005	0,8322	0,6945	0,4084	0,1750	0,0358	$4,964\cdot10^{-4}$	$8,158\cdot10^{-7}$	$1,038\cdot10^{-49}$
0,01	0,8523	0,7285	0,4093	0,2198	0,0555	$1,343\cdot10^{-3}$	$5,105\cdot10^{-6}$	$2,655\cdot10^{-43}$
0,02	0,8730	0,7642	0,5162	0,2761	0,0857	$3,633\cdot10^{-3}$	$3,195\cdot10^{-5}$	$6,787\cdot10^{-37}$
0,05	0,9014	0,8137	0,6027	0,3784	0,1524	$1,354\cdot10^{-2}$	$3,611\cdot10^{-4}$	$2,015\cdot10^{-28}$
0,1	0,9232	0,8534	0,6776	0,4688	0,2355	$3,664\cdot10^{-2}$	$2,259\cdot10^{-3}$	$5,152\cdot10^{-22}$
0,2	0,9458	0,8952	0,7619	0,5888	0,3639	$9,913\cdot10^{-2}$	$1,414\cdot10^{-2}$	$1,318\cdot10^{-15}$
0,5	0,9763	0,9535	0,8894	0,7945	0,6471	0,3697	0,1598	$3,911\cdot10^{-7}$
1	1	1	1	1	1	1	1	1

Distribution of the Radial Gradient in Interplanetary Space in the Steady-State Spherical Symmetric Case

The case when Λ is independent of the distance from the Sun. Using formula (9.123) from [87], we find, on the basis of (A4.15), an expression for the relative radial gradient

$$\beta \equiv \frac{dn(r, R, t)/dr\cdot 100 r_\delta}{n(r, R, t)} = \frac{100(j+1)ur_\delta}{2\varkappa_0}\frac{\Phi\left(\gamma+2, 3, \frac{2}{3}\frac{ur}{\varkappa_0}\right)}{\Phi\left(\gamma+1, 2, \frac{2}{3}\frac{ur}{\varkappa_0}\right)}\ \%/1\text{AU} \qquad \text{(A4.26)}$$

When the distribution of the cosmic ray intensity is determined from formula (A4.18), the values are

$$\beta = \frac{100ur_\delta}{\varkappa_0}\ \%/1\text{ AU} \qquad \text{(A4.27)}$$

The case $\Lambda \sim r$. According to (A4.23),

$$\beta = \frac{100\varkappa_1 r_\delta}{r}\ \%\ 1\ \text{AU} \qquad \text{(A4.28)}$$

where α_1 is determined from expression (A4.24).

/62

Determination of the Dimensions of the Modulation Region through Simultaneous Measurement of the Modulation Depth and the Relative Radial Gradient

It can be easily seen that when simultaneous measurements of the observation depth and the radial gradient are used, r_0, the radius of the modulation region, can be found uniquely. In fact, using for the case Λ = const the approximate expressions for the modulation depth (A4.18) and the relative radial gradient (A4.27), we obtain

$$r_0 = r + \frac{100 \ln |n_0/n(r)|}{\beta} r_\delta. \qquad \text{(A4.29)}$$

For the case $\Lambda \sim r$, we obtain from (A4.23) and (A4.28),

$$r_0 = r \left[\frac{n_0}{n(r)}\right]^{100 r_\delta/\beta r}. \qquad \text{(A4.30)}$$

In (A4.29) and (A4.30), the quantities $n_0/n(r)$ and β are measured experimentally. Therefore, the uncertainty in u and Λ has no effect on the determination of r_0. Substituting the r_0 which was found in (A4.18) and (A4.23), we can then find $u/\varkappa_0$.

Accounting for the Lag in the Processes in Interplanetary Space Relative to the Phenomena of the Sun

It was shown above that the solution of the diffusion equation with transfer taking into account the particle inhibition in interplanetary space is almost the same as the solution which is obtained from the condition for the equality of the diffusion and convective flux. This condition implies that

$$\frac{n(r, R, t)}{n_0(R)} = \begin{cases} \exp\left[-\int_r^{r_0} \frac{u}{\varkappa_0} dr\right], & \text{when } \Lambda = \text{const}, \\ \exp\left[-\int_r^{r_0} \frac{\alpha_1}{r} dr\right], & \text{when } \Lambda \sim r, \end{cases} \qquad \text{(A4.31)}$$

where α_1 is determined from the expression (4.24).

Taking into account that the lag in the change of state of the interplanetary medium at the distance r is r/u, and the lag in the change in the dimension of the modulation region r_0 is r_0/u, we obtain

$$\frac{n(r, R, t)}{n_0(R)} = \begin{cases} \exp\left[-\int_r^{r_0(t-r_0/u)} \frac{u}{\varkappa_0}(t - r/u)\,dr\right], & \text{when } \Lambda = \text{const}, \\ \exp\left[\int_r^{r_0(t-r_0/u)} \alpha_1(t - r/u)\frac{dr}{r}\right], & \text{when } \Lambda \sim r. \end{cases} \tag{A4.32}$$

Suppose that the minimum values of the parameters attained near the minimum solar activity (with a certain lag) are $r_{0\ min}$, $(u/\varkappa_0)_{min}$, $\alpha_{1\ min}$, and the maximum values are $r_{0\ max}$, $(u/\varkappa_0)_{max}$, $\alpha_{1\ max}$. We will assume that in first approximation the parameters r_0, $u/\varkappa_0$ and α_1 vary harmonically with a period of 11 years, i.e.,

$$r_0 = r_{0\max} - (r_{0\max} - r_{0\min})\left[1 + \cos\omega\left(t - \frac{r}{u}\right)\right]; \tag{A4.33}$$

$$\frac{u}{\varkappa_0} = \left(\frac{u}{\varkappa_0}\right)_{max} - \frac{(u/\varkappa_0)_{max} - (u/\varkappa_0)_{min}}{2}\left[1 + \cos\omega\left(t - \frac{r}{u}\right)\right]; \tag{A4.34}$$

$$\alpha_1 = \alpha_{1\max} - \frac{\alpha_{1\max} - \alpha_{1\min}}{2}[1 + \cos\omega(t - r/u)]; \tag{A4.35}$$

where $\omega = 2\pi/T$; T = 11 years, $r_{mean} = 1/2(r_{0\ max} + r_{0\ min})$ and t is measured from the instant at which the minimum solar activity occurs, i.e., from the beginning of the cycle. /63

Substituting (A4.33) and (A4.34) in (A4.31), we obtain for the case Λ = const

$$\frac{n(r, R, t)}{n_0(R)} = \exp\left\{-\left(\frac{u}{\varkappa_0}\right)_{mean}(r_0 - r) + \left[\left(\frac{u}{\varkappa_0}\right)_{max} - \left(\frac{u}{\varkappa_0}\right)_{min}\right]\frac{u}{\omega} \times \right. \\ \left. \times \sin\frac{\omega(r_0 - r)}{u}\cos\omega\left(t - \frac{r_0 + r}{2u}\right)\right\}, \tag{A4.36}$$

where

$$(u/\varkappa_0)_{\text{mean}} = \frac{1}{2}\left[\left(\frac{u}{\varkappa_0}\right)_{\max} + (u/\varkappa_0)_{\min}\right].$$

Since for 11-year variations

$$\frac{\omega(r_0 - r)}{u} \leqslant 1, \quad \frac{u}{\omega}\sin\frac{\omega(r_0 - r)}{u} \approx r_0 - r \text{ and}$$

$$\frac{n(r, R, t)}{n_0(R)} = \exp\left\{(r_0 - r)\left[-\left(\frac{u}{\varkappa_0}\right)_{\text{mean}} + \left(\left(\frac{u}{\varkappa_0}\right)_{\max} - \left(\frac{u}{\varkappa_0}\right)_{\min}\right) \times \right.\right. \quad \text{(A4.37)}$$

$$\left.\left. \times \cos\omega\left(t - \frac{r_0 + r}{2u}\right)\right]\right\},$$

where r_0 is determined from expression (A4.33). From (A4.37) it can be seen that the maximum and minimum intensity of the cosmic rays are shifted by $(r_0 + r)/2u$ relative to the minimum and maximum solar activity, respectively.

We will now consider the case $\Lambda \sim r$. Substituting (A4.33) and (A4.31), and using formula (2,641.2) from [87], we obtain

$$\frac{n(r, R, t)}{n_0(R)} = \exp\left\{-\alpha_{1\,\text{mean}} \ln\frac{r_0}{r} - \frac{\alpha_{1\max} - \alpha_{1\min}}{2} \times \right.$$

$$\left. \times \left[\cos\omega t\left(\text{ci}\,\frac{\omega r_0}{u} - \text{ci}\,\frac{\omega r}{u}\right) - \sin\omega t\left(\text{si}\,\frac{\omega r_0}{u} - \text{si}\,\frac{\omega r}{u}\right)\right]\right\}, \quad \text{(A4.38)}$$

where $\alpha_{1\,\text{mean}} = 1/2\ (\alpha_{1\,\max} + \alpha_{1\,\min})$ and ci and si are, respectively the cosine and sine in the integral. An analysis of the expression (A4.38) shows that in the case $\Lambda \sim r$, the lag relative to changes in the solar activity is considerably smaller than in the case $\Lambda = \text{const}$ (for equal r_0/u). This is due to the fact that for $\Lambda \sim r$, the regions closest to the Sun are most effective for producing the modulation.

REFERENCES

1. Dorman, L. I., Variatsii kosmicheskikh luchey, [Cosmic Ray Variations], Moscow, Gostekhizdat Press, 1957. /64

2. Dorman, L. I., Variatsii kosmicheskikh luchey i issledovaniye kosmosa, [Cosmic Ray Variations and a Study of the Universe], USSR Acad. of Sci. Publ., 1963.

3. Dorman, L. I. and Gushchina, R. T., in the collection Kosmichekiye luchi, No. 8, 158 (1967).

4. Makino, T. and Kondo, I., Proc. Internat. Conf. Cosmic Rays, 1, London, 564 (1965).

5. Shea, M. A., Smart, D. F., and McCracken, K. G., J. Geophys. Res., 70 (17), 1417-4130 (1965).

6. Finch, H. P. and Leaton, B. R., Monthly Notices Roy. Astron. Soc., Geophys. Suppl., 1967, p. 314.

7. Hensen, D. C. and Cain, J. C., J. Geophys. Res., 67, No. 9 3568 (1962).

8. Dorman, L. I., in the collection Kosmicheskie luchi, No. 3, 174 (1961).

9. Viskov, V. V. and Dorman, L. I., in the collection Kosmicheskie luchi, No. 7, 197 (1965).

10. Boos, E. J. and Dorman, L. I., in the collection Kosmicheskie luchii problemy kosmofiziki, [Cosmic Rays and Problems in the Physics of the Universe], Novosibirsk, 1965, p. 229.

11. Mathew, P. M., Canad. J. Phys., 37, 85 (1959).

12. Lindgrean, S. and Lindholm, F., Tellus, 13, 280 (1961).

13. Wada, M., Japan Inst. Phys. Chem. Res., 54, 335 (1960); 55, 7 (1961).

14. Carmichael, H., Bercovitch, M. and Steljest, J. F., Proc. Internat. Conf. Cosmic Rays, 2, Jaipur, 350 (1963).

15. Kaminer, N. S., Ilgach, S. F. and Khadakhanova, T. S., Geomagnetizm i aeronomiya, No. 4, 653 (1964); No. 5, 946.

16. Kaminer, N. S., Ilgach, S. F., and Khadakhanova, T. S., Geomagnetizm i aeronomiya, 4 (6), 1116 (1964).

17. Bercovitch, M. and Robertson, B. C., Proc. Internat. Conf. Cosmic Rays, 1, London, 489 (1965).

18. Kaminer, N. S. and Khadakhanova, T. S., Geomagnetizm i aeronomiya, 6, 921 (1966).

19. Kaminer, N. S., Ilgach, S. F.. Khadakhanova, T. S., in the collection Kosmicheskie luchi, No. 8, 117 (1967).

20. Dorman, L. I., Zh Eks Teor Fiz , 26, 504 (1954).

21. Compton, A. H., and Turner, R. N., Phys. Rev., 52, 700 (1937).

22. Lockwood, J. A. and Calawa, A. R., J. Atmos. & Terrest. Phys., 11, 23 (1957).

23. Dubinsky, J., Chaloupka, P. and Kowalski, T., Mat -fyz casop., 10 (1), 57 (1960).

24. Gushchina, R. T., Dorman, L. I. and Kaminer, N. S., Izv Akad Nauk SSSR, Ser Fiz , 30 (11), 1722 (1966).

25. Dorman, L. I., Izv Akad Nauk SSSR, Ser Fiz, 30 (11), 1722 (1966).

26. Viskov, V. V., Dorman, L. I., Krupitskaya, T. I., in the collection Kosmicheskie luchi, No. 8, 242 (1967).

27. Dorman, L. I., Geomagnetizm i aeronomiya, 6 (6), 1096 (1966).

28. Bachelet, F., Balata, P., Dyring, E. and Iucci, N., Nuovo cimento, 35, 23 (1965).

29. Dorman, L. I. and Kovalenko, V. A., Geomagnetizm i aeronomiya, 6 (5), 922 (1966).

30. Chapman, S., Nature, 140, 423 (1937).

31. Johnson, T. H., Rev. Mod. Phys., 10, 193 (1938).

32. Hayakawa, S. and Nishimura, J. N., J. Geophys. Res., 55, 221 (1950).

33. Treiman, S. B., Phys. Rev., 89, 130 (1953); 93, 544 (1954).

34. Kondo, I., Nagashima, K., Iosida, S., and Vada, M., Trudy Mezhdunar. konf. po kosmicheskim lucham, [Proceedings of the International Conference on Cosmic Rays], Vol. 4, USSR Acad. Sci. Publ., 1960, p. 210.

35. Dorman, L. I., Blokh, Ya. L., Kaminer, N. S., in the collection Kosmicheskie luchi,No.4, 5 (1961).

36. Dorman, L. I., Inozemtseva, O. I., in the collection Kosmicheskie luchi, No. 4, 237 (1961).

37. Dorman, L. I., Inozemtseva, O. I., Geomagnetizm i aeronomiya, 2 (3), 453 (1962).

38. Störmer, C., Arch. sci. phys. et natur., 32, 277, 413 (1911).

39. Ray, E. C., Phys. Rev., 101, 1142 (1956).

40. Dorman, L. I., Tyasto, M. I., in the collection Kosmicheskie luchi, No. 7, 121 (1965).

41. Dorman, L. I. and Inozemtseva, O. I., in the collection Kosmicheskie luchi, No. 7, 131 (1965).

42. Dorman, L. I., Tyasto, M. I., and Smirnov, V. S., Geomagnetizm i aeronomiya, 5 (5), 913 (1965).

43. Asaulenko, L. G., Dorman, L. I., Smirnov, V. S. and Tyasto, M. I., Geomagnetizm i aeronomiya, 5 (5), 809 (1965).

44. Dorman, L. I., Tyasto, M. I., and Fedorova, E. A., Izv Akad Nauk SSSR, Ser Fiz , 30 (100), 1830 (1966).

45. Makino, T. and Kondo, I., Proc. Internat. Conf. Cosmic Rays, Vol. 1, London, 1965, p. 564.

46. Akasofu, C. and Chapman, S., J. Geophys. Res., 66 (5), 1321 (1961).

47. Webber, W. R. and Quenby, J. J., Philos. Mag., 4 (41), 654 (1959).

48. Parker, E., Interplanetary Dynamical Processes, N. Y., 1963.

49. Ginzburg, B. L., Pikel'ner, S. B., and Shklovskiy, I. S., Astron zh , 32 (6), 503 (1955).

50. Dorman, L. I., Trudy Mezhdunar konf po kosmicheskim lucham [Proceedings of the International Conference on Cosmic Rays], Vol. 4, USSR Acad of Sci Publ, 1960, p. 328.

51. Alaniya, M. V., Dorman, L. I., Shatashvili, L. Kh., in the collection Kosmicheskie luchi, No. 8, 84 (1967).

52. Dorman, L. I., Geomagnetizm i aeronomiya, 6 (2), 231 (1966).

53. Neher, N. V. and Naderson, H. R., J. Geophys. Res., 69 (9), 1911 (1964).

54. Dorman, L. I. and Miroshnichenko, L. I., Geomagnetizm i aeronomiya, 5 (3), 377 (1965).

55. Dorman, I. V. and Dorman, L. I., Geomagnetizm i aeronomiya, 5 (5), 666 (1965).

56. Shishov, V. I., Geomagnetizm i aeronomiya, 3 (4), 484 (1964).

57. Fibish, M. and Abraham, P. B., J. Geophys. Res., 70 (11), 2475 (1965).

58. Dorman, L. I., Miroshnichenko, L. I., in the collection Kosmicheskie luchi, No. 8, 194 (1967).

59. Shishov, V. I., Geomagnetizm i aeronomiya, 6 (2), 223 (1966).

60. Krymskiy, G. F., Geomagnetizm i aeronomiya, 4 (6), 977 (1964).

61. Kuz'min, A. I., Variatsii kosmichekikh luchey vysokikh energiy, [High Energy Cosmic Ray Variations], Nauka Press, 1964.

62. Dorman, I. V. and Dorman, L. I., J. Geophys. Res., 72, 1513 (1967).

63. Simpson, J. A., Preprint No. 25, Vatican, 1963, p. 323.

64. Dorman, I. V. and Dorman, L. I., in the collection Kosmicheskie luchi, No. 7, 5 (1965).

65. Dorman, L. I., Luzov, A. A. and Mamrukova, V. P., Dokl Akad Nauk SSSR, 172, 833 (1967).

66. Dorman, L. I., Geomagnetizm i aeronomiya, 6 (2), 231 (1966).

67. Dorman, L. I., in the collection Kosmicheskie luchi, No. 8, 305 (1967).

68. Dorman, L. I., Trudy Mezhdunar konf po kosmicheskim lucham [Proceedings of the International Conference on Cosmic Rays], Vol. 4, USSR Acad of Sci Publ., 1960, p. 328.

69. Vedenov, A. A., Velikhov, E. P. and Sagdeev, R. Z., Yadernyy sintez, 2, 11 (1961).

70. Dorman, I. V. and Dorman, L. I., Geomagnetizm i aeronomiya, 7 (6) (1967).

71. Dorman, I. V. and Dorman, L. I., Izv Akad Nauk SSSR, Ser. Fiz., 31 (8) (1967).

72. Fan, C. Y., Gloeckler, G. and Simpson, J. A., Proc. Internat. Conf. Cosmic Rays, Vol. 1, London, 1965, p. 380.

73. Balasubrahmanyan, V. K., and McDonald, F. B., J. Geophys. Res., 69 (15), 3289 (1964).

74. Ormes, J. F. and Webber, W. R., Proc. Internat. Conf. Cosmic Rays, Vol. 1, London, 1965, p. 349.

75. Freier, P. S. and Waddington, C. J., Phys. Rev. Letters, 13, 108 (1964).

76. McDonald, F. B. and Ludwig, G. H., Phys. Rev. Letters, 13, 783 (1964).

77. Dorman, I. V. and Dorman, L. I., Geomagnetizm i aeronomiya 5 (4), 666 (1965).

78. Dorman, I. V. and Dorman, L. I., Izv Akad Nauk SSSR, Ser Fiz , 30 (11), 1239 (1966).

79. Gloeckler, G. and Jokipii, J. K., Phys. Rev. Letters, 17, 203 (1966).

80. Fan, C. Y., Gloeckler, G., Hsich, K. C. and Simpson, J. A., Phys. Rev. Letters, 16, 813 (1966).

81. Fan, C. Y. and Simpson, J. A., Proc. Internat. Conf. Cosmic Rays, Vol. 1, London, 1965, p. 109.

82. Ginzburg, V. L. and Syrovatskiy, S. I., Proiskhozhdeniye kosmicheskikh luchey, [The Origin of Cosmic Rays], USSR Acad. Sci. Publ., 1963.

83. Dorman, L. I., Proc. Internat. Conf. Cosmic Rays, Vol. 2, Jaipur, 1963, p. 76.

84. Kamke, E., Spravochnik po obyknovennym differentsial'nym uravneniyam [Handbook on Ordinary Differential Equations], Fizmatgiz Publ., 1967.

85. Yanke, Ye., Emde, F., Tablitsy funktsiy s formulami i krivymi [Table of Functions with Formulas and Curves], Moscow, Goskhimizdat Publ., 1949.

86. Dorman, L. I., in the collection Kosmicheskie luchi, No. 4, 128 (1961).

87. Gradshteyn, I. S. and Ryzhik, I. M., Tablitsy integralov summ, ryadov i proizvedeniy [Tables of Integrals, Sums Series and Products], Fizmatgiz Publ., 1962.

N75 16454

ENERGY SPECTRUM OF GALACTIC ELECTRONS IN THE ENERGY RANGE $2 \cdot 10^{10} - 2 \cdot 10^{11}$ eV

V. I. Zatsepin, V. I. Rubstov, and N. S. Svirzhevskiy

ABSTRACT

New experimental data on the energy spectrum of galactic electrons up to the energies $\sim 2 \cdot 10^{11}$ eV were obtained in the summer of 1967 by a scintillation telescope lifted to the stratosphere at 32 km. The geometrical factor of the telescope was 1200 sq. cm steradians, i.e., three times as great as the geometrical factor of previously employed installations. The results confirm the previous measurements and are in disagreement with the data obtained by Daniel and Stephens.

In the summer of 1967 the investigations of the energy spectrum of electrons which began earlier were continued [1]. The main emphasis in these investigations was on movement in the high energy range. An instrument whose geometrical factor was 1200 $cm^2 \cdot$steradians, which exceeds three times the geometrical factor of the apparatus used earlier, was constructed for this purpose. The instrument consisted of three identical telescopes, whose centers were situated at the vertices of an equilateral triangle whose side was 380 mm long.

Figure 1 shows the schematic diagram of one telescope. The principle by which the electrons were isolated was the same as before [1]. The absorber Pb_1 could be removed and placed in sequence above one of the telescopes. The scintillator S_1 was added to provide the capability for eliminating events caused by nuclear interactions in the displaceable lead block when it was above the neighboring telescope. The scintillators and absorber had the form of circular disks with a 30-cm diameter. The thickness of each absorber was 3t-units. The triple coincidence circuit S_2, S_3, S_4 served as the master, requiring an energy release greater than 0.2 I_μ, 6 I_μ and 50 I_μ, respectively (I_μ is the ionization isolated in each scintillator by the relativistic μ-meson. The scintillator S_1 required an ionization $> 0.2\ I_\mu$. In each recorded event, a mark indicated the presence or absence of ionization in the scintillator S_1. During processing, only

those events were sampled, when, along with the master, ionization occurred in S_1 (quadruple coincidence circuit $S_1S_2S_3S_4$). The amplitude of the signal from S_2, S_3 and S_4 was analyzed using amplitude analyzers.

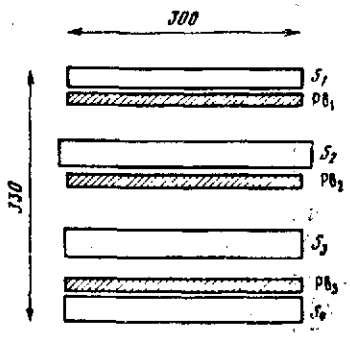

Fig. 1. Schematic diagram of scintillation telescope S_1, S_2, S_3, S_4 -- Plastic scintillators; Pb_1, Pb_2, Pb_3 -- Lead scintillators

This article reports the results of the preliminary precoessing of the data available to us. To construct the energy spectrum, we sampled for the time being only high energy events ($\geq$ 20 BeV).

Out of all events caused by single charge particles and satisfying the required release of energy in the scintillator, only those were selected which were not accompanied by ionization in the scintillators S_1 or S_2 of the neighboring telescopes. /68 The events that were not accompanied represented approximately 20% of all "single charge" events. The remaining events were caused by local nuclear reactions in the substance of the telescopes, which follows from an analysis of the high altitude behavior of the events "that were accompanied."

The results obtained from processing the data are shown in Fig. 2. The values of the electron intensities which are plotted in the graph were obtained by averaging the data from all three telescopes, and the errors correspond to the scatter in the data. The diagram shows also our former data as well as the data of other authors. The new data confirmed our former results. However, the data clearly disagreed with the results of R. R. Daniel and S. A. Stephens [2] both with regard to the absolute intensity of the electron flux and with regard to the inclination of the spectrum. We plotted in the same diagram the upper limit for the intensity of the γ-quanta and electrons with E > 470 BeV according to the data from the Bristol group [3]. The total primary flux of γ-quanta and electrons, according to

[4], is considerably smaller than that which can be expected by extrapolating the electron spectrum of Daniel and Stephens. At the same time, this result apparently does not contradict the extrapolation of our spectrum in the high energy range.

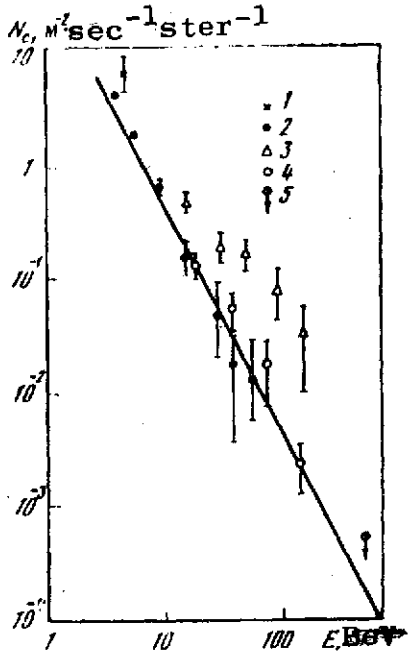

Fig. 2. Total energy spectrum of galactic electrons.

1--data [4]; 2--our previous data [1]; 3--data [2]; 4--our new data; 5--upper limit for the intensity of γ-quanta and electrons according to the data [3]

In conclusion, it is our pleasant duty to express our gratitude to A. N. Charakhch'yan for useful comments and constant interest in the work, to Yu. F. Chekhovskikh for his help in carrying out the experiments, and to G. G. Zorina and V. I. Obryvalova for their help in processing the results that were obtained.

REFERENCES

1. Rubitsov, V. I., Zatsepin, V. I., Izv Akad Nauk SSSR, Ser Fiz, 31, 1233 (1967).

2. Daniel, R. R., Stephens, S. A., Proc. Internat. Conf. Cosmic Rays, 1, London, 1965, p. 335.

3. Fowler, P. H., Proc. Internat. Conf. Cosmic Rays, 5, Jaipur, 1963, p. 182.

4. Bland, G. I., Boella, G., Degli Antoni, G., Phys. Rev. Letters, 17, 813 (1966).

N75 16455

THE RELATION BETWEEN THE CHEMICAL COMPOSITION OF SOLAR COSMIC RAYS AND THE DURATION SPECTRUM OF RADIOSPLASHES

N. P. Tsimakhovich

ABSTRACT

The comparison of durations of the centimeter and meter components of the radiosplashes corresponding to the chromospheric flares with the known chemical composition of the radiated nuclei has shown a greater duration of the centimeter component for the splashes wherein protons are dominating, and vice versa.

A conclusion is made about the interrelation of heavy nucleus emission and the processes which occur in the upper layers of the solar corona.

Measurements carried out on space rockets and artificial Earth satellites have shown that during certain flares on the Sun, not only protons are injected into interplanetary space, but also heavy nuclei [1 - 6]. To explain the origin of the heavy nuclei, B. M. Vladimirskiy proposed the preferred acceleration mechanism of heavy nuclei on the Sun [7]. It is assumed that the protons are formed along the path of the nuclear flux during collisions in the solar atmosphere. This implies that pure proton bursts lie deep in the chromosphere and pure nuclear bursts in the corona. This concept agrees with the classification of bursts into chromosphere and corona bursts [8, 9]. S. I. Akin'yan has shown that the depth of the burst is reflected in the initial frequency of the corresponding radiosplash [10].

We proposed the hypothesis that the spectral properties of the radiosplash are indicators of the chemical composition of the particle flux [11]. To verify this proposition, schematic diagrams of radiosplashes were set up for 17 cases of solar cosmic ray flares whose chemical composition was known [12]. The schematic diagrams are given in the form shown below for the four most characteristic frequency ranges, around 9000, 3000, 600 and 200 MHz. The cases considered by us are subdivided into two groups: A--12 cases of proton radiation associated with large chromospheric flares (Class > 2) and B--5 cases without protons preceded by small bursts and in some cases not even by these.

In Group A (Table 1) cases No. 6 and No. 8 with a very large number of protons are singled out. The assumption can be made that the corresponding flares occurred at very great depth which is confirmed by the radio spectrum characterized by the long duration of the event in the centimeter range (Fig. a). In cases No. 11 and No. 12, the proton content is small. Here, it is assumed that the process developed in higher layers of the solar atmosphere. Hence, the meter range is apparently more

Table 1. A. SOLAR COSMIC RAYS EMITTED DURING CHROMOSPHERIC FLARES

Case No.	Chromospheric Flares					Particles		$\frac{\Delta I\ 200\ MHz}{\Delta I\ 3000\ MHz}$
	Yr.	Data	Beginning Time	Coord. Points	Class	p^+/α	α/M	
1	1958	23 III	09 h 47 min	14°S73°E	3+	1	?	1.8
2	1959	10 V	20.55	17N50E	3	1	?	1.4
3		10 VII	20.06	20N60E	3+	1.4	—	4.2
4		14 VII	03.25	17N04E	3+	1	?	4.8
5		16 VII	21.14	16N31W	3	1	?	1.6
6	1960	4 V	10.00	13N90W	2	⩾50	—	0.2
7		20 VIII	06.25	18N87W	2+	⩾1	?	30.0
8		3 IX	00.37	18N88E	2+	30—40	42	0.3
9		12 XI	13.15	27N04W	3+	1	~70	0.8
10		15 XI	02.07	25N35W	2+	1	~100	3.0
11	1961	12 VII	09.50	07S23E	3	⩾1	?	0.3
12		18 VII	09.21	07S59W	3+	6	?	0.9

developed and the radiosplash is absent in the 3-cm range (Fig.c, d). The schematic diagrams of the radiosplashes of the remaining seven cases in Group A have both a developed meter and centimeter range, for example, No. 5 (Fig. d). This relation holds regardless of where the flare occurred on the Sun. Clearly the flares presented took place at higher levels than the other flares. /70

Since it is known that the duration of the meter range of the radiosplash is generally greater for central flares, we will consider pairwise the characteristics of two central and two extreme flares with different proton composition. For the study,

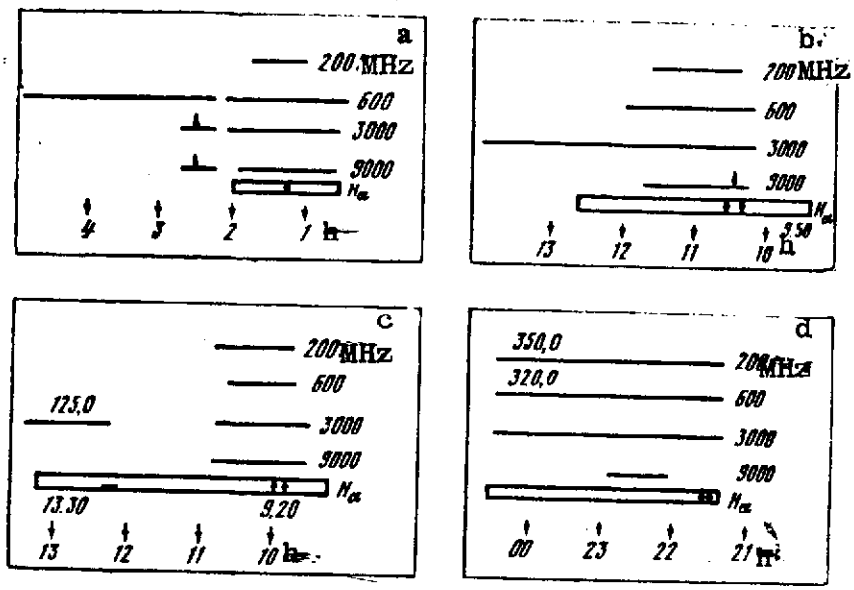

Fig. RADIO SPECTRUM

No. of case: a-8, b-11, c-12, d-5

we will take cases No. 5 and No. 11 (see Figs. c and d) and Nos. 12 and 8 (see Figs. a and c). The first pair of radiosplashes which corresponds to central flares shows a pronounced dependence of the duration of the meter and centimeter components on the nuclear composition of the bursts: for No. 5 the ratio for the duration of the meter and 10-cm components is 2, and for No. 11 it is 0.3. In flares on the boundary, it is much less pronounced: for No. 12 the ratio of the two components is 0.9 and for No. 8, it is 0.3.

Thus, in flares on the boundary, the nuclear effect may be superposed by the effect of the different directivity of the meter and centimeter components of radiosplashes. In the central part of the solar disk, the flares containing fewer protons are characterized by a more clearly pronounced duration of the meter component of the radiosplash compared to the centimeter component.

The cases in group B (Table 2) are analyzed analogously. The events on September 12, 1959, occurred against the background of a solar noise in the meter range. Therefore, the possible short-lived increases in the radio flares are not singled out in the meter component. With regard to the microwave range,

splashes were not detected in the 3-cm range. Short-lived splashes occurred at 10 cm and at 37.5 cm, at 10 h. 00 min. and at 11 h. 30 min. Universal time (UT), respectively.

Table 2. SOLAR COSMIC RAYS EMITTED WITHOUT CHROMOSPHERIC FLARES

/71

Case No.	Year	Data	Beginning Time	Duration in min	Particles	
					z	p'
13	1959	12 IX	11 h 27 min	17	⩾15	None
14		12 IX	12.57	13	⩾15	"
15		12 IX	15.23	25	⩾15	"
16		13 IX	07.07	7	~2	
17	1960	1 XII	11.20	12	12÷14	?

The acceleration of these fluxes must take place shortly before they are recorded in interplanetary space. Only subflares are detected on the Sun at this time and only after the corpuscular phenomenon near the Earth comes to an end. The events in the emission also began later. However, because all three types of phenomena occur approximately at the same time, they can be referred to the same process, taking place, apparently, in the upper layers of the Sun's atmosphere. The latter is indicated by the solar noise and the absence of microwave splashes. As a result of this, sudden perturbations which are related primarily to microwave splashes were not observed in the ionosphere.

If we accept the alternative hypothesis that various nuclear acceleration mechanisms exist on the Sun, it will not contradict the possibility of indicating the chemical composition of solar cosmic rays with the aid of the radio spectrum. In fact, the assumption can be made that the acceleration mechanisms that are active in the deep and high layers of the Sun's atmosphere are different, which is very probable because of the great difference in the physical properties of these layers. Then the processes in the deep layers generate primary or secondary proton fluxes which are indicated by splashes with a developed microcomponent. The processes in the high layers generate heavy nucleus fluxes and are accompanied by radiosplashes in the dead range.

It must be mentioned that the available data about heavy nucleus fluxes are insufficient to form a final opinion. However, certain preliminary concepts can be proposed. Taking into consideration the short duration of the nuclear effects and the fact that they are not related to the important events in the optical or radio range, the assumption can be made that they occur

comparatively frequently, although until now they have been recorded only occasionally. In fact, two space rockets recorded, during their flight, four cases. Since the level of solar activity at that time was relatively low, we can assume that the frequency of the nuclear splashes represents a mean value. Even if we take it as an index indicating the frequency of the phenomenon, we can conclude that within one month at least 20 - 30 cases occur in which heavy nuclei are emitted from the Sun. This corresponds to an abundance of events in the dead range.

The scatter, in the time when the splashes, radio and nuclear events occur, confirm the complexity of the sporadic solar activity effects, taking place very often without optical phenomena, in accordance with the concepts developed by D. Wentzel [13]. This refers primarily to corona flares. Since these are usually Class 2 flares, the conclusion can be made that "unseen flares" take place in the upper layers of the Sun's atmosphere.

Thus, the recording of the radio flares on the Sun in the four characteristic frequency ranges can serve as an indicator of the chemical composition of the nuclei emitted from the Sun.

REFERENCES

1. Kurnosova, L. V., Razorenov, L. A. and Fradkin, M. I., Iskusstv Sputniki Zemli, No. 5, 19 (1960).

2. Kurnosova, L. V., Razorenov, L. A. and Fradkin, M. I., Iskusstv Sputniki Zemli, No. 6, 132 (1961).

3. Ginzburg, V. L., Kurnosova, L. V., Razorenov, L. A. and Fradkin, M. I., Usp. Fiz Nauk, 82, 585 (1964).

4. Kurnosova, L. V., Razorenov, L. A. and Fradkin, M. I., Iskusstv Sputniki Zemli, No. 12, 31 (1962).

5. Kurnosova, L. V., Razorenov, L. A. and Fradkin, M. I., Iskusstv Sputniki Zemli, No. 15, 66 (1963).

6. Kurnosova, L. V., Pogachev, V. I., Razorenov, L. A. and Fradkin, M. I., Trudy FIAN, 23, 3 (1964).

7. Vladimirskiy, B. M., Izv Krym Astrofiz. Observ., 33, 151 (1965).

8. Slonim, Yu. M., Astron Zh, 39, 798 (1962).

9. Slonim, Yu. M., Solnechnyye dannyye, No. 4, 67 (1963).

10. Akun'yan, S. I., Solnechnyye dannyye, No. 10, 58 (1965).

11. Cimahovica, N., Zvaigznota debess, 26, ziema, 16 (1965).

12. Cimahovica, N., Zvaigznota debess, 34, ziema, 7 (1967).

13. Wentzel, D., Astrophys. J., 32, 185 (1961).

N75 16456

III. MODULATION EFFECTS OF COSMIC RAYS

SOLAR ACTIVITY AND COSMIC RAYS IN THE PERIOD 1963-1965

A. G. Zusmanovich, Ye. V. Kolomeyets, R. A. Chumbalova, Yu. A. Shakhova

ABSTRACT

The article presents the results of investigations of the interrelation between the intensity of cosmic rays and various indices of solar activity during January 1963 to June 1965.

In papers [1 - 3] it was shown that a considerable lag exists in the maximum intensity of cosmic rays from the minimum solar activity which is determined from the sunspot number. Thus, the minimum sunspot number in the last solar activity cycle is observed in the third quarter of 1964, and the maximum intensity in May 1965, which gives a lag of 9-10 months. Having determined in this way the time lag in the intensity of cosmic rays relative to solar activity, the authors in [2 - 4] found that the modulation region extends up to 80-160 AU.

Analogous dimensions of the modulation region were found on the basis of the data about the 27-day variations in the cosmic ray intensity in [5]. However, in papers [6, 7] in which the data about the intensity of cosmic rays in the stratosphere were compared with the solar activity determined from sunspot groups, it was found that the modulation region extends approximately up to 7 AU. Paper [8] has shown that the dimension of the modulation region is at most 20 AU and that the most likely value is 8-12 AU. The authors of [9], who studied the relation between the intensity of the cosmic rays and the sunspot number, their area, and the intensity of the magnetic field, found that the lag in the maximum cosmic ray intensity relative to the minimum solar activity was the same for all three activity indices that had been selected, and that it was 2-3 months, which gives dimensions of the modulation zone on the order of 10-12 AU. In paper [10], the intensity of cosmic rays was correlated with the radiation at the corona line λ 5303 Å, and it turned out that the correlation coefficient was very high (0.96). In addition to this, the authors of [10] assume that no shift in the intensity of the cosmic rays relative to the radiation at the line 5303 Å exists, i.e., that the modulation zone does not exceed several AU. Earlier it was shown [11, 12] that the radiation at the line 5303 Å can be used as an index of solar activity.

This paper presents the results of investigations of the relation between the intensity of cosmic rays and various indices of solar activity in the period January 1963 - June 1965, i.e., during minimum solar activity.

1. The Correlation Between the Intensity of Cosmic Rays and Radiation at the Corona Line 5303 Å

/74

Radiation at the line 5303 Å was taken from paper [13] from the data in the stations Pictou-Midi (France) and Kislovodsk (USSR). All data were broken up into five heliolatitude bands: I (40 - 80°) N, II (10 - 40°) N, III ± 10°, IV (10 - 40°) S, V (40 - 80°) S, (Fig. 1). From Fig. 1 it can be seen that the minimum radiation at the line 5303 Å occurred in March-April 1965, which is especially evident from the data for the equatorial band III.

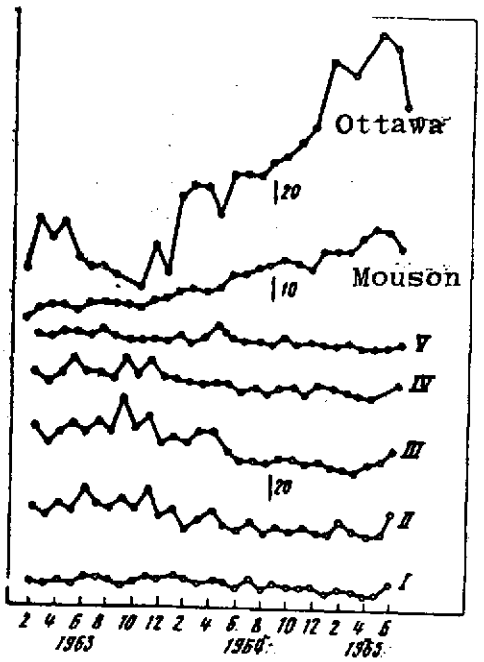

Fig. 1. Changes in the intensity of cosmic rays at the Mouson and Ottawa stations top, and the radiation intensity at the corona line 5303 Å in five solar bands bottom, in the period 1963-1965. Scale in relative units.

Thus, if we take as an index of the solar activity the radiation at the corona line 5303 Å, the lag in the maximum intensity of cosmic rays (May 1965) from minimum solar activity is 1-2 months. Table 1 gives the values of the correlation coefficient for the radiation at the line 5303 Å and the intensity of cosmic rays obtained on the basis of the data from neutron monitors (Ottawa, Mouson, Uankayo) and measurements carried out in the stratosphere (Murmansk). The largest values of the correlation coefficient were obtained for a phase shift

of 1-2 months. In addition to this, it can be seen that the highest correlation with the radiation is observed in band III, which indicates the great effectiveness of the equatorial zones in the modulation of cosmic rays in the period investigated.

2. The Correlation between the Intensity of the Cosmic Rays and the Sunspot Number

The correlation between the total number of spots on the entire disk, according to the data [13] and also the number of sunspots in the two solar latitude bands: $\pm 20^{\circ}$ and $\pm(20\text{-}90^{\circ})$ according to the data [14] and the intensity of cosmic rays was studied (Table 2). From Table 2 it can be seen that the highest correlation coefficient is obtained for a shift of 3-4 months.

Figure 2 gives the relations between the change in the intensity of the cosmic rays and the intensity at the line 5303 Å in various bands and the sunspot number (on the entire disk in different belts). On the basis of the values of the correlation coefficients and the graphs in Fig. 2, the conclusion can be made that the radiation at the corona line 5303 Å is a better index of solar activity than the sunspot number. When the time lag is 1-2 months, the dimensions of the modulation zone obtained are 8-10 AU. The dimensions of the modulation zone r_0 are determined from the equality for the pressure of the solar wind and the interstellar magnetic field

$$\frac{n_p m_p u^2}{2r_0^2} = \frac{H_{IM}^2}{8\pi}$$

where n_p is the concentration of the solar wind plasma on the orbit of the Earth, m_p is the mass of the proton, H_{IM} is the intensity of the magnetic field outside the region occupied by the solar plasma fluxes, and u is the velocity of the wind. Assuming that the mean velocity of the fluxes is $\sim 2\cdot10^7$ cm/sec, $H_{IM} = (5\cdot10)\cdot10^{-6}$ Oe [15] and $n_p = 1\text{-}2$ cm^{-3}, we obtain $r_0 = 10\text{-}16$ AU. /75

Table 1

/75

Station	Shift in mos	Band I	Band II	Band III	Band IV	Band V
Murmansk	0	−0,45±0,06	−0,56±0,05	−0,71±0,04	−0,61±0,05	−0,37±0,07
	1	−0,45±0,06	−0,55±0,05	−0,71±0,04	−0,55±0,05	−0,33±0,07
	2	−0,37±0,06	−0,56±0,05	−0,71±0,04	−0,56±0,05	−0,33±0,07
	3	−0,32±0,06	−0,56±0,05	−0,67±0,04	−0,52±0,05	−0,32±0,07
	4	−0,30±0,06	−0,58±0,05	−0,66±0,04	−0,49±0,06	−0,29±0,07
Mouson	0	−0,44±0,06	−0,51±0,06	−0,70±0,04	−0,44±0,06	−0,33±0,07
	1	−0,42±0,06	−0,51±0,06	−0,70±0,04	−0,56±0,05	−0,33±0,07
	2	−0,37±0,06	−0,53±0,06	−0,69±0,04	−0,53±0,06	−0,29±0,07
	3	−0,34±0,06	−0,56±0,06	−0,70±0,04	−0,54±0,06	−0,30±0,07
	4	−0,27±0,07	−0,57±0,04	−0,64±0,05	−0,50±0,05	−0,29±0,07
Ottawa	0	−0,46±0,06	−0,57±0,05	−0,71±0,04	−0,51±0,05	−0,32±0,06
	1	−0,41±0,06	−0,52±0,06	−0,74±0,03	−0,59±0,04	−0,37±0,06
	2	−0,33±0,07	−0,50±0,06	−0,69±0,05	−0,49±0,05	−0,32±0,07
	3	−0,28±0,07	−0,56±0,05	−0,69±0,05	−0,49±0,05	−0,30±0,07
	4	−0,24±0,07	−0,57±0,05	−0,56±0,05	−0,42±0,06	−0,27±0,07
Uankayo	0	0	−0,58±0,05	−0,59±0,05	−0,39±0,06	−0,17±0,08
	1	−0,05±0,08	−0,51±0,05	−0,66±0,05	−0,46±0,06	+0,06±0,08
	2	−0,13±0,08	−0,40±0,06	−0,51±0,05	−0,38±0,06	−0,12±0,07
	3	0	−0,54±0,05	−0,62±0,05	−0,38±0,06	−0,13±0,07

Table 2

Station / Band	Shift, months						
	0	1	2	3	4	5	6
Mouson	−0,43±0,06	−0,46±0,05	−0,46±0,05	−0,51±0,05	−0,53±0,05	−0,40±0,06	−0,41±0,06
Ottawa	−0,40±0,06	−0,43±0,06	−0,46±0,05	−0,51±0,05	−0,51±0,05	−0,35±0,06	−0,35±0,06
Uankayo	−0,36±0,06	−0,43±0,06	−0,45±0,05	−0,59±0,04	−0,43±0,06	−0,37±0,06	−0,36±0,06
± (0—20°)	−0,55±0,05	−0,54±0,05	−0,52±0,05	−0,52±0,05	−0,50±0,05	−0,47±0,05	−0,44±0,05
± (20—90°)	+0,42±0,06	+0,35±0,06	+0,26±0,07	+0,28±0,06	+0,23±0,07	+0,17±0,07	+0,18±0,07

The observed corona radiation lines come from highly ionized atoms. They are formed in metastable states. This means that the life of the excited state before radiation is shorter than the time interval between the collisions during which the excitation energy is transferred to the colliding particle. The lines 5303 and 6374 Å used by us belong to the ionized iron atom that has lost 13 and 9 electrons (Fe_{XIV} and Fe_X). Such lines are excited by the electron bombardment (the excitation is proportional to N_e^2, where N_e is the electron concentration) in the inner corona and the radiation (excitation proportional to N_e/r^2) in the outer corona [16, 17]. Ratios of the intensities of the corona lines can be used to determine the temperature inside the corona [11-18]. If there are N(I - x) ions per unit volume in the p-th level of ionization and the remaining Nx ions are in the (p + 1)-th level, /76

$$\frac{x}{1-x} = \frac{S(p \to p+1)}{\alpha(p+1 \to p)},$$

where S(p → p + 1) is the collision ionization coefficient at the p-th level of ionization and α (p + 1 → p) is the recombination coefficient. These coefficients are [16]:

$$S(p \to p+1) = 3 \cdot 10^{-8} T^{1/2} \chi_p^2 e^{-\frac{11600}{T}\chi_p},$$
$$\alpha(p+1 \to p) = 1{,}5 \cdot 10^{-11} Z^2 T^{-1/2},$$

where Z is the charge of the ion in the (P + 1)-th ionization level, χ_p is the ionization potential of the p-th state in electron volts, and T is the temperature. Comparing the lines 5303 and 6374 Å we have

$$\frac{N_{Fe_{XIV}}}{N_{Fe_X}} = \frac{N_{XIV}}{N_{XIII}} \frac{N_{XIII}}{N_{XII}} \frac{N_{XII}}{N_{XI}} \frac{N_{XI}}{N_X} =$$
$$= 9 \cdot 10^4 \chi_{13}^2 \chi_{12}^2 \chi_{11}^2 \chi_{10}^2 \exp\left[-\frac{11600(\chi_{13} + \bar{\chi}_{12} + \chi_{11} + \bar{\chi}_{10})}{T}\right] \cdot T^4,$$

or

$$\frac{I5303}{I6374} \simeq 3 \cdot 10^{24} \exp\left(-\frac{1{,}3 \cdot 10^7}{T}\right) \cdot T^4.$$

The calculations show that for the intensity values which were averaged over the disk, this ratio was 4.4 for June 1963, and 1.68 for May 1965. Thus, the mean temperature of the corona changed by several percent. However, for the band of solar latitudes ± 30° the ratio of I_{5303} to I_{6374} changed by a factor of 9.8, which gives approximately a 10% change in the temperature. Thus, the temperature of the corona decreases from the maximum solar activity to the minimum, while the intensity of the corona lines above the active solar regions increases [19].

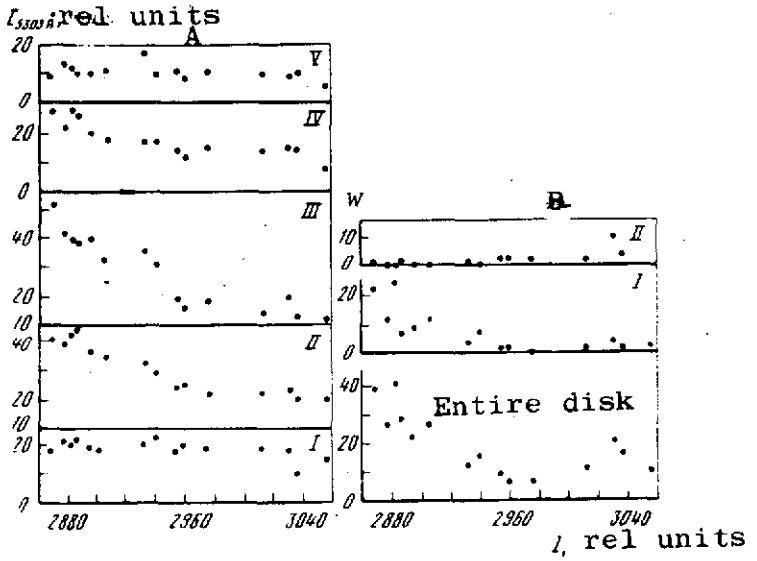

Fig. 2. Cosmic Ray intensity at the Ottawa station vs. the intensity of (a) the corona line 5303 Å and (b) the sunspot number.

Roman numerals indicate solar latitudes

According to the theory of E. Parker [20, 21] the velocity of the quiet solar wind is a function of the corona temperature. For a temperature of the corona of ~900,000° (for $I_{5303}/I_{6374} = 5$) the wind velocity on the Earth's orbit is ~ 400 km/sec. /77

Thus the radiation at the corona line 5303 Å and the ratio of I_{5303} to I_{6374} are a measure of the effect of the solar activity on the intensity of the cosmic rays, where the higher correlation between the intensity and the line 5303 Å indicates that the radiation at the line 5303 Å is a better index of solar activity than the sunspot number.

REFERENCES

1. Katzman, J. and Rose, D. C., Canad. J. Phys., 40, 1919 (1962).

2. Dorman, I. V. and Dorman, L. I., in the collection Kosmicheskie luchi, No. 7, 5 (1965).

3. Dorman, I. V. and Dorman, L. I., in the collection Kosmicheskie luchi, No. 8, 65 (1967).

4. Dorman, I. V. and Dorman, L. I., in the collection Kosmicheskie luchi, No. 8, 100 (1967).

5. Alaniya, M. V., Dorman, L. I. and Shatashvili, L. Kh., in the collection Kosmicheskie luchi No. 8, 84 (1967).

6. Charakhch'yan, A. N. and Charakhch'yan, T. N., Geomagnetizm i aeronomiya, 6 (3), 486 (1966).

7. Charakhch'yan, A. N. and Charakhch'yan, T. N., Geofizicheskiy byull., No. 17, 3 (1966).

8. Quenby, J. J., Proc. Internat. Conf. Cosmic Rays, Vol. 1, London, 1965, p. 3.

9. Kolomeyets, Ye. V. and Shakhova, Yu. A., Sbornik dokl. XXXI nauch. conf. Ural'sk, [Collection of Papers Read at the 31st Scientific Conference in Ural'sk], 1967, p. 148.

10. Hatton, C. J., Marsden, P. L. and Willets, A. C., Proc. Internat. Conf. Cosmic Rays, Mod. VI-50, Calgary, 1967.

11. Sarabhai, V., Proc. Internat. Conf. Cosmic Rays, Vol. 1, Jaipur, 1963, p. 190.

12. Sarabhai, V. and Subramanian, G., Proc. Internat. Conf. Cosmic Rays, Vol. 1, London, 1965, p. 170.

13. Quarterly Bulletin on Solar Activity, 1962-1965.

14. Solnechnye dannye za 1962-1965 gg, [Solar Data in the Years 1962-1965], Nauka Press, 1965.

15. Ginz'burg, V. L. and Syrovatskiy, S. I., Proiskhozhdeniye kosmicheskikh luchey, [Origin of Cosmic Rays], USSR Acad. of Sci. Publ., 1963.

16. Brandt, J. and Hodge, P., Astrofizika solnechnoy sistemy, [Astrophysics of the Solar System], Foreign Lit. Publ., 1967.

17. Shklovskiy, I. S., Fizika solnechnoy korony, [Physics of the Solar Corona], Fizmatgiz Publ., 1962.

18. Shklovskiy, I. S., Izv Krym Astrofiz Obser, 6, 105 (1951).

19. In the collection Solnechnaya sistema, [The Solar System], edited by D. Koyper, Vol. 1, Foreign Lit. Publ., 1957.

20. Parker, E. N., Proc. Internat. Conf. Cosmic Rays, Vol. 1, Jaipur, 1963, p. 173.

21. Parker, E. N., Dinamicheskie protsessy v mezhplanetnom prostranstve, [Dynamical Processes in Interplanetary Space], Foreign Lit. Publ., 1965.

N75 16457

THE COSMIC RAY BURST ON 28 JANUARY 1967

N. P. Chirkov, G. F. Krymskiy, I. S. Samsonov,
V. I. Ipat'ev

ABSTRACT

The solar cosmic ray flare which took place on January 28, 1967, is analyzed. Energy responses and the diffusion coefficient ($D = 6.5 \cdot 10^{21}$ cm^2/sec^{-1}) are determined. Periodic variations of the cosmic rays with an amplitude of 0.10 - 0.20% and a period of 35 to 40 min are discovered during the decrease phase of the flare.

On January 28, 1967, at 8 h 50 min UT a cosmic ray flare occurred in Tiksi, whose maximum occurred approximately at 12:00, and which ended early on January 20, i.e., the flare lasted approximately 24 hours. Figure 1 compares the data about the cosmic rays that were recorded in this period in several stations. The table gives the time when the maximum began and the amplitudes of the flare for these stations. The table and Fig. 1 show that the flare was almost isotropic and began on the average at 8 h 30 min. The amplitude up to 1.1 - 1.2 BV was the same within 1 - 2%, and for large pulses (up to 5 BV) the amplitude dropped in accordance with the law $\sim R_c^{-\gamma}$, with $\gamma = 1.8$. /78

Weak anisotropy was observed in the initial stage of the flare, which was characterized by a faster increase in the intensity in Deep River and Goose Bay than in other stations, and also by a somewhat earlier beginning of the flare at the stations (at 8 h 28 min and 8 h 22 min, respectively), i.e., the shock zone was apparently in Europe.

The intensity of the cosmic rays as a function of time can be expressed [1] in the form

$$n(t) = A\tau^{-\frac{3}{2-\alpha}} e^{-\frac{1}{\tau}},$$

where A is a constant and /79

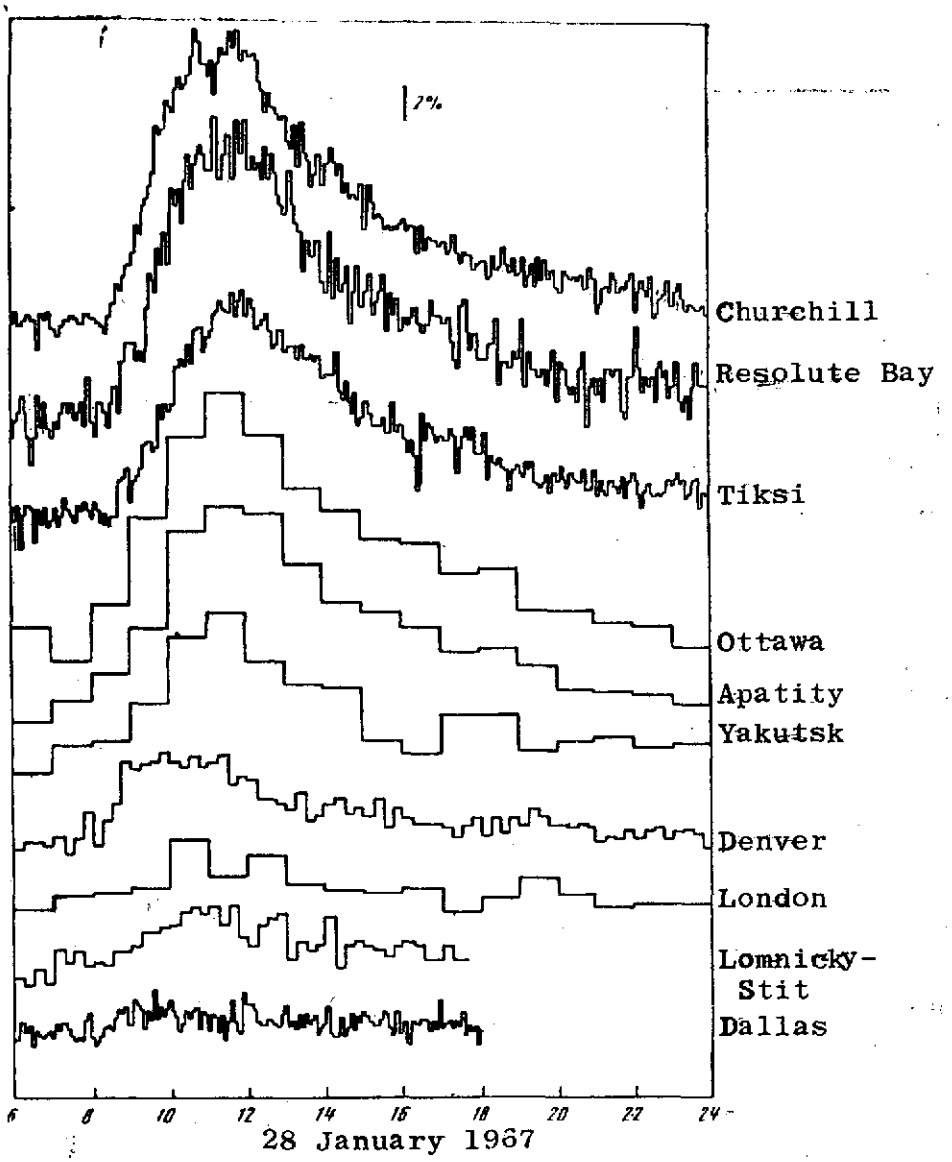

Fig. 1. Cosmic ray flare on January 28, 1967, on the basis of the data from neutron monitors mounted at the stations Churchill, Resolute Bay, Tiksi, Ottawa, Apatity, Yakutsk, Denver, London, Lomnicky-Stit, Dallas

$$\tau = \frac{2-\alpha}{\left(\frac{r_\delta}{r_\odot}\right)^{2-\alpha}+1}\frac{Dt}{r_\odot^2},$$

Here r_δ is the distance from the Sun to the Earth, $r_\odot$ is the radius of the Sun, D is the diffusion coefficient and t is time from the beginning of the flare. The parameter α characterizes the relation between the diffusion coefficient and the distance: $D(r) \sim r^\alpha$. When $\alpha = 0$, equation (1) becomes the usual diffusion equation.

Station	R_e BV	Beginning Time UT	Maximum Time	Amplitude, %
Resolute Bay	0,05	8 h 32.5 min 42.5 min	11,9 h ± 0,2 min	17,0±0,5
Alert	0,05	8.32.5±2,5	11,0±0,2	15,0
Inuvik	0,18	8.27.5±5,0	11,1±0,3	13,0
Churchill	0,21	8.27.5±2,5	10,7 ÷ 11,7	17,5
Goose Bay	0,52	8.22.5±5,0	11,3±0,3	12,5
Tiksi	0,53	8.47 5±2.5	11,7±0,2	13,0
Apatiti	0,64	8.30±30	11,5±0,5	13,0
Deep River	1,02	8.27 5±5,0	11,2±0,2	14,0
Ottawa	1,08	8.30±30	11,5±0,5	16,0
Sulphur	1,14	8.32±2,5	11,4±0,3	22,0
Vatutsk	1,70	8.30±30	11,5±0,5	9,5
London	2,73	8.30±30	10,5±0,5	4,0
Denver	2,91	8.22 5±7.5	10,1±1.2	5,0
Lomnicky-Stit	4,0	8.37.5±7,5	11,0±0,6	3,5
Dallas	4,4	8.32 5±2.5	9,5±0,5	1,5

Figure 2 gives the experimental data for Churchill which were smoothed using a moving average, using 12 and 5 min data, and the calculated curves for various values of α. In order that the curves agree, the time at which the flare began had to be shifted forward by 1 h, i.e., the assumption was made that the flare occurred approximately at 7 h 30 min. The latter generally agrees with the time when the chromospheric flare began in the visible range. Thus, according to the data available in the Crimean astrophysical observatory which we received, a Class 1 flare was observed on the 28th of January at 7 h 28 min, and in the active region with the coordinates 23°S and 19°E, at 8 h 58 min. At the same time, a radiosplash was observed at the frequency

3100 MHz with increased activity in the meter range. In the active zone mentioned above, there were also less than four subflares.

It can be seen from Fig. 2 that after the maximum, the intensity dropped faster than $t^{-8/2}$. The best agreement was observed when $\alpha = 1.2$, i.e., the drop in the intensity took place in accordance with the law $t^{-37.5}$. The approximation of the data from the Tiksi and Resolute Bay stations also confirms that $\alpha = 1.0 - 1.2$, and gives as the beginning of the burst $\sim$ 7 h 30 min.

The known values of the beginning (7 h 30 mon) and of the maximum ($\sim$ 11 hr 30 min) of the flare can be used to determine the mean length of the free travel.

$$\lambda = \frac{R_0^2}{(2-\alpha)\,ct_{max}} = 6{,}5\cdot 10^{11}\ \text{cm}$$

and the diffusion coefficient $D = \frac{\lambda c}{3} = 6{,}5\cdot 10^{21}\ \text{cm}^2/\text{sec}$

The values of λ and D that were obtained are considerably smaller than those obtained earlier, which is due to the fact that the active region was in the southern hemisphere and the eastern solar hemisphere, since the solar cosmic rays were apparently incident to the lines of force in the interplanetary magnetic field at a large angle. /80

The 5-min data from the supermonitors can be used to study cosmic ray variations whose period is less than 1 hour. For this purpose moving averages were obtained from the 3- and 5-min values and the 12- and 5-min values for the period of the flare. The second series was subtracted from the first series and, using the periodogram analysis method, the quasi-periodicity was found:

Station	Period	Amplitude
Resolute Bay. . . .	35'	0.19±0.02
Tiksi.	40	0.11±0.03
Churchill	40	0.16±0.03

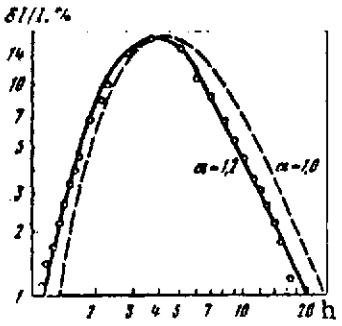

Fig. 2. Calculated (dashes) values for various values of α and the experimental values (points) of the relative cosmic ray intensity on January 28, 1967, vs. time t measured from the beginning of the flare

This periodicity in the fluctuations of the cosmic ray intensity is probably related to the fluctuations of the lines of force in the interplanetary magnetic field.

REFERENCES

1. Krymskiy, G. F., Doctoral dissertation, Scientific Research Institute of Nuclear Physics, Moscow State University, 1966.

2. Dorman, L. I., Variatsii kosmicheskikh lucheyi issledovanie kosmosa, [Cosmic Ray Variations and a Study of the Universe], USSR Acad. of Sci. Publ., 1963.

N75 16458

SOLAR ACTIVITY AND ITS RELATION TO CERTAIN PARAMETERS OF PHENOMENA IN THE GEOPHYSICAL COMPLEX

T. S. Razmadze, A. M. Chkhetiya

ABSTRACT

Results of a detailed analysis of solar activity in 1957-1965 are compared with the data on solar activity with variations of cosmic ray activity, and geomagnetic, ionospheric and terrestrial currents. Cosmic ray variations are investigated with reference to the asymmetry of solar hemispheres. All storms in the IGY are classified and a symbolic diagram of the time sequence is drawn up

This article presents briefly the results of a detailed analysis of solar activity in the IGY-IYQS (1957-1965), which was carried out on the basis of the cyclical law using the main characteristics of sunspots (areas and relative numbers) and on the basis of the results obtained from a study of the relation between the solar activity and variations in the intensity of cosmic radiation. The results of a study of the relation between geophysical phenomena of corpuscular origin (cosmic rays, geomagnetic, ionospheric and terrestrial fluxes) with solar flares in the IGY period [1-3] are also presented. /84

In the period studied, the activity in the solar hemispheres did not develop entirely synchronously, the common maximum was observed in September-October 1957 (by areas) and in October-December (by the relative sunspot numbers). The minimum was observed in June 1964 (by both indices of the solar activity).

An east-west and north-south asymmetry was detected in the development of the activity in cycle No. 19. Almost in the entire interval studied, the activity in the western solar hemisphere was greater than in the eastern hemisphere. In the development epoch and at the maximum of the cycle, the total activity was greater in the southern hemisphere, and towards the end of the cycle, in the northern hemisphere. The maximum activity occurred in January 1959. In the initial epoch of cycle No. 20, the activity in the northern hemisphere is highly dominant.

To compare the data about the solar activity with variations in the intensity of the neutron component of the cosmic variation, we used the linear correlation method. Figure 2 gives the graphs for the change in the correlation coefficients (the ordinate), respectively, by all the data about the solar activity

(by the areas s and the number of sunspots w) and by the data for various hemispheres (E, W, N, S) in the maximum epoch (1957-1962) (Fig. 2,a) and minimum (1960-1965) solar cycle (Fig. 2b). The corresponding data from the Norikura station were used for the cosmic rays (see Fig. 1). The values of the time shift k were plotted on the abscissa in months.

On the basis of the value of the coefficients, when the shift in the data that are compared is 0 (k = 0), the conclusion can be made that the activity of the Sun (by spots) and the variations in the intensity of the neutron component of the cosmic rays are highly negatively correlated, both in the maximum epoch, and the minimum epoch of the cycle under consideration. This confirms the conslusion about the possible modulation of cosmic rays also at the minimum in the 11-year solar cycle [4].

The results of the "shifted" correlation (k > 0) show that in the time interval studied, the effect of the Sun on cosmic ray variations may be considered as consisting of several effects related to the activity of various hemispheres of the Sun which lag from one another by different time intervals. In addition to this, the conclusion can be drawn that the north-south asymmetry in the development of the solar activity is reflected in the relation with the cosmic ray variations. In the maximum epoch, the greatest effect of the Sun occurs when the shift is zero, which also occurs in the case when the activity was studied in different hemispheres of the Sun. Other effects (by the curve for the southern hemisphere in the third and tenth months of the time shift and 4 - 6 and 11th months in the northern hemisphere) represent a smaller fraction in comparison with the first effect. During the minimum epoch, the effects of the Sun corresponding to various time shifts, in the given case for the zero and 10-month shift become comparable. The facts that were pointed out here can also be observed when the total activity of the Sun is studied (see curves Σs, Σw).

By comparing the two bottom curves in Fig. 2, it can be seen that the values of the correlation coefficients by the given relative sunspot numbers are consistently good (with a minor exception within the error range) and are slightly higher than the corresponding values of the coefficients by areas of the spots for both extremes of the solar cycle, which indicates the great "cosmic effectiveness" of the first solar activity index.

We will give the results of a comparison of variations in the intensity of cosmic rays I (the mean over the Zugspitz-Climax stations), the intensity of the horizontal component of the Earth's magnetic field H, the critical frequencies of the ordinary wave in the F2 layer of the ionosphere f_0F2, the maximum

amplitudes of the latitudinal component of the fluxes E_y on Earth (in MV/km) in the IGY period. This period was also studied in articles [5, 6]. In the first article, the geomagnetic perturbations were compared with phenomena on the Sun, and in the second article, the perturbations in the intensity of cosmic rays with geomagnetic phenomena. In article [7] it was shown that to compare the elements of the electromagnetic complex, it was useful to use smoothed curves. /85

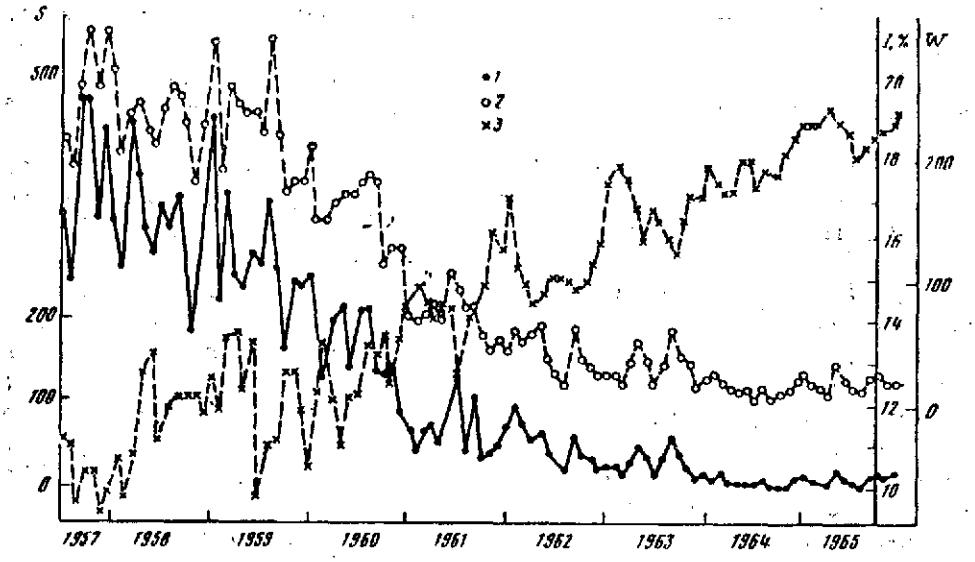

Fig. 1. Cyclical curves. 1--Area of spots s (in parts per million of the solar disk); 2--Sunspot number w; 3--Intensity of cosmic rays I (in %).

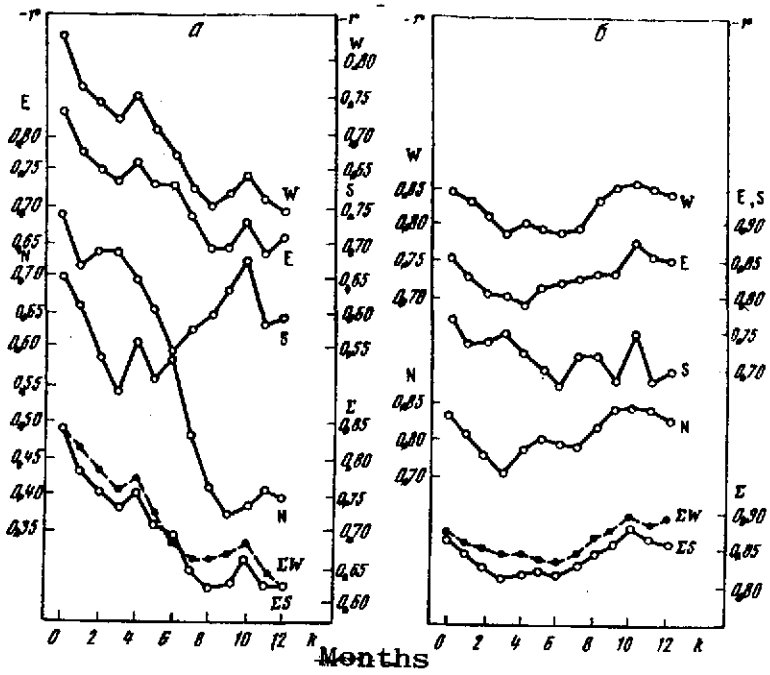

Fig. 2. Changes in the correlation coefficient between the intensity of cosmic rays and characteristics of sunspots obtained from mean monthly values when the data which were compared were shifted by different numbers of months k for (a) the maximum epoch and (b) the minimum epoch of the solar cycle.

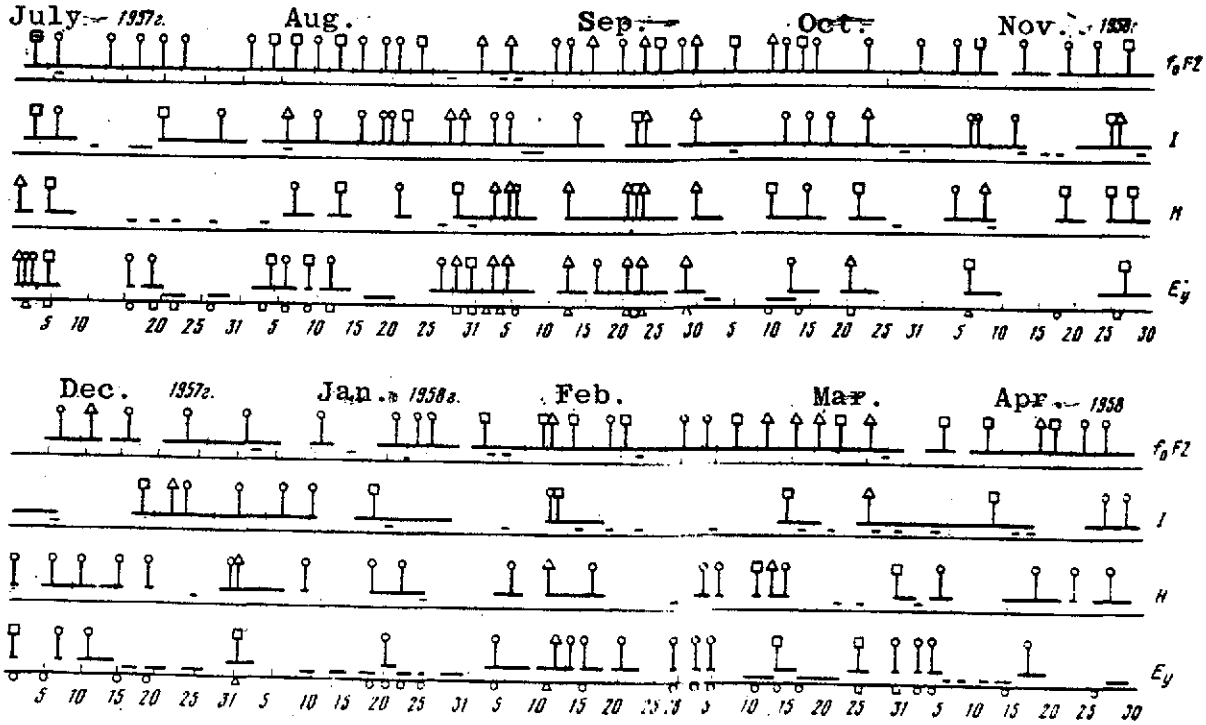

Fig. 3

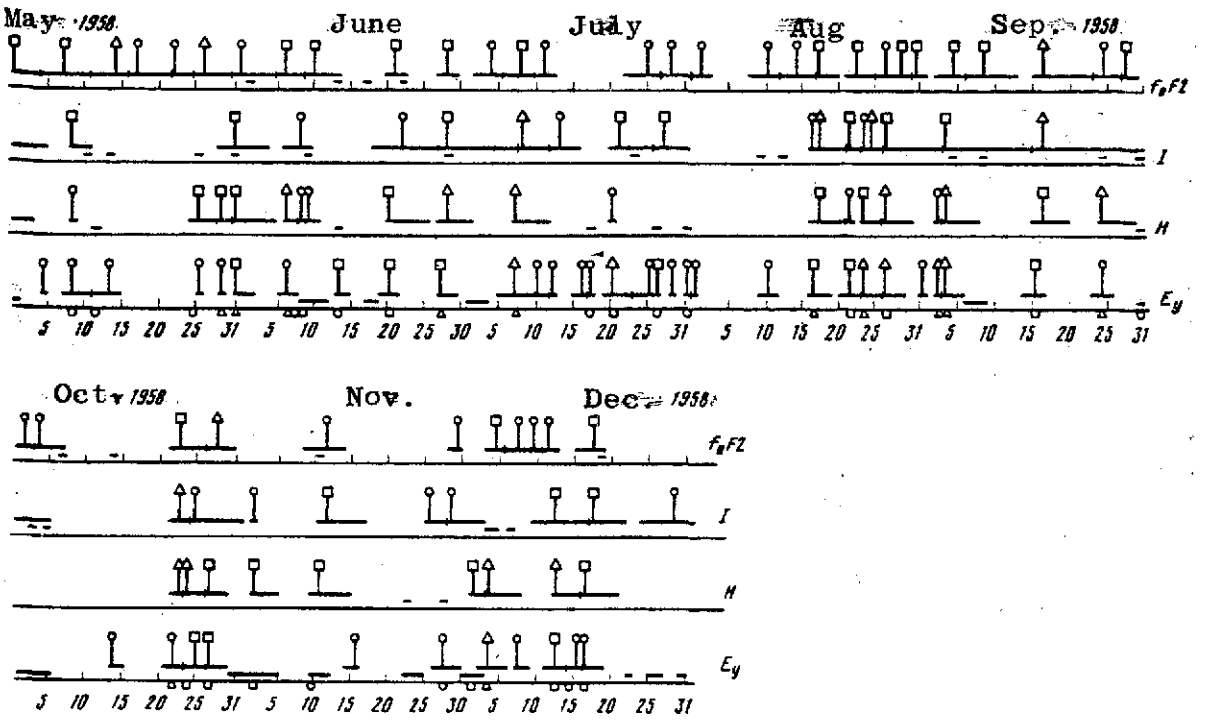

Fig. 3. Symbolic diagram for the time sequence of cosmic ray bursts, magnetic, ionospheric and terrestrial fluxes in the IGY period. Symbols in text.

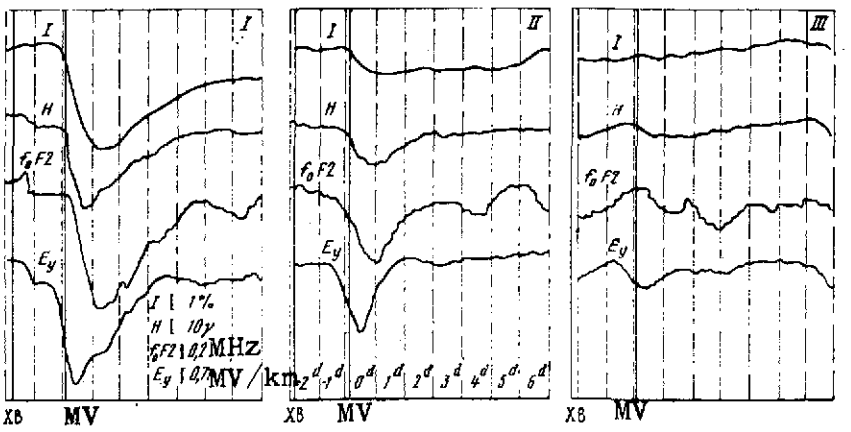

Fig. 4. Curves of cosmic rays, magnetic, ionospheric and terrestrial fluxes in the ICY period averaged over three groups of storms, (I)--great, (II)--moderate, and (III)--small.

The classification by the following groups was made on the basis of the curves for the phenomena that were mentioned above:

I. Great storms (triangle), $\Delta I > 5\%$; $\Delta f_0F2 > 4$ MHz; $\Delta H > 100\ \gamma$; $\Delta E_y > 15$ mV/km

II. Moderate storms (square), $3\% < \Delta N \leq 5\%$; 2 MHz $< \Delta f_0F2 \leq 4$ MHz; $70\ \gamma < \Delta H \leq 100\ \gamma$; 9 mV/km $< \Delta E_y \leq 15$ mV/km;

III. Small storms (circle), $\Delta I \leq 3\%$; $\Delta f_0F2 \leq 2$ MHz; $\Delta H \leq 90\ \gamma$; $\Delta E_y \leq 9$ mV/km;

IV. Perturbations (shaded circle), in I, f_0F2, H, E_y.

On the basis of these criteria, just as in the diagram in article [6], we set up a symbolic diagram for the time sequence of variations in the parameters studied due to storms in accordance with the above classification (Fig. 3). The figure shows by month (horizontal lines) the duration of the storms and indicates their intensity at the instant when the largest depression is observed.

To detect the connection between these phenomena, the method of epoch superposition was used. The data from the smoothed curves for the phenomena in the electromagnetic complex were averaged over three groups of storms, large storms (I), moderate storms (II), and small storms (III). The values when the magnetic storms began were taken according to [8] as the zero days. The boundaries were the two days which preceded the zero day and the six successive days. In Fig. 4 the vertical lines indicate the averages from all cases when the magnetic storms (MS) and chromospheric flares (CF) began.

Figure 4 shows the following.

1. The variations in the cosmic rays are most highly correlated with the phenomena in the electromagnetic complex in the period of great and very great magnetic storms. The degree of correlation decreases as the intensity of the magnetic storms decreases, until it vanishes completely.

II. On the average, the greater the velocity of the corpuscular flux, the more intense the corresponding storm (for example, $v_{g.s} = 1 \cdot 10^8$ cm/sec; $v_{m.s} = 0.9 \cdot 10^8$ cm/sec; $v_{s.s} = 0.8 \cdot 10^8$ cm/sec). /86

III. In the case of great storms (I) (which were mainly caused by solar flares whose power was 3.3^+, which are accompanied by a radiosplash of type IV), a slight increase was detected in the variations of the critical frequencies of the ordinary wave

in the F2 layer and in the ionosphere. This additional ionization is apparently the result of the bombardment of the F2 layer by low energy particles generated during the flares.

The correlation coefficients (0.7 - 0.9) for all components in the complex studied show high correlation in the case of great storms. To estimate quantitatively the relation between the quantities I and H, f_0F2, E_y we found the regression lines using the method of least squares. Figure 5 shows that to a 1% change in the intensity of the neutron component of cosmic rays corresponds a change in the intensity of the horizontal component of the Earth's magnetic field of 10γ, a change in the critical frequency of the ordinary wave in the F2 layer of 0.35 MHz, and a change in the maximum amplitude of the latitudinal component of terrestrial fluxes of 0.8 MV/km.

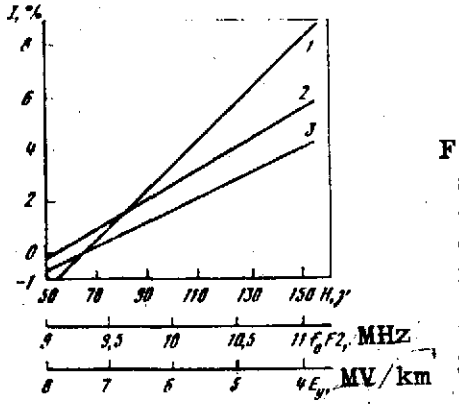

Fig. 5. Regression lines for the intensity of cosmic rays and the parameters of ionospheric and geomagnetic phenomena on the one hand, and also terrestrial fluxes on the other hand.

1--$I = K_1H + b_1$; 2--$I = K_2F2 + b_2$; 3--$K_3E_y + b_3$

REFERENCES

1. Solnechnye dannye za 1957-1965 gg, [Solar Data for the Years 1957-1965], USSR Acad. of Sci. Publs.

2. Gnevysheva, R. S., Katalogi deyatel'nosti Solntsa za 1956-1959 gg, [Catalogues of Solar Activity for 1956-1959], Publications of the Main Astronomical Observatory of the USSR Acad. of Sci. in Pulkov.

3. Cosmic Ray Intensity during the I.S.Y. and 1959-1965, Tokyo.

4. Dorman, I. V. and Dorman, L. I., in the collection Kosmicheskie luchi, No. 7, 5 (1965).

5. Mustel', E. R., Yegorova, N. B., Solnechnaya aktivnost', No. 1, 5 (1961), USSR Acad. of Sci. Publs.

6. Bashle, F., Balata, P., Konforto, Ye. and Marini, G., Trudy Mezhdunar. konf. po kosmicheskim lucham, [Proceedings of the International Conference on Cosmic Rays], IV, USSR Acad. of Sci. Publs., 1950.

7. Chkhetiya, A. M., in the collection Nekotoryye voprosy issledovaniya elektromagnitnogo polya Zemli, [Certain Problems in the Study of the Earth's Electromagnetic Field], Tbilisi, Georgian SSR Acad. of Sci. Publs., 1965, p. 105.

8. Meada, H., Sakyari, K., Ondon, T. and Yamamoto, M., Ann. Geophys., 18 (4), 305 (1962).

N75 16459

ATMOSPHERIC EFFECTS AND SIDEREAL-DIURNAL VARIATIONS IN EXTENDED AIR SHOWERS

/87

N. N. Efimov, D. D. Krasil'nikov,
S. N. Nikol'skiy, F. K. Shamsutdinova

ABSTRACT

The paper presents the results of observations recorded during 1959-1964 on the variations of the extended air shower intensity with an average power of 1.4×10^4 and 1.4×10^5 particles at sea level.

The effect of disintegrating particles and the essential role of cascades formed above the lower third of the atmosphere are examined. However, the authors failed to discover anisotropy of initial particles with an energy of $10^{14} - 10^{15}$ eV with an accuracy of up to 0.1%.

The equipment for protracted observations of extended air showers at sea level used by us was already described in articles [1, 2]. The characteristics of the experimental data on which this report is based are given in Table 1. In this table C (3; 1.0; 3.8) are the triple coincidences between the groups of counters G-M with an area of 1.0 m^2, at a distance of 3.8 m from one another ("local installation"); C (6; 1.0; 57) are the sixfold coincidences between the two local installations at a distance of 57 m from one another, $\bar{N}$ is the mean power of the extended air shower by the number of charged particles, $\bar{f}$ and n are the mean counting rate and the total number of showers used in the analysis, respectively.

The geometric effect of the change in the density of the atmosphere is estimated from the variation of the altitude at the level h_0 - 100 mb using the altitude coefficient α_H which was calculated earlier [3]. α_T is the temperature equivalent of the altitude coefficient, and α_h is the observed barometric coefficient.

Figure 1 shows the relation between the intensity of the extended air shower (with the barometric correction) vs. the change $H_{h_{0-100}}$, the altitude of the layer, at pressure h_0 = 100 mb. The altitudes of other isobar levels vary with the same phase,

Table 1. CHARACTERISTICS OF THE EXPERIMENTAL MATERIAL

Type of coincidences	$\bar{N}$	$\bar{f}$, hr^{-1}	n	A_n, % per mb	α_T, % per °C	α_h, % per mb
C(3; 1,0; 3,8)	$1{,}4\cdot10^4$	409	$4{,}5\cdot10^7$	$-0{,}059$	$-0{,}21$	$-0{,}75\mp0{,}015$
C(6; 1,0; 57)	$1{,}4\cdot10^3$	48	$5{,}2\cdot10^6$	$0{,}013$	$0{,}05$	$-0{,}91\mp0{,}023$

as the altitudes of the h_0 = 100 mb level but their oscillations amplitude increases with the altitude. In Yakutsk the seasonal spread of the changes in the altitude of the layer at a pressure of 500 mb is 500 m, and of the 100 mb layer, 1200 m.

In Fig. 1 the mean monthly altitude of the layer at the pressure h_0 = 100 mb and the corresponding mean monthly terrestrial temperature obtained from 5-year data are plotted on the abscissa. The variations in the intensity of the extended air shower together with the mean monthly values for the same period are plotted on the ordinate. The errors at the points represent mean errors from the readings of four identical installations.

It can be seen that as $H_{h_{0-100}}$ increases, the intensity of the showers recorded by the local installations drops faster for C (6, 1.00; 57) the relation becomes steeper and even negative when the values of $H_{h_{0-100}}$ are large. This effect of the atmospheric density can be explained as the decay effect of pions. When they disintegrate, the pions are knocked out from the nuclear cascade, which leads to a reduced power of the shower.

Figure 2 gives the variations in the intensity of the extended air shower during the passage of cyclones (see also [4]). The cyclone periods are interesting because the temperature changes in layers above the 700-mb layer have opposite sign than those in the lower third of the atmosphere. The results show that after the corrections for the barometric and local geometric effects, a residual variation is observed. The latter is by its character the geometric effect of the atmospheric layers above the 700-mb level. This indicates that the angles of jump of the pions with an energy of 10^{11} - 10^{12} eV generated at the altitudes on the order of 4 - 6 km have a substantial effect on the formation of the three-dimensional distribution function of air shower particles at sea level. /88

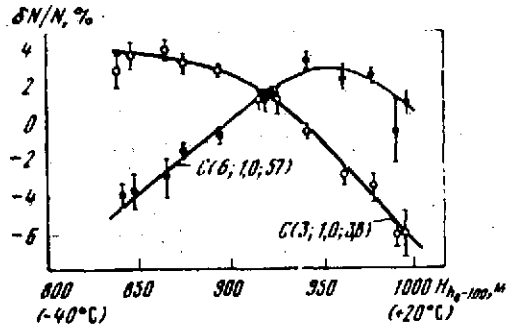

Fig. 1. Variations in mean monthly values of the intensity of extended air shower with barometric corrections vs. changes in the altitudes of the layer with pressure h_0 = 100 mb (or temperature above the surface of the Earth) according to 5-year data.

When sidereal-diurnal variations are studied, the usual temperature corrections cannot be used, since the daily fluctuations in the state of the atmosphere have specific features: the daily temperature curve in the layer near the Earth leads the temperature changes of the higher layers in phase and the amplitude of the temperature fluctuations is greatest near the Earth.

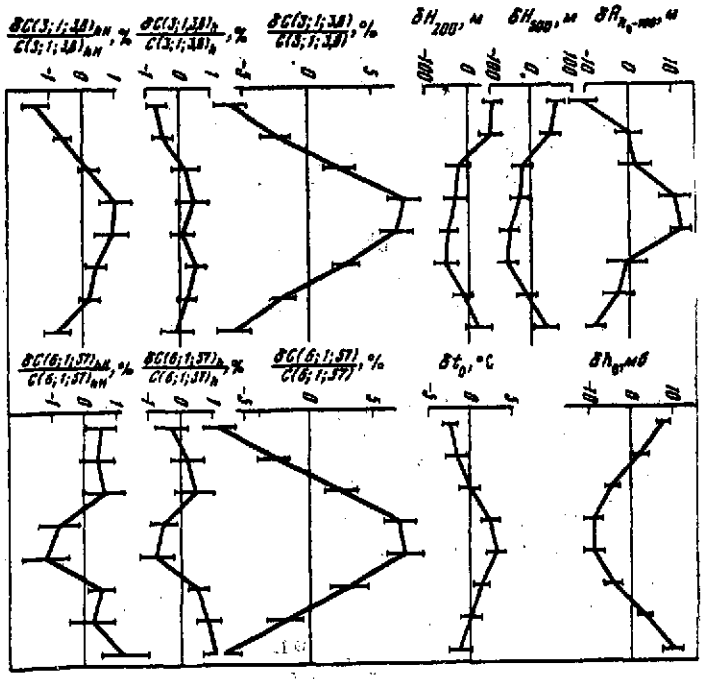

Fig. 2. Variations in the intensity of the extended air shower during the passage of cyclones. Depending on the character of the change in pressure, the passage time of the cyclones was broken up into 8 periods.

The extended air shower intensity is shown without corrections, with barometric correction, with barometric and geometric correction

One method for taking into account the atmospheric effect in the study of sidereal-diurnal variations in extended air showers was proposed in [5]. In this study, the so-called complex temperature coefficient $\beta_T e^{ir}$ is introduced, where β_T /89
is the magnitude of the temperature coefficient, τ is the phase shift between the daily temperature variation vector and the temperature component of the daily variation of the extended air shower.

From the daily-solar variation in the pressure given in Table 2, using α_n, we find the vector for the barometric component of the daily variation. Subtracting it from the daily-solar variation in the intensity of the extended air shower, we obtain the expected vector for the temperature component. Comparing the latter with the daily-solar temperature variation vector, we find the magnitudes of the temperature coefficient β_T and the phase shift τ between these two vectors, 0.08% per $^{\circ}$C and 2 h for C (3; 1.0; 3.8), and 0.08% per $^{\circ}$C and 4 h for C (6; 1.0; 57). In both cases, as was to be expected, the vector of the temperature component lags the terrestrial temperature vector.

Table 2. FIRST HARMONICS OF THE DAILY VARIATIONS IN PRESSURE h_0, TEMPERATURE IN THE LAYER NEAR THE SURFACE OF THE EARTH T_0 AND THE EXTENDED AIR SHOWER INTENSITY WITHOUT CORRECTIONS

Measured Magnitudes	Solar time		Sidereal time	
	A, %	t, hrs	A, %	t, hrs
h_0, mb	0,22±0,03	3,3±0,5	0,15±0,6	23,1±0,3
T_0, °C	3,6 ±0,1	13,3±0,2	1,3±0,1	6,9±0,3
C(3; 1,0; 3,8)	0,11±0,03	3,8±0,9	0,04±0,02	11,7±2,2
C(6; 1,0; 57)	0,45±0,06	16,8±0,6	0,31±0,08	10,9±1,0

Next, using α_n, β_T, τ, we find the vector sum of the barometric and temperature components of the sidereal-diurnal variations. Subtracting this sum from the vector of the observed sidereal-diurnal air shower variations we find finally the true sidereal-diurnal variation vector. The results are given in Table 3.

Table 3. AMPLITUDES AND TIMES FOR THE MAXIMUM OF THE FIRST HARMONIC OF THE SIDEREAL-DIURNAL VARIATIONS IN THE INTENSITY OF EXTENDED AIR SHOWERS ACCORDING TO DATA FROM OBSERVATIONS CARRIED OUT IN AUGUST 1959-JULY 1964 IN YAKUTSK

Type of Coincidence	A, %	τ, hrs
C(3; 1,0; 3,8)	0,05±0,07	6,5±5,3
C(6; 1,0; 57)	0,08±0,09	10,0±4,3

Thus, the primary cosmic rays with the energy $E_0 = 10^{14} \div 10^{15}$ eV do not detect anisotropy with an accuracy up to ~ 0.1%.

REFERENCES /90

1. Krasil'nikov, D. D., Tr Yakutsk Filiala Akad Nauk SSSR, Ser Fiz, No. 3 (1960).

2. Efimov, N. N., Materialy XIII nauch. sessii Yakutskogo filiala SO AN SSSR, [Proceedings of the 13th Scientific Conference of the Yakutsk Branch of the Siberian Department of the USSR Acad. of Sci.], Materials of the Yakutsk Branch of the Siberian Department of the USSR Academy of Sciences, 1961.

3. Krasil'nikov, D. C., Tr. Yakutsk Filiala Sib Otd Akad Nauk SSSR, Ser. Fiz., No. 4 (1962).

4. Krasil'nikov, D. C., Atakova, M. M., Efimov, N. N., et al., Kosmicheskie luchi i problemy kosmofiziki, [Cosmic Rays and Problems in Astrophysics], Novosibirsk, 1964, p. 111.

5. Efimov, N. N., Geomagnetizm i aeronomiya 7 (3), 1967.

N75 16460

COMPARISON OF THE RESULTS OF SIMULTANEOUS COSMIC RAY MEASUREMENTS IN THE STRATOSPHERE AT THE OLENIA AND APATITY STATIONS

L. L. Lazutin

ABSTRACT

The results of regular measurements of the cosmic ray intensity in the stratosphere obtained by the Olenia (Physics Institute named after P. N. Lebedev of the Academy of Sciences, USSR) and Appatity (Polar Geographical Institute of the Kola Branch of the Academy of Sciences, USSR) high latitudinal stations during September-December 1966 are compared. The present paper estimates the agreement between the results obtained by closely located stations by means of various radiosondes, RK-2 (PIL [Physics Institute named after Lebedev]) and RKL-5 (PGI [Polar Geographical Institute]. The assumption about the substantial contribution of auroral x-ray radiation to the fluctuation of the radiosonde counting rate at high altitudes is confirmed.

Regular cosmic ray measurements in the stratosphere at the high latitudinal stations Apatity (PGI [Polar Geographic Institute]) and Olenia (PIL [Physics Institute named after Lebedev]) are carried out according to a coordinated program which makes it possible to obtain valuable data about particle fluxes that originate in the Sun and near the surface of the Earth. Unfortunately, the considerable differences from the radiosondes RK-2 (PIL) [1] and RKL-4 [2] (PGI) made it difficult to carry out a simultaneous analysis. In order to eliminate the differences in the recording part of the equipment, PIL developed, and uses in the experiments since 1966, the RKL-5 radiosonde which combines the input elements of the PIL RK-2 radiosonde with the feed system of the RKL-4 radiosonde.

This article gives the results of a comparison of the measurements made in Apatity and Olenia in the last four months of 1966. Over 300 radiosondes were launched in this period at these two stations.

Number of flights	Olenia	Apatity
Total.	142	177
Above 20 g/cm^2 . . .	82	126
Above 10 g/cm^2 . . .	43	57
Simultaneous (Δt take-offs < 3 h). . . .	70	70

For the comparison, flights were selected that passed the two stations with an interval not exceeding 3 h between takeoffs, which attained the maximum Pfotzer altitude (~ 40 g/cm^2). Seventy such flights were selected in each station. The figure gives the mean monthly altitude curves that were averaged over the selected flight. The tables give the mean radiosonde counting rate $\bar{N}$ at the Pfotzer maximum and at the atmospheric depth 20 g/cm^2, as well as the magnitude of the standard deviation of the 3-min values

$$\sigma_{rec} = \sqrt{\frac{\sum_i (N_i - \bar{N})^2}{n}},$$

where N_i is the counting rate averaged over three min, n is the number of 3-min recording intervals in the given range of pressures, and the mean root square error determined by the full counting rate is

$$\sigma_{cr} = \frac{\sqrt{\Sigma 3N_i}}{3n} = \frac{\sqrt{3n\bar{N}}}{3n} = \sqrt{\frac{\bar{N}}{3n}}.$$

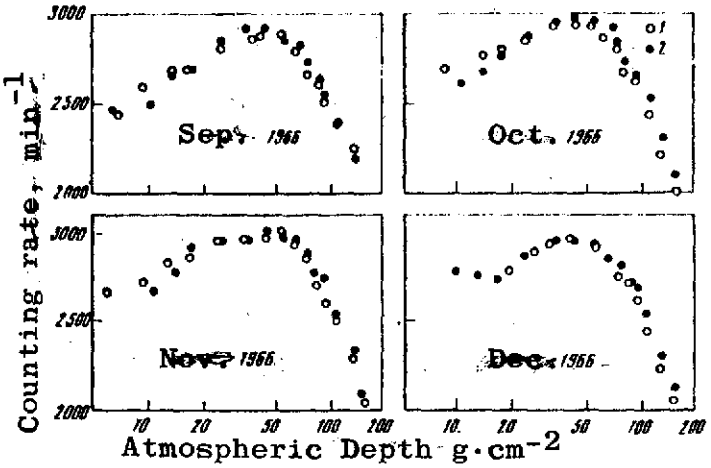

Fig. Mean monthly altitude curves for the cosmic ray intensity averaged over the selected flights.

1--Olenia; 2--Apatity

/91

It can be seen from the table that $\sigma_{cr} << \sigma_{rec}$, which is understandable since σ_{rec} is determined in addition to the statistical error, also by the instrumental error and the true variations in the intensity of the radiation in the stratosphere.

Month	Olenia				Apatity				Δp, g·cm^{-2}
	$\bar{N}$, min^{-1}	n	σ_{rec}	σ_{cr}	$\bar{N}$, min^{-1}	n	σ_{rec}	σ_{cr}	
Sep	2705	11	71	9	2703	34	127	5	16÷20
Oct	2830	10	55	10	2767	23	92	6	
Nov	2830	5	81	14	2854	12	66	9	
Dec	—	—	—	—	2735	9	133	10	
Sep	2890	27	17	6	2917	35	113	5	40÷50
Oct	2940	20	5	7	2963	24	86	6	
Nov	2965	12	5	9	2996	16	27	8	
Dec	2935	12	9	9	2931	12	42	9	

Returning to the comparison of the results from the flights, we note that the measurements up to 20 g·cm^{-2} agree with great accuracy. The differences which can be seen in the diagram and which occur at a high altitude are related both to the low statistical accuracy of the averaging and to the great fluctuations in the radiation at these altitudes. Since fewer and fewer flights participate in the analysis as the altitude increases, the nonsimultaneity of the recording will give greater and greater differences. The source of these considerable fluctuations at the latitude at which the observations were made is apparently the inhibiting x-ray radiation of the auroral electrons. If we assume, as in [3], that the mean loss of electrons with energy in excess of 25 keV in 24 h is 3·10 cm^{-2}, or per minute $N \sim 2 \cdot 10^7$ cm^{-2}.min^{-2}, we can estimate the contribution of the x-ray radiation to the counting rate ΔN_p from the formula

$$\Delta N_p = \frac{NSC}{KR},$$

where S is the effective area of the counter (in cm^2), C is the sensitivity coefficient of the counter to x-ray radiation, K is the conversion factor for converting the electron flux to the photon flux at the boundary of the atmosphere, and R is the attenuation coefficient of the photon flux at the recording depth. /92

Taking the values of N given above and also S = 16 cm^2, C = 0.01 [4], K = 10^4 [3] and R for the atmospheric depth 10 $g \cdot cm^{-2}$ of order of 2-4, we obtain the result that ΔN consists of 100-200 pulses per min, i.e., 4-10% of the total counting rate. Taking into consideration the fact that the fluctuations in the auroral electron flux can exceed several times the mean level even in quiet periods, we can assume that the results of the estimate confirm the hypothesis about the substantial contribution of auroral x-ray radiation to the fluctuations in the radiosonde counting rate at high altitudes. If we assume that the auroral electron bursts take place in a narrow latitudinal zone, we can conclude that the tendency to exceed the counting rate at high altitudes at the Olenia station in September-November (see diagram) indicates that Olenia lies closer in these months to the maximum of the zone of auroral electron bursts.

REFERENCES

1. Charakhch'yan, A. N., in the Collection Kosmicheskie luchi, No. 3, 134 (1961).

2. Lazutin, L. L., Frantsuz, E. T., Izv Akad Nauk SSSR, Seriya Fiz 28 (12), 2085 (1964).

3. Anderson, K. A., "A review of balloon measurements of x-rays in the auroral zone," Univ. of Calif., Berkeley, USB-64/4, 1964.

4. Khitun, V. A., Schetchiki yadernogo izlucheniya i schetnyye ustroystva, [Nuclear Radiation Counters and Counting Devices], Gosenergoizdat, 1959.

N75 16461

ALTITUDINAL, DIURNAL AND LATITUDINAL DEPENDENCES FOR IONIC CONCENTRATIONS FORMED BY CORPUSCULAR FLUXES IN THE STRATOSPHERE AND MESOSPHERE

Yu. A. Bragin

ABSTRACT

On the basis of over 15 rocket measurements of ionic concentrations below 80 km, the authors compare the height, daily and latitudinal dependences between positive ionic concentrations and cosmic ray intensity below 60 km as well as between ionic concentrations and corpuscular streams within the 60-80 km altitude range. It is shown that ionic concentration and cosmic ray intensity below 60 km at night are likely to be interrelated, in conformity with Chapman's theory of the simple layer. In daytime, all phenomena are aggravated by photodetachment and ion exchange reactions with the participation of ozone. Between 60-80 km, besides ordinary cosmic rays, there must exist an additional corpuscular stream.

Until now, more than 15 measurements of charged particles with the same sign (small positive ions) were carried out on rockets below 60 km, at medium latitudes in the USSR and in the Pacific Ocean [1-4], on the basis of which the conclusion can be made that approximately in the place where the maximum cosmic ray intensity formed by secondary particles is observed, the maximum ionic concentration occurs.

In order to better understand the laws that govern the altitudinal and daily measurements of the concentration profiles, Fig. A shows the most characteristic profiles during the day, in the evening, at night, and in the morning. /93

The maximum concentration at night is lower the higher the Sun. During the day, there are fewer ions at the maximum than at night. On light days, the total increase in the night concentration in the stratosphere and upper troposphere has several maxima and minima. Obviously, such daily variations in the ionized layer in the stratosphere are not related to the source, the cosmic rays, if we assume that the amplitude of the daily variations in cosmic ray intensity did not exceed 10% of the mean value in the stratosphere. Probably at night the ionic maximum in the stratosphere and the maximum of the ionizing agent, the cosmic rays, coincide, i.e., the ionized layer in the stratosphere can probably be adequately described using Chapman's

theory of a simple layer. During the day, more complex phenomena take place that are probably related to the photodetachment of electrons from the negatively charged ions and with ionic exchange reactions in which ozone participates [5].

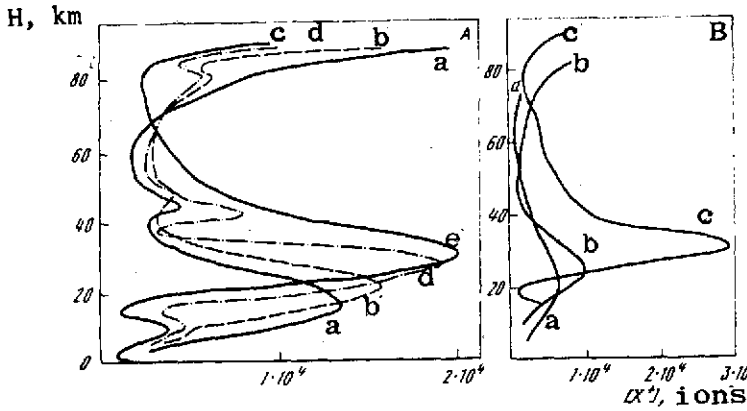

Fig. Most characteristic ionic concentration profiles

A--During the day (a), in the evening (b), at night (c), in the morning (d);
B--Night profiles obtained at the equator (a), at 30° in the Pacific Ocean and at medium latitudes in the USSR (c)

Figure B shows three night profiles of the ionic concentrations obtained at the equator, approximately at 30°N in the Pacific Ocean and at medium latitudes in the USSR, which reflect the latitudinal dependence of the ionic concentration. The location and magnitude of the ionic concentration maxima correspond to the latitudinal distribution of the maxima for the intensity of secondary cosmic particles, i.e., the curve X^+ corresponds to the curve $\sqrt{I}$ ($X^+ \approx \sqrt{g} \approx \sqrt{I}$, where g is the ionizing rate under the effect of the cosmic particles, and I is the intensity of their flux).

In order to explain the high ionic content $X^+ \approx 5 \cdot 10^3$ ion/cm^3 during the day and at night compared to the electrons at altitudes of 60-80 km, we must assume that an ionizing corpuscular stream exists in this region, which is different from the ordinary cosmic ray flux. Its intensity for electrons with an energy of 10^5 eV is - 10 - 10^3 cm$^2 \cdot$sec^{-1}, and for protons with an energy of 10^7 eV it lies in the range 1 - 10^2 cm$^{-2} \cdot$sec^{-1} [6]. Particles with such energies are found in the Earth's radiation belts.

At first sight, these are the very important conclusions about the relation between corpuscular streams and the ionic concentration below 90 km.

REFERENCES

1. Bragin, Yu. A., Kosmicheskie issledovaniya 3 (1), 168 (1965).

2. Bragin, Yu. A., Kosmicheskie issledovaniya 4 (3), 453 (1966).

3. Bragin, Yu. A., Kosmicheskie issledovaniya 5 (3), 478 (1967).

4. Bragin, Yu. A., Kosmicheskie issledovaniya 5 (6), 951 (1967).

5. Bragin, Yu. A., Danilov, A. D., and Kostko, O. I., Space Res. 8, London, 353 (1967).

6. Bragin, Yu. A., Kostko, O. K., Repnev, A. I., and Shvidkovskiy, Ye. G., Kosmicheskie issledovaniya 5 (1) 1967.

N75 16462

THE EFFECT OF COSMIC RAYS ON THUNDERSTORM ELECTRICITY

Yu. A. Bragin

ABSTRACT

The inflow of charges of small ions, formed by cosmic rays, into thunderstorm cells is estimated on the basis of rocket measurements of ionic concentrations below 90 km. Out of the two processes that form the thunderstorm charge (generation and separation of charges), the former is supposed to be caused by cosmic rays, and the nature of separation is assumed to be the same as in other thunderstorm theories

Many theories exist which explain the nature of the thunderstorm; however, all these theories are beset by certain difficulties and none of them can be acknowledged to be completely valid [1, 2]. Any theory of the thunderstorm must presuppose mechanisms for the processes that generate the electric charges and the neutral medium with their subsequent separation which have the property that the rate at which the charge Q accumulates in the thunderstorm cell corresponds to the observed quantity $\frac{dQ}{dt} \approx 0.5 - 1$ C/km^3·min. This is equivalent to a current density of 10^{-12}A/cm^2, the vortex of the cell at 10-12 km must be positively charged and the base negatively, and the negative charge must move downward [1 - 4].

The necessary rate at which the charge accumulates in the thunderstorm cell can, in principle, be the result of the ionizing activity of cosmic rays in the atmosphere. Two mechanisms are assumed. The first is the direct ionization of the neutral medium by cosmic rays. The rate at which charged particles are formed at an altitude of 10 km is approximately 50 ion/cm^3·sec and above [5], which corresponds to 0.5 C/km^3·min. If we assume that the separation processes in the thunderstorm occur faster than the recombination, which is not clear at all, the direct ionization of the medium by cosmic rays in the thunderstorm cell can charge the entire thunderstorm or at least a considerable part of it.

The second source for the accumulation of the charge in the thunderstorm cell is the surrounding air which is ionized below 60 km by cosmic rays. We will estimate the rate at which

the charges from the surrounding air arrive in the thunderstorm cloud. We will assume that the velocity v of the rising air current forming the thunderstorm cell is 5 m/sec in the upper part of the cell (the horizontal velocity component with which the cloud moves is even greater). When the velocities are smaller, the water vapors cannot rise to an altitude of 10-12 km, and, hence, a thunderstorm cell cannot be formed [4].

Figure 2 in article [6] and also the data in article [7] /95
show that the maximum ionization of small ions in the stratosphere can descend to the troposphere (as a rule in the second half of the day) where the concentration values for ions with the same sign reach $X^+ \approx 2 \cdot 10^4$ ion/cm^3. This means that through one square centimeter every second $v \cdot X^+ \cdot 1.6 \cdot 10^{-19} = 1.6 \cdot 10^{-12}$ amperes will pass, or through 1 km^2 approximately 1 C per minute. Even a greater amount of electricity is contributed to the vortex of the thunderstorm cloud by the horizontal current component. It is sufficient to maintain the thunderstorm charges.

Suppose now that the upper part of the thunderstorm cell containing condensation nuclei enters the zone which contains $2 \cdot 10^4$ small ions of the same sign. Theory and experiment [2] have shown that in the presence of condensation nuclei an equilibrium in the concentration of large and small ions is reached in several tenths or hundreds of seconds, such that the ratio in the concentration of small positive to negative ions is 1.25, i.e., in the time indicated an excess of small positive ions with a charge $0.25 \cdot 2 \cdot 10^4 \cdot 1.6 \cdot 10^{-19}$ C/cm^3 (or 1 C/km^3) is accumulated at the vortex of the thunderstorm cloud, which must be balanced by a negative charge of the same magnitude concentrated at the condensation nuclei in large particles.

The processes which separate the charges in the thunderstorm begin only when it begins to rain, i.e., when the heavy formations in the cloud begin to drop [1 - 4]. Hence, the negative charge of heavy ions will be carried down through gravity. As a result, the top of the thunderstorm cell has a positive charge and the bottom a negative charge.

Thus, in the two processes responsible for the formation of the thunderstorm (generation and separation) generation is caused either directly or indirectly by cosmic rays, and the nature of the separation is obviously the same, as in most other theories of the thunderstorm.

REFERENCES

1. Israel, H., Atmöspharische Electrizität, [Atmospheric Electricity], Vol. I, Leipzig, 1957; Vol. II, Leipzig, 1961.

2. Coroniti, S. E. (Ed.), Problems of Atmospheric and Space Electricity, Amsterdam, Elsevier, 1965.

3. Chalmers, I. A., Recent Advances in Atmospheric Electricity, London, Pergamon, 1959.

4. Tverskoy, P. N., Kurs meteorologii, [A Course in Meteorology], Leningrad, Gidrometeoizdat, 1962.

5. Spravochnik po geofizike, [Handbook on Geophysics], Nauka Press, 1965.

6. Bragin, Yu. A., "Altitudinal, diurnal and latitudinal dependences for ionic concentrations formed by corpuscular fluxes in the stratosphere and mesosphere," in this collection.

7. Bragin, Yu. A., Kosmicheskie issledovaniya 5 (30) 478 (1967).

N75 16463

POSSIBILITY OF CONTROLLING THE EARTH'S NEGATIVE CHARGE AND THE UNITARY VARIATION OF ITS ELECTRIC FIELD BY COSMIC RAYS

Yu. A. Bragin, S. S. Vorontsov, A. A. Kocheyev

ABSTRACT

The dependence of the atmospheric conductivity upon the cosmic ray intensity, the possibility of charge generation in thunderstorms by cosmic rays, the dependence of the troposphere electricity on the stratosphere, the relationship between the unitary variation of the Earth's electric field intensity and that of cosmic ray intensity (daily, yearly and 11-year latitudinal dependence of both values), deny first, the exceptional role of the tropospheric processes in maintaining the terrestrial charge and unitary variation, and, second, compel one to consider the cause mentioned above to be the result of the influence of cosmic rays.

The variation in the Earth's negative charge Q is determined by the balance of the charge I_{ch}, and the discharge I_d of the spherical capacitor of the Earth, the ionosphere ($\frac{dQ}{dt} = I_{ch} - I_d$).

The intensity E of the Earth's electric field depends on the Earth's charge and conductivity of the Earth's capacitor, the ionosphere. The total conduction current and the current in the charge can be expressed by the integral

$$I_p = \int_S \vec{j}\, dS = \int_S eE\lambda\, dS = \int_S eE\Sigma n_i\mu_i\, dS.$$

The conductivity of the atmosphere $\lambda = \sum_i n_i\mu_i$ is determined by the concentration n_i and the mobility μ_i of the ions formed during the ionization of the atmosphere by cosmic rays. On the other hand, it is known that the recharging of the capacitor Earth-ionosphere takes mainly place during thunderstorms and peak discharges [1 - 3]. This current depends on the processes which generate and separate the charges in the thunderstorm, on the conductivity and the wind near the peak period. The thunderstorm activity, as shown in [4], apparently also depends on cosmic rays. Thus the discharge currents and, hence, also

the Earth's charge obviously depend on the cosmic ray intensity. In addition to this, the parameters of atmospheric electricity studied depend on the thermodynamic and dynamic state of the atmosphere, mainly the troposphere, since it represents the main part of the leakage resistance of the Earth-ionosphere capacitor, in which the processes that separate the charges take place [1, 2, 5, 6]. A widely held opinion is that the tropospheric electricity is regulated by thermodynamic and dynamic tropospheric phenomena, i.e., the charge and discharge currents depend mainly on the latter [2, 3, 6-9].

Until very recently, the most popular theory for the formation of discharge currents, the maintenance of the negative charge of the Earth and variations in the Earth's electric field was the Earth's discharge theory during thunderstorms [2, 6, 7, 10]. Recently, studies appeared which subjected this theory to criticism. Other hypotheses are also proposed [2, 9, 11-13].

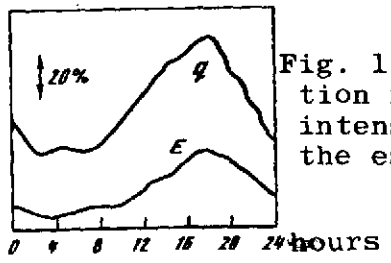

Fig. 1. Daily variation in the ionization rate q due to cosmic rays and the intensity E of the electric field of the earth.

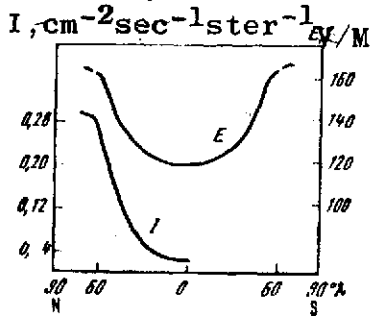

Fig. 2. Latitudinal dependences for the cosmic ray intensity I and the intensity of the electric field of the Earth E.

The displacement of the maximum ionic concentration in 24 hours from the stratosphere to the troposphere [14] invalidates the proposition that the troposphere plays an exceptionally important role in the processes that maintain the Earth's charge. The possibility that charges are generated in the thunderstorm by cosmic rays [4], the dependence of the conductivity of the cosmic ray intensity, the relationships between the electricity /97

in the troposphere and stratosphere, the relationship between the unitary variation in the intensity of the Earth's electric field and variations in cosmic ray intensity or the rate at which ions are formed when air is ionized by cosmic rays (see below) compel us to seek the cause for the unitary variation in the effect of cosmic rays.

We will consider several observations pertaining to the intensity of the Earth's electric field and cosmic rays.

Figure 1 gives the daily variations in the ionization rate due to cosmic rays and the unitary variation in the intensity of the Earth's electric field [6, 7]. Both curves show that the maxima coincide at 18 hours and the minima at 4 hours UT.

Figure 2 shows the latitudinal dependence of the intensity of the cosmic rays and the intensity of the Earth's electric field [7, 15]. The latitudinal dependence for both quantities is the same.

The yearly cosmic ray variation $\delta I/I$ and the variation in the intensity of the electric field E are given in Fig. 3 [16, 7, 17]. It can be seen that the maxima and minima in the cosmic ray intensity coincide. The variation in the μ-meson component coincides with the yearly variation in E.

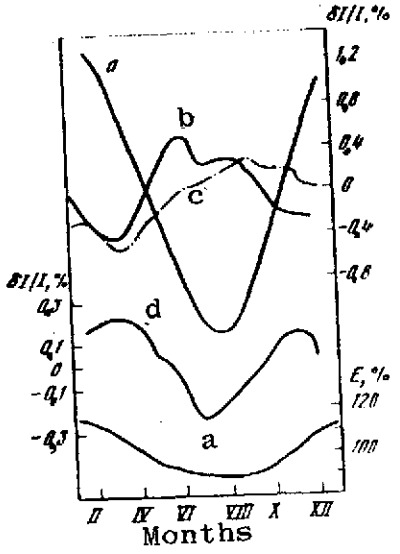

Fig. 3. Yearly cosmic ray variation $\delta I/I$

a--Meteorological effect not eliminated; b, c--meteorological effect eliminated; d--variations in μ-meson component of cosmic rays; and e--variations in intensity of the electric field E [17].

Figure 4 shows the 11-year variations in the cosmic ray intensity in antiphase with solar activity, and variations in the intensity of the field [15, 7]. Figures 1 - 4 show the selected most characteristic curves obtained from many measurements.

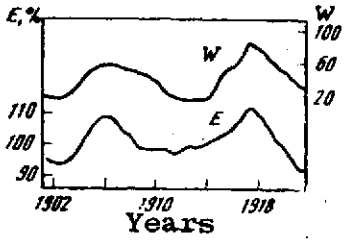

Fig. 4. 11-year variations in the intensity of cosmic rays in antiphase with solar activity W, and variations in the intensity of the field E

The direct and inverse dependence of E on I in various cases can be explained by the fact that the cosmic rays have an effect both on the charge and discharge process of the Earth-ionosphere capacitor. For the time being it is not clear which processes are dominant in which case.

For the time being, it is difficult to propose a concrete mechanism for the effect of cosmic rays on the Earth's charge. However, the quest for this mechanism should not be abandoned since the assumption that was made above, namely that the electricity in the troposphere is regulated by the cosmic rays, justifies this quest.

REFERENCES

1. Bragin, Yu. A., Kosmicheskie issledovaniya 5 (1) (1967).

2. Coroniti, S. C. (ed.), Problems of Atmospheric and Space Electricity, Amsterdam, Elsevier, 1965.

3. Tverskoy, P. N., Kurs meteorologii, [A Course in Meteorology], Leningrad, Gidrometeoizdat, 1962.

4. Bragin, Yu. A., "The Effect of Cosmic Rays on Thunderstorm Electricity," in this collection.

5. Chalmers, I. A., Recent Advances in Atmospheric Electricity, London, Peegamon, 1959.

6. Israël, H., Atmosphärische Elektrizität, [Atmospheric Electricity], Vol. I, Leipzig, 1957.

7. Israël, H., Atmosphärische Elektrizität, [Atmospheric Electricity], Vol. II, Leipzig, 1961.

8. Frenkel', Ya. I., Teoriya atmosfernogo elektrichestva, [Theory of Atmospheric Electricity], Moscow-Leningrad, Gostekhizdat, 1949.

9. Imyanitov, I. M. and Chubarina, E. V., Electrichestvo svobodnoy atmosfery, [Electricity in the Free Atmosphere], Gidrometeoizdat, 1965.

10. Wilson, C. T., "The maintenance of the Earth's electric charge," N 5, 1922 [sic].

11. Khrgian, A. Kh., Lobodin, T. V., "Evaluation of currents in the Earth's charge in thunderstorm activity zones," Geofizicheskiy byull., No. 16, 82 (1965).

12. Mulisen, K., The Influence of Water on the Atmospheric Electrical S. Field, London, Pergamon, 1958.

13. Gerasimenko, V. I., "Contributions to the problem of the causes of the unitary variation of the electric field of the atmosphere," Uch Zap Leningr Vyssh Inzh Morsk uchilishcha im. Makarova, No. 10, 1958.

14. Bragin, Yu. A., "Altitudinal, diurnal and latitudinal dependences for the ionic concentrations formed by corpuscular fluxes in the stratosphere and mesosphere," in this collection.

15. Spravochnik po geofizike, [Handbook on Geophysics], translated from the English, Nauka Press, 1965.

16. Dorman, L. I., Variatsii kosmicheskikh luchey, [Cosmic Ray Variations], Moscow, Gostekhizdat, 1957.

17. Nestorov, G., Dokl Bolgarskoy AN 16 (4) (1963).

N75 16464

EFFECT OF THRESHOLD RIGIDITY VARIATIONS ON THE ELECTRON PRODUCTION RATE IN THE ATMOSPHERE

L. I. Dorman, T. M. Krupitskaya, M. I. Tyasto

ABSTRACT

Current systems formed during magnetic disturbances cause threshold energy variations of cosmic ray particles. The latter, in turn, are a source of electron production in the terrestrial atmosphere. The paper gives the calculations of the electron production rate with the count of threshold variations during magnetic disturbances

One reason for the formation of electrons in the atmosphere are cosmic rays of solar or galactic origin, which, in turn, are affected by the solar wind, interplanetary magnetic fields, and, in particular, the Earth's magnetic field. The primary flux of cosmic rays I near the boundary of the atmosphere can be expressed as

$$I = \int_{E_{\text{по min}}}^{\infty} D(E)\,dE,$$

where the lower limit of integration is determined either by the cutoff of the primary spectrum or by the atmospheric cutoff, or by the geomagnetic rigidity cutoff. This paper investigates the effect of changes in the magnetic cutoff during magnetic perturbations on the rate at which electrons are produced in the upper atmosphere. /99

It was shown earlier that the geomagnetic rigidity cutoff varies considerably during auroral storms as a result of the formation of current systems in this period [1]. In this case, the current which reduces the horizontal component at the equator by the amount ΔH, flows along the parallel envelope in the western direction with a force which is proportional to the cosine of the latitude. Figure 1 gives the variations in the threshold energies ΔR_c that were calculated in [1] as functions of R_c, for ΔH at the equator and for the radii of the current envelope.

In general, the rate at which the electrons q_i caused by the flux of cosmic particles I are produced, depends on the depth p at which the observations are carried out in the atmosphere, the form of the differential spectrum $D_i(E_{KO})$ and the energy losses through ionization to cosmic ray particles when they pass the atmosphere $\varepsilon(E_{KO}, p)$ [2]

$$q_i = \frac{\rho(p)}{Q} \int_{E_{KO\,min}}^{\infty} D_i(E_{KO})\,\varepsilon_i(E_{KO}, p)\,dE_{KO},$$

where $\rho(p)$ is the density of the atmosphere at the level with pressure p g/cm^2; $D_i(E)$ is the spectrum of primary particles of type i on the boundary of the atmosphere; E_{KO} is the kinetic energy of the primary particles on the boundary of the atmosphere in MeV, $\varepsilon_i(E_{KO}, p)$ are the energy losses to ionization MeV·g^{-1}·cm^2. /100

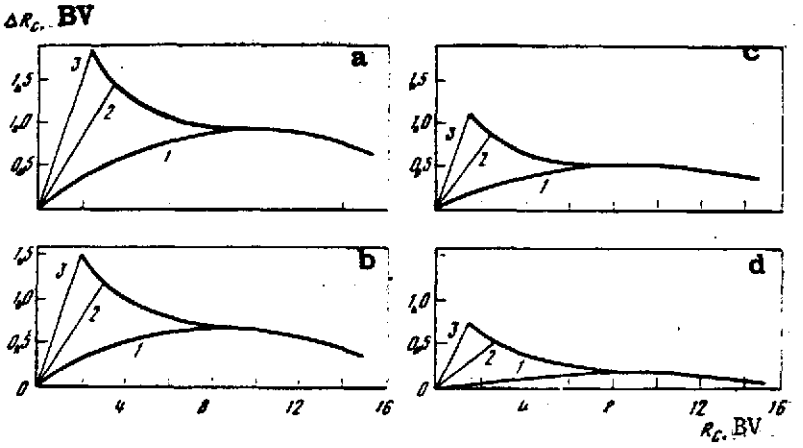

Fig. 1. Variations in threshold rigidity ΔR_c vs R_c

Curves 1, 2 and 3--for current envelope radii equal to 3, 5, and 9 times the radius of the Earth; a--ΔH = 400; b--300; c--200; d--100 γ

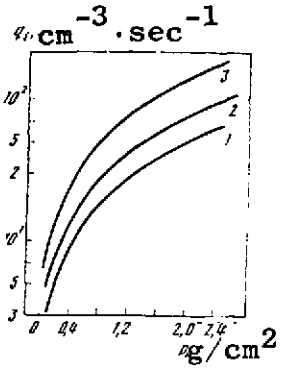

Fig. 2. Profile for the electron production rate q for the undisturbed period at the geomagnetic latitudes

1--40; 2--50; 3--55°

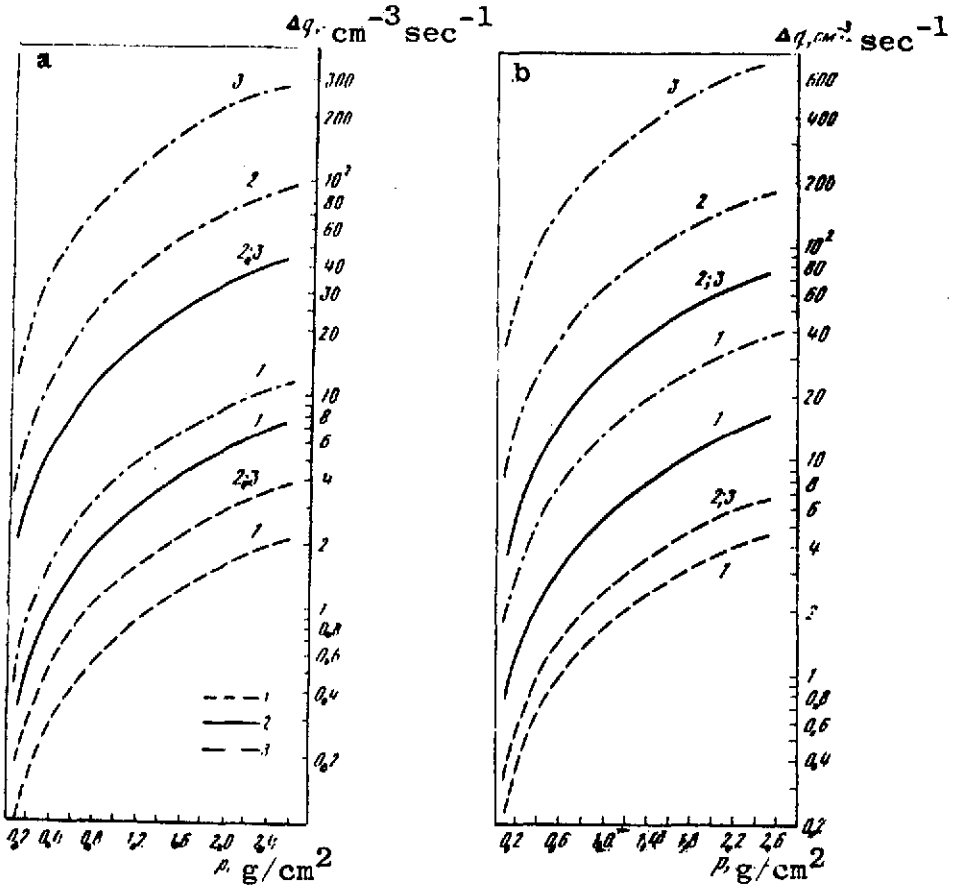

Fig. 3. (continued next page)

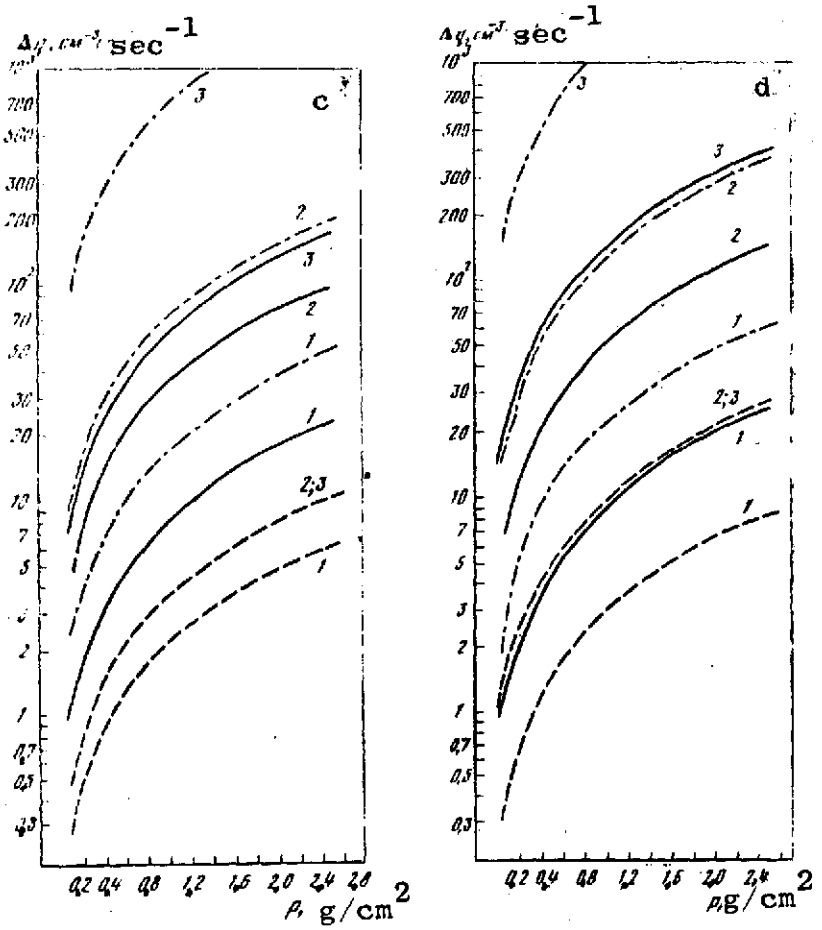

Fig. 3. Profiles for the variations in the electron production rate at the latitudes I - 40; II - 50; III - 55°. Curves 1, 2, and 3, respectively, for envelope radii equal to 3, 5, and 9 times the radius of the Earth

a--ΔH = 100; b--200; c--300; d--400 γ

In first approximation we can assume that the flux of primary cosmic particles consists of protons. The profiles for the electron production rate were calculated for galactic cosmic rays arriving in the vertical direction and from the spectrum $D_i(E_{KO}) = kE_{KO}^{-2}$ where k is a coefficient ($k \approx 1$) [2].

Figure 2 shows the profiles for the electron production rate for the undisturbed period.for the geomagnetic latitudes. Figure 3 shows the calculated profiles for variations in the electron production rate Δq_i in the layer D under the effect of

galactic cosmic rays

$$\Delta q_i = q_{id} - q_{iu},$$

where q_{id}, q_{iu} are the rates at which the electrons are produced in the disturbed and undisturbed period.

From Fig. 3 it can be seen that the rate at which the electrons are produced at the given geomagnetic latitude depends both on the dimensions of the radius of the current envelope and on the magnitude of the disturbance in the horizontal component ΔH. The quantity Δq_i is larger the greater the latitude /101
and the greater the radius of the spherical envelope for the given value ΔH. For example, at the latitude 50°, for $\Delta H = 300\ \gamma$ at the depth 2 g/cm^2 when a = 3.5, for $9R_E\Delta q_i$ = 18.78 and 136 el/cm^3·sec, respectively, which is 24, 100 and 177% of the undisturbed value of q_i at the given depth.

REFERENCES

1. Dorman, L. I. and Tyasto, M. M., in the collection Kosmicheskie luchi, No. 7, 131 (1965).

2. Dorman, L. I., Variatsii kosmicheskikh luchey i issledovanie kosmosa, [Cosmic Ray Variations and a Study of the Universe], Moscow, USSR Acad of Sci Publ., 1963.

N75 16465

SECULAR VARIATIONS OF L, B-COORDINATES

/102

I. V. Getselev, E. V. Gorchakov, V. A. El'tekov

ABSTRACT

The calculation results of L, B-coordinates for different years from 1957 to 1967 are given. Periodic calculations of the geomagnetic coordinates for different epochs are considered to be very urgent.

In many cases, the densities of charged particle fluxes in the Earth's radiation belts depend considerably on the space. In sectors where the gradient rises or falls they can be L^{10-20}; therefore, even small deviations in the value of L from the real value, can lead to considerable errors in the study of the dynamics of the processes. Since, at the present time, L, B-coordinates are used which were calculated from the state of the Earth's magnetic field in the years 1955-1960, apparently an evaluation of the values of the secular variations in the L, B-coordinates is useful, on the basis of which recommendations could be made with regard to the periodicity with which they should be calculated for the drawing of maps.

At the present time, to calculate the epoch variations in the quantities L and B, spherical harmonic analysis is used with 48 coefficients in the expansion. Using the calculation formulas obtained by this method [1] we find an expression for the absolute magnitudes of the variations in the intensity of the geomagnetic field ΔB

$$\Delta B = \frac{Br}{B}\Delta B_r + \frac{B_\theta}{B}\Delta B_\theta + \frac{B_\varphi}{B}\Delta B_\varphi, \qquad (1)$$

where B_r, B_θ, B_φ are components of the intensity B of the Earth's magnetic field and ΔB_r, ΔB_θ, ΔB_φ are the absolute values of the variations corresponding to the components. To calculate the change in the relative magnitude of the variation $\Delta B/B$, we write the computational formula for the quantity $\Delta B_\varphi/B_\varphi$ for the component B_φ in the following form

$$\frac{\Delta B_\varphi}{B_\varphi} = \frac{\left(\frac{R}{r}\right)^3 \Delta T_1 + \left(\frac{R}{r}\right)^4 \Delta T_2 + \left(\frac{R}{r}\right)^5 \Delta T_3 + \left(\frac{R}{r}\right)^6 \Delta T_4 + \ldots + \left(\frac{R}{r}\right)^{n+2} \Delta T_n}{\sum_{n=1}^{\infty} \left(\frac{R}{r}\right)^{n+2} \sum_{m=0}^{n} m \left(g_n^m \cos m\varphi - h_n^m \sin m\varphi\right) \frac{P_n^m(\cos\theta)}{\sin\theta}}, \qquad (2)$$

where ΔT_1, ΔT_2, ΔT_3, . . . are values of the quantity ΔT_n, equal to

$$\Delta T_n = \sum_{m=0}^{n} m \left(\Delta g_n^m \cos m\varphi - \Delta h_n^m \sin m\varphi\right) \frac{P_n^m(\cos\theta)}{\sin\theta}, \qquad (3)$$

for n = 1, 2, 3, . . . ; g_n^m and h_n^m are the Gaussian coefficients Δg_n^m and Δh_n^m are the variations in the Gaussian coefficients in the period under consideration, and P_n^m are the associated Legendre polynomials. The ratio (2) shows that the contribution of the higher harmonics to the relative magnitude of the variation $\Delta B_\varphi / B_\varphi$ decreases as the altitude increases. The same applies to the relative change in the variations of other components and of the quantity B itself.

The magnitude of the variation in the parameter L depend both on the values ΔB_r, ΔB_θ, ΔB_φ and ΔB, and also on the shift in the magnetic line of force in space, which is determined by the variation in the intensity of the Earth's magnetic field. The change in the three-dimensional coordinates of any point of the line of force as a function of the variation in the intensity of the magnetic field of the preceding point can be calculated from the formulas

$$\Delta r = \frac{B\Delta B_r - B_r \Delta B}{B(B+\Delta B)} \Delta S; \quad \Delta\theta = \frac{1}{r} \frac{B\Delta B_\theta - B_\theta \Delta B}{B(B+\Delta B)} \Delta S;$$
$$\Delta\varphi = \frac{1}{2\sin\theta} \frac{B\Delta B_\varphi - \varphi_\varphi \Delta B}{B(B+\Delta B)} \Delta S, \qquad (4)$$

where ΔS is the distance between the points under consideration on the line of force. /103

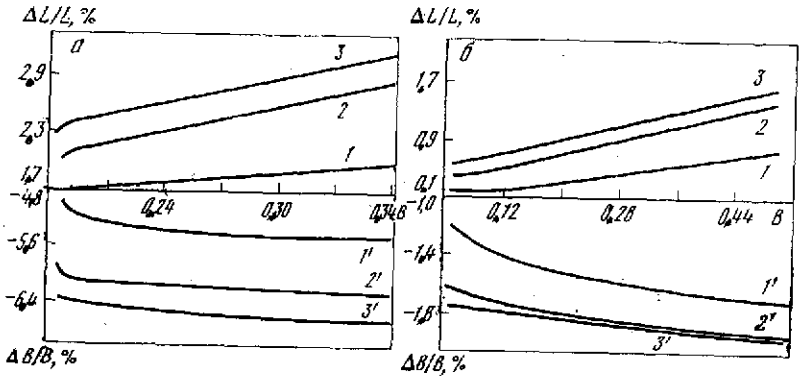

Fig. Variation in the quantities $\Delta L/L$ and $\Delta B/B$ ($\lambda = 270^{\circ}$) along the magnetic lines of force

a - L = 1.1; b--2.02; 1.1' = 1960; 2, 2' - 1965; 3, 3' - 1967

To calculate L in terms of the intensity of the magnetic field B_0 at the equator of the magnetic line of force, we can derive the following relation between the quantities $\Delta L/L$ and $\Delta B_0/B_0$:

$$\frac{\Delta L}{L} = 1 - \sqrt[3]{1 - \frac{\Delta B_0}{B_0}}. \qquad (5)$$

An analysis of relations (1), (2), (4), (5) enables us to draw the following conclusions: 1) the quantities $\Delta B/B$ and $\Delta L/L$ must decrease as the altitude increases; 2) the value of $\Delta L/L$ is smaller than the value of $\Delta B/B$ for the same point.

The quantitative evaluation of the relative magnitudes of the variations L and B was made on an electronic computer. The sequence of calculations was as follows. The magnetic line of force was constructed on the basis of the Gaussian coefficients in 1955 and the values of L and B were calculated for the points on this line. For each point, the values of L and B were calculated on the basis of the Gaussian coefficients in 1960 [3], 1965 and 1967 (the variant of B. R. Liton) and the quantities $\Delta B/B$ and $\Delta L/L$ were calculated.

The computational results are given in the diagram and in Tables 1 and 2. The results that were obtained fully agree with our conclusions.

Table 1

Epoch	$\frac{\Delta B}{B}$, %				$\frac{\Delta L}{L}$, %			
	$L = 1,1$	$L = 1,28$	$L = 2,02$	$L = 2,57$	$L = 1,1$	$L = 1,28$	$L = 2,02$	$L = 2,57$
1960/1955	−4,98	−3,11	−1,02	−0,758	1,7	1,05	0,34	0,25
1965/1960	−0,9	−0,72	−0,49	−0,43	0,34	0,26	0,18	0,15
1967/1965	−0,48	−0,51	−0,25	−0,193	0,25	0,16	0,08	0,06
1967/1955	−6,36	−4,33	−1,76	−1,38	2,29	1,47	0,60	0,46

Table 2

/104

Epoch	$\frac{\Delta I}{I}$, %				
	$R = 1,016\ R_3$	$R = 2R_3$	$R = 3R_3$	$R = 4R_3$	$R = 5R_3$
1960/1955	1,95	0,29	0,13	0,12	0,11
1965/1960	0,54	0,16	0,11	0,09	0,04
1967/1965	0,12	0,04	0,03	0,02	0,01

It should be noted that the values of ΔB/B calculated relative to 1955, exceed several times the experimental data. This is apparently due to the somewhat higher values of the coefficients in 1955. Therefore, when the results obtained are evaluated, it is necessary to take into account the data calculated for 1960, 1965 and 1970, whose Gaussian coefficients were determined more accurately.

When the last remark is taken into consideration, the following conclusions can be made. At low altitudes the relative magnitude of the variation can attain for B ~ 1%, for L ~ 0.5%, i.e., it will introduce an additional error in these quantities. Therefore, it is useful to calculate the values of L. B once every 5 years, at a time when the geomagnetic field is analyzed. For distances exceeding $2R_E$ the calculations of

L, B can be carried out once every 10 years, since the relative magnitudes of the secular variations at these altitudes are 2-3 times smaller than near the surface of the Earth.

REFERENCES

1. Getselov, I. V., El'tekov, V. A., Volga, V. I. and Kuznetsov, V. A., "Comparative analysis of errors in various methods used to calculate L, B-coordinates," in this collection.

2. Finch, H. F., and Leaton, B. R., "The earth's main magnetic field-epoch 1955," Monthly Notices Roy. Astron. Soc., Geophys. Suppl. 7, 314 (1957).

3. Fougere, P. F., "Spherical harmonic analysis 2, new model derived from magnetic observatory data for epoch 1960," J. Geophys. Res. (1964).

N75 16466

POSSIBLE ISOTOPIC SHIFTS WITH CHANGES IN THE GEOMAGNETIC FIELD

Yu. P. Bulashevich, V. M. Yershov, V. F. Zakharchenko

ABSTRACT

The geomagnetic fields of the past geological epochs are studied on the basis of observations on the rock residual magnetization. This paper evaluates the shifts in the isotopic composition of the same elements in the rocks affected by cosmic rays. The possibility of using the shifts in the isotopic composition for revealing geomagnetic field inversions is discussed. Geomagnetic field inversion periods traced by the rock residual magnetization are in good agreement with the periods of the greatest qualitative changes in the animal world throughout the last 500 million years.

Paleomagnetic studies lead to the conclusion about geomagnetic field inversions [1 - 4] taking place in $n \cdot 10^5$ - $n \cdot 10^6$ years [5 - 11].

Several hypotheses exist about the possible character of the inversions of the Earth's magnetic field:

a) The decomposition of the dipole field into multiple components and the formation of a field with the opposite sign,

b) Turning of the dipole without reducing the intensity of the field to zero [15, 10],

c) Reduction of the intensity of the field to zero and the formation of a field with opposite sign [1, 2, 6, 11].

The variations in the Earth's magnetic field during the inversion periods have an effect on the cosmic radiation intensity which they increase by a factor of three at the equator. During solar flares the intensity of the cosmic radiation increases manyfold.

R. Uffen [12] proposed the hypothesis that cosmic radiation during inversion periods had an effect on the development of life on Earth. Later J. Simpson [13] who compared the available data about the development of 17 orders and classes of life organisms, the geomagnetic field inversions, organic activity, climatic changes, sea regressions and transgressions, demonstrated satisfactory agreement between the epochs in which certain families of live organisms perished on a wide scale

and the periods of most frequent variations in the polarity of the magnetic field. The changes in the fauna with the rock residual magnetization in the deep-water Antarctic core are in almost full agreement. The data about the correlation between the magnetic field inversions and the changes in the animal world are still inadequate to prove the cause for these related phenomena, but they are adequate for assuming its existence.

Articles [5, 14] point out the difficulties in the study and in obtaining reliable results about the magnetic field during transition epochs. It is of interest to study the variations in the intensity of cosmic rays on Earth in periods of geomagnetic field inversions.

As a result of the interaction of cosmic ray particles with the substance, both radioactive and stable isotopes are formed. The accumulation of stable cosmogenic elements during the prolonged action of cosmic rays on the substance of the Earth's surface can lead to a deviation in the isotopic ratios from the normal ratios. The Earth's magnetic field reduces the cosmic ray intensity of rays reaching the surface. Therefore, the absence or considerable weakening of the field during a particular geological period can be reflected in the isotopic composition of the chemical elements of rocks.

The changes in the isotopic composition arising during the accumulation of products resulting from the splitting of nitrogen, oxygen and argon nuclei in the atmosphere were determined in [15]. Thus, lithium isotopes, Li^6 and Li^7, are generated in the atmosphere with approximately the same yield and reach the Earth's surface, and a greater part of these are dissolved in oceans. The natural mixture contains 7.5% Li^6 and 92.5% Li^7. Therefore, the products resulting from the splitting will increase the relative isotope Li^6 content in the oceans. Quantitative estimates made on the assumption that the cosmic ray intensity will remain the same as now for a period of $4 \cdot 10^9$ years gives a change in the isotopic composition which is approximately equal to 0.03%. At the same time attention is drawn to the fact that the higher value of the intensity in the past could have been caused by the weakened magnetic field.

To determine certain characteristics of cosmic radiation, /106
A. P. Vinogradov, et al., [14] carried out a radio chemical and mass spectrometric study of iron meteorites. It turned out that, as a result of the thoroughgoing splitting of iron over a period of $4.5 \cdot 10^9$ years, stable isotopes from A^{36} to Mn^{55} accumulated in the meteorite in amounts on the order of magnitude of 10^{-8} - 10^{-9} g/year. The isotopic composition of cosmogenic chemical elements differs substantially from the composition of rocks on Earth.

Thus, under the influence of cosmic rays, changes take place in the isotopic composition of elements in the atmosphere, hydrosphere and lithosphere. The intense movement of particles in the atmosphere and in the hydrosphere make it impossible to relate the observations in these media to definite periods in the history of the geomagnetic field. The cosmogenic isotopes in the lithosphere must be studied on the basis of the products resulting from the splitting of an element which is sufficiently prevalent, of great atomic weight, which can be found in the rocks that are used to determine the paleomagnetism. Iron satisfies these requirements.

Suppose that N_i/N_k is the ratio of two isotopes of a chemical element corresponding to their percentage content in rocks on Earth. n_i and n_k atoms of the corresponding isotopes will accumulate in one unit of volume in a certain time interval. As a result, a shift will occur in the ratio of the i-th isotope to the k-th isotope, which is equal to

$$\Delta(i/k) = \frac{\frac{N_i + n_i}{N_k + n_k} - \frac{N_i}{N_k}}{N_i/N_k} 100\% = \frac{\frac{n_i}{N_i} - \frac{n_k}{N_k}}{1 + \frac{n_k}{N_k}} 100\%. \qquad (1)$$

Let us assume that $N_i < N_k$. Then the shift will be larger the less prevalent the i-th isotope and the greater its efficiency in the splitting reaction. Also taking into account that n_k/N_k is always smaller than 1, we can obtain the estimate using the approximate formula

$$\Delta(i/k) \simeq \frac{n_i}{N_i} 100\% = \Phi\sigma_i t \cdot \frac{N_{Fe}}{N_i} 100\%, \qquad (2)$$

where Φ is the stream of the neutron component of the cosmic rays, σ_i is the production cross section for the i-th isotopes and N_{Fe} is the number of iron atoms per unit volume of the rock, and t is the radiation time.

Considerable deviations from the percentage content found in the products resulting from the splitting of iron in rocks prevalent on Earth were found in [15] for the isotope pairs K^{40} K^{41}, Ca^{46}/Ca^{40}, Ti^{49}/Ti^{48}, V^{50}/V^{51}. Quantitative estimates of the isotope shifts lead to quantities of the same order of magntiude

for all pairs that were enumerated. In the case of potassium we obtain

$$\Delta(K^{40}/K^{41}) = 1{,}3\cdot10^{-13}\frac{Fe}{K}\Phi t\%, \qquad (3)$$

where Fe/K is the ratio of the iron to potassium content in the sample, which in rock is on the order of magnitude 10^2. If the rock sample is irradiated for t - $4\cdot10^9$ years by a flux of 10^{-2} particles/cm^{2}sec (at the mountain level) the magntiude of the shift will be $6\cdot10^{-4}$%. The maximum duration of the geomagnetic field inversion period is estimated to be 10^6 years. Therefore, the magnitude of the shift $\Delta(K^{40}/K^{41})$ during the inversion period will be smaller by three orders of magnitude. This indicates that a study of the isotopic composition of chemical elements for paleomagnetic purposes requires specially prepared samples. If iron minerals are selected, for example, magnetite, the Fe/K ratio can clearly be increased by 1 - 2 orders of magnitude.

The estimates that were given above were obtained on the assumption that no catastrophic increases in the cosmic ray intensity occurred during the geological time intervals of interest. /107

Recently, a hypothesis was proposed about the solar origin of the Earth's magnetic field [16] according to which the geomagnetic field was formed by powerful solar proton streams, and the inversion of the field took place through demagnetization of the Earth and magnetization in the opposite direction. The streams mentioned are on the order of 10^{10}cm^{-2}.sec^{-1}. A study of the isotopic shifts of the elements in the corresponding layers on the Earth's surface can be used as a basis for verifying the proposed hypothesis.

The Neptune method can turn out to be useful in the detection of inversions that originated several million years ago. In the mutual reaction of cosmic ray neutrons with U^{238}, Np^{237} is formed with a half-decay period of $2.2\cdot10^6$ years. If at some instant t = 0 an additional neutron stream Φ appears acting for a time period T, the Np^{237}/U^{238} ratio can be estimated at the instant when the measurements are made. When $\Phi = 10^{-2}$cm^{-2}.sec^{-1}, T = 10^5 years and $\sigma(n,2n) = 4.5\cdot10^{-24}$cm^2, the ratio is 10^{-13}, for all times less than the half decay period. The value of the Np^{237} and U^{238} ratio in uranium pitch that was measured experimentally [17] was greater by one order of magnitude, which is probably due to the great background of spontaneous neutron fission.

REFERENCES

1. Petrov, G. N. and Rybak, R. S., in the collection Magnetizm gornykh porod i paleomagnetizm, [Magnetism of Rocks and Paleomagnetism], Krasnoyarsk, Siberian Branch of the USSR Acad. of Sci. Publs., 1963.

2. Lin'kova, T. I., in the collection Nastoyashchee i proshloe magnitnogo polya Zemli, [The Present and Past of the Earth's Magnetic Field], Nauka Press, 1965.

3. Opdyke, N. D., Glass, B., Hays, I. D., and Foster, I., Science 154, 3747 (1966).

4. Aparin, V. P. and Vlasov, A. Ya., in the collection Nastoyaschee i proshloe magnitnogo polya Zemli, [The Present and Past of the Earth's Magnetic Field], Nauka Press, 1966.

5. Vlasov, A. Ya. and Kovalenko, G. V., in the collection Magnetizm gornykh porod i paleomagnetizm, [Magnetism of Rocks and Paleomagnetism], Krasnoyarsk, Siberian Branch of the USSR Acad. of Sci. Publs., 1963.

6. Petrova, G. N., Kaporovich, I. G., Makarova, E. V. and Rybak, R. S., in the collection Nastoyaschee i proshloe magnitnogo polya Zemli, [The Present and Past of the Earth's Magnetic Field], Nauka Press, 1965.

7. Einarsson, T., Neues Jahrb. Geol. und Paläontol. Monatsh., No. 4, 159-175 (1957).

8. Cox, A., Doell, R. R., and Dalrymole, G. B., Science 144, 3626 (1964).

9. Bukha, V., in the collection Nastoyashchee i proshloe magnitnogo polya Zemli, [The Present and Past of the Earth's Magnetic Field], Nauka Press, 1965.

10. Helsley, C. E., Trans. Amer. Geophys. Union 44 (1) (1963).

11. Harrison, C. T. and Somagajulu, B. L. K., Nature 212, 5067 (1966).

12. Uffen, R. I., Nature 198, 4876 (1963).

13. Simpson, J. G., Bull. Geol. Soc. America 77, 197-204 (1966).

14. Vinogradov, A. P., Lavrukhina, A. K., and Revina, L. D., Geokhimiya, No. 11, 955-966 (1961).

15. Johanson, S. A. E., Tellus 11 (1) (1959).

16. Danvillier, M. A., C. r. Acad. Sci., No. 13, 263 (1966).

17. Gorshkov, G. V., Zyabkin, V. A., Lyatkovskaya, N. M. and Tsvetkov, O. S., Estestvennyy neytronnyy fon atmosfery i zemnoy kory, [The Natural Neutron Background of the Atmosphere and the Earth's Core], Atomizdat Publications, 1966.

N75 16467

CALCULATIONS OF THE COSMIC RAY MODULATION IN INTERPLANETARY SPACE TAKING INTO ACCOUNT THE POSSIBLE DEPENDENCE OF THE TRANSPORT TRAVEL FOR THE SCATTERING OF THE PARTICLES AND OF THE VELOCITY OF THE SOLAR WINDS ON THE ANGLES THEY MAKE WITH THE HELIOEQUATOR PLANE

(The Case of Isotropic Diffusion)

L. I. Dorman, Z. Kobilinski

ABSTRACT

The modulation of galactic cosmic rays is studied by the magnetic heterogeneities stream on the assumption that the diffusion coefficient is reduced whereas the solar wind velocity is increased with the growth of the angle θ (between the Sun's rotation axis and the direction of solar plasma motion).

The stationary plane problem of isotropic diffusion is solved as it applies to two cases:

(1) with due account of particle retardation by the antiphermium mechanism;

(2) without an account of the above mechanism.

This problem is solved by the grid method in the polar coordinate system. The results of the calculations are followed by a discussion of the method of solution and of the errors.

The change in the solar wind characteristics which depends on the angle θ affects only slightly galactic cosmic ray modulation with the parameter $d = 2/3 \cdot U_0 r_0 / \varkappa_0$ varying between 0.02 and 5.0, where r_0 is the radius of the body under consideration, $\varkappa_0$ and U_0 are the diffusion coefficients and the solar wind velocity in the helioequator plane, respectively.

1. Fundamental Equations

In the diffusion approximation when the assumption is made that the density of the energy of cosmic particles in interplanetary space is much smaller than the density of the energy of the magnetic fields and the kinetic energy of motion of the plasma, the space-time variation in the cosmic ray density in the volume subjected to the modulating effect of the Sun can

be determined from the following anisotropic diffusion equation:

$$\frac{\partial n}{\partial t} - \frac{1}{r^2}\frac{\partial}{\partial r}\left(-r^2 u_{dr} n + r^2 \varkappa_{rr}\frac{\partial n}{\partial r} + r\varkappa_{r\theta}\frac{\partial n}{\partial \theta} + \frac{r\varkappa_{r\varphi}}{\sin\theta}\frac{\partial n}{\partial \varphi}\right) -$$
$$- \frac{1}{r\sin\theta}\frac{\partial}{\partial \theta}\left(-\sin\theta u_{dr\,\theta} n + \sin\theta \varkappa_{\theta r}\frac{\partial n}{\partial r} + \frac{\sin\theta \varkappa_{\theta\theta}}{r}\frac{\partial n}{\partial \theta} + \frac{\varkappa_{\theta\varphi}}{r}\frac{\partial n}{\partial \varphi}\right)$$
$$- \frac{1}{r\sin\theta}\frac{\partial}{\partial \varphi}\left(-u_{dr\,\varphi} n + \varkappa_{\varphi r}\frac{\partial n}{\partial r} + \frac{\varkappa_{\varphi\theta}}{r}\frac{\partial n}{\partial \theta} + \frac{\varkappa_{\varphi\varphi}}{r\sin\theta}\frac{\partial n}{\partial \varphi}\right) -$$
$$- \frac{2}{3}\frac{u}{r}\frac{\partial}{\partial R}(Rn) = F(r, \theta, \varphi, R, Z, t) \qquad (1)$$

where the boundary and initial conditions are determined by the concrete model for the variations [1].

The cosmic ray density in interplanetary space is $n(r, \theta, \varphi, R, Z, t)$, where, θ, φ are heliocentric spherical coordinates, R and Ze are the hardness and the charge of the particles and t is time. In equation (1), F is the source function $\varkappa_{ik}$ is the tensor diffusion coefficient, u is the velocity with which the plasma moves, u_{dr} is the drift velocity of the cosmic rays due to the radial motion of the plasma emitted from the rotating Sun. The last term in the left member of the equation describes the retardation by the antiphermium mechanisms, i.e., the systemmatic loss of energy in the particles due to the preferential scattering during the retarded collisions of the particles with the magnetic inhomogeneities [1, 2].

In the r, θ, φ coordinate system, the anisotropic diffusion tensor has the form

$$\varkappa_{ik} = \varkappa_0 \begin{pmatrix} C_1^2 + \alpha_1 C_2^2 & C_2\alpha_2 & -C_1C_2(1-\alpha_1) \\ -C_2\alpha_2 & \alpha_1 & -\alpha_2 C_1 \\ -C_1C_2(1-\alpha_1) & \alpha_2 C_1 & C_2^2 + \alpha_1 C_1^2 \end{pmatrix}, \qquad (2)$$

where

$$\alpha_1 \equiv \frac{R^2}{R^2 + 9\cdot 10^3 A^2 H^2}; \quad \alpha_2 \equiv \frac{3\cdot 10^2 AHR}{R^2 + 9\cdot 10^4 A^2 H^2}; \qquad (3)$$

$$C_1 \equiv (1 - \sin^2\psi \sin^2\theta)^{1/2}; \quad C_2 \equiv \sin\psi \sin\theta \tag{4}$$

and H_0 is the intensity of the large-scale magnetic field, $\chi_\theta = v\Lambda/3$; Λ is the transport travel for the scattering particles, and Ψ is the angle between the magnetic lines of force and the direction of the radial motion of the magnetic inhomogeneities. /109

In the presence of inhomogeneities in the field on the background of the large-scale regular field if we denote the relative role played by the large-scale field by $\beta \sim H_0/(H_0 + h)$, where h is the intensity of the magnetic field in the inhomogeneities, we have, for the components of the drift velocity vector of the particles the following expressions

$$u_{dr.r} = \frac{\beta u \Omega^2 (r - r_\odot)^2}{u^2 + \Omega^2 (r - r_\odot)^2} + \frac{2(1-\beta)u}{3}; \quad u_{dr.\theta} = 0;$$
$$u_{dr.\varphi} = \frac{\beta u^2 \Omega (r - r_\odot)\sin\theta}{u^2 + \Omega^2 (r - r_\odot)^2}. \tag{5}$$

Here $r_\odot$ is the radius of the Sun, $\Omega = 2\pi/T$ is the angular frequency for the rotation of the Sun ($T \approx 27$ days).

When the regular interplanetary field is absent ($H_0 = 0$), according to [3], $\alpha_1 = 1$, $\alpha_2 = 0$ and according to [2]

$$\varkappa_{ik} = \varkappa_0 \begin{pmatrix} 1 & 0 & 0 \\ 0 & 1 & 0 \\ 0 & 0 & 1 \end{pmatrix}, \tag{6}$$

i.e., isotropic diffusion occurs.

Since $\beta = H_0/(H_0 + h) = 0$, we obtain, according to (5), for the drift velocity of the particles

$$u_{dr.r} = \frac{2}{3}u; \quad u_{dr.\theta} = u_{dr.\varphi} = 0. \tag{7}$$

In this case we obtain from equation (1) the isotropic cosmic ray diffusion equation in interplanetary space:

$$\frac{\partial n}{\partial t} - \frac{1}{r^2}\frac{\partial}{\partial r}\left(-r^2\cdot\frac{2}{3}un + r^2\varkappa_0\frac{\partial n}{\partial r}\right) - \frac{1}{r\sin\theta}\frac{\partial}{\partial\theta}\left(\frac{\sin\theta}{r}\varkappa_0\frac{\partial n}{\partial\theta}\right) - \\ - \frac{1}{r\sin\theta}\frac{\partial}{\partial\varphi}\left(\frac{\varkappa_0}{r\sin\theta}\frac{\partial n}{\partial\varphi}\right) - \frac{2}{3}\frac{u}{r}\frac{\partial}{\partial R}(Rn) = F(r, \theta, \varphi, R, Z, t). \qquad (8)$$

There are reasons for assuming that a regular interplanetary magnetic field with lines of force in the shape of spirals of Archimedes exists up to a distance of several astronomical units from the Sun, and that this field is disturbed by relatively small fluctuations $h < H_0$. The anisotropic diffusion of cosmic rays occurs in this region. Farther the magnetic field becomes turbulent and extends up to a distance on the order of 100 AU [3]. The isotropic diffusion of cosmic rays described by equation (8) must occur in this field.

2. Stationary Models for the Isotropic Diffusion of Galactic Cosmic Rays Taking into Account Retardation by the Antiphermium Mechanism

2.1. Spherical Symmetric Model

Article [1] studied the isotropic diffusion of galactic cosmic rays. The author ignored the effect of the region around the Sun where anisotropic diffusion exists because of the relatively small dimensions of this region. For galactic cosmic rays we must set $F = 0$ in equation (8), since there are no galactic particle sources within the modulation zone. In the stationary spherical symmetric case $\left(\frac{\partial n}{\partial\theta} = \frac{\partial n}{\partial\varphi} = 0\right)$ the term $\frac{\partial n}{\partial t}$ can be ignored on the assumption that the dependence of u, $\varkappa_0$, r_0 (the radius of the modulation zone) on time is sufficiently weak, which is valid to a large extent with regard to 11-year variations. We then obtain the equation /110

$$\frac{1}{r^2}\frac{\partial}{\partial r}\left(r^2\cdot\frac{2}{3}un - r^2\varkappa_0\frac{\partial n}{\partial r}\right) - \frac{2}{3}\frac{u}{r}\frac{\partial}{\partial R}(Rn) = 0 \qquad (9)$$

with the boundary conditions

$$n(r, R, Z)_{r=0} < 8; \quad n(r, R, t)|_{r=r_0} = n_0(R), \qquad (10)$$

where $n_0(R)$ is the density of the cosmic rays of rigidity R, beyond the boundaries of the modulating zone, and t is considered as the parameter.

Using the separation of variables method and assuming that $\varkappa_0$ is independent of r and that the dependence of $\varkappa_0$ on R can be ignored in the interval in which R varies as the particles penetrate the modulating zone and that $n_0(R) = kR^{-\gamma}$, in article [1], the equation

$$\rho \frac{d^2B}{d\rho^2} + \left(2 - \frac{2}{3b}\rho\right)\frac{dB}{d\rho} - \frac{2}{3b}(1+\gamma)B = 0, \tag{11}$$

was obtained from equation (9), or, using the notation d = 2/3b and selecting the most realistic value $\gamma = 2.5$, the equation

$$\rho \frac{d^2B}{d\rho^2} + (2 - d\rho)\frac{dB}{d\rho} - 3{,}5dB = 0 \tag{12}$$

with the boundary conditions B(1, t) = 1, B(0, t) < ∞, where $B = n/n_0$, $\rho = r/r_0$. The solution of equation (11) is expressed in terms of the degenerate hypogeometric functions

$$B = \frac{n(\rho, R, t)}{n_0(R)} = \frac{\Phi\left(\gamma + 1, 2, \frac{2\rho}{3b}\right)}{\Phi\left(\gamma + 1, 2, \frac{2}{3b}\right)}. \tag{13}$$

The results, which were calculated using this formula, are given in [1] and were compared with the solution of the equation obtained from the conditions for the equality of the diffusion and convective flux for the cosmic rays in interplanetary space [4]:

$$\frac{1}{r^2}\frac{\partial}{\partial r}\left(r^2 un - r^2 \varkappa_0 \frac{\partial n}{\partial r}\right) = 0; \tag{14}$$

$$n(r, R, t)|_{r=0} < \infty; \quad n(r, R, t)|_{r=r_0} = n_0(R). \tag{15}$$

where $B = e^{-\frac{ur_0}{\varkappa_0}(1-\rho)} = e^{-\frac{3}{2}d(1-\rho)}$ is the solution of the given equation. This comparison has shown that the differences were small.

2.2. A Model which takes into Account the Possible Dependence of the Transport Travel for the Scattering and the Velocity of the Solar Wind on the Angle with the Helioequator Plane

According to contemporary concepts about the situation in interplanetary space, we should expect that the transport travel for the scattering Λ and the velocity of the solar wind u depend not only on the distance from the Sun, but also on the heliolatitudes. The purpose of the calculations is to study the sensitivity of the cosmic ray density distribution to the degree of asymmetry of the problem. /111

Assuming for a variation of long periodicity that the density n of galactic cosmic rays is independent of the azimuth angle φ, we obtain a plane problem for the unknown density $n(r, \theta, R, t)$. Since a stationary problem is being solved, t is a parameter. The boundary of the region considered is a sphere with radius r_0. The effect of the region near the Sun where anisotropic diffusion occurs is ignored.

The equation describing the distribution of the cosmic ray density is obtained from (8)

$$\frac{1}{r^2}\frac{\partial}{\partial r}\left(r^2\frac{2}{3}un - \varkappa r^2\frac{\partial n}{\partial r}\right) - \frac{1}{r\sin\theta}\frac{\partial}{\partial\theta}\left(\frac{\sin\theta}{r}\varkappa\frac{\partial n}{\partial\theta}\right) - \frac{2}{3}\frac{u}{r}\frac{\partial}{\partial R}(Rn) = 0 \qquad (16)$$

with the boundary conditions

$$n(r, \theta, R, t)|_{r=r_0} = n_0; \quad n(r, 0, R, t)|_{r=0} < \infty. \qquad (17)$$

We assume that the transport travel for the scattering Λ and the velocity of the solar wind u depend on the angle θ as follows

$$\Lambda = \Lambda_0(2 - \sin\theta); \quad u = \frac{1}{2}u_0(1 + \sin\theta)$$

or

$$\varkappa = \varkappa_0 (2 - \sin\theta), \tag{18}$$

where $\varkappa_0$, Λ_0, u_0 are, respectively, the diffusion coefficient, the transport travel and the velocity of the solar wind in the helioequator plane.

Under this assumption, in the direction of the Sun's pole $\varkappa$ is twice as large and u 1/2 times as large as in the helioequator plane. Such variation in the solar wind parameters of the continuously expanding corona of the Sun can occur near the solar activity maximum. During high solar activity, the corona has almost complete spherical symmetry, since, during minimum activity, the density of the corona is considerably lower above the poles than above the equator [4, 5]. Here, as in Section 2.1, we ignore the dependence of the diffusion coefficient on the rigidity and we assume that the diffusion coefficient is independent of the distance from the Sun and that $n_0 = kR^{\gamma}$, $\gamma = 2.5$.

After a change and separation of the variables, we obtain

$$\rho^2 \frac{\partial^2 B}{\partial \rho^2} + \frac{\partial^2 B}{\partial \theta^2} + \left[2\rho - d \frac{\frac{1}{2}(1 + \sin\theta)}{2 - \sin\theta} \rho^2 \right] \frac{\partial B}{\partial \rho} +$$
$$+ \frac{2 \operatorname{ctg}\theta (1 - \sin\theta)}{2 - \sin\theta} \frac{\partial B}{\partial \theta} - 3{,}5d \frac{\frac{1}{2}(1 + \sin\theta)}{2 - \sin\theta} \rho B = 0, \tag{19}$$

with the boundary conditions

$$B|_{\rho=1} = 1; \qquad B|_{\rho=0} < \infty \tag{20}$$

and

$$d = \frac{2}{3} \frac{u_0 r_0}{\varkappa}; \quad B = \frac{n(\rho, \theta, R, t)}{n_0(R)}; \quad \rho = \frac{r}{r_0}.$$

2.3. Method of Solution

We have a plane problem which we solve using the grid method in the polar coordinate system (ρ, θ). Since the problem is symmetric with respect to the helioequator plane, we take only 1/4 of the circle (Fig. 1). For the approximate numerical integration of equation (19) we pass through two families of lines /112

$$\rho = ih \quad (i = 1, 2, \ldots, n),$$
$$\theta = \left(k - \frac{1}{2}\right) l \quad (k = 1, 2, \ldots, m), \tag{21}$$

where h, l are the step sizes in the grid obtained in this manner.

The problem is to determine approximately the values $B_{i,k}$ of the function $B(\rho, \theta, R, t)$ at the nodes of this grid. For each interior node (i, k) we set up a difference equation by replacing at the point $\left[ih, \left(k - \frac{1}{2}\right) l\right]$ the derivatives in equation (19) by the differences. These arithmetic relations are completely analogous to those relations which are used in the numerical solution of the differential equation of the eliptic type in Cartesian coordinates [6, 7].

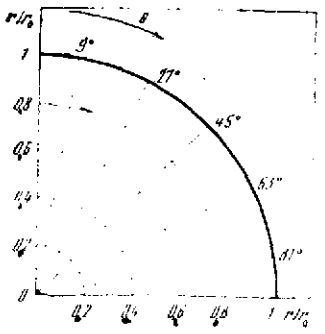

Fig. 1. Polar coordinate system used for solving the plane problem by the method of grids.

In this case, the derivatives are replaced by the following differences:

$$\left(\frac{\partial^2 B}{\partial \rho^2}\right)_{i,k} \approx \frac{B_{i+1,k} - 2B_{i,k} + B_{i-1,k}}{h^2}; \quad \left(\frac{\partial B}{\partial \rho}\right)_{i,k} \approx \frac{B_{i+1,k} - B_{i-1,k}}{2h};$$
$$\left(\frac{\partial^2 B}{\partial \theta^2}\right)_{i,k} \approx \frac{B_{i,k+1} - 2B_{i,k} + B_{i,k-1}}{l^2}; \quad \left(\frac{\partial B}{\partial \theta}\right)_{i,k} \approx \frac{B_{i,k+1} - B_{i,k-1}}{2l}. \tag{22}$$

The grid is shifted half a step in the direction θ (see Fig. 1) in order to avoid the direction $\theta = 0^o$ where the coefficient of the derivative $\partial B/\partial\theta$ is infinite and the derivative itself is zero. From physical considerations, it follows that the modulation depth $B = n/n_0$ must be a continuous function which is symmetric with respect to the direction $\theta = 0^o$, whose values must not differ very much at a distance of a single step (for a small step size) since the diffusion coefficient and the velocity of the solar wind which have an immediate effect on the cosmic ray density also change very little at such distances. Therefore, this procedure will not distort the results near the direction $\theta = 0^o$.

The value of the function at the coordinate center is found by means of parabolic interpolation using the mean values of the function in the neighboring nodes for $i = \pm 1, \pm 2$ [8]. The physical considerations confirm also here the correctness of the method, since the value of the unknown function at the origin must not differ by much from the values in the neighboring nodes.

Thus, we obtain a system of linear algebraic equations, whose number is equal to the number of unknowns and at the same time to the number of interior nodes in the grid

$$B_{i,k} = \frac{A_{i,k}}{F_{i,k}} B_{i+1,k} + \frac{C_{i,k}}{F_{ik}} B_{i-1,k} + \frac{D_{ik}}{F_{ik}} B_{i,k+1} + \frac{E_{ik}}{F_{ik}} B_{i,k-1}; \tag{23}$$

where

$$A_{ik} = i^2 + \left[i - \frac{d}{4} \frac{1 + \sin\left(k - \frac{1}{2}\right) l}{2 - \sin\left(k - \frac{1}{2}\right) l} \right];$$

$$C_{ik} = i^3 - \left[i - \frac{d}{4} \frac{1 + \sin\left(k - \frac{1}{2}\right) l}{2 - \sin\left(k - \frac{1}{2}\right) l} i^2 h \right];$$

$$D_{ik} = \frac{1}{l^2} + \frac{\operatorname{ctg}\left(k - \frac{1}{2}\right) l \cdot \left[1 - \sin\left(k - \frac{1}{2}\right) l\right]}{l\left[2 - \sin\left(k - \frac{1}{2}\right) l\right]};$$

$$E_{ik} = \frac{1}{l^2} - \frac{\operatorname{ctg}\left(k - \frac{1}{2}\right) l \cdot \left[1 - \sin\left(k - \frac{1}{2}\right) l\right]}{l\left[2 - \sin\left(k - \frac{1}{2}\right) l\right]}; \qquad (24)$$

$$F_{ik} = 2i^2 + \frac{2}{l^2} + 3{,}5 \cdot \frac{d}{2} \cdot \frac{1 + \sin\left(k - \frac{1}{2}\right) l}{2 - \sin\left(k - \frac{1}{2}\right) l} ih.$$

From the conditions for the symmetry of the problem

$$B_{i-1} = B_{i,1}; \quad B_{i,m+1} = B_{i,m}, \qquad (25)$$

follows, and at the coordinate origin we have

$$B_0 = \frac{4}{3} \cdot \frac{1}{m} \sum_{k=1}^{m} B_{1,k} - \frac{1}{3} \cdot \frac{1}{m} \sum_{k=1}^{m} B_{2,k}. \qquad (26)$$

At the nodes on the boundary we have equality

$$B_{n,k} = 1. \qquad (27)$$

The problem is solved with the aid of three grids (Table 1)

Table 1. POLAR COORDINATE SYSTEM FOR THE SOLUTION OF THE PLANE PROBLEM USING THE METHOD OF GRIDS

Grid Characteristics

N	Variable					
	ρ			θ		
	No. of nodes, n	Stepsize L	No. of nodes, m	Stepsize		No. of interior nodes in the grid
				Radians	Degrees	
I	5	0,2	5	$\frac{\pi}{10} \approx 0{,}314$	18°	21
II	10	0,1	15	$\frac{\pi}{30} \approx 0{,}105$	6°	136
III	30	$\frac{1}{30} \approx 0{,}033$	45	$\frac{\pi}{90} \approx 0{,}0349$	2°	1306

Using the step sizes shown in Table 1, the coefficients (24) are positive at all nodes of the grid, and it can be proved [7], that the iterative Seidel method which we used converges.

The calculations were carried out for the following values of the parameter d: 0.02, 0.05, 0.1, 0.5, 1.0, 2.0, 5.0 on the BESM-6 electronic computer. /114

When the computational results for the three grids (I-III) are available, the convergence of the method of grids for the problem under consideration can be verified directly. To do this, we compare the values $B^N_{i,k}$ which were obtained by solving the problem using the grid N (N is an index equal to I or II), with the solution of the problem using the finest grid III at the points (i, k) of the grid which are the common nodes of all three grids or of the two finer grids (II and III). The relative differences between the $B^N_{i,k}$ were calculated for these nodes in grid I or II, and the $B^{III}_{i,k}$ in grid III

$$\delta^N_{i,k} = \frac{B^N_{i,k} - B^{III}_{i,k}}{B^{III}_{i,k}}. \qquad (28)$$

Table 2 gives the values $\Delta^N_{i,k} = \delta^N_{i,k} \cdot 100\%$ for the nodes where the lines $\rho = 0.8, 0.6, 0.4, 0.2$ intersect with the lines $\theta = 9, 27, 45, 63, 81^\circ$ (these are the common nodes in all three grids) and for the coordinate origin and certain common nodes in grids II and III ($\rho = 0.9, 0.7, 0.5, 0.3, 0.1$).

This is illustrated in Fig. 2 which gives the values of δ_{ik}^{N} for the 21 common points in all three grids as a function of the geometric mean $s = \sqrt{h\zeta}$ of the step size, which characterizes the individual grids. The abscissa is in logarithmic scale.

It can be seen from Fig. 2 and from the table that the sequence of solution obtained from refining the grid converges in the entire region to the exact solution of the problem when the values of the parameter d lie in the range 0.02 - 5.0.

The sequence of solutions, as was to be expected, converges faster near the boundary than in the central part of the grid. As the parameter d increases, convergence is slower. When $d = 0.02$ and 0.05, the solutions obtained using grids I, II and III do almost not differ from one another and, therefore $\Delta_{i,k}^{N}$ is given in the table only at the coordinate origin. For $d = 0.1$ only the relative differences between the values in the first and third grid are given (Δ_{ik}^{I}); therefore, at all nodes except the coordinate origin $\Delta_{ik}^{II} < 0.01\%$. For $d = 1.0$, 2.0, 5.0 Δ_{ik}^{N} are given for a large number of nodes. When $d = 5.0$, the Δ_{ik}^{II} exceeds 4% for $\rho = 0.1$, and for the coordinate origin we even have $\Delta_{ik}^{II} = 22.53\%$, since for $d = 1.0$, these values are, respectively, 0.3% and 6.26%. It is also obvious that the change in ρ has a greater effect on the Δ_{ik}^{N} than θ.

2.4. Estimate of the Error in the Results

The error in the solution of the partial differential equation of the elliptic type obtained using the method of grids consists of the following three errors:

a) the error resulting from the approximation of the differential equation by a difference equation,

b) the error resulting from the approximation of the boundary conditions;

c) the computational errors.

We will discuss these types of errors.

When we replace the differential equation by the difference equation (using formula (22)) we make an error that can be estimated using the majorant method of S. A. Gershgorin [7, 8]: /117

Table 2

$$\Delta_{ik}^{N} = \delta_{i,k}^{N} \cdot 100\%$$

d	ρ	N	θ				
			9°	27°	45°	63°	81°
0,02	0,0	I	1,29				
		II	0,11				
0,05	0,0	I	0,76				
		II	0,29				
0,1	0,8	I	0,02	0,01	0,01	0,00	0,00
	0,6	I	0,03	0,02	0,01	0,00	0,00
	0,4	I	0,04	0,03	0,02	0,01	0,00
	0,2	I	0,05	0,04	0,03	0,02	0,01
	0,0	I	1,53				
		II	0,59				
0,5	0,8	I	0,08	0,05	0,05	0,03	0,02
		II	0,01	0,00	0,00	0,00	0,00
	0,6	I	0,17	0,13	0,11	0,07	0,05
		II	0,01	0,01	0,01	0,01	0,01
	0,4	I	0,27	0,24	0,19	0,14	0,10
		II	0,02	0,01	0,01	0,01	0,01
	0,2	I	0,40	0,38	0,35	0,31	0,27
		II	0,01	0,01	0,01	0,00	0,00
	0,0	I	7,69				
		II	2,86				
1,0	0,8	I	0,18	0,13	0,14	0,15	0,15
		II	0,02	0,02	0,02	0,03	0,04
	0,6	I	0,43	0,35	0,34	0,33	0,31
		II	0,05	0,05	0,06	0,07	0,07
	0,4	I	0,77	0,69	0,65	0,60	0,56
		II	0,10	0,10	0,10	0,11	0,12
	0,2	I	1,33	1,34	1,28	1,26	1,23
		II	0,19	0,19	0,20	0,20	0,20
	0,1	II	0,31	0,31	0,33	0,34	0,35
	0,0	I	16,36				
		II	6,26				
2,0	0,8	I	0,38	0,35	0,44	0,56	0,63
		II	0,04	0,06	0,09	0,12	0,15
	0,6	I	1,07	0,96	1,07	1,23	1,33
		II	0,15	0,16	0,21	0,27	0,31
	0,4	I	2,07	1,96	2,02	2,15	2,23
		II	0,31	0,32	0,37	0,43	0,47
	0,2	I	3,91	3,91	4,01	4,15	4,23
		II	0,59	0,60	0,64	0,69	0,72
	0,1	II	0,91	0,95	1,01	1,07	1,12
	0,0	I	32,65				
		II	11,97				
5,0	0,9	II	0,07	0,10	0,14	0,16	0,14
	0,8	I	1,20	1,17	1,48	1,64	1,55
		II	0,23	0,23	0,32	0,38	0,38
	0,7	II	0,37	0,42	0,55	0,66	0,69
	0,6	I	3,66	3,39	3,87	4,44	4,75
		II	0,62	0,67	0,84	1,01	1,10
	0,5	II	0,95	1,00	1,19	1,42	1,58
	0,4	I	7,85	7,41	7,79	8,66	9,51
		II	1,40	1,45	1,64	1,90	2,12
	0,3	II	2,02	2,06	2,22	2,42	2,68
	0,2	I	15,68	15,36	15,53	16,21	16,95
		II	2,90	2,92	3,03	3,21	3,38
	0,1	II	4,17	4,21	4,32	4,49	4,64
	0,0	I	51,66				
		II	22,53				

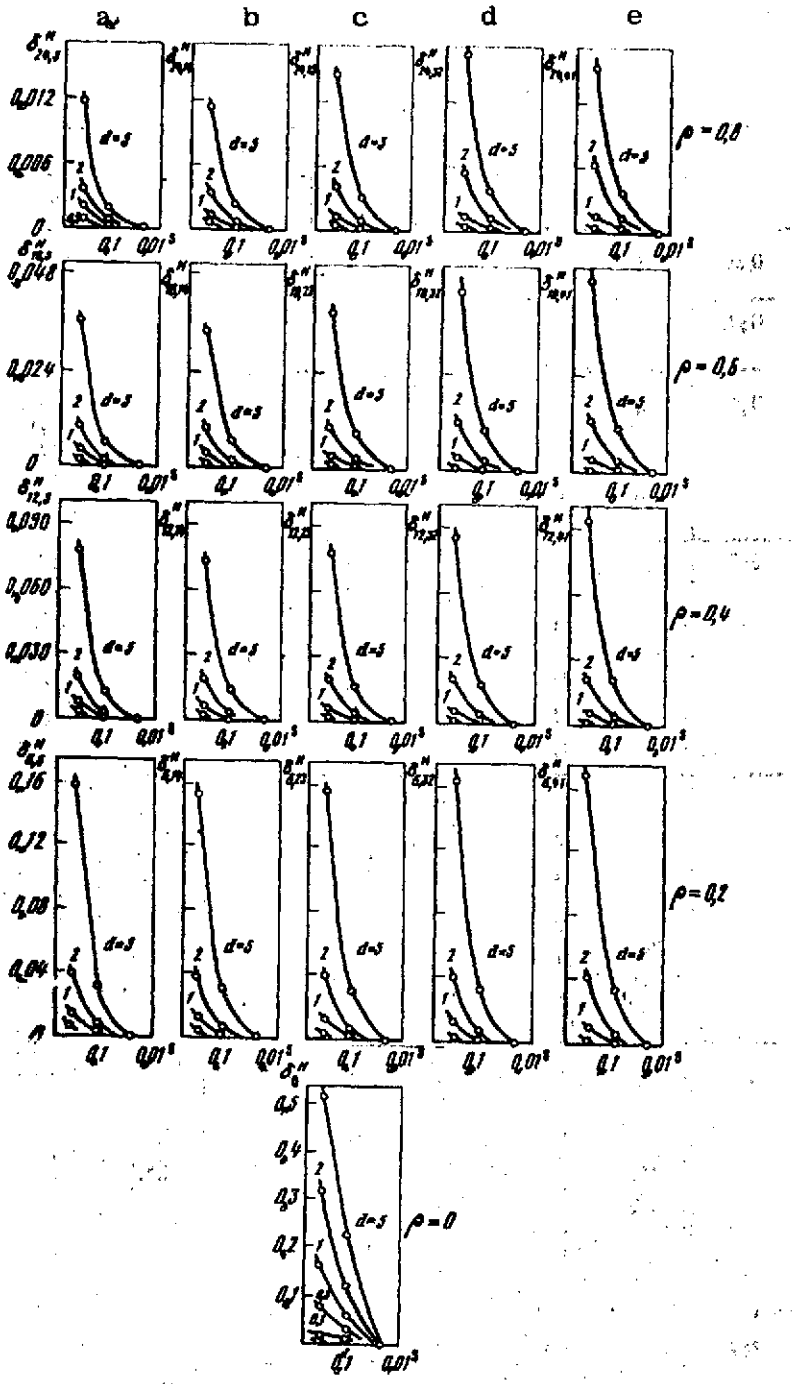

Fig. 2. Relative differences $\delta^N_{i,k}$ vs. the geometric mean $s = \sqrt{h\,l}$ of the grid step size for the common nodes of all three grids used.

a--$\theta = 9^\circ$, b--27°, c--45°, d--63°, e--81°

$$|\varepsilon_{ik}| \leqslant |\eta_{ik}| + \frac{h^2}{24} \frac{\max_G \{(a^2 + \alpha^2 b) M_4 + 2(|c| + \alpha^2 d) M_3\}}{\min_G \left\{\frac{a}{p^2} + \frac{b}{g^2} - \frac{|c|}{p} - \frac{|e|}{g}\right\}} \times$$
$$\times \left(1 - \frac{(\rho_i - \rho_0)^2}{p^2} - \frac{(\theta_k - \theta_0)^2}{g^2}\right), \qquad (29)$$

where $\alpha = 1/h$, a, b, c, e are the coefficients (functions of ρ and θ) of the derivatives in the elliptic equation, G is the region in which the equation is solved, p, g are the semiaxis of the ellipse with axes parallel to the coordinate axes and centered at the point (ρ_0, θ_0) containing in its interior the region G, and M_k is the upper bound of the absolute values k of the x-derivatives of the unknown solution in the region G.

In our problem the boundary of the given region coincides with the boundary of the grid; therefore, the error at interior points and at points on the boundary resulting from an approximation of the boundary conditions (usually described by η_{ik}), is zero.

But here we must take into account the error committed when the function is interpolated at the coordinate origin ζ_{ik}. This error has the greatest effect on the results at the coordinate origin

$$|\zeta_0| \leqslant \frac{1}{6} M_4 h^4 + \frac{4}{3} \frac{1}{m} \sum_{k=1}^{m} |\varepsilon_{1,k}| + \frac{1}{3} \frac{1}{m} \sum_{k=1}^{m} |\varepsilon_{2,k}| \qquad (30)$$

and decreases as the distance from the origin increases $[\zeta_{ik}] \leq [\zeta_0]$.

The first term in the right member of inequality (30) denotes the interpolation error from the Lagrange polynomial which passes through the four points ($i = \pm 1, \pm 2$), the second and third term take into account the errors in the values of the function at the interpolation nodes [7].

The estimate of the error in the numerical solution of the problem using formula (29) and taking into account (3) has the disadvantage that it contains the maximum absolute values of the third and fourth derivatives of the unknown solution. A preliminary estimate of these derivatives is difficult to obtain and attempts to calculate them from the values of the solution

found using numerical differentiation formulas which can be obtained from the Lagrange interpolation polynomial for various intervals did not give satisfactory results. The reason for this is the fact that even though the function and interpolation polynomial can be very close, the derivatives can differ considerably.

In addition to this, the computational error has a considerable effect on the calculation of the derivatives. Therefore, we will obtain a rough estimate of the absolute error for the solution of the given differential equation using the Runge method [7]. When we plot ρ and θ in rectangular coordinates, it is obvious that the problem must be solved so that the grid is rectangular. In each of the three cases, the step sizes h and l are constant in the entire grid, and the angle θ is in radians. The step sizes h and l were selected in the cases II and III in such a way (see Table 1) that approximately $h \approx l$ so that we can assume that we have a square grid. Then, assuming that the error in the solution is r when a square grid with step size h is used, the error at the point $(\rho, \theta) = i \cdot h, k \cdot h)$ can be represented approximately in the form

$$\varepsilon_h(\rho, \theta) = p(\rho, \theta) h^r, \tag{31}$$

where the coefficient $p(\rho, \theta)$ is independent of h.

Then we have, respectively for grid III (step size h) and for grid II (step size 3h) /118

$$\varepsilon_{ik}^{III} \approx p(ih; kh) h^r; \quad \varepsilon_{ik}^{II} \approx p(ih, kh) 3^r h^r \approx 3^r \varepsilon_{ik}^{III}. \tag{32}$$

If $B(\rho, \theta)$ is the exact solution of the problem at the point $(\rho, \theta) = (ih, kh)$; B_{ik}^N is the approximate solution obtained by the method of grids using the grid N,

$$B(\rho, \theta) = B_{ik}^{II} + \varepsilon_{ik}^{II}; \quad B(\rho, \theta) = B_{ik}^{III} + \varepsilon_{ik}^{III}, \tag{33}$$

which implies

$$\varepsilon_{ik}^{III} \approx \frac{B_{ik}^{III} - B_{ik}^{II}}{3^r - 1}. \tag{34}$$

Solving the Dirichlet problem by the above method and using an approximation at the nodes on the boundary, with the aid of the Collatz equations, the error with respect to h is on the order r = 2. In our calculations, the nodes on the boundary have exact values, and in the center, the order of magnitude of the error relative to h is r = 4. However, the grid is only approximately square, so that we will not distort the results of the calculated errors, if we assume that the order of magnitude of the error is also r = 2. This can only lead to a somewhat higher value of the estimated error near the boundary and near the coordinate origin.

Table 3 $|\epsilon_{ik}| \cdot 10^6$ ACCORDING TO FORMULA (35)

d	ρ	θ 9°	27°	45°	63°	81°
0,02	0,8	0	0	0	0	0
	0,6	0	0	0	1	1
	0,4	1	1	1	2	2
	0,2	3	4	4	4	4
	0,1	7	7	8	8	8
	0,0	130				
0,05	0,8	0	0	0	1	1
	0,6	1	1	1	1	1
	0,4	1	2	2	2	2
	0,2	3	3	3	4	4
	0,1	6	6	6	7	7
	0,0	339				
0,1	0,8	2	1	1	0	1
	0,6	3	2	2	2	1
	0,4	4	3	3	2	2
	0,2	6	6	5	5	4
	0,1	10	10	12	13	11
	0,0	654				
0,5	0,8	7	6	5	5	5
	0,6	13	9	8	9	7
	0,4	15	12	10	8	7
	0,2	21	20	22	19	18
	0,1	32	31	29	24	22
	0,0	1960				

d	ρ	θ 9°	27°	45°	63°	81°
1,0	0,9	9	9	12	14	18
	0,8	21	19	24	31	35
	0,7	33	29	35	41	45
	0,6	46	42	46	51	54
	0,5	57	54	56	59	65
	0,4	69	66	67	68	68
	0,3	82	80	78	78	77
	0,2	99	98	98	97	96
	0,1	138	140	144	148	150
	0,0	2471				
2,0	0,9	21	26	41	59	72
	0,8	36	52	74	98	114
	0,7	75	77	98	122	136
	0,6	99	98	116	134	144
	0,5	118	116	127	139	145
	0,4	133	130	134	139	142
	0,3	142	138	139	139	139
	0,2	150	148	146	145	143
	0,1	172	173	178	182	184
	0,0	1733				
5,0	0,9	66	87	115	117	97
	0,8	135	146	173	169	146
	0,7	185	181	192	179	157
	0,6	212	194	187	167	147
	0,5	214	190	170	145	127
	0,4	200	174	147	122	106
	0,3	171	150	123	100	87
	0,2	134	119	110	83	73
	0,1	94	89	81	74	69
	0,0	269				

Table 4. $\sigma_{ik} \cdot 10^6$ ACCORDING TO FORMULAS (37-38) /119

N	ρ	θ									
		μ = 10⁻⁶					μ = 10⁻⁷				
		9°	27°	45°	63°	81°	9°	27°	45°	63°	81°
II	0,9	2	2	2	2	3	0	1	0	0	0
	0,8	5	5	5	4	4	0	1	1	0	1
	0,7	8	7	7	7	8	0	0	0	1	1
	0,6	12	12	11	11	11	1	1	1	1	1
	0,5	17	16	16	15	16	1	1	1	1	2
	0,4	24	23	22	22	21	2	2	2	2	2
	0,3	35	33	33	33	31	3	2	3	3	3
	0,2	52	50	49	48	47	5	5	4	4	5
	0,1	85	83	80	79	78	8	8	7	7	7
	0,0	91					8				
III	0,9	10	11	10	10	10	1	1	1	1	1
	0,8	22	21	22	22	22	2	1	2	2	2
	0,7	37	37	37	36	35	3	3	4	4	3
	0,6	57	56	55	53	53	5	5	5	4	5
	0,5	83	82	81	78	77	7	8	8	7	7
	0,4	120	118	116	113	112	11	11	11	10	11
	0,3	180	177	173	169	167	17	16	16	15	15
	0,2	280	282	277	272	270	24	26	25	25	25
	0,1	535	530	523	516	486	49	48	48	47	47
	0,0	1143					103				

Then from (34) we have

$$\varepsilon_{ik}^{III} \approx \frac{B_{ik}^{III} - B_{ik}^{II}}{8}. \tag{35}$$

Table 3 gives (to six significant digits) the values of the absolute error $|\varepsilon_{ik}|$ in the final results calculated from formula (35) at certain common nodes of grids II and III with the given coordinates ρ and θ. It can be seen from the table that the error increases as the distance from the boundary increases and as the parameter d increases.

The computational error consists of the error resulting from the solution of a system of difference equations and the rounding error. With regard to the latter, on the basis of the estimates given by V. Vasov and G. Forsyth [9], when the calculations are made on a computer using the finite-difference method for the elliptic problem, the rounding errors when

compared to the errors of the method can probably be ignored.

When the number of digits behind the decimal on which the values of the solution of the system of difference equations after the ν-th iteration $B_{ik}^{(\nu)}$ must not differ from the values of the solution after the $(\nu + 1)$-th iteration $B_{ik}^{(\nu+1)}$ must not differ are determined, it is necessary to try, on one hand to save machine time, and on the other hand, to retain the required accuracy of the results. On the basis of article [8], we concluded that to retain four significant digits in the solution (the successive iterations must be terminated after the inequality

$$B_{ik}^{(\nu+1)} - B_{ik}^{\nu} \leqslant \mu = 10^{-7}. \tag{36}$$

is satisfied.

In order to check the error committed during the computations using the interpolation method for the chosen μ, we carried out the calculations for the values $\mu = 10^{-6}$ and 10^{-8} in two cases: when the parameter d was 0.02 and 1.0, respectively. Since the difference between the case d = 0.02 and 1.0 is small, we give here only the results when the parameter d is 1.0. /120

Table 4 gives the values of:

$$\sigma_{ik} = B_{ik}^{N}(\mu = 10^{-6}) - B_{ik}^{N}(\mu = 10^{-8}) \tag{37}$$

and

$$\sigma_{ik} = B_{ik}^{N}(\mu = 10^{-7}) - B_{ik}^{N}(\mu = 10^{-8}) \tag{38}$$

to six significant digits for certain common nodes in grids II and III. It can be seen that σ_{ik} increases as the distance from the coordinate origin decreases and that it depends little on the angle θ. The number of equations when grid II is used is less than 136, and for the same values of μ the number of significant digits in the solution of the system of equations is 4 for $\mu = 10^{-6}$ and 5 for $\mu = 10^{-7}$, while in the case of grid III (1306 equations) the number of significant equations in the solution will be less by one at those nodes where $0.4 \geq \rho \geq 0.1$

and is equal to 3 and 4, respectively.[1] As μ decreases from 10^{-6} to 10^{-7}, the number of significant digits in the solution of the system of equations increases by one.

It can be seen from the table that the choice $\mu = 10^{-7}$ is the correct choice. The values of σ_{ik} which were given for the grid III in the case $\mu = 10^{-7}$ can be taken approximately as the values of the error in the solution of the problem which is obtained by using the interpolation method in solving the system of difference equations.

In summary, we will evaluate the total absolute error ζ_{ik} in the results given in Table 5. For d = 0.02, 0.05, 0.1 all the numbers in Table 5 are correct (when $0.1 \leq \rho \leq 0.9$ to four significant digits and when $\rho = 0$ to three significant digits).

For d = 0.5, 1.0, 2.0, 5.0, the data are as follows:

$d = 0{,}5$	
$0{,}1 \leqslant \rho \leqslant 0{,}9$	All digits are correct
$\rho = 0$	$\lvert \xi_0 \rvert \leqslant 0{,}02$
$d = 1{,}0$	
$0{,}3 \leqslant \rho \leqslant 0{,}2$	All digits are correct
$0{,}1 \leqslant \rho \leqslant 0{,}2$	$\lvert \xi_{ik} \rvert < 0{,}0002$
$\rho = 0$	$\lvert \xi_0 \rvert < 0{,}003$
$d = 2{,}0$	
$\rho = 0{,}9$	$\lvert \xi_{ik} \rvert \leqslant 0{,}0001$
$0{,}2 \leqslant \rho \leqslant 0{,}8$	$\lvert \xi_{ik} \rvert \leqslant 0{,}0002$
$\rho = 0{,}1$	$\lvert \xi_{ik} \rvert \leqslant 0{,}0002$
$\rho = 0$	$\lvert \xi_{ik} \rvert \leqslant 0{,}002$
$d = 5{,}0$	
$0{,}7 \leqslant \rho \leqslant 0{,}9$	$\lvert \xi_{ik} \rvert \leqslant 0{,}0002$
$0{,}4 \leqslant \rho \leqslant 0{,}6$	$\lvert \xi_{ik} \rvert \leqslant 0{,}0003$
$0{,}1 \leqslant \rho \leqslant 0{,}3$	$\lvert \xi_{ik} \rvert \leqslant 0{,}0002$
$\rho = 0$	$\lvert \xi_{ik} \rvert \leqslant 0{,}001$

2.5. Evaluation of the Results

Figure 3 shows the modulation depth $B = n/n_0$ as a function of $\rho = r/r_0$ for constant values of the angle θ in the

1. When we say that the number a is an approximation of the exact number with n significant digits, we mean that the absolute error $\Delta = |A - a|$ does not exceed the unit in the decimal system which is expressed in terms of the n-th significant digit of the approximate number.

interval from 1 to 89° for the values of the parameter

$$d = \frac{2}{3}\frac{u_0 r_0}{\kappa_0}.$$

Figure 4 gives the modulation depth for various values of d. Figure 5 gives the modulation depth as a function of the angle θ for constant values of ρ. Figure 6 gives the same relation for different values of d. /123

It can be seen that the relation proposed for the characteristics of the solar wind as a function of the angle with the helioequator does not have a considerable effect on the modulation of galactic cosmic rays for variations in the parameter d in the range 0.02 to 5.0. As the parameter d decreases, i.e., as the diffusion coefficient κ_0 increases, or as the product $u_0 r_0$ decreases, the density of the particles in the region under consideration increases and at the same time the difference between the densities in various directions decreases.

Hence, for various d, the density in the directions θ = 1 and 80° differs at most (in %) as follows.

d	ρ	%	d	ρ	%
5,0	0,8	25,36	0,5	0,53	6,2
2,0	0,7	16,46	0,1	0,5	1,5
1,0	0,63	10,6	0,02	0,5	0,30

The difference in the density for various angles θ decreases near the coordinate origin and near the boundary of the region under investigation.

In the above spherical symmetric cases, the density of the particles is smaller than in the model with the dependence on θ, which applies especially to the coordinate origin. This difference decreases as the value of the parameter d decreases (for example, for d = 1.0 the difference between (19) and (11) at the coordinate origin is 11.3%, while for d = 0.1 it is 4.2% and for d = 0.02, it is only 0.9%). For d < 1.0, the spherical model that takes into account retardation by the antiphermium mechanism gives a density of the particles which is somewhat smaller than in Parker's model [4].

Table 5

$B = n/n_0$

d	$\frac{r}{r_0}$	θ												
		1°	9°	17°	25°	33°	41°	45°	49°	57°	65°	73°	81°	89°
0,02	0,9	0,9981	0,9981	0,9980	0,9979	0,9978	0,9976	0,9976	0,9975	0,9974	0,9972	0,9971	0,9970	0,9970
	0,8	0,9961	0,9960	0,9959	0,9957	0,9955	0,9953	0,9951	0,9950	0,9947	0,9945	0,9943	0,9942	0,9941
	0,7	0,9939	0,9938	0,9937	0,9934	0,9932	0,9928	0,9927	0,9925	0,9921	0,9918	0,9916	0,9914	0,9913
	0,6	0,9916	0,9915	0,9913	0,9911	0,9907	0,9904	0,9902	0,9900	0,9896	0,9892	0,9889	0,9887	0,9887
	0,5	0,9891	0,9891	0,9889	0,9886	0,9882	0,9879	0,9876	0,9874	0,9870	0,9867	0,9864	0,9861	0,9861
	0,4	0,9865	0,9865	0,9863	0,9860	0,9857	0,9853	0,9851	0,9849	0,9845	0,9841	0,9839	0,9837	0,9836
	0,3	0,9838	0,9837	0,9836	0,9833	0,9831	0,9827	0,9825	0,9824	0,9820	0,9817	0,9814	0,9813	0,9812
	0,2	0,9809	0,9809	0,9808	0,9806	0,9804	0,9801	0,9799	0,9789	0,9796	0,9793	0,9791	0,9790	0,9789
	0,1	0,9779	0,9779	0,9778	0,9777	0,9776	0,9775	0,9774	0,9773	0,9772	0,9770	0,9769	0,9768	0,9768
	0,0	0,975												
0,05	0,9	0,9953	0,9953	0,9951	0,9948	0,9945	0,9941	0,9940	0,9938	0,9934	0,9931	0,9928	0,9927	0,9926
	0,8	0,9903	0,9902	0,9899	0,9894	0,9888	0,9882	0,9879	0,9876	0,9869	0,9864	0,9859	0,9856	0,9854
	0,7	0,9849	0,9848	0,9844	0,9838	0,9830	0,9822	0,9818	0,9814	0,9805	0,9798	0,9791	0,9787	0,9786
	0,6	0,9792	0,9790	0,9786	0,9779	0,9771	0,9762	0,9757	0,9752	0,9742	0,9733	0,9726	0,9721	0,9720
	0,5	0,9732	0,9730	0,9725	0,9718	0,9710	0,9700	0,9695	0,9690	0,9680	0,9671	0,9663	0,9658	0,9656
	0,4	0,9668	0,9666	0,9662	0,9655	0,9647	0,9638	0,9633	0,9628	0,9618	0,9609	0,9602	0,9598	0,9596
	0,3	0,9601	0,9599	0,9596	0,9590	0,9583	0,9575	0,9571	0,9566	0,9558	0,9550	0,9544	0,9539	0,9538
	0,2	0,9531	0,9530	0,9527	0,9523	0,9517	0,9511	0,9508	0,9505	0,9498	0,9492	0,9487	0,9484	0,9483
	0,1	0,9458	0,9457	0,9456	0,9453	0,9450	0,9447	0,9445	0,9443	0,9439	0,9436	0,9433	0,9431	0,9431
	0,0	0,940												
0,1	0,9	0,9908	0,9906	0,9903	0,9898	0,9891	0,9884	0,9881	0,9877	0,9870	0,9863	0,9858	0,9854	0,9853
	0,8	0,9809	0,9807	0,9800	0,9791	0,9780	0,9768	0,9761	0,9755	0,9742	0,9731	0,9721	0,9715	0,9713
	0,7	0,9704	0,9701	0,9693	0,9681	0,9667	0,9651	0,9642	0,9634	0,9617	0,9602	0,9590	0,9582	0,9578
	0,6	0,9593	0,9589	0,9580	0,9567	0,9551	0,9533	0,9523	0,9513	0,9494	0,9477	0,9463	0,9454	0,9450
	0,5	0,9475	0,9471	0,9462	0,9449	0,9433	0,9414	0,9404	0,9393	0,9374	0,9356	0,9341	0,9332	0,9328
	0,4	0,9352	0,9349	0,9340	0,9328	0,9312	0,9294	0,9284	0,9274	0,9255	0,9238	0,9225	0,9215	0,9212
	0,3	0,9223	0,9220	0,9213	0,9202	0,9189	0,9173	0,9165	0,9156	0,9140	0,9125	0,9113	0,9105	0,9101
	0,2	0,9089	0,9087	0,9082	0,9074	0,9063	0,9051	0,9045	0,9039	0,9026	0,9015	0,9005	0,8999	0,8997
	0,1	0,8950	0,8949	0,8946	0,8941	0,8935	0,8929	0,8925	0,8922	0,8915	0,8908	0,8903	0,8899	0,8898
	0,0	0,883												

Table 5 (continued)

d	$\frac{r}{r_0}$	θ											
		1°	9°	17°	25°	33°	41°	45°	49°	57°	65°	73°	81°	89°
0,5	0,9	0,9588	0,9579	0,9561	0,9535	0,9505	0,9471	0,9553	0,9435	0,9400	0,9368	0,9342	0,9325	0,9318
	0,8	0,9155	0,9141	0,9111	0,9068	0,9016	0,8957	0,8927	0,8896	0,8837	0,8783	0,8739	0,8709	0,8698
	0,7	0,8706	0,8690	0,8653	0,8600	0,8534	0,8461	0,8422	0,8384	0,8309	0,8241	0,8186	0,8149	0,8135
	0,6	0,8245	0,8228	0,8189	0,8131	0,8060	0,7980	0,7938	0,7895	0,7813	0,7739	0,7679	0,7639	0,7623
	0,5	0,7776	0,7760	0,7721	0,7665	0,7594	0,7514	0,7473	0,7430	0,7348	0,7274	0,7215	0,7175	0,7160
	0,4	0,7301	0,7287	0,7252	0,7201	0,7137	0,7064	0,7026	0,6987	0,6912	0,6845	0,6790	0,6754	0,6739
	0,3	0,6824	0,6812	0,6785	0,6743	0,6690	0,6629	0,6598	0,6566	0,6503	0,6447	0,6401	0,6371	0,6359
	0,2	0,6348	0,6340	0,6321	0,6291	0,6253	9,6210	0,6187	0,6164	0,6119	0,6078	0,6045	0,6023	0,6014
	0,1	0,5879	0,5874	0,5864	0,5849	0,5829	0,5807	0,5795	0,5782	0,5759	0,5737	0,5720	0,5708	0,5703
	0,0	0,550												
1,0	0,9	0,9260	0,9243	0,9206	0,9156	0,9096	0,9030	0,8996	0,8961	0,8893	0,8832	0,8782	0,8748	0,8735
	0,8	0,8504	0,8478	0,8421	0,8339	0,8241	0,8132	0,8076	0,8019	0,7908	0,7808	0,7728	0,7674	0,7652
	0,7	0,7746	0,7717	0,7649	0,7552	0,7434	0,7302	0,7234	0,7165	0,7032	0,6913	0,6817	0,6752	0,6727
	0,6	0,6996	0,6966	0,6897	0,6797	0,6673	0,6535	0,6464	0,6392	0,6253	0,6128	0,6028	0,5962	0,5936
	0,5	0,6260	0,6234	0,6170	0,6076	0,5959	0,5828	0,5760	0,5692	0,5560	0,5441	0,5347	0,5284	0,5259
	0,4	0,5548	0,5526	0,5471	0,5390	0,5290	0,5176	0,5117	0,5058	0,4942	0,4839	0,4757	0,4703	0,4681
	0,3	0,4865	0,4848	0,4806	0,4744	0,4665	0,4576	0,4530	0,4483	0,4392	0,4311	0,4246	0,4202	0,4185
	0,2	0,4218	0,4207	0,4179	0,4138	0,4085	0,4025	0,3994	0,3962	0,3901	0,3845	0,3800	0,3771	0,3759
	0,1	0,3614	0,3609	0,3596	0,3576	0,3551	0,3521	0,3507	0,3490	0,3460	0,3433	0,3411	0,3396	0,3390
	0,0	0,316												
2,0	0,9	0,8741	0,8707	0,8637	0,8541	0,8328	0,8303	0,8238	0,8173	0,8046	0,7930	0,7837	0,7774	0,7749
	0,8	0,7523	0,7477	0,7370	0,7224	0,7050	0,6858	0,6759	0,6661	0,6470	0,6299	0,6162	0,6071	0,6034
	0,7	0,6373	0,6322	0,6207	0,6044	0,5848	0,5633	0,5523	0,5413	0,5201	0,5014	0,4865	0,4766	0,4727
	0,6	0,5307	0,5260	0,5151	0,4994	0,4805	0,4596	0,4490	0,4384	0,4181	0,4002	0,3861	0,3768	0,3731
	0,5	0,4336	0,4297	0,4204	0,4068	0,3904	0,3722	0,3629	0,3536	0,3360	0,3204	0,3082	0,3002	0,2970
	0,4	0,3468	0,3438	0,3366	0,3261	0,3131	0,2986	0,2912	0,2839	0,2698	0,2574	0,2477	0,2413	0,2387
	0,3	0,2708	0,2687	0,2638	0,2564	0,2472	0,2370	0,2317	0,2264	0,2163	0,2074	0,2004	0,1957	0,1939
	0,2	0,2056	0,2045	0,2016	0,1972	0,1918	0,1856	0,1824	0,1792	0,1730	0,1675	0,1631	0,1603	0,1591
	0,1	0,1516	0,1511	0,1499	0,1481	0,1458	0,1432	0,1418	0,1405	0,1378	0,1354	0,1334	0,1322	0,1317
	0,0	0,116												
5,0	0,967	0,9180	0,9142	0,9070	0,8978	0,8871	0,8753	0,8691	0,8630	0,8509	0,8398	0,8308	0,8247	0,8222
	0,933	0,8395	0,8332	0,8208	0,8046	0,7858	0,7654	0,7549	0,7444	0,7239	0,7054	0,6905	0,6805	0,6765
	0,9	0,7651	0,7570	0,7409	0,7197	0,6952	0,6688	0,6553	0,6418	0,6159	0,5928	0,5743	0,5620	0,5571
	0,8	0,5667	0,5570	0,5364	0,5088	0,4772	0,4438	0,4270	0,4106	0,3796	0,3529	0,3320	0,3184	0,3131
	0,7	0,4060	0,3973	0,3782	0,3524	0,3228	0,2920	0,2768	0,2620	0,2347	0,2116	0,1941	0,1828	0,1784
	0,6	0,2803	0,2737	0,2587	0,2381	0,2164	0,1902	0,1783	0,1668	0,1458	0,1284	0,1153	0,1070	0,1038
	0,5	0,1856	0,1810	0,1706	0,1562	0,1395	0,1222	0,1138	0,1058	0,0911	0,0790	0,0700	0,0644	0,0622
	0,4	0,1167	0,1140	0,1076	0,0986	0,0881	0,0771	0,0717	0,0666	0,0572	0,0495	0,0437	0,0401	0,0387
	0,3	0,0689	0,0675	0,0641	0,0592	0,0534	0,0473	0,0442	0,0413	0,0359	0,0314	0,0281	0,0259	0,0251
	0,2	0,0374	0,0368	0,0354	0,0332	0,0306	0,0278	0,0264	0,0250	0,0224	0,0202	0,0185	0,0174	0,0170
	0,1	0,0183	0,0181	0,0177	0,0171	0,0163	0,0155	0,0150	0,0146	0,0137	0,0130	0,0124	0,0120	0,0119
	0,0	0,010												

Remark: When $r/r_0 = 1.0$, B = 1.0 for all values of θ.

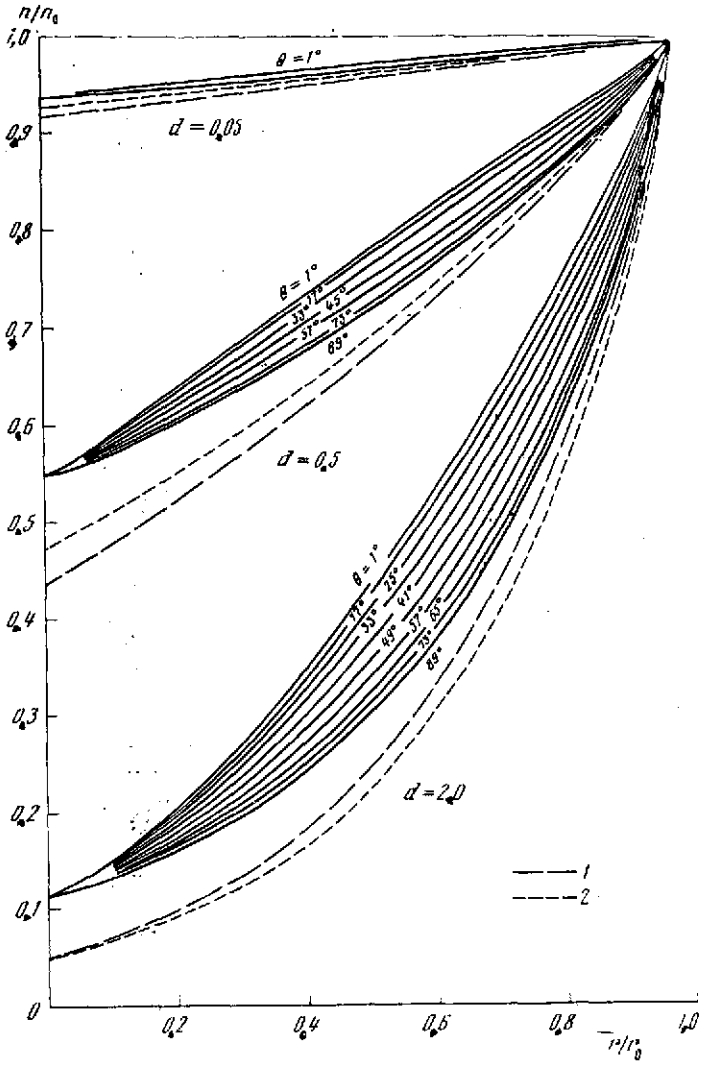

Fig. 3. Modulation depth $B = n/n_0$ vs. $\rho = r/r_0$ for d = 0.05, 0.5, 2.0 for the directions given above in the model that takes into account retardation by the antiphermium mechanism (results obtained from solving eqs. (19), (20)

1--modulation depth vs. distance in the case of a spherical symmetric model according to formula (13), 2--$B = n/n_0$ vs. ρ in the case when the diffusion and convective cosmic ray streams are equal, according to formula (15), for the appropriate d.

/124

3. Stationary Isotropic Diffusion Models of Galactic Cosmic Rays without Taking into Account Retardation by the Antiphermium Mechanism

3.1. Spherical Symmetric Model

In the stationary spherical symmetric case, when retardation by the antiphermium mechanism is not taken into account, the three-dimensional distribution of the density of galactic cosmic rays is described by equation (9) without the last term in the left member:

$$\frac{1}{r^2}\frac{\partial}{\partial r}\left(r^2\cdot\frac{2}{3}un-r^2\varkappa_0\frac{\partial n}{\partial r}\right)=0 \tag{39}$$

using the same boundary conditions /125

$$n(r,R,Z)|_{r=0}<\infty;\quad n(r,R,Z)|_{r=r_0}=n_0(R), \tag{40}$$

where R, and Z are parameters.

It is assumed that $\varkappa$ is independent of ρ. After the change of variables $\rho = r/r_0$, $B=\frac{n(r,R,Z)}{n_0(R)}$ we obtain the equation

$$\frac{d}{d\rho}\left[\rho^2\left(\frac{2}{3}uB-\frac{\varkappa_0}{r_0}\frac{dB}{d\rho}\right)\right]=0 \tag{41}$$

or

$$\rho\frac{d^2B}{d\rho^2}+(2-d\rho)\frac{dB}{d\rho}-2dB=0\ ;\ B|_{\rho=0}<\infty;\ B|_{\rho=1}=1. \tag{42}$$

The solution of the equation is

$$B=e^{-\frac{2}{3}\frac{u(r_0}{\varkappa_0}(1-\rho)}=e^{-d(1-\rho)}. \tag{43}$$

The values of the modulation depth as a function of ρ are given in Table 6 for selected values of d from the interval $0.02 \leq d \leq 5.0$.

Table 6. $B = n/n_0$ VS. ρ

d	ρ												
	0,0	0,01	0,02	0,05	0,1	0,2	0,3	0,4	0,5	0,6	0,7	0,8	0,9
0,02	0,9802	0,9804	0,9806	0,9812	0,9822	0,9841	0,9861	0,9881	0,9900	0,9920	0,9940	0,9960	0,9980
0,05	0,9512	0,9517	0,9522	0,9536	0,9560	0,9608	0,9656	0,9704	0,9753	0,9802	0,9851	0,9900	0,9950
0,1	0,9048	0,9057	0,9066	0,9094	0,9139	0,9231	0,9324	0,9418	0,9512	0,9608	0,9704	0,9802	0,9900
0,5	0,6065	0,6094	0,6126	0,6218	0,6376	0,6703	0,7047	0,7408	0,7788	0,8187	0,8607	0,9048	0,9512
1,0	0,3679	0,3716	0,3753	0,3867	0,4066	0,4493	0,4966	0,5488	0,6065	0,6703	0,7408	0,8187	0,9048
2,0	0,1353	0,1391	0,1409	0,1496	0,1653	0,2019	0,2466	0,3012	0,3679	0,4493	0,5488	0,6703	0,8187
5,0	0,0067	0,0071	0,0075	0,0087	0,0111	0,0183	0,0302	0,0498	0,0821	0,1353	0,2231	0,3679	0,6065

Remark: When $\rho = 1.0$, $B = 1.0$ for all values of d.

3.2. A Model which Takes into Account the Possible Dependence of Δ on the Angle with the Heliequator Plane

In order to study the sensitivity of the distribution of the cosmic ray density to the asymmetry of the parameters that determine the solar wind in the case when retardation by the antiphermium mechanism is not taken into account, we solve a problem which is analogous to that described in Section 2.2. We assume here that the diffusion coefficient is independent of the rigidity and the distance from the Sun. The relation of the diffusion coefficient and the velocity of the solar wind as a function of the θ are the same as in (18). Then

$$\frac{1}{r^2}\frac{\partial}{\partial r}\left(r^2\frac{2}{3}un-\varkappa r^2\frac{\partial n}{\partial r}\right)-\frac{1}{r\sin\theta}\frac{\partial}{\partial\theta}\left(\frac{\sin\theta}{r}\varkappa\frac{\partial n}{\partial\theta}\right)=0 \tag{44}$$

with the boundary conditions

$$n(r,\theta,R,t)|_{r=r_0}=n_0;\ n(r,\theta,R,t)|_{r=0}<\infty, \tag{45}$$

where R, t are parameters. After the change of variables $\rho = r/r_0$, $B = n/n_0$ we obtain the following equation:

$$\rho^2\frac{\partial^2 B}{\partial\rho^2}+\frac{\partial^2 B}{\partial\theta^2}+\left[2\rho+d\frac{\frac{1}{2}(1+\sin\theta)}{2-\sin\theta}\rho^2\right]\frac{\partial B}{\partial\rho}+\frac{2\operatorname{ctg}\theta(1-\sin\theta)}{2-\sin\theta}\frac{\partial B}{\partial\theta}-$$
$$-2d\frac{\frac{1}{2}(1+\sin\theta)}{2-\sin\theta}\rho B=0 \tag{46}$$

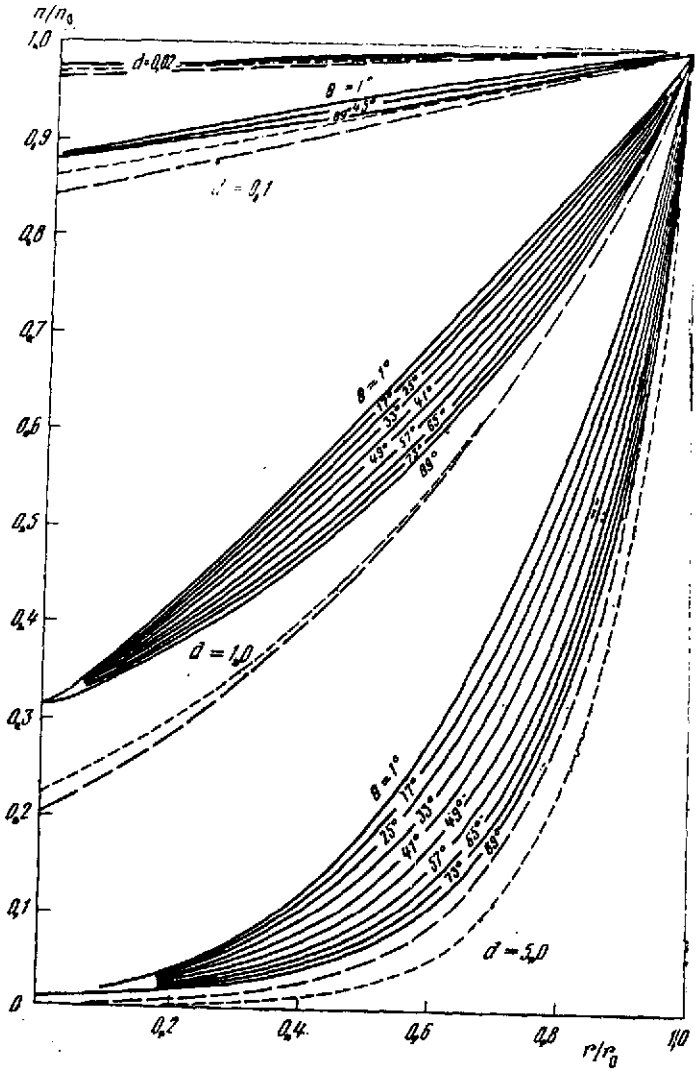

Fig. 4. Modulation depth $B = n/n_0$ vs. distance $\rho = r/r_0$ for d = 0.02, 0.1, 1.0, 5.0 for the directions given above in the model that takes into account retardation by the antiphermium mechanism (results obtained from solving equations (19), (20).

Same notation as in Fig. 3.

/126

with the boundary conditions

$$B|_{\rho=1} = 1;\ B|_{\rho=0} < \infty. \tag{47}$$

Equation (46) differs from equation (19) only by a factor in the coefficient of the last term in the left member.

The problem is solved using the same method described in Section 2.3, using three grids, for which the data are given in Table 1 for the same values of the parameter d.

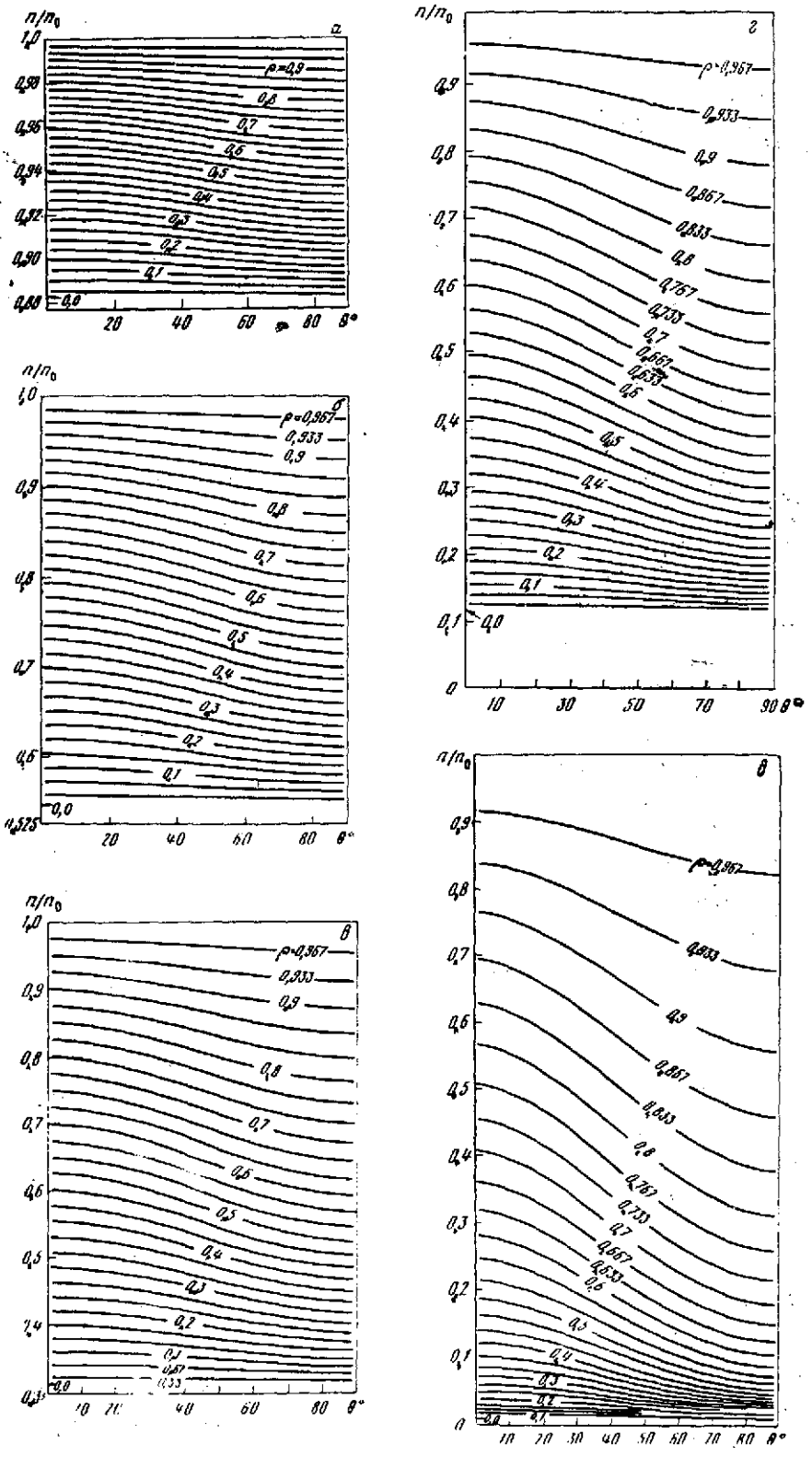

Fig. 5. Modulation depth $B = n/n_0$ vs. the direction (cont'd)

θ for various distances $\rho = r/r_0$ in the case of the model that takes into account retardation by the antiphermium mechanism. The diagram gives curves for distances from $\rho \approx 0.033$ to $\rho \approx 0.967$ in intervals of 0.033 for: a - d = 1.0; b - 0.5; c - 1.0; d - 2.0; e - from $\rho = 0.1$ to $\rho = 0.967$ when d = 5.0.

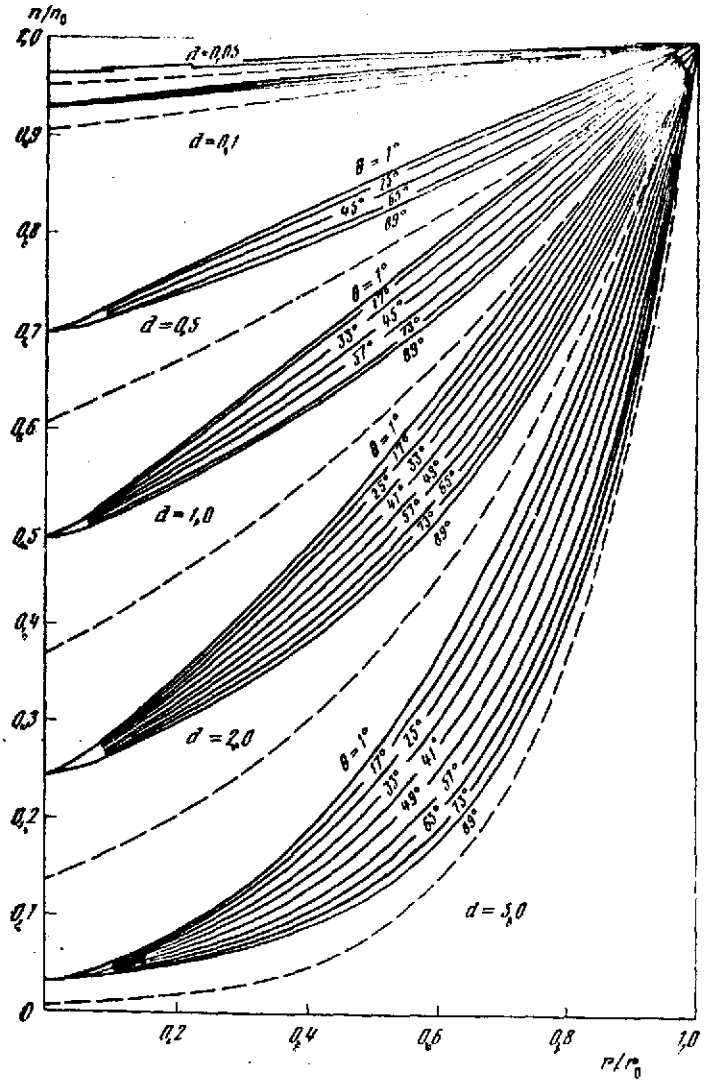

Fig. 6. Modulation depth $B = n/n_0$ vs. distance $\rho = r/r_0$ for d = 0.05, 0.1, 0.5, 1.0, 2.0, 5.0 for the directions given above for the model that does not take into account retardation by the antiphermium mechanism (results obtained from solving equations (46), (47)).

Dashed line shows B vs. ρ in the spherical symmetric case according to formula (43) for the corresponding d.

Table 7. EXAMPLE FOR THE CONVERGENCE OF THE METHOD OF GRIDS WHEN $\Delta_{ik}^{N} = \delta_{ik}^{N} \cdot 100\%$ IS CALCULATED ACCORDING TO FORMULA (28)

d	ρ	N	θ				
			9°	27°	45°	63°	81°
0,02	0,0	I	0,16				
		II	0,06				
0,05	0,0	I	0,43				
		II	0,16				
0,1	0,0	I	0,87				
		II	0,33				
0,5	0,8	I	0,05	0,04	0,03	0,02	0,01
		II	0,01	0,00	0,00	0,00	0,00
	0,6	I	0,12	0,09	0,07	0,05	0,04
		II	0,01	0,01	0,01	0,01	0,01
	0,4	I	0,13	0,15	0,13	0,09	0,06
		II	0,02	0,02	0,01	0,01	0,01
	0,2	I	0,27	0,25	0,23	0,21	0,18
		II	0,03	0,03	0,03	0,02	0,02
	0,0	I	4,54				
		II	1,75				
1,0	0,8	I	0,12	0,09	0,09	0,08	0,07
		II	0,01	0,01	0,01	0,01	0,02
	0,6	I	0,28	0,23	0,21	0,18	0,15
		II	0,03	0,03	0,03	0,03	0,03
	0,4	I	0,48	0,43	0,39	0,34	0,30
		II	0,06	0,05	0,05	0,06	0,05
	0,2	I	0,81	0,79	0,77	0,74	0,72
		II	0,10	0,10	0,10	0,10	0,10
	0,1	II	0,17	0,18	0,18	0,19	0,20
	0,0	I	9,43				
			3,59				
2,0	0,8	I	0,28	0,24	0,28	0,32	0,34
		II	0,04	0,04	0,05	0,07	0,08
	0,6	I	0,71	0,64	0,67	0,71	0,85
		II	0,08	0,10	0,12	0,14	0,16
	0,4	I	1,36	1,28	1,28	1,29	1,28
		II	0,19	0,20	0,22	0,24	0,24
	0,2	I	2,55	2,55	2,60	2,65	2,67
		II	0,39	0,40	0,41	0,41	0,43
	0,1	II	0,67	0,69	0,73	0,76	0,79
	0,0	I	20,02				
		II	7,49				
5,0	0,9	II	0,04	0,05	0,07	0,04	0,04
	0,8	I	0,83	0,76	0,88	0,85	0,66
		II	0,12	0,13	0,18	0,19	0,15
	0,7	II	0,23	0,25	0,31	0,35	0,33
	0,6	I	2,45	2,24	2,42	2,55	2,53
		II	0,39	0,41	0,49	0,55	0,57
	0,5	II	0,59	0,61	0,71	0,81	0,66
	0,4	I	4,60	4,90	5,06	5,38	5,63
		II	0,84	0,90	0,99	1,12	1,20
	0,3	II	1,27	1,30	1,40	1,53	1,63
	0,2	I	10,47	10,47	10,79	11,31	11,74
		II	1,91	1,95	2,06	2,19	2,30
	0,1	II	3,37	3,46	3,64	3,85	4,00
	0,0	I	49,90				
		II	19,68				

Table 8

$B = n/n_0$

d	$\frac{r}{r_0}$	θ											
		1°	9°	17°	25°	33°	41°	45°	49°	57°	65°	73°	81°	89°
0,02	0,9	0,9989	0,9989	0,9989	0,9988	0,9987	0,9986	0,9986	0,9986	0,9985	0,9984	0,9983	0,9983	0,9983
	0,8	0,9978	0,9977	0,9976	0,9975	0,9974	0,9973	0,9972	0,9971	0,9970	0,9968	0,9967	0,9966	0,9966
	0,7	0,9965	0,9965	0,9964	0,9962	0,9961	0,9959	0,9958	0,9957	0,9955	0,9953	0,9952	0,9951	0,9950
	0,6	0,9952	0,9951	0,9950	0,9949	0,9947	0,9945	0,9944	0,9942	0,9940	0,9938	0,9936	0,9935	0,9935
	0,5	0,9938	0,9937	0,9936	0,9934	0,9932	0,9930	0,9929	0,9928	0,9926	0,9923	0,9922	0,9920	0,9920
	0,4	0,9923	0,9922	0,9921	0,9920	0,9918	0,9916	0,9915	0,9913	0,9911	0,9909	0,9907	0,9906	0,9906
	0,3	0,9907	0,9907	0,9906	0,9904	0,9903	0,9901	0,9900	0,9899	0,9897	0,9895	0,9893	0,9892	0,9892
	0,2	0,9890	0,9890	0,9889	0,9888	0,9887	0,9886	0,9885	0,9884	0,9883	0,9881	0,9880	0,9879	0,9879
	0,1	0,9873	0,9873	0,9873	0,9872	0,9872	0,9871	0,9870	0,9870	0,9869	0,9868	0,9867	0,9867	0,9867
	0,0	0,986												
0,05	0,9	0,9973	0,9973	0,9972	0,9970	0,9968	0,9966	0,9965	0,9964	0,9962	0,9960	0,9959	0,9958	0,9957
	0,8	0,9944	0,9943	0,9941	0,9939	0,9936	0,9932	0,9930	0,9928	0,9925	0,9921	0,9918	0,9917	0,9916
	0,7	0,9913	0,9912	0,9910	0,9906	0,9902	0,9897	0,9895	0,9892	0,9887	0,9883	0,9879	0,9877	0,9876
	0,6	0,9880	0,9879	0,9876	0,9872	0,9867	0,9862	0,9859	0,9856	0,9851	0,9846	0,9842	0,9839	0,9838
	0,5	0,9845	0,9844	0,9841	0,9837	0,9832	0,9826	0,9823	0,9820	0,9815	0,9809	0,9805	0,9802	0,9801
	0,4	0,9808	0,9807	0,9804	0,9800	0,9796	0,9790	0,9787	0,9784	0,9779	0,9774	0,9769	0,9767	0,9766
	0,3	0,9769	0,9768	0,9766	0,9762	0,9758	0,9753	0,9751	0,9748	0,9743	0,9739	0,9735	0,9733	0,9732
	0,2	0,9728	0,9727	0,9726	0,9723	0,9720	0,9716	0,9714	0,9712	0,9709	0,9705	0,9702	0,9700	0,9700
	0,1	0,9685	0,9685	0,9684	0,9682	0,9681	0,9679	0,9677	0,9676	0,9674	0,9672	0,9671	0,9670	0,9669
	0,0	0,965												
0,1	0,9	0,9947	0,9945	0,9943	0,9940	0,9937	0,9933	0,9931	0,9928	0,9924	0,9920	0,9917	0,9915	0,9914
	0,8	0,9887	0,9887	0,9883	0,9878	0,9872	0,9865	0,9861	0,9857	0,9850	0,9843	0,9837	0,9834	0,9832
	0,7	0,9827	0,9825	0,9820	0,9813	0,9805	0,9796	0,9791	0,9786	0,9776	0,9767	0,9760	0,9755	0,9753
	0,6	0,9761	0,9759	0,9754	0,9746	0,9737	0,9728	0,9720	0,9715	0,9704	0,9694	0,9685	0,9680	0,9678
	0,5	0,9692	0,9690	0,9685	0,9677	0,9667	0,9656	0,9650	0,9644	0,9632	0,9622	0,9613	0,9608	0,9603
	0,4	0,9619	0,9617	0,9612	0,9605	0,9595	0,9585	0,9579	0,9573	0,9562	0,9552	0,9544	0,9538	0,9536
	0,3	0,9543	0,9541	0,9537	0,9530	0,9522	0,9513	0,9508	0,9503	0,9493	0,9484	0,9477	0,9472	0,9470
	0,2	0,9463	0,9462	0,9458	0,9454	0,9447	0,9440	0,9437	0,9433	0,9425	0,9419	0,9413	0,9409	0,9408
	0,1	0,9380	0,9379	0,9377	0,9375	0,9375	0,9371	0,9365	0,9363	0,9359	0,9355	0,9352	0,9350	0,9349
	0,0	0,931												

Table 8 (continued)

d	r/r0	θ 1°	9°	17°	25°	33°	41°	45°	49°	57°	65°	73°	81°	89°
0,5	0,9	0,9742	0,9736	0,9725	0,9710	0,9691	0,9670	0,9659	0,9648	0,9626	0,9606	0,9590	0,9579	0,9575
	0,8	0,9467	0,9459	0,9440	0,9414	0,9381	0,9345	0,9326	0,9306	0,9269	0,9235	0,9207	0,9189	0,9181
	0,7	0,9279	0,9169	0,9146	0,9113	0,9071	0,9025	0,9001	0,8976	0,8928	0,8885	0,8850	0,8826	0,8817
	0,6	0,8880	0,8869	0,8844	0,8807	0,8762	0,8710	0,8683	0,8656	0,8603	0,8555	0,8516	0,8490	0,8480
	0,5	0,8570	0,8560	0,8535	0,8499	0,8453	0,8401	0,8374	0,8346	0,8292	0,8244	0,8205	0,8178	0,8168
	0,4	0,8253	0,8243	0,8221	0,8187	0,8145	0,8097	0,8071	0,8046	0,7998	0,7951	0,7914	0,7890	0,7880
	0,3	0,7928	0,7921	0,7902	0,7874	0,7838	0,7798	0,7776	0,7755	0,7712	0,7674	0,7643	0,7623	0,7614
	0,2	0,7599	0,7593	0,7580	0,7560	0,7534	0,7504	0,7488	0,7473	0,7441	0,7413	0,7391	0,7375	0,7369
	0,1	0,7267	0,7264	0,7257	0,7246	0,7232	0,7216	0,7207	0,7199	0,7182	0,7167	0,7155	0,7146	0,7143
	0,0	0,699												
1,0	0,9	0,9504	0,9494	0,9470	0,9438	0,9399	0,9356	0,9333	0,9310	0,9265	0,9223	0,9190	0,9167	0,9158
	0,8	0,8989	0,8972	0,8934	0,8880	0,8815	0,8742	0,8704	0,8665	0,8590	0,8521	0,8466	0,8428	0,8414
	0,7	0,8460	0,8440	0,8395	0,8329	0,8248	0,8158	0,8111	0,8063	0,7970	0,7886	0,7818	0,7773	0,7755
	0,6	0,7923	0,7903	0,7856	0,7786	0,7700	0,7603	0,7552	0,7501	0,7402	0,7312	0,7240	0,7192	0,7172
	0,5	0,7385	0,7366	0,7320	0,7253	0,7170	0,7075	0,7026	0,6976	0,6879	0,6792	0,6722	0,6675	0,6656
	0,4	9,6848	0,6832	0,6792	0,6733	0,6658	0,6574	0,6530	0,6485	0,6398	0,6320	0,6258	0,6216	0,6199
	0,3	0,6318	0,6306	0,6274	0,6227	0,6167	0,6098	0,6062	0,6026	0,5956	0,5892	0,5841	0,5807	0,5794
	0,2	0,5800	0,5791	0,5769	0,5737	0,5695	0,5647	0,5622	0,5597	0,5547	0,5503	0,5467	0,5443	0,5433
	0,1	0,5298	0,5293	0,5283	0,5266	0,5245	0,5221	0,5208	0,5195	0,5170	0,5147	0,5128	0,5116	0,5111
	0,0	0,490												
2,0	0,9	0,9082	0,9059	0,9010	0,8942	0,8861	0,8770	0,8723	0,8674	0,8580	0,8493	0,8423	0,8375	0,8356
	0,8	0,8164	0,8130	0,8054	0,7947	0,7817	0,7673	0,7598	0,7522	0,7375	0,7241	0,7133	0,7060	0,7031
	0,7	0,7263	0,7226	0,7139	0,7016	0,6865	0,6697	0,6610	0,6522	0,6352	0,6199	0,6077	0,5995	0,5962
	0,6	0,6395	0,6359	0,6274	0,6150	0,5998	0,5819	0,5741	0,5653	0,5483	0,5331	0,5210	0,5129	0,5097
	0,5	0,5570	0,5538	0,5462	0,5350	0,5212	0,5058	0,4976	0,4898	0,4743	0,4606	0,4496	0,4423	0,4395
	0,4	0,4796	0,4770	0,4708	0,4616	0,4502	0,4374	0,4307	0,4240	0,4112	0,3997	0,3906	0,3846	0,3822
	0,3	0,4081	0,4062	0,4017	0,3949	0,3864	0,3768	0,3718	0,3668	0,3571	0,3484	0,3415	0,3370	0,3352
	0,2	0,3430	0,3419	0,3390	0,3347	0,3294	0,3232	0,3200	0,3168	0,3105	0,3049	0,3004	0,2974	0,2962
	0,1	0,2850	0,2845	0,2833	0,2814	0,2789	0,2761	0,2746	0,2731	0,2702	0,2676	0,2655	0,2641	0,2635
	0,0	0,243												
5,0	0,967	0,9342	0,9314	0,9259	0,9185	0,9098	0,9000	0,8948	0,8895	0,8790	0,8693	0,8613	0,8558	0,8536
	0,933	0,8702	0,8654	0,8556	0,8425	0,8269	0,8096	0,8005	0,7913	0,7732	0,7565	0,7429	0,7337	0,7300
	0,9	0,8083	0,8020	0,7891	0,7716	0,7509	0,7280	0,7160	0,7040	0,6805	0,6592	0,6418	0,6302	0,6255
	0,8	0,6370	0,6290	0,6114	0,5874	0,5590	0,5281	0,5123	0,4965	0,4664	0,4397	0,4185	0,4045	0,3989
	0,7	0,4893	0,4817	0,4644	0,4404	0,4121	0,3817	0,3663	0,3511	0,3225	0,2977	0,2783	0,2656	0,2607
	0,6	0,3658	0,3595	0,3450	0,3246	0,3004	0,2746	0,2617	0,2490	0,2253	0,2050	0,1894	0,1793	0,1754
	0,5	0,2655	0,2608	0,2499	0,2345	0,2161	0,1964	0,1866	0,1770	0,1592	0,1440	0,1323	0,1249	0,1219
	0,4	0,1863	0,1832	0,1759	0,1654	0,1528	0,1393	0,1326	0,1259	0,1136	0,1031	0,0950	0,0899	0,878
	0,3	0,1258	0,1240	0,1197	0,1135	0,1059	0,0976	0,0935	0,0894	0,0817	0,0751	0,0701	0,0668	0,0655
	0,2	0,0813	0,0805	0,0784	0,0753	0,0715	0,0673	0,0652	0,0630	0,0590	0,0555	0,0527	0,0510	0,0502
	0,1	0,0502	0,0500	0,0493	0,0483	0,0470	0,0455	0,0448	0,0440	0,0425	0,0412	0,0402	0,0395	0,0392
	0,0	0,033												

Remark: When r/r_0 = 1.0, B = 1.0 for all values of θ.

The convergence of the method of grids for the problem under consideration is checked by comparing the values of the solution B^N_{ik} that were found by solving the problem, using grids I and II with the values of the solution for grid III (B^{III}_{ik}) at certain common nodes (i, k) of these grids. /13

Table 7, like Table 2 gives the values $\Delta^N_{ik} = \delta^N_{ik} \cdot 100\%$, where the δ^N_{ik} are determined from formula (28). It can be seen from the table that the sequence of solutions obtained from refining the grid converges to the exact solution of the problem for values of the parameter d in the range 0.02 to 5.0. When d = 0.02, 0.05 and 0.1, the solutions obtained using grids I, II and III almost do not differ from one another, so that Δ^N_{ik} is given in the table only for the coordinate origin. For d = 0.5, the values of Δ^I_{ik} and Δ^{II}_{ik} are given only for nodes common to all three grids (i.e., for ρ = 0.8, 0.6, 0.4, 0.2 and 0.0). For d = 1.0, 2.0, 5.0, Δ^N_{ik} are also given in the table for the common nodes of grids II and III, i.e., when ρ = 0.1 and φ = 0.9, 0.7, 0.5, 0.3 (for d = 5.0). As d increases, the convergence is slower, especially near the coordinate origin.

The values of the modulation depth $B = n/n_0$ are given in Table 8 and shown in Fig. 5 for various values of the parameter d. The absolute value of the error ε_{ik} resulting from the approximation of the differential equation by a system of difference equations is estimated using the Runge method. Table 9 gives the values of the absolute error in the final results to six significant digits, which were calculated using formula (35) at certain common nodes of grids II and III, with the given coordinates ρ and θ. It can be seen from the table that the error increases as the distance from the boundary increases and as the parameter d increases.

The total absolute error in the results ζ_{ik} in the solution of the problem given in Table 9 will be estimated by taking into account the errors in the interative method used to solve the systems of difference equations σ_{ik}. The error in the iterative method must not differ much from the analogous error (29) discussed in Section 2.4. Therefore, from the standpoint of the solution method, equations (19) and (46) do not differ, and the error depends mainly on the number of difference equations that must be solved and on μ (36) whose value was also here 10^{-7}. For d = 0.02, 0.05, 0.1 all values given in Table 9 are correct (for $0.1 \leq \rho \leq 0.9$ up to four significant digits and for ρ = 0, up to three significant digits). /13

Table 9. VALUES OF THE MODULI OF THE ABSOLUTE ERRORS IN THE FINAL RESULTS ε_{ik} ACCORDING TO FORMULA (35)

d	ρ	θ 9°	27°	45°	63°	81°
0,02	0,8	0	0	0	0	0
	0,6	1	1	1	1	1
	0,4	2	2	2	2	3
	0,2	4	4	5	5	5
	0,1	8	8	8	8	8
	0,0	68				
0,05	0,8	0	0	0	0	0
	0,6	0	0	0	1	1
	0,4	0	1	1	2	2
	0,2	3	3	3	4	4
	0,1	6	6	7	7	7
	0,0	192				
0,1	0,8	1	0	0	0	0
	0,6	1	1	0	1	1
	0,4	1	1	0	1	2
	0,2	1	1	2	3	3
	0,1	4	4	4	5	5
	0,0	387				
0,5	0,8	6	4	4	3	3
	0,6	13	10	8	7	10
	0,4	19	16	14	12	10
	0,2	27	26	24	22	20
	0,1	39	39	40	40	39
	0,0	1530				

d	ρ	θ 9°	27°	45°	63°	81°
1,0	0,9	6	5	6	8	9
	0,8	14	12	14	16	17
	0,7	22	19	21	23	23
	0,6	31	27	28	29	29
	0,5	39	36	36	36	35
	0,4	48	45	44	43	42
	0,3	59	56	55	54	52
	0,2	75	74	73	72	70
	0,1	115	117	120	123	125
	0,0	2201				
2,0	0,9	16	17	25	34	41
	0,8	36	36	47	60	68
	0,7	56	55	67	80	87
	0,6	64	75	85	95	101
	0,5	96	94	101	108	111
	0,4	116	114	117	120	121
	0,3	137	135	136	136	135
	0,2	166	165	165	165	165
	0,1	239	242	249	255	259
	0,0	2276				
5,0	0,9	44	53	66	58	45
	0,8	96	100	114	103	89
	0,7	141	136	143	131	111
	0,6	174	163	159	144	128
	0,5	193	176	165	149	143
	0,4	199	183	166	148	135
	0,3	197	182	164	147	136
	0,2	192	182	167	154	146
	0,1	201	208	203	200	197
	0,0	813				

For d = 0.5, 1.0, 2.0, 5.0, the data are as follows:

$d = 0{,}5$
$0{,}1 \leqslant \rho < 0{,}9$ — All values are correct
$\rho = 0$
$d = 1{,}0$
$0{,}2 \leqslant \rho < 0{,}9$ — Corr. to 4 signif. digits
$\rho = 0{,}1$ — $|\xi_{0}| < 0{,}0002$
$\rho = 0$ — $|\xi_{ik}| < 0{,}003$

$d = 2{,}0$
$0{,}7 \leqslant \rho \leqslant 0{,}9$ — Correct to 4 signif. digits
$0{,}2 \leqslant \rho \leqslant 0{,}6$ — $|\xi_{ik}| < 0{,}0002$
$\rho = 0{,}1$ — $|\xi_{ik}| < 0{,}0003$
$\rho = 0$ — $|\xi_{0}| < 0{,}003$
$d = 5{,}0$
$\Sigma\rho = 0{,}9$ — $|\xi_{ik}| < 0{,}0001$
$0{,}5 \leqslant \rho \leqslant 0{,}8$ — $|\xi_{ik}| < 0{,}0002$
$0{,}1 \leqslant \rho \leqslant 0{,}4$ — $|\xi_{ik}| < 0{,}0003$
$\rho = 0$ — $|\xi_{0}| < 0{,}001$

3.3. Evaluation of Results

Figure 6 gives the modulation depth $B = n/n_0$ vs. $\rho = r/r_0$ for various values of the angle θ in the interval 1 to 89° for the following values of the parameter $d = 2/3 \cdot r_0 u_0/\varkappa_0$: 0.05, 0.1, 0.5, 1.0, 2.0, 5.0. The modulation depth vs. the distance which was calculated from formula (43) in the spherical symmetric case is given for a comparison. It can be seen that when retardation by the antiphermium mechanism is not taken into account, the proposed relation between the characteristics of the solar wind and the angle with the helioequator plane also does not have a considerable effect on the modulation of galactic cosmic rays when the parameter d varies in the range 0.02 to 5.0.

The maximum difference in the density in the directions $\theta = 189°$ is as follows:

d	ρ	%
5.0	0.8	23.8
2.0	0.7	14.0
1.0	0.6	7.5
0.1	0.5	0.8
0.05	0.467	0.2

The density of the particles is considerably smaller than in the case when the retarding mechanism is taken into account. Comparing the corresponding spherical symmetric models (see Figs. 3, 4 and 6) we see that the density of the particles in all these cases differs approximately by the same amount.

REFERENCES

1. Dorman, L. I. in the collection Kosmicheskie luchi, No. 8, 305 (1967).

2. Dorman, L. I., Trudy Mezhdunar konf po kosmicheskim lucham, [Proceedings of the International Conference on Cosmic Rays], Vol. 4, USSR Acad. of Sci. Publs., 1960, p. 328.

3. Dorman, L. I., Izv Akad Nauk SSSR, Ser. Fiz, 8 (1968).

4. Parker, E., Dinamicheskie protsessy v mezhplanetnoy srede, [Dynamical Processes in the Interplanetary Medium], Foreign Lit. Publs., 1965.

5. van Biesbroeck, C., The Sun, G. P. Kuiper, Univ. of Chicago Press, Chicago, 1953, p. 601.

6. Yushkov, P. P., Trudy Leningr tekhn in-ta kholodil'n prom , 14, 315-323 (1956).

7. Berezin, I. S., and Zhidkov, N. I., Metody vychisleniy, [Numerical Methods], Fizmatgiz, 1962.

8. Collatz, L., Chislennye metody resheniya differentsial'nykh uraveniy, [Numerical Methods for the Solution of Differential Equations], Foreign Lit. Publs., 1953.

9. Fazov, V. and Forsythe, G., Raznostnye methody resheniya differentsial'nikh uravneniy v chastnykh proizvodnykh, [Difference Methods for the Solution of Partial Differential Equations], Foreign Lit. Publs., 1963.

N75 16468

IV. MEASUREMENTS FROM SATELLITES AND ROCKETS

A STUDY OF COSMIC RAYS ON THE ARTIFICIAL MOON SATELLITES "LUNA-11" AND "LUNA-12"

N. L. Grigorov, V. G. Kurt, V. N. Lutsenko
V. L. Maduyev, N. F. Pisarenko, I. A. Savenko

ABSTRACT

In the period from the end of August 1966 to January 1967 the primary cosmic radiation fluxes beyond the terrestrial magnetosphere were measured by means of the equipment mounted on the satellites "Luna-11" and "Luna-12." The altitude dependence of cosmic rays near the lunar surface as well as the intensity of protons and electrons of solar origin in the moon's vicinity were determined. The paper considers the general variation time of the intensity of protons with $Ep \geq 50$ MeV and $Ep > 1.8$ MeV throughout the period from August 28, to October 1, 1966, and from October 25, 1966, to January 5, 1967. The solar flares (August 28 and September 2) were followed by sharp increases of proton fluxes.

The correlation of proton intensity with the parameters characterizing the solar and geomagnetic activities and the specific features of the angular distribution of the proton flux as revealed during measurements are given. Data on electron fluxes studied on September 1 and 8, 1966, when short-term increases in the electron intensity were observed are given.

Experiments which studied the corpuscular radiation in the space near the moon that started on the satellite "Luna-10" [1 - 3] were continued on the satellites "Luna-11" and "Luna-12."

The equipment, which was mounted in the artificial satellite "Luna-11," consisted of a gas-discharge and scintillating counter. The SVG-9 gas discharge counters were protected by a brass screen which was 2 $g \cdot cm^{-2}$ thick from all sides except at the window. The diameter of the mica window was 5 mm and it was 1.2 $mg \cdot cm^{-2}$ thick. To protect the window from soft solar ultraviolet radiation, a gold layer that was 0.3 $mg \cdot cm^{-2}$ thick was sprayed over the window. In front of the mica window was a collimator with an angle of taper of 60°. Outside the conical collimator the ferrite plates of a magnetic filter were inserted in all counters but they were magnetized only in one counter (No. 2). The magnetic field in

counter No. 2 had such magnitude that electrons with energy less than 100 keV were almost completely deflected, and when the energy of the electrons was 1 MeV and above, the recording effectiveness was close to 1. In addition to electrons, counter No. 2 (with the magnetized ferrite) recorded through the mica window protons with energy greater than 0.5 MeV while counter No. 1 recorded electrons with energy $E_e > 30$ keV and protons with energy $E_p > 0.5$ MeV. Thus, the difference in the intensities measured by counters No. 1 and No. 2 was caused by electrons with energy greater than 30 keV. Counter No. 3 was the same as counter No. 1, the only difference being that it was mounted in a different direction. When the Sun was in the field of view of the SBT-9 counters, they could record the x-ray radiation from the Sun. The geometrical factor of counters No. 1 2 and 3 for the particles recorded through the mica window was 0.15 $cm^2 \cdot$steradian.

The equipment also included a gas-discharge counter, No. 4 of the STS-5 type, which was screened on all sides by an aluminum plate that was 3 $g \cdot cm^{-2}$ thick. The scintillation counter consisted of an FEU-16 photomultiplier with a CsJ (Tl) crystal that was 1 mm thick, whose diameter was 12 mm with a conical collimator with angle of taper 60° that was 10 mm high and had a 10 mm diameter in the part next to the crystal. The CsJ (Tl) crystal was covered by a 2.7 $mg \cdot cm^{-2}$ thick aluminum foil. The axis of counter No. 3 made a 90° angle with the direction of the axes of counters Nos. 1 and 2. The axes of the collimators of counters Nos. 1 and 2 were parallel to the axes of the scintillation counter. /136

At the output of the FEU were integral discriminators through which pulses passed to the counters corresponding to an energy release in the crystal of $E_1 > 30$ keV, $E_2 > 300$ keV and $E_3 > 1.5$ MeV. Taking into account the absorption in the foil and in the insensitive surface layer of the CsJ (Tl) crystal, electrons with energy $E_e > 60$ keV and protons with energy $E_p > 0.9$ MeV could be recorded by the first threshold, $E_e > 300$ keV and $E_p > 1.0$ MeV, respectively, by the second threshold, and protons with energy 100 MeV $> E_p > 1.8$ MeV by the third threshold. The geometrical factor of the scintillation counter for the particles that entered it through the collimator was 1.3 $cm^2 \cdot$steradian, and for the penetrating isotropic flux of particles, it was 0.66 cm^2.

The counting rate of the sensors was recorded by logarithmic ratemeters with a reading accuracy of $\sim 20\%$ and a time constant equal to 8 sec. The characteristics of the sensors are

given in Table 1. The ratemeters were interrogated once every 6.75 sec in communication sessions with frequency 1. The duration of the communication sessions fluctuated from 2 to 40 minutes. The "Luna-11" satellite was launched in the Earth's orbit on the 28th of August 1966. The orbital pericynthion was 130 km, the apocynthion was 1230 km, and the inclination of the orbit to the plane of the Moon's equator was $\sim 10^{\circ}$.

Table 1. CHARACTERISTICS OF THE SENSORS

Sensor	Protection $g \cdot cm^{-2}$	Window $mg \cdot cm^{-2}$	Geometric factor $cm^2 \cdot ster$	Energy threshold, keV	Recommended particles and threshold energies	Orientation of counters relative to axis of rotation	Magnetic filter
SBT-9 (Counter No1)	2	1,5	0,15	—	$E_p > 0,5$ Mev $E_e > 30$ keV	90°	not magnetized
SBT-9 (Counter No2)	2	1,5	0,15	—	$E_p > 0,5$ MeV $E_e > 300$ keV	90°	magnetized
SBT-9 (Counter No3)	2	1,5	0,15	—	$E_p > 0,5$ MeV $E_e > 30$ keV	0°	not magnetized
Scintillating (SI(T2)) counter	3	2,7	1,3	I—30	$E_p > 0,9$ MeV $E_e > 60$ keV	90°	—
	3	2,7	1,3	II—300	$E_p > 1,0$ MeV $E_e > 300$ keV	90°	—
	3	2,7	1,3	III—1500	$E_p - 100$ MeV $> E_e > 1,8$ keV	90°	—
STS-5	3	—	4,5*		$E_p > 50$ MeV $E_e > 5$ keV	Global	—

*The effective area for the isotropic flux is given in cm^2.

During the entire measurement period (from August 28 to October 1, 1966) the "Luna-11" satellite rotated about its own axis with a period T = 122 sec and the direction of the axis of rotation was close to the direction of the axis of counter No. 3. The axes of counters Nos. 1, 2 and of the scintillation counter were perpendicular to the axis of rotation, which made it possible to measure the angular distribution of the radiation fluxes. From the analysis of the data about corpuscular radiation,

x-ray radiation and the readings of the light sensor mounted aboard, it followed that the angle between the axis of rotation and the direction to the Sun was close to 90°.

The same equipment was mounted on the "Luna-12" satellite which operated from October 25, 1966, to January 5, 1967. The main orbital parameters of "Luna-12" were as follows: the inclination of the orbital plane to the Moon's equator was 17°, the apocynthion was 1740 km, and the pericynthion was 95 km. The rotation period of the satellite was T = 255 sec. /137

Study of Primary Cosmic Rays

As already mentioned in [1], the mean intensity of primary radiation on the "Luna-10" satellite in April 1966 was 4.7 ± 0.4 $cm^{-2} \cdot sec^{-1}$. The results of analogous measurements that were made on the satellite "Luna-11" and "Luna-12" are given in Table 2.

Table 2. RESULTS OF MEASUREMENTS MADE ON SATELLITES IN 1966

Satellite	Period when measurements were made	Type of counter	Geometrical factor cm^2	Flux $cm^{-2} \cdot sec^{-1}$
"Luna-10"	April	SBT-9	2.6	4.7±0.4
"Luna-11"	September	STS-5	4.3	3.7±0.4
"Luna-12"	October-November	STS-5; CBT-9 SBT-9M	4.5; 2.4; 2.8	4.0±0.4

The table shows a drop in the primary cosmic radiation flux as the solar activity increases in comparison with the value 5.35 $cm^{-2} \cdot sec^{-1}$ obtained on the "Luna-9" in February 1966. The smallest value of the flux, 3.7 $cm^{-2} \cdot sec^{-1}$, was obtained in September 1966, which was due to a large number of solar flares and the concommitant Forbush drops (Fig. 1). Figure 2 shows the time curve for the intensity of the cosmic rays in October-November 1966. This period is characterized by relatively low solar activity. The data about the primary radiation flux during this entire period show approximately the same level of intensity. The slight drop in the intensity toward the end of October 1966 is due to the Forbush drop that was recorded at that time. The same value of the intensity $\left(4 \frac{part \cdot cm^{-2} \cdot sec^{-1}}{cm^2 \cdot sec}\right)$

was obtained on the "Cosmos-159" artificial satellite in June 1967 at a distance of 30-50 thousand km from Earth. It should be mentioned that the results given here obtained on the basis of data from moon satellites were obtained in those cases when the satellites were outside the Earth's magnetosphere.

The measurements given for various distances from the lunar surface made it possible to obtain the altitude curve for the cosmic ray intensity. If only primary radiation occurs near the Moon, the altitudinal dependence of the counting rate I(h) of the counter recording the global cosmic ray flux results from the fact that the moon screens part of the space. If $\Omega(h)$ is the solid angle at which the moon is visible from a point at a distance h from the surface, n_0 is the cosmic ray intensity per unit in the solid angle, and S is the area of the counter,

$$I(h) = n_0 S 4\pi - n_0 S\Omega(h) = n_0 S 4\pi \left[1 - \frac{\Omega(h)}{4\pi}\right],$$

/139

where $n_0 S 4\pi$ is the counting rate of the counter in interplanetary space ($h \to \infty$). Further

$$\frac{I(h)}{I(\infty)} = 1 - \frac{\Omega(h)}{4\pi}; \quad \Omega(h) = 2\pi\left[1 - \frac{\sqrt{1 + 2R_M/h}}{1 + R_M/h}\right]$$

where R_M is the radius of the moon. If we assume that the lunar surface is a source of isotropic albedo radiation of intensity αn_0 the intensity of this radiation at the altitude h will be proportional to the solid angle $\Omega(h)$ under which the instrument sees the moon. Then $\frac{I(h)}{I(\infty)} = 1 - (1 - \alpha)\frac{\Omega(h)}{4\pi}$.

Measurements made on the "Luna-10" showed the presence of albedo radiation ($\alpha \sim 12\%$) in the altitude range 400-900 km. On the "Luna-11" and "Luna-12" satellites, this range was extended to 100-1700 km. The results of the measurements were broken up into groups corresponding to altitude ranges of Δh = 100 km. The mean intensity I(h) was determined in each group. Figure 3 gives the altitudinal dependence of the quantity $I(h)/I(\infty)$ averaged over the measurements made on all three moon satellites. For "Luna-10" the radiation intensity

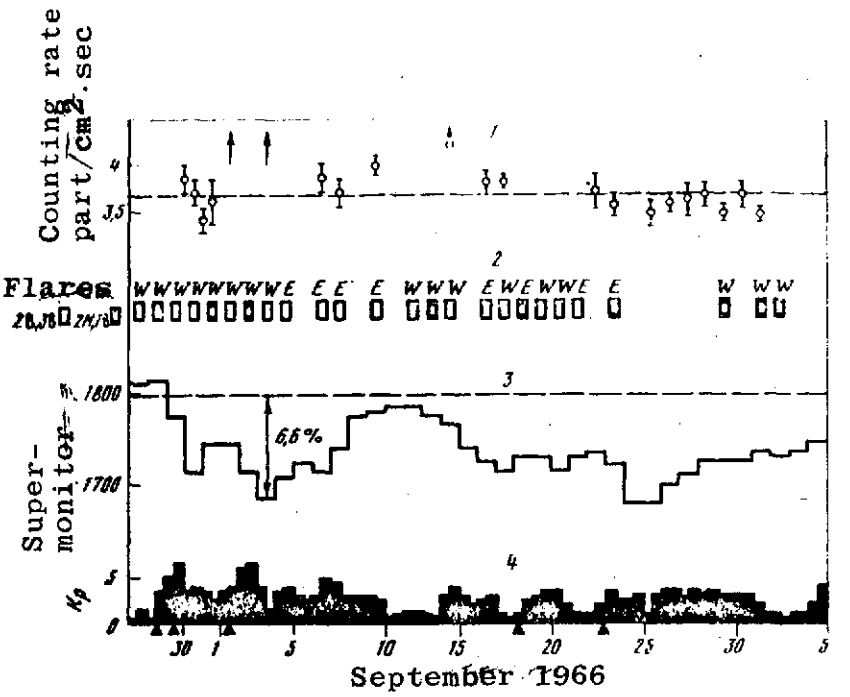

Fig. 1. Readings of the STS-5 counter (1), (2) readings of the neutron supermonitor (Moskva), (3) and the K_p-index in September 1966 (4).

Triangles indicate the beginning of sudden auroral storms, and the arrows instants at which the counting rate increases sharply.

in free space $I(\infty)$ was measured directly. Since reliable measurements of $I(\infty)$ were not available on "Luna -11" and "Luna-12," this quantity was calculated from measurements made at the altitudes 900-1000 km on the assumption that the ratio of the intensity to the intensity in open space at these altitudes is the same as for the "Luna-10."

The curves give the calculated value of $I(h)/I(\infty)$ for the albedo equal to 0 and 25%. It can be seen that at low altitudes the albedo increases approximately up to 25%. We note that measurements on "Luna-9" on the surface of the Moon gave a value $\alpha = 26\%$ [4]. Possibly, the reason why the albedo decreases as the altitude increases is the small magnetic field of the Moon [5] and the deflected soft albedo radiation.

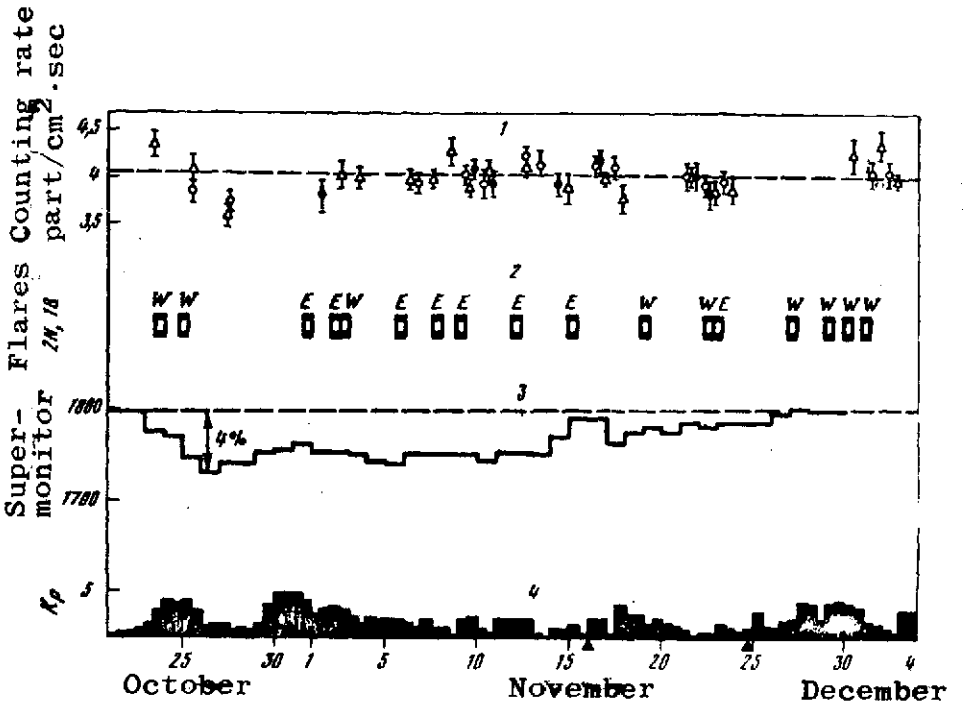

Fig. 2. Readings of gas-discharge counters (1) (dark circle STS-5, triangle SBT, light circle SBTM), solar flares (2), readings of the neutron supermonitor (Moskva) (3) and the K_p-index in October-December 1966 (4)

Remaining notation the same as in Fig. 1.

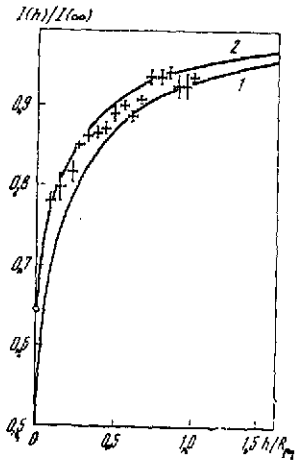

Fig. 3. Altitudinal curves for the cosmic radiation around the Moon according to the data from the "Luna-10," "Luna-11," and "Luna-12" satellite data.

The distance from the lunar surface is plotted on R_L on the abscissa, and the ratio of the intensity at the given altitude to the intensity at infinity is plotted on the ordinate.

1--α = 0, 2--α = 0.25.

Recording of the Proton Component of Solar Cosmic Rays

Measurements of the corpuscular radiation beyond the Earth's magnetosphere make it possible to obtain the most complete information about solar cosmic rays. Such measurements were made on the artificial moon satellites "Luna-11" and "Luna-12" in the period between August 24, 1966, and January 5, 1967.

The greatest amount of information was obtained for the intensity of protons in two energy intervals: 1.8 - 100 MeV (scintillation counter, $E_{III} > 1500$ keV) and $E > 50$ MeV (the STS-5 counter). We note that for solar protons with a sharply dropping spectrum, these intervals correspond, for all practical purposes, to two points in the entire spectrum: $E_p > 1.8$ MeV and $E_p > 50$ MeV. For galactic cosmic rays the intensity of the protons is small in the interval 1.8 - 100 MeV.

Figure 4 gives the change in the proton intensity over time with $E_p > 50$ MeV and $E_p > 1.8$ MeV (mean value for each period). The first group includes galactic cosmic rays whose intensity was, according to our measurements. approximately 4 $cm^{-2} \cdot sec^{-1}$. It can be seen from Fig. 4 that in most periods, the intensity of protons with $E_p > 50$ MeV corresponds to the galactic background. Two substantial increases in the intensity were only recorded on August 28 and September 2. In the last case, the intensity exceeded the background value by 2 orders of magnitude. With regard to the intensity of protons with $E_p > 1.8$ MeV, it fluctuated considerably and was beyond the range of the instrument. The maximum values were observed with a lag of several hours to 1.5 days in comparison with the maxima of protons with $E > 50$ MeV.

The figure below gives the graph for the motion of the active regions on the visible disk of the Sun (longitude as a function of time) and the coordinates of the most powerful flares. The latitudes of the active regions did not change, for all practical purposes, during two successive revolutions of the Sun. During the measurements, two intervals with high solar activity were observed on "Luna-11": from August 27 to September 4, and from September 17 to September 21. This intensification in the activity is due to the passage of three active regions with latitude 7, 22 and 23°N of long duration /141
over the disk of the Sun. More than 90% of all recorded flares of Class 1B, 2B and 3B occurred in these regions, and the most active region was the region with 23°N.

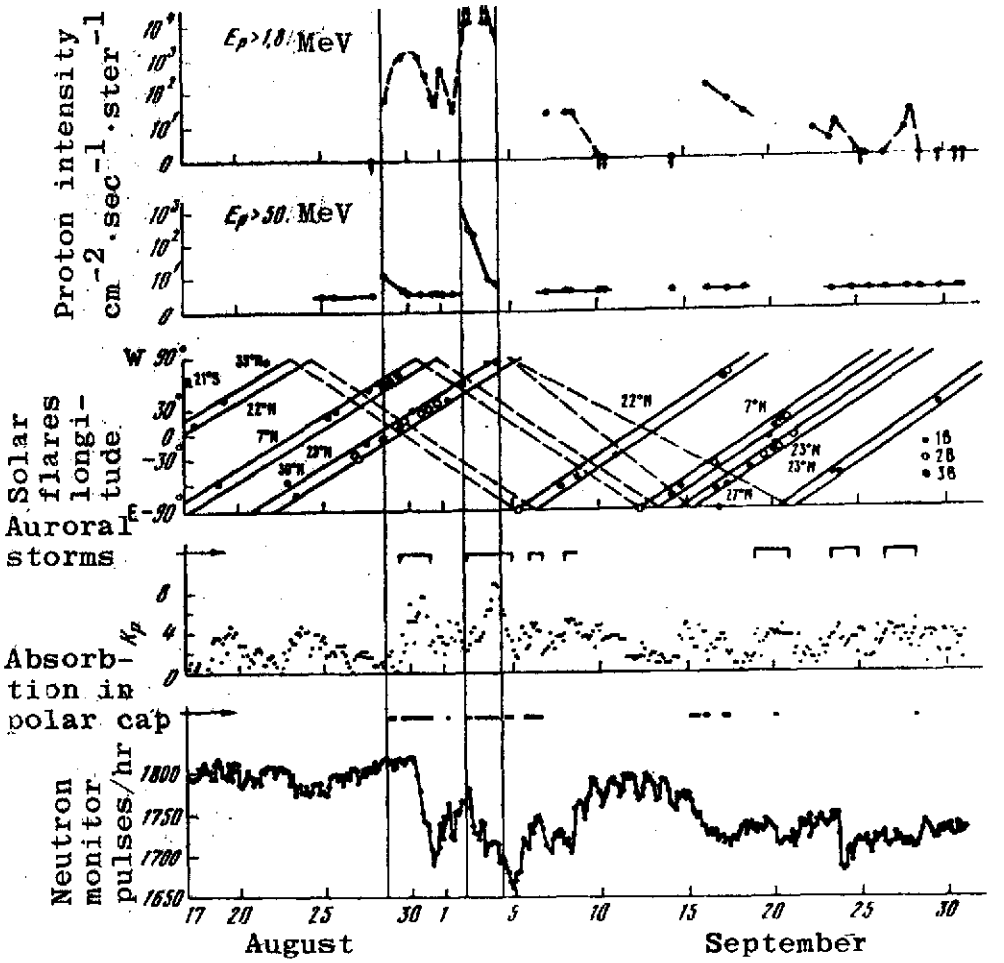

Fig. 4. Proton intensity, solar and geophysical data during the operation of the "Luna-11" artificial satellite.

Figure 4 shows that the increases in the intensity of protons with $E_p > 50$ MeV on the 28th of August and the 2nd of September followed flares of Class 3B in the active region 23°N. We note that the measurements on the 28th of August were carried out 3 hours after the optical flare began, whereas on the 2nd of September only after 14 hours. Nevertheless, in the second case, the intensity of the protons was higher by one order of magnitude. The considerably greater effect from the second flare can be explained by the fact that the location of the flare on the second of September at 60°W was more favorable for the arrival of protons in the vicinity of the Earth-Moon system.

The values of the K_p-index, the readings of the neutron monitor (Moskva, the three-hour means) and the auroral storms and the absorption of radio waves in the polar cap are given in the bottom part of the diagram. It can be seen that the flares which occurred on the 28th of August, and especially on the 2nd of September, were accompanied by powerful geomagnetic disturbances and Forbush-drops which are highly correlated with the changes in the intensity of the protons in the vicinity of the Moon. The third equally powerful flare in the active region 23°N under consideration occurred on the limb on the 4th of September. The nearest communication session after this flare was only the 7th of September; however, a comparison of our measurements with the geophysical data allows us to conclude that the effect of the protons from this flare was considerably smaller than that of the flare which occurred on the 2nd of September. In the same way as for the flare that occurred on the 28th of August, this fact agrees with the concepts about the interplanetary magnetic field, whose lines of force are bent along a spiral of Archimedes.

The intensity of protons with $E_p > 400$ MeV was measured on the artificial earth satellite "Proton-3" simultaneously with the measurements made on "Luna-11." During the period following the flares on August 28 and September 2, no increase in the intensity above the cosmic background was detected (within a 10% range from the background). When these data are combined with the results obtained on "Luna-11," it is possible to estimate the character of the spectrum of the solar protons at the measurement instant. If we adopt for the complete spectrum of the protons the law $N(E) \sim E^{-\gamma}$ we obtain for γ the values 1 and 1.7 for August 28 and September 2, respectively.

The intensity of protons with $E_p > 50$ MeV from the flare which occurred on the 2nd of September varied according to $N(t) \sim t^{-3,4}$ (time was measured from the beginning of the optical flare). The estimate of the complete proton flux based

on this dependence on t and various assumptions about the instants for the maximum of the flux (from 2 to 6 hours after the optical flare began) varies from 10^8 to 10^9 cm^{-2}, which corresponds to an absorption of protons with $E_p > 50$ MeV from 10 to 100 rad. According to the data in article [6], the event which occurred on the 2nd of September was the most powerful event since July 18, 1961. The maximum intensity of protons with $E_p > 1.8$ MeV $N(E_p > 1.8 \text{ MeV}) \geq 10^4 cm^{-2} \cdot sec^{-1} \cdot ster^{-1}$ does not contradict the value $N(E_p > 2 \text{ MeV}) = 7.5 \cdot 10^4 cm^{-2} \cdot sec^{-1}$, obtained during simultaneous measurements on the 1963-38C satellite (partial report in [6]). According to the data in article [6], the drop in the proton flux with $E_p > 5$ MeV continued until the 9th of September.

When the active regions passed the visible disk of the Sun for the second time, the greatest flare activity was recorded in the period between September 17 to September 21. At that time, the most powerful flares (3B) were observed in the active regions 22 and 0.7°N. Although with regard to power and location these flares were close to the flares that occurred on the 28th of August and 2nd of September, their proton effectiveness was considerably smaller. After the 4th of September we observed an increase in intensity only for protons with $E_p > 1.8$ MeV.[2] The intensity of protons with $E_p > 50$ MeV /142
in all communication periods was close to the galactic background. The readings of the neutron monitor and the geomagnetic data also indicate the smaller effectiveness of the flares that occurred between September 17 - 21.

In several measurement periods it was possible to determine the angular distribution of the flux in the plane perpendicular to the axis of rotation. We note that the axis of rotation of "Luna-11" was close to the orbital plane and made an $\sim 80°$ angle with the direction to the Sun. In the period on August 31 when the moon was not in the field of view of the sensors, radiation was recorded, which was isotropic within the limits of the measurement accuracy.

The periodically recurring "off-scale readings" in the SBT-9 and SBT-9M counters were due to the recording of solar x-ray radiation. The galactic cosmic ray background was 10 pulses/sec for the SBT-9 and SBT-9M counters and the first two thresholds of the scintillation counter. For the third

2. It should be mentioned that a part of these increases may be due to the presence of recurrent fluxes with a period of 27 days [7].

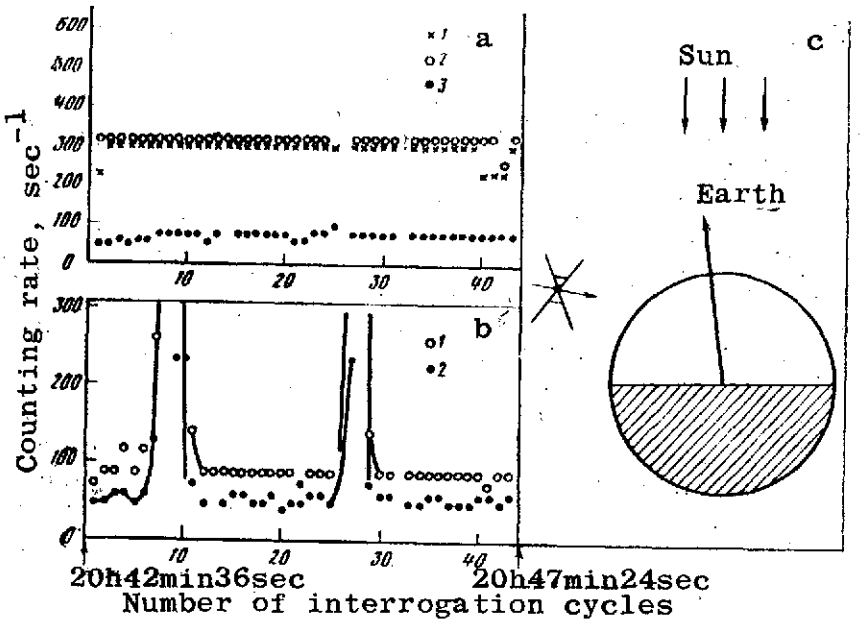

Fig. 5. Example of the recording of anisotropic proton flux on August 31, 1966.

a--CsI sensor; 1--E_1 > 30 keV; 2--E_2 > 300 keV; 3--E_3 > 0.5 MeV; b--sensors: 1--SBT-9, 2--SBT-9M, 3--position of satellite on orbit.

Arrow indicates the direction of the satellite's axis of rotation. The cones of rotation correspond to the position of the scintillation counter and the SBT-9 (No. 1) and SBT-9M (No. 2) counters.

threshold (E_{III} > 1500 keV) the background did not exceed 1 pulse/sec. Figure 5 also shows the location of the satellite at the instant when the measurements were made and the projection of its axis of rotation on the orbital plane.

The period of the operation of the "Luna-12" artificial moon satellite is characterized by smaller flare activity. The intensity of protons with E_p > 50 MeV corresponded to the cosmic background in all periods, and only in two measurement periods on the 13th and 16th of December 1966, proton fluxes with E_p > 1.8 MeV were recorded (Fig. 6). These fluxes may be due to the flares of Class 2B which occurred on the 9th and 10th of December on the eastern part of the solar disk.

During the period on the 13th of December, a rapid increase in the intensity of the protons by a factor of three was observed at 13 h 51 min, Moscow time, (the two points in Fig. 6) which coincided with the beginning of the Forbush drop on Earth. The increase was observed for a period of 9 min, after which the flux decreased.

The period on December 13 gives an example of anisotropy of a flux which is not related to the screening of the field of view of the detectors by the Moon. Figure 7 gives a small part of this period until the flux begins to increase. The right side shows the location of the satellite at the instant when the measurements were made and the projection of its axis of rotation on the orbital plane. The Moon and the Sun are not in the field of view of the sensors. The arrows indicate the instant when the axes of the detectors make the smallest angle with the direction to the Sun. The counting rate of the SBT-9 counter directed along the axis of rotation in the direction opposite to the moon remained constant and was 30 pulses/sec. The galactic background for all SBT-9 counters was ~ 10 pulses/sec, for the first scintillation counter threshold, the background was ~ 3 pulses/sec and for the second and third thresholds the background was ~ 1 pulse/sec. Anisotropy of the flux was observed during the entire measurement period which lasted 66 minutes.

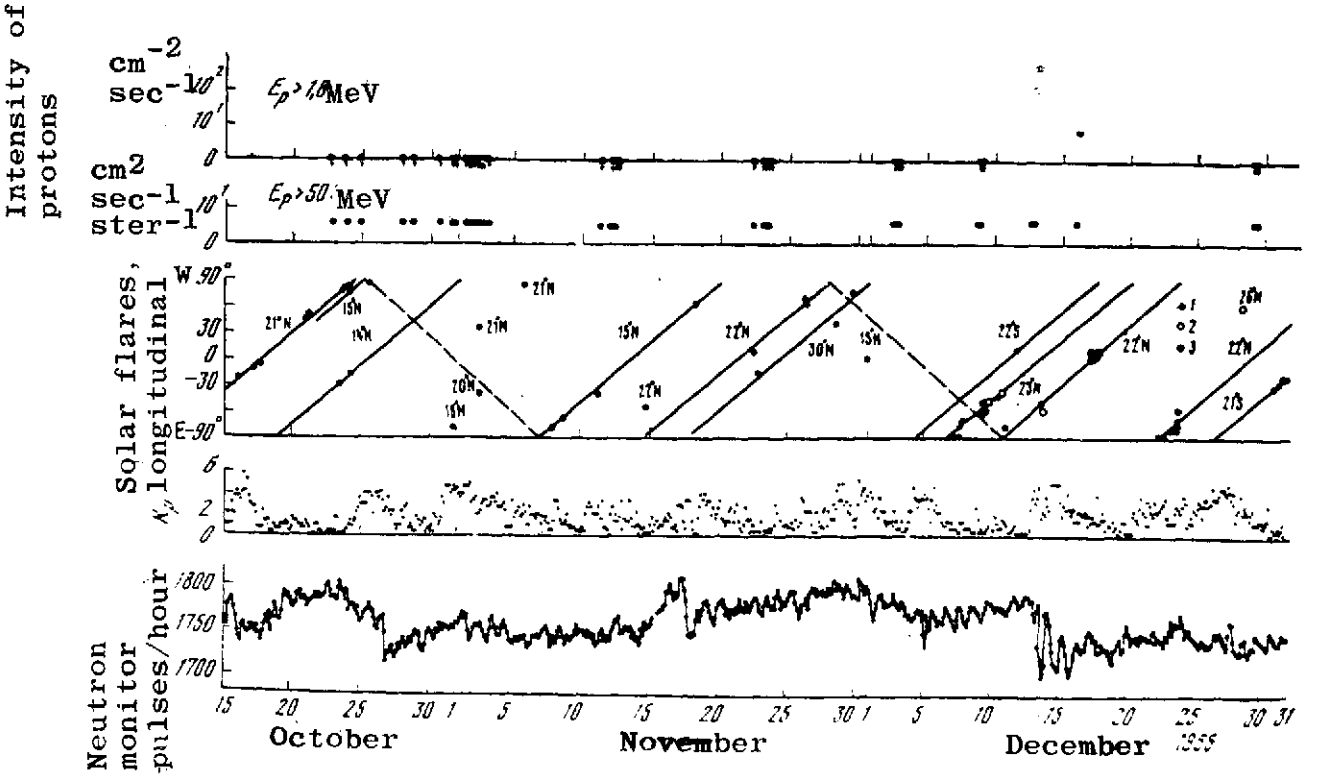

Fig. 6. Intensity of protons, solar and geophysical data in the operational period of the "Luna-12" artificial moon satellite.

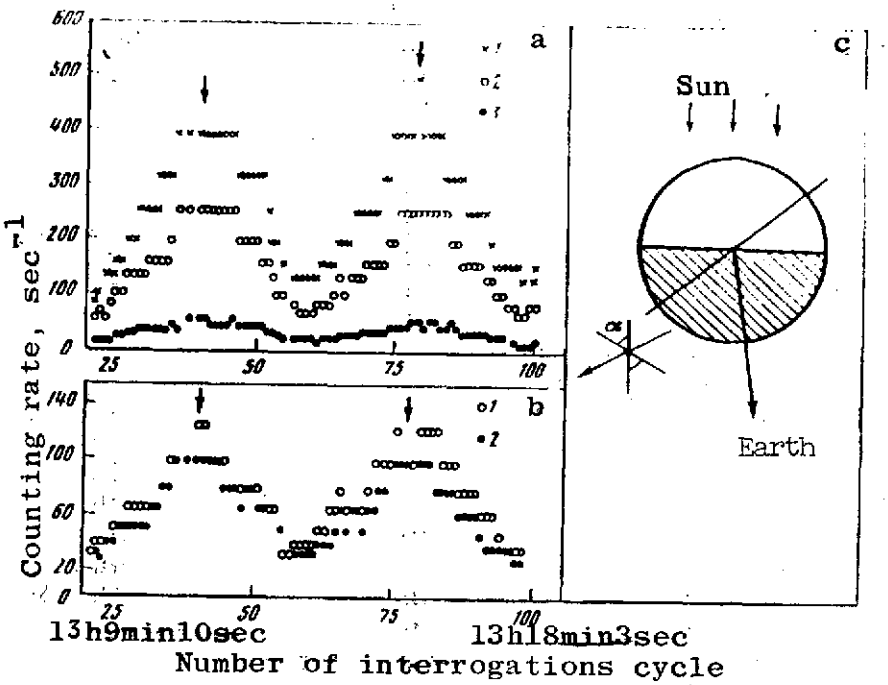

Fig. 7. Examples of a recording of an anisotropic flux of protons on December 13, 1966.

a--CsI counter: 1- $E_1 > 30$ keV, 2--$E_2 > 300$ keV, 3--$E_3 > 1.5$ MeV, b--counters: 1--SBT-9 and 2--SBT-9M; c--position of "Luna-12" satellite in the session. The arrow indicates the axis of rotation of the satellite, and the cones α corresponds to the instant marked in the left part of the figure by vertical arrows. The scintillation counter and the SBT-9 (No. 1) and SBT-9M (No. 2) counters rotate in the orbital plane of the satellite.

Investigation of the Electron Component of Solar Cosmic Rays on the "Luna-11" Artificial Moon Satellite

At the time when the artificial moon satellite "Luna-11" was launched (August 1966), there were only two known studies [8, 9] which reported the detection of electrons of solar origin with an energy of tens and hundreds of kiloelectron volts. Many aspects of this pehnomena are still not known adequately. Therefore, the task of the experiment was to identify reliably electrons of such energies on the background of the wide spectrum of protons and to study their propagation

in interplanetary space. The period between August 28 to October 1, 1966, was characterized by increased solar activity. The series of powerful flares that started on August 28 was accompanied by intense proton and electron fluxes in the space around the Moon [10].

One example of the recording of electrons with an energy $E_e > 30$ keV in the space near the Moon, is given in Fig. 8. This diagram shows the results of the measurements made on September 8, 1966, between 13 h 10 min 59 sec to 13 h 30 min 7 sec (Moscow time). The measurement instant and the ordinal number of the corresponding measurement are plotted on the abscissa, and the counting rate of the counters is plotted on the ordinate. During the entire 20-min measurement cycle, the counting rate of the scintillation counter by the first and second thresholds and the counting rates of counters Nos. 1 and 2 varied periodically and in phase, while the measurement periods coincided with the rotation period of the "Luna-11" satellite about its own axis. Figure 8 shows clearly that the radiation recorded by the SBT-9 (No. 1) counter and the first threshold of the scintillation counter consists mainly of electrons with an energy from 30 to 300 keV. The modulation may be caused both by the anisotropy of the radiation recorded as well as by the partial superposition of the solid angle of the counters by the Moon. /14

It can be seen from Fig. 8 that at the maximum of the recorded intensity, the electron flux with $E_e > 30$ keV was on the order of $N \approx 800$ $cm^{-2} \cdot sec^{-1} \cdot ster^{-1}$ and the electron flux with energies $E_e > 60$ keV was on the order of $N \approx 300$ $cm^{-2} \cdot sec^{-1} \cdot ster^{-1}$, i.e., the complete spectrum of the electrons was characterized by the exponent $\gamma \approx 1.5$. In this period, as in preceding measurement periods, in addition to large electron fluxes, there were proton fluxes with an energy of $E_p > 1.0$ MeV in space that were recorded by the second and third threshold of the scintillation counter and counters Nos. 1 and 2. These proton fluxes were on the order of 10^{-2} $10^{-2} cm^{-2} \cdot sec^{-1} \cdot ster^{-1}$.

An interesting case of a short-range increase in the electron flux in the September 1, 1966, period is given in Figs. 9 and 10. In that period, from the instant when the measurements began until the instant T_1 = 21 h 2 min 22 sec, the scintillation counter and counters Nos. 1, 2, and 3 recorded soft radiation (protons with E > 1 MeV) that exceeded several times the galactic cosmic ray background. Sharp increases in the counting rate of counters Nos. 1 and 2, recurring with a period of 122 sec (indicated in Fig. 1 by the arrows) are due /14

to the recording of solar x-ray radiation. Because of the high threshold, the scintillation counter did not record this radiation.

/145

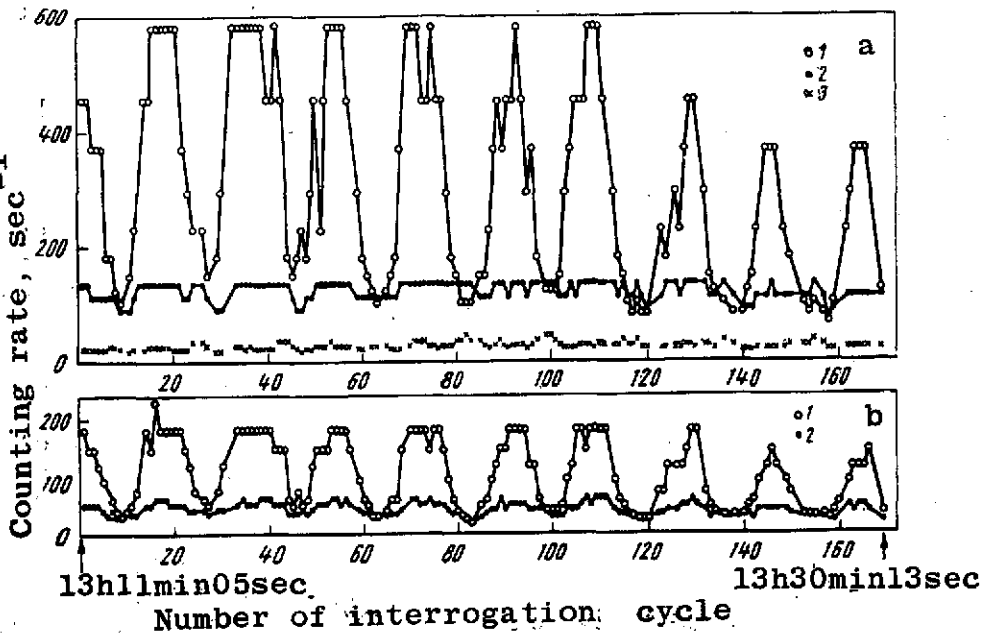

Fig. 8. Readings of the counters in the second session on September 8, 1966.

a--Results of measurements by scintillation counter with energy thresholds $E_1 > 30$ keV (1), $E_2 > 300$ keV (2), and $E_3 > 1.5$ MeV (3); b--measurements with SBT-9 counters (No. 1) without magnet (1) and SBT-9M (No. 2) with magnet (2).

At the instant T_1, the SBT-9 counters Nos. 1 and 3 and also the first scintillation counter threshold recorded a rapid increase in the counting rate. Taking into account the time constant of the ratemeters, the statement can be made that the time during which the intensity increased did not exceed 10 sec. Figure 9 shows that the particles that caused the increase in the counting rate at the instant T_1 were almost not recorded by counter No. 2, and that the energy released by them in the CsJ(Tl) crystal is a magnitude between 30 to 300 keV. These conditions can only be satisfied by electrons with an

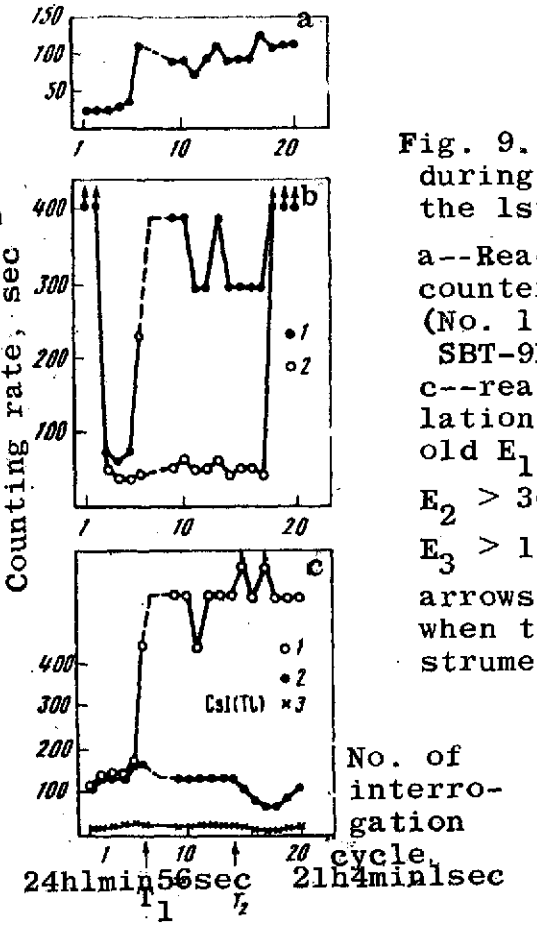

Fig. 9. Counter readings during the first session on the 1st of September 1966.

a--Readings from the SBT-9 counter (No. 3), b--SBT-9 (No. 1) counter (1) and SBT-9M (No. 2) counter (2), c--readings of the scintillation counter with threshold $E_1 > 30$ keV (1); $E_2 > 300$ keV (2), and $E_3 > 1.5$ MeV (3). The arrows indicate the instant when the readings on the instruments were off-scale.

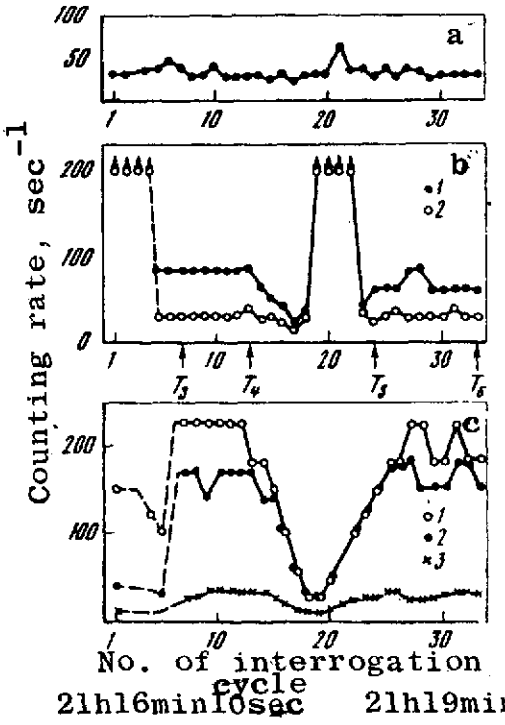

Fig. 10. Instrument readings during the second period on September 1, 1966.

The same symbols as in Fig. 9.

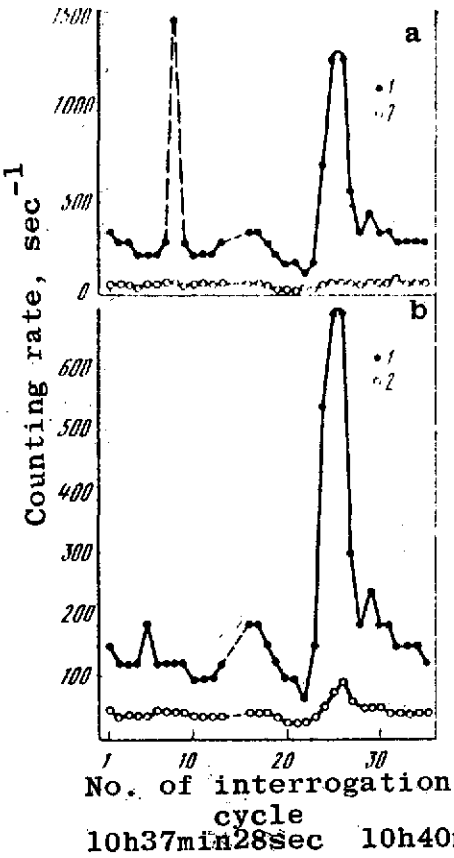

Fig. 11

energy between 30 to 300 keV. The intensity of these electrons that is determined from the difference of the counting rate of counters Nos. 1 and 2 is $N_e \sim 1700$ cm^{-2}.sec^{-1}.ster^{-1}. At the same time, the intensity determined from the counting rate of the first and second scintillation counter thresholds is $N \sim 300$ cm^{-2}·sec^{-1}·ster^{-1}. If this difference in the intensities is due to the difference in the energy thresholds, the complete electron spectrum which is taken in the form of a power function $N(E) \sim E^{-\gamma}$, we will have $\gamma \approx 2.5$ in the energy interval from 30 to 60 keV.

In the next measurement period, 16 min later (see Fig. 10), the intensity of the electron flux decreased by a factor of 5 - 7. Thus, the duration of the electron "burst" was on the order of 1/4 of an hour. The sharp increases in the counting rate of counters Nos. 1 and 2 which recurred synchronously with the rotation of the satellite as in the previous period are due to the recording of solar x-ray radiation. The decrease in the counting rate which can be seen well in Fig. 10 at all thresholds of the scintillation counter and in counter No. 1 in the

interval between the instants T_R and T_5 are due to the screening of the field of view of these counters by the Moon.

The second case of a short-term increase in the electron flux was recorded on the 8th of September 1966 at 10 h 40 min (Moscow time). The measurement period which lasted approximately 3.5 min, began at 10 h 37 min 30 sec (Fig. 11). It can be seen from Fig. 11 that in the time interval from 10 h 37 min 30 sec to 10 h 40 min 00 sec, an electron flux with energies $E_e > 30$ keV, $N \sim 600$ $cm^{-2} \cdot sec^{-1} \cdot ster^{-1}$ and with energy $E_e > 60$ keV, $N \sim 200$ $cm^{-2} \cdot sec^{-1} \cdot ster^{-1}$ was present. At 10 h 40 min 07 sec, a sharp increase in the electron flux occurred which was recorded by counter No. 1 and the scintillation counter (first threshold).

At the intensity maximum the electron fluxes were: for $E_e > 30$ keV, $N = 4 \cdot 10^3$ $cm^{-2} \cdot sec^{-1} \cdot ster^{-1}$, and for $E_e > 300$ keV, $N = 1.2 \cdot 10^3$ $cm^{-2} \cdot sec^{-1} \cdot ster^{-1}$. A higher intensity of the electron flux was observed for a period of 25 sec, after which it dropped to the previous value. It should be noted that this phenomenon was observed at the period when the "Luna-11" was on the dark side of the moon, not within direct visibility of the Sun, so that the possibility of recording the x-ray radiation from the Sun was not present.

We would like to draw attention to certain particular features of the cases in which the electrons were recorded that were discussed above:

1) A rapid increase in the electron flux with an almost unchanged proton flux was observed at 21 h 2 min 22 sec on September 1, 1966, and at 10 h 40 min 7 sec on September 8, 1966.

2) A simultaneous variation in the electron flux with energies $E_e > 30$ keV and $E_e > 60$ keV in these sessions.

In both these cases, the increase in the intensity of the electrons took place several times in a time interval $\lesssim 10$ sec. Two different models can be proposed to explain the features mentioned above.

1. Electrons with different energies are emitted simultaneously by some source at a distance not greater than $5 \cdot 10^5$ km, so that the variance of the velocities does not lead to a scatter in the arrival time exceeding 10 sec. Such source can be the shock waves in interplanetary space that are formed /14

during the collisions of magnetized plasma moving with different velocities. We note that in the period on September 8 the angle Sun-Earth-Moon was 90^{o}, so that the electrons propagating along the lines of force of the geomagnetic field could not arrive in the vicinity of the Moon.

2. The electron fluxes exist for a long time. The rapid increase and drop in the flux are due to the fact that the flux is localized in space either in the magnetic tube or in a cloud of magnetized plasma that moves with the velocity of the solar wind, which causes rapid and simultaneous changes in the counting rate for electrons with an energy $E > 30$ keV and $E > 60$ keV. The estimate for the dimensions of the region where the electrons are localized is 10^4 - 10^5 km.

The simultaneous measurements of the radiation in the vicinity of the Moon and far from the Earth-Moon system have great promise for explaining the nature of the electrons recorded in the space around the Moon.

In conclusion the authors express their gratitude to T. N. Markelova and D. P. Sukhov for the preparation and calibration of the magnetic filters, and to M. A. Zel'dovich, L. F. Vlasenko and L. L. Lifshits for their help in processing the telemetered information.

REFERENCES

1. Grigorov, N. L., Maduyev, V. L., Pisarenko, N. F. and Savenko, I. A., Dokl Akad Nauk SSSR 170 (3), 565 (1966).

2. Grigorov, N. L., Maduyev, V. L., Madel'shtam, S. L., et al., Dokl Akad Nauk SSSR 170 (3), 567 (1966).

3. Grigorov, N. L., Maduyev, V. L., Pisarenko, N. F. and Savenko, I. A., Kosmicheskie issledovaniya 4 (6), 842 (1966).

4. Vernov, S. N. Vakulov, P. V., Gorchakov, E. V., et al., Dokl Akad Nauk SSSR 169 (4), 1044 (1966).

5. Zhuzgov, L. N., Dolginov, Sh. Sh., and Eroshenko, E. G., Kosmicheskie issledovaniya 4 (6), 880 (1966).

6. Maisley, A. I. and Goedeke, A. D., Canad. J. Phys. 46 (10), 766 (1968).

7. O'Gallagher, I. I. and Simpson, I. A., Phys. Rev. Letters 16, 1212 (1966).

8. Van-Allen, I. A. and Krimgis, S. M., J. Geophys. Res. 10 (23), 5731 (1965).

9. Anderson, K. A. and Lin, R. P., Phys. Rev. Letters 16 (24), 1121 (1966).

10. Grigorov, N. L., Lutsenko, V. N., Maduyev, V. L., et al., Kosmicheskie issledovaniya 5 (6), 891 (1967).

N75 16469

THE STUDY OF COSMIC RAYS ON THE "PROTON" ARTIFICIAL EARTH SATELLITE

/149

N. L. Grigorov, I. A. Savenko, R. N. Basilova, N. N. Volodichev, S. I. Voropayev, L. F. Kalinkin, G. P. Kakhidze, V. A. Labutin, A. S. Melioranskiy, E. A. Pryakhin, I. D. Rapoport

ABSTRACT

Investigations were carried out with the space stations of the "Proton" series to study the physics of cosmic rays (1). The "Proton-1" and "Proton-2" had identical equipment and the measurement programs differed in minor and unessential details. The SEZ-13 device for the search of particles with a fractional electrical charge and the SEZ-11 device for the measurement of high energy electrons were mounted on the "Proton-3" satellite. The mode of action of the SEZ-11 device differed from that of the SEZ-12 device used in the "Proton-1" and "Proton-2" satellites for similar purposes. Some of the results that were obtained are presented. The following people contributed to the report: Part I, Kakhidze, G. P. and Rapoport, I. D.; Part 2, Kalinkin, L. F., Melioranskiy, A. S. and Pryakhin, E. A.; Part 3, Basilova, R. N., and Voloditchev, N. N., Part 4, Kalinkin, L. F. and Labutin, V. A.

The SEZ-13-01 device was mounted on the "Proton-3" artificial earth satellite for the search of relativistic particles with fractionally charged quarks in primary cosmic rays beyond the boundaries of the atmosphere. The principle on which it operated and the block diagram for the device are described in articles [1, 2].

The device has the capability to record single particles with a fractional charge if the energy E_0 of the particle is such that $E_0/Mc^2 \geq 0.85$. The system which records the amplitudes of the pulses consists of a proportional counter, an amplifier and a 64-channel amplitude analyzer with a switch mechanism, and it records particles with a charge e/3 and a signal to noise ratio 4:1. The control instruction regulates the linear transmittance if the amplitudes V_i of the pulses in each of the 12 proportional counters satisfy the condition $0.006 \leq \frac{V_i}{V_{prob}} \leq 0.67$ where V_{prob} is the most probable amplitude

of the pulses.

Control measurements carried out at sea level have shown that the probability that the control instruction will be triggered is $W_{meas} \sim 1.5 \cdot 10^{-5}$, and that the counting rate of the quadruple coincidence circuits is 23.1 pulses/sec. The telemetering channels record the amplitudes of the pulses from the proportional counters when the control instruction arrives to the linear transmitters. The instant when the control instruction passes through is recorded telemetrically. The control instruction can be triggered by the calibration device through single cosmic ray particles. Such events are also recorded by the telemetering channel. After the control instruction pulse is transmitted to the linear transmitters, the first pulse at the output of the wave generator is formed with a lag of 10-8 msec. This makes it possible to reset the triggers of the counters before the arrival of the first pulse in the train. The resetting of the triggers simplifies the processing of the telemetered information.

The calibration instruction generates the control instruction when the output pulses from the quadruple coincidence circuits are in a counting circuit whose capacitance is 2^{18}. Therefore, the time interval between the calibration pulses is proportional to the intensity of the primary cosmic rays that were recorded by the device as the quadruple coincidences of pulses from the extreme and middle counters in the device. The instrument records from 350 to $6 \cdot 10^3$ pulses/sec^{-1}, depending on the geomagnetic latitude. The rate at which the control instruction is counted by the transmitters will vary depending on the counting rate of the quadruple coincidences.

At high latitudes when the counting rate of the quadruple coincidences is $6 \cdot 10^3$ pulses/sec^{-1} and the probability of triggering the control command by a relativistic single particle is $\sim 1.5 \cdot 10^{-5}$, the frequency of the control instruction was, on the average, 1 every 10 sec. Since the scanning of the entire information pertaining to the passage of one particle through the instrument was about 9 seconds, the probability that two or more control instructions will be generated during the scanning time was high at high latitudes, i.e., the recorded event will not refer to a single particle. Therefore, sectors of the trajectory with small geomagnetic latitudes were used for the processing and those events were sampled when the particles passed through the device which were recorded by more than two telemetering points.

In the data from 16 sessions 72 cases were recorded when calibrating protons passed through the device. On the basis of these calibration pulses, the mean amplitude $\bar{V}$ was determined for each proportional counter out of the total number of pulses in the train (the maximum recorded number of pulses in the train was 63) and its probable value $V_{prob} = 0.7\ \bar{V}$. These values are given in Table 1. When the probable values of the pulse amplitudes generated by a particle with charge e are known, it is possible to determine the values of the amplitudes generated by a particle with charge e/3. The probable values of these amplitudes must be 2 - 4. These are also given in Table 1. /150

TABLE 1

No. of proportional counter*	Mean amplitude of the pulse $\bar{V}$	Probable value of the amplitude of the pulse V_{prob}	Probable value of the amplitude of the pulse for particles with a charge e/3, V_{prob} (e/3)	No. of proportional counter*	Mean amplitude of the pulse $\bar{V}$	Probable value of the amplitude of the pulse V_{prob}	Probable value of the amplitude of the pulse for particles with a charge e/3, V_{prob} (e/3)
1	33	24	2,7	6	31	22	2,4
2	40	29	3,2	9	43	31	3,4
3	39	27	3,0	10	44	32	3,5
4	43	31	3,4	11	30	22	2,4
5	38	27	3,0	12	36	26	2,9

*Measurements have shown that the proportional counters 7 and 8 had mean amplitude values of the pulses that were considerably lower, which were eliminated from the study when the restuls were processed.

When cases similar to those involving quarks were sampled, the data had to satisfy the following requirements.

1. The readings of the counter device for the control instructions had to correspond to the recording of a single particle.

2. In all channels of the amplitude analyzer, no signal was allowed with an amplitude exceeding the trigger threshold of the upper level discriminator which was 16 pulses

in the train. For 7.38, 53 and 99 sessions 895 triggerings of the control instruction were recorded from single particles and 131 events satisfying the requirements that were enumerated. It turned out that the observed amplitudes were zero in all cases in a large number of counters.

These 131 cases were divided into two groups, the first group with a maximum amplitude in one of the counters of 8 pulses in the train ($\sim 1/9$ of the most probable pulse generated by the particle with the charge e) and the second with a maximum amplitude of 16 pulses in the train. These groups represented respectively, 110 and 21 cases. Figure 1 gives for these groups the distribution of the number of amplitudes whose values were zero. The occurrence of such number of zero values of the amplitudes can be explained by the overloaded amplifiers of the recording channels caused by the passage of a multiple-charge primary particle through the device.

Since a particle with a charge e/3 can generate a zero amplitude with probability $< 10\%$ in one of the counters, we required that in all counters the amplitudes of the particles with this charge which was selected lie in the interval from 1 to 8 pulses and that there be no more than two zero values of the amplitude. In 60 h not a single case was recorded which satisfied the conditions that have been enumerated.

An analysis of the appearance of small signals (less than 10 pulses in the train) in the counters at the instant when the calibrated protons were recorded, makes it possible to estimate the effective time during which no multicharged particles which could overload the amplifiers passed through the device. This estimate gives an effective time which is 60% of the measurement time. From here one can obtain an upper bound for the particle flux with the charge e/3. It is assumed that the effective time during which the device was not in the shadow of the Earth is 65% of the entire flight time. The measurement time taking into account the overloading effects and the overshading was $8.4 \cdot 10^4$ sec. The geometrical factor of the device was $\Gamma = 3 \cdot 10^3 \text{cm}^2 \cdot \text{steradian}$ /151

$$I(e/3) = \frac{1}{3 \cdot 10^3 \cdot 0.84 \cdot 10^5} \approx 4 \cdot 10^{-9} \text{cm}^{-2} \cdot \text{sec}^{-1} \cdot \text{ster}^{-1}.$$

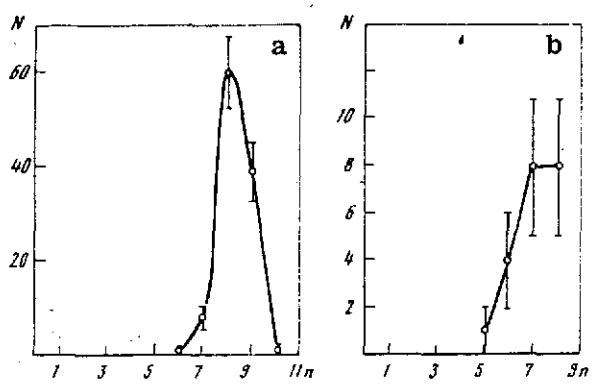

Fig. 1. Distribution of the number of zero amplitude values in the proportional counters calculated for the passage of a single particle which in one counter gives a maximum amplitude of the pulse for (a) 8 and (b) 16 pulses in the train.

The number of zero amplitudes (n) in one recorded event is plotted on the abscissa and the number of cases (N) is plotted on the ordinate.

The cosmic ray particles that pass through the interplanetary space from the point where they are generated to the surface of the Earth's atmosphere, pass through approximately 3 g/cm^2 interstellar gass substance. The cosmic rays interact with the gas. Using the upper estimate for the stream I(e/3) it is possible to estimate the upper limit of the cross section in which the primary protons with different energies E of the particles with the charge e/3 are generated. If the proton flux with energy $\geq$ E is denoted by I_0 ($\geq$ E),

$$\sigma(e/3) = \frac{I(e/3)\,A}{NQI_0},$$

where N is the Avogadro number, Q is the mean amount of substance passed through by the protons in galactic space, and A is the atomic weight of the atoms in the interstellar medium. (A = 1). For particles with energy E $\geq 10^{11}$ eV, $I_0 \approx 10^{-3}$cm^{-2}·sec^{-1}·ster^{-1}, and, hence, $\sigma(e/3) \leq 2\cdot10^{-30}$cm^2.

Measurement of High Energy γ-Quanta

The measurement of hard global γ-radiation fluxes that were carried out on the "Proton-2" artificial earth satellite with the aid of the γ-quanta GG-1 spectrometer were used with the data about the orientation of the object determined from magnetometer readings. The device was described earlier in articles [3, 4] which also gave certain results pertaining to the measurement time. The orientation of the satellite was

either not taken into account at all, or was determined approximately on the basis of certain indirect criteria. The dependence of the intensity of γ-quanta on the geographical latitude was noted, which indicated a relation between the recorded radiation and the charged particle fluxes.

The relation between the intensity of the measured γ-quanta I_γ and the values of the limiting hardness P for angles in the interval $\Delta\alpha = 0.60^\circ$ between the axis of the device and the direction to the zenith was studied in order to make the mechanisms of the effect of the charged particles on the recording of the neutral radiation and the detection of the primary γ-radiation flux more precise. /152

Figure 2 gives the relations $I_\gamma(P)$ for the three threshold energy values of the γ-quanta E_γ: ≥ 16, ≥ 50 and ≥ 170 MeV. It can be seen that $I_\gamma(P) \neq$ const. Hence, also for the given $\Delta\alpha$ the primary γ-quanta are simulated by charged particles. The following sources of such simulations can be pointed out: 1) the direct adding of charged particles due to the small recording effectiveness of the anti-coincidence system ϵ_{AC}, 2) recording of the γ-radiation caused by the charged particles as a result of the interaction with the body of the object (~ 1 g/cm^2) within the limits of the angle of view of the device; 3) the random coincidences from neutral radiation globally incident to the device which is recorded differently by its detectors; 4) the adding of charged particles due to a reduction in ϵ_{AC} when the counting rates of the anti-coincidence detector are large in regions with somewhat higher radiation intensity (high geographical latitudes) when the amplification factor of the photomultiplier can be reduced, and, as a result, the effective triggering threshold of this detector can be increased; 5) the recording of secondary γ-radiation from the substance in the atmosphere traveling within the solid angle when the electrons or positrons formed by this radiation in the converter are subsequently scattered into the solid angle.

The data in Fig. 2 allow us to conclude that the simulations mentioned in Section 1 are not the decisive factor. In fact, in this case we would expect a similarity between the spectra of the γ-quanta $I_\gamma(P)$ and the charged particle spectra $I_z(P)$. However, the relations $I_\gamma(P)$ are different for different threshold values E_γ and have a form that is different from the spectrum of the charged particles [6]. In addition, to explain the observed intensity of the γ-quanta, it is necessary to assume a recording effectiveness of the anti-coincidence system

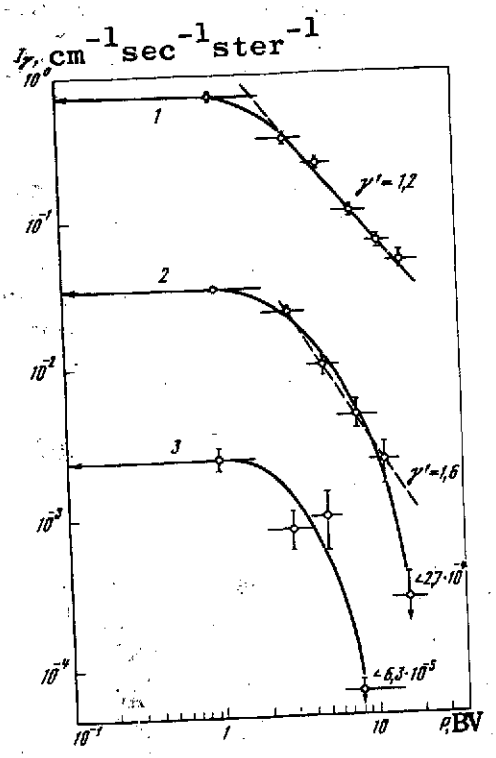

Fig. 2. γ-radiation intensity with various energies $E_\gamma \geq 16$ (1), ≥ 50 (2) and ≥ 170 MeV (3) vs. hardness P for the angular interval 0 - 60° between the axis of the device and the vertical axis.

Dashed lines indicate power spectra.

which is considerably smaller than the magnitude $\varepsilon_{AC} \gtrsim 0.997$ which was found experimentally. At the present time, it is difficult to point out a preferential source for the γ-quanta simulations. Certain quantitative data do not contradict the assumption that the processes mentioned in points 3 - 5 can occur in fact, since the observed simulations are also observed at the lowest energy threshold of the γ-radiation. Hence, we can assume that the recorded γ-quanta are mainly secondary. /153

For E > 50 MeV for P > 14 BV and $E_\gamma \geq 170$ MeV for P > 6 BV not a single γ-quantum was recorded during the entire measurement period, which was 1 h and 3.7 h, respectively. The upper bounds for the intensity that were obtained from here are $I_\gamma(E_\gamma \geq 50$ MeV) $< 2.7\cdot10^{-4}$ and $I_\gamma(E_\gamma \geq 170$ MeV) $< 6.3\cdot10^{-5}$ quanta·cm^{-2}·sec^{-1}·ster^{-1}·MeV^{-1}. The last quantity also refers to $I_\gamma(E_\gamma \geq 500$ MeV). Fig. 3 gives, together with the data of other authors [7-11], the values of the upper limits for the intensity of γ-quanta referred to the unit energy interval: $2.3\cdot10^{-6}$, $9\cdot10^{-7}$ and $6.3\cdot10^{-8}$ quanta. cm^{-2}·sec^{-1}·ster^{-1}·MeV^{-1} for the regions E_γ 50-170, 170-500 and 500-1500 MeV. These values agree with the results obtained by

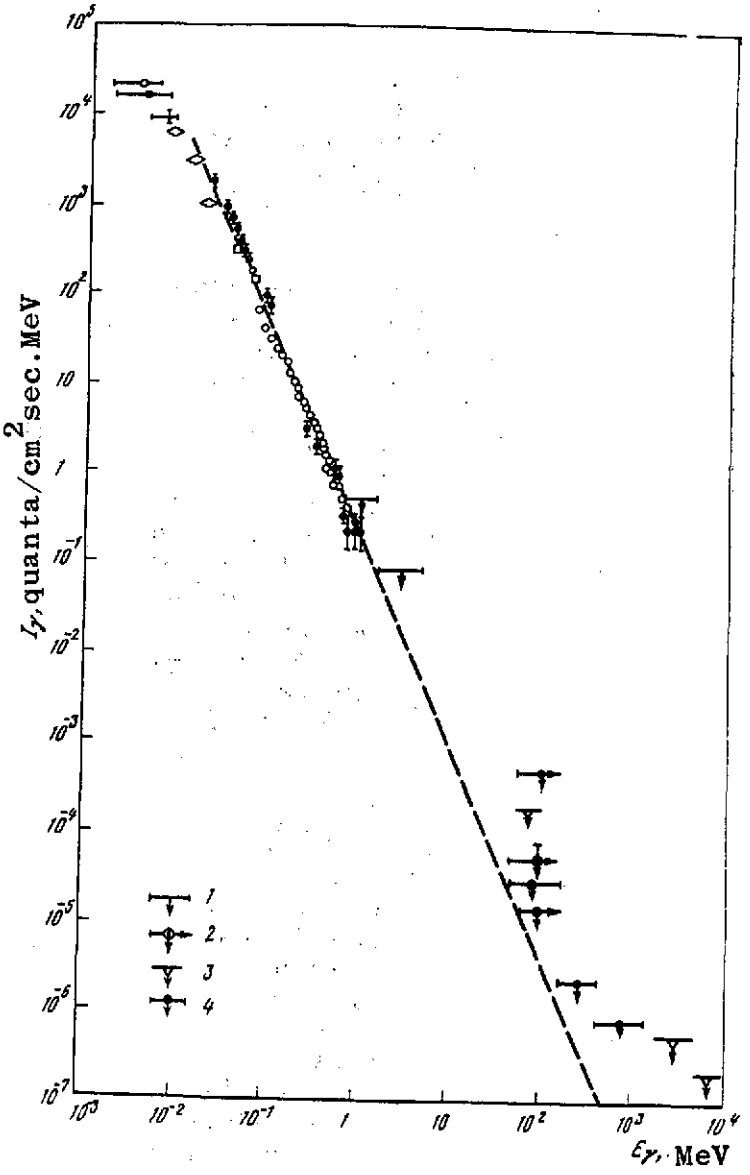

Fig. 3. Differential spectrum of primary cosmic global x-ray and γ-radiation.

Fragment of graph given in article [7] supplemented by the results from this article (1), and also articles [8, 9] (2) and [10, 11] (3, 4)

U. L. Kraushar, et al., from satellites [8, 9[which are one order of magnitude below the magnitudes measured in experiments on balloons [10, 11]. At the same time, all data referring to the region $E_\gamma \geq 50$ MeV are approximately one order of magnitude below the values extrapolated from the range 2 keV - 1 MeV, where the radiation is mainly explained by the inverse Compton effect.

Study of Heavy Nuclei in Cosmic Rays on the "Proton-1" and "Proton-2" Artificial Earth Satellites

Superheavy nuclei in cosmic rays with a charge $Z > 30$ (SH-nuclei) are the least studied range of nuclear charges. At the present time, it is assumed that the relative abundances of these nuclei in cosmic rays and in the universe coincide [12], and, for example, the ratio to very heavy nuclei with $Z \geq 20$ (VH-nuclei) is 10^{-3} [13].

After the data obtained from the "Proton-1" and "Proton-2" artificial earth satellites were published [14, 15] several additional papers which studied superheavy nuclei appeared. In the study of R. Yolker, et al., [16] that was carried out using an original method which measured the number of nuclei on the traces left by these in meteorites, the given ratio of nuclear fluxes with $Z > 32$ to VH-nuclei is on the order of magnitude of the relative abundance of these nuclei in the universe. J. Ormes, et al., [13], who carried out the measurements using the Cerenkov scintillation method, obtained for the ratio of the groups SH/VH the value $1.6 \cdot 10^{-2}$, which agrees well with other results, and exceeds by one order of magnitude the ratio for the abundance of these nuclei in the universe. For nuclei with $Z > 36$, the abundance of these nuclei in cosmic rays and in the universe, according to the measurements of these authors, approximately coincides.

An unexpected result was obtained by P. Fowler, et al., [17] with the aid of a detector whose total area was $4.5 m^2$ containing four photoemulsion layers interspersed with lead absorbers. According to their data in a considerable part of the range of charged nuclei $Z > 40 - 83$ the abundance of the nuclei on cosmic rays is practically constant. The abundance of nuclei with $Z > 40$ and $Z > 48$ in cosmic rays is lower by one order of magnitude, and with $Z > 83$, taking into account the interaction of the nuclei in the substance in front of the detector, is almost two orders of magnitude greater than the mean abundance of the nuclei in the universe. This abundance of nuclei with a charge > 83 compels the authors to assume that the sources of the cosmic rays are relatively very rich in transbismuth elements and that very heavy particles pass a thicker layer of the substance than the light particles. /155

The results of the studies that were mentioned are summarized in Table 2 which gives, for a comparison, the data obtained from the "Proton-1" and "Proton-2" artificial earth satellites, and the relative abundances of superheavy particles in the universe that were averaged over the studies [18 - 20]. The abundances of nuclei measured from the

Table 2

Ratio of the nuclear groups	Data from different measurements				The relative abundance of superheavy nuclei in the universe according to studies [18-20].
	"Proton-1", "Proton-2" [14,15]	Yolker et al. [16]	Ormes et al. [13]	Fowler et al. [17]	
$\frac{N(Z \geqslant 30)}{N(VH)}$	$3{,}2 \cdot 10^{-2}$	—	$1{,}6 \cdot 10^{-2}$	—	$\simeq 2{,}5 \cdot 10^{-3}$
$\frac{N(Z \geqslant 32)}{N(VH)}$	—	$(1{,}6 - 3{,}7) \cdot 10^{-4}$	—	—	$\simeq 1{,}0 \cdot 10^{-3}$
$\frac{N(Z \geqslant 36)}{N(VH)}$	—	—	$1{,}2 \cdot 10^{-3}$	—	$\simeq 0{,}6 \cdot 10^{-3}$
$\frac{N(Z \geqslant 40)}{N(VH)}$	$1{,}3 \cdot 10^{-2}$	—	—	$3{,}4 \cdot 10^{-3}$	$\simeq 2{,}2 \cdot 10^{-4}$
$\frac{N(Z \geqslant 48)}{N(VH)}$	$3 \cdot 10^{-3}$	—	—	$2{,}1 \cdot 10^{-3}$	$\simeq 1{,}3 \cdot 10^{-4}$
$\frac{N(Z \geqslant 83)}{N(VH)}$	—	—	—	$0{,}8 \cdot 10^{-3}$	$\simeq 2{,}1 \cdot 10^{-7}$

"Proton-1" and "Proton-2" artificial earth satellites are referred to the nuclei with $Z > 20$, so that they are somewhat lower than in studies [14, 15] where they were referred to $Z \geq 21$.

The measurement data from the "Proton-1" and "Proton-2" artificial satellites lead to the conclusion that the content of superheavy nuclei in cosmic rays is higher than their content in the universe. Therefore, we will dwell on certain methodological points which could give such higher values.

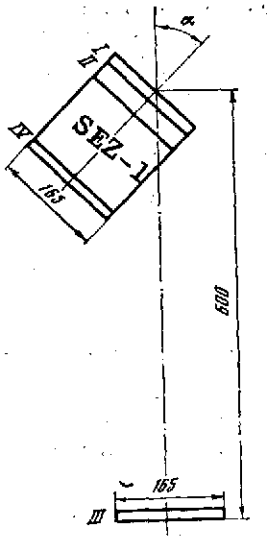

Fig. 4. Geometry of the experiment. I-IV - counters

1. The passage of nuclei with a charge Z = 20 - 28 through the Cerenkov detector at an angle to the axis of the device which is nearly 90° with the simultaneous triggering of the lower scintillation counter by a δ-electron or random coincidence with an arbitrary particle passing through this counter. In this case, we could expect that at the output from the Cerenkov counter an amplitude of the signal must be formed which is proportional to the path of the particle in the Cerenkov counter, which can trigger higher thresholds corresponding to the largest Z. This possibility was verified experimentally. The Cerenkov SZE-1 spectrometer, which is analogous to those that were mounted in the satellites, read for various values of the angles α between the axis of the device and the direction to the zenith (Fig. 4) the amplitude distributions of the pulses from the μ-mesons of the cosmic rays shown in Fig. 5. It can be seen that as the angle α increases, the amplitude at the output from the Cerenkov counter not only does not increase, but, on the contrary, drops. This is explained by the fact that as the angle α increases, more and more of the Cerenkov light is incident to the upper surface of the Cerenkov detector which is covered by dull black paint. The amplitude increases as the angle increases only in the case when the detector is covered by white paint with a high reflectance coefficient which follows from a study of the amplitude distributions of the pulses from the μ-mesons and for α = 70° shown in Figs. 5 and 6. In all cases the spectra were read off from the same number of μ-mesons. Thus, the simulation of superheavy nuclei by less heavy nuclei when these travel along a long path is eliminated in the Cerenkov detector.

2. Simulation of superheavy nuclei by scintillations in the admixtures in the windshield material of the photoelectron multiplier. These types of simulations should not depend on the orientation of the device with respect to the vertical axis, since the light from the scintillations propagates isotropically. Therefore, to detect this type of simulation, special sectors were selected in the trajectory of motion of the "Proton-2" artificial earth satellite, in which the axis of the instrument was oriented upward and downward. The results are given in Table 3, which gives the measurement time, the number of nuclei with $Z \geq 2 \geq 42 \geq 48$ and the ratios of superheavy nuclei to nuclei with $Z \geq 2$ for various directions of the instrument axis. In spite of the fact that the intensities differ (by a factor of 5) the ratios of the remaining nuclei in various groups do not change, which speaks against the simulation of superheavy nuclei by scintillations. It should be noted that the intensity does not drop to zero when the axis of the instrument is oriented downward, because the input aperture of the instrument is not completely shaded by the Earth. /156

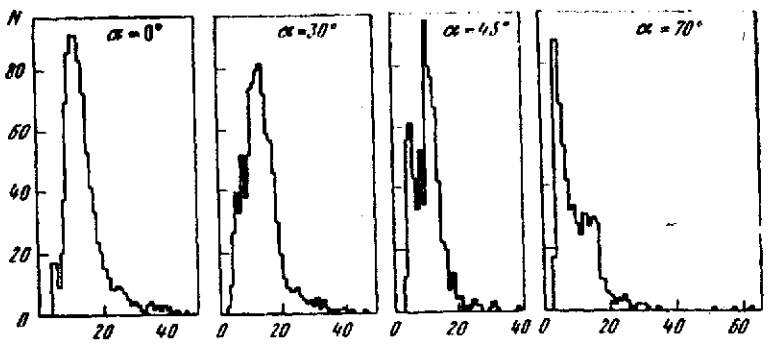

Fig. 5. The amplitude distributions of the pulses from the μ-mesons of cosmic rays read by the SEZ-1 as a function of the angle α

The numbers of the channels of the amplitude analyzer are plotted on the abscissa and the number of events in the given channel are plotted on the ordinate

Table 3

Orientation of the axis of the device	t, min	$N(Z \geq 2)$	$N(Z \geq 42)$	$N(Z \geq 48)$	$\frac{N(Z \geq 42)}{N(Z \geq 2)}$	$\frac{N(Z \geq 48)}{N(Z \geq 2)}$
Upward	≈1590	$4{,}36 \cdot 10^5$	27	5	$(0{,}6 \pm 0{,}1) \cdot 10^{-4}$	$(0{,}1 \pm 0{,}05) \cdot 10^{-4}$
Downward	≈1515	$9{,}69 \cdot 10^4$	5	2	$(0{,}5 \pm 0{,}2) \cdot 10^{-4}$	$(0{,}2 \pm 0{,}15) \cdot 10^{-4}$

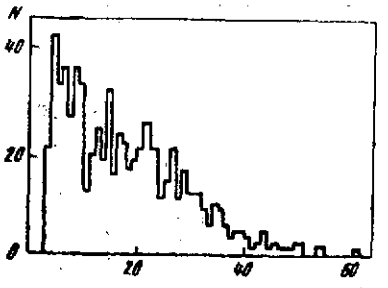

Fig. 6. Amplitude distribution of pulses from μ-mesons of cosmic rays for $\alpha \sim 70^{\circ}$, when the upper surface of the Cerenkov detector is covered by white paint with a high coefficient of reflectance.

The same quantities as in Fig. 5 are plotted on the axes.

In previous studies in which the results of a study of the energy spectra of various groups of nuclei obtained with the aid of the Cerenkov SEZ-1 spectrometer mounted in the space stations "Proton-1" and "Proton-2" are discussed, it was reported that the exponents for the complete spectra obtained for protons, helium nuclei in the group C, N, O, nuclei in the H-group (with a charge $Z \geq 10$) and VH-group ($Z \geq 20$) satisfy the values 1.5 [21] and that the spectra of the charging groups with $4 \leq Z \leq 6$, $6 \leq Z \leq 10$, $10 \leq Z \leq 21$, and $Z \geq 21$ resemble the spectrum of helium nuclei [22]. These conclusions were of a preliminary character, since we did not have data about the orientation of the satellites. At the present time, the data about the orientation are available for the "Proton-2" artificial earth satellite, which can be used to construct the energy spectra for various charging groups. /157

This article considers the complete spectra by rigidity for protons and helium nuclei that were measured on November 5, 1965, on 45 - 52 sectors of the trajectory of the "Proton-2" artificial earth satellite. The character of the change of the orientation of the device on this sector of the trajectory can be seen well in Fig. 7, which shows the dependence of the number of nuclei with $Z \geq 2$ that were recorded in a time interval of 387 sec of flight time. The transverse axis of the device was almost stabilized in space and was oriented in such a way that the device was not shaded, for all practical purposes, by the Earth at high southern latitudes, the region of maximum intensity, and it was almost completely shaded at northern high latitudes, the region where the maximum was low.

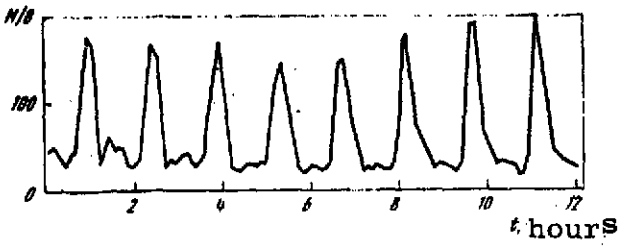

Fig. 7. The intensity of nuclei with $Z \geq 2$ and kinetic energy $E \geq 400$ MeV neutrons vs. the measurement time t

To construct the spectra, sectors were selected where the shading of the instrument by the Earth was 0, which corresponded to an angular interval of 0 - 52° which the transverse axis of the instrument made with the direction to the zenith. It follows from the above that practically all the information used in this article was obtained in the southern hemisphere. The total measurement time in this study was approximately 5 h.

Figure 8 shows the complete spectra by rigidity for protons and helium nuclei in the range 1 - 18 BV. The values of the magnetic rigidity which was determined taking into account the elevation above sea level are plotted on the abscissa, and the intensity is plotted on the ordinate. The errors on the abscissa and ordinate are mean square errors. The exponents of the spectra satisfied the value 1.5 in the range 6 - 19 BV. The averaged value of the ratio of proton intensities to helium nuclei in the magnetic rigidity range 2 - 18 BV is 9.0 ± 0.5, which agrees with the data given in article [23].

The measured intensity of protons with energy $\geq$ 400 MeV which was 0.40 $cm^{-1} \cdot sec^{-1} \cdot ster^{-1}$ does not contradict the results of measurements made on 4-6 October and 3-6 December 1965 on the "Luna-7" and "Luna-8" stations which gave, in interplanetary space, an intensity of protons with energy greater than 30 MeV of 0.43 $cm^{-2} \cdot sec^{-1} \cdot ster^{-1}$ and 0.47 $cm^{-2} \cdot ster^{-1}$, respectively [24].

Measurement of High Energy Electrons on the "Proton-3" Artificial Earth Satellite

The measurements of high energy electrons were continued on the space station "Proton-3" with the aid of the SEZ-11 device. The operational principle of this instrument was similar to that of the apparatus used in study [25] for analogous purposes in experiments made on balloons. It consists of a /158
scintillation and Cerenkov counter and a scintillation mica spectrometer of electron energy forming the telescope (Fig. 9).

The scintillation counter consisting of a plastic scintillator (1.5 cm thick) (1) and an FEU-16 photomultiplier (2) is tuned to maximum sensitivity and only the passage of a particle through it is recorded. The Cerenkov counter consists of a plexiglas radiator which is 3 cm thick, whose diameter is 8 cm (3), which is in optical contact with an FEU-52 photomultiplier [4].

The interval corresponding to the optimal recording of one singly charged relativistic particle is selected from the pulse spectrum of the Cerenkov counter. These signals, together with the pulses from the scintillation counter and energy spectrometer are recorded by a triple coincidence circuit.

Because of the directional effect of the Cerenkov light, mainly particles arriving from the upper hemisphere are recorded (to improve the sensitivity of the Cerenkov counter the top end of the radiator is blackened).

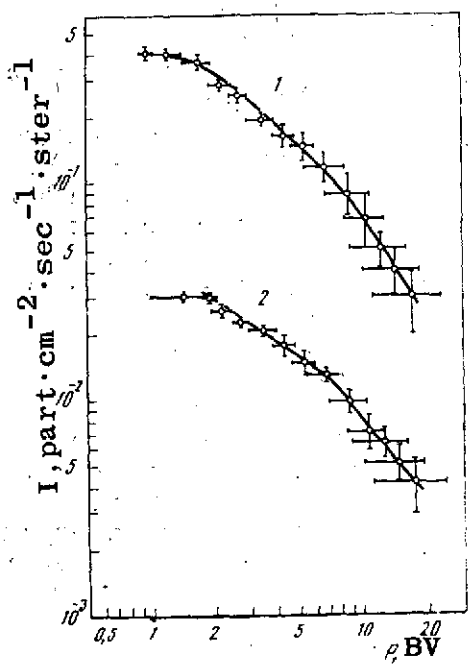

Fig. 8. Complete spectra by rigidity for protons (1) and helium nuclei (2).

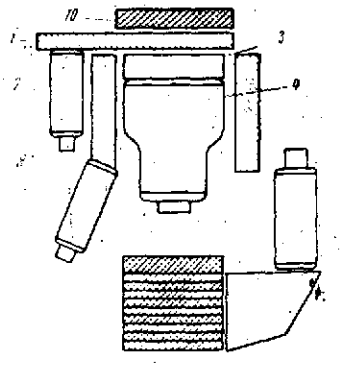

Fig. 9. Schematic diagram of the instrument.

For explanation, see text.

The electron energy spectrometer consists of alternating lead layers (5) and the scintillating plastic mass (6) whose area is 10 x 10 cm^2. The thickness of the first Pb layer is 1 cm, and of the remaining four layers, 0.5 cm each; the thickness of each of the five plastic mass layers is 0.5 cm. The scintillating light is recorded by an FEU-13 photomultiplier (8) with the aid of a light guide (7). The system that selects the amplitudes of the pulses from this detector has four integral thresholds, for which, on the basis of calculations using the cascading curves [26, 27], the following energy values of the electrons E_e can be set up: 0.04, 0.3, 1.0, 3.5 GeV (the first threshold is significant in the method and its purpose is not to determine the energy of the electrons). To protect the charged particles from showers outside the aperture of the instrument, the Cerenkov counter is surrounded by a cylinder made from the scintillating plastic mass (9). The signals from this detector are connected to the anti-coincidence circuit with the pulses from the telescope.

On the side of the input window of the instrument is a lead filter which is 1.5 cm thick (10). The measurements are made when the filter is not present. The measurements are carried out without the filter "O" ("open") and with the filter, which covers the aperture of the telescope "Z" ("closed"). When the filter is in the first position, both electrons N_e, and also heavier particles (mainly protons, N_p) are recorded: /15

$$N_0 = N_e + N_p. \tag{1}$$

When the filter is closed, high energy electrons undergo cascading multiplication with probability close to 1. The corresponding signals from the Cerenkov counter are outside the interval of amplitudes associated with the recording of a single particle

$$N_c = KN_p . \tag{2}$$

The attenuation factor for the proton flux K = 0.92 due to the filter is calculated from the known magnitude of the cross section of the nonelastic interaction of high energy neutrons with the lead [28]. From (1) and (2) we obtain

$$N_c = N_0 - 1.09\, N_c \tag{3}$$

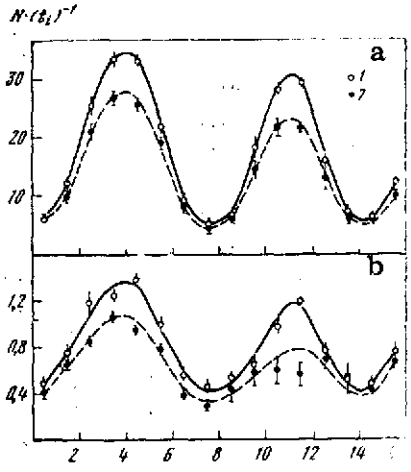

Fig. 10. Counting rate when the filter is in (1) the open and (2) the closed position at various energy thresholds.

a--$E_e \geq 1.0$ BeV; b--$E_e \geq 3.5$ BeV

The measurement time during flight when the filter was in either position was ~ 1.5 h. The electron flux can be determined from (3) when the geometrical factor of the instrument $\Gamma = 11.2$ cm^2·ster and the recording effectiveness of single charged particles by the Cerenkov counter $\varepsilon = 0.59$ are taken into account, which are obtained from the measurements of the μ-mesons of cosmic rays at sea level.

The data available at the present time about the results of the measurements make it possible to obtain preliminary information about the values of the electron fluxes that are averaged over the longitude and the angles which determine the orientation of the object.

When the results were processed, the time during which the instrument operated was broken up into periods of equal duration, i.e., 1 revolution of the satellite about the Earth. Each period, in turn, was divided into equal intervals of $t_i \approx 6.5$ min ($i = 1 - 14$, and t_1 was the interval which corresponded to the position of the object in the southern hemisphere near the equator when the satellite moved from the north to the south). The averaged values $N_0(t_i)$ and $N_Z(t_i)$, that were averaged over the periods and obtained in 300 flight hours are given in Fig. 10.

We can expect that at the second ($E_e \geq 0.3$ BeV) and even the third ($E_e \geq 1$ BeV) energy thresholds, the recording effectiveness of the electrons when the filter is closed is not zero, because of the small number of particles in the shower

and the fluctuations in their number and their distribution by energy (this quantity will be made more precise later). For energies $E_e > 3.5$ BeV this factor plays a less important role.

From the data in Fig. 10, it is possible to obtain the values of the global electron fluxes with energies $1 \leq E_e \leq 3.5$ BeV averaged over the intervals t_4, t_5, t_{11}, t_{12} ("high" latitudes) and t_3, t_6, t_{10}, t_{13} ("Medium" latitudes): $(2 \pm 0.4) \cdot 10^{-4}$ and $(0.7 \pm 0.5) \cdot 10^{-4}$ $cm^{-2} \cdot sec^{-1} \cdot ster^{-1}$, respectively. Because of the above inequality, which does not give zero recording effectiveness when the filter is closed, we can assume that these values are somewhat lower.

Clearly for medium, and also to a considerable extent high latitudes, electrons with energies $E < 3.5$ BeV are mainly secondary. As shown in in article [29], at the altitudes attained in experiments with balloons, the secondary electron radiation has considerable magnitude for $E_e \sim 10^2 - 10^3$ MeV. The present data indicate that at satellite altitudes (200 - 600 km) this radiation remains sufficiently intense. An analogous result applying to electrons with energies ~ 300 MeV was also obtained during the "Proton-1" and "Proton-2" artificial earth satellite flights. The following authors contributed mainly to the separate sections of the report: the first part, G. P. Kakhidze and I. D. Rapoport, the second part, L. F. Kalinkin, A. S. Melioranskiy and E. A. Pryakhin, the third part, R. N. Basilova and N. N. Volodichev, the fourth part, S. I. Voropaev, L. F. Kalinkin and V. A. Labutin. /160

The authors express their gratitude to Yu. F. Galaktionov, L. V. Kuleshov and L. S. Bratolyubov-Tsylukidze for their help in processing the experimental data, and to L. V. Kurnosov and L. A. Razorenov for their participation in the evaluation of the results obtained on superheavy nuclei.

REFERENCES

1. Grigorov, N. L., Rapoport, I. L., Savenko, I. A. and Skuridin, G. A., Kosmicheskie issledovaniya 2 (5), 724 (1964).

2. Grigorov, N. L., Kakhidze, G. P., Rapoport, I. D. and Savenko, A. I., in the collection Kosmicheskie luchi, No. 11 (1969).

3. Grigorov, N. L., Kalinkin, L. F., Melioranskiy, A. S., et al., Izv Akad Nauk SSSR, Seriya Fiz, 30, 1765 (1966).

4. Grigorov, N. L., Kalinkin, L. F., Melioranskiy, A. S., et al., Kosmicheskie issledovaniya 5 (1), 124 (1967).

5. Garmire, G. and Kraushaar, W. L., Space Sci. Rev., 4, 123 (1965).

6. Ormes, I. F. and Webber, W. R., Proc. Internat. Cosmic Ray Conf., Vol. 1, London, 1965, p. 349.

7. Rocchia, R., Rotherflug, R., Boclet, D., Ducras, G. and Labeyrie, J., Space Research VII 2, Wien (1966).

8. Kraushaar, W. L., Clark, G. W., Helmken, H., Higbie, P., and Agogino, M., Astrophys. J. 141, 845 (1965).

9. Kraushaar, W. L., Clark, G. W., and Garmire, G., Canad. J. Phys. 46 (10), 414 (1968).

10. Anand, K. G., Daniel, R. R. and Stephens, S. A., Cand. J. Phys. 46 (10), 652 (1968).

11. Duthie, I. G., Haffner, E. H., Kaplan, E. M., and Fazio, G. G., Phys. Rev. Letters 10, 364 (1963).

12. Ginzburg, V. L., and Syrovatskiy, S. I., Proiskhozhdeniye kosmicheskikh luchey, [The Origin of Cosmic Rays], USSR Acad. of Sci. Publs., 1963.

13. Ormes, J. F., von Rosenvinge, T. and Webber, W. R., Technical Report GR-92 of School of Physics and Astronomy, Univ. Minnesota, Jan. 1967.

14. Volodichev, N. N., Grigorov, N. L. and Savenko, I. A., Izv Akad Nauk. SSSR, Seriya Fiz, 31 (8), 1231 (1967).

15. Volodichev, N. N., Grigorov, N. L. and Savenko, I. A., Kosmicheskie issledovaniya 5 (3), 434 (1967).

16. Fleischer, R. L., Price, R. B., Walker, R. M., Maurette, M., and Morgan, G., J. Geophys. Res. 72 (1), 355 (1967).

17. Fowler, P. H., Adams, R. A., Cowen, V. G., and Kidd, J. M., "The charge spectrum of very heavy cosmic ray nuclei," Preprint, Univ. Bristol, April 1967.

18. Sues, H. G. and Urey, H., Rev. Mod. Phys. 28, 53 (1956) (L. Sues, H. Urey, UFN 62, 101 (1957).

19. Cameron, A. G. W., Astrophys. J. 129, 676 (1956).

20. Aller, L. H., Abundance of the Elements, N. Y., Interscience, 1961 (L. Aller, Rasprostranennost' khimicheskikh elementov, Foreign Lit. Publs., 1963).

21. Volodichev, N. N., Grigorov, N. L., Nesterov, V. E., et al., Izv Akad Nauk SSSR, Seriya Fiz, 30 (11), 1763 (1966).

22. Volodichev, N. N., Grigorov, N. L. and Savenko, I. A., Kosmicheskie issledovaniya 5 (3), 436 (1967).

23. Webber, W. R., Proc. IX Internat. Conf. Cosmic Rays, London, 1966.

24. Vernov, S. N., Vakulov, P. V., Gorchakov, E. V., Logachev, Yu. I., Lyubimov, L. P., Nikolaev, A. G., and Pereslegina, N. V., Dokl Akad Nauk SSSR 169 (5), 1044 (1966).

25. Rubtsov, V. I., Izv Akad Nauk SSSR, Seriya Fiz 30, 1289 (1966).

26. Ivanenko, I. P. and Samosudov, B. Ye., Yadernaya fizika 5, 622 (1967).

27. Dovzhenko, O. P., and Pomanskiy, A. A., Zhur Exper Teor Fiz. 45, 268 (1963).

28. Barashenkov, V. S., Secheniya vzaimodeystviya elementarnykh chastits, [Intersection Cross Sections of Elementary Particles], Moscow, Nauka Press, 1966.

29. Verma, S. D., J. Geophys. Res. 72, 915 (1967).

30. Grigorov, N. L., Klintsov, Yu. S., Nesterov, V. Ye., et al., Izv Akad Nauk SSSR, Seriya Fiz. 30, 1778 (1966).

N75 16470

MEASUREMENT OF PROTON SPECTRA ON SATELLITES FROM THE "COSMOS" SERIES OF ARTIFICIAL SATELLITES

Ye. Ye. Kovalev, V. I. Ostroumov, S. S. Skvortsov, L. T. Smirennyy

ABSTRACT

In 1966-1967 measurements were performed at altitudes from 200 to 400 km to determine the fluxes and spectra of protons by means of nuclear emulsions of the BR-2 and Ya-2 types. The proton spectra within the range up to 8 BeV are presented. The spectra obtained are the basis for estimating radiation hazards.

In accordance with the program of scientific investigations (announced by Tass on 16 March 1962) we carried out, during 1965-1967, measurements of fluxes and energy spectra of heavy charged particles inside hermetic sectors of satellites from the "Cosmos" series at altitudes of 200-400 km.

The nuclear emulsion layers were collected in piles consisting of 15 - 20 layers whose diameter was 50 mm, which were placed in circular hermetic aluminum containers with the same diameter whose wall was 0.3 g/cm^2 thick. The samples were sealed in hermetic parts of the satellite and also in polyethylene spheres placed in these parts whose radius was 5, 10, 15 cm, in order to study the attenuation and accumulation of the radiation in a substance with equivalent fibers. Charged particle tracks were sampled for the measurements whose angle of dip was $\pm 10^{\circ}$. The energy of protons up to 50 MeV was determined from the travel to energy ratio [1].

In the range 50-400 MeV, the energy of the protons was determined with the aid of the ionization method. For this purpose, every checker constructed the graduating curve which related the energy of the protons to their ionization, which was expressed in terms of the number of grams per 100 μm of travel. Tracks of slowed down protons as well as tracks of π- and μ-mesons and relativistic electrons from easily identifiable $\pi \rightarrow \mu \rightarrow e$ decays were used to construct the curves. The energy of the protons in the range 50-400 MeV and the number of protons with an energy > 400 MeV were determined in this manner. Figure 1 gives the results of the measurements of the proton spectra in the range 400 MeV with various polyethylene filters in the cabin of the satellite when the altitudes of the apogee was ~ 300 km. A comparison of the spectra that were obtained with the proton spectrum of the internal belt obtained by

S. Freeden and R. White [2] at altitudes of ~1200 km has shown that in our case the initial spectrum of protons in the internal band at altitudes ~ 300 km is somewhat softer. /162

To determine the energy spectrum of the protons in the range > 400 MeV, we made an analysis of the stars in the photoemulsion by the number of rays. We started out with the assumption that neutrons with a certain energy can create stars whose ray composition depends on the energy of the neutrons. Suppose that the density of the stars with a given number of rays n, formed by the neutrons in a definite energy interval E_k, is dN_n^k/dV. Then

$$\frac{dN_n^k}{dv} = \frac{1}{\lambda_n(E_k)} P_n(E_k), \tag{1}$$

where $P_n(E_k)$ is the neutron flux (neutrons/cm^2) in the energy interval E_k(MeV), forming stars with the number of rays n, $\lambda_n(E_k)$ is the length of the open travel of the neutron with energy E_k necessary to form a star with a number of rays n.

The total density of the stars with the given number of rays n will be

$$\frac{dN_n}{dV} = \sum_k \frac{dN_n^k}{dV}, \tag{2}$$

or using formula (1)

$$\frac{dN_n}{dV} = \sum_n^k \frac{1}{\lambda_n(E_k)} P_n(E_k). \tag{3}$$

Letting n = 3, 4, . . . k, we obtain from (3) a system of linear equations for determining the energy spectrum of the neutrons ($P(E_k)$), where the energy intervals E_k are selected in the entire energy range of the neutrons. The function $\lambda_n(E_k)$ can be taken from the experimental data on accelerators in the energy band from 100 MeV to 23 BeV. Since the numerical values

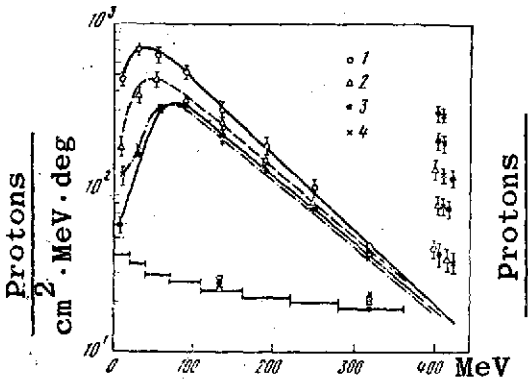

Fig. 1

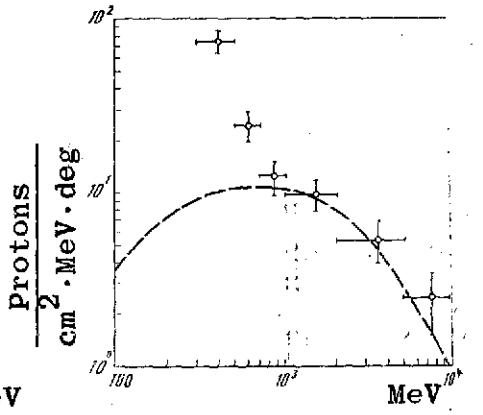

Fig. 2.

Fig. 1. Differential energy spectra of protons beyond various polyethylene filters of various thickness in the hermetic sector of a satellite from the "Cosmos" series.

1 - 0.3; 2 - 5; 3 - 10; 4 - 15 g/cm^2.

Fig. 2. Differential energy spectrum of protons in the energy range 400 MeV.

The experimental points and the differential energy spectrum of the galactic cosmic ray protons are shown during minimum solar activity, which was constructed from the data in the literature, taking into account the geomagnetic cutoff rigidity (dashed line).

in (3) are given or are determined with a certain error, it is useful to write expression (3) as an overdetermined system of equations, so that the number of selected energy intervals is smaller than the number of equations ($k < n$), and solve this system using the least squares method with the aid of electronic computers. /133

The spectrum which was obtained in this manner (Fig. 2) differs considerably from the spectrum of protons of galactic origin in the energy range 300-700 MeV. This can be explained by the contribution of protons from the internal radiation belt. Some increase in the proton flux in the energy range > 3 BeV occurred, apparently, due to the impurity of multiray stars resulting from the interaction of fast α-particles of galactic origin with photoemulsion nuclei, or due to the great recording effectiveness of multiray stars compared to stars with fewer rays. It was found that the ray distributions from

stars found in the samples behind polyethylene layers of various thickness did not differ one from another within the statistical error.

To calculate the proton doses with energies up to 400 MeV, we used the data on specific filter mesh doses published in article [3]. When the doses caused by the protons with higher energies were determined, their specific doses were taken as being equal to the proton doses with an energy of 400 MeV.

The magnitudes of the doses that were calculated on the basis of the proton spectra that were obtained are given in the table.

FILTER MESH DOSES OF PROTONS IN THE HERMETIC SECTOR OF A SATELLITE FROM THE "COSMOS" SERIES WITH APOGEE ALTITUDE ~ 300 km, WITH FLIGHT PATH ANGLE 65°, mrem/day

Thickness of the filter, g/cm^2	Dose		
	Surface	Mean Mesh	At a depth of 5 cm
0,3	35/46*	7,4/18,6	12/23,2
5,0	23/34	5,6/16,8	8,4/19,6
10	16/27	4,4/15,5	8/19,2
15	15/26	4,0/15,2	8/19,2

*In the numerator E_p < 400 MeV, in the denominator the full dose

The following conclusions can be made on the basis of the data that were presented.

1. The distribution of the dose along the depth of the body is not uniform. The surface dose exceeds almost by a factor of two the dose at the cover depth of the main haemopoeitic organs.

2. A larger screening filter leads only to a considerable reduction in the surface dose, since the screen absorbs only soft protons.

In addition, it can be seen that the main contribution to the surface dose behind thin filters comes from protons whose energy is less than 400 MeV, i.e., mainly protons from the internal radiation belt. Behind a thick filter, the contribution to the mean mesh dose of galactic protons (with energy

greater than 400 MeV) exceeds almost by a factor of three the contribution of protons from the radiation belt.

REFERENCES

/164

1. Barkas, W. H. and Young, D. M., YCRL-2579, September, 1954.

2. Freeden, S. C. and White, R. S., Phys. Rev. Letters, 3, 9 (1959).

3. Zerby, C. D. and Kinney, W. E., Nucl. Instrum. and Methods, 36, 125 (1965).

N75 1647

MEASUREMENT OF SPECTRA AND NEUTRON FLUXES ON ARTIFICIAL EARTH SATELLITES FROM THE "COSMOS" SERIES

V. Ye. Dudkin, Ye. Ye. Kovalev, M. R. Novikova,
Yu. V. Potapov, S. S. Skvortsov, L. N. Smirennyy

ABSTRACT

In 1966-1967 measurements were carried out at the altitudes of 200 to 400 km to determine the spectra and fluxes of fast neutrons inside the hermetically sealed artificial earth satellites of the "Cosmos" series. The detectors used were nuclear emulsions of the B9 and BR types and an emulsion of the P9 type, filled with Li and P. Spectra and fluxes of neutrons in the range of energies from thermal energies to 10 MeV are presented. Neutron doses are also estimated.

In accordance with the program of scientific research on satellites from the "Cosmos" series, measurements of fluxes and spectra of neutrons at altitudes of 200-400 km from the surface of the Earth were carried out in 1966-1967. The neutron detectors used were nuclear emulsions of the P-9 and BR type. Spectra and neutron fluxes with energies from thermal energies to $E_n \sim 10$ MeV were measured. The energy distributions of fast neutrons ($E_n = 1 \div 10$ MeV) were determined from recoil protons. The recoil protons that were formed during the np-scattering of neutrons on the emulsion hydrogen were recorded.

The energy distribution of neutrons was obtained by differentiating the spectrum of the recoil protons

$$\frac{dN}{dE}\,dE = -\frac{d}{dE}\left(\frac{dP}{dE}\,\frac{1}{f}\right)\frac{E}{n\sigma V}\,dE, \qquad (1)$$

where dP/dE is the number of recoil protons in the volume V of the emulsion with energy in the interval E, E + dE, f is a correction coefficient that takes into account the protons that leave the emulsion layer, n is the number of hydrogen atoms in 1 cm^3 of the emulsion and $\sigma(E)$ is the n, p-scattering cross section.

For computational convenience the spectrum of recoil protons in expression (1) is represented in analytical form (as a sum of exponentials).

Neutron fluxes with various energies were obtained with the aid of equation (1) for $E_n > 1$ MeV. In the energy range of neutrons with $E_n < 1$ MeV, the measurements were less reliable because of the large inspection error during the recording of short-travel recoil proton tracks. Therefore, the flux of low energy neutrons was determined in another manner. Special emulsions with a filler were used. The filler that was used was $Li_2B_4O_7$ salt with a boric acid admixture. The great lithium (~ 30 mg/cm^3) and boride (~ 160 mg/cm^3) content in the emulsion and also the use of bonds enriched by B^{10}, made it possible to reduce considerably the sensitivity of the detector to thermal and intermediate neutrons.

In the emulsion, the splitting of $Li^6(n, \alpha)T$ and $B^{10}(n, \alpha)Li^7$ was recorded. The simultaneous irradiation of the emulsions with the lithium and boride filler and without the filler made it possible to separate reliably the decomposition products of Li^6 and B^{10} from the recoil protons. The number of fissions in 1 cm^3 of the N_0 emulsion can be represented in the form /165

$$N_0 = \int_E^\infty N(E)\sigma(E)ndE, \qquad (2)$$

where N(E) is the spectrum of the neutrons, neutrons/(cm^{2}MeV), n is the number of Li^6(B^{10}) atoms in 1 cm^3 of the emulsion, and σ(E) is the reaction cross section of Li^6 + n or B^{10} + n.

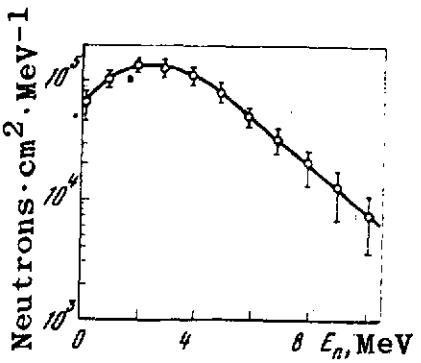

Fig. Differential spectrum of neutrons in the hermetic satellite from the "Cosmos" series at altitudes of 200 - 400 km.

Let us transform expression (2) to the form

$$N_0 = \bar{\sigma} n \int N(E)\,dE = \bar{\sigma} n I, \qquad (3)$$

where $I = \int N(E)\,dE$ is the neutron flux, neutrons/cm^2, $\bar{\sigma}$ is the cross section of the reaction averaged over the neutron spectrum. When $\bar{\sigma}$ was calculated, it was assumed that the form of the spectrum in the energy range $E_n < 1$ MeV was analogous to that obtained in article [1] and was close to 1/E. The neutron fluxes with energy less than 1 MeV that were determined with the aid of equation (3) agree with an accuracy up to 15% in the count of the number of fissions of Li^6 and B^{10}.

The measurements of neutrons at the altitudes 200 - 400 km that were carried out on various satellites from the "Cosmos" series have shown that the form of the neutron spectrum does almost not depend on the orbital parameters. The figure shows the characteristic spectrum of the neutrons in the hermetic part of the satellite. The given spectrum is an average over the satellite trajectory. A particular feature of the spectra that were measured is the presence of a maximum when the energy is $\sim$ 1 MeV. This indicates the vaporizing nature of the neutron spectra formed during inelastic proton interactions from cosmic radiation with the shell and the spacecraft, and with oxygen and nitrogen in the atmosphere. The energy distribution of fast neutrons that was measured in articles [1, 2] on the boundary of the atmosphere ($\sim$ 12 km) and at the altitudes 300-600 km has an analogous form.

The mean flux of neutrons along the satellite orbit with energy ($E_n \lesssim 10$ MeV) which was obtained by integrating the energy distribution is 1.2 $\pm$ 0.4 neutrons/cm^2·sec. This quantity exceeds considerably the values of the albedo fluxes obtained in studies [1 - 3] that were formed as a result of the nuclear interactions of protons from cosmic radiation with oxygen and nitrogen in the air rebounding from the boundary of the atmosphere. The difference can be explained by the fact that along with the albedo neutrons, we recorded in our experiments also neutrons that were leaving the shell and the spacecraft. As the data of article [2] indicate, they contribute substantially to the total flux of the neutrons that are recorded. It should be mentioned that an exact quantitative comparison of the measured fluxes with the data of other authors is difficult, because of the different geometry of the experiments. In addition to this, the fluxes of albedo neutrons depend considerably

on the coordinates of the point at which the observations are carried out in space, and they varied considerably in a wide range from ~ 0.08 to 1.1 neutrons·cm^{-2}·sec^{-1} [1 - 3].

The neutron doses inside the satellite sectors were calculated on the basis of the measured neutron spectra. The contribution of the neutrons to the total dose in rem units was 10 - 15%, according to these calculations, which indicates that it is necessary to take into account the neutrons in the estimate of the radiation hazard of flights. /166

REFERENCES

1. Hess, W. N., et al., Phys. Rev., 116, 445 (1959).

2. Bame, S. J. and Conner, J. P., J. Geophys. Res., 68, 1221 (1963).

3. Trainor, I. H. and Lockwood, I. A., J. Geophys. Res., 69, 3115 (1964).

THE POSSIBILITY OF USING SUPERCONDUCTIVE SYSTEMS IN THE ANALYSIS OF THE COMPOSITION OF COSMIC RAYS

O. P. Anashkin, B. M. Belitskiy, V. B. Brodskiy,
L. V. Kurnosova, N. N. Mikhaylov, L. A. Razorenov,
T. M. Sidyakina, M. I. Fradkin

N75 1647

ABSTRACT

The experimental results on the use of superconductive systems on board of spacecraft are described. To ensure low temperatures in the cryostat under weightlessness, helium was used at a pressure above the critical pressure (a pressure of 2.4 atm and initial temperature of 5.2°). In flight, the temperature was controlled at six points, while the pressure and intensity of the magnetic field were controlled in the solenoids.

The methodical test proved it possible to mount special installations on satellites, with extensive magnetic fields based on superconductive alloys, and particularly, low weights and low power consumption magnetic analyzers.

There are many problems whose solution requires the creation of sufficiently strong magnetic fields aboard satellites and space rockets. In particular, the magnetic fields are necessary for the analysis of charged particles by the sign of the charge and by energy. The usual permanent magnets and electromagnets can only be used with difficulty, the former because of their great weight, and the latter because of their high energy consumption. These difficulties are removed to a considerable extent when superconductive solenoids are used to create strong magnetic fields. In this case, the weight is mainly determined by the weight of the superconductive wire and the cryostat, and there is practically no energy consumption.

At the present time, the design of superconductive solenoids for various purposes is well understood in laboratory conditions. However, there is no experience with these devices when they are lifted on rockets and satellites. The application of superconductive devices during space flights can encounter many difficulties. First, it is necessary to ensure the preservation of the cooling helium solenoid both on the active sector of the flight, and also beyond, under weightlessness. Next, when current is fed into the solenoid on Earth, before the satellite is launched, it is necessary to ensure the preservation of the superconductivity on the active flight sector. Usually, liquid helium is used to cool the solenoids. The

cryostat contains a two-phase system: liquid helium in the lower part and gas in the upper part and in the neck. Under weightless conditions, the liquid helium can flow along the walls and enter the neck. At the same time, very intense vaporization and drop of the helium on the cryostat can occur. As a result, if some preventive measures are not taken, the entire helium quickly vaporizes.

It is more convenient to use helium at a pressure that is slightly higher than the critical pressure. In this case, the helium represents a homogeneous mass and the problem of spreading of the liquid phase under weightless conditions does not exist. It can be shown that the "cold margin" in the case of work with helium in the post-critical state differs little from the "cold margin" in the vessel with the liquid helium. The temperature near the critical point (5.2°K) differs little from the liquid helium temperature (4.2°K) and it is suitable for maintaining the solenoid in the superconductive state. /167

During the experiment it was necessary to check the operation of the superconductive solenoids cooled by the helium in the post-critical state aboard the satellite when current was introduced into the solenoid on Earth before the satellite was launched. Such methodical experiment was carried out aboard the "Cosmos-140" satellite. To carry out the methodical experiment, a special cryostat was constructed whose general form is shown in Fig. 1. To maintain a constant pressure of 2.4 atm.abs., which exceeds somewhat the critical pressure (P = 2.26 atm.abs.), a system of regulating valves was installed in the instrument. A pneumatic relay was used to control the valve. Two small solenoids made from a superconductive wire and the 65-BT alloy were placed in the cryostat. Wire temperature sensors were used to measure the temperatures at several points of the cryostat.

The vessel was launched on the flight at a temperature of 5.2 - 5.3°K and a pressure of 2.4 atm.abs., i.e., with the helium in the post-critical state. The current was introduced in the solenoids on Earth and the solenoids were closed with the aid of wrenches. In one solenoid the field was 9.5 thousand oersted and in the second field, slightly more than 13 thousand oersted. Data about the operation of the temperature sensor, the field sensors and the pressure sensor were obtained during the flight.

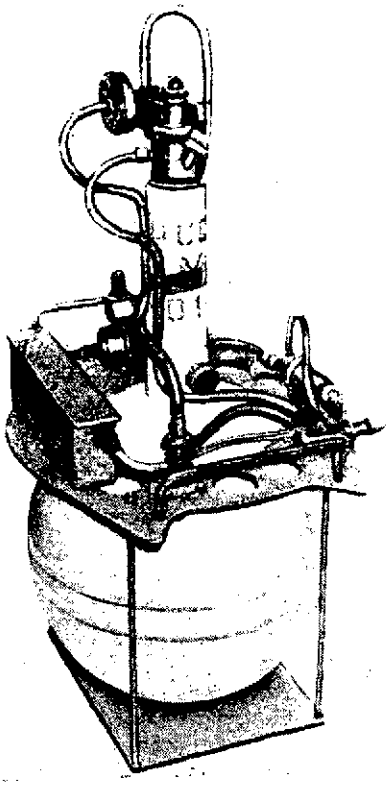

Fig. 1. General view of the cryostat

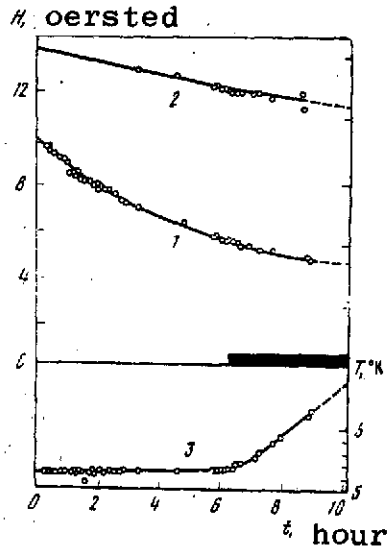

Fig. 2. Variations in the intensity of the magnetic field in the solenoids and the temperature rise in the cryostat during flight.

Explanation in text.

The main results of the measurements were as follows: /168

1. The instrument withstood well the active sector of the flight, on this sector the temperature in the cryostat and the intensity of the field in each solenoid did not vary for all practical purposes.

2. During the first 6 hours of the orbital flight, the temperature in the cryostat according to the data from all sensors varied very slowly and increased by no more than approximately $0.1^{\circ}K$.

3. The pressure in the cryostat remained constant during the entire flight.

4. Six hours after the flight began, the satellite was turned in such a way that the centrifugal force of 10^{-3} g was oriented in the direction of the cryostat neck, i.e., in the direction opposite to the force of gravity in ground conditions. After this, a considerable rise in the temperature began in the cryostat. The heating of the system after the artificial "gravitational force" directed to the neck was introduced, can be explained by the formation of directed convection in the vessel in which the cooling gas began to "descend" to the neck and the hot gas condensed in the working part of the dewar vessel. This should lead to the discharge of preferred cold gas through the valve, and consequently to a faster heating of the system.

Figure 2 gives the variation in the field in each solenoid with time in ground conditions (solid curves 1 and 2). The visible damping of the field is caused by the imperfection of the contacts that were used which could easily be eliminated. The important thing is that the damping of the field during flight was exactly the same as during the conditions on ground (the points indicate flight data). Curve 3 gives the temperature vs. time according to the data from one sensor. It can be seen that the temperature rise began from the instant when the "artificial gravity" appeared (black thick strip). When the temperature reached the value at which the magnitude of the current in the solenoids was critical, a stall occurred in the field.

The following conclusions can be made on the basis of the data obtained.

1. Under space flight conditions helium can be used as the cooling agent at a pressure above the critical pressure.

2. The great static and vibrational loads on the active flight sector do not disturb the superconductive state of the wire in the solenoid windings.

3. The presence of even small forces that simulate gravity, can have considerable effect on the operation of the system. When superconductive devices designed for operation in space are constructed, it is necessary to take into account all possible rotations of the satellite.

4. The methodical experiment that was carried out shows that it is really possible to create on the satellite devices with large magnetic fields, in particular, magnetic particle analyzers with low weights and power consumption.

V. NUCLEAR AND ELECTROMAGNETIC INTERACTIONS
A STUDY OF THE INTERACTION OF NEUTRAL AND CHARGED PARTICLES

V. M. Kim

N75 16473

ABSTRACT

Preliminary experimental data on the number of charged neutral nuclear-active particles were obtained by the Tien-Shan installation at 200 BeV. The ratio of the number of charged particles to the number of neutral particles was 2.1 ± 0.3.

Nuclear-cascade curves in iron and distributions over the portions of energy transferred to neutral pions in lead were obtained for avalanches generated by charged and neutral particles. The characteristics of interactions of the charged neutral particles at the existing experimental errors showed no difference.

The interactions of neutral and charged particles were studied at the Tien-Shan installation. The installation consisted of an ionized calorimeter, five upper Pb series and 15 low Fe series. The calorimeter was covered by two rows of counters of the hodoscope. The counters in the first row of the hodoscope were perpendicular to the counters in the second row. Above the calorimeter (2.5 m) was a block consisting of 5 *cm* Pb.

The ratio of the number of charged particles to the number of neutral particles was measured with and without tracking (with an energy not exceeding 10^{-8} eV). This ratio turned out to be equal to C/N = 2.1 ± 8.3. Thus, if the ratio of the number of protons to the number of neutrons at our altitude is 1.2, the charged pions represent 31^{+6}_{-7}% of the entire flux of nuclear-active particles.

Averaged nuclear-cascade curves were obtained for charged and neutral particles that interact in the iron rows of the ionizing calorimeter (Fig. 1). The calorimeter depth is plotted on the abscissa. It can be seen from the figure that the points coincide within the experimental errors. Each curve was constructed from 100 events with different energies (from 100 to 1000 BeV) the λ absorption corresponding to these curves were 250 ± $g \cdot cm^{-2}$. /170

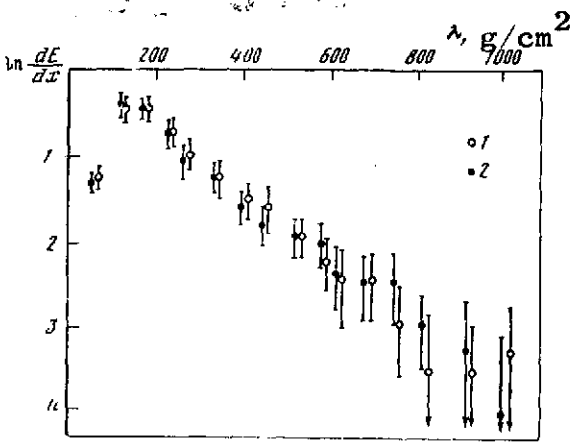

Fig. 1. Nuclear-cascade curves in iron for neutral (1) and charged (2) particles

Figure 2 shows the distribution $K_{n_\varphi}^{0}$ for the charged and neutral particles which interacted in the lead. In the distribution for the charged particles, about half the particles are charged pions; if half of them had a larger K_{π^0}, we would observe the maximum in the range 0.6 - 1.0. Unfortunately, the statistic is not large and the distributions coincide within the statistical error. Both distributions correspond to the mean value

$$K_{\pi^0} = 0{,}25 \pm 0{,}08.$$

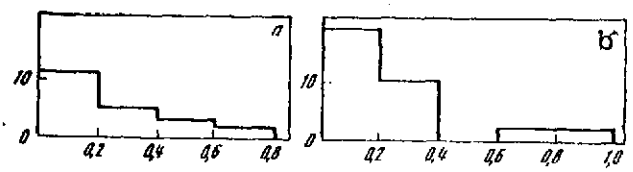

Fig. 2. Distribution by parts of energy transferred in the lead to neutral ions, for charged particles (21 events) (a) and neutral particles (33 events) (b)

On the abscissa, parts of the transferred energy, on the ordinate, the number of cases

Thus, using these methods we were able to find the differences between the interacting neutrons and pions within the experimental error. The statistical errors are large, especially for the distribution K_{π^0}.

The author expresses his gratitude to S. A. Slavatinskiy for use comments.

REFERENCES

1. Guseva, V. V., Denisov, E. V., Dobrotin, N. A., et al., Izv Akad Nauk SSSR, Seriya Fiz, 30, 1574 (1966).

N75 16474

MEASUREMENT OF THE RELATIVISTIC INCREASE IN PRIMARY IONIZATION FORMED BY A CHARGED PARTICLE IN A STREAMER CHAMBER

/171

V. A. Davidenko, B. A. Dolgoshein, V. K. Semenov, S. V. Somov

ABSTRACT

The relative contribution of the secondary ionization to the measured ionization depending on the time of delay of the high-voltage pulse supply is estimated.

The specific primary ionization formed by a charged particle in a streamer chamber can be measured in the case when, during the time between the passage of the particle and the time when the high-voltage pulse arrives at the electrode of the chamber, the secondary ionization electrons diffuse at a distance which is smaller than the radius of the streamer. Under this condition the secondary ionization electrons do not appear in the form of separate streamers but are recorded either as one streamer that grew in the group of electrons (in the case when little energy is transferred) or have the form of a characteristic branch on the tract (in the case when a large amount of energy is transferred).

Figure 1 gives for Ne, Ar, and He the time curves for the lag in the relative contribution of secondary ionization to the measured ionization. It follows from the relations that are given, that when the characteristic radius of the streamer is ~ 0.4 mm at a pressure close to atmospheric pressure, with a real variable minimum lag in the arrival of the high-voltage pulse (100-200 nsec), He is most suitable for measuring the primary ionization. Therefore, when the possibility of measuring primary ionization was verified experimentally, the chamber was filled with helium up to a pressure of 0.4 atm.

The tracks of electrons with energy ~ 1.7 MeV from the source Sr^{90} were photographed through a triple-cascade electron-optical converter. The experimental data obtained, which depended on the time lag in the root mean square deviations of the number of streamers on the given length of the track, are given in Fig. 2 in units of the standard Poisson deviation.

C-4

The data given indicate a gradual transition from the Poisson distribution which characterizes the primary ionization to the Landau distribution describing the fluctuations in the total ionization. Qualitatively, this transition is illustrated in Figs. 3 and 4, in which the experimental histograms that were obtained for lag times of 0.25 and 15 msec are compared with the Poisson distribution and the Landau distribution. Thus, Figs. 2 - 4 show that for small time lags, we can measure the primary ionization, and for large time lags, the total ionization formed by the particle in the gas of the chamber. From the standpoint of the measurement accuracy of ionizing capacity, the most preferable measurement is the measurement of primary ionization. /172

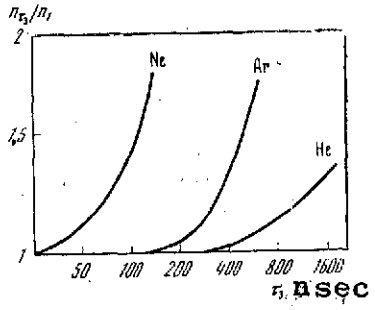

Fig. 1

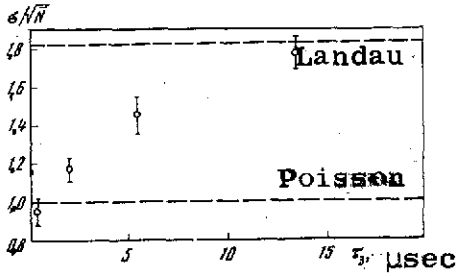

Fig. 2 /171

Fig. 1. Ratio of measured ionization to primary ionization vs. the time lag. The gas pressure is 1 atm, and the radius of the streamer is 0.4 mm

Fig. 2. Root mean square deviations for the number of streamers on the given length of the track vs. time lag

As shown in Fig. 5, the results obtained from measuring the primary ionization in a sufficiently wide interval do not depend on the operating regime of the chamber (the form and amplitude of the high-voltage pulse, the time lag and the length of the streamer). Using these results, we measured the relativistic increase in primary ionization in the interval E/mc^2 from 3 to 500. When the relativistic increase was measured, the chamber was filled with helium up to a pressure of 0.6 atm. The lag in the arrival of the high-voltage pulse was 200 nsec. The chamber was exposed to a beam of electrons with known pulse obtained from the electronic FIAN SSSR [Physics Institute named after P. N. Lebedev of the Academy /173

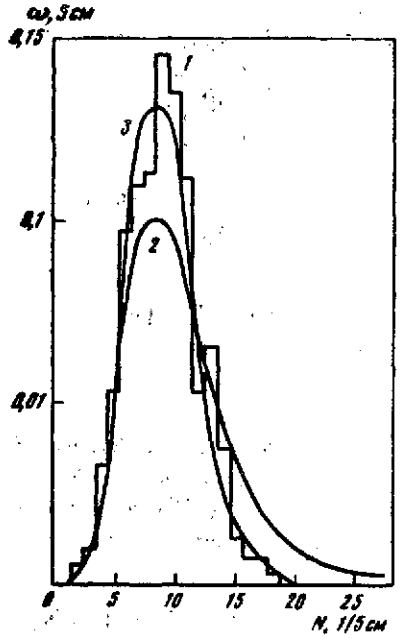

Fig. 3

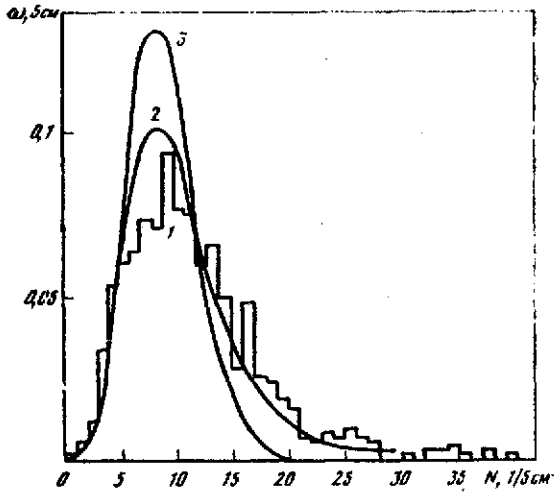

Fig. 4

Fig. 3. Comparison of distribution obtained experimentally (1) the number of streamers per unit length of track with Poisson distributions (2) and Landau distributions (3) at an He pressure of 0.4 atm, time lag 250 nsec.

Fig. 4. Comparison of the distribution for the number of streamers per unit length of track obtained experimentally at an He pressure of 0.4 atm, with time lag of 4 4 msec with the Poisson and Landau distribution.

Same notation as in Fig. 3.

of Sciences, USSR] synchroton. The experimental data from the measurement of the relativistic increase in primary ionization are given in Fig. 6.

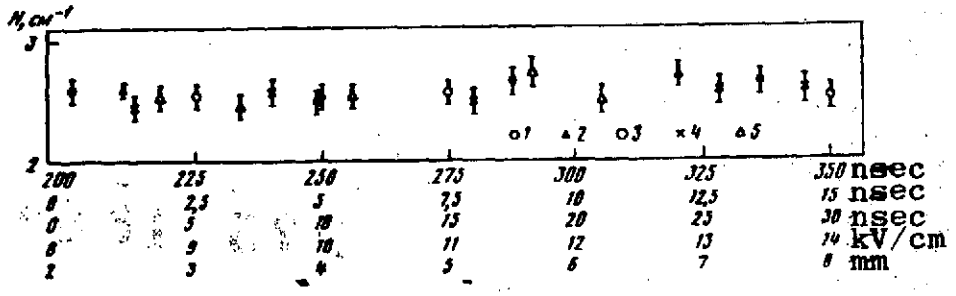

Fig. 5. Effect of change in the operating regime of the chamber on the number of streamers obtained at an He pressure of 0.6 atm.

1--Lag, 2--decay time, 3--build-up time, 4--intensity, 5--length of streamer.

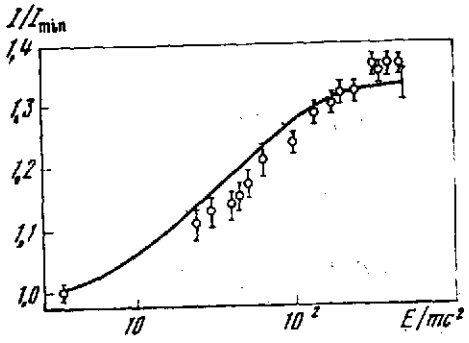

Fig. 6. Relativistic increase in primary ionization measured in the streamer chamber filled with helium at a pressure of 0.6 atm.

Solid curve--theoretical calculation of P. Budini [1] in which corrections were introduced for the overlap of the streamers, points indicate experimental data.

The authors express their gratitude to Professor P. A. Cerenkov for providing the possibility of working with the FIAN synchrotron.

REFERENCES

1. Budini, P., Taffara, L. and Viola, C. Nuovo Cimento, 18 (5) (1960).

VI. PROBLEMS OF METHOD AND EQUIPMENT INSTALLATION FOR THE SEARCH OF HEAVY NONRELATIVISTIC PARTICLES AT SEA LEVEL

A. M. Gal'per, V. A. Gomozov, A. F. Iyudin, Yu. D. Kotov, B. I. Luchkov, A. A. Prilepin, A. I. Rogovskiy

N75 16475

ABSTRACT

A detector of heavy nonrelativistic sea-level particles is described. Selection of events is based on the dependence of the particle path on particle mass at a given speed. Cerenkov counters with $\beta_{tr} = 0.59$ are used as speed selectors.

Mounted above the detector is a scintillation counter for measuring the ionization caused by a particle. The particle track is recordeu by spark chambers.

In the last few years many studies were made that were devoted to the search for quarks [1 - 10]. Relativistic particles with a small charge were sought in cosmic rays both at sea level [1] and mountain altitudes [3]. In all these studies, essentially the same principle was used: the ionization was measured in several counters that were placed one above another. In article [2] a spark chamber was used to increase the reliability with which the results were interpreted. In the studies that were made, the existence of relativistic particles leading to ionization corresponding to a fractional charge was not demonstrated. These problems were discussed in detail at the Moscow Conference on quarks on March 3-4, 1966.

In this connection, we proposed a principle, and an installation was prepared that made it possible to record nonrelativistic heavy particles in cosmic rays both with a fractional charge (1/3e) and a non-fractional charge (1e). The block diagram of the installation is given in Fig. 1. The heavy particles were selected on the basis of the relation between the particle path and its mass for the given velocity.

The velocity selector used consisted of two Cerenkov counters (CH1 and Ch2) made from blocks of heavy TF-3 glass whose dimensions were 200 x 200 x 80 mm. The threshold rate of the counters was $\beta_{tr} = 0.59$. Events were recorded when the pulses of the scintillation counters C1 and C2 coincided in the absence of pulses from the Ch1 and Ch2. Thus, particles were selected which passed through the entire installation whose velocity in

Ch1 and Ch2 was less than β_{tr}. A block of lead which was 136 g/cm^2 thick was mounted between Ch2 and C2. Therefore, particles whose mass was less than 3 BeV and $\beta \leq \beta_{tr}$ were absorbed in it. The dimensions of C1 and C2 were 160 x 160 x 15 mm.

Three spark chambers, each in two 10-mm intervals, make it possible to select single particles passing through the installation. To determine the charge of the heavy particles and to separate them from the muons, protons, deuterons and α-particles which can be recorded in the counts of the Cerenkov counters, the scintillation counter I that measured the ionization was used. The counter was a scintillator with dimensions 130 x 130 x 50 mm, which was visible in the FEU-49 photomultiplier through a plexiglas light guide. The geometrical factor of the installation was 35 cm^2·ster. The design of the installation makes it possible to take easily into account a geometrical factor up to $2 \cdot 10^3$ cm^2·ster. The pulses from the counters C1 and C2 arrive at the CC coincidence circuit through the amplifiers with a lag of 50 nsec with a resolution time of 16 nsec. The pulses from Ch1 and Ch2 arrive to the shaping circuit (SC) at the output from which a pulse is generated whose duration is 100 nsec, if a pulse arrived at the input from at least one Cerenkov counter. The pulse from the shaping circuit arrives at the anti-coincidence circuit (AC) in the forbidden channel. The pulse from I arrives at the input of the amplifier of the C1-8 oscillograph. The scanner of the oscillograph is activated by the pulse from the anti-coincidence circuit. The screen of the oscillograph and the spark chambers are photographed by a photorecorder of the RFk-5 type. To eliminate the effect of pickups from the ionization chamber, a high voltage pulse arriving to the ionization chamber from the pulse voltage generator was delayed by 1.2 msec before the anti-coincidence circuit was triggered.

/175

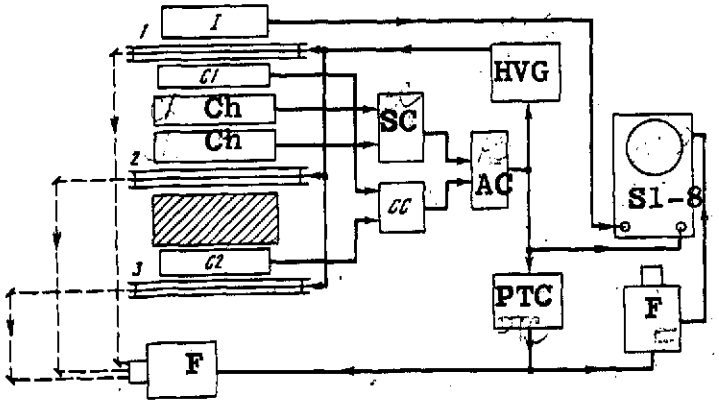

Fig. 1. Block diagram of the installation.

I--Ionizing spectrometer counter; C1, C2--scintillation coincidence counters; Ch1, Ch2--threshold Cerenkov counters; 1 - 3--spark chambers; HVG--high voltage pulse generator; SC--shaping circuit; CC--coincidence circuit; AC--anti-coincidence circuit; PTC--photo camera triggering circuit; F--RFK-5 photocameras; S1-8--oscillograph

The installation is graduated daily by the cosmic muons when Ch1 and Ch2 are switched on. The distribution halfwidth in the counter I obtained from the muons is 25%. The effectiveness of the Cerenkov counters which is measured for muons from the ratio of the counting rate of the triple-coincidences (C1, C2, Ch) to the counting rate of the double coincidences (C1, C2) is 98.5% for each Cerenkov counter. Fig. 2 gives the ionization distribution in the counter from muons, protons, deuterons and α-particles that can be recorded during the coincidence loss of the Cerenkov counters. The amplitude resolution curve for muons was used when the distributions were constructed. It was assumed that the pulse spectra of μ, p, d and α were similar at sea level. Figure 2 shows that the probability that protons and muons will be recorded in the interval 2.5 - 3.5 is $\leq 10^{-3}$ (by ionization). Since the probability of coincidence losses in the Cerenkov counters is $\leq 1.5 \cdot 10^{-2}$, the flux can be detected at the level $(1.5 \cdot 10^{-2})^2 \cdot 10^{-3} = 2 \cdot 10^{-7}$ from the number of protons. /17

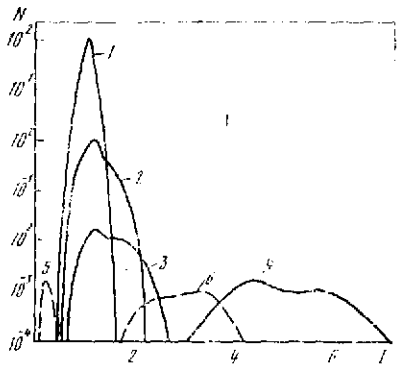

Fig. 2. Distribution by ionization in counter I of (1) muons, (2) protons, (3) deuterons, and (4) α-particles which can be recorded in the counts of the Cerenkov counters. Dashed curves indicate assumed distributions of quarks with a charge 1/3 e (5) and 1e (6) and mass 10 BeV

The ionization (in relative units) is plotted on the abscissa, and the number of cases on the ordinate

The installation was used at sea level for a period of 30 hours. In this period, the operating rate was 3 h^{-1}. However, after the traces in the spark chamber and the pulses from the ionizing counter were analyzed, not a single "quark-like case" remained.

In conclusion, the authors express their gratitude to V. G. Kirillov-Ugryumov and I. L. Rozental for their interest in this study.

REFERENCES

1. Sunyar, A. W. and Schwarzchild, A. Z., Phys. Rev., 136, B 1157 (1964).

2. Buhler-Broglin, A., Nuovo cimento, 45 (20) (1966).

3. Bowen, Th., Delise, D. A., Kalbach, R. M. and Mortara, L. B., Phys. Rev. Letters, 13, 728 (1964).

4. Barton, J. C. and Stockel, A. M., Phys. Rev. Letters, 17, 360 (1966).

5. Dorfan, D. E., Eades, J., Lederman, L. M., Lee, W. and Ting, C. C., Phys. Rev. Letters, 14, 999 (1965).

6. Hagopian, V., Selove, W., Ehrlich, R., Leboy, E., et al., Phys. Rev. Letters, 13, 280 (1964).

7. Bingham, H. H., Dickinson, M., Diebold, R., Kosh, W., et al., Phys. Rev. Letters, 9, 201 (1964).

8. Chupka, W. A., et al., Phys. Rev. Letters, 17, 60 (1966).

9. Sinanoglu, O., et al., Phys. Rev. Letters, 17, 785 (1966).

10. Bennet, W. R., Phys. Rev. Letters, 17, 1196 (1966).

THE FEASIBILITY OF CONSTRUCTING A STABILIZING PLATFORM FOR A COSMIC RAY STATION

I. A. Akhmadeyev, V. M. Bednazhevskiy, E. P. Tolpygin

N75 16476

ABSTRACT

The paper considers the feasibility of constructing platforms stabilizing cosmic ray stations on a spacecraft using a three-stage universal joint. The stabilization system consists of three independent electrohydraulic drives.

Hydrocylinders of the BGU-3P type are recommended as actuating mechanisms for horizontal stabilization, while hydromotors PM No. 2.5A or MP = 0.25/10, MB = 0.4/10, MB-0.63/10 are recommended for azimuth stabilization.

The PD No. 1.5 pump is suitable for use as a variable capacity pump.

One way of stabilizing a cosmic ray station on a space craft is the use of a three-stage universal joint with a stabilization system consisting of three independent electrohydraulic drive mechanisms. We will consider the position of the cardan above the transverse axis of the spacecraft near the stern.

Selection of the Types of Hydraulic Mechanisms /1'

The moments acting on the cardan are determined from the equations given in article [1].

For the drive mechanism which triggers rolling motion, the equation

$$I_c\ddot{\theta} + mr_1^2\ddot{\theta} + mgr_1\sin\theta - mr_1r_2\ddot{\psi}\cos(\psi-\theta) + mr_1r_2\dot{\psi}^2\sin(\psi-\theta) + M_{fr} = M_{st} \quad (1)$$

is valid, where I_c is the central moment of inertia, θ is the angle at which the platform deviates from the true vertical, m is the mass of the station and the cardan; g is acceleration due to gravity; r_1 is the radius of the pendular motion, r_2

is the displacement of the center of oscillation of the spacecraft relative to the center of gravity of the cardan suspension; ψ is the angle of roll of the spacecraft; M_{fr} is the frictional moment; and M_{st} is the moment necessary to maintain the platform in horizontal position. To calculate the required value of M_{st}, we will take the following values of the quantities in equation (1),

$$\psi = 30^{\circ};\ T = 15 \text{ sec};\ \theta = 30';\ I_c = 900 \text{ kg}\cdot\text{m}\cdot\text{sec}^2;$$

$$M_{fr} = 60 \text{ kg}\cdot\text{m};\ r_2 = 10 \text{ m};\ m - 1350 \text{ kg}\cdot\text{sec}^2/\text{m};$$

T is the oscillation period.

For the most unfavorable case, when all moments have the same sign, $M_{st.max}$ (in kg·m) for various values of the pendular radius r (in m) has the values:

$M_{st.max} = 61$ when $r_1 = 0$; $M_{st.max} = 210$ when $r_1 = 0.1$;

$M_{st.max} = 370$ when $r_1 = 0.2$.

For the drive mechanism which triggers pitching motion, the equation for the moments has the form

$$I_c\ddot{\theta} + mr_1^2\ddot{\theta} + mgr_1 \sin\theta - mr_1r_2\ddot{\psi}\sin(\psi - \theta) - mr_1r_2\dot{\psi}^2\cos(\psi - \theta) + M_{fr} = M_{st} \tag{2}$$

The mnemonic subscripts in the equation have the same meaning as in equation (1), however, for pitching motion. M_{st} will be calculated for the following values of the quantities in equation (2),

$$\psi = 30^{\circ},\ T = 15 \text{ sec};\ \theta = 30';\ I_c = 1800 \text{ kg}\cdot\text{m}\cdot\text{sec}^2;\ r_2 = 60 \text{ m}.$$

The maximum required values of the moments in this case are

$M_{st.max} = 62$ kg·m for $r_1 = 0$; $M_{st.max} = 800$ kg·m for $r_1 = 0.1$ m.

In the case when the platform is in the middle of the spacecraft,

$$M_{st.max} = 210 \text{ kg·m for } r_1 = 0.1 \text{ and } r_2 = 10 \text{ m.}$$

The hydrocylinder of the PGU-3B type [2] whose working piston diameter is 6.5 cm with a maximum travel of 85 cm and a nominal pressure of 100 atm which weighs 12.5 kg can be used as the actuating mechanism (AM) for the hydraulic drive mechanisms. In this case, to insure rolling angles of $\pm 30^{\circ}$, the distance from the cardan axis to the spot where the hydrocylinder is mounted must be $\simeq$ 80 cm. To obtain $M_{st.max}$ = 800 kg·m, a pressure of 30 atm is needed. For a discharge velocity ψ = 0.22 1/sec the required consumption is 10 liters/min.

The parameters that were mentioned ensure the serial variable capacity pumping of the PD No. 1.5 type [2] with the following engineering characteristics: maximum capacity 26.5 liters/min, a nominal pressure of 100 atm, a weight of 20 kg. The electromotive drive can be any drive with a power not less than 2.25 keV on the shift and n = 2950 rpm. /17

When the same type of pump is used in the azimuthal stabilization drive as the triggering mechanism, the hydromotor of the PM No. 2.5 type [2] with a transmission of i $\simeq$ 30 through the ball-roller path can be used as the hydraulic drive. If transmission takes place through a simple reductor i = 2 = 3, hydraulic motors with a large moment of the MP-0.25/10, MP-0.4/10 or MP-0.63/10 type can be used as the triggering mechanism. The lowest permissible pendular motion radius of the cardan whose axis of rotation lies along the transverse axis of the spacecraft is 0.3 - 0.4 m for the selected hydraulic drive, and for the cardan ring whose axis is perpendicular to the transverse axis up to 0.1 - 0.2 m when the platforms are on the stern, and up to 0.3 - 0.4 m, when the platforms are in the middle part of the spacecraft.

Structural Diagram of the Drive Mechanism

The hydraulic drive mechanism consists of the following elements: an electromechanical converter, a hydraulic amplifier of the "nozzle-valve" type, a slide valve hydraulic amplifier, a pump with variable capacity and the triggering mechanism. The hydraulic drive mechanism has rigid feedback from the pipe of the variable capacity pump to the slide valve. The output element of the hydraulic drive is the electromechanical converter through whose coil arrives the control voltage from the electronic amplifier, and the output is the shaft (or rod) of the triggering

mechanism. The simplified structural diagram of the drive mechanism selected on the basis of studies [3 - 5] taking into account many nonlinearities has the form shown in Fig. 1, where $W_i(p)$ ($i = 1, 2, \ldots, 5$) are the transfer functions that characterize the links

$W_1(p) = \frac{i(p)}{U_y(p)} = \frac{k_1}{T_1 p + 1}$ the windings of the electromagnetical converter;

$W_2(p) = \frac{\Delta P_1(p)}{M_0(p)} = \frac{k_2}{T_2^2 p^2 + 2\xi_2 T_2 p + 1}$ the "nozzle-throttle" hydraulic amplifier;

$W_3(p) = \frac{X(p)}{\Delta P(p)} = \frac{k_3}{T_3 p + 1}$ the slide valve hydraulic amplifier;

$W_4(p) = \frac{\beta(p)}{\Delta X(p)} = \frac{k_4}{p(T_4 p + 1)}$ the pipe of the variable capacity pump;

$W_5(p) = \frac{p\varphi(p)}{\Delta\beta(p)} = \frac{k_5}{T_5^2 p^2 + 2\xi_5 T_5 p + 1}$ the triggering mechanism with the load

$W_{fd}(p) = \frac{\beta_2(p)}{M_1(p)} = k_6(T_6 p + 1)$ feedback after loading

/179

The coefficients and time constants of the transfer functions have the following values:

$k_1 = 0.1 \frac{ma}{b}$; $T_1 = 2 \cdot 10^{-3}$ sec; $b_i = 0.18$ ma;

$k_2 = 1$ kg·cm^{-2}·ma

$T_2 = 4.6 \cdot 10^{-3}$ sec; $\xi_2 = 0.32$; $k_3 = 6.4 \cdot 10^{-2}$ cm^{1}kg^{-1}·cm^2;

$T_3 = 0.01$ sec; $c_3 = 0.26$ kg/cm^2; $b_x = 0.02$ cm; $c_x = 0.1$ cm;

$k_4 = 100$ rad/cm·sec; $T_4 = 2.3 \cdot 10^{-2}$ sec; $c_4 = 7.4 \cdot 10^{-2}$ cm;

$b_\beta = 0.524$ rad; $k_{fd} = 11.6$ kg·cm^{-2}·rad; $T_6 = 0.065$ sec.

For the drive mechanism which triggers the rolling and pitching motion, the values are:

Rolling Motion:	Pitching Motion:
$T_5 = 0.05$ sec	$T_5 = 0.07$ sec
$\xi_5 = 0.4$	$\xi_5 = 0.5$
$k_5 = 1.17$ sec^{-1}.	$k_6 = 0.35 \cdot 10^{-6}$ kg^{-1}·cm^{-1}.

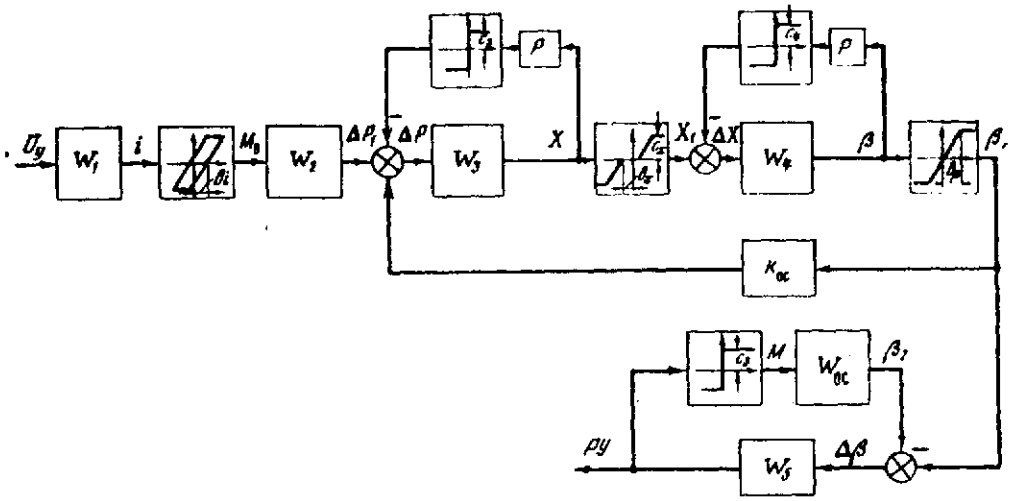

Fig. 1. Structural diagram of the hydraulic drive mechanism.

For the azimuth stabilization drive (when it operates on the hydromotor PM No. 2.5A with $i = 30$ and $I_c = 2100$ kg·msec^2) $k_5 = 5.5$ sec^{-1}, $T_5 = 0.35$ sec, $\xi_5 = 2.75$; $k_6 = 5 \cdot 10^{-5}$ kg^{-1}·cm^{-1}.

The length of the pipes connecting the pump with the triggering mechanism was taken as 2 m in the calculations. In practice it must be selected as small as possible. During the linearization of a number of nonlinearities in the regulated part of the hydraulic drive a variable voltage $c\omega = 440$ 1/sec and $U = 60$ V is supplied to the high-resistance coils of the electromechanical converter.

The experimental amplitude-phase characteristics of the open-drive mechanism (input value U_y, output value, P_y, A--rotary angle of the pipe) when a linearized voltage is supplied are shown in Fig. 2 and coincide, for all practical purposes, with the characteristics that were calculated on the basis of the structure given in Fig. 1. These relations (Fig. 2) are also preserved when the dynamics of the "variable capacity pump-loaded hydromotor" branch are taken into account.

From Fig. 2 it can be seen that the characteristics of the drive mechanism depend considerably on the magnitude of the input signal. Experimental and theoretical studies have shown that the part of the hydraulic drive mechanism from the electromechanical converter including the pipe of the variable capacity

pump can be described by the transfer function 9 (see Fig. 1)

$$W_{hd}(p) = \frac{\beta(p)}{U_y(p)} = \frac{k_{hd}e^{-\tau p}}{T_{hd}p + 1},$$

where $k_{hd} = 1.25 \cdot 10^{-2}$ rad/V is the amplification factor of the part described; T is the time constant and τ is the time lag.

The quantities τ and T_{hd} vary with the variation in the input voltage. These relations are plotted in Fig. 3. The experience obtained from using the above-mentioned hydraulic drive system in stabilization systems has shown that it will ensure the required accuracy during operation under spacecraft conditions. This question can be analyzed in greater detail in a study devoted to an investigation of the dynamics of the stabilizer under more precise disturbing interactions.

/180

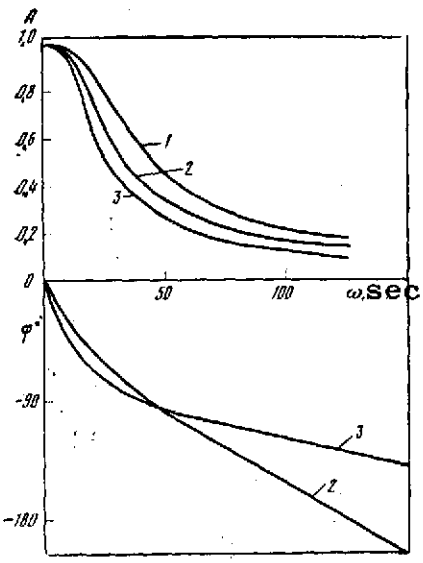

Fig. 2

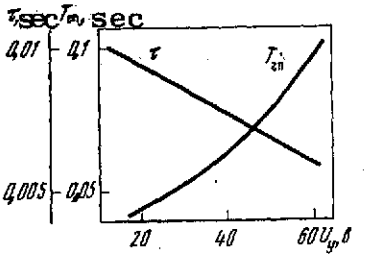

Fig. 3

Fig. 2. Amplitude-phase characteristics for various values of the input voltage

1--when U_u = 20 V

2--when U_y = 40 V

3--when U_y = 60 V

A--Relative amplitude of the rotary angle of the pump pipe; φ--phase.

Fig. 3. The relations $\tau = f(U_y)$ and $T_{hd} = f(U_y)$.

Conclusions

1. It is possible to construct a stabilizing platform in a cosmic ray station using a hydraulic drive mechanism.

2. It is useful to use a pump of the PID No. 1.5 type as the variable capacity pump.

3. The triggering mechanisms of the drives can be: type PGU-3B hydrocylinders; for azimuth stabilization a hydromotor of the PIM No. 2.5A type, or hydromotors with a large moment of the MP-0.25/10, MP-0.4/10 and MP-0.63/10 type, depending on the design of the universal joint.

4. The regulated part of the hydraulic drive mechanism can be represented in approximate calculations as an aperiodic branch with a lag which simplifies considerably the analysis and synthesis of the closed drive mechanism.

REFERENCES

1. Akhmadeyev, I. A., "One method of stabilizing a telescope and a neutron monitor on a spacecraft," in the collection Kosmicheskie luchi, No. 12, 155 (1970).

2. Gidravlicheskoe oborudovanik. Katalog-spravochnik, [Hydraulic Equipment. Handbook-Catalogue], No. 1, Moscow, 1967.

3. Gamynin, N. W., Osnovy sledyashchego gidravlicheskogo privoda, [Basic Principles of a Hydraulic Servomechanism], Oborongiz Publs., 1962.

4. Tolpygin, Ye. P., Nelineynost' kharakteristik reguliruye mogo gidroprivoda ob"emnogo tipa, [The Nonlinearity of the Characteristics of a Regulated Hydraulic Drive Mechanism of the Displacement Type," Gidroprivody i gidroavtomatika, [Hydraulic Drives and Hydraulic Automation], Vol. II, Leningrad, 1968.

5. Kulagin, A. V., Demidov, Yu. S., Prokof'ev, V. N. and Kondakov, L. A., Osnovy teorii i konstruirovaniya ob"enmykh gidroperedach, [Fundamentals in the Theory and Design of Hydrostatic Transmission Gears], Moscow, "Vysshaya shkola" Publs., 1963.

N75 16477

LARGE NEUTRON COUNTERS FOR SUPERMONITORS

/181

Ya. L. Blokh, L. I. Dorman, V. K. Koiyava, V. Kh. Leonov, Kh. Narziev, V. G. Chaykovskiy

ABSTRACT

The paper describes large neutron counters of the CHM-15 type designed for the neutron supermonitor with an area of about 20 m^2. Statistical accuracy of the counters is 0.1% per 2 hours. Dimensions: length--2 m; diameter--150 mm; pressure--200 mm Hg. The counters are filled with BF_3 gas containing over 80% of B^{10}.

In an analysis of data from a world-wide network of stations which record continuously cosmic rays, the statistical accuracy of each individual station is inadequate for most investigations. In order to detect certain small effects, we used averaged data from these stations [1 - 4]. But this method is not very justified, since the data from these stations depend on their location on the surface of the Earth and can differ considerably.

Therefore, recently, devices with great statistical accuracy, so-called super instruments [5] became the object of attention. A neutron supermonitor for large neutron counters [6] was developed in Canada. These counters are 2000 mm long and their diameter is 150 mm. The working volume of the counters is 30 times larger than the volume of the old counters that were 1000 mm long, whose diameter was 40 mm. These counters were used in a monitor developed by George Simpson [7]. These counters made it possible to design and use for recording a neutron monitor, whose effective area was on the order of 20 m^2, i.e., one order of magnitude higher than that of the Simpson monitor [7]. Analogous large counters for the recording of slow neutrons were developed in the Soviet Union. These counters were designed for a neutron supermonitor, whose statistical accuracy is on the order of 0.1% in 2 hours.

The main requirement on the neutron monitor is that it ensure a constant recording level for a long time period with an accuracy not worse than 0.1%. The main requirements on the CHM-15 counters were determined by the particular current manufacturing technological features of large neutron counters, and also by the stable electronic features (amplifier, discriminator, feed sources, etc.) that operate 24 hours over many years.

The CHM-15 counters are filled with BF_3 gas enriched by more than 80% with the isotope B^{10}. The counters are manufactured from a steel pipe (steel X19H9T and X18H10T) whose walls are not more than 1 mm thick. A tungsten wire, whose diameter is 0.06 mm, is used as the anode. C-49-2 glass serves as the insulator, and the outlets for the wires in the insulator are made from the H29K18 alloy. Hermetization is obtained through argon-arch welding. In addition to the two main electrodes, there are also two other protective rings (one on each side).

For greater reliability, the outlets from the anode and cathode are doubled and read out from both ends of the counter. The maximum length is 2090 ± 10 mm, and the maximum diameter is 150 ± 3 mm. The effective working length is 200 mm. The gas pressure in the counter is on the order of 200 mm Hg. The range of the counter characteristics does not exceed 200 V. And the inclination of the plateau of the counter characteristic is not more than 3% per 100 V. The range of the plateau of the discrimination characteristics is not less than 10 mV at the output for a sensitivity on the order of 35 mV. The inclination of the plateau of the discrimination characteristic is 0.15 (in % for a % change in the threshold of the discriminator). The nominal operating voltage is in the range 2600-2800 V. The background noise from the counter due to radioactivity does not exceed 5 pulses/min, which is 1-2% of the number of recorded neutrons of cosmic origin. The resistance in the installation of the outlet from the anode does not exceed 10 megohm. The counter preserves its parameters in the temperature interval 30 - 40°C. The measured differential spectra of the counters that were prepared have shown that they have a minimum which is adequate for discriminating noise from the neutron pulses.

However, the spectra obtained were worse than those in the Canadian counters. This is explained by the fact that the gas that was used does not have the necessary quality. However, these data show that when the required stability of the amplifier and of the feed voltages are maintained, the CHM-15 counters can be used for the continuous recording of cosmic rays. /1

REFERENCES

1. Dorman, I. L., Variatsii kosmicheskikh luchey, [Cosmic Ray Variations], Gostekhizdat, 1957.

2. Dorman, I. L., Variatsii kosmicheskikh luchey i issledovanie kosmosa, [Cosmic Ray Variations and a Study of Space], USSR Acad. of Sci. Publs., 1963.

3. Dorman, I. L., Blokh, Ya. L. and Kaminer, N. S., in the collection Kosmicheskie luchi, No. 4, 5 (1951).

4. Ya. L. Blokh, Dorman, L. I. and Kaminer, N. S., Trudy Mezhdunar. konf. po kosmicheskim lucham, [Proceedings of the International Conference on Cosmic Rays], Vol. 4, Moscow, 1960, p. 178.

5. Palmeira, R. and Williams, R., Nuovo cimento 8, 353 (1958).

6. Carmichael, H., NM-64. Neutron Monitor Specification, Deep River Laboratory, 3 August 1962.

7. Simpson, J. A., Neutron Monitor, Chicago, 1955.

EFFECT OF ELECTRON DIVERGENCE IN AIR GAPS ON THE MEASUREMENT OF THE ENERGY OF CASCADES IN EMULSION CHAMBERS

A. V. Apanasenko, L. T. Baradzey, Ye. A. Kanevskaya, Yu. A. Smorodin

N75 16478

ABSTRACT

The effect of an increase in electron density in the vicinity of the cascade axis caused by an avalanche passing through the gap between lead filters of the emulsion chamber was investigated experimentally. Optical densities were measured in circles with radii 48, 58, 84 and 140 μm in three x-ray films spaced at 400, 800 and 1200 μm from the filter surface having a thickness of 6 cascade units. The optical densities of blackening spots caused by electron-photon cascades of 1-2, 2-7 and > 7 BeV energies were measured.

The number of electrons inside the circles with radii 25, 50, 100 and 150 μm were calculated in three showers with energies 4.4×10^{11}, 7×10^{11} and 10^{12} eV found in three layers of 400 micron nuclear emulsion without a substrate.

The results prove the presence of a gap between the filter and the nuclear emulsion which results in the underestimation of energy by several tenths of a percent.

For energies exceeding 10^{12} eV, the energy of γ-quanta is the only quantity which is accessible to measurement in practice and which characterizes the energy distribution among the particles generated in nuclear interactions. This fact explains the interest in methods which measure the energy of electron-photon cascades with the aid of nuclear and x-ray emulsions in which three-dimensional resolution which is adequate for measuring the energy of individual γ-quanta is attained.

The methods which are currently used to measure the energy of cascades, are based on a comparison of the densities of the cascade electrons at small distances from the axis which is determined by counting the electron traces in the nuclear emulsions or by photometering the black spots on x-ray films with the density of the electrons calculated in accordance with three-dimensional cascade theory.

Theoretical calculation of the three-dimensional distribution of electrons were carried out for a homogeneous medium, whereas in emulsion chambers, filters made from a heavy material are used (usually lead) which is interspersed with emulsion layers. The thickness of the gaps between the filters is, as a rule, a magnitude $\sim 10^3$ μm which is comparable with the length of the cascade unit in the lead. In article [1] the result was obtained that in first approximation, the taking into account the homogeneity of the medium reduces to an increase in the Mollier radius. The three-dimensional distribution of electrons in the cascade developing in such a medium broadens. /183

The three-dimensional distribution of the electrons moving at different angles to the avalanche axis changes when the cascade passes through the gap between the filter and the photo material. The three-dimensional distribution of electrons which is found in the emulsion layer will differ from the distribution of the electrons in the filter.

To investigate this effect, we measured the densities of the black spots which pass successively through the same cascade on film. The measurements were carried out with x-ray films of the PT-6 type. The PT-6 film whose total thickness is 240 μm has two 35 μm thick emulsion layers, one on each side of the celluloid base.

The films were exposed under a lead filter to 6-cascade units in paper envelopes. Each envelope contained three films. The thickness of the packet wall was ~ 200 μm and the thickness of the paper inserts between the films was ~ 80 μm. When the packet was assembled, air gaps of ~ 30-40 μm could be formed between the layers. The total distances from the lower surface of the lead filter to the middle of the films were, respectively, ~ 400, 800 and 1200 μm. These distances could fluctuate in individual packets. An estimate of the fluctuations gives the value $\sim 20\%$.

To increase the accuracy of the comparison of the black spots all three films were developed simultaneously. Black spots from γ-quanta with an energy from 1 to 200 BeV, whose zenith angle did not exceed 30° were sampled. The films were photometered on a microphotometer [2]. The mean optical black spots $D = \lg\frac{I_0}{I}$ were measured in circles with radii $r_1 = 48$, $r_2 = 58$, $r_3 = 84$ and $r_4 = 140$ μm. The average results of the measurements are given in Table 1. The number at the top represents the ratio D_i of the black spots in the film studied to the black spots D_{ib} in the upper film, the number at the bottom represents the ratio of the energy of the cascades

determined from the black spots in the given and the upper films. The ratio of these energies, which is given in the table, was close to the ratio of the mean densities of the electrons in the circles of the given radius. The results given in Table 1 show that the effect of the divergence of the cascade electrons in the gap leads to a systematic error which reduces the measured energy of the cascade. The magnitude of the effect decreases somewhat as the energy of the cascades increases. It should be noted that the results were obtained for a fixed thickness of the filter of 6 t-units. When thicker filters are used, one can expect an increase in the effect both in cascades with low and high energies. /184

TABLE 1.

Cascade energy, BeV	Film	r = 48 μm	r = 58 μm	r = 84 μm	r = 140 μm
1—2	Mean 800 μm from Pb	0,91±0,03	0,87±0,03	0,89±0,03	0,94±0,06
		0,90±0,05	0,85±0,05	0,88±0,05	0,91±0,11
	Lower 1200 μm from Pb	0,80±0,04	0,79±0,04	0,82±0,03	0,81±0,06
		0,76±0,04	0,77±0,04	0,80±0,06	0,75±0,10
2—7	Mean 800 μm from Pb	0,92±0,02	0,91±0,02	0,88±0,02	0,90±0,03
		0,86±0,03	0,88±0,03	0,84±0,03	0,82±0,06
	Lower 1200 μm from Pb	0,86±0,02	0,82±0,02	0,80±0,02	0,87±0,03
		0,75±0,04	0,75±0,03	0,71±0,04	0,80±0,05
7	Mean 800 μm from Pb	0,94±0,02	0,96±0,02	1,0±0,03	0,97±0,04
		0,80±0,06	0,86±0,07	1,0±0,06	0,96±0,08

This effect was also investigated through a direct count of the number of electrons. Three layers of an emulsion, each 400 μm thick without a substrate were exposed under 6 t-units of lead. The nuclear emulsions were immediately behind the packet with the x-ray films. The distance between the first and second layers of the nuclear emulsion was 1100 μm, and between the second and third, 420 μm. The number of particles in circles whose radii were 25, 50, 100 and 150 μm, respectively, were measured in three showers with energies 0.44, 0.74, 1 BeV. Particles making an angle $\theta < 10^{\circ}$ with the shower axis, which corresponded to an energy of the particles of $\sim 1 \cdot 10^{8}$ eV, were counted [3]. In the circle whose radius was 150 μm, the proportion of the particles with an angle $> 10^{\circ}$ which were ignored, when the energy of the shower was determined, was approximately 20%.

Table 2 gives for each shower the ratio of the number of particles counted in the second layer (n_{II}) to the number of particles counted in the first emulsion layer (n_I) and also the ratio for the number of layers in the third (n_{III}) and the second (n_{II}) emulsion layers. The same table gives the results of the measurements of the energy in the corresponding layers.

The set of all data obtained with the x-ray films and the nuclear emulsions does not contradict the linear relations for the correction as a function of the size of the gap.

TABLE 2

Shower	Ratio	r = 25 μm	r = 50 μm	r = 100 μm	r = 150 μm
№ 1 E=0,44 BeV $\alpha = 33°$	n_{II}/n_I	0,54±0,08	0,72±0,10	0,68±0,10	0,66±0
	E_{II}/E_I	0,64±0,09			
	n_{III}/n_{II}	0,75±0,10	0,72±0,10	0,85±0,12	0,79±0,11
	E_{III}/E_{II}	0,80±0,11			
№ 2 E=0,7 BeV $\alpha = 53°$	n_{II}/n_I	0,64±0,09	0,66±0,09	0,72±0,10	0,66±0,09
	E_{II}/E_I	0,70±0,10			
	n_{III}/n_{II}	0,64±0,09	0,69±0,10	0,86±0,12	0,83±0,12
	E_{III}/E_{II}	0,80±0,11			
№ 3 E = 1 BeV $\alpha = 23°$	n_{II}/n_I	0,69±0,10	0,69±0,10	0,73±0,10	0,73±0,10
	E_{II}/E_I	0,71±0,10			
	n_{III}/n_{II}	0,74±0,10	0,77±0,11	0,74±0,10	0,83±0,12
	E_{III}/E_{II}	0,77±0,11			

Thus, when the energy of electron-photon cascades is measured with the aid of nuclear or x-ray films, it is necessary to introduce a correction that takes into account the effect of the divergence of the electrons in the gap between the filter and the emulsion surface. /185

REFERENCES

1. Nishimura, I., Progr. Theor. Phys. Japan Suppl., 32 72 (1964).

2. Baradzey, L. T., Kanevskaya, Ye. A. and Smorodin, Yu. A., Trudy FIAN im. P. N. Lebedeva, [Publ. of the Physics Inst. of the USSR Acad. of Sci.], 46, (1970).

3. Apanasenko. A. V. and Shcherbakova, M. N., in the collection Kosmicheskie luchi, No. 12, 121 (1970).

N75 16479

DESCRIPTION OF AN IONIZATION CALORIMETER COMPLEMENTED WITH PROPORTIONAL COUNTERS

Kh. P. Babayan, N. G. Boyadzhyan, V. V. Vasil'tsov,
N. L. Grigorov, V. A. Sobinyakov, V. Ya. Shestoperov

ABSTRACT

The paper describes an ionization calorimeter with a system of proportional counters which are used to determine the charge of the particles incident to the calorimeter and to estimate the number of the secondary charged particles.

Several years ago we designed an ionization calorimeter with a working area of 10 m^2, for the study of nuclear interactions of particles with an energy of 10^{11} - 10^{13} eV [1]. The measurements that were made at the high-mountain Erevan Physical Institute yielded a great deal of experimental material.

However, it should be mentioned that in the analysis of the experimental material, in a number of cases, the information obtained from the installation was inadequate.

It is known that at mountain altitudes the π-mesons can comprise up to 30 - 40% of the total nuclear-active particle flux with energies above 10^{12} eV [2]. However, it is possible that the characteristics of the interactions of neutrons and pions with nuclei differ from one another. At the same time, the apparatus used did not allow us to determine the nature of the nuclear-active particle incident to the installation in each individual case. Therefore, when the data that we obtained were interpreted, we were forced to use, in a number of cases, the experimental data of other authors and certain indirect considerations.

In order to circumvent this difficulty and to increase the information obtained about the interaction of particles with energies 10^{11} - 10^{13} eV, the ionization calorimeter is now equipped with several series of proportional counters. The installation uses proportional counters whose cross section is rectangular and whose dimensions are 3000 x 55 x 110 mm^3. In each counter it is possible to measure the ionization created in it when one to several hundreds of relativistic particles pass through it. A detailed description of the counter is given in article [2]. /186

A schematic diagram of the modified installation is given in the diagram. Below the top lead filter 1, whose function is to absorb the electron-photon component is the target-filter 3, in which the nuclear-reactive particles undergo interactions. The substance of the filter, its thickness and its distance from the ionization calorimeter can vary, depending on the physical problem. There are two proportional counters above the filter and two below it [4]. Each row consists of 26 counters. The top rows are designed to determine the presence or absence of a charge in the nuclear-active particles. In the first case, the interactions that are studied can be caused both by neutrons and also by π-mesons, in the second case, only by neutrons. The two lower rows of counters are designed to estimate the number of charged particles generated as a result of the interaction of the nuclear-particle in the filter. The axes of the counters in neighboring rows are located in mutually perpendicular directions, in order to determine the coordinates of the charged nuclear-active particles.

Below is the ionization calorimeter (5) with iron filters (2), which is described in detail in article [1]. The study of the nuclear interactions, as before, can be carried out using the method of controlled photoemulsions (6). Three rows of proportional counters which are located in the ionization calorimeter are used to generate the signal which controls the operation of the counter.

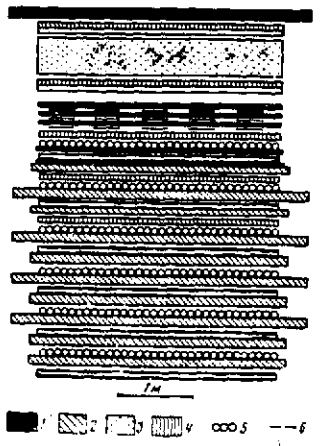

Fig. Schematic diagram of the installation.

Explanation in text.

REFERENCES

1. Babayan, Kh. P., Grigorov, N. L., Sobinyakov, V. A. and Shestoperov, V. Ya., in the collection Kosmicheskie luchi, No. 8, 182 (1966).

2. Grigorov, N. L., Zhur Exper Teor Fiz., 45 (12), 1920 (1963).

N75 16480

A DISCHARGE-CONDENSATION METHOD FOR THE DETECTION OF TRACES OF CHARGED PARTICLES

Z. Sh. Mandzhavidze, V. N. Roynishvili

ABSTRACT

A new discharge-condensation method is suggested for detecting the traces of charged particles. The chamber designed on the basis of this method possesses a high time resolution (several microseconds) and a greater memory time (dozens of milliseconds). Photographed traces of cosmic particles in the discharge-condensation chamber are given.

In this study we were able to implement a new discharge-condensation method for detecting traces of charged particles, which unifies, to a considerable degree, a number of specific features of such elementary particle detectors as spark and condensation chambers.

The high resolution of spark chambers and the greater memory time of the isolated event which is characteristic of condensation chambers, are of considerable interest. Combining these features in one instrument, and also the total isotropy, the good three-dimensional resolution, the great brightness of the traces, and the possibility of using as the working medium practically all the gas gives us reason to assume that the discharge-condensation method will be applied to the physics of elementary and high-energy particles.

The essence of the discharge-condensation method is that the traces are detected in two stages with the successive use of the discharge and condensation recording principles.

In the first stage, the ionization electrons generated by the charged particles in the working gas mixture with the condensate are accelerated in the pulsed electric field, and initiate the gas discharge. However, the amplitude and the duration of the pulse are selected in such a manner that the discharge does not pass into the visible stage, and is interrupted at the Townsend avalanche stage. Thus, primary ionization is intensified by several orders of magnitude. This stage ensures that the event is isolated in time with high resolution which is several μsec, and the fact that the information about the event, which was isolated as a result of the gas intensification, is a dense column of ions, is responsible for the great memory time which is several tens of a msec.

In the second stage, the oversaturated vapor ionic condensation takes place along the trajectory of the particle. However, the degree of oversaturation is selected approximately 2 - 3 times below the threshold value necessary for the primary ionic condensation, which, however, is adequate for the condensation of dense accumulations of ions, i.e., the trace after gas intensification in the first stage. Thus, condensation takes place only on the traces that were isolated, which were subjected to gas intensification. The chamber is completely insensitive to other traces.

The necessary oversaturation must be formed by known methods that are used in Wilson chambers and in diffusion chambers. To obtain the traces of particles by the discharge-condensation method, we used a cylindrical Wilson chamber whose diameter was 30 cm and whose height was 10 cm with the usual expansion mechanism. A high-voltage pulse from the generator of the Arkad'ev-Marks type was fed between the counts by an electrode located near the front glass of the chamber and by a perforated grid mounted in front of a rubber diaphragm. The duration of the pulse was regulated by an air gas-discharge arrestor, which shunted the chamber. The chamber was filled with pure neon at a pressure of 1.1 atm, and the condensate used was ethyl alcohol. The discharge-condensation chamber was controlled by the telescope of the scintillation counters. The delay time between the instant when the particle passed through the chamber and the instant when the high voltage pulse was fed to the electrodes did not exceed 1 μsec.

The experiments were carried out when the chamber was in /188
two positions relative to the separating system. In one series of experiments, the position of the chamber was such that the counters isolated the particles which intersected the chamber at a small angle relative to the direction of the electric field. The diagram gives a photograph of the trace of the particle when the position of the chamber was such that the particles causing the coincidence passed through the chamber at a large angle relative to the direction of the electric field. The photographs were made through the front glass of the chamber and the mesh electrode.

In both series of experiments, the degree of expansion of the chamber was 1.04, the illumination delay time was 40 msec, the power of the pulse source of the light was ~ 80 joules, and the aperture ratio was 1:22. It should be mentioned that these conditions are not optimal and that in the future they can be improved.

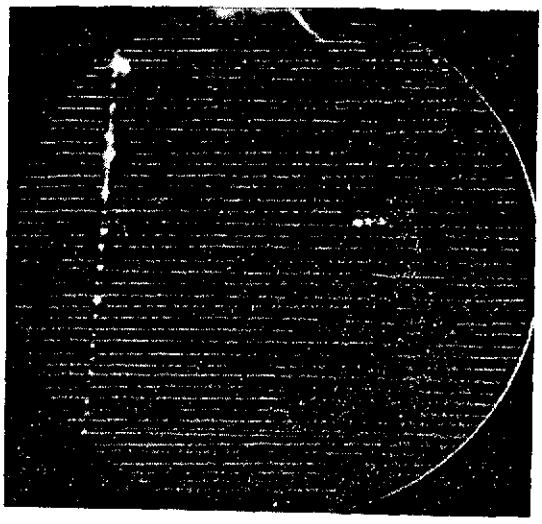

Fig. Particle trace in discharge-condensation chamber.

The photographs were made along the direction of the electric field of the pulse.

The high time resolution, several microseconds, makes it possible to use the discharge-condensation chamber in beams of great intensity with a flux of $\sim 10^5$ particles in the cycle, and the great memory of the event isolated as a result of the gas intensification, several tens of milliseconds, facilitates considerably the control of the discharge-condensation chamber when complex and rare events are studied, when it is necessary to analyze a great amount of information from the control counters.

The only requirement which the working medium must satisfy in the discharge-condensation chamber is that it must ensure a gas intensification of the primary ionization in the pulsed electric field by several orders of magnitude. Practically all gases, including hydrogen, satisfy this condition. The use of hydrogen as the working medium in a discharge-condensation chamber is very important since a hydrogen discharge-condensation chamber which can be regulated and exposed to high-intensity beams is not inferior to a liquid-hydrogen chamber in effectiveness, using the working medium as the target.

The authors express their gratitude to Ye. L. Andronikashvili /189
for his constant interest in this work, and to A. K. Dzhavrishvili for his considerable help and useful criticisms, and to N. K. Chernyshev and N. S. Grigalashvili for their participation in tuning the apparatus.

N75 16481

A SYSTEM FOR MULTICHANNEL RECORDING AND AUTOMATIC READING OF INFORMATION

E. A. Bogomolov, Ye. Ya. Yevstaf'ev, V. K. Karakad'ko, N. D. Lubyanaya, V. A. Romanov, M. G. Totubalina, M. A. Yamshchikov

ABSTRACT

The paper considers a system for the recording and processing of telescope data for measurements of EW asymmetry. The information is recorded by 45 channels on a continuously moving 35-mm film. The dead time of the recorder is about 0.1 sec. A sorting electronic circuit is used to reduce the errors when the statistical time distribution of the pulses is recorded.

The recorded information is read out by means of photoresistors. The phototransmitter signals are fed either to the mechanical recorder unit for preliminary processing, or to a logical circuit which controls the operation of the punching device. The punched tape is processed by an electronic computer.

A system on board which records the information from telescopes in the study of the spectrum and the cosmic ray composition in the range 2 - 8 BeV is described in article [1]. In the first experiments, the information was recorded on magnetic tape with the aid of tape drives that are analogous to those described in article [2]. In one instrument two magnetic tapes were used which made it possible to record the information in six channels, out of which two were time channels. Later an auto-recorder was prepared in which a number of parameters (temperature, pressure, etc.) were recorded in sequence on photo paper which was placed on a rotating drum.

The striving to obtain more complete information about each particle recorded by the telescope led to the development of a multichannel recording device. First, these devices (when the recording was done on a 35-mm film) were used for duplicating the magnetic recordings, and later preference was given to them since they can be used to record the information from a large number of channels and in addition had smaller dimensions and weight. /190

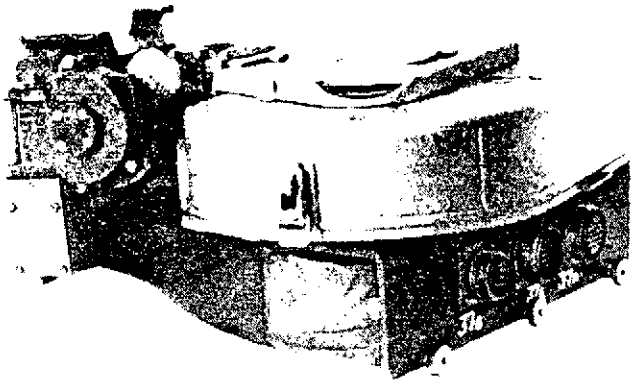

/189

Fig. 1. Film-drive for multichannel recording

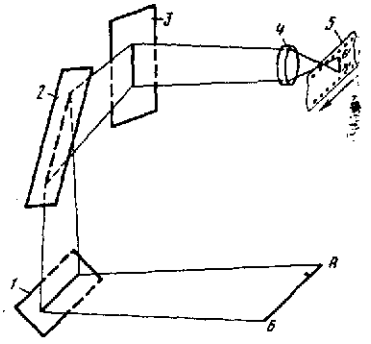

Fig. 2. The path of rays in the film-drive device shown in Fig. 1.

1 - 3--mirrors;
4--objective;
5--film

The device uses two film-drives. The first is a specially prepared photo camera in which the instrument panel is recorded once every 8 min. On the panel are eight mechanical counters whose purpose is to count the pulses in various channels of the telescope, and a sample manometer at 60 atm used to record the variable pressure of the gas in the Cerenkov gas counter, three microamperemeters for recording the temperature at various points on the instrument and the feed voltage, the electronic circuits, and also a mechanical pressure gauge inside the device. The photographs are taken on a 35-mm film and the capacity of the cassettes is 50 m. The main purpose of this photo apparatus is to record the pressure and temperature of the gas in the gas counter; in addition, it makes the operational processing of the basic experimental data possible.

In the second film drive device (Fig. 1), the commutation K-24-11 lamps are photographed on continuously moving film with the aid of the "Orion" objective. The device uses a cassette whose capacity is 120 m. The speed at which the film moves can be varied, depending on the expected duration of the experiment. In the experiments that were carried out, it was ~ 12 m/h. To reduce the dimensions of the device, a mirror system is used. The path of the rays in the system is shown in Fig. 2.

The number of photographed lamps is 45. Out of these, seven are used to control the operation of various nodes in the instruments and also for time marks. To obtain more complete information using the same number of lamps, their brightness is modulated. Eleven lamps are used for counting the pulses in various channels of the telescope. Each of them is connected to the arm of the counting cell. The image on the film is obtained in the form of dashes. The remaining 27 lamps are at the output of 32- and 16-channel analyzers, and also the outputs of the five main channels of the telescope. They give standard flares (the duration of the burning is 65 μsec and the lamp voltage is 15 V. The number of the analyzer channel to which the pulse arrives and the coincidences of the main channels of the telescope are determined with their aid. /191

The dead time of this recording system is comparatively large, and it is determined by the burning time of the lamps. To reduce the counting errors during the recording of the statistical time distribution of the pulses, a sorting electronic circuit is used. It directs the pulse which arrives during the time when the lamps burn along the "doubling" track. A separate group of lamps is lit for this track. Such a circuit makes it possible to reduce considerably the number of counting errors when the 32 channels of the analyzer which is controlled by interrogating the main channels of the telescope are loaded. For example, when $n = 4.6$ pulses/sec, the counting error is $\sim 26\%$ (when the lamps burn for 65 μsec and when the "double" is introduced, the error is reduced to 4% [3].

The large volume of information and the necessity to process it in various ways required the design of an automatic AC counter. The main task of the AC is the transfer of the events recorded on the film to a standard punched tape which is processed on an electronic computer. The block diagram of the AC is given in Fig. 3. The film which contains the information is pulled through a special drive through the instrument where it is checked on a "Mikrofot" film. The speed at which the film moves can be varied, depending on the character of the counting. The sensors which are used are small-dimension SF2-1 photoresistors placed serially on the "Mikrofot" screen. The signals from the BFD photosensors are connected to the normalization and counter (NCB) block, where the mechanical recorders are located. These are used to count the number of pulses in various channels of the telescope (second group of lamps). For the preliminary processing of the information, the BFD is connected to the BMR mechanical recorder block which contains a diode matrix and mechanical recorders. It is designed to receive the spectrum from the 32- and 16-channel analyzers both when the information is read from the film and also directly from the instrument when it is tuned.

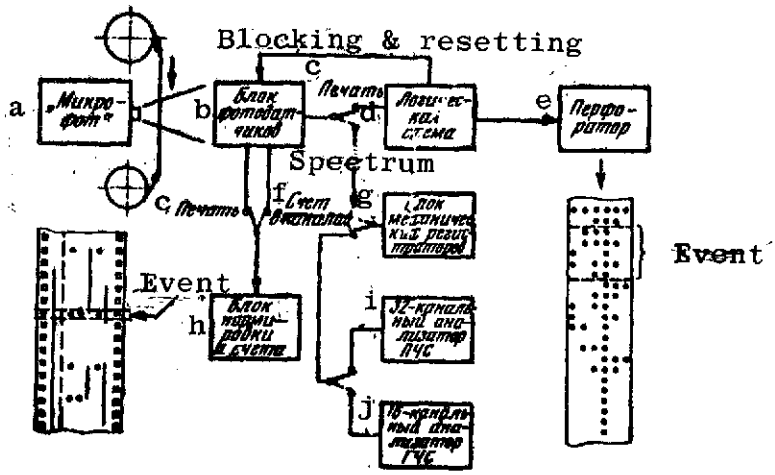

Key:
a. "Mikrofot"
b. Photosensor block
c. Printing
d. Logical Circuit
e. Perforator
f. Counting in channels
g. Mechanical recorder block
h. Normalization & counter block
i. PChS 32-channel analyzer
j. GChS 16-channel analyzer

Fig. 3. Block diagram of automatic counter

When the information is transferred from the film to the punched tape, the BFD is connected to the LC logical circuit. The function of the LC is to interrogate in sequence all BFD channels and to start the PT punched tape. In addition to this, the LC blocks the BFD during the interrogation, and also when the next drive is mounted. In this operating regime, the BNS is used to normalize various time intervals over time.

The authors express their sincere gratitude to I. M. Zheleznov for the design of the firm drive devices and also to G. S. Pyatigorskiy for his help in the development of the AC system.

REFERENCES

1. Bogomolov, E. A., Karakad'ko, V. K., Lubyanaya, N. L., et al., "A Telescope for the study of cosmic radiation in the range 2 - 8 eV/s," Dokl na Vses konf po kosmicheskim lucham, [Read at the International Conference on Cosmic Rays], Alma-Ata, 1966 -- Kosmicheskie luchi, No. 12, 67-70 (1970).

2. Barsukov, V. T., Belyaevskiy, A. I., Bocharkin, V. K., et al., PTE, No. 5, 119 (1966).

3. Gol'danskiy, V. I., Kutsenko, A. V. and Podgoretskiy, M. I., Statistika otschetov pri registratsii yadernykh chastits, [Statistics of Readings during the Recording of Nuclear Particles], Fizmatgiz Publs., 1959.

N75 16482

INSTALLATION FOR THE STUDY OF THE ANGULAR DISTRIBUTION OF COSMIC MUONS WITH SUPER-HIGH ENERGIES AT LARGE ZENITH ANGLES

V. V. Borog, V. G. Kirillov-Ugryumov, A. A. Petrukhin, V. V. Shestakov

ABSTRACT

An Installation consisting of an ionization calorimeter and a counter hodoscope can be used to record cascade showers caused by the electromagnetic interactions of muons with super-high energies in the cosmic ray horizontal flux. The direction of the muons is determined by a hodoscope consisting of 2196 counters of the GS-30 type. The information obtained makes it possible to restore the angular and energy distribution of the cosmic muons, which, in turn, makes it possible to determine the mechanism of their generation. The accuracy with which the angle of the passing particle is determined is discussed in detail in addition to the causes which can introduce distortions, such as shower accompaniment of neutrons, escape of shower electrons from the calorimeter, random coincidences, etc.).

Calculations [1] have shown that the angular distribution and intensity of cosmic muons of super-high energies depend considerably on the processes in which they are formed, and, hence, their study can yield information about the generation of unusual particles in nuclear interactions at energies that exceed by one order of magnitude the energy of the muons studied. The method used in the study, the recording of cascade showers formed due to electromagnetic interactions of the muons with the substance uses the fact that the cross sections of these processes are known from the theory and that the energy of the electromagnetic cascade can be measured with the aid of an ionization calorimeter.

The installation (Fig. 1) consists of the calirometer K and the three "walls" of the gas-discharge Geiger counters GS-30: A, B, C. The ionization calorimeter which was described earlier [2, 3] consists of six rows of cylindrical rectangular ionization chambers, whose axes are horizontal in the even rows and vertical in the odd rows. Only the electronic circuits were modified somewhat so that the existing system can detect the perpendicular passage of approximately 60 relativistic electrons through the ionization chamber. When the thickness of the iron absorber between the rows of the chamber is 5.3 radiation units, this installation can record cascade showers with energies $\gtrsim$ 60 BeV in at least theee chamber rows.

The direction of motion of the muon, and, consequently, also the position of the shower axis are determined roughly by the coordinate grid formed by the ionization chambers, and more accurately with the aid of the walls A and B of the hodoscope. When the numbering is the same, the chambers actuated with the same ordinal number in the closest neighboring even (odd) rows corresponds to the passage of the storm with the axis in the zenith (azimuth) angular interval from 70 to 90°. Using the information about the passage of the muon through even one wall of the hodoscope, makes it possible to subdivide this interval into four parts that are approximately equal with a gap on the order of 5°. Each wall represents a set of 96 cells, each cell combining six gas-discharge GS-30 counters. The dimension of the cell, which is 20 x 60 cm^2, is given by six diameters and the length of the working part of the counters. The non-effectiveness of the recording which is related to the presence of gaps between the counters, the dead time and other factors does not exceed 15%.

Figure 2 shows the block diagram of the installation. The pulses from the cells of the A01-A96 and B01-B96 hodoscope arrive to the mixers-shapers, the walls A-SFA and the walls B-SFB. /193
The double coincidence circuit CC2 isolates the cases when the muons pass through both walls. The anti-coincidence circuit CAC ensures that the events are selected which are not accompanied by the passage of the particle through the cells in the top row of counters B01-B12. The necessity of such sampling is dictated by the fact that the passage of 2 - 3 relativistic particles along the filament of the chamber with a vertical axis corresponds to the ionization in it above the threshold, and the cascades which are formed at the top and bottom of the housing, as well as the wide atmospheric showers can be recorded with great effectiveness.

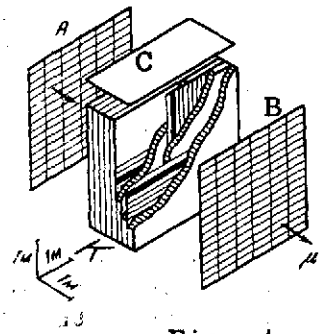

Fig. 1

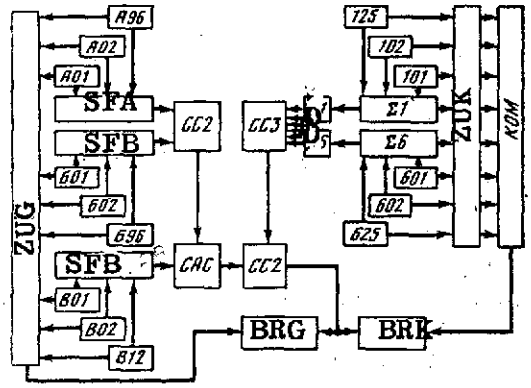

Fig. 2

Fig. 1. Installation layout. K--ionization calorimeter; A, B and C--"walls" of gas discharge counters.

Fig. 2. Block diagram of control and recording system. Explanation in text.

The signals from the amplifiers K01-K25 from the K-th row, whose amplitude is proportional to the ionization induced in the corresponding chamber by the shower electrons are added in the summing amplifier ΣK of this row. If the total ionization exceeds the threshold value given by the discriminators D1-D6 in three or more rows the coincidence circuit CC3 is activated which generates the so-called calorimetric tract signal. Further, another coincidence circuit CC2 samples events of the type (A + B + C + K) when the signals from the calorimetric track and the CAC circuit arrive to it. At the same time in the memory devices ΣUK of the calorimeter memory in the ZUG hodoscope memory device, the information from all channels is stored and then the recording blocks BRK and BRG, respectively, ensure that it is recorded.

The possibility exists in the installation to disconnect the counters in the B row from the anticoincidence circuits CAC, and also to connect it to the coincidence circuit with A and B (events of the type A + B + K and A + B + C + K). This may become necessary when muon beams are studied in wide atmospheric showers which travel under large zenith angles.

In the ideal case, the passage of the muon will be recorded by actuating the single cells in the walls A and B which correspond to the entry and the leaving of the muon of the installation. However, the calorimetric track signals are delayed relative to the instant when the muon passes through the installation by the time $T_{del} \leq 20$ μsec which is related to the collection time of the electrons in chambers with the given geometry [4] and the time characteristics of amplifiers and follow-up circuits. The probability of a random coincidence is determined from the total number of counters, the mean counting rate of each counter, and the memory time. Since the intensity of the pulses at the output of the mixer-shaper circuit is on the order of $3 \cdot 10^3$ pulses/sec, and the hodoscope memory time must exceed somewhat the maximum T_{del}, the probability that the ideal picture will be disturbed through the random triggering of some other cell in the installation is approximately 10%, taking into account the information from the calorimeter. /194
This probability can be reduced considerably when the memory in the hodoscope memory device is based on the SAS signal. After the maximum T_{del}, recording or erasing takes place, depending on whether or not the calorimetric track signal arrived.

From the standpoint of indeterminacy of locating the coordinate where the passage takes place through the walls of the hodoscope, in addition to the "random" triggering of the counters of electrons and photons accompanying the muons with super-high energies and the electrons of the shower itself which were not recorded in the calorimeter substance, or which were

scattered back, also represent a danger. When the probability that an additional cell of the hodoscope will be actuated due to the passage of the electron or photon generated during the interaction of the muon with the substance in the surrounding housing is estimated, it is taken into account that the counters are placed in aluminum boxes in walls whose density is ~ 1 g/cm^2. The estimate is in excess of 10%. It is difficult to estimate theoretically the effect of avalanche electrons, and for the time being experiments do not contradict the assumption that for showers near the surface of the iron absorber, the output wall of the hodoscope functions effectively, and for showers that begin in the middle of the calorimeter, the inverse current is negligible.

Thus, the installation that was described can record electromagnetic cascades with an energy $\gtrsim 60$ GeV caused by the interaction of cosmic muons with the substance of the absorber in the zenith angle interval from 65 to 90°, and for 2/3 of these, it is possible to determine the zenith angle with an accuracy of $\pm 3°$.

In conclusion, the authors express their gratitude to Ye. S. Vanchugin, A. A. Plastunov, S. N. Filyushin, and V. K. Chernyatin for their help in assembling and tuning the installation.

REFERENCES

1. Zatsepin, G. T. and Kuz'min, V. A., Zhur Exper Teor Fiz, 39, 1677 (1960).

2. Borog, V. V., Kirillov-Ugryumov, V. A., Petrukhin, A. A., et al., in the collection Fizika elementarnykh chastits [The Physics of Elementary Particles], Atomizdat, 1966, p. 59.

3. Borog, V. V., Kirillov-Ugryumov, V. G., Petrukhin, A. A., et al., Izv Akad Nauk SSSR, Seriya Fiz, 30, 1669 (1966).

4. Kirillov-Ugryumov, V. G., Petrukhin, A. A. and Shestakov, V. V., Prib Tekh Eksp, 4. 59 (1965).

N75 16483

CERTAIN PROBLEMS IN THE DEVELOPMENT AND DESIGN OF SCINTILLATION AND CERENKOV COUNTERS

V. S. Chukin

ABSTRACT

The paper examines the feasibility of increasing the effectiveness of the scintillation and Cerenkov counters through improving light collection of the recorded radiation on the photoelectric cathode of the photomultiplier. The paper lists optical and mechanical characteristics ensuring optical contact between the elements of the optical system and particularly between the elements of the "detector photoelectric multiplier light guide system."

An example of how to select a detector of the directional plexiglas Cerenkov counter is given. Also presented are the experimentally obtained amplitude distributions during the recording of cosmic ray μ-mesons. The necessity to obtain agreement between the characteristic spectrum of the photocathode of the photomultiplier and the spectrum of the recorded radiation is stressed.

The effectiveness of scintillation and Cerenkov counters is determined in many ways by how well the light of the recorded radiation is collected on the photoelectric cathode of the photomultiplier. The intensity of the Vavilov-Cerenkov radiation is considerably below the light outburst in the scintillator. Therefore, the problem of collecting the light is especially important in the design of Cerenkov counters.

The light collection can be improved: first, through an effective optical coupling of the elements of the "detector-light guide-photomultiplier" system and the use of transparent materials for the recorded radiation, second: by using various reflecting covers; third, by the appropriate calculation of the geometry of the detector and the entire optical system; fourth, by using a highly effective photomultiplier whose spectral characteristic agrees well with the spectrum of the recorded radiation.

It is known that in order to reduce the fraction of reflected light when the elements of optical systems are coupled, in particular in the "detector-light guide-photomultiplier system," various substances are used, i.e., optical contacts. The most effective optical connections are obtained when a

contact is used whose refractive index is close to the refractive indices of the elements which are connected. Usually Canada balsam, immersion, vaseline diffusion and other oils are used for this purpose. However, the use of the optical contacts that were mentioned, hinges on the design of special devices which ensure good mechanical contact in combination with constant pressure on the coupled elements, which hinder the contact from leaving the coupling zone. In instruments that were specially designed, in which after the final tuning no provisions are made for disassembling the optical elements, contacts must be used which have adhesive properties. A study of the optical properties of the contacts led to the complete elimination by the user of such contacts as Canada balsam, immersion oil, etc. [1 - 3].

Various types of resins that are produced by our industry have been widely used since 1961 as optical contacts. The high adhesion of some types (for example, ED-6) makes it possible to use them without polymerization as temporary contacts also in cases when the optical elements are disassembled. Silicon-organic vaselines and silicon oils are also used in optical contacts that are disassembled [4]. The use of the organic couplings developed by the workers in the institute in cooperation with the USSR Academy of Sciences with an optical adhesive composition based on cyanate acrylate [5] have great promise for couplings that are not disassembled.

Figure 1 gives the data for the relative transmission capacity in the range 2200-600 Å for various contacts in a thin layer. It can be seen that among the contacts which have the best transparency in the ultraviolet range of the spectrum, the adhesive-contact ensures the best coupling which is not disassembled.

The use of highly effective coatings reflecting the diffusion increases the fraction of the collected light and makes it possible to design counters with the same sensitivity on the entire volume of the detector, in spite of the disadvantageous form of the detector for the collection of the light. Thus, the use of the VL-548 paint (developed in the State Research and Planning Institute-4) in a scintillation counter with a detector whose diameter is 200 mm and h = 20 mm, made it possible to obtain a homogeneous light collection in 96% of the volume of the detector [6]. The best metal reflector is Al spray-coated in a vacuum. When the gas threshold Cerenkov counters were prepared [1], the reflecting surfaces of the mirrors and the surfaces of the parabolic reflectors were coated with aluminum, and an aluminum mylar film was glued to the internal cylindrical surface, which also had high reflectance properties. The effectiveness of the counters that were prepared in this manner attained 96%. /196

The importance of selecting properly the geometry of the detector can be illustrated on the example of an oriented plexiglas counter [3].

The counter had to satisfy the following requirements: 1) maximum light collection; 2) minimum thickness of the radiator; 3) the independence of the amount of collected light from the spot where the particle passed through; 4) recording of particles arriving in only one direction.

The substance of the radiator, optical plexiglas (polymethyl acrylate) had better transparency than the usual substance (Fig. 1, curve 8) [7] in the wavelength range of interest (taking into account the Vavilov-Cerenkov spectrum).

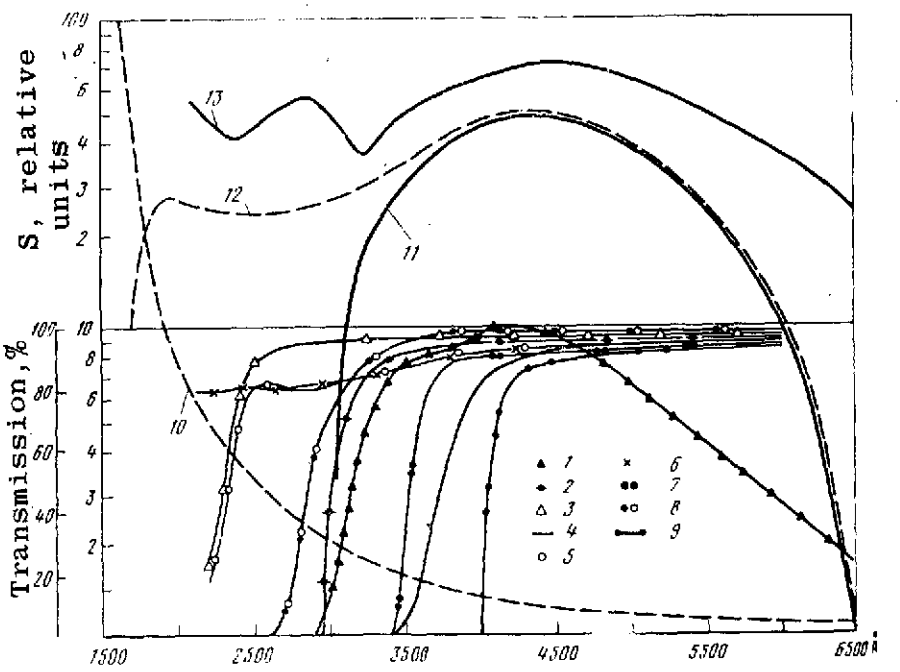

Fig. 1. Certain spectral-optical characteristics

1--spectral characteristic of the 13B photomultiplier; 2--transmission spectrum of the adhesive composition based on ED-5 epoxy resin (thickness of layer 40 μm; 3--transmission spectrum of adhesive composition based on monomeric cyanide acrylates (30 μm layer); 4--Canada balsam transmission spectrum (30 μm layer); 5--vaseline oil transmission spectrum (30 μm layer); 6--"KV-3" organic silicon gasoline transmission spectrum (50 μm layer); 7--"1-Sh-35" organic glass transmission spectrum (sample thickness 3.2 mm); 8--transmission spectrum of more

(continued next page)

(Caption, Figure 1, continued)

transparent organic glass (sample 3.2 mm); 9--transmission spectrum of scintillating plastic substance based on polystyrene (sample 10 mm); 10--Vavilov-Cerenkov radiation spectrum (for illustration purposes); 11--spectral characteristic of the CsSb S-11 photocathode (the material of the window is glass) [8]; 12--spectral characteristic of the CsSb S-13 photocathode (the material of the window is melted quartz) [8]; 13--spectral characteristic of photomultiplier with multi-alkaline photocathode (the material of the window is melted quartz) [8].

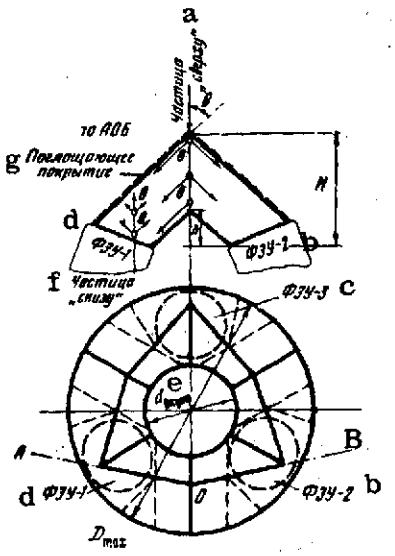

Key:
a. Particle "on top"
b. Photomultiplier-2
c. Photomultiplier-3
d. Photomultiplier-1
e. $d_{internal}$
f. Particle at bottom
g. Absorbing coating

/197

Fig. 2. Diagram illustrating the selection of the basic dimensions of the detector of an oriented Cerenkov counter

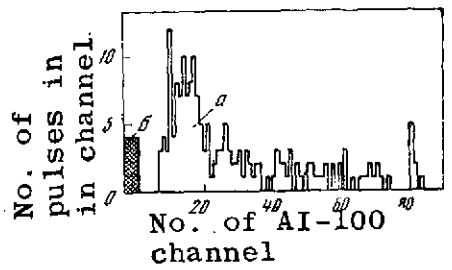

Fig. 3. Distribution of amplitudes of pulses from oriented Cerenkov counter

a--straight position of counter; b--reverse position

To improve the uniformity of the light collection, we used three photomultipliers of the FEU-53 type. It is known that the Vavilov-Cerenkov radiation is characterized by the orientation. The radiation angle θ is related to the velocity of the particle β and the refractive index of the medium n by the relation $\theta = \arccos 1/n\beta$. For a particle velocity of $\beta \approx 1$ and $n = 1.5$ (plexiglas) $\theta_{max} = 48^{\circ}$. If we know θ_{max}, the dimensions of the detector (D_{max} and $d_{internal}$) which are determined by the solid angle of the installation, the number of photomultipliers, and the diameter of photocathode, the height (H) of the detector (which will ensure the light collection in the zone of the radiator and which is at an equal distance from the two neighboring photomultipliers (Fig. 2)) can be determined. The shape of the detector is such that the path along which the particles travel in the detector is approximately the same for all admissible recording directions. In order that the Vavilov-Cerenkov radiation generated by the particles coming "from below" do not arrive at the photomultiplier, an absorbing coating is applied to the upper edges of the detector. The recording efficiency of the μ-meson cosmic ray counter was determined both in the straight and opposite directions (the counter was rotated 180°. The distributions of the amplitudes that were obtained when the μ-mesons were recorded in both positions of the counter are given in Fig. 3.

The efficiency of the counters increases considerably when the spectral characteristic of the photomultiplier agrees with the spectrum of the recorded radiation. The technical quantum efficiency of the photocathodes which basically determines the efficiency of the photomultiplier as a whole, depends on the transparency of the material of the rear window turned toward the light of the recorded radiation, the photon absorption in the cathode, and the quantum efficiency of the cathode itself. In the ultraviolet range of the spectrum of light waves, the technical quantum efficiency is determined by the transparency of the material of the photomultiplier window. Thus, the range of the spectral sensitivity of the photomultiplier with the usual antimony-piezo cathode applied to melted quartz broadens

considerably in the ultraviolet direction [8] which is extremely important for ensuring agreement with the Cerenkov radiation spectrum (see Fig. 1, curve 9). To obtain a still greater efficiency of the photomultiplier, multi-alkaline cathodes are applied to the melted quartz window (see Fig. 1, curve 12).

REFERENCES

/198

1. Bolyshev, V. A., Kapustin, I. N., Kurnosova, L. V., et al., Ustanovka dlya registratsii elektronnoy komponenty pervichnogo kosmicheskogo izlucheniya, [Installation for Recording the Electron Component of Primary Cosmic Radiation], Preprint, Physics Institute of the USSR Acad. of Sci., 1966.

2. Balyshev, V. A., Kapustin, I. N., Kurnosova, L. V., et al., in the collection Kosmicheskie luchi, No. 11, 160 (1969).

3. Chukin, V. S., Preprint, Physics Institute of the USSR Acad. of Sci., No. 96, 1967.

4. Antonov, R. P., Zhinkin, D. Ya., Korneyeva, G. K., et al., "Organic silicon couplings for optical contacts," Prib Tekh Eksp, No. 6, 180 (1969).

5. Korshak, V. V., Polyakova, A. M., Chukin, V. S., Semyantsev, V. N., "Optical properties of polycyanate acrylates and compounds based on them," Dokl Akad Nauk SSSR, 178 (2), 370 (1968).

6. Logachev, V. I., Sinitsina, V. G. and Chukin, V. S., O sobiranii sveta v bol'shom plasticheskom stsintillyatore, [Light Collection in a Large Plastic Scintillator], Preprint, Physics Institute of the USSR Acad. of Sci., 1966.

7. Rubtsov, M. A., Frolova, M. I. and Chukin, V. C., "Organic glass for the detectors of Cerenkov counters," Prib Tech Eksp, No. 4, 59 (1969).

8. Engstrom, R. W., and Matheson, R. M., IRE Trans., N S-7, N 2-3, 1960, p. 52.

N75 16484

STUDY OF SPARK CHAMBERS FILLED WITH VARIOUS GAS MIXTURES

G. S. Akopyan, N. Kh. Bostandzhyan, G. A. Marikyan,
K. A. Matevosyan

ABSTRACT

This paper reports the performance of the four-layer spark chamber filled with alcohol vapors at 45 torr, "very pure" neon at 1 - 4.6 atm and also filled with only "very pure" neon at 1 - 2.9 atm. The curves of particles recording efficiency vs. the delay time in the chamber pulse supply and the number of operations are given. This efficiency decreases with an increase in the delay time and any addition of alcohol vapors increases the drop in the efficiency with time. However, alcohol vapors improve the localization of tracks along which the particles move and make them three to four times as narrow compared to the tracks inside the chamber filled with "very pure" neon.

The four-layer spark chamber that was studied had a metallic body whose shape was rectangular with a transparent wall for photographing the tracks. The distance between the electrodes in all layers was 10 mm, and the working area of the electrodes (5-mm thick iron) was 8.30 cm^2. To fill it with the necessary mixture of gases, the chamber was pumped-out to a pressure of 10^{-3} torr.

The measurements were carried out under the following experimental conditions:

a) To seal the body of the chamber, a vacuum rubber packing was used. The electrodes in the chamber were separated from one another by polystyrene columns. The transparent wall was made from organic glass. The chamber was filled with "very pure" neon;

b) to eliminate vaporization sources inside the chamber, indium metal was used, and the electrodes were insulated from one another and from the wall by porcelain insulators, and the wall from organic glass was replaced by glass calculated for a pressure of 8 atm·tech. The chamber was filled with "very pure" neon;

c) under the conditions mentioned in point b), the chamber was filled with an alcohol vapor mixture up to a pressure of 45 torr and with "very pure" neon up to the necessary pressure

In the conditions (a) when the delays in the supply of the working pulse are greater, a reduced recording efficiency of the particles is noted with the passage of the working time in the spark chamber [1, 2]. The first day after the chamber was filled with the working gas (pressure 1 and 4 atm·tech) the sparks in the compartments are formed in the direction of the electric field, which agrees with the data of other authors [3, 4]. After several days, when the total number of triggerings of the chamber was $2 \cdot 10^4$ at a pressure of 5 atm·tech. with an accuracy of 30%, sparks were formed along the path of the particle, however, always with a smaller slope than the slope of the true trajectory. /199

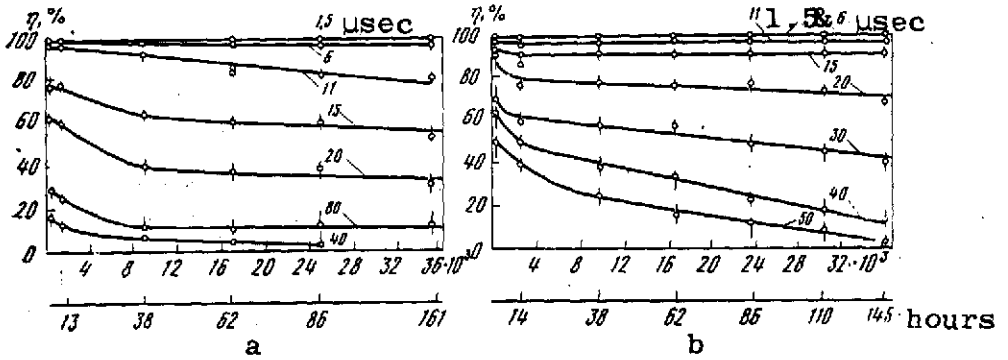

Fig. 1. Efficiency vs. number of times the chamber filled with "very pure" neon was triggered.

a--pressure 1 atm·tech; b--pressure 2.9 atm·tech. The number of times the chamber was triggered is plotted on the abscissa (the time that elapsed after it was filled with the gas is given below) and the efficiency in % is plotted on the ordinate. The numbers on the curves are the delay time (in μsec) in supplying the working pulse to the spark chamber.

Under the conditions (b) a reduction in the recording efficiency of the particles as the number of triggerings increases takes place much more slowly than under the conditions (a). The dependence of the efficiency on the number of times the chamber was triggered is given in Fig. 1 for various values of the delay time with which the working pulse is supplied. The chamber operating in conditions (b) does not make it possible to determine the direction of the recorded particle

in a particular compartment. The tracks which are obtained are spread and have the direction of the electric field regardless of the direction of the particle and the magnitude of the delay time in the supply of the working pulse ($\geq$ 1.5 μsec) and the gas pressure in the chamber (2.9 atm·tech). The spreading of the tracks increases as the delay increases which can be clearly seen in Fig. 2.

In the conditions (c) the quality of the tracks in the spark chamber improves considerably (Fig. 2); however, the drop in the recording efficiency of the particles accelerates with the time during which the chamber operates. Figure 3 gives the recording efficiency of the particles versus the number of times the chamber was triggered for various values of the delay time with which the working pulse was applied. In this case, the degree of localization of the spark on the particle path increases. Even at a pressure of the gas mixture equal to 1 atm·tech), slanted tracks are observed (relative to the electric field).

We carried out microscopic measurements of the observed width of the tracks during various operating regimes of the spark chamber. A reduced width of the tracks was observed with the time which occurred after the chamber was filled with the working gas. This is most evident when the chamber operates under the conditions (a), when in 1 week the width of the tracks decreases on the average by a factor of 1.5. Under the conditions (b) the width of the tracks decreases in two months only 1.25 times as much, and under conditions (c), even less. Table 1 gives the width of the tracks that were recorded during the first day when the spark chamber operated under various conditions. It is clearly seen that in the mixture of "very pure" neon and alcohol vapors, the tracks are 3 - 4 times as narrow as in the "very pure" neon without any admixtures. Under conditions (a), /200
the tracks that are obtained are also narrow, but on the average, are twice as wide as in the presence of alcohol vapors in the chamber.

The recording effectiveness of the particles vs. the delay time in the supply of the high-voltage pulse was also studied for spark chambers filled with a mixture of "very pure" neon and chemically pure helium. Two chambers whose dimensions were 20 x 15 cm^2 were used for this purpose with a 6-cm gap between the electrodes. One of them was filled only with "very pure" neon and the second with a mixture of neon and helium in various proportions. The total pressure in the chambers was 600 torr.

TABLE 1. MEAN WIDTH OF TRACKS (in mm)

Conditions under which the chamber operates	Pressure, technical atm	Delay time, μsec			
		1.5	6	10	15
a	1,0	1,76±0,25	—	—	—
	4,0	1,71±0,25	—	—	—
б	1,0	2,6±0,6	3,2±0,8	—	—
	2,9	2,2±0,5	4,4±0,9	5,2±1,0	—
в	1,0	0,83±0,12	1,01±0,15	—	1,05±0,15
	4,6	0,93±0,12	1,13±0,15	—	1,32±0,20

The results of these measurements are given in Table 2. The recording efficiency of the particles when the delays in the feeding pulse of the chambers were <3 μsec were not determined by us, but the curve for this efficiency as a function of the delay time in the range ≥ 3 μsec agrees with the fact that during 1 μsec delays the efficiency of the chamber is $> 90\%$ for all gas mixtures that were studied. From Table 2 it can be seen that as the delay time increases, the recording efficiency of the particles in the chamber filled with a neon and helium gas mixture decreases, and that this decrease takes place more rapidly the greater the amount of helium in the mixture.

TABLE 2. RECORDING EFFICIENCY OF PARTICLES (in %)

Gas mixture	Delay time, μsec						
	3	8	13	18	28	38	50
Ne	98±2	98±2	97±2	96±2	93±3	94±3	91±3
Ne+0,5% He	91±5	83±5	67±6	56±5	46±6	42±6	40±7
Ne+0,75% He	72±6	55±6	30±5	19±4	14±3	12±4	10±3
Ne+1,5% He	55±6	36±5	22±5	12±4	3±2	—	—
Ne+5% He	48±5	18±3	6±2	—	—	—	—

It follows from what was presented above that the addition of a small amount of gas to the "very pure" neon leads to a reduced recording efficiency of the particles (for large delays in the supply of the high-voltage feeding pulse to the spark chamber) but the quality of the tracks is improved and the accuracy with which the spot where the particle passes through is determined is also improved. /201

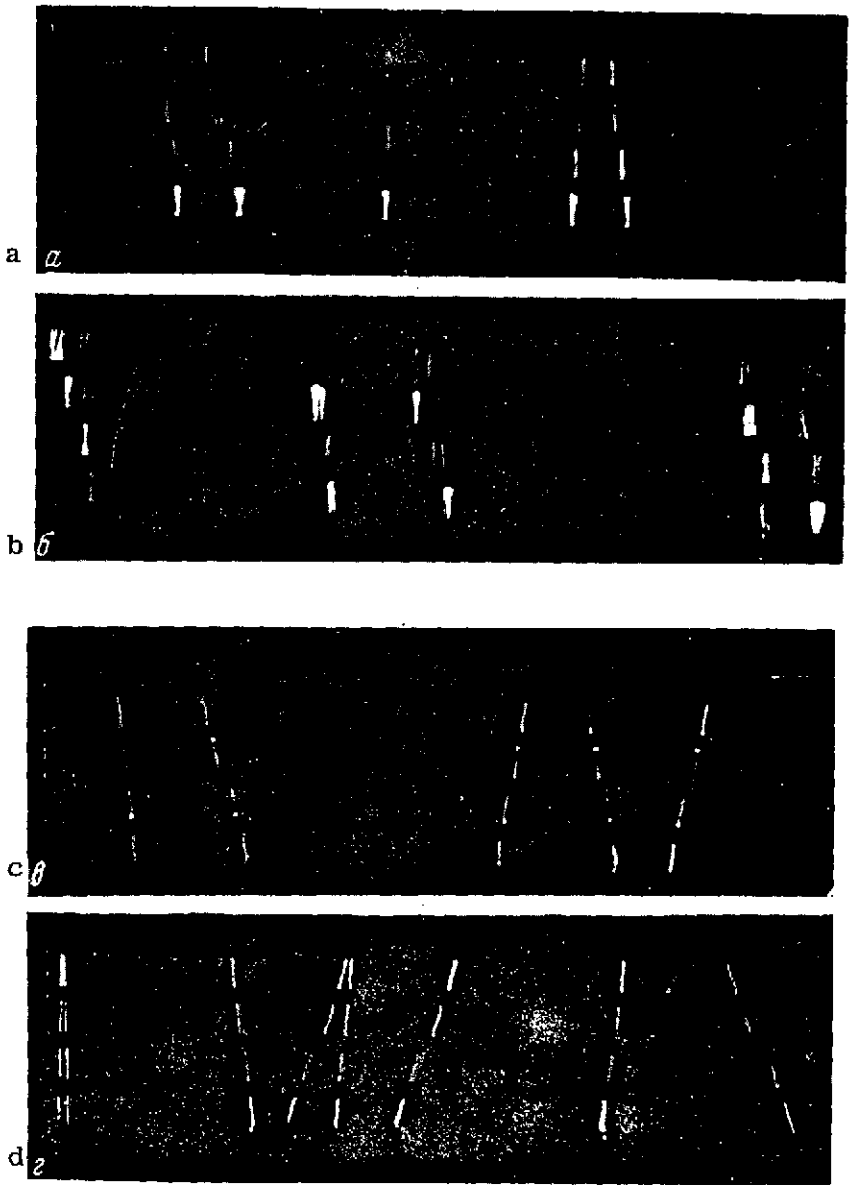

Fig. 2. Photographs of particle tracks.

a--pressure 2.9 atm·tech, delay time 1.5 μsec; b--2.9 atm·tech, 11.0 μsec; c--1.0 atm·tech, 1.5 μsec; d--4.6 atm·tech, 1.5 μsec

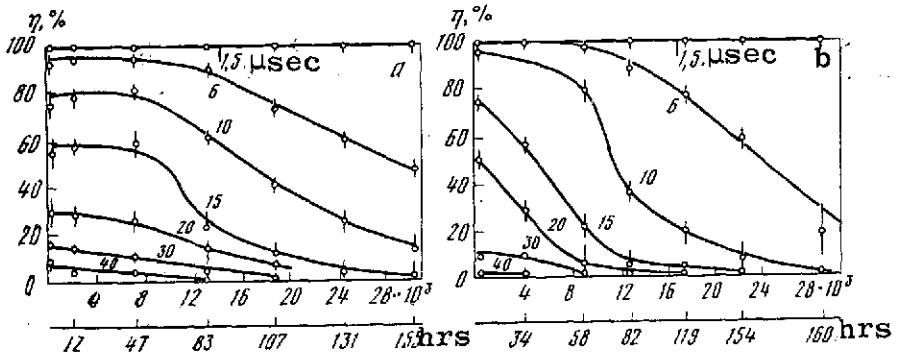

Fig. 3. Efficiency vs. the number of times the spark chamber filled with a mixture of "very pure" neon and alcohol vapors was triggered.

a--pressure 1 atm·tech; b--pressure 4.6 atm·tech. Remaining symbols the same as in Fig. 1.

REFERENCES

1. Bostandzhyan, N. Kh., Marikyan, G. A. and Matevosyan, K. A., Izv Akad Nauk Arm SSR, Fizika, 1, 55 (1966).

2. Akopyan, G. S., Bostandzhyan, N. Kh., Marikyan, G. A. and Matevosyan, K. A., Trudy Vses. konf. po kosmicheskim lucham, [Proceedings of the National Conference on Cosmic Rays], Alma Ata, 1966. In the collection Kosmicheskie luchi, No. 2, 93-95 (1970).

3. Dayon, M. I. and Leksin, G. A., Usp Fiz Nauk, 80, 281 (1963).

4. Novikov, L. S., Prib Tekh Eksp, No. 4, 45 (1965).

N75 16485

A THREE-ELECTRODE STREAMER CHAMBER

N. N. Nurgozhin

ABSTRACT

A three-electrode streamer chamber has been designed with basic components consisting of two glass boxes with overall dimensions 1.00 x 500 x 200 mm^3 filled with neon at 1 atm. Serving as a high-voltage pulse source is a nanosecond voltage pulse generator with cutoff discharges at 16 atm nitrogen pressure. The discharges are designed for obtaining an adjustable pulse with an amplitude of 600 kV and a nanosecond pump. To match the chamber electrodes with the oscillator, the electrodes are manufactured in the shape of a three-wire strip line. The cutoff discharger plugin and the operating instructions are also described here.

The paper contains photographs of particles traces inside the chamber in addition to the oscillograms of the corresponding high voltage pulse applied to the chamber.

The development of the method of streamer (track spark) chambers [1 - 3] opens up new possibilities for the study of the nature and interaction of elementary particles. However, the weak glowing brightness of the streamers, which makes their recording by the usual photographic means difficult, the increase in the intensity of the electric field in the chamber for the purpose of increasing the glowing brightness of the streamers, and difficulties in the removal of strong electromagnetic noise which accompanies the operation, all these limit the possibility of applying streamer chambers to the study of nuclear interactions of cosmic ray particles. The main technical difficulties in the way of using streamer chambers in large physical experiments were solved when it was developed in Alma-Ata. /202

The basis element of the streamer chamber are two glass boxes whose dimensions are 1000 x 500 x 200 mm^3 described in article [4] filled with neon to a pressure of 1 atm, which were placed between the duralumin and mesh electrodes. The source for the high-voltage pulse is the nanosecond pulse generator with cutoff dischargers to obtain a regulated pulse duration, which were developed in the Nuclear Physics Scientific Research Institute at the Tomsk Polytechnical Institute [5, 6]. Figure 1 shows schematically the entire installation. The accumulation capacitor 7 with a capacitance of 100 nfarad charged from the

voltage pulse generator (C_{sp} = 14,300 nfarad; U_{max} = 200 kV, the KVG-II-30 - 0.1) capacitor when the internal discharge is pierced (at a nitrogen pressure of 16 atm) puts out a 300 kV pulse with a $2 \cdot 10^{-2}$ front to the transmission line with a wave resistance ρ = 1000 ohm, whose amplitude is doubled at the open end and reaches 600 kV. The transmission line consists of a series of segments, which, when connected, provide the necessary pulse duration. /203

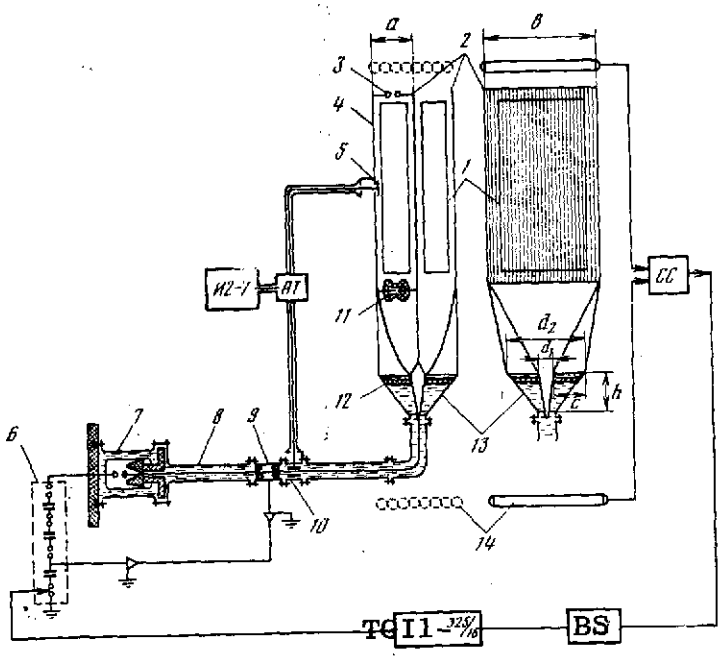

Fig. 1. Feed pulse and chamber control circuit. /202

1--glass boxes; 2--mesh electrodes; 3--air-shunting discharger; 4--duraluminum electrode; 5-10--capacitance dividers; 6--voltage pulse generator; 7--accumulation capacitor; 8--transmission line; 9--discharge under pressure; 11--cutoff discharger peak-plane (not used); 12--insulator; 13--coaxial tapered line; 14--Geiger counter; CC--coincidence circuit; BS--block for pulse shaping; AT--attenuator; 12-7--nanosecond time interval meter

To match the electrodes of the chamber with the transmission line of the generator, they were manufactured in the shape of a three-wire strip line [7]. For d/b = 0 (the thickness d of the plates is considerably smaller than their width b), ρ = 100 ohm and the distance between the plates is a = 224 mm (determined by the gap in the chamber), and the thickness of the plates is b = 560 mm. The smooth transition from the coaxial transmission line to the electrodes in the chamber is made in the form of the coaxial tapered line 13. The wave resistance of the coaxial tapered line (h = 250 mm, c = 210 mm, d_1 = 82 mm,

d_2 = 500 mm) is equal to the wave resistance of the strip line [7]. The full use of such a closed system in the high-voltage generator and the three-electrode system in the chamber reduces considerably the electromagnetic noise accompanying the operation of the streamer chamber.

The chamber is regulated by the telescope of the Geiger counters which isolate the cosmic radiation particles that passed through the volume of the chamber. The pulse from the coincidence circuit actuates the generator on the horizontal thytratron whose pulse ignites the first spark interval of the voltage generator. The delay in the supply of the high-voltage pulse is ~ 1 μsec.

To limit the duration of the pulse, a two-electrode cutoff discharger 9 is used at a nitrogen pressure of 16 atm. The tests of the discharger have shown that it ensures a duration of the rear front of the pulse of 2 nsec (Fig. 2). The method for connecting the discharger 9 and its operation with the streamer chamber are given below.

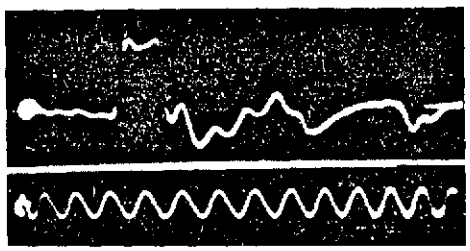

Fig. 2. Oscillogram of pulse with cutoff discharger with capacitance divider 10 (see Fig. 1).

Period of graduated oscillations 10 nsec.

/202

The discharger 9 is mounted at the end of the transmission line. The trace in the chamber has the shape shown in Fig. 3,a (in two projections). If, in addition the air shunting discharger 3 is used on the opposite side where the high-voltage pulse is supplied, which is attached to the end of the electrode plates, the trace in the chamber becomes uniform and has the shape shown in Fig. 3,b.

The discharger 9 is separated from the plate of the streamer chamber by a sector of the transmission line as shown in Fig. 1. The discharger was filmed in such a fashion that it did not break down during the propagation of the incident wave, but did break down during propagation from the open end (the charged streamer chamber is the open end) of the reflected wave leading to a doubling of the voltage. The breakdown in the internal wire of the discharger 9 occurred during the propagation of the

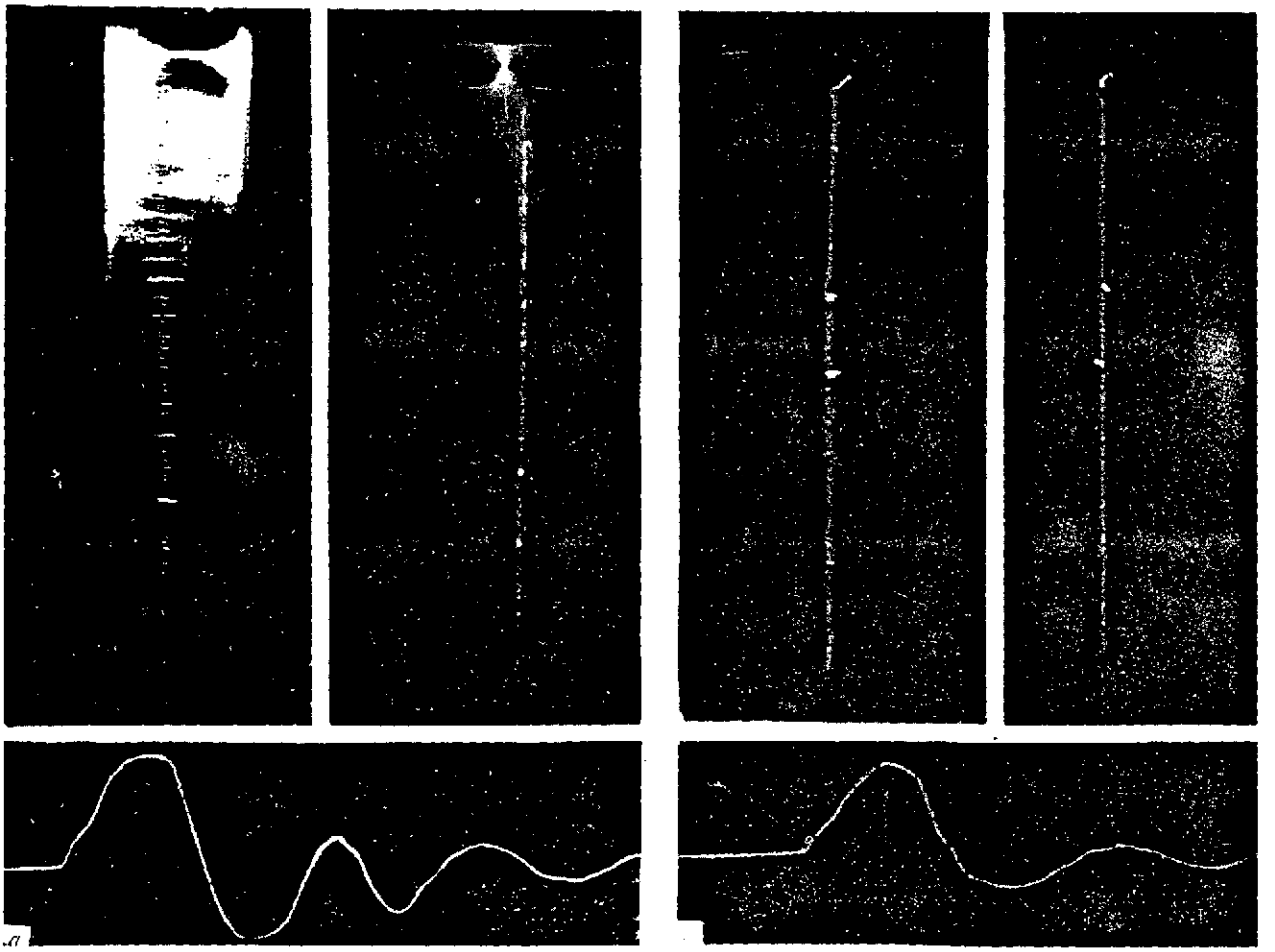

Fig. 3. Photographs of particle traces in the chamber and oscillograms of the corresponding high-voltage pulse in the chamber. (Continued on next page).

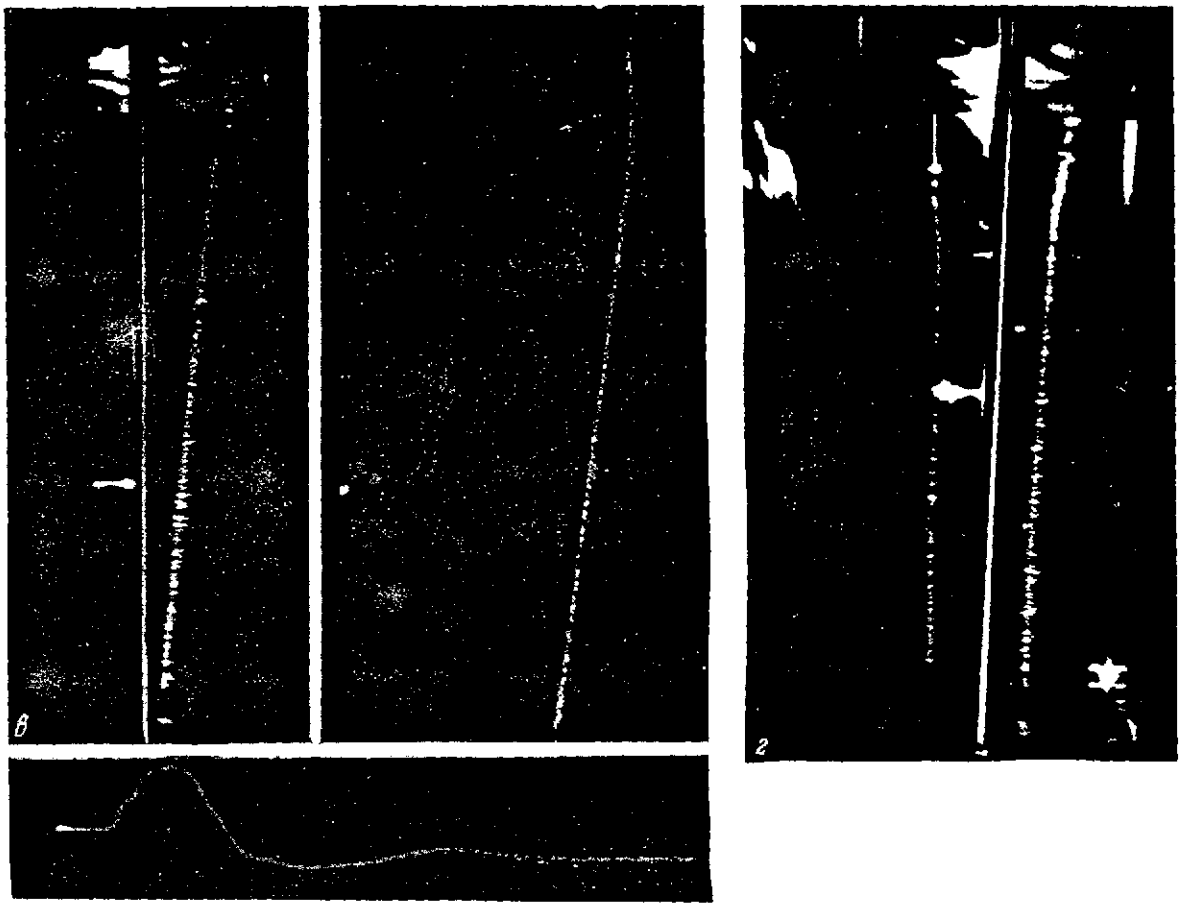

Fig. 3. Photographs of particle traces in the chamber and oscillograms of the corresponding high-voltage pulse in the chamber.

a--spark discharger 9 mounted at the end of the transmission line; b--using an air shunting discharger; c--discharger 9 separated from the plate of the streamer chamber by the transmission line sector with two additional connected shunting dischargers at the end of the electrode plates; d--shower consisting of two particles photographed through the side wall of the chamber.

The shape of the pulse and the remaining data are the same as in Fig. 3,c.

incident wave and the spark which was formed in the process served as the source of the electrons without the additional supply of a triggering pulse. The photographs of the traces in this regime are given in Figs. 3, c and 3,d.

The photographs were made with a Jupiter-8 objective (1:2) on aerial photofilm of the 13 type, whose sensitivity was 1000 units All-Union State Standards. The high-voltage pulse was picked up using a capacitance divider placed above the electrode of the chamber with the aid of a PK-71 cable and I2-7 cable (l ≈ 50 m).

It can be seen from the photograph that when the chamber is fed by single voltage pulses, more stable and bright traces are obtained with good localization of the light.

In Fig. 3,b the length of the streamers (~ 2 mm) is approximately equal to their width (≈ 1 mm) and their brightness is adequate for making photographs, even perpendicularly to the electric field.

In conclusion, the author expresses his gratitude to Professor Zh. S. Takibaev and to Yu. T. Lukin, Candidate of Physical-Mathematical Sciences for their interest in this article and also to I. M. Nikolaev and T. Zh. Imanbakov for their help in this work.

/204

REFERENCES

1. Mikhaylov, V. A., Roynishvili, A. N. and Chikovani, G. E., Zh. Exper Teor Fiz 46, 1228 (1964).

2. Dolgoshein, B. A. and Duchkov, B. I., Zh Exper Teor Fiz, 46, 1953 (1964).

3. Rudenko, N. S., Zh Exper Teor Fiz, 49, 1394 (1965)

4. Nurgozhin, N. N., "Increasing the isotope properties of a discharge spark chamber with large gaps," in this collection.

5. Vorob'ev, G. A. and Rudenko, N. S., Prib Tekh Eksp, No. 1, 109 (1965).

6. Vorob'ev, G. A., Rudenko, N. S., Tsvetkov, V. I. and Kozlov, M. I., Prib Tekh Eksp, No. 1, 186 (1967).

7. Meynke, Kh. and Gundlakh, F., Radiotekhnicheskiy spravochnik, [Radio Engineering Handbook], Vol. 1, Gosenergoizdat Publs., 1960.

· N75 16486

INCREASING THE ISOTROPIC PROPERTIES OF A DISCHARGE SPARK CHAMBER WITH A LARGE GAP

N. N. Nurgozhin

ABSTRACT

Investigations were carried out to record particle tracks in the form of sparks or streamers running at different angles toward the electric field of the chamber. The investigations were performed with two discharge spark chambers consisting of boxes glued with ED-6 epoxy resin. Each box consisted of 8 mm glass plates with overall dimensions 100 x 50 x 20 cm. The chambers were filled with neon at 1 atm. The spark chambers were powered by a pulse with an amplitude of 300 kV applied from a pulse generator.

The recording of particle tracks in the form of sparks took place at track angles $\varphi < 30^{\circ}$ with respect to the electrical field. When $\varphi > 40^{\circ}$ the tracks are recorded in the form of streamers. Particle traces with respect to the angle are given.

A fully isotropic discharge spark chamber of large area recording greater quantities of particles is said to be feasible.

In the last few years many studies were published whose purpose was to impart to spark chambers with a large gap isotropic properties during the recording of the traces of charged particles [1 - 7]. However, many of these studies have not been widely applied in practice, first because of the limited brightness of the traces, second because of technical difficulties, which limit the dimensions of the chamber. In our opinion the most promising solution of the problem of increasing the isotropy of discharge spark chambers with a large gap, is the recording of particle tracks not only in the form of spark channels, but also in the form of streamers [8].

In the study we used two discharge spark chambers (IRK) that were boxes glued together from 8-mm glass plates, whose overall dimensions were 1000 x 500 x 200 mm^3 with ED-5 epoxy resin, that were pumped up to a pressure of 10^{-3} - 10^{-4} torr, and filled with neon to a pressure of 1 atm.tech which were placed between metallic electrodes that were 1.5 mm thick. The chambers were pumped and filled in a metallic casing.

The pulse feeding and control circuits are shown in Fig. 1. /205
A specific feature of the feeding circuit is the use of a powerful voltage pulse generator (VPG), and a compensation node (C_H, P_O, SR) for shaping pulses with an amplitude of 300 kV with a steep front, whose activity can be regulated [9].

The gas-discharge counters above and elow the chamber (one counter with dimensions 550 x 32 on each side), connected to the coincidence circuits isolated the particles that passed through the working volume of the chamber in the plane parallel to the plane of the film and triggered the control circuit of the voltage pulse generator. The indeterminacy in the estimate of the angle was $\pm 6^{o}$, and the delay in the supply of the high-voltage pulse was 1 μsec.

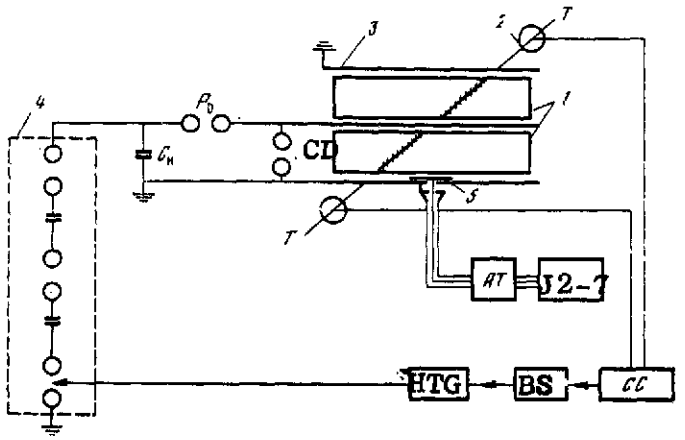

Fig. 1. Feeding pulse circuit and control circuit of the chamber.

1--glass chambers; 2--gas-discharge counters; 3--metallic electrodes; 4--discharge pulse voltage generator (S_{sp} = 2500 nfarad, U_{max} = 200 kV); 5--capacitance divider; C_H--accumulation capacitance (250 nfarad); P_O--peak air discharger; CD--cutoff discharger; I2-7--nanosecond time interval meter; CC--coincidence circuit; BS--pulse shaping block; HTG --high-voltage tiratron generator; AT--attenuator.

Figure 2 shows the oscillogram of the high-voltage pulse in the chamber which was picked up with the aid of the capacitance divider placed over an electrode in the chamber. A pulse

of variable polarity is obtained after the first pulse is cut off as a result of the oscillations of the capacitance discharge of the plates of the chamber through the cutoff discharger. The number of oscillations depends on the damping in the chamber-cutoff discharger plate system and it is regulated by varying the breakdown interval of the cutoff discharger (CD).

Fig. 2. Oscillogram of high-voltage pulse amplitude 300 kV, brightness marks 200 nsec.

The positions of the chamber remained unchanged during the experiment; however, the position of the counters that sampled the particles arriving at various angles φ to the direction of the electrical field in the chamber were changed. When the pulse duration is great, starting from the angle $\varphi \geq 30^{\circ}$, a "forest" of sparks of small brightness is observed on the track which propagates from the main spark along the electrical field to the electrode in the chamber. As the angle φ increases, the "forest" of sparks becomes more and more bright and the chamber passes into the projection state [10]. If the duration of the main pulse is reduced by decreasing the spark discharge distance of the cutoff discharger, clear spark channels are observed in the chamber which follow the particle trajectory only up to the angles $\varphi \leq 30^{\circ}$, and when $\varphi \geq 40^{\circ}$, the track of the particle consists of individual streamers and the chamber passes into the streamer state [3, 4]. As the angle φ increases, the brightness of the streamers decreases provided the duration of the main pulse does not increase. /206

Figure 3 shows the photographs of the traces of cosmic rays for various values of the angle φ.

The photographs were made using a Jupiter-8 objective (1:5.6 and 1:2.8) on aerial photofilm of type 13 with a sensitivity of 100 units All-Union State Standards. It should be mentioned that the bottom chamber operates in the projection state and shows only the direction of the trajectory of the particles. However, during shunting with a special resistance R_n = 5 kohm, the chamber passes into the streamer state (Fig. 3,d).

The widths of the particle tracks shown in Figs. 3,c and d, are 6 and 10 mm, respectively. As the tracks become more narrow, their brightness also decreases (approximately in the same way as when the angle φ increases), and they are not recorded on the film, although sufficiently clear traces can be observed visually.

Figure 4 gives the photographs of showers which show along with the recording of the tracks in the form of spark channels narrow streamer tracks. The mean dimension of the streamers is 3-5 mm. A specially shaped high-voltage pulse is needed to obtain such tracks in streamer chambers [3, 4].

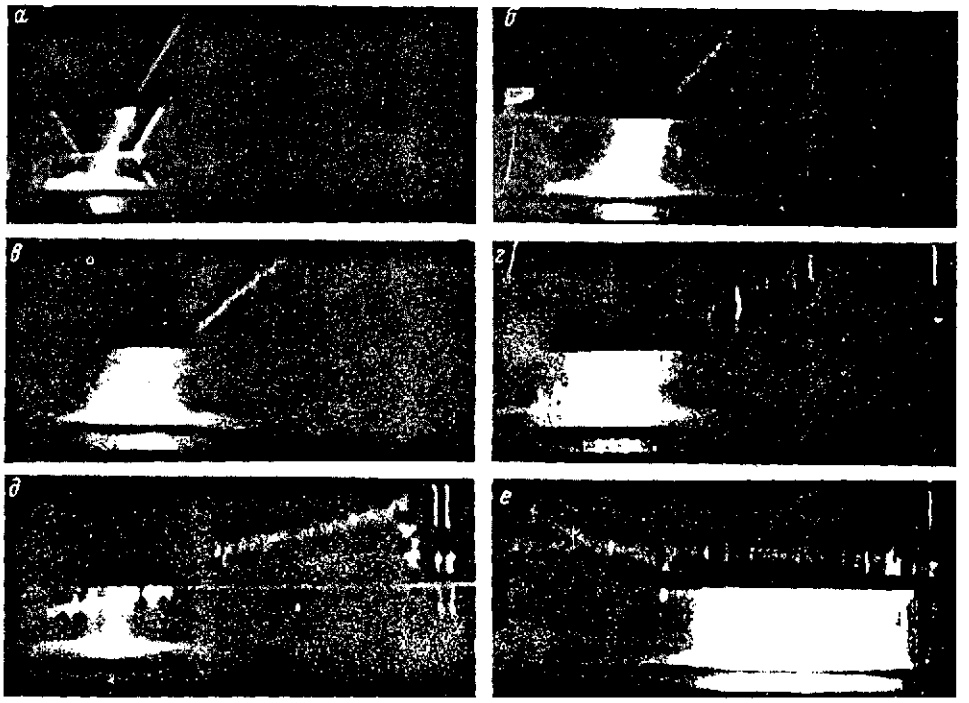

Fig. 3. Photographs of the particle tracks depending on the angle φ

a--30°; b--40°; c--55°; d--65°; e--75°; f--φ = 90°.

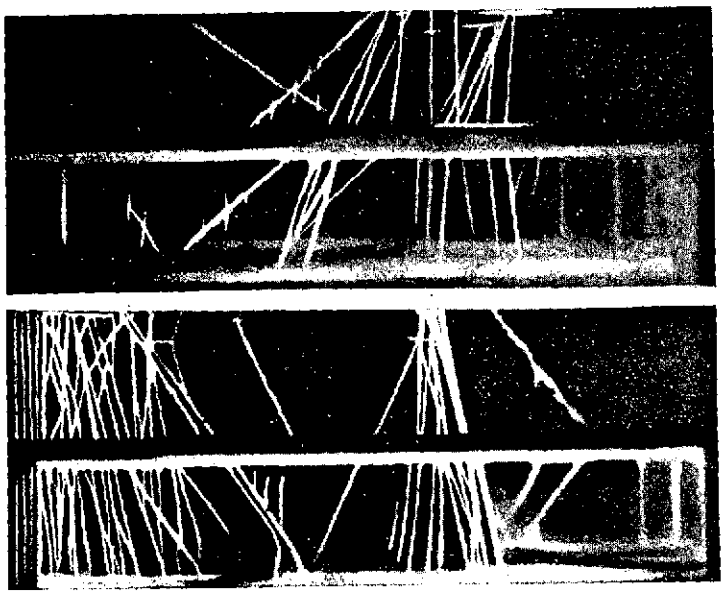

Fig. 4. Photographs of showers with narrow streamer tracks

On the basis of experimental data, the following picture can be given for the development of a spark discharge when a large number of particles intersecting its working volume at different angles pass simultaneously through the chamber. The spark channel along the track develops faster than the channels along the electrical field, and the rate at which it develops increases as the tracking angle φ decreases. In addition, a large number of such spark channels in the shower shortens the feeding pulse. The discharges which develop only in the direction of the field for particles passing at large angles ($\varphi > 40^{\circ}$) do not make the transition to the spark stage and are localized near the particle trajectory in the form of streamers. In addition to this, the spark tracks of the shower illuminate the weak streamer traces, thus making it possible to photograph them. Thus, for traces with $\varphi > 40^{\circ}$, the spark tracks of the shower resemble the shunting discharger in the streamer chamber. Such self-regulation of the duration of the high-voltage feeding pulse and the additional illumination due to the pulses can be very important in the recording of many particles passing simultaneously through the chamber at different angles, and for obtaining a high shower effectiveness of the chamber regardless of the slope of the traces.

Summarizing what has been said, we conclude that a completely isotropic discharge spark chamber with a large gap which is highly efficient with regard to the number of particles recorded can be developed by increasing the intensity of the electric field and by improving the parameters of the high-voltage pulse.

In conclusion, the author expresses his gratitude to Professor Zh. S. Takibaev and to T. Lukin, Candidate of Physical Sciences, for their interest in this study, and to G. P. Kozlov and V. A. Anan'eva for their help with the work.

REFERENCES

/207

1. Fukui, S., Hayakawa, S., Tsukishima, T. and Nukushima, H., Nucl. Instrum. and Methods, 20, 195 (1963).

2. Cavalleri, G., Gatte, E. and Redaelli, C., Nuovo cimento, 6, 1282 (1962).

3. Mikhaylov, V. A., Roynishvili, V. N. and Chikovani, G. E., Zh Teor Eksp Fiz, 46, 1229 (1964).

4. Dolgoshein, B. A. and Duchkov, B. I., Zh Teor Eksp Fiz, 46, 1953 (1964).

5. Butslov, M. M., Komarov, V. I. and Savchenko, O. V., Zh Teor Eksp Fiz, 46, 2245 (1964).

6. Domaskinskiy, A. E., et al., Materialy rabochego soveshchaniya po iskrovym kameram, [Reports read at the Conference on Spark Chambers], Dubna, 1966 -- Preprint, Joint Institute of Nuclear Research, 1966, pp. 13-2958.

7. Alakov, A. V., Babushkina, O. P., Bolotov, V. N. and Devishev, M. I., Preprint, Physics Institute of the USSR Academy of Sciences, No. 40, 1967.

8. Nurgozhin, N. N., and Kalibaev, M. A., in the collection Kosmicheskie luchi, No. 12, 98 (1970).

9. Nurgozhin, N. N., Simpozium po nanosekundnoy radioelektronike v yadernoy fizike, [Symposium on Nanosecond Radio Electronics in Nuclear Physics], Dubna, 1967.

10. Doyon, M. I., Voprosy fiziki elementarnykh chastits, [Problems in the Physics of Elementary Particles], Yerevan, Armenian SSR Acad. of Sci., 1963.

N75 16487

GAS THRESHOLD CERENKOV COUNTERS

V. I. Logachev, V. G. Sinitsyna, V. S. Chukin

ABSTRACT

The report describes two designs of gas threshold Cerenkov counters for recording electrons of primary cosmic rays with $E_e \geq 5$ MeV, without recording protons with $E_p < 10$ BeV. Also presented are design and technological measures which ensure maximum light collection of the Cerenkov radiation originating on the photocathode of the photomultiplier inside the radiator.

The paper shows the dependence of the reflection factor on the length of the light wave for different coatings as well as for the throughput of the different optical materials employed. A range of methods for determining the efficiency of the counters during the recording of cosmic ray μ-mesons and ways of increasing it further are given.

When an installation for the recording of the electronic components of primary cosmic radiation was developed, it was necessary to have a detector that recorded electrons with $E_e \geq 5$ MeV, which did not record protons with $E_p < 10$ BeV [1].

The energy threshold of the gas Cerenkov counter (GCC) is determined by the refractive index n as

$$E_{threshold} = \frac{E_0}{\sqrt{2(n-1)}}. \quad (1)$$

The refractive index n of the gas is a function of its density, so that using the gas as the Cerenkov gas counter radiator, the threshold of the counter can be set at a definite value by changing the pressure. On the basis of the threshold energy from the protons $E_{threshold} > 10$ BeV/nucleons from formula (1), we obtain $n - 1 < 5 \cdot 10^{-3}$. Such refractive index of the radiator can be obtained at comparatively small gas pressures ($p < 10$ atm) by using freon or ethylene. In the Cerenkov gas counter designs, vaseline was used at a pressure of 5 atm·tech. For ethylene $(n - 1) \cdot 10^4 - 6.96$ at 0°C and 760 mm Hg;

therefore, at a pressure of 5 atm·tech, the energy threshold of the counter for protons is $E_{threshold} \approx 12$ BeV.

Since the efficiency of the threshold Cerenkov gas counter depends mainly on how well the light from the Vavilov-Cerenkov radiation generator in the radiator is collected on the photocathode of the photomultiplier, special attention was paid to the optics of the counter, and measures were taken to ensure a maximum reflectance coefficient of the internal surfaces. Since the efficiency of the counters also depends on the quantum output of the amplification factor and the noise level of the photomultiplier, the photomultipliers operating in the counters were selected carefully. /208

A characteristic feature of the designs under consideration is that the photomultiplier which scans the volume of the radiator lies inside the solid angle of the sensitivity of the installation. Such design of the circuit, in addition to ensuring the conditions for attaining high efficiency, made it also possible to design a compact structure for the node controlling parts of the installation.

The first variant of the counter (Fig. 1) was in the form of a cylinder whose diameter was 140 mm and whose length was $l = 700$ mm. At the focus of the aluminized spherical mirror 5, made from ShKh-15 steel is the plexiglas window3, through which the light arrives at the photocathode of the FEU-53 photomultiplier. A semiconductive pulse light source based on gallium phosphite (GaP) which is used to calibrate the counter during the control test period is mounted directly in front of the photocathode of the photomultiplier in the plexiglas window. The optical contact between the plexiglas window, the photomultiplier and the semiconductive light source is obtained on an epoxy resin base, which, in addition to high mechanical-engineering properties, transmits light well in the range 3000-6000 Å [1 - 3].

The top part of the counter (Fig. 2) is made from 1X18H9T steel in the form of a reflector which improves considerably the light collection. The reflector represents a surface of revolution. The generatrix of this surface is the branch of the parabola passing through the edge of the plexiglas window through which the photomultiplier scans the internal volume of the gas counter. The focus of the parabola lies on the edge of the photocathode of the photomultiplier (the point F in Fig. 2). The axis of the parabola X - X is oriented along the axis of the counter O - O. Such reflector makes it possible to collect effectively the light from the particles passing within the solid angle of sensitivity of the installation ($2\alpha - 17^{o}$). Al is sprayed on the surface of the reflector and to the internal surface of the cylindrical part of the counter (wall thickness /210

δ = 1 mm) is glued an aluminized mirror image reflecting mylar film (ϵ = 0.06, A_s = 0.13). It is also possible to apply to the internal surface of the cylindrical part a highly effective coat of reflecting V1-548 paint (Fig. 3).

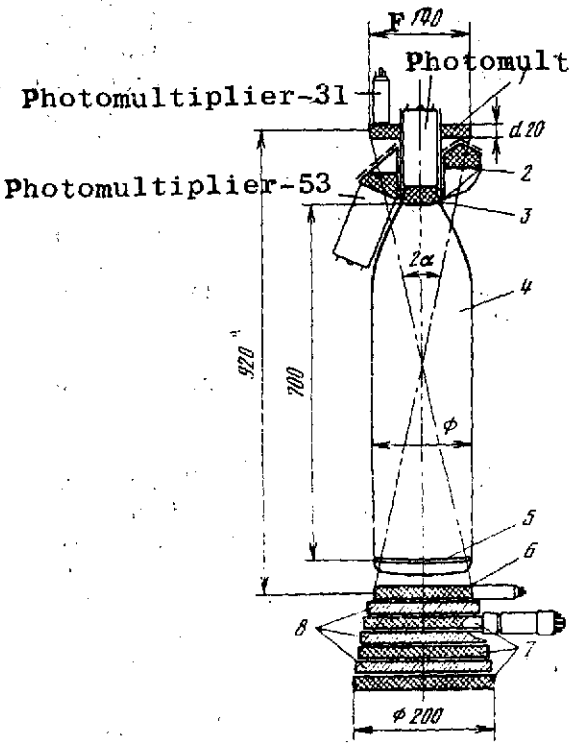

Fig. 1. First variant of gas Cerenkov counter.

1 and 6--telescope from scintillation counters; 2--oriented Cerenkov counter; 3--window of Cerenkov gas counter; 4--Cerenkov gas counter; 5--spherical mirror (f = 700 mm); 7--measurement scintillation counters; 8--lead filters

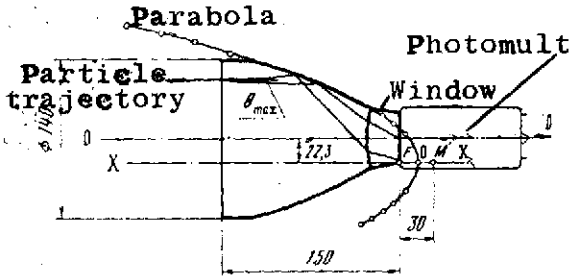

Fig. 2. Diagram explaining the structure of the profile of the Cerenkov gas counter reflector

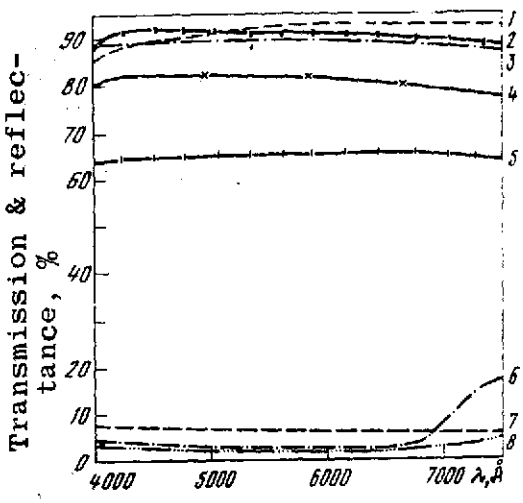

Fig. 3. Reflectance coefficient vs. length of light wave.

Measurements were carried out on the SF-10 spectrophotometer using Taylor's method; 1--VL-458 paint; 2--aluminum (99, 99) sprayed in vacuum; 3--aluminized mylar film; 4-- photographic plate = 4; 5--Al, etched with alkaline; 6--Al, blackened galvanically; 7--NTs-25 black enamel; 8--CuO (blackened galvanically)

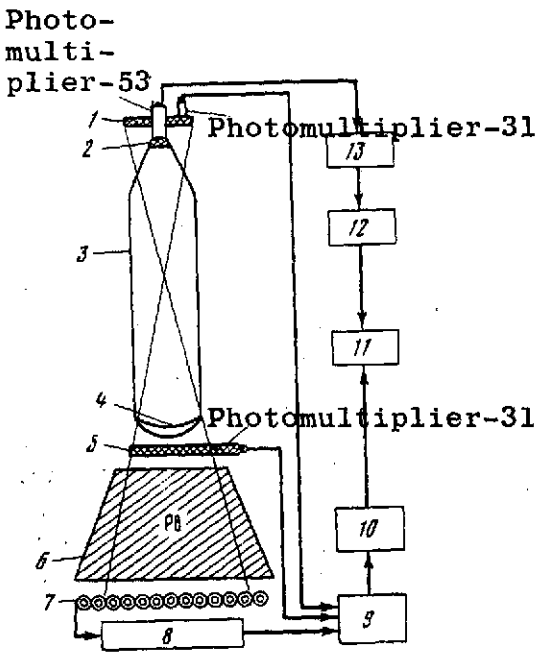

Fig. 4. Block diagram of installation for determining the effectiveness of the counters.

1--top scintillation counter of telescope; 2--plexiglas window; 3--Cerenkov gas counter; 4--spherical mirror; 5--bottom scintillation counter of telescope; 6--lead filter; 7--gas-discharge counters of STS-2 telescope; 8--adder; 9--coincidence circuit; 10--AI-100 triggering circuit; 1--AI-100 amplitude analyzer; 12--amplifier; 13--emitter follower

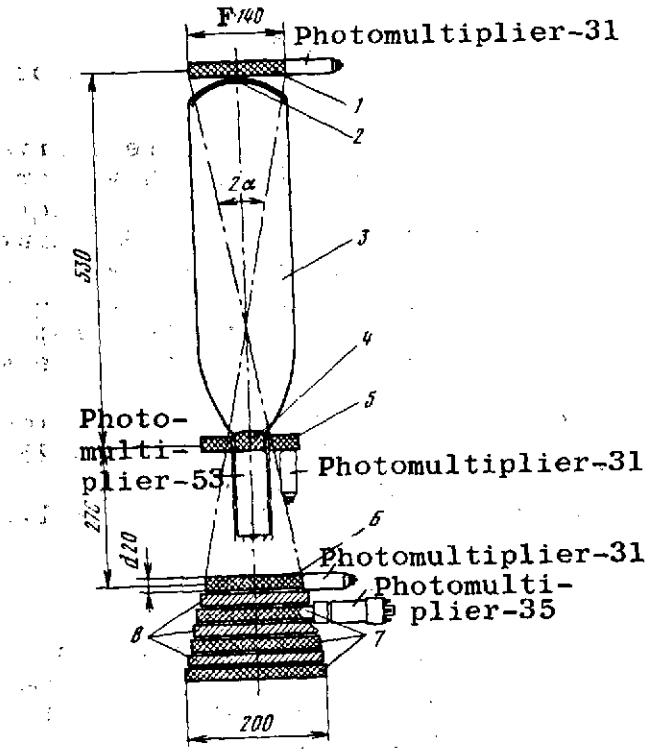

Fig. 5. Second Cerenkov gas counter variant.

1, 5, 6--telescope from scintillation counters (d = 20 mm); 2--blackened surface; 3--Cerenkov gas counter; 4--scintillation counter meters; 8--lead filters

The efficiency of the counters was determined from single-charged cosmic particles. The block diagram of the installation used to determine the efficiency is given in Fig. 4. To eliminate the recording of μ-mesons which trigger the telescope of the scintillation counters (d = 20 mm) and which do not give light in the gas Cerenkov counter (E < 2 BeV), a lead filter which was 1 m thick was used (> 1000 g/cm^2). The amplitude analyzer was triggered by the telescope from the scintillation counters 1 and 5 and the gas-discharge counters placed under the lead 7. The efficiency of the Cerenkov gas counter of the given type was 93-96% [1].

During the development the design and other control experiments, attention was paid to the possible effect of various factors in the surrounding medium on the constancy of the parameters of the counters and also on their possible variation with time. To control the gas pressure, a sensor was mounted on the counter which measured the pressure with an accuracy of ± 1.5%. To control the temperature, sensors were used which measured the temperature with an accuracy of ± 2.5%.

The relations for the parameters of the main elements of the counter and the installation as a whole were determined as functions of the temperature. The results of the tests have shown that the apparatus was fully operational under the given experimental conditions, when the temperature varied from -5 to +45°C, and that the parameters did not change with time within the accuracy of the measurements.

In the second variant of the Cerenkov gas counter (Fig. 5), the volume of the radiator is scanned by the photomultiplier from below upward and the light arrives directly at the photocathode of the photomultiplier without the losses which occur when it is reflected from the mirror. A screen was fixed in the top part of the counter to which a highly effective light-absorbing coating was applied (see Fig. 3, curve 8). This design of the structure made it possible to do without the oriented plexiglas Cerenkov counter, since the light generated by the particles arriving from below, arrives at the absorbing screen due to the orientation of the Vavilov-Cerenkov radiation, and is not recorded by the photomultiplier. The data about the magnitude of the pulse in the first variant of the counter that were obtained experimentally made it possible to reduce the length of the gas radiator to 500 mm, by observing carefully the manufacturing specifications for the reflecting elements.

REFERENCES

/211

1. Bolyshev, V. A., Kapustin, M. N., Kurnosova, L. V., et al., Ustanovka dlya registratsii elektronnoy komponenty pervichnogo kosmicheskogo izlucheniya, [Installation for the Recording of the Electron Component of Primary Cosmic Radiation], Preprint, Physics Institute of the USSR Acad. of Sci., 1966.

2. Bolyshev, V. A., et al., in the collection Kosmicheskie luchi, No. 11, 1969.

3. Chukin, V. S., Preprint, Physics Institute of the USSR Acad. of Sci., 1967.

N75 16488

BACKGROUND ESTIMATION IN A (νe)-DIFFUSION DETECTOR

V. I. Glotov

ABSTRACT

Background conditions for detecting (γe)-diffusion are discussed with reference to the utilization of a hodoscope system consisting of wide-area flat Geiger counters connected for coincidence and of a controllable spark chamber.

When calculating the background, any organic compounds synthesized from C, O_2 and H_2 (for example, organic glass) with radioactive admixtures (U, Th and their allied products) is presumed to be the preferrable material for the construction of the detector.

The number of background events simulating the effect sought is estimated by analyzing the spectrum of the organic glass γ-radiation caused by the disintegration and fission of long-lived isotopes and by nuclear reactions with the participation of α-particles and neutrons.

When neutrino experiments are carried out, attention must be paid to the radioactive background of the structural materials from which the detector is made [1, 2]. It is especially important that such background be taken into account during the recording of the diffusion of solar neutrino on the electron because of the small magnitude of the effect sought. During diffusion the neutrino is repelled forward in a narrow solid angle [3]. This recoil electron can be recorded in a hodoscope system consisting of flat Geiger counters of large area (200 x 100 cm^2) [4] connected for coincidence, or in a spark chamber which is controlled by such counters. Such and other detectors must be oriented toward the Sun.

The presence of U, Th admixtures in the substance from which the detector is made, and their daughter products leads to the formation of background electrons in the detector volume which can simulate recoil electrons from the neutrino. In this connection, this article examined the possible sources for the generation of background electrons as well as the distribution of these electrons by energy.

Background electrons are formed as a result of the β-disintegration of radioactive elements and as a result of the

diffusion of background photons also on electrons. The background photons, in turn, are generated in the disintegration of radioactive elements and also in nuclear reactions (α, γ), $(\alpha, \alpha\gamma)$, $(\alpha, n\gamma)$, (n, γ), $(n, n'\gamma)$. β-disintegration and the Compton diffusion of photons with energy $E_\gamma < 3$ MeV form the soft part of the complete spectrum of background electrons with energy $E_e \lesssim 3$ MeV. The photons that accompany the aforementioned nuclear reactions form the hard part of the electron spectrum with energy 4 MeV $< E_e <$ 13 MeV. The intensity of high-energy electrons clearly depends on the chemical composition of the material of the detector.

The energy spectra of the electrons were calculated under the following assumptions: a) the detector (the walls of the counters and the plates of the spark chambers) were made from an organic substance, synthesized from oxygen, hydrogen and carbon), for example, organic glass), b) the impurities of the substance include a mixture (1:3) of uranium and thorium in radioactive equilibrium with the daughter products; c) the detector is imbedded in an infinite space filled with the material from which the detector itself is made, d) extraneous sources in the background not connected with the substance of the detector do not exist. It was found that the rate at which the electrons with energy $E_e < 3$ MeV were generated in organic glass was $\sim 10^9 \cdot m/day^{-1} \cdot cm^{-3}$, and with energy $E_e > 4$ MeV, $\sim 3 \cdot 10^2 \cdot m/day^{-1} \cdot cm^{-3}$, respectively, (m is the amount in grams of the U and Th mixture (1:3) in one gram of organic glass).

The number of background triggerings of the coincidence circuits in the hodoscope system and the number of background tracks in the spark chamber were calculated on the basis of the energy spectra of the electrons that were obtained. It was assumed that /21
the background triggering of the coincidence circuits is brought on by the following effects: a) the multiple Compton effect; b) the simultaneous generation in the β-disintegration of the electron and photon which "trigger" the necessary number of counters; c) through various combination of random coincidences; d) through the passage of a long-range background electron. The number of background triggerings of the coincidence circuits was calculated for various recording thresholds of the electrons and for various coincidence multiplicities. The resolution time of the counters was taken as 10^{-5} sec. The thickness of the walls of the counters was determined by selecting the coincidence multiplicity and the recording threshold of the recoil electron. It was found that for $E_{threshold} > 5$ MeV and for the selected coincidence multiplicity, coincidence circuits were

mainly triggered by long-range electrons. This was also true of the spark chamber. The background in the spark chamber can be reduced by introducing an appropriate criterion for the selection of the tracks by the angle [3]. The nuclear reaction C^{13} $(\alpha, n\gamma)$ which generates γ-quanta with $E_\gamma >$ MeV is responsible for the generation of long-range electrons. This reaction is caused by α-particles which belong to the radioactive families Ra and RdTh. The figure compares the magnitude of the effect with the background level in the hodoscope system with quadruple and quintuple coincidences (and in the spark chamber). The background was calculated for $m \approx 10^{-9}$ g/g. The accuracy of the background estimation is not below 100%.

The author expresses his gratitude to A. E. Chudakov, G. T. Zatsenin and B. V. Tolkachev for useful criticisms and recommendations.

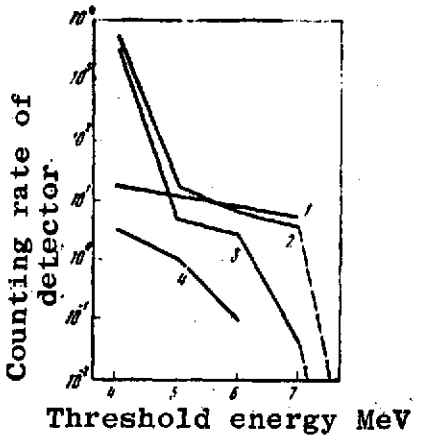

Fig. Comparison of the magnitude caused by neutrino diffusion on the electrode with the background.

1--effect [3]; 2--background in hodoscope for quadruple coincidences; 3--background in hodoscope for quintuple coincidences; 4--background in spark chamber.

REFERENCES

1. Glotov, V. I., Elpidinskiy, A. V., Zagrebin, V. A., in the collection Kosmicheskie luchi, No. 10, 92, (1969).

2. Glotov, V. I., Gamma-aktivnost' organicheskikh veshchestv, vyzvannaya radioaktivnymi zagryazneniyami, [Gamma-Activity of Organic Substances Caused by Radioactive Contamination], Preprint, Physics Institute of the USSR Acad. of Sci., No. 105, 1967.

3. Domogatsky, G. V. and Zatsepin, G. T., Proc. IX Internat. Conf. Cosmic Rays, Vol. 2, London, 1965.

4. Bondarev, B. V., Mikheev, S. P., Sborshchikov, V. G. and Tolkachev, B. V., "Flat Geiger counter with many wires," in the collection Kosmicheskie luchi, No. 12, 88-90 (1970).

N75 16489

COMPARATIVE ANALYSIS OF ERRORS IN DIFFERENT METHODS OF CALCULATING L, B-COORDINATES

I. V. Getselev, V. A. El'tekov, V. I. Volga, V. A. Kuznetsov

ABSTRACT

Due to considerable difficulties of calculating L, B-coordinates, several simplified methods are currently used. The relative errors in L, B-coordinates calculated by approximate methods are given.

It is suggested that different methods be used to calculate L, B-coordinates in the solution of various problems.

In the study of the geometric position and the dynamics of radiation belts, the most widely used method is the method of representing particle fluxes in so-called L, B-coordinates. The usefulness of this method is that the characteristics of the fluxes are related naturally to the characteristics of the geomagnetic field, and many functional relations which depend on the coordinates of three-dimensional space can be reduced to functions of two variables when this method is used.

It is known [1] that the leading center of the trajectory moving in a stationary geomagnetic field describes the drift surface which is determined by the conditions for the preservation of the first $\mu(r, t)$ and second $I(r, t)$ adiabatic invariants. Instead of μ and I, C. E. McIlwain [2] proposed to use a pair of numbers B and L. The first is the modulus of the intensity of the magnetic field at the reflectance points and the second is a parameter, which in the case of a dipole field, is equal to the maximum distance of the line of force from the dipole expressed in terms of the Earth's radius. In a non-dipole field, L does not have a simple geometrical interpretation, but it is related to the values of B and I at the reflecting points by the same formulas as in the dipole case. In addition to this McIlwain introduced effective envelopes which are characterized by a constant L, which in a non-dipole field coincide only approximately with the true envelopes. This makes it possible to associate the fluxes with values of B and L at the observation point, and not at the reflecting point, but it leads to a certain inaccuracy whose consequences can only be evaluated with considerable difficulty.

Leaving aside this problem, we will consider certain methods for calculating the L, B-coordinates, and we will give a relative estimate for them. We note that to process the experimental data successfully, B and L must be calculated with an accuracy not worse than 1%.

The model of the central dipole turns out to be too coarse even for distances of $\sim 5R_E$, as can be seen from the figure and the table. Therefore, it is necessary to take into account higher harmonics in the Gaussian series expansion of the geomagnetic potential. According to the program that we coded, the B and L were calculated both by taking into account different numbers of harmonics, altogether up to six, and also on the basis of the noncentral dipole model [3]. In the first case, to calculate L, the line of force was constructed, after which L was calculated either in terms of B or I or in terms of the minimum value of B on the line of force. It was found that the difference in the results did not exceed 0.5%, which was mentioned in [4]. Since a systematic calculation of L requires a great deal of machine time, we give a comparison of the results only for B (see table).

We note that the relative errors for L are several times smaller than the corresponding errors for B.

TABLE. MAXIMUM RELATIVE ERROR IN DIFFERENT MODELS, %

Distance R_E	Model			Distance R_E	Model		
	CD	ED	DQ		CD	ED	DQ
1	20	5	4	4	5	2	1
3	10	3	2	5	3	1	0,5

Taking the calculations based on the 48-term potential (6 harmonics) as the exact values, the following table of the maximum relative errors can be set up for various models: the central dipole (CD), the eccentric dipole (ED) and the dipole with the quadruple (DQ). It can be seen from the table that the ED model is not sufficiently reliable up to distances of $\sim 4R_E$. For these distances, the calculations based on the multipole representation with a sufficient number of harmonics can be used. /214

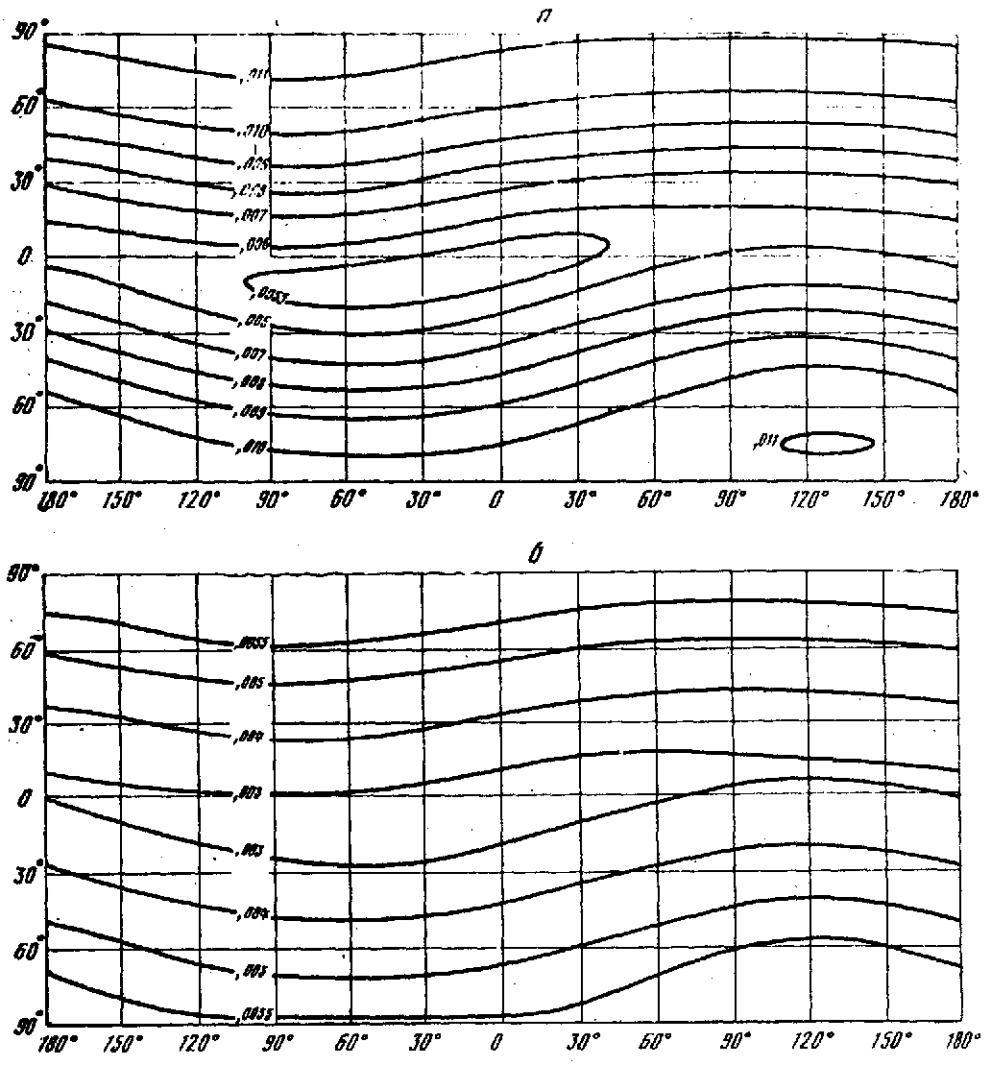

Fig. Isolines B at altitudes 18,000 km (a) and (24,000 km (b)

REFERENCES

1. Northrop, T. and Teller, E., in the collection Solnechnyye korpuskulyarnye potoki i ikh vzaimodeystviye s magnitnym polem Zemli, [Solar Corpuscular Fluxes and Their Interaction with the Earth's magnetic field[, Foreign Lit. Publs., 1962.

2. McIlwain, C. E., J. Geophys. Res., 66, 3681 (1961).

3. Ben'kova, I. P., Vinnikova, T. L., and Tyurmina, L. O., Geomagnetizm i aeronomiya, 4, 917 (1964).

4. Stone, E. C., J. Geophys. Res., 68, 4157 (1963).

N75 16490

AN INSTRUMENT FOR THE STUDY OF THE COMPOSITION OF THE ELECTRON COMPONENT OF COSMIC RAYS

E. A. Bogomolov, V. K. Karakad'ko, N. D. Lubyanaya, V. A. Romanov, M. G. Totuvalina, M. A. Yamshchikov

ABSTRACT

A telescope consisting of three spark chambers and two control scintillations counters has been designed and is used for investigating the composition of the cosmic ray electron component within the range of energies from 1.0 to 10.0 BeV by the EN assymetry method. The geometrical factor of the telescope is ~ 20 cm^2.ster. Discharges are recorded in the chambers on a photo film. The telescope is oriented to the azimuth with an accuracy of ± 3°.

A study of the charging composition of the electron component of primary cosmic rays contributes to the full understanding of questions related to their origin and propagation. In the studies that were published in the last few years, relatively reliable data about the number of positrons in cosmic rays are given only for the energy ranges from 0.2 - 0.5 BeV [1]. With regard to energies above 0.5 BeV, the available experimental data are scarce, and the measurement errors are large. It is rather difficult to obtain exact data about the charging composition of the electron component because of its relatively low intensity (~ 1% of the total cosmic ray intensity) and the complexity of separating primary electrons and positrons from secondary ones.

At the present time, two methods are used to separate the electrons and positrons: by analyzing their deviation in the magnetic field of the device [1, 2] and by studying the east-west asymmetry of the electron component [3, 4]. The second method, which is simpler, was used in this study.

General Characterization of the Instrument

To study the composition of the electron component in the energy range 1.0 - 10.0 BeV, a telescope was prepared which was designed to operate on high-altitude balloons. During the flight the telescope is oriented alternately along the Earth's magnetic field east and west. The orientation system is analogous to that described in [5]. The accuracy of the orientation by azimuth is ± 3°. The zenith angle of the telescope during the measurements was 45 or 60°.

The telescope consists of three spark chambers and two regulating scintillation counters. Figure 1 shows the the exterior (with casing removed) and Fig. 2 shows the block diagram of the telescope. The top spark chamber determines the direction of motion of the charged particle arriving in the telescope and it separates the showers formed in the residual atmosphere and on the substance of the outer shell of the instrument. The total amount of the material for the first interval of the spark chamber is ~ 0.1 of the radiation length. The middle and bottom chambers are shower chambers whose thickness is ~ 17 radiation lengths. The geometrical factor of the telescope is ~ 20 $cm^2 \cdot ster$. The telescope lies in a hermetic aluminum casing with two longitudinal windows covered by plexiglas. The chamber intervals and the auxiliary instruments are photographed through these windows. The device weighs approximately 300 kg. /216

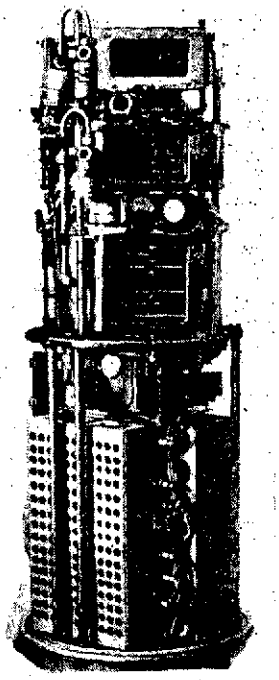

Fig. 1. Outer form of the telescope (casing removed)

Spark Chambers

The casings of the spark chambers are steel cylinders with a 340 mm diameter and the heights of the top, middle and bottom chambers are 90, 120 and 200 mm, respectively. In

each casing are two plexiglas windows for scanning the spark intervals. The number of electrodes in the chambers is 5, 5 and 7, respectively, for the top, middle and bottom chamber. The gaps between the electrodes are 12 ± 0.2 mm. The high-voltage pulse feed circuit for the electrodes of the spark chambers is shown in the block diagram (see Fig. 2). The electrodes in the top chamber are made from 0.05 mm thick aluminum foil which is glued to the plexiglas edges.

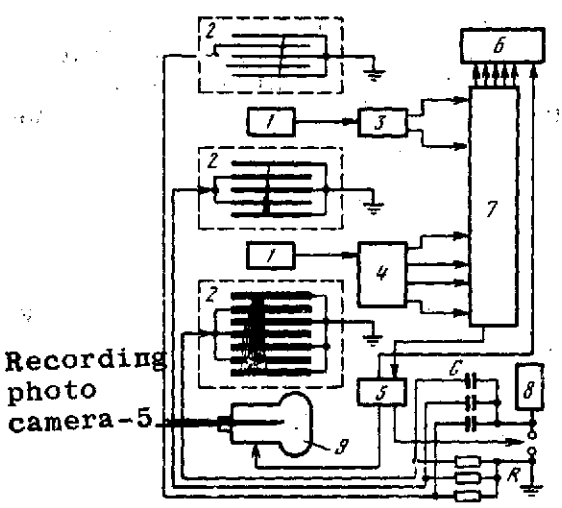

Fig. 2. Block diagram of telescope.

1--scintillation counters; 2--spark chambers; 3--differential discriminator; 4--threshold device; 5--control block; 6-- mechanical counters; 7--coincidence circuits; 8--high-voltage transformer; 9--recording photo camera.

To obtain sufficiently hard electrodes with a good surface in the shower chambers, hollow steel plates were used in which lead disks with a 160 mm diameter that were 5 mm thick were inserted in the top chamber, and 10 mm thick disks in the bottom chambers. After they were soldered, the plates were ground. The thickness of each plate in the middle chamber was ~ 1 radiation length and in the bottom chamber ~ 2 radiation lengths.

To increase the recording efficiency of the shower particles, dielectric plates were inserted in the gaps in the middle and bottom chamber adjacent to the high-voltage electrodes. In the middle chamber, bakelite plastic plates were used (1 mm thick) and in the bottom chamber, plexiglas plates (1.8 mm thick). The interiors of the middle and bottom chamber are connected.

Scintillation Counters, Radio Engineering Circuits and Photo Recording

The scintillation counters are located in the gaps between the chambers. The diameter of the plastic scintillators of both counters is 100 mm, and the thickness is 30 mm. They are scanned on the side by FEU-15 photomultipliers. To improve the light collection, the scintillators are covered with white enamel. The pulses from the top counter arrive to the differential discriminator and from the bottom counter to a series of threshold devices. The pulses that pass the discriminator and the threshold devices arrive at the coincidence circuits ($\tau = 10^{-7}$ sec). The passage of single single charged relativistic particles through the top scintillator which coincides with the passage of one or more than one, more than two or more than three such particles through the bottom scintillator is recorded. The signal from the output of the coincidence circuit corresponding to the passage of more than three particles through the bottom scintillator is used to trigger the spark chambers. The pulses from all outputs of the coincidence circuits are recorded by mechanical counters. The discriminator and threshold devices use tunnel diodes. /217

In the switch circuit for the voltage pulse to the chambers, the discharger described in [8] is used.[1] The triggering circuit of the discharger is mounted on a 6 B-B lamp. The anode voltage of the lamp is ~ 1200 V. The total lag from the instant when the particle passes through both scintillators until the high-voltage pulse is supplied to the electrodes in the chambers is ~ 0.3 μsec. The front of the high-voltage pulse is ~ 40 nsec.

An 11 - 17 kV voltage was used to tune the telescope. A high-voltage transformer with stabilization was used to obtain this voltage. In the working range of temperatures and input voltages, the changes in the high-voltage do not exceed ± 100 V. The maximum power of the transformer at the output is ~ 15 W. With such power, up to three events can be recorded per second.

The RFK-5 photo camera is used for the photorecording. On one frame, the intervals of the spark chambers in two projections, the mechanical counters, the signal lamps, the control instruments and the clocks are photographed. The time necessary to photograph one frame and to move the film is 0.5 sec. In this time, the triggering circuit of the discharger is blocked.

---

1. The dischargers were kindly supplied by G. M. Gorodinskiy and E. M. Kruglov, for which the authors are deeply grateful.

Tuning of the Telescope

The telescope was tuned by cosmic radiation μ-mesons. During the tuning, the voltage of the photomultiplier in the bottom counter was raised to such a value that the pulses from the single particle triggered the threshold device corresponding to the passage of more than three particles through the bottom scintillator. In this case, the instrument recorded with the thresholds of the discriminator that were selected approximately 90% of single-charged relativistic particles passing through the telescope. The tuning of the spark chambers was reduced to the selection of the accumulation capacitances C, the shunting resistances R (see Fig. 2) and the amplitude of the high-voltage pulse supplied to the chambers when these were filled with helium or technically pure neon.

The brightness of the sparks is not great because of the presence of the dielectric plates in the gaps in the shower chambers. Therefore, a high aperture lense (Jupiter-3) is used for the photo recording and an aerial photo film whose sensitivity is 1500 units All-Union Standards. The depth of focus of such objective is small, which requires that the system of mirrors collecting the images of all photographed objects on one frame be carefully adjusted.

In addition to the sparks, diffusion light appears in the gaps when dielectric plates are used. Its brightness drops as the distance from the spark increases, and it is somewhat different in various gaps, which is apparently related to the scatter in the size of the gaps. The size of the sparks which was determined from the photographs is 1 - 2 mm (recalculated for the object) and it depends on the photographing conditions and /218
the development of the photo film. The size of the sparks, as a rule, increases somewhat near the dielectric plate. When the slope of the particle trajectory makes an angle of 12° to 15° with the axis of the chamber, the spark follows the track.

Breakdowns occurred in chambers filled with helium up to a pressure of 1.1 - 1.2 atm for a voltage of ~ 16 kV. The selected feed voltage for the chambers was 15.3 kV. In this case, for the top and middle chamber, the most effective were C = 2500 nfarad and R = 300 ohm, and for the bottom chamber, C = 5000 nfarad and R = 300 ohm. When the chambers were stressed with neon of technical purity to the same pressure, all other conditions being equal, the brightness of the sparks and of the diffusion light increased considerably. This made it possible to reduce the voltage to 14.0 kV. The optimal image of the spark with the previous capacitances was obtained with R = 100 cm. Subsequently, all work was carried out using neon of technical purity.

During the testing, the top chamber was connected both with and without the dielectric plates. In the first case, it was not possible to select conditions for which the quality of the image was satisfactory. In the presence of the dielectric, the ratio of the brightness of the sparks to the brightness of the diffusion light in this chamber was smaller than in the shower chambers. In the second case, to increase the effectiveness of the intervals, the plates that were formerly grounded, were connected with the earth through a resistance of 400-500 ohm. Nevertheless, lapses often occurred in one of the four gaps of the chamber. This is permissible, since the requirements on the effectiveness of the intervals for the top chamber are lower than for the remaining chambers. Therefore, the second variant for connecting the top chamber was selected.

The shower chambers were refilled approximately once a month. It turned out that in the first 2 - 3 days, the brightness of the sparks decreased, and then the changes in the brightness became less noticeable. When the tracks of the μ-mesons were photographed, the lapses in the gaps during the first week were not more than 0.3% of the total number of sparks. In 18 - 20 days, they increased to 3% and in 28 - 30 days to 5%. It was also noted that during the same time after the chambers were refilled, the effectiveness of the intervals dropped somewhat with an increase in the number of triggerings of the chambers, which is possibly related to the release of gases from the dielectric plates in the discharge.

After the telescope was tuned, the voltage on the photomultiplier of the bottom counter was reduced to a working value, and the showers were recorded. For the given thresholds, the telescope was triggered ~ once every hour. Several showers were recorded with 10 - 15 particles in the gap. Because of the small shower counting statistic at earth level, it was not possible to determine the effectiveness of the intervals of the shower chambers for several particles.

Testing of the Telescope

In the summer of 1967 the device was tested in the stratosphere at an altitude of 32 km. The spark chambers were refilled 3 days before the flight. During the flight, the telescope was oriented east and west in accordance with a given program. The measurements were made in 4- and 1-minute intervals, while the telescope was turned by 180°. The signal from the magnetic field sensor which is proportional to the angular deviation of the telescope, was transmitted to the instrument which was photographed during each triggering of the chambers. It turned out that the turn and damping oscillations of the telescope took 20 - 30 sec in most cycles.

Approximately 2600 frames were obtained on the drift sector. (The mean frequency with which the telescope was triggered was ~ 10 min^{-1}.) Mainly these are photographs of nuclear interactions in the middle chamber, which is related to the low effectiveness with which the electrons are isolated by the control circuit of the chambers. When the number of recorded nuclear interactions is large, the processing of the information obtained is much more complex. However, in the analysis of photographs, the isolation of the /219
nuclear interactions is easier, because of the large number of intervals and the comparatively large thickness of the material on the particle track, so that the long-range particles formed in the nuclear interactions are easily tracked.

The photographs show well the development of showers in the middle and bottom chambers. In the beginning of the shower when the particles diverge little, it is often difficult to isolate individual sparks. This is possibly due to the presence of the dielectric in the chamber gaps. The data from the mechanical counters show that the operation of the control circuit of the chambers was satisfactory during the entire flight. The photographs of nuclear interactions obtained during the flight made it possible to estimate the effectiveness of the intervals of the shower chambers when they are used for a large number of particles. (The estimate was obtained for the bottom chamber.)

Photographs were used in which the electron-photon shower with a large number of particles was accompanied by one or several long-range particles, as well as photographs with images of a jet of particles after the nuclear interaction. In the first case, the number of sparks differed considerably in different gaps. In the second case, it usually varied negligibly. Photographs were selected in which the number of sparks in each gap was ≥ 5. (In most cases, the number of sparks was 5 - 10). In these photographs straight tracks were selected which had sparks in the first and last gap which were easily traced on the background of the number of sparks in the remaining gaps.

150 such tracks which were recorded on various flight sectors were examined. Passage through the gap was only noted in four tracks. This gives for the recording effectiveness of a particle in the interval during the passage of 5 - 10 particles a value of $\sim 99\%$. Of course, the effectiveness of the chamber may be somewhat higher when such method is used to sample the events; nevertheless, it is undoubtedly fully adequate for the recording of showers with a large number of particles.

Summary

As a result of the tests it was established that the device that was prepared can be used to study the charging composition of the cosmic ray electron component from primary cosmic rays.

The spark chambers of the device record with high efficiency the electron-photon showers. The large amount of material on the path of the particles and the large number of spark intervals make it possible to trace well the development of the shower in the chambers.

To facilitate the processing of the information obtained, it was necessary to improve the control system which controls the chambers in order to increase the efficiency with which the electron-photon showers are separated from the showers caused by nuclear interactions.

REFERENCES

1. Hartman, R. C., Astrophys. J., 150, 371 (1967).

2. Hartman, R. C., Meyer, P. and Hilderbrand, R. H., J. Geophys. Res., 70 (11), 2713 (1965).

3. Bland, C. J., Boella, G., Degli Antoni, G., Dilworth, C., Scarsi, L., Sironi, G., Agrinier, B., Koechlin, Y., Parlier, B., and Vesseur, J., Phys. Rev. Letters, 17,

4. Daniel, R. R., Stephens, S. A., Proc. 9th Sympos. Cosmic Rays, Elementary Particle Phys., and Astrophys., Bombay, 1965. Bombay, 1966, pp. 54-57. /220

5. Bogomolov, Z. A., Karakad'ko, V. K., Dubyanaya, N. D., et al., Dokl na Vses Konf po fizike kosmicheskikh luchey, [Reports Read at the All-Union Conference on the Physics of Cosmic Rays], Alma-Ata, 1966.

6. Novikov, L. S., Prib Tekh Eksp, No. 4, 45-48 (1965).

7. Fukui, S. and Zacharow, B., Nucl. Instrum. and Methods, 23, 24-28 (1963).

8. Gorodinskiy, G. M., Damaskinskiy, Ye. A., Denisov, A. S., et al., Prib Tekh Eksp, 2, 68 (1967).

N75 16491

SPARK CALORIMETER--AN INSTRUMENT FOR DETERMINING PARTICLE ENERGY OF COSMIC RADIATION

A. A. Alakoz, V. N. Bolotov, M. I. Devishev, L. P. Klimanova, A. P. Shmeleva

ABSTRACT

In 1964 a spark calorimeter was installed at the NOR-Amberd Station (2000 m above sea level). The advantages of this calorimeter over the ionization calorimeter are illustrated.

Ionization calorimeters[1] in which the showers are usually recorded either with the aid of ionization chambers or with the aid of a scintillator [2] are widely used to measure the energy of nuclear-active cosmic rays particles in the range of several hundreds BeV. In 1964 a calorimeter in which large area wide gap spark chambers were used as the shower detectors was installed in the Nor-Amberd Station (2000 m above sea level). The energy is determined from the number of tracks in the spark chambers in the intermediate layers of the substance of the calorimeter. The recording effectiveness of a large number of particles (up to several hundreds) in wide-gap chambers is close to 100% [3]. Spark calorimeters (spark meters) are useful in the measurement of energy in installations already containing spark chambers, when, for example, the combination of spark chambers with an ionization calorimeter leads to great technical difficulties.

The main disadvantage of a spark meter is the limited energy range in which it can be used successfully. By selecting appropriate filters, it is possible to obtain, in the energy range 10 - 500 BeV, an accuracy in the determination of particle energy which is the same as that obtained when ionization calorimeters are used. The possibility of using the spark meter for higher energies is limited, because the accuracy with which the shower particles are counted drops quickly as a result of the merging of the tracks, mainly in the center of the shower.

From here it is obvious that the selection of the substance in the spark meter is of paramount importance. The most advantageous combination turned out to be the use of combined iron and organic glass filters. A light substance (organic glass) absorbs low-energy particles in the showers, and thus reduces considerably the number of tracks observed in the chambers.

The direction of the charged particles is determined by the spark track in the chamber which is located above the spark meter with an accuracy of $\sim 10^{-3}$ rad [3]. The direction of neutral particles is reconstructed from the form of the nuclear showers in the spark meter. The accuracy with which the direction of the neutral particles is determined is within $2 \cdot 10^{-2}$ rad, which is better by almost one order of magnitude than the resolution of the ionization calorimeter.

The energy of the nuclear-active particles is determined from the number of tracks N_Σ in the chambers of the spark meter $E_0 = k(N)N_\Sigma$. When the recording efficiency of the particles in the chambers is 100%, the indeterminacy in the energy is primarily related to fluctuations in the development of the nuclear cascade. To estimate the accuracy with which the energy is determined from the number of particles in the calorimeter, we calculated the variance for this number, using the Monte Carlo method, in the energy range 50 to 5000 GeV. /221

We took into account fluctuations related to: 1) different travels of the neutron before the interaction; 2) different proportions of energy remaining in the neutron after the interaction; 3) the distribution of the energy transferred between charged and neutral π-mesons; 4) fluctuations in electron showers. The calculations were carried out for three observation levels and three types of filters: 1) from a light substance (Al, organic glass); 2) combined (Pb or Fe + 0.3 nuclear units organic glass); 3) iron. The last can be used to estimate the lower bound for the variance (since the fluctuations in the highly ionizing particles that occurred were not taken into account in determining the energy by the ionizing calorimeter). All characteristics of the elementary interaction were taken from the data in article [4] which were recalculated for the nucleus [5]. The number of electrons in the showers from π^0-mesons were calculated from articles [6, 7]. /222

The value of the proportionality coefficient k(N) between the mean number of particles in the spark meter ($\bar{N}_\Sigma$) and the energy of the incident particle E_0 (Fig. 2) was obtained as a result of the calculations. Between the dotted lines lies the range of possible values k, which is related to the variance for the given number of particles in the spark meter for the given energy E_0, and vice versa.

Figure 3 gives the relation between the variance for the given number of particles and the number of observation levels for various energies of the incident neutrons and for various

filters. It can be seen from the curves that for the given energy of the incident neutron, the variance decreases as the number of observation levels increases. For a fixed number of observation levels, the variance increases slightly as the energy increases.

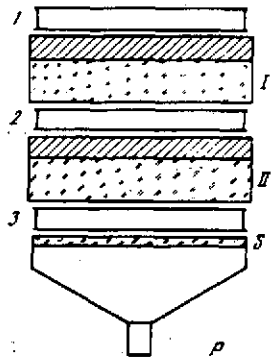

Fig. 1. Schematic diagram of spark meter with combined filters

1 - 3--spark chambers; I - II--parts of calorimeter; S--scintillator, P--photomultiplier

/221

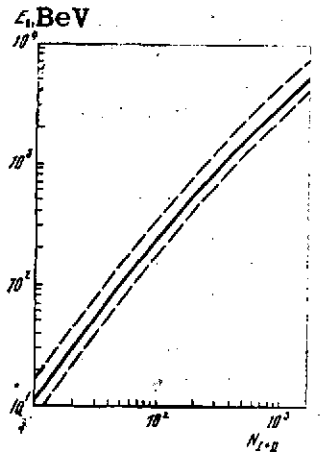

Fig. 2. Energy of incident nucleons vs. number of particles recorded on two observation levels

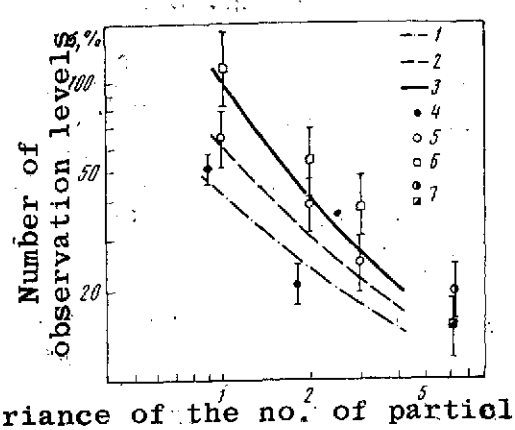

Fig. 3. Variance in number of secondary particles vs. number of observation levels.

Curves--calculated using Monte Carlo method; 1 for E_0 - 110 BeV and iron + organic glass filter; 2--E_0 - 120 BeV and iron filters; 3--E_0 - 1200 BeV and iron filter. Experimental points: 4--spark meter E_0 - 50-500 BeV; 5--ionization calorimeter E_0 - 80-200 BeV; 6--ionization calorimeter E_0 - 200-800 BeV; 7--ionization calorimeter [9] (a) variance for number of particles; (b) number of observation levels.

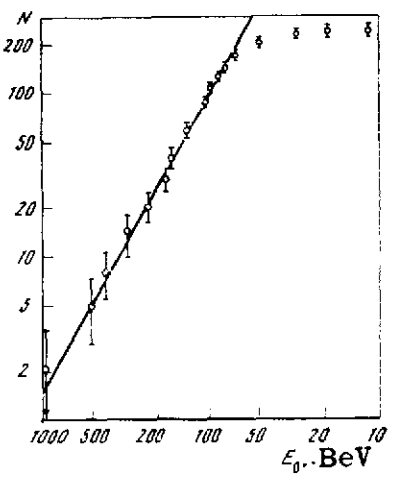

Fig. 4. Integral range spectrum of neutrons at altitude 200 m above sea level (a) BeV

An attempt was made to estimate the variances experimentally. /222 To do this, the relative distribution of the number of particles recorded at various observation levels in the spark meter and ionization calorimeter were used [8, 9]. This eliminated the distribution associated with the spectrum of decreasing energies. For the spark meter, the correlation coefficients between the number of particles on the individual levels were taken from the calculations, and for the calorimeter, the correlation between

the number of particles on a particular level and the total energy released were ignored. The experimental values of the variances that were thus obtained are plotted in Fig. 3 as points.

The satisfactory agreement between the experimental and calculated values of the variances confirms the correctness of the choice in the calculation of the main nuclear interaction characteristics. The form of the integral range spectrum (Fig. 4) and also the intensity of cosmic neutrons at the altitude 2000 m above sea level were determined with the aid of the spark meter. The experimental points are described sufficiently well by a straight line with slope ($\gamma_n = 1.85 \pm 0.2$, which agrees with the data of other authors about the spectrum of cosmic protons and the complete spectrum of nuclear-active particles ($\gamma_p = 1.8 + 0.1$; $\gamma = 2.0 + 0.15$) [10]. The intensity of the neutrons according to our data is $(7.9 + 1.2)\,m^{-2}.ster^{-1}.h^{-1}$.

The experience gained from using the spark meter has shown that along with a relatively good accuracy with which the energy is determined (25-30% in the range up to several hundred BeV) it has certain advantages over the ionization calarimeter, namely simplicity of manufacture, tuning and use, clarity and simplicity with which the events are processed and a high three-dimensional resolution.

REFERENCES

1. Grigorov, N. L., Murzin, V. S., Rapoport, I. D., Zh Eksp Teor Fiz 34, 506 (1958).

2. Grigorov, N. L., Dobratin, N. A., Zhdanov, G. B. and Takibaev, Zh. S., Izv Akad Nauk SSSR, Seriya Fiz 28, 1741 (1964).

3. Bolotov, V. N., Devishev, M. I., Klimanova, L. F., Duchkov, B. I. and Shmeleva, A. P., Dokl. na Vses. soveshch. po fizike kosmicheskikh luchey, [Reports Read at the National Conference on the Physics of Cosmic Rays], Apatity, 1964.

4. Galstyan, D. A., Zhdanov, G. B., Tret'yakova, M. I., Chernyavskiy, M. I. and Shcherbakova, M. A., Izv Akad Nauk SSSR, Seriya Fiz 30 (10), 1958 (1966). /223

5. Lebedev, A. N., Slavatinskiy, S. A. and Tolkachev, B. V., Zh Eksp Teor Fiz 46, 6 (1964).

6. Ott, K., Z. Naturforsch., 9a, 488 (1954).

7. Crawford, D. F. and Messel, H., Nucl. Phys., 61, 145 (1965).

8. Akopyan, G. S., et al., Izv Akad Nauk SSSR, Seriya Fiz 22 (10) (1965).

9. Denisov, E. V., et al., Izv Akad Nauk SSSR, Seriya Fiz 30 (10) (1966).

10. Grigorov, N. L., Izv Akad Nauk SSSR, Seriya Fiz 28, 1801 (1964).

N75 16492

GENERALIZATION OF FORMULAS FOR IONIZATION ENERGY LOSSES AND COLLISION CROSS SECTION IN THRESHOLD DETECTORS

V. K. Yermilova, L. P. Kotenko, G. I. Merzon, V. A. Chechin

ABSTRACT

Two types of formulas were obtained for $(-dE/dx)$ and the number of collisions per unit of path length $(dN/dx) = \text{const}$, which depend on W_m, with due account of the polarization effect of the medium.

The relations for the specific energy losses $-dE/dx$ and the collision cross section σ which depend on the velocity of the charged particle change considerably if collisions are recorded in which the energy transfer W is above a certain level W_m [1, 2]. In particular, if W_m is close to the ionization potential I_i of the internal electron shells of the atoms of the medium, the relativistic increase $-dE/dx$ and the level of the plateau are much higher than predicted by the Bete-Bloch formula, where it is assumed that $W_m = 0$ [3, 4]. This fact must be taken into account in the case of detectors which are only sensitive to those ionization and activation events in which a sufficiently large energy is transferred. We will call such detectors threshold detectors. Bubble chambers ($W_m \gtrsim 300$ eV) and nuclear photoemulsions ($W_m \simeq 170$ eV [5]) have the highest threshold. The existence of the threshold $W_m = I_1$, where I_1 is the first ionization potential must also be taken into account when the primary ionization in gases is calculated.

An increase in the relativistic ionization rate when $W_m \approx I_i$ indicates ways for creating new instruments or for implementing regimes which make it possible to measure the ionization of relativistic particles with great accuracy.

In this article we present the formulas for $-dE/dx$ and the number of collisions per unit length of path $dN/dx = \text{const} \cdot \sigma$ as functions of W_m that we obtained taking into account the polarization effect of the medium. The Bete-Bloch [3, 5] and Budini [6] formulas are special cases of these formulas when $W_m = 0$.

Formulas for $(-dE/dx)_{W_m<W<T}$ and $(dN/dx)_{W_m<W<T}$

Two types of formulas were obtained for $(-dE/dx)_{W_m<W<T}$ and $(dN/dx)_{W_m<W<T}$, where T is the maximum energy transferred in the collisions.

(A). The atoms of the medium were considered as discrete oscillators whose frequencies corresponded to the mean ionization potentials of the electron shells. The corresponding expressions and their derivation are given in articles [1, 2].

(B). The atoms of the medium were considered as oscillators with a continuous frequency spectrum. The method used for the calculations was analogous to the previous method. The dielectric constant of the medium $\varepsilon(\nu)$ was calculated from the distributed forces of the oscillators $f(\nu)$ which coincide with an accuracy up to a constant coefficient with the cross section of the photo effect measured for a number of substances in the energy interval 10 - 10^6.

The results are conveniently represented in a form which is similar to the Bete-Bloch formula, which takes into account the correction for the effect of the density of the medium /224

$$\left(-\frac{dE}{dx}\right)=\frac{A}{\beta^2}\left\{\int_{W_m/\omega_0}^{T/\omega_0} f(\nu)\,d\nu\left[\ln\frac{2mc^2\beta^2T}{\omega_0^2\nu^2(1-\beta^2)}-\beta^2\right]+\right.$$
$$\left.+\ln\frac{T}{W_m}\int_0^{W_m/\omega_0} f(\nu)\,d\nu-\delta\right\}, \qquad (1)$$

$$\left(\frac{dN}{dx}\right)=\frac{A}{\beta^2}\left\{\int_{W_m/\omega_0}^{T/\omega_0}\frac{f(\nu)\,d\nu}{\omega_0\nu}\left[\ln\frac{2mc^2\beta^2}{\omega_0\nu(1-\beta^2)}-\right.\right.$$
$$\left.\left.-\beta^2+\left(1-\frac{\omega_0\nu}{T}\right)\right]+\left(\frac{1}{W_m}-\frac{1}{T}\right)\int_0^{W_m/\omega_0} f(\nu)\,d\nu-1\right\}, \qquad (2)$$

where ν is the frequency expressed in units of the plasma frequency ν_0 and $\omega_0 = h\nu_0$). The first and second terms in (1) and (2) correspond to the excitation and ionization processes with an energy transfer W from W_m to T. The second terms have a Rutheford character and contribute to the collisions with the external electrons whose coupling energy is less than W_m (these

terms vanish when $W_m = 0$). The last terms take into account the effect of the density of the medium and Cerenkov radiation[1]

$$\delta = \frac{A}{\beta^2}\left\{\int_{W_m/\omega_0}^{T/\omega_0} f(\nu)\,d\nu\left[\ln\frac{(1-\beta^2)}{\sqrt{(1-\beta^2 R_e\varepsilon)^2+\beta^4 I m^2\varepsilon}}+\right.\right.$$
$$\left.\left.+\beta^2(1-R_e\varepsilon)\right]+2\int_{W_m/\omega_0}^{T/\omega_0}\left(\beta^2-\frac{R_e\varepsilon}{|\varepsilon|^2}\right)\nu d\nu\right\}, \qquad (3)$$

$$\Delta = \frac{A}{\omega_0\beta^2}\left\{\int_{W_m/\omega_0}^{T/\omega_0}\frac{f(\nu)\,d\nu}{\nu}\left[\ln\frac{(1-\beta^2)}{\sqrt{(1-\beta^2 R_e\varepsilon)^2+\beta^4 I m^2\varepsilon}}+\right.\right.$$
$$\left.\left.+\beta^2(1-R_e\varepsilon)\right]+2\int\left(\beta^2-\frac{R_e\varepsilon}{|\varepsilon|^2}\right)d\nu\right\}. \qquad (4)$$

In the transition to describe oscillator forces, expressions (1) - (4) coincide with the formulas that were obtained in the approximation (A).

As the velocity of the particle increases ($\beta \to 1$) $(-dE/dx)_{W_m<W<T}$ and $(dN/dx)_{W_m<W<T}$ reach a plateau whose level depends considerably on W_m. For small values of W_m ($W_m \ll I_i$) distant collisions whose relativistic increase is suppressed, to a large extent by the effect of the density of the medium, play an important role. For very large W_m ($W_m \gg I_i$) when all atomic electrons can be considered free, only the Rutheford terms remain in formulas (1) and (2) and the relativistic increase is absent. The greatest relativistic increase takes place in the intermediate case when $W_m \backsim I_i$ (Fig. 1).

Evaluation of the Results

We will use the data from calculations based on the model of discrete oscillators for liquid Xe, $CBrF_3$ and C_3H_8 used in

1. For the last terms in formulas (3) and (4) that correspond to the Cerenkov radiation, the integration is carried out over the region where $\beta^2 R_e\varepsilon(\nu) > 1$.

bubble chambers (for a large number of frequencies, the discrete oscillator model gives results which are close to those obtained from the exact formulas (1) - (4). The maximum relativistic increase turns out to be considerably higher than at $W_m = 0$ and is for $\langle dN/dx\rangle_{W_m<W<T}$ in Xe, $CBrF_3$ and C_3H_8, respectively, ~ 50, 35 and 25% (see Fig. 1). It is interesting that the experiments for $CBrF_3$ (Fig. 2) and our data for C_3H_8, where the relativistic increase in the density of the traces is, respectively, (32 ± 5) and (10 - 15)% agrees only with the calculations for $\langle dN/dx_{W_m<W<T}\rangle$, but not for $\langle -dE/dx\rangle_{W_m<W<T}$. This means that the probability that a bubble will be formed in a bubble chamber does not depend on the magnitude of the local heating if the energy released exceeds the threshold value. When the length of the tracks in $CBrF_3$ is approximately 1m, it is possible to separate the ions and protons with a pulse of 3 - 30 BeV/c by the relativistic increase in the density.

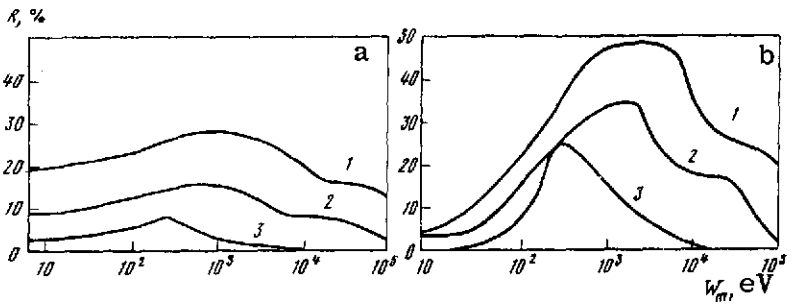

Fig. 1. Relativistic ionization rate vs. threshold energy W_m in Xe, $CBrF_3$ and C_3H_8

a-- $R = \frac{(-dE/dx)_{plateau}}{(-dE/dx)_{min}} - 1$ b-- $R = \frac{(dN/dx)_{plateau}}{(dE/dx)_{min}} - 1$

1--Xe, T = 300 keV; 2--$CBrF_3$, T = 232 keV; 3--C_3H_8, T = 127 keV

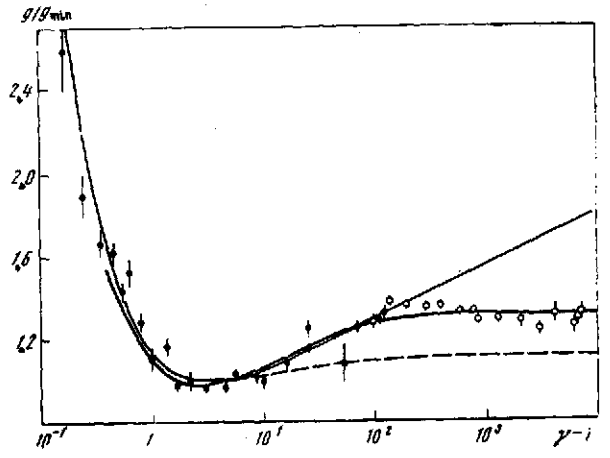

Fig. 2. Normalized density of traces g/g_{min} vs. kinetic energy of particle in a bubble chamber filled with $CBrF_3$ at 37.5°C

Middle curve was calculated according to the formula for $(dN/dx)_{W_m<W<T}$ at W_m = 0.09 keV and T = 232 keV, top and bottom curves were calculated according to the Bete-Bloch formula without and with the correction for the density effect, respectively. The experimental data were taken from article [7].

The increase in threshold energy W_m must take place in spark chambers containing electronegative impurities. These impurities hinder the development of the discharge when the ionization density is small, which is equivalent to an increase in W_m. We intended to check the effect of the electronegative /226 impurities on the relativistic increase in the ionization with the aid of a multi-layer spark chamber operating in the regime of a counter with low effectiveness. It is advantageous to use such chamber which records the trajectory and measures the ionization in the separation of particles at high energies.

The authors are grateful to A. I. Alikhanyan for his attention to the work, to A. T. Matachun and F. I. Strizhevskaya for carrying out the calculations and to L. P. Kuzina for her help in processing the results.

REFERENCES

1. Kotenko, L. P., Merzon, G. I. and Chechin, V. A., Yadernaya fizika, 5, 815 (1967).

2. Kotenko, L. P., Merzon, G. I. and Chechin, V. A., Proc. Internat. Conf. Instrum. for Energy Physics, p. 140.

3. Steruheimer, R. M., Phys. Rev., 88, 851 (1952).

4. Steruheimer, R. M., Phys. Rev., 103, 511 (1956).

5. Zhdanov, A. P., and Kuks, I. M., Usp nauchn fotografii XII, 53 (1966).

6. Budini, P., Nuovo cimento, 18, 43 (1956).

7. Hoffman, J. and Hugentobler, Helv. phys. acta, 38, 783 (1956).

N75 16493

DISTORTION OF THE ALTITUDE DEPENDENCE AND ENERGY SPECTRUM OF THE NEUTRON COMPONENT NEAR THE EARTH'S SURFACE

G. V. Gorshkov, O. S. Tsvetkov

ABSTRACT

The results of the altitude distribution of slow (cadmium difference) and fast (supercadmium) neutrons from 2000 m down to sea level are given. The neutron energy spectrum is calculated by the cadmium ratio.

The distrotion in the neutron cosmic radiation field in the atmospheric layer near the surface of the Earth has not been studied extensively [1, 2]. At the same time, the distortion in the neutron field, both by intensity and by the energy spectrum is considerable, as theoretical calculations have shown [1], and must be taken into account when the results of measurements carried out on Earth and in the free atmosphere at various altitudes are compared. These data may also turn out to be important in the estimation of the neutron distribution from nuclear explosions and neutron sources used in geophysical search methods for useful fossils and in the solution of a number of other problems [3 - 5].

R. Edge [2], who studied the altitude distribution of cosmic radiation neutrons from the Earth's level to 400 m with the aid of BF_3 counters on a television tower, did not detect distortions in the energy spectrum near the Earth's surface, even though he did detect a distortion in the altitude dependence.

This article gives the results of measurements of the altitude distribution of slow (cadmium difference) and fast (supercadmium) neutrons from an altitude of 2000 m down to sea level above the water surface. The distortions in the energy spectrum were estimated from the cadmium ratio.

Proportional neutron counters with working lengths of 942 mm and a 34-mm working diameter filled with boron trifluoride enriched to 85% with the B^{10} isotope were used by us as the indicator. Ten such counters were combined in two identical groups (five counters in each) and placed in a hermetic duralumin box at a distance of 5 cm from one another. The radio-engineering circuit of the installation which used semiconductor instruments was based on the circuit developed in [6] for the neutron monitor. The circuit had two independent channels

/227

connected for coincidence with a third channel, the noise elimination channel. The device was fed from batteries which ensured a continuous operation of the device for 500 hours.

The measurements were made in April-May 1966 above Lake Ladoga (geomagnetic latitude 56°N, sea level) with the aid of a light two-seat YaK-12 airplane at altitudes from 2000 m to 25 m, and with the aid of a boat on the level of the lake. The distance from the shore at all measurement points was at least 1 km.

To determine the intensity of the supercadmium neutrons, it was necessary to take into account the residual background of the proportional counters, caused mainly by the natural impurity in the substance of the counter by radioactive elements. The value of this background, which was 0.48 ± 0.01 pulses·min^{-1} per counter was determined by us in special experiments by a comparison of the effects measured in water (the lake), using a cadmium screen in two neutron fields with the same spectral composition, with the relative intensity which was known [7]. The results of the measurements that were corrected for the barometric effect are given in the diagram with the mean statistical errors. An analysis of the curves in the diagram shows that in the equilibrium region of the atmosphere (800 - 950 g·cm^{-2}), the travel of the neutron-forming cosmic radiation component is approximately 145 g·cm^{-2} which agrees with the measurement data of many foreign scientists. Starting with a pressure of approximately 975 g·cm^{-2} (about 500 m above sea level), the effect of the water surface becomes apparent, as a result of which the distribution of the neutron density as they approach the water surface deviates considerably from the law for the altitude distribution in the equilibrium region of the atmosphere. Curve 2 (the cadmium difference) passes through the minimum at the pressure 1020 g·cm^{-2} (about 150 m above sea level) and then rises rather steeply to sea level at the pressure 1049 g·cm^{-2} at which the density of the slow neutrons is 3.5 times as large as at the minimum. Curve 3 shows that the intensity of fast neutrons, in contrast to slow neutrons, drops to the surface of the water and decreases approximately by a factor of three at the lake level compared to the intensity extrapolated for this point from the equilibrium region. The presence of a minimum in curves 1 and 2 is explained by a disturbance in the equilibrium between the rate at which the neutrons are formed and the rate at which they are absorbed.

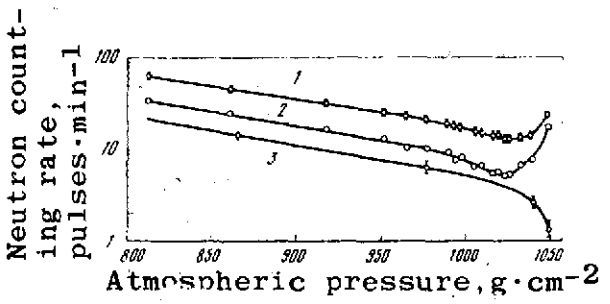

Fig. Distribution for the density of neutrons in low layers of the atmosphere above the surface of the water: 1--effect recorded by unprotected counters; 2--effect caused by slow neutrons (cadmium difference); 3--effect caused by supercadmium neutrons (with energy above 0.4 eV)

An increase in the density of the slow neutrons near the water surface takes place as a result of the following processes: 1) the reflection of slow atmospheric neutrons from the water; 2) the diffusion of atmospheric neutrons slowed down in the water /228 and 3) the diffusion of neutrons formed in the surface layer and slowed down in it.

The cadmium ratio which characterizes the spectrum of the slow neutrons includes supercadmium neutrons in the equilibrium region of the atmosphere (see Fig.) and it is close to 2.5:1 which agrees with the data of other authors [8 - 12] if we take into account the natural background of the counters. This ratio increases as the distance from the water surface decreases and attains the value 12: 1 approximately near the surface of the water.

It should be noted that the method for observing the changes in the energy spectrum used in [2] (surrounding the counters with various paraffin layers) is less sensitive to differences in the initial sectors of the energy spectra. Therefore, it did not detect in practice a noticeable difference between the spectra of the neutrons in the free atmosphere and near the Earth's surface (above the soil). In addition to this, we would expect that this effect above dry areas (soil) will manifest itself to a lesser degree and will depend on the water content in the soil.

The number of readings of the counter filled with boron trifluoride is related to the rate at which the neutrons q are formed in air in the equilibrium region by the following relation [1]:

$$q = n \frac{\sigma_a}{\sigma_b} \cdot \frac{780}{V_p} ,$$

where n is the neutron counting rate, pulses·sec^{-1}; σ_a and σ_b are the thermal absorption cross sections for neutrons in the air and in boron trifluoride, respectively, calculated per molecule in barn, V is the working volume of the detector, in cm^3; P is the pressure of the BF_3 gas in the counter in atm. In computing q the neutron counting rate was used which was recorded by the unprotected detector (slow + supercadmium neutrons) which was extrapolated to the lake level from the equilibrium region, taking into account the attenuation in the neutron density in the counter (self-screening effect).

The rate at which neutrons with energy less than 0.5 MeV were formed in 1 g of air per second at sea level (1033 g·cm^{-2}) for the geomagnetic latitude 56°N was determined and was equal to $(3.2 \pm 0.2) \cdot 10^{-5}$.

In conclusion, the authors express their gratitude to M. I. Timoshin for his help in the measurements.

REFERENCES

1. Bethe, H. A., Korf, S. A. and Placzek, G., Phys. Rev., 57, 573 (1940).

2. Edge, R. D., Phys. Rev., 145, 1023 (1966).

3. Lingenfetrer, R. E., Canfield, E. H. and Hess, W. H., J. Geophys. Res., 66, 2665 (1961).

4. Zakharchenko, V. F., Izv Akad Nauk SSSR, Seriya Fiz 30 (11), 1813 (1966).

5. Boella, G., et al., Nuovo cimento, 29, 103 (1963).

6. Leonov, V. Kh. and Mazaryuk, E. A., Geomagnetizm i aeronomiya, 4 (6), 1101 (1964).

7. Gorshkov, G. V. and Tsvetkov, O. S., Atomnaya energiya, 26 (1), 27 (1969).

8. Agnew, H. M., et al., Phys. Rev., 72, 203 (1947).

9. Yuan, L. C. L., Phys. Rev., 76, 1267 (1949).

10. Simpson, I. A., Phys. Rev., 83, 1175 (1951).

11. Poole, M. I., et al., Process in Nuclear Energy, Vol. 2, London, 1958, p. 91.

12. Gorshkov, G. V., Zyabkin, V. A., Lyatovskaya, N. M. and Tsvetkov, O. S., Estestvennyy neytronnyy fon atmosfery i zemnoy kory, [Natural Neutron Background of the Atmosphere and the Earth's Core], Atmoizdat Publs., 1966.

N75 16494

THE EFFECT OF THERMAL NEUTRON FIELD SLAGGING CAUSED BY CYLINDRICAL BF_3 COUNTERS IN DIFFUSION MEDIA

G. V. Gorshkov, O. S. Tsvetkov, R. M. Yakovlev

ABSTRACT

During investigations of the cosmic ray neutron component, and particularly during absolute measurements of the slow neutron intensity and the rate of neutron formation, as well as in the course of these measurements using a group of parallel counters immersed in a moderator, the question arises of how to take into account the distortions of the thermal neutron field introduced by the counters. This paper sets forth the results of calculations carried out by means of diffusion theory and transport approximation (first collision method) in addition to the experimental data of the effect of distortions of the density of the thermal neutron flux which takes place every time the CHM-8 and CHMO-5 type counters are placed in the diffusive media (paraffin, water, plexiglas).

The reduction of the density of the thermal neutron flux is proved to be substantial and should be included during the investigations. For example, the CHM-8 type counter immersed in the water will have a ratio: $\varphi_R/\varphi_\infty = 0.76$, where φ_R is the density of the thermal neutron flux on the surface of the counter, φ is the flux density in the absence of the counter.

In the investigation of the neutron component of cosmic rays, in particular during absolute measurements of the intensity of slow neutrons and the rate at which neutrons are formed, as well as during relative measurements by a group of parallel counters immersed in a decelerator, difficulties arise when the distortions in the field of thermal neutrons introduced by the counters are taken into account. This article gives the results of computations carried out in transport approximation (first collision method) for the attenuation of the field of thermal neutrons formed in counters of the CHM-8 and CHMO-5 type. The deflection of the thermal neutron field was also obtained near the counters and in the air (shade effect) and in various decelerating media (water, paraffin, plexiglas) for which the calculations were carried out on the basis of diffusion theory. To verify the calculations that were made, we measured the distribution of the density of the thermal neutrons at various distances from the counter in the water.

When the neutron counter is placed in a diffusive medium, the neutron flux in the vicinity of the counter which acts as the absorbing body becomes smaller. The distortion in the density of the thermal neutron flux is caused by the following factors: 1) an attenuation of the neutron flux when it passes through the counter which acts as the absorbing body (the self-screening effect); 2) distortion of the neutron flux due to a disturbance in the diffusion characteristics of the medium near the counter (deflection effect of the field). The last effect is characteristic of absorbing media with a small transport length of the path. The reduction in the flux in this case occurs as a result of the fact that the neutrons that were absorbed in the counter no longer participate in the diffusion process, and the supply of neutrons from the surrounding medium cannot compensate the absorption of neutrons in the counter. For counters filled with BF_3 (enriched 85% by the B^{10} isotope) the macroscopic absorption cross section of the neutrons Σ_a is considerably larger than the macroscopic cross section Σ_s (in particular for the CHM-8 counter it is $\Sigma_a/\Sigma_s \simeq 200$). Therefore, to find the probability β that the neutrons will be absorbed in the counter, we use the transport approximation (first collision method) [1].

For an infinitely long solid cylinder in a homogeneous neutron field (for the case $\Sigma_a r \ll 1$)

$$\beta = 2\Sigma_a r - \frac{8}{3}\Sigma_a^2 r^2, \tag{1}$$

where r is the radius of the counter.

The self-screening coefficient f_s is related to the probability β by the simple relation

$$f_s = \frac{\bar{\varphi}_v}{\bar{\varphi}_s} = \frac{\beta}{(2-\beta)\Sigma_a r}, \tag{2}$$

where $\bar{\varphi}_v$ is the neutron flux averaged over the volume of the cylinder, and $\bar{\varphi}_s$ is the flux averaged over the surface of the cylinder.

The full self-screening coefficient is

$$f_0 = \frac{\bar{\varphi}_v}{\varphi_\infty} = \frac{\beta}{2\Sigma_a r}, \tag{3}$$

where φ_∞ is the neutron flux in the absence of an absorbing body. The values of f_s and f_0 that were obtained for counters in an air medium (vacuum) are given below: /230

CHM-9--f_s = 0.97 and f_0 = 0.93; CHMO-5--f_s = 0.99 and f_0 = 0.96.

Thus the density of the neutrons in the air which was measured by the counters must be corrected by the multiplicative factor $1/f_0$.

When the counter is immersed in decelerating media with a small transport length of the path (water, paraffin, plexiglas) in which the absorption cross section is considerably smaller than the diffusion cross section, to determine the distortions in the thermal neutron field in the vicinity of the counter, the diffusion approximation is used. The density of the thermal neutron flux at the distance R from the axis of the cylinder φ_R is determined, according to [1], from the following expression

$$\varphi_R = \varphi_\infty \left[1 - F \frac{K_0(\varkappa R)}{K_0(\varkappa r)}\right], \tag{4}$$

where

$$F = \frac{1}{1 + 2D\varkappa \frac{K_1(\varkappa r)}{K_0(\varkappa r)} \frac{2-\beta}{\beta}}; \tag{5}$$

D is the diffusion coefficient of the medium;

$$\varkappa^2 = \frac{\Sigma_a'}{D},$$

where Σ_a' is the macroscopic asorption cross section of the thermal neutrons by the medium, K_0 ($\varkappa$R) and k_1 ($\varkappa$R) are Bessel functions, and β is determined from expression (1).

The values of the deflection coefficient for the field of thermal neutrons that were calculated with the aid of these formulas in the vicinity of the CHM-8 and CHMO-5 counters that were immersed in the decelerating media: water, paraffin and plexiglas are given in Tables 1 and 2. The deflection of the thermal neutron field φ_R/φ_∞ caused by the CHM-8 counter in water is also shown in the diagram (solid curve).

TABLE 1. DEFLECTION OF THERMAL NEUTRON FIELD IN THE VICINITY OF A COUNTER OF THE CHM-8 TYPE IN DECELERATING MEDIA

Distance from the axis of the counter, cm	Water	Paraffin	Organic glass	Distance from the axis of the counter, cm	Water	Paraffin	Organic glass
1,7	0,79	0,78	0,80	4,0	0,94	0,94	0,93
2,0	0,83	0,81	0,83	6,0	0,98	0,98	0,96
2,5	0,87	0,86	0,87	8,0	0,99	0,99	0,99
3,0	0,90	0,89	0,90	10,0	0,996	0,997	0,995

TABLE 2. DEFLECTION OF THERMAL NEUTRON FIELD IN THE VICINITY OF A COUNTER OF THE CHM-8 TYPE IN DECELERATING MEDIA

Distance from the axis of the counter, cm	Water	Paraffin	Organic glass	Distance from the axis of the counter, cm	Water	Paraffin	Organic glass
1,7	0,82	0,80	0,84	4,0	0,95	0,95	0,95
2,0	0,85	0,84	0,86	6,0	0,98	0,98	0,97
2,5	0,89	0,88	0,89	8,0	0,99	0,99	0,99
3,0	0,92	0,91	0,92				

The values of the total attenuation coefficient for the thermal neutron field are given in Table 3. /231

TABLE 3. COEFFICIENT FOR THE TOTAL DEFLECTION OF THE DENSITY OF THE THERMAL NEUTRON FLUX $\bar{\varphi}_v/\varphi_\infty$ CAUSED BY INTRODUCING THE COUNTER IN DIFFUSIVE MEDIA

Type of counter	Water	Paraffin	Organic glass
CHM-8	0,75	0,73	0,76
CHMO-5	0,82	0,80	0,82

To check the computational results, we carried out measurements of the distribution of the density of the thermal neutrons near a counter of the CHM-8 type immersed in a retarder (fresh water). The experiment was reduced to the following. The counter which was placed in a thin-wall duralumin 38-mm diameter pipe was introduced in the thermal neutron field created in the fresh water (a tank whose overall dimensions were 180 x 120 x 120 cm) with the aid of a Po + Be source. After this, the density of the thermal neutrons was determined in succession at a distance R from the counter axis and the density of the neutrons at the same point, without the counter, i.e., the ratio φ_R/φ_∞ was determined. The density φ_R and φ_∞ was measured using the method of activating a rhodium foil (Rh^{203}) and a set of silver foils in the form of disks whose diameters were 10, 20, 30 and 40 mm which were 100 mg·cm^{-2} thick. The guided activity was measured 30 sec after irradiation with the aid of the β-counter of the CBT-10 type connected through a preamplifier to an installation of the PS-20 type.

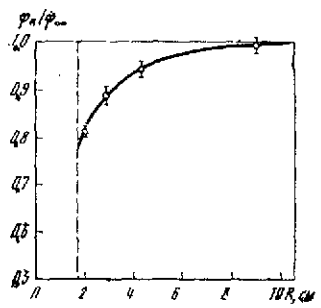

Fig. Deflection of the thermal neutron field caused by a counter of the CHM-8 type in water φ_R/φ_∞ vs. the distance from the axis of the counter R.

The results with the mean weighted errors that were obtained are plotted in the figure, from which it can be seen that the agreement between the calculated values $\bar{\varphi}_R/\varphi_\infty$ (solid curve) and the values which were found experimentally is satisfactory. Thus, the distortion in the field of the thermal neutrons caused by counters of the CHM-8 and CHMO-5 types is very substantial in the media that were considered above, and it must be taken into account in investigations.

In conclusion the authors thank Yu. S. Martynov and M. I. Timoshin for their help during the measurements.

REFERENCES

/232

1. Megreblian, P. and Kholms, D., Teoriya reaktorov, [Theory of Reactors], Moscow, Gosatmizdat, 1962, pp. 174-177.

N75 16495

STUDY OF COSMIC RAY MOTION IN COSMIC SPACE NEAR THE EARTH

V. K. Budilov, V. I. Ivanov, L. V. Kozak, L. A. Mirkin, I. G. Tsukerman

ABSTRACT

The paper presents data on experimental installations developed in the cosmic ray variations laboratory in Kazgu (Alma-Ata). Various experiments on modelling the interaction of plasma with the geomagnetic field as well as the plasma distribution in quiet and disturbed fields are described.

The characteristics of the meson supertelescope using scintillators (effective area, 10 m^2) for vertical alignments designed to study microvariations of the cosmic rays and their interrelation with magnetospheric fluctuations and the study of solar wind parameters are given

In the last few years several studies [1 - 3] were devoted to the study of the interaction of the dipole with the magnetic field with the aid of models. The clarity and definiteness make this method very promising. In the cosmic ray Kazgu laboratory (Kazakh State University in Kirov) an installation was developed which models the Earth's magnetosphere. The installation consists of a vacuum cylindrical chamber, whose diameter is 1100 mm, which is 1600 mm long with a pumping system consisting of an initial vacuum pump of the BH-1 type and a vacuum set of the BA-5-4 type. This system makes it possible to obtain a vacuum of 10^{-5} mm Hg. A magnetized steel ball (terella) of radius r_T = 2.5 cm, whose magnetic moment is M_T - 2500 gauss·cm^3 is suspended in the center of the chamber. At a distance R = 36 cm from the axis of the terella is an electromagnet for which the distance between the poles is r_{em} = 30 cm. The magnetic moment of this electromagnet can vary from 0 to $5.4 \cdot 10^6$ gauss·cm^3, depending on the power of the feeding current. The field of the terella can be disturbed in various ways with the aid of this electromagnet, obtaining a parallel-antiparallel or transverse position of the terella field and the disturbing dipole, changing the magnetic moment of the latter [4]. The disturbing field which was selected had a dipole form, on the basis of the theoretical assumptions in [5], that the disturbed field in the Earth's magnetosphere can be represented as the sum of the fields of the initial dipole and the perturbing dipole.

Both a constant and variable electrical voltage was fed to the terella. It could vary in amplitude within wide limits. For the appropriate voltage and pressure, a discharge was formed in the chamber. The motion of the particle in the discharge plasma was controlled by the magnetic field of the terella and the disturbing electromagnet. Consequently, the processes taking place in the magnetosphere of the terella can be evaluated from the character and form of the belts of the captured plasma.

This article gives the results obtained on an installation from modelling the space near the Earth. For the appropriate voltage on the sphere, a discharge appears in the chamber, and the charged particles captured by the field of the terella form a radiation belt around the equator (Fig. 1a). If, for the same voltage, a disturbing magnet is switched on, then for an intensity of the magnetic field at its poles between 800 to 1100 gauss, an additional belt of captured plasma appears from the perturbing side at a distance $R = 2.5\ r_T$ (see Fig. 1b). /233

When the perturbing field is further increased, the belt disappears. In particular, it should be noted that this picture is observed only in the case of fields that have parallel directions. In the case of fields with opposite directions, the additional belt is not observed.

A further increase of the potential of the sphere increases the discharge between the terella and the walls of the chamber. For this increased voltage, in addition to the equatorial ring, the sphere whose radius is $\sim 3\ r_T$ begins to glow (Fig. 2). When the magnetic field of the disturbing magnet is oriented parallel to the field of the terella, "polar caps" are formed at the poles, which are bounded in latitude approximately by the 55^o parallel, whose light intensity is higher, the greater the perturbing field. Figures 2a and b show, respectively, the discharge on the undisturbed and disturbed terella (the voltage on the poles of the disturbing electromagnet is 1500 gauss).

For greater electric potentials on the terella, when the disturbing magnetic field increases, the discharge region elongates gradually and takes on the form of drops and the beginning of the drop is located on the equator of the terella. This effect is observed in both cases when the fields of the disturbing magnet and terella are in parallel and antiparallel positions. Figures 3a, b show, respectively, the photographs of the discharge when the field of the terella is undisturbed, and with a disturbing field, which is parallel and antiparallel to the field of the terella. In the absence of a disturbance, the radius of the glowing sphere is $r - 4\ r_T$. When the intensity of the disturbing field on the poles of the magnet is 1600 gauss, the distance from the beginning of the drop is $5r_T$.

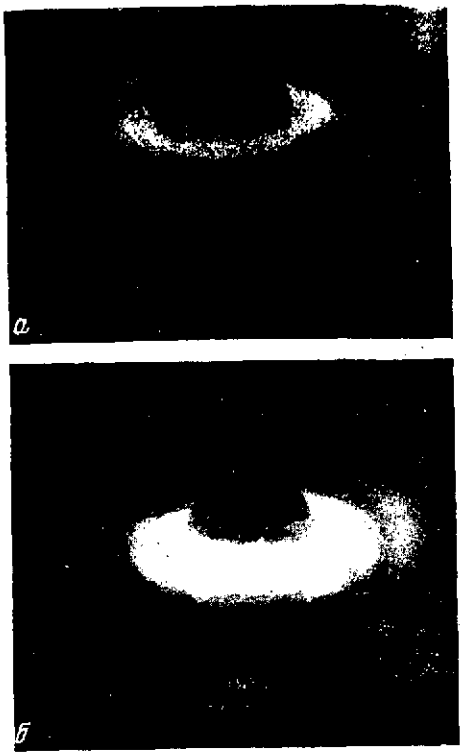

Fig. 1. Captured plasma belt in the magnetosphere of the terella

a--without disturbed field
b--with disturbed field

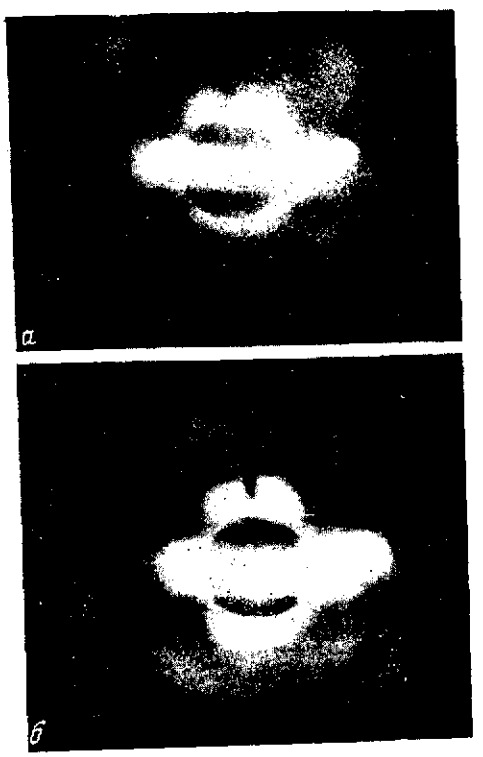

Fig. 2. Formation of "polar caps" during disturbance of the magnetic field of the terella

a--undisturbed magnetosphere of the terella
b--disturbed magnetosphere of the terella

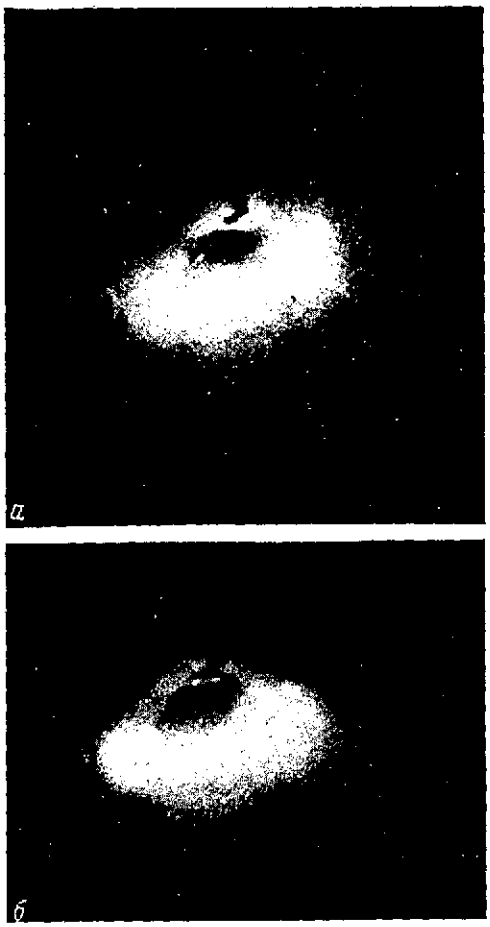

Fig. 3. Change in the form of the discharging sphere with the change in the disturbing field

a--disturbing field parallel to field of the terella
b--disturbing field anti-parallel to the field of the terella

To study short periodic variations of cosmic rays, a telescope was developed in Kazgu which was mounted on plastic scintillators. The theoretical expected counting rate in the vertical direction was $1.5 \cdot 10^5$ pulses/min which ensures a statistical error better than 0.25%. The data which were obtained experimentally were $1.4 \cdot 10^5$ counts per minute for double coincidences. When the installation was developed, special attention was given to the following factors for the real accuracy of the device: 1) the random coincidences were ~ 0.1%; 2) the end effects in the scintillators (four connected blocks in one counter) were constant over time and reduced the total counting intensity by less than 0.001%; 3) the magnitude of the error introduced by the effect of a change in room temperature of $\pm 5^{\circ}C$ can be ignored, because for $t^{\circ} \leq 40_0 C$, the amplification properties of the transistors vary very insignificantly [6]. /234

The installation consists of two cubes displaced along the edge (l = 3.3 m), 16 scintillation detectors (the area of each is 1 m^2), located at the vertices of the cube, and four paired detectors in the center of the cubes. The geometry that was selected makes it possible to record in the following directions: vertical direction, 10 channels at an angle of 45° from the west, south, east, and north, and four channels from the northwest and southeast, and from the northeast and southwest, two channels each. In addition to this, possible directions are the directions mentioned above at angles of 20, 33, 54° with a somewhat smaller statistical weight. The dependence of the intensity of the recorded particles on the zenith angle is shown in Figs. 4a, b. Figure 5 shows the values of the asymptotic directions from which the particles arrive for the point with the Alma-Ata coordinates. The graphs were constructed on the basis of the calculations of K McCracken and R. Chasson [7, 8].

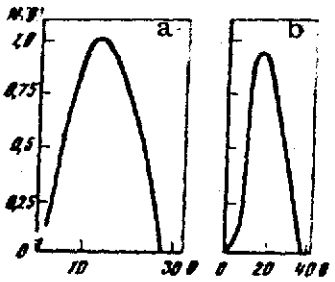

Fig. 4. Directional diagram of telescope

a--vertical; b--slanted direction

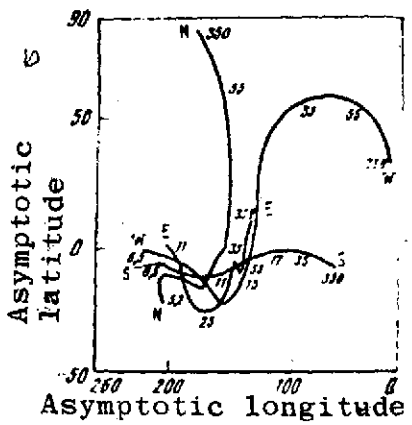

Fig. 5. Asymptotic directions for the arrival of particles in Alma-Ata at an angle of 48° (numbers near the curves indicate the hardness of the particles, BeV)

The scintillation counter represents a light reflecting container which can be disassembled. Its design was selected on the basis of the calculations that we made and the experimental work [9]. The degree of inhomogeneity of the counter was ~ 9%. When the output pulse was calculated, the ionization losses of the meson in the scintillator were determined by the Bete-Bloch formula in Bregg's approximation, and they were 9.66 MeV [10]. The number of photons obtained as a result of the passage of a single particle is

$$N = \frac{\Delta\varepsilon}{\omega} = \frac{9{,}66 \cdot 10^6}{120} = 8{,}6 \cdot 10^4 \text{ photons}$$

where ω is the excitation energy for the plastic scintillators used in the installation, which was equal to 120 eV.

The calculations that were made show that per photocathode when the reflectance coefficient of the walls of the light collector is $\varkappa = 0.2$ and the diffusion obeys the law $\cos^4\theta$,

$$N_\phi = \omega_c \omega_k \varkappa N_c \text{ photons}$$

where ω_c is the probability that a quantum will arrive at a photocathode during mirror reflectance, ω_k is the probability that it will remain in the cone during diffusion scattering, N_c is the number of quanta in the light collectors that left the plastic.

Consequently, the pulse when the photomultiplier is loaded will be

$$U = \frac{2}{c} = \frac{\theta\beta k N_\phi e}{C_{вх}} \approx 0{,}007 \text{ V}$$

where θ is the probability that the electron will be discharged from the photomultiplier cathode, which is ~ 0.1; β is the coefficient for the collection of the electrons on the first dynode which is ~ 0.9, and k is the amplification factor of the photomultiplier. The pulses that were obtained experimentally have an amplitude of the same order of magnitude.

The basic circuit of the electronic block is represented in Fig. 6. All nodes of the circuit are assembled on diffused base transistors (P402). The emitter follower with $k_y = 0.8$ is based on two transistors. The stability of the transistor parameters over time and also the thermal stability are ensured by using large emitter loads (direct current) and it is < 1% in 8 h of operation. The input resistance is ~ 500 kohm.

The main amplifier has $k_y = 60$. To prevent overloading of the amplifier, a diode amplitude limiter is used [11]. For such a limiter, the amplitude on the input pulses is < 100 mV, and it does not vary, for all practical purposes. As the amplitude of the input pulse increases, the resistance of the diode increases sharply, which leads to a decrease in the output signal. A similar cell is also at the output of the amplifier.

The discriminator used is a single flip-flop oscillator with a millivolt triggering threshold, which is used in combination with a diode discriminator [12]. The absolute value of the triggering threshold may vary from 5 to 600-700 mV. The pulse which is picked up from the common emitter-resistor is ~ 1.6 V and it arrives to the coincidence circuit. The coincidence circuit is assembled on semiconductor D2D diodes and has the following parameters: a selection coefficient > 7, a resolution time $\tau \sim 1$ μsec. The discriminator at the output of the coincidence circuit is analogous to the one described above, and the amplitude of the output signal, which is ~ 1.5 V makes it possible to record using standard counting installations. /235

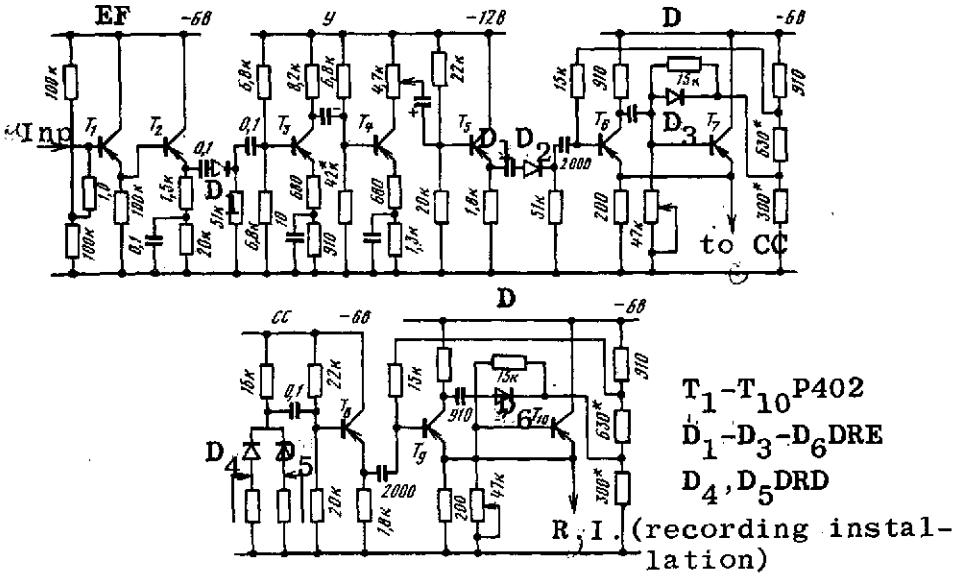

Fig. 6. Basic electronic circuit of telescope channel

REFERENCES

1. Quinn, R. G., Nature, 208, 5008 (1965).

2. Osborne, F. J., Bachynsky, M. P. and Gorne, J. V., Appl. Phys. Letters, 5, 77 (1964).

3. Danielson, L. and Lindberg, L., Phys. Fluids, 7, 1878 (1964).

4. Malforms, K. C., Arkiv mat. astron. och. fys., A32, (8) (1965).

5. Hones, E. W., J. Geophys. Res., 68, 1209 (1963).

6. Ovechkin, Yu., Rekomendatsii po primeneniyu poluprovodinkovykh priborov, [Recommendations for the Use of Semiconductor Instruments], Moscow, 1966.

7. McCracken, K. G., Rao, U. R., Fowler, B. C., Shea, M. A., and Smart, D. F., IQSY Instruction Manual, No. 10, 1965.

8. Baker, P., Chasson, R. L., and Kisselbach, V. J., Nature, 211, 354 (1966).

9. Egorov, G. A., et al., Izv Akad Nauk SSSR, Seriya Fiz., 31, 1789 (1965).

10. Starodubtsev, S. B. and Romanov, A. M., Proiskhozhdenie zaryazhennykh chastits cherez veshchestvo, "Passage of Charged Particles Through a Substance], Tashkent, Izd-vo Adak Nauk Uzb. SSR, [Publ. of the Uzbek Acad. of Sci.], 1963.

11. Radkevich, I. A., Prib Tekh Eksp, No. 3, 95 (1963).

12. Soshnin, L. D., Prib Tekh Eksp, No. 4, 138 (1960).

N75 16496

DETERMINATION OF COUPLING COEFFICIENTS AT VARIOUS ZENITH ANGLES ON THE BASIS OF THE COSMIC RAY AZIMUTH EFFECT

S. A. Bel'skiy, B. A. Dmitriev, A. M. Romanov

ABSTRACT

The value of EW asymmetry and coupling coefficients at different zenith angles were measured by means of a double coincidence crossed telescope which gives an opportunity to measure simultaneously the intensity of the cosmic ray hard component at zenith angles from 0 to 84° in opposite azimuths. The advantages of determining the coupling coefficients by the cosmic ray azimuth effect as compared to their measurement by the latitudinal effect are discussed.

At the present time, a great deal of attention is given to the study of the anisotropy of cosmic radiation. Since cosmic rays from the sources of the anisotropy arrive at the observation point at different zenith angles and azimuths, it is important to know the coupling coefficients between the primary and secondary radiation in these directions. This article gives the preliminary results of measurements of the coupling coefficients at different zenith angles by the azimuth cosmic ray effect. The measurements were carried out at sea level at geomagnetic latitude $\lambda = 57^{\circ}$ with a perfected device [1], representing a crossed double coincidence telescope, which can be used to measure simultaneously the intensity of the hard component of cosmic rays at eight zenith angles between 0 to 84° in opposite azimuths.

The measurement of the coupling coefficients at the given point using this method is free of many disadvantages inherent in the method in which the coupling coefficients are determined by the latitudinal effect. First, it is not necessary to introduce corrections for the meteorological effects, since the differences in the counts of crossed telescopes with different azimuths and the same zenith angles are used. Second, certain errors due to the possible unstable operation of the apparatus are eliminated automatically. Third, the results of the measurement depend little on the change in the total level of the cosmic radiation. Finally, when the recording point is selected appropriately, the azimuthal effect at large zenith angles can exceed the magnitude of the effect which occurs during the change of the geomagnetic latitude.

The recording part of the device that was used for the hard component of the cosmic rays is shown schematically in Fig. 1. The electronic circuit of the device is described in [1]. The telescope used counters of the SI-5G types. The azimuth was changed by rotating the platform on which the device was mounted. In addition to this, the telescope could turn 180° in the vertical plane (see supplements No. 1 and No. 2 in Fig. 1) which made it possible to vary the thickness of the absorber (lead) from 93 to 186 $g \cdot cm^{-2}$. The energy threshold of the recorded protons was varied from 170 to 280 MeV, and for muons from 107 to 180 MeV.

Figure 2 shows the zenith angular relation for an absorber which is 93 $g \cdot cm^{-2}$ thick (solid curve) and 186 $g \cdot cm^{-2}$ thick (dashed curve) when the installation is oriented east-west.

The increase in the intensity of the cosmic rays at large zenith angles as the thickness of the absorber increases is apparently related to the second transient minimum [2].

The amplitude of the east-west asymmetry was calculated from the formula /237

$$A = \frac{2(N_W - N_E)}{N_N + N_E},$$

where N_E and N_W are the intensities of the cosmic rays arriving from the eastern and western direction at the given zenith angle. The amplitude of the east-west asymmetry increases as the zenith angle increases (Fig. 3). However, at the zenith angle $\xi = 84°$ for an 186 $g \cdot cm^{-2}$ absorber it already begins to drop. The table gives the values of the coupling coefficients which were calculated from the relation

$$W_\xi^3(\Delta\varepsilon) = -\frac{\Delta N_\xi(\Delta\varepsilon)}{N_\xi^3(\Delta\varepsilon)\,\Delta\varepsilon},$$

where $\Delta N_\xi = N_\xi^W - N_\xi^E$, and $\Delta\varepsilon = \varepsilon_\xi^W - \varepsilon_\xi^E$. The minimum values of ε_ξ^E and ε_ξ^W at which the primary particles can arrive at the boundary of the atmosphere from the eastern and western directions were calculated for $\lambda = 57°$ taking into account the Earth's

shadow cone [3, 4]. The table also gives the values of the integral multiplicities that were calculated using the values of the coupling coefficients obtained from relation [5]

$$m_\xi(\Delta\varepsilon) = \frac{W_\xi^3(\Delta\varepsilon)\, N_\xi^3(\Delta\varepsilon)}{D(\varepsilon)},$$

where D(ε) is the differential spectrum of the primary cosmic radiation taken from [5]. The data that were obtained show that the method which determines the coupling coefficients by the azimuthal effect is promising.

ϑ, deg	ε_ξ^0, BeV	ε_ξ^3, BeV	W_ξ^3, % BeV			$m_\xi \cdot 10^{-3}$
			93 g·cm^{-2}	186 g·cm^{-2}	93 g·cm^{-2}	186 g·cm^{-2}
36	1,62	0,625	3,8±0,2	2,9±0,2	0,79±0,05	0,56±0,05
48	3,65	0,613	1,8±0,1	1,3±0,1	1,64±0,09	1,2±0,1
60	8,37	0,603	0,97±0,05	0,86±0,05	3,4±0,2	3,3±0,2
72	22,0	0,598	0,40±0,03	0,40±0,03	7,5±0,6	7,9±0,4
84	46,6	0,595	0,22±0,02	0,15±0,02	9±1	7±1

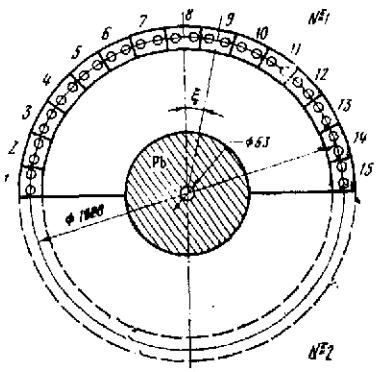

Fig. 1. Instrument diagram

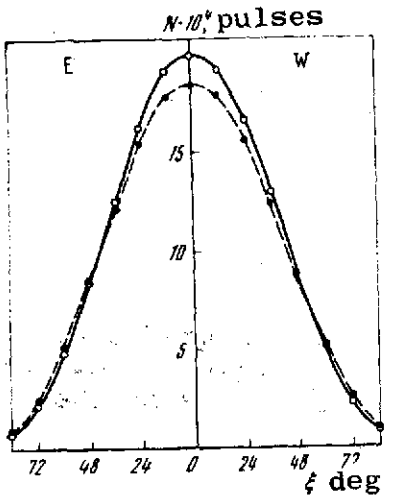

Fig. 2. Zenith angular dependence of the hard cosmic ray component

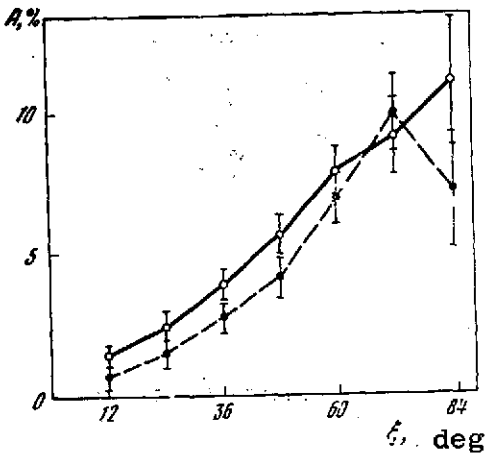

Fig. 3. Amplitude of east-west asymmetry vs. zenith angle for hard cosmic ray component

More complete information can be obtained during measurements at medium and low latitudes for several orientation values of the telescope by azimuth. This would make it possible to obtain the relation for the coupling coefficients at different zenith angles for various energies. /238

REFERENCES

1. Bel'skiy, S. A. and Romanov, A. M., Izv Akad Nauk SSSR, Seriya Fiz., 29 (9), 1672 (1965).

2. Hauser, Von I., Ann. Phys., 5, 327 (1960).

3. Alpher, Br. R. A., J. Geophys. Res., 65, 137 (1950).

4. Schremp, E. T., Phys. Rev., 54, 158 (1938).

5. Dorman, L. I., Variatsii kosmicheskikh luchey, [Cosmic Ray Variations], Gostekhizdat Publs., 1957.

N75 16497

MEASUREMENT OF SUPERSMALL QUANTITIES OF Ar^{37} AND H^3

G. E. Kocharov, V. O. Naydenov

ABSTRACT

The results of measurements made on supersmall quantities of Ar^{37} and H^3 by a low-background installation based on miniature proportional counters are presented (ø 1, 3, 4 mm). The article considers the sensitivity limit for the recording of Ar^{37} and H^3.

We already reported [1 - 4] the development of a low-background installation based on a miniature proportional counter used for the recording of supersmall quantities of Ar^{37} and H^3.

For definiteness we will assume that the duration of a single experiment is 70 days, i.e., the background is measured for 35 days and the effect, together with the background is measured for 35 days.[1] Figures 1 and 2 show the minimal amounts of Ar^{37} and H^3 amenable to measurement versus the width of the energy window. These relations were constructed from the experimental values of the counting rate of the background pulses for various operating regimes of a low background installation, taking into account the recording efficiency (η). Figure 1 also gives the relations for a detector with zero background assuming a 30% statistical accuracy and the data of Davis [5, 6]. From the figure it can be seen that the optimal width of the window is ~ 1 keV. The limiting counting sensitivity for the counter under consideration when the measurement time is 70 days is ~ 40 Ar^{37} atoms.

Since the energy spectrum of tritium is asymmetric, the recording sensitivity depends both on the width of the window and on the selected lower discrimination threshold. It can be seen that the limiting sensitivity for the sample of the 4-mm diameter counter under consideration is $\sim 4.10^4$ atoms. A reduction of the dimensions of the counter which lead to a

1. The half-life of Ar^{37} is 35 days; therefore, a duration of the experiment which is 70 days is nearly optimal. For tritium (half-life 12.4 years) we must speak about a sensible experiment time. In this article, we took, for convenience, the same time as for Ar^{37}.

reduced background, increases the role of the so-called wall effect, and changes the characteristics (resolution, stability, etc.) of the counter. As the investigations that we carried out have shown, the aforementioned effects are not a hindrance to miniaturization up to a diameter of 3 (for tritium) and 1 mm (for Ar^{37}).

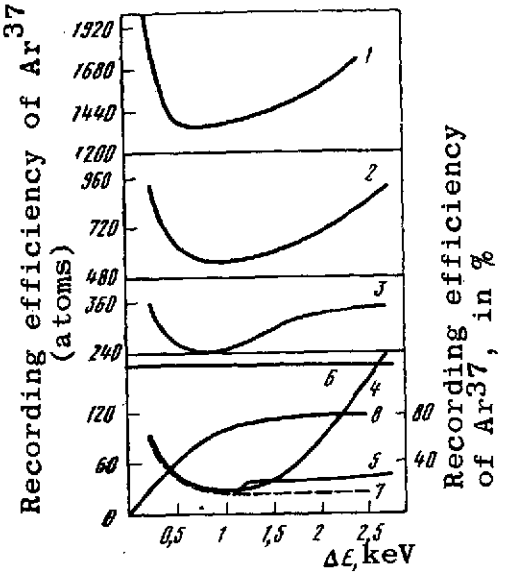

Fig. 1. Recording sensitivity of Ar^{37} in a counter whose diameter is 4 mm and whose length is 54 mm vs. the width of the energy window for various types of protection

1--without protection; 2--iron screen; 3--iron screen and anticoincidences; 4--iron and mercury screen together with anticoincidences; 5--Davis counters [5] ø 3 mm, l = 12 mm; 6--David Geiger counter [6]; 7--ideal counter with zero background; 8--recording efficiency of Ar^{37}.

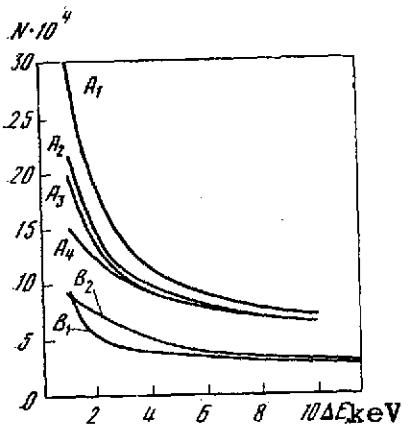

Fig. 2. Recording sensitivity of tritium (atoms) vs. the width of the energy window ($\Delta E = E_b - E_L$) and lower discrimination threshold (E_L) for counters with ø 5 and 4 mm in protection regime "iron and mercury screen together with anticoincidences

A--counter ø 5 mm; 1-4--E_L = 1.5, 2.5, 3.4, 4.5 keV, respectively; B--counter ø 4 mm; 1-2--E_L = 1.5, 3.5 keV, respectively.

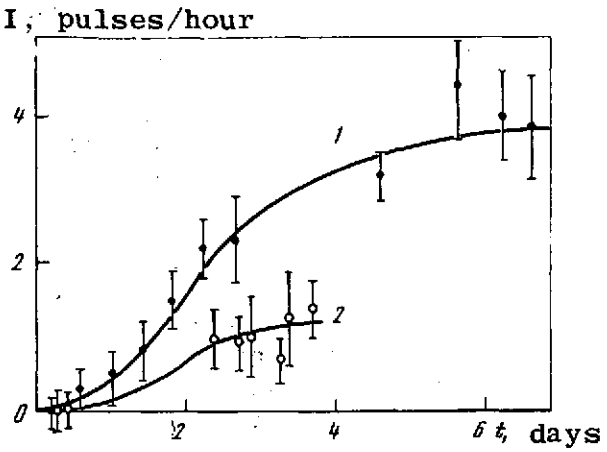

Fig. 3. Memory effect for Ar^{37} in the remaining counter ø 3 mm and l = 12 mm

When supersmall amounts of radioactive gases are measured, special attention must be given to the so-called memory effect. This effect consists of the following: when the counter is filled with the working gas together with the radioactive substance investigated, a part of the latter can be incorporated in the walls and ends of the counter. As a result, during other measurements, a part of the substance that was incorporated can again enter the working gas, distorting the results of the measurements. The memory effect of tritium is well-known; it is mainly determined by the presence of a film of water and other compounds containing water on the internal surface of the counter. An effective way of combatting this effect is repeated pumping with subsequent flushing of the interior with hydrogen. For one steel counter, the memory effect was 0.3% in 4 days after the tritium was removed from the counter. The counter was first pumped for 3 hours, and then it contained the working gas (90% Ar + 10% CH_4) for 16 hours and then it was pumped again for 5 hours. /240

The absence of data about the memory effect for argon (inertial gas) and the necessity to measure supersmall amounts of Ar^{37} led to the necessity to study in detail the phenomenon that was mentioned. We will consider briefly the results that we obtained. After a single pumping of the counter containing $5 \cdot 10^6$ Ar^{37} atoms and filling it with the inertial working mixture, we observed an increase in the counting rate of the background pulses with time (Fig. 3, curve 1). Since the true background of this counter had been measured by us earlier for a long time, it was easy to determine the rate at which the Ar^{37} was released into the working volume. It turned out that it was 25 atoms per hour in the first 39 hours and 100 atoms in

1 hour in the next 30 hours. After 5 days, the counting rate reached the plateau. After this, the counter was pumped and filled with the working gas. The memory effect was observed again, but this time in a smaller amount (Fig. 3, curve 2). The background level for the given counter returned to the true level after the counter was pumped many times and flushed with the working gas. It is rather difficult to explain the substantial memory effect for Ar^{37}.

In conclusion, we give the values of the smallest amounts of Ar^{37} and tritium that we measured. In a ø 5 mm and l = 54 mm counter, the absolute count per hour was $3 \cdot 10^{-5}$ tritium atoms, in a ø 3 mm and l = 12 mm counter, it was 370 Ar^{37} atoms in 110 hours.

REFERENCES

1. Kocharov, G. E. and Naydenov, V. O., Dokl na Vses konf po yadernoy spektroskopii, [Reports Read at the All-Union Conference on Nuclear Spectroscopy], February 1964.

2. Kocharov, G. E., Dokl na Vses konf po kosmicheskim lucham, [Reports Read at All-Union Conference on Cosmic Rays], Apatity, 1964.

3. Viktorov, S. V., Kocharov, G. E. and Naydenov, V. O., Zh Exp Teor Fiz, 36, 199 (1966).

4. Kocharov, G. E. and Naydenov, V. O., Prib Tekh Eksp, No. 3, 5 (1966).

5. Davis, R., Phys. Rev. Letters, 12, 303 (1964).

6. Davis, R., Radiat. Sci. Res. 1, London, Pergamon Press, 1958, p. 728.

N75 16498

PLASTIC SCINTILLATION COUNTERS WITH AN AREA OF 2 m^2

T. A. Yegorov, N. N. Yefimov, D. D. Krasil'nikov, I. Ye. Sleptsov

ABSTRACT

Two designs of plastic scintillation counters with an area of 2 m^2 scanned in each case by a single photomultiplier of the FEU-49 type are described.

The radial dependence of their light collection at the place of the path of the detected particle does not exceed 10% while the half-width of the differential distribution of the pulse amplitudes from nonfiltered cosmic radiation at sea level is 90-95%, and 65%, the plastic thickness being 5 cm and 10 cm, respectively. The temperature coefficient of the counter is 0.32% per 1°C.

Recently, as has been shown many times [1 - 3], the need arose to design scintillation counters of large dimensions. Such counters are needed for the observation of cosmic rays in neutrino physics, gamma-ray astronomy, in all cases when we are forced to use large effective areas of the detectors to increase the light intensity of the observation installation. The use of counters of large dimensions, controlled by a single photomultiplier, while decreasing the number of radioelectronic elements can increase the reliability and facility of the experiment, and reduce considerably the cost of such detectors. /241

But an increase in the area of the scintillators is related to a general decrease in the light collected, and the formation of a radial dependence of the light collected on the place where the detected particle arrives, if special measures are not taken [3]. Among these, radial dependence is the least acceptable, since it can worsen considerably the resolving power of the scintillation counter as a counter of the number of detected particles.

The radial dependence can be reduced by a sophisticated selection of the geometry of the reflector, by selecting the proper light-reflecting coating, and by the mutual position of the photoelectron multiplier and the plastic scintillators in the counter. In this study, all three methods are used.

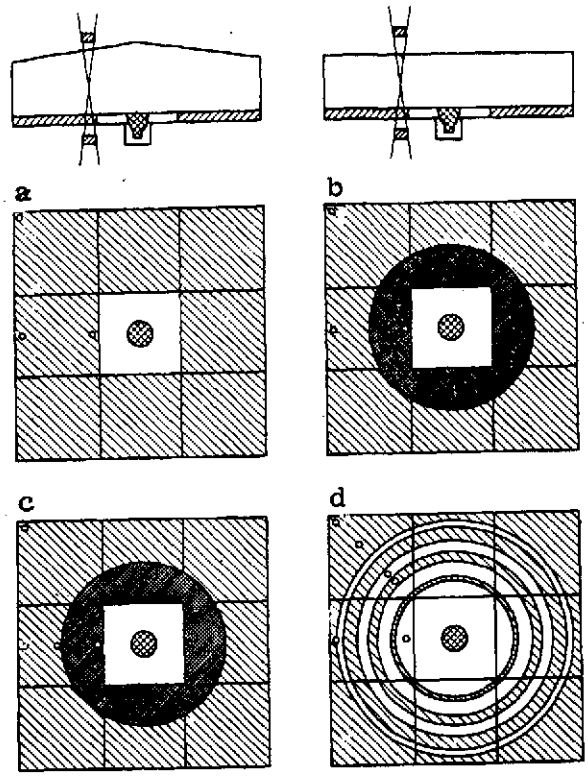

Fig. 1. Two designs of scintillation counters with different light-reflecting coatings

The circles denote sectors where the amplitudes were measured on the photomultiplier anode during the passage of single vertical particles

The radial dependence was picked up for each scintillation counter (Figs. 1 and 2) which included eight blocks of plastic scintillators (PS) each of which (50 x 50 x 5 cm) was made from polystyrene with a scintillating additive (p-terphenyl, ~ 1% and POPOP ~ 0.05%). All blocks are scanned by one FEU-49B photomultiplier. The ratio of the area of the cathode of the photoelectron multiplier to the area of the light-reflecting surface is $\sigma_{FEU}/\sigma_{ref} \simeq 3.3 \cdot 10^{-3}$.

The walls of the reflector have a diffuse-reflective coating with a reflectance coefficient ~ 0.80 - 0.90. In addition to this, light-reflecting coatings with various reflectance coefficients were used in the counter proposed, which is important for reducing the inhomogeneity in the light collected in the counter. /242

Figure 1 shows two types of reflectors and several types of light-reflecting coatings: for a reflector with the upper part in the form of a pyramid two types of coatings (a and b), and for a reflector with a flat top part, two types of coatings (c and d). The latter is more easily manufactured. The circles

show the sectors of the counters which were investigated, in which the amplitudes on the photomultiplier anode which corresponded to the pulses formed during the passage of one vertical particle within an angle of ~ 0.1 ster through a particular sector of the counter were measured. The measurements were carried out when the voltage on the photocathode was ~ 1600 V. In cases a and c, the five edges of the scintillators were painted with white enamel, i.e., one transparent surface was left for the photon yield. In cases b and d, all edges of the scintillators are transparent. In cases b and d, in the blocks of the scintillating plastics in the central part, the reflecting coatings have a very low reflectance coefficient (~ 0.08), in case d the light reflecting coating is applied on top of the scintillator blocks in the form of concentric circles which narrow at the edge of the counter. The white screens are applied to lengthen the optical paths for the light radiation from the central sectors of the counters. Case a is shown without additional attenuating coatings.

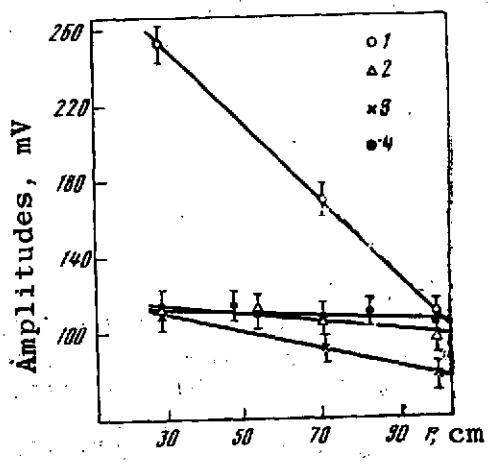

Fig. 2. Distribution of most probable amplitudes of the photomultiplier anode during the passage of single vertical particles at different distances from the center of the counter

1-4--corresponding counter variants; a-g--shown in Fig. 1

The counter was calibrated by the vertical μ-mesons and the equilibrium electron component of the cosmic radiation. To isolate the vertical particles, a telescope was used, which was mounted on fast counters, on the FEU-52 photomultiplier with a purple glass whose dimensions were 8 x 8 x 5 cm. The multichannel AI-100 amplitude pulse analyzer was used as the recording device. When the peaks of the probable amplitudes of the pulse from the photomultiplier were determined, the V. Zimmerman linearization method was used [4].

The radial dependence is shown in Figure 2. Here it can be seen that the use of the reflector structures proposed and even of coarse gradations in the light-reflecting coatings, makes it possible to obtain satisfactory light collection from such a

large dector area when the design of the counter is not complex. The light collection is evened out in various sectors of the counter on the basis of the worst sector of the counter. The radial dependence obtained for the counter variants that were studied was, respectively, for cases a, b and c, 56, 14 and 30% when the half-width of the differential distributions was 115, 95, 98% of the total cosmic radiation component. In case d, the radial dependence does practically not exist, and the half-width of the distribution is 90% for a plate thickness of 5 cm and 65% for 10 cm.

The temperature dependence of various photomultipliers and of the purple glass usually differs considerably. When the amplitude of the pulses from the photomultiplier, as a rule, only decreases as the temperature drops, the luminescence yield from the purple glass is different for different purple glasses. Thus, for certain types of purple glass, the luminescence yield varies little in a wide range of temperatures. For other types of purple glass, the temperature dependence is stronger and it is sometimes characterized by a change of sign. The temperature quenching [5] depends on the concentration of the admixtures and decreases as the concentration increases. It was found that the temperature effect of the purple glass manufactured in the Kharkov reactive chemical plant has opposite sign than the temperature effect of the photomultiplier and that is compensates the latter to a considerable extent. /243

The temperature dependence was read for two selected combinations: 1) only one FEU-49 photomultiplier was subjected to temperature fluctuations and 2) the FEU-49 photomultiplier together with the plastic scintillator were tested in the temperature range from -24 to +28°C. The AI-100 thermostat chamber was used in the study, and to study the photomultiplier, a TKh-3B support light source was used. During all measurements, a complete collection of the charge in the output circuits of the photomultiplier was ensured. The results show that as the temperature drops, the amplitude at the output of the photomultiplier decreases, and the light yield from the plastic scintillator increases which leads to a decrease in the temperature dependence of the entire counter. The temperature coefficients are, respectively:

$$\beta_{PM} = 1.8\%/^{\circ}C \text{ and } \beta_{PM + PG} = 0.32\%^{\circ}C.$$

REFERENCES

1. Abrosimov, A. T. and Blokh, Ya. L., in the collection Kosmicheskie luchi, No. 7, 240 (1965).

2. Yudin, E. P., Dovzhenko, O. I. and Denisov, E. V., Prib Tekh Eksp, No. 4, 77-82 (1965).

3. Egorov, T. A., Efimov, N. N. and Krasil'nikov, D. D., Izv Akad Nauk SSSR, Seriya Fiz., 29 (9), 1788 (1965).

4. Zimmermann, W., Rev. Scient. Instrum., 32 (9), 77 (1961).

5. Rozman, I. M. and Kilin, S. F., Uspekhi Fiz Nauk, 19 (3), 466 (1955).

N75 16499

THEORY OF FLUCTUATIONS OF EXTENDED AIR SHOWERS

L. G. Dedenko

ABSTRACT

The Monte Carlo method was used to calculate the probability distribution functions of shower characteristics for primary protons at sea level. The calculation was based on the following model of the elementary event: the interaction paths are 90 g/cm^2 for nucleons and 120 g/cm^2 for pions. The nonelasticity coefficient for nucleons is uniformly distributed between 0.1 and 0.9, and for pions it is equal to 1. Isobaric pions are taken into account. The spectra of secondary particles were determined using Cocconi's approximation formula. The calculation for the nuclei was carried out on the assumption of a breakup of the nucleus into component nucleons. The mean number of particles and the variances of the distributions for electrons when the number of muons was fixed, and for muons when the number of electrons was fixed, were calculated. A comparison with the experiment was made. The best agreement is obtained for the primary composition, which is the same as that at low energies.

At the present time good experimental data are available about the muon component of wide showers for a fixed number of electrons on the observation level, and on the electron component for a fixed number of muons [1]. It is of interest to compare these data with the quantities that were calculated according to some model of the elementary event. The degree of agreement with the experiment can be used as an index of how well the model was selected.

Let

$$f(N_e; N_\mu; A; E; x) - \quad (1)$$

be the probability distribution of the number of electrons N_e and muons N_μ in the shower at the observation level x from a primary particle with energy E and atomic number A. Let

/244

$$B_A e^{-\gamma A^y} - \quad (2)$$

be the energy spectrum of such particles, where B_A is the proportion of nuclei with atomic weight A in the primary cosmic radiation, γ_A is the exponent of the energy spectrum and $y = \ln (E/1\ \text{BeV})$. Then the distribution function of the number of electrons for the primary nucleus with atomic weight A when the number of electrons is fixed can be written in the following form:

$$\varphi(N_e/N_\mu;\ A) = F_A \int e^{-\gamma_A y} f(N_e;\ N_\mu;\ A;\ y)\, dy. \tag{3}$$

where F_A is a normalizing constant. For a complex composition of the primary radiation, the distribution function for the number of electrons can be determined as follows:

$$\varphi(N_e/N_\mu) = \sum_A B_A \varphi(N_e/N_\mu;\ A)/F_A. \tag{4}$$

where the summation must be carried out over all nuclei in the primary radiation. The distribution function for the number of muons when the number of electrons is fixed is determined analogously. We calculated the function $f(N_e;N_\mu;A = 1;E;x)$ by the Monte Carlo method on an electronic computer on the basis of the model of the elementary event which we described earlier [2]. The coefficients of skewness and excess for this distribution function usually did not exceed 1. Therefore, in first approximation, it can be assumed that the electrons and muons in the shower are normally distributed

$$f(N_e;\ N_\mu;\ A = 1;\ E) = \frac{\exp\left\{-\frac{1}{2(1-r^2)}\left[\left(\frac{N_e - \bar{N}_e}{\sigma_e}\right)^2 + \frac{2r(N_e - \bar{N}_e)(N_\mu - \bar{N}_\mu)}{\sigma_e \sigma_\mu} + \left(\frac{N_\mu - \bar{N}_\mu}{\sigma_\mu}\right)^2\right]\right\}}{2\pi\sigma_e\sigma_\mu\sqrt{1-r^2}}, \tag{5}$$

where r is the correlation coefficient, σ_e, σ_μ, $\bar{N}_e$, $\bar{N}_\mu$ are the standard deviations and means, respectively, for the number of electrons and muons.

If we use the hypothesis about the break-up of the nucleus into A component nucleons, the distribution function for the nucleus can be determined using the central limit theorem from probability theory as we did earlier [3]. The diagram shows the results of the calculations for the mean number of electrons and muons in the shower for a fixed number of muons and electrons, respectively. The set of curves 1 was calculated for the pure primary proton composition, the set 2 for a complex composition when the relative proportion of B_A nuclei is the same as that at low energies:

A	1	4	14	31	51
B_A	0,31	0,22	0,12	0,21	0,14

the set 3 for the case when in the primary radiation there are only nuclei with atomic weight A-31. The curve at the top reflects in each case the dependence of the mean number of muons on the fixed number of electrons, and the bottom curve the dependence of the mean number of electrons on the fixed number of muons. In case 3, both curves merge into a single line. The circles indicate the experimental data from study [1]. It can be seen from the figure that best agreement with the experiment was obtained for the complex composition of primary radiation. The pure proton composition can be made to agree with the experiment provided the model of the elementary event is modified. Another argument can also be raised against a primary composition consisting only of nuclei with atomic weight A-31. The standard deviation ratios of the distribution function (4) which were determined experimentally are in the interval 0.7 - 0.5, in the range for the number of electrons and muons under consideration, and for curve 3, in the interval 0.2 - 0.1. The standard deviation ratios for the case of a complex composition of the primary radiation agree well with the experiment, and, for the pure proton composition, not quite as well. The ultimate explanation of the nature of the primary particles and the model of the elementary event require additional information about the absolute intensity of showers with the given number of electrons and muons as well as information about wide showers at other observation levels.

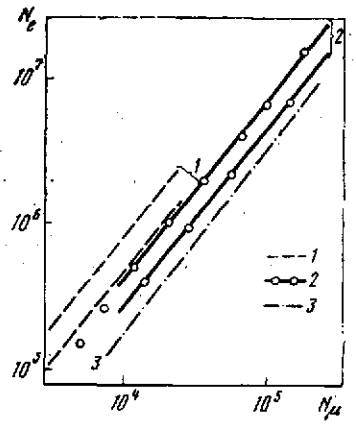

Fig. Mean number of electrons and muons vs. the fixed number of muons and electrons at the observation level.

1--for a pure proton primary composition; 2--for a complex composition; 3--for a composition consisting only of nuclei with atomic weight A = 31. Circles indicate experimental data from study [1]

REFERENCES

1. Abrosimov, A. T., Atrashkevich, V. B., Belyaeva, I. F., et al., Izv Akad Nauk SSSR, Seriya Fiz., 32 (3), 463 (1968).

2. Dedenko, L. G., Izv Akad Nauk SSSR, Seriya Fiz., 32, (3) (1968).

3. Dedenko, L. G., Zhur Eksp Teor Fiz, 46, 1859 (1964).

☆ U. S. GOVERNMENT PRINTING OFFICE: 1975—635-047 / 51